LOW MELTING POINT ALKALI METAL BOROHYDRIDE MIXTURES FOR HYDROGEN STORAGE

By

YINZHE LIU

A thesis submitted to the University of Birmingham for the degree of DOCTOR OF PHILOSOPHY

School of Metallurgy and Materials
College of Engineering and Physical Sciences
University of Birmingham
April 2018

SYNOPSIS

Metal borohydrides have been considered as most promising solid-state H_2 storage media, due to their relatively high volumetric hydrogen capacities and low hydrogen operating pressures, when compared with other storage methods. However, their high dehydrogenation temperatures and limited reversibility have so far prevented their use in commercial applications. Therefore, efforts to understand their hydrogen sorption mechanisms have become very important, as they may provide insights into how to: "tune" the composition and/or microstructure to attain more favourable reaction pathways; as well as lower the temperature and pressure conditions required for achieving hydrogen cycling stability.

This work investigated the structural and compositional changes during heating in several borohydrides ($LiBH_4$, $NaBH_4$, KBH_4) and their low-melting-point mixtures ($0.62LiBH_4$-$0.38NaBH_4$, $0.75LiBH_4$-$0.25KBH_4$) synthesised by ball milling. The crystal and vibrational structures of these compounds were characterized using lab-based X-ray diffraction (XRD) and Raman/Infrared (IR) spectroscopy. Their thermal stabilities and hydrogen sorption mechanisms were studied using Differential Scanning Calorimetry (DSC), Thermal Programmed Decomposition connected with Mass Spectrometer (TPD-MS), Pressure-Composition Isotherms apparatus (PCI), XRD and Raman/IR spectroscopy.

Reactions forming solid solutions or bimetallic borohydrides were observed in the as-milled low-melting-point borohydride mixtures. Under Ar, the $0.62LiBH_4$-$0.38NaBH_4$

mixture could release 10.8 wt.% of hydrogen at 650 °C, whilst the $0.75LiBH_4$-$0.25KBH_4$ led to 8.9 wt.% hydrogen evolution at 700 °C. The dehydrogenation peak temperatures for these alkali borohydrides mixtures were strongly affected by their metal cations and therefore located in the temperature range higher than $LiBH_4$. In addition, these mixtures had poor cycling stabilities under the conditions used for H_2 sorptions (500 °C, 1 bar H_2, 10 h for desorption, and 400 °C 130 bar H_2, 12 h for re-absorption). The reversible hydrogen contents were reduced dramatically by 80% starting from the 2nd cycle, maintaining 4-15% of the initial hydrogen capacity at the 3rd cycle.

The destabilization effects on dehydrogenation of $LiBH_4$, $0.62LiBH_4$-$0.38NaBH_4$, $0.75LiBH_4$-$0.25KBH_4$ were demonstrated for two selected additives: micron-sized SiO_2, and nano-sized Ni. These additives did not change the low melting points; rather, they resulted in lower dehydrogenation temperatures via the formation of more stable compounds (such as Li_2SiO_3 and Li_4SiO_4 from SiO_2, and Ni_4B_3 from Ni). However, they often decreased the hydrogen evolution and facilitated the formation of metal dodecaborates. Moreover, the addition of nano-sized Ni did not significantly improve the cycling stability under the experimental conditions used, but it led to partially reversible $LiBH_4$.

Therefore, it was concluded that before practical use of a low-melting-point alkali metal borohydride mixture is possible, there is a need for: further compositional optimization with respect to the rehydrogenation conditions, in parallel with the use of nano-confinement of the mixture via an infiltration approach.

ACKNOWLEDGEMENTS

First of all, I would like to express my sincere appreciation to the School of Metallurgy and Materials in the University of Birmingham and funding from the People Programme – Marie Curie Actions of the European Union Seventh Framework Programme FP7/2007-2013/ (under REA grant agreement° 607040 - Marie Curie ITN ECOSTORE), to provide me with a platform and financial support for my PhD research.

I would like to thank specially Prof. David Book, as my PhD supervisor, for his constant encouragement and instructive guidance, and Prof. Marcello Baricco and Prof. Bjørn Hauback for accepting my secondment plan at their institution for completing very exciting experiments.

I owe a great deal of thanks to all the ECOSTORE members and the people I met during secondments in the University of Turin (Italy) and the Institute for Energy Technology (Norway) for their kind help during my PhD studies. In particular, a special thank you to Dr. Anna Wołczyk, Dr. Michael Heere and Mrs. Erika Michela Dematteis for their continuous assistance and advices.

I shall also extend my sincere gratefulness to the members of the Hydrogenation Materials Group, both past and present, Dr. Daniel Reed, Dr Shahrouz Nayebossadri, Mr. Simon Cannon, Dr. Sheng Guo, Dr. Luke Hughes, Dr. Lydia Pickering, Dr. Joshua Edwin Vines, Mr. Christos Paterakis, Dr. Luis Contreras Vasquez, Mr. Cao Yuan, Mrs. Carmel Greenwood, Mr. Sheng Sun, Mr. He Niu for all their kindness help and guidance.

The last but not the least, I would like to show appreciation to my parents and my best buddy Dr. Chen Jia for their love, encouragement and support.

TABLE OF CONTENTS

LIST OF ILLUSTRATIONS

LIST OF TABLES

LIST OF ABBREVIATIONS

AC	Activated Carbon
AFC	Alkaline Fuel Cell
BET	Brunauer–Emmett–Teller
CALPHAD	CALculation of PHAse Diagrams
Cap.	Capacity
CCD	Charge-Coupled Device
CMK-3	Ordered Mesoporous Carbon No.3
CNCs	Carbon Nanocages
COFs	Covalent-Organic frameworks
Com.	Combination bands
DC	Direct Current
DFT	Density Functional Theory
DME	DiMethyl Ether
DMFC	Direct Methanol Fuel Cell
DOE	U.S. Department of Energy
DSC	Differential Scanning Calorimetry
EDS	Energy-dispersive x-ray Spectroscopy
EELS	Electron Energy Loss Spectroscopy
FCC	Face-Centred Cubic
FTIR	Fourier Transformation Infrared Spectroscopy
Hex./HEX	Hexagonal
HKUST-1	Hong Kong University of Science and Technology No.1
HP-DSC	High Pressure DSC
HSAG	High Surface Area Graphite
HSC	Enthalpy-Entropy-Capacity
IFE	Institute for Energy Technology
IMS	Industrial Methylated Spirit
IR	Infrared
LiCa	$0.68LiBH_4$-$0.32Ca(BH_4)_2$
LiK	$0.75LiBH_4$-$0.25KBH_4$
LiK-Ni	$0.86(0.75LiBH_4$-$0.25KBH_4)$-0.14Ni
LiK-Si	$0.95(0.75LiBH_4$-$0.25KBH_4)$-$0.05SiO_2$
LiMg	$0.55LiBH_4$-$0.45Mg(BH_4)_2$
LiNa	$0.62LiBH_4$-$0.38NaBH_4$
LiNa-Ni	$0.91(0.62LiBH_4$-$0.38NaBH_4)$-0.09Ni
LiNa-Si	$0.95(0.62LiBH_4$-$0.38NaBH_4)$-$0.05SiO_2$
liq	liquid
M(BH4)n	Metal borohydrides
MCFC	Molten Carbonate Fuel Cell
MCM-41	Mobil Composition of Matter No.41

MHx	Metal Hydrides
MOFs	Metal-Organic Frameworks
Mono.	Monoclinic
MOx	MOFs
MS	Mass Spectrometry
NMR	Nuclear Magnetic Resonance
Ortho./ORT	Orthorhombic
P	Pressure
PAFC	Phosphoric Acid Fuel Cell
PCI	Pressure-Composition Isotherms
PEM	Proton Exchange Membrane
PEMFC	Proton Exchange Membrane Fuel Cell
PPN	Porous Polymer Networks
PROX	PReferential Oxidation
RF-CA	Resorcinol-Formaldehyde Carbon Aerogels
RF-CC	Resorcinol-Formaldehyde Carbon Cryogels
RGA	Residual Gas Analyser
RHCs	Reactive Hydride Composites
RT	Room Temperature
SBA-15	Santa Barbara Amorphous type material No.15
SEM	Scanning Electron Microscope
SGTE	Scientific Group Thermodata Europe
sh	shoulder
SOFC	Solid Oxide Fuel Cell
SS	Solid Solution
T or Temp.	Temperature
TEM	Transmission Electron Microscope
TG	TG
TGA	ThermoGravimetric Analysis
TGA-DSC	Thermogravimetry DSC
TPD	Thermal Programmed Decomposition
TPD-MS	Thermal Programmed Decomposition connected with Mass Spectrometer
VSM	Vibrating Sample Magnetometry
XRD	X-ray diffraction
ZZCO	Porous $ZnO/ZnCo_2O_4$
χ	electronegativity

CHAPTER 1 INTRODUCTION

1.1 Global Energy Overview

Demand for energy has continued to increase along with global social development and population growth since 1950, and is projected to peak in 2035 (Figure 1.1) (Ren et al. 2017). Fossil fuels, such as coal, oil and gas, have been widely used to meet this demand over the last century. However, these are non-renewable energy resources, which can cause both serious air pollution and climate change (Gilman et al. 2008). In addition, they are unevenly distributed all over the world and will inevitably be exhausted in the future. Governments are tackling the issue of energy security as well as solutions to the global climate change threat (Shafiee & Topal 2009; Mohr et al. 2015).

The Paris climate Agreement established on 12 December 2015 enters into force on 22 April 2016 (Uniteed Nations Framework Convention on Climate Change 2015). It aims to actively respond to the climate change threat by limiting global warming[1]. The UK government is committed to reduce at least 80 % of greenhouse gas emissions compared to its 1990 level by 2050, and at some points in the second half of this century (e.g. 2050s-70s) to net zero emission (Bell et al. 2016). This requires a change of economy and research direction towards low-carbon energy supplies.

[1] The Paris climate Agreement (2015) aims to limit the global warming to well below 2 °C above pre-industrial levels within this century, as well as by increasing the ability to adapt to the adverse impact of current climate change, fostering climate resilience and low greenhouse gas emissions development without threatening food production (Klein et al. 2017)

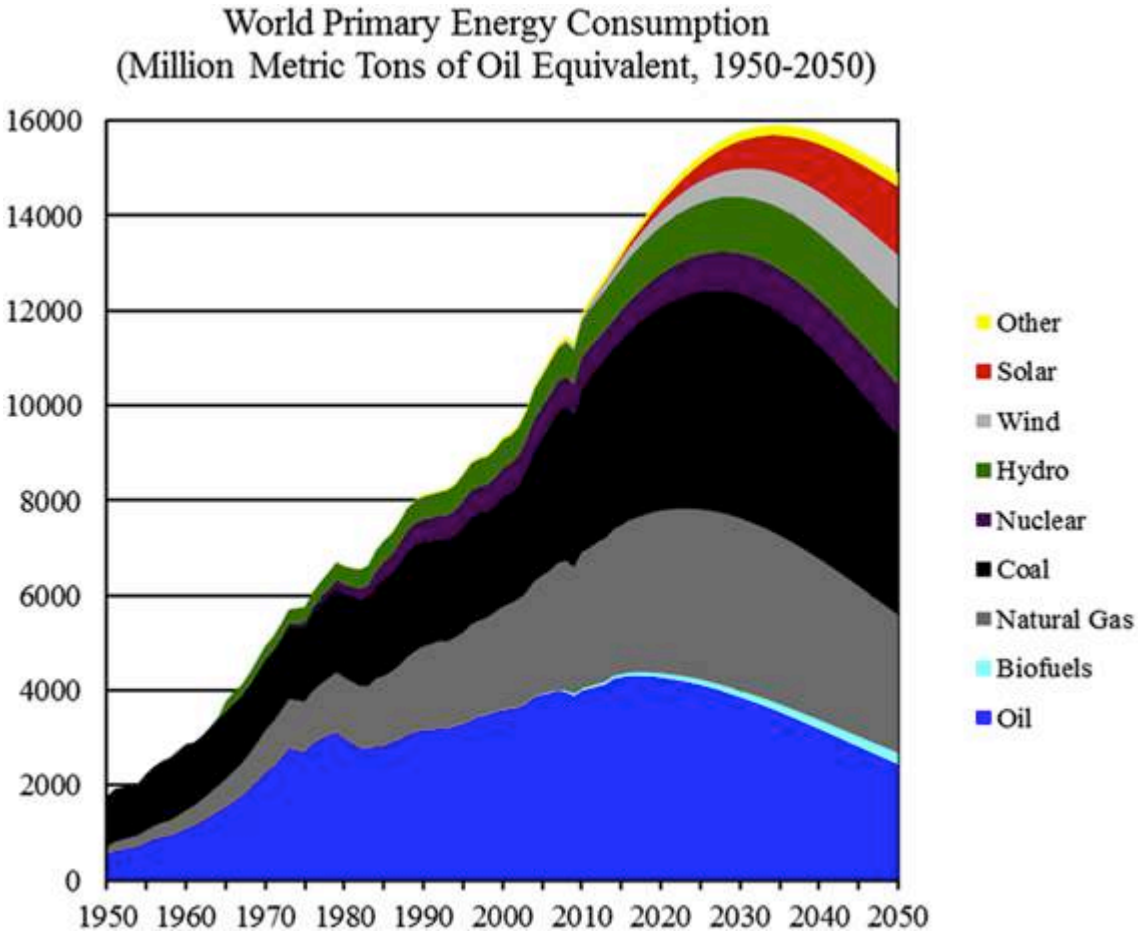

Figure 1.1 Illustration of world primary energy consumption (Ren et al. 2017).

Thus, sustainable development requires a search for alternative renewable and low-carbon (or carbon-free) energy resources and vectors. The well-accepted clean and renewable energy sources are solar, wind, water, geothermal, bioenergy and nuclear power, providing energy in terms of electricity generation, air and water heating/cooling (Hussain et al. 2017). These resources exist over wide geographical areas, in contrast to the traditional fossil fuels that are usually concentrated in a certain number of countries, although there are still some restrictions on effectively harvesting them. Alternatively, electricity generation from fuel cells using the chemical energy of hydrogen (or methanol or ethanol) provides a potential, clean and efficient approach to supply energy,

as well as to reduce carbon pollution and fossil fuel consumption (Boudghene Stambouli & Traversa 2002). In general, fuel cells are lightweight with excellent energy conversion efficiency compared to other conventional thermomechanical methods, and are feasible for a wide range of applications: transportation, portable/stationary power supplies (Mahato et al. 2015).

1.2 Fuel Cell and Hydrogen Infrastructure Technologies

1.2.1 Basics of Fuel Cell

The concept of a fuel cell is analogous to a conversion device, where the chemical energy stored in the fuel is converted to electricity through an electrochemical reaction rather than by combustion. Its basic principle was discovered in the 1840s (Andújar & Segura 2009), consisting of an electrolyte layer in contact with two electrodes (anode and cathode) on either side (Figure 1.2). The electrolyte is an electron insulator that only permits positive ions to transfer from the anode to the cathode (and negative ions from the cathode to the anode).

Depending on the choice of electrolyte and fuel, the fuel cell can be simply categorized into six major types (Kirubakaran et al. 2009), including:

1) Proton exchange membrane fuel cell (PEMFC);
2) Alkaline fuel cell (AFC);
3) Phosphoric acid fuel cell (PAFC);
4) Molten carbonate fuel cell (MCFC);
5) Solid oxide fuel cell (SOFC);
6) Direct methanol fuel cell (DMFC).

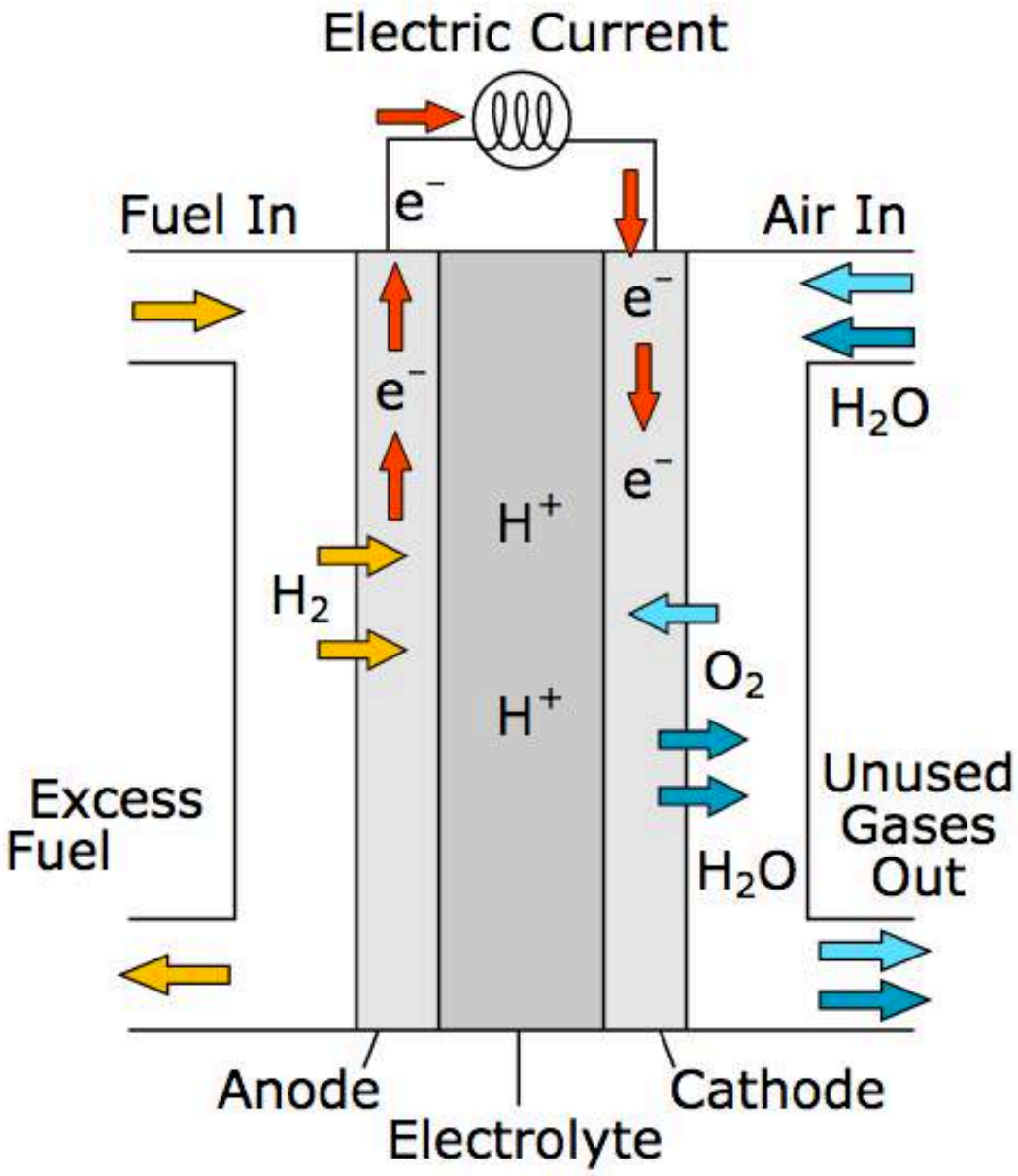

Figure 1.2 A schematic diagram of a H_2 PEM fuel cell during operation (Mattuci 2015).

H_2 has been proposed as a potential carbon-free vector due to its highest energy density among the known fuel materials on a weight basis (U.S. Department of Energy 2017b), and it is therefore the most commonly used fuel. In a H_2 PEM fuel cell (Figure 1.2), the H_2 is continuously fed to the anode electrode while the oxygen (from air) is constantly sent to the cathode terminal. At the anode, H_2 dissociates into two protons (H^+) and two

electrons (e^-). Each free electron moves through an external electrical circuit (producing electrical current) to the cathode side in order to recombine with oxygen (O_2) and protons, forming pure water (H_2O) (Peighambardoust et al. 2010). The chemical reactions at the electrodes and the overall reaction are as follows:

$$H_2 \xrightarrow{anode} 2H^+ + 2e^- \qquad \textbf{Equation 1.1}$$

$$O_2 + 4H^+ + 4e^- \xrightarrow{cathod} 2H_2O \qquad \textbf{Equation 1.2}$$

$$2H_2 + O_2 \xrightarrow{overall} 2\,H_2O \qquad \textbf{Equation 1.3}$$

In general, as a consequence of the low voltage of a single fuel cell (e.g. 0.6-0.8 V), a stack of cells is electrically connected in order to obtain a higher voltage feasible for practical use (Züttel et al. 2008). In addition, several key challenges have been addressed to the development of fuel cell technologies, such as cost and durability, the production & storage, and the delivery of hydrogen (particularly for on-board application) (U.S. Department of Energy 2017c).

At the state of the art, the fuel cells have been successfully applied for means of transport. Several H_2 fuel cell vehicles are commercially available, such as: Hyundai Tucson (since 2014), Toyota Mirai (since 2015) and Honda Clarity (since 2016) (Agarwal & Saxena 2014; Yoshida & Kojima 2015; Rosli et al. 2017). Apart from that, applications in motorcycle, boats, trains and aeroplanes have also been reported (O'Hayre et al. 2017).

1.2.2 Hydrogen Infrastructure

H_2 is the simplest element, containing a proton and an electron. It is rarely stored naturally on the earth; however, it can form a large variety of stable compounds such as water, oil and natural gas. In general, it can be produced through thermochemical, electrolytic or photolytic processes.

The core concept in the thermochemical approach is fuel processing (i.e. Reforming in Figure 1.3), where the conversion of hydrogen-containing materials (e.g. gasoline, ammonia or methanol) into a H_2 rich stream occurs (Holladay et al. 2009).

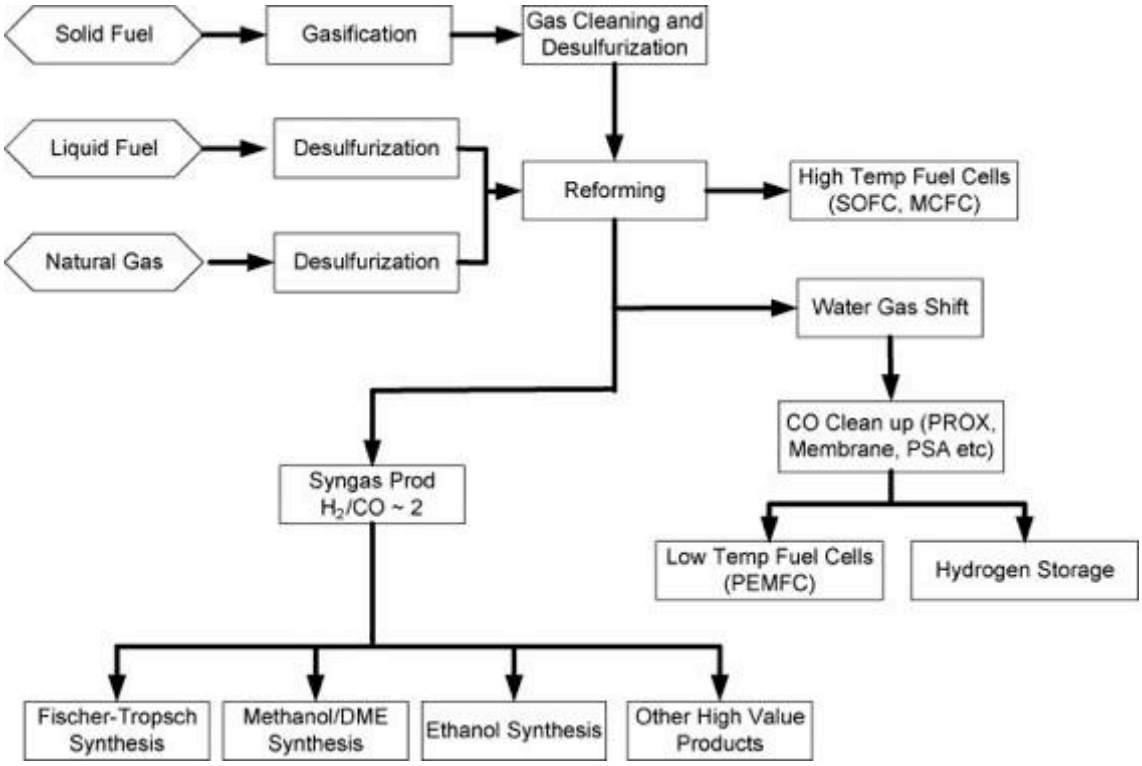

Figure 1.3 A schematic of thermochemical production of H_2 (Holladay et al. 2009)[1].

[1] **The PROX stands for PReferential Oxidation, and DME represents Dimethyl ether.**

The large-scale industrial H_2 production uses stream reformation of methane in the 700-1100 °C temperature range (Holladay et al. 2009), which follows:

$$CH_4 + H_2O \rightarrow CO + 3H_2 \quad \Delta H = 206 \text{ kJ mol}^{-1} \qquad \textbf{Equation 1.4}$$

$$CO + H_2O \rightarrow CO_2 + H_2 \quad \Delta H = -41 \text{ kJ mol}^{-1} \qquad \textbf{Equation 1.5}$$

In practice, the water-gas-shift reaction (Equation 1.5) is essential to adjust the H_2/CO ratio in order to produce more H_2. The by-products will be removed from the gas stream afterwards, leaving essentially pure H_2.

Alternatively, H_2 can be obtained from water electrolysis, where water is split into its constituents by electricity (Zeng & Zhang 2010). H_2 is harvested at the cathode during operation (Figure 1.4):

$$2H_2O \xrightarrow{electrolysis} 2H_2 + O_2 \qquad \textbf{Equation 1.6}$$

In practice, the reaction kinetics can be accelerated through using alkaline solution, solid-polymer electrolytes or selected catalyst (Ni et al. 2007). Moreover, the electrolysis approach is a near-zero greenhouse gas emissions process, especially when the electricity is from clean and renewable sources, such as photocatalytic water splitting (Ahmad et al. 2015).

After production, H_2 must be safely transported to the point of use, such as a dispenser at refuelling stations for vehicles or stationary power facilities. However, due to its low

specific and volumetric densities, the current solutions use compressed gas trucks, cryogenic liquid trucks or gas pipelines, depending on the demand and delivery distance (Yang & Ogden 2007). Reducing delivery cost, increasing energy efficiency, maintaining H_2 purity and minimizing H_2 leakage during transportation are the key challenges for the development of H_2 delivery infrastructures (U.S. Department of Energy 2017a).

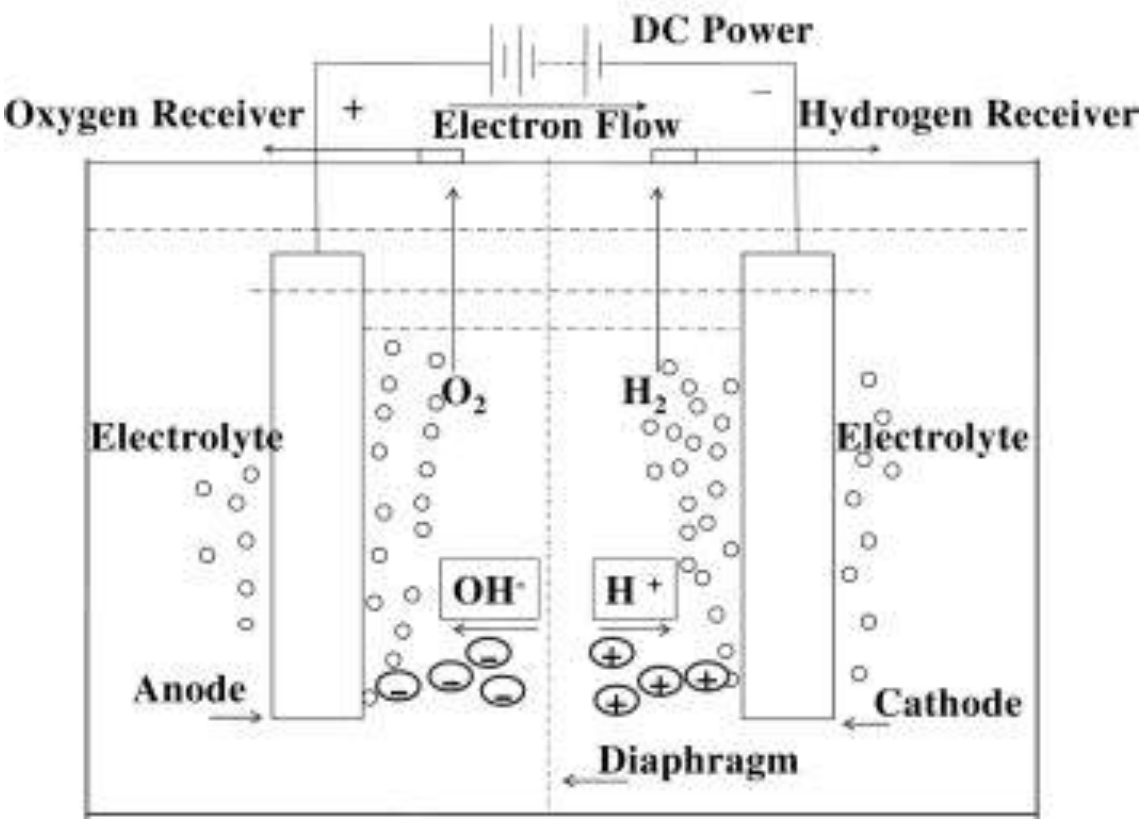

Figure 1.4 A schematic diagram of a basic water electrolysis system (Zeng & Zhang 2010)[1] .

Apart from the above, H_2 storage is one of the main bottlenecks for the widespread introduction of the fuel cell and H_2 technologies, especially for mobile applications. This will be discussed in Chapter 2.

[1] DC stands for Direct Current.

1.3 Scope of this Thesis

This work will focus on understanding the H_2 storage property and the decomposition mechanism of lithium borohydride based systems, consisting of 11 chapters:

- Chapter 2 will give a general introduction of the H_2 storage methods, outlying the criteria for the potential storage systems in mobile applications.
- Chapter 3 will give an overview of the synthesis, structure and H_2 storage property for typical borohydrides, and the common solutions to tailor their thermodynamic and to modify their reaction kinetics during dehydrogenation.
- Chapter 4 will summarize the known eutectic metal borohydride systems, including their eutectic behaviours and H_2 storage properties.
- Chapter 5 will state the aims and importance of this project.
- Chapter 6 will describe the experimental apparatus and procedures.
- Chapter 7 will present and discuss the results of $LiBH_4$-based systems ($LiBH_4$, $LiBH_4$-SiO_2, $LiBH_4$-Ni) and the effect of the additive particle size with respect to dehydrogenation.
- Chapters 8 and 9 will present and discuss the results of $LiBH_4$ based low melting point borohydride systems ($0.62LiBH_4$-$0.38NaBH_4$, $0.75LiBH_4$-$0.25KBH_4$). Reducing the dehydrogenation temperature and improving the reversibility by using selected additives (micron-sized SiO_2 or nano-sized Ni) will be presented.
- Chapter 10 will give a general discussion and emphasize the relationship between the key findings and the previous literature.
- Finally, the conclusion and outlook will be given in Chapter 11.

CHAPTER 2 HYDROGEN STORAGE

Since H_2 has the highest energy per mass (120 MJ kg^{-1}) among all the fuels (Figure 2.1) (U.S. Department of Energy 2017b), it becomes a potential carbon-free energy vector (no net CO_2 emission) in the fuel cell technologies. But, its low ambient temperature density (0.08988 kg m^{-3}) leads to a low energy per unit volume (0.01 MJ L^{-1}) that requires a large space when stored in ambient conditions (e.g. ~11 m^3 for 1 kg H_2) (Züttel 2003). Therefore, high-efficient storage technologies are required, and this becomes one of the key challenges for enabling the hydrogen and fuel cell technologies in particular applications: stationary power, portable power and transportation.

The U.S. Department of Energy (DOE) has set targets for H_2 storage in applications for automotive (i.e. light-duty full cell vehicles), material handling and portable power applications (U.S. Department of Energy 2017b). These target values in Table 2.2 were designed for the entire system, including other associated functional components in the storage system, such as tank, piping, regulators, etc. This means that the hydrogen storage material in use must exhibit a much higher gravimetric capacity in order to compensate the mass increase of the system hardware. However, for the stationary applications, the H_2 densities are not such a critical issue and the cost becomes a more important factor.

A number of H_2 storage technologies has been investigated that can be categorised into two major groups: 1) physical storage, such as storage of H_2 as a compressed gas or as a liquid (at -252.9 °C or lower); and 2) materials-based storage, where H_2 is stored via

physical contact with material (such as adsorbed on the surface of a high-surface area solid) or through forming ionic/covalent chemical bonds (such as hydrolysis, interstitial metal hydrides, complex hydrides and chemical storage systems) (U.S. Department of Energy 2017b). This chapter will review a few hydrogen storage technologies, including their current status, advantages and limitations.

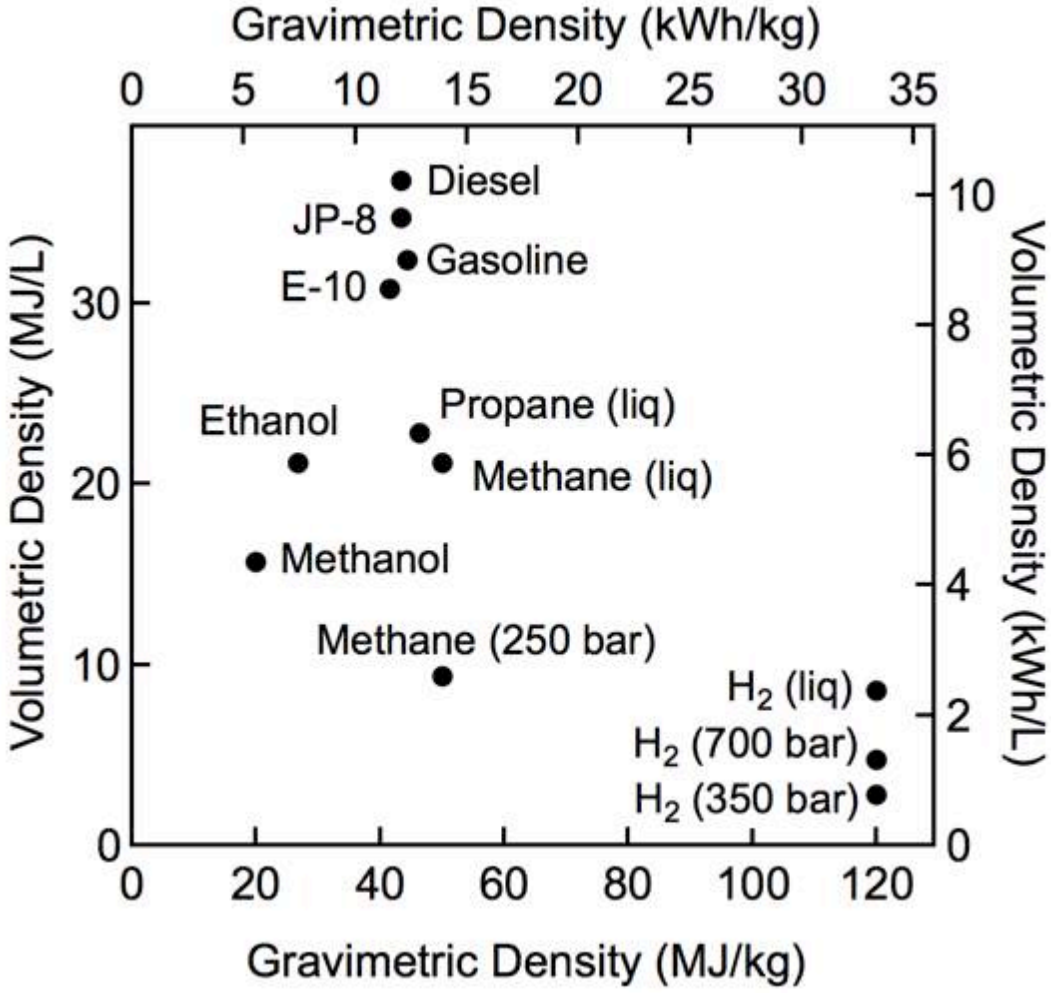

Figure 2.1 Comparison of energy densities for different fuels (U.S. Department of Energy 2017b)[1].

[1] 'liq' is the abbreviation for 'liquid'.

Table 2.1 DOE technical system targets for 2020[1].

		Light-Duty Full Cell Vehicles	Material Handing Equipment	Rechargeable Low Power Portable Equipment	Rechargeable Medium Power Portable Equipment
System Capacity					
H_2 Cap.	g H_2	n.a.	2000	<1	>1-50
Gravimetric Cap.	kg H_2 per kg	0.045	n.a.	0.03	0.03
Volumetric Cap.	kg H_2 per L	0.03	0.05	0.04	0.04
Cost					
System Cost	£ per kg H_2	n.a.	~500	~10	~15
Fuel cost	£ per kg H_2	~250	~200	n.a.	n.a.
Durability/Operability					
Operating Temp.	°C	-40/60	-40/60	-40/60	-40/60
Min/Max delivery T	°C	-40/85	-40/85	10/85	10/85
Min/Max delivery P	bar	5/12	3/12	1.5/3	1.5/3
Operational cycle life	Cycles	1500	5000	n.a.	n.a.
Charging/Discharging Rates					
System fill time	min	3-5	2.8 (for 2 kg H_2)	n.a.	n.a.
Min full flow rate	(g/s)/kW	0.02	0.02	0.02	0.02
Avg. flow rate	(g/s)/kW	0.004	n.a.	n.a.	n.a.
Time to full flow at 20 °C	s	5	5	5	5
Time to full flow at -20 °C	s	15	15	10	10
Transient response at operating temperature 10%–90% and 90%–0% (based on full flow rate)	s	0.75	0.75	2	2
Fuel Quality	% H_2	Meets applicable standards			
Heath and Safety					
Permeation and leakage	-				
Toxicity	-	Meets applicable standards			
Safety	-				

[1] T or Temp. is the short form for Temperature; whilst P stands for Pressure.

2.1 Storage of Hydrogen as a Compressed Gas

The compressed gaseous H_2 is currently the widest used and best understood storage technology. The infrastructure requirements of handling the compressed H_2 already exist. The associated technical and safety concerns of storage and transportation have largely been resolved (Acosta et al. 2014).

This method is suitable for the large stationary H_2 storage and it is currently equipped in the modern H_2 fuelling stations for full cell vehicles (elementenergy 2015). For mobile applications, the high-pressure H_2 tank is well established and allows the DOE target to be partially met. Handling a high-pressure gas requires not only special design of the tank but also other associated engineering challenges, as the gas pressure needs to be reduced from storage pressure (high) to working condition (low).

Table 2.2 summarises the common compressed gaseous H_2 tanks (Barthelemy et al. 2017).

Table 2.2 Compressed gaseous H_2 tank types.

Type	Description	Approximate Max Pressure
I	Metal tank (steel or Al)	Steel: 200 bar Al: 175 bar
II	Metal tank (Al) with filament windings like glass fibre/aramid or carbon fibre around the metal cylinder	Al/glass: 260 bar steel/carbon: 300 bar steel/aramid: 300 bar
III	Tanks made from composite material, fiberglass/aramid or carbon fibre with a metal liner (steel or Al)	Al/glass: 300 bar Al/aramid: 430 bar Al/carbon: 700 bar
IV	Composite tanks such as carbon fibre with a thermoplastic polymer liner	plastic/carbon: 660 bar
V	Composite tanks such as carbon fibre with no polymer liner needed	

The Toyota Mirai, one of the latest commercial fuel cell vehicles unveiled in 2014, has two state-of-the-art carbon fibre reinforced composite (Type IV) tanks (Kane 2014). They can store approximately 5 kg H_2 at 700 bar (max. 875 bar) with system gravimetric and volumetric capacities of 0.057 kg H_2 kg^{-1} and 0.04 kg H_2/L respectively (Kane 2014). These values are higher than the DOE 2020 targets listed in Table 2.1, but still lower than the ultimate capacity targets (e.g. 0.065 kg H_2 kg^{-1} and 0.05 kg H_2 L^{-1}) (U.S. Department of Energy 2017b). The H_2 stored in the Toyota Mirai enables 300 miles cruising range (max. speed at 111 mph) with a full charge, and the refuelling time is approximately 3 min (Kane 2014). Therefore, the compressed gaseous H_2 storage technology has been considered as a near-term solution for mobile application. However, its high cost due to the carbon fibre based composite materials needs to be reduced by using novel materials without compromising the system capacity and safety.

Alternatively, a range of hybrid tank systems combining a high-pressure tank and H_2 storage materials (such as metal hydrides, reactive hydride composites and metal-organic frameworks) have also been proposed (Takeichi et al. 2003; Lototskyy & Yartys 2015; Cao et al. 2015; Cao et al. 2016; Urbanczyk et al. 2016). They have the advantage of relatively higher volumetric H_2 capacity; however, a special heat exchange design is needed to perform hydrogen release and uptake from storage materials (Gkanas et al. 2016).

2.2. Storage of Liquefied Hydrogen

To be converted into liquid, H_2 must be cooled below its critical point (-240.2 °C) or below -253 °C to avoid boiling at atmospheric pressure (Flynn 2004). Thus, extra

energy input is required to maintain this low temperature during practical use. The liquefied hydrogen has a much higher volumetric energy density (8 MJ/L) than its gaseous form (2.5 or 5 MJ/L for compressed H_2 at 345 bar or at 690 bar), which is more attractive for the extension of vehicular cruising range and the application of large-scale energy storage from the infrastructure point of view (Durbin & Malardier-Jugroot 2013; Klebanoff 2016). The extra energy spent for H_2 liquefaction can possibly be compensated by the easiness of delivery and storage in an advanced design (Mori & Hirose 2009).

In practice, a metallic double-walled vessel is normally used for cryogenic storage, where the inner vessel is equipped with a special designed vacuum multilayer insolation to isolate the ultra-low temperature liquid (cold) from its working environment (hot) (Mori & Hirose 2009) (Figure 2.2).

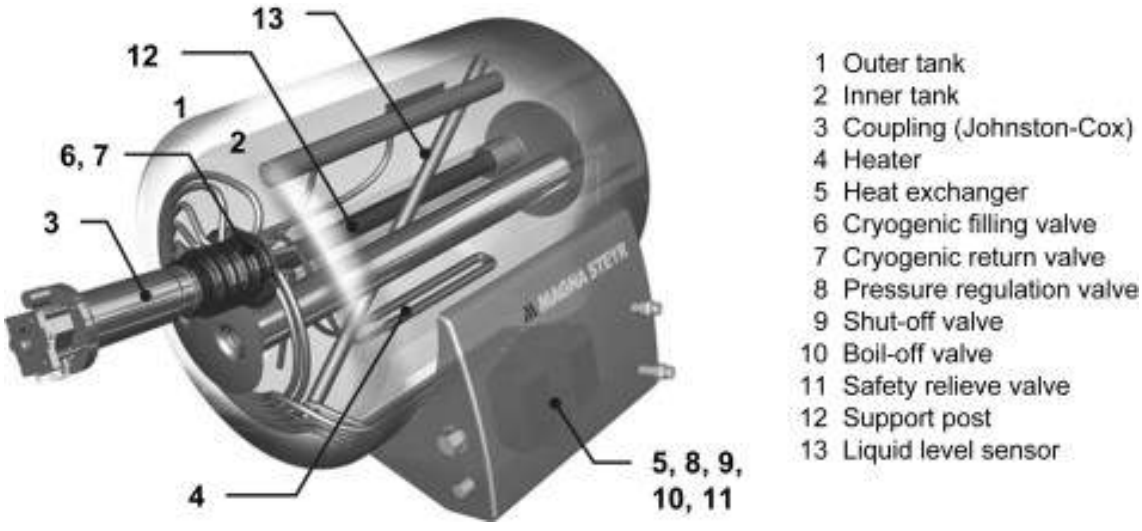

Figure 2.2 A schematic diagram of a liquefied hydrogen tank designed by Magna Steyr (Mori & Hirose 2009).

Alternatively, advanced methods that combine the compression and cryogenic storage of H_2 are proposed, such as cooled-compressed H_2 gas and pressurized liquid H_2 (Ahluwalia et al. 2010; Durbin & Malardier-Jugroot 2013). The former technique cools down the compressed H_2 to -196 °C in order to form a more compact and denser gas, which increases the volumetric capacity and requires less energy input than the conventional method (operating at -253 °C or lower) (Ahluwalia et al. 2010). The later technique based on the concept that the liquefied H_2 is slightly compressible (e.g. from 0.07 kg L^{-1} H_2 at 1 bar to 0.09 kg L^{-1} H_2 at 237 bar, at -252 °C), which also leads to a compact tank with higher capacity (Durbin & Malardier-Jugroot 2013).

2.3 Storage of Hydrogen on High Surface Area Materials

Due to the van der Waals force, H_2 can be adsorbed onto the surface of materials (or being held within pore structures) through either dipole/induced-dipole or induced-dipole/induced-dipole interaction with atoms on the surface (Bénard & Chahine 2007), known as physisorption. It has excellent performance at low temperatures (e.g. -196 °C) since the energy required for these interactions is normally very low (typically 4-10 kJ mol^{-1} H_2) (Walker 2008).

A number of high surface area materials with different structures have been demonstrated as candidates for physisorption of H_2, such as carbon-based structures (e.g. activated carbons, carbon nanotube-based structures or graphene) (Rzepka et al. 1998; Ozturk et al. 2015; Klechikov et al. 2015), open porous structures (e.g. metal-organic frameworks (MOFs), covalent-organic frameworks (COFs) and porous polymer networks (PPN)) (Wood et al. 2007; Goddard et al. 2008; Langmi et al. 2014). In

general, the storage gravimetrical capacity of physisorption reaches ~3-6 wt.%-total at cryogenic temperature and atmospheric pressure (Gogotsi et al. 2005; Bénard & Chahine 2007; Baburin et al. 2015). It can be enhanced by pressurization (Bénard & Chahine 2001; Z. Yang et al. 2007), especially in COFs (e.g. 21 wt.% of hydrogen can be stored in COF-108 at 100 bar) (Knighten et al. 2007).

The main advantages of this simple storage technology are 1) relatively low operating pressures; 2) rapid sorption kinetics; 3) high purity of H_2; (Roszak et al. 2016). However, no material has so far exhibited the most ideal adsorbing properties required for mobile applications (Roszak et al. 2016). Their low average adsorption energy, heterogeneous surface, mesoporosity and poor volumetric packing are the major challenges. The low H_2 capacities, low operating temperatures and the reduced system volumetric capacity caused by the volume of host materials are the major disadvantages (Thomas 2007; Niaz et al. 2015).

2.4 Storage of Hydrogen through a Reaction with Water

By reacting with water, a large range of chemical compounds release H_2 during hydrolysis in ambient conditions, such as $NaBH_4$ (Mao & Gregory 2015), MgH_2 (Tegel et al. 2017) and NaSi (Wallace 2012). The hydrolysis reaction can be easily controlled by adjusting the pH value or using catalysts (Amendola et al. 1999; Amendola et al. 2000). Usually, high active heterogeneous catalysts (such as ruthenium (Ru), rhodium (Rh) or platinum (Pd) based noble metal catalyst or cobalt-boron based catalysts) can be used to control the reaction kinetics by regulating the contact area between the catalyst and solution (Muir & Yao 2011). However, hydrolysis reactions are normally not

directly reversible on-board, where the "spent fuel" has to be removed from the reaction vessels and recharge H_2 off-board (National Renewable Energy Laboratory 2007).

One of the typical examples is the hydrolysis utilization and regeneration of $NaBH_4$ (Figure 2.3). In theory, 1 g of $NaBH_4$ produces 2.37 L of hydrogen, which is identical to 10.8 wt.% of hydrogen on a reactants-only basis under standard temperature and pressure conditions (Nunes et al. 2016):

$$NaBH_4 + 2H_2O \xrightarrow{RT} NaBO_2 + 4H_2 \quad \Delta H = -75 \text{ kJ mol}^{-1} H_2 \qquad \text{Equation 2.1}$$

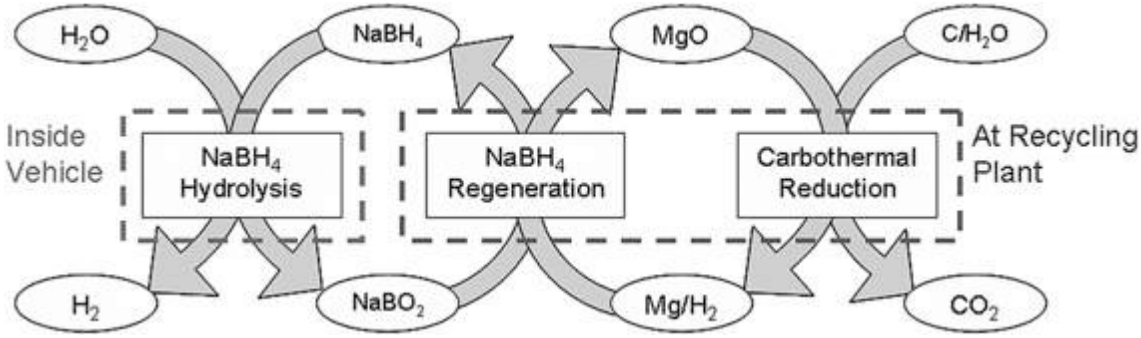

Figure 2.3 A schematic of $NaBH_4$ hydrolysis utilization and regeneration process for mobile application (Kojima & Haga 2003).

However, this theoretical capacity by weight is significantly reduced in practice due to the added mass of the solvent and the by-products ($NaBO_2$), as well as the excess weights of storage/reaction vessels (Mohring & Luzader 2001). For example, the $NaBH_4$-based hydrogen on Demand^{TM} system possesses a system gravimetric capacity of about 4 wt.% and 0.022 kg H_2 L^{-1} (Kutz 2015).

The "spent fuel" (slurry mainly contains $NaBO_2$) can be recycled by heating with MgH_2 at 550 °C in 70 bar H_2 for 2 h, forming $NaBH_4$ and MgO (Equation 2.2). Furthermore,

MgO can be recycled through a redox reaction with Si, and their oxidation product SiO_2 can then be reduced back to Si through a carbon-thermal treatment (Kojima & Haga 2003), as illustrated in Figure 2.3.

$$NaBO_2 + 2MgH_2 \xrightarrow{550\,^{\circ}C+70\ bar\ H_2} NaBH_4 + 2MgO \qquad \textbf{Equation 2.2}$$

However, due to the drawbacks and limitations of the hydrolysis of $NaBH_4$, the DOE issued a "NO-GO" recommendation and excluded it from potential H_2 storage media for mobile applications (National Renewable Energy Laboratory 2007).

2.5 Metal Hydrides Systems

2.5.1 Traditional Metal Hydrides

Metal hydrides are versatile. They are the most technologically relevant class of H_2 storage materials and are suitable for many other applications, such as neutron moderation (Vetrano 1971), nuclear reactor (F. S. Yang et al. 2010), electrochemical cycling (Young & Nei 2013), direct fuel cell (Lototskyy et al. 2017), thermal storage (Felderhoff & Bogdanović 2009), purification/separation (Chen et al. 2013), heat pumps (compressor) (Lototskyy et al. 2014) and etc.

In general, the alkali and alkaline earth metals are inclined to form stoichiometric ionic hydrides, except BeH_2 (covalently bonded) (Dekock & Gray 1989) and MgH_2 (mix of ionic and covalent bonds) (Noritake et al. 2002). The transition-metal hydrides are usually non-stoichiometric, where variable compositions may be available (e.g. $PdH_{0.015}$, $PdH_{0.607}$ (Adams & Chen 2011)).

Metal hydrides (MH_x) are fabricated through reaction between metals (or alloys) and H_2, where H_2 is absorbed into the interstitial sites. Thus, the overall storage capacity of a metal hydride strongly depends on the amount of interstitial sites available (Züttel 2003). The general H_2 absorption reaction can be expressed as

$$\boldsymbol{M + (x/2)H_2 \leftrightarrow MH_x + heat} \qquad \textbf{Equation 2.3}$$

where M stands for metal/alloy and MH_x represents its corresponding hydride (Sandrock & Bowman 2003). The thermodynamic aspect of this H_2 absorption process is often described using Pressure-Composition Isotherms (PCI). For example, Figure 2.4 illustrates H_2 absorption in a typical intermetallic compound.

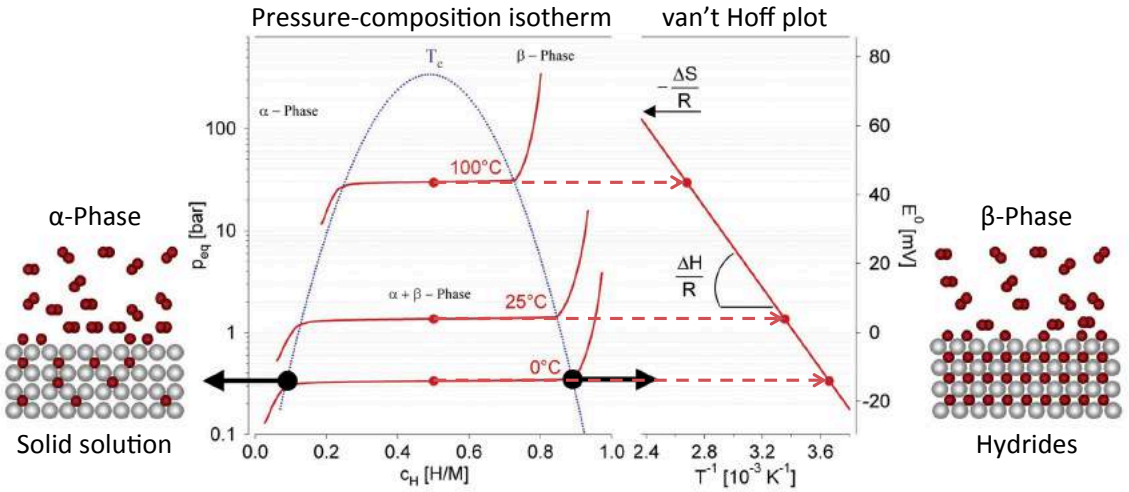

Figure 2.4 Determination of enthalpy of reaction from the slope of the van't Hoff plot using the equilibrium pressure in the pressure-composition isotherms for H_2 absorption in a typical intermetallic compound, revised from (Züttel 2003).

Applying H_2 to the metal/alloy phase at a certain temperature initiates the H_2 absorption process. At low pressure, H_2 molecules disassociate at the surface and diffuse into the

metal lattice as H atoms in low concentrations, forming a solid solution (α-Phase). This phase has the same crystal structures as the host metal/alloy, possibly with a weak lattice expansion to accommodate the H atoms (Züttel 2003).

With the increasing H_2 pressure, the ordered hydride phase (β-Phase) starts to nucleate, and the pressure reaches a plateau in the isotherms where the solid solution and ordered hydride phase coexist (α+β-Phase). The length of this plateau determines the amount of H_2 stored in the system, and the equilibrium pressure (P_{eq}) at the plateau is related to enthalpy (ΔH_f) and entropy (ΔS_f) of formation as a function of temperature by the van't Hoff equation (Züttel 2003):

$$\ln(\mathbf{P}/\boldsymbol{P_0}) = \Delta \boldsymbol{H_f}/\boldsymbol{RT} - \Delta \boldsymbol{S_f}/\boldsymbol{R} \qquad \textbf{Equation 2.4}$$

where P is the plateau pressure at a certain temperature (T), P_0 is the standard pressure at 1 bar and R is the gas constant (8.3145 J mol^{-1} K^{-1}). Therefore, by plotting the plateau pressure (ln P) against the inverse temperature (1/T) from a number of pressure-composition-temperature isothermal measurements, the enthalpy and entropy of formation for a certain material can be easily obtained from the slope and intercept on the van't Hoff plot, respectively (Züttel 2003). Besides, no plateau behaviour exists above a critical temperature (T_c), exhibiting a continuous α to β phase transition.

After being fully hydrogenated, the H_2 pressure rises steeply again with the concentration in the pure hydride phase (β-Phase) (Züttel 2003).

The sorption process is reversible. Desorption of H_2 from the host metal is achieved by simply increasing temperature or reducing pressure.

One of the typical metal hydrides is MgH_2. It is relatively low cost and is one of the most promising reversible metal hydrides with high hydrogen capacities (7.6 wt.% and 0.11 kg H_2 L^{-1}) (Jain, Lal, et al. 2010). However, its relatively high thermal stability (desorption temperature > 300 °C), sluggish kinetics in H_2 sorptions (caused by poor decomposition of H_2 on Mg surface and slow diffusion of H_2 in the bulk MgH_2/Mg) and unsatisfactory heat management become the major obstacles for its practical application (Wang & Wang 2017). To overcome these drawbacks, a number of strategies have been applied to tune the H_2 storage performance, such as alloying (H. Wang et al. 2016), nano-scaling (Sadhasivam et al. 2017), nano-confinement (Huen et al. 2017) and additive-addition (catalysts, other metal hydrides) (Wang & Wang 2017).

Besides MgH_2, other types of metal hydrides, such as A_2B, AB, AB_2, AB_3, AB_5 alloys (A is usually a group III or IV or a rare-earth metal forming a stable hydride; B is a transition metal which is unable to form a stable hydride but helps to catalyse the dissociation of H_2 molecules) are investigated (Sandrock 1999; Züttel 2003; Zhu et al. 2013; Manickam et al. 2015). For instance, $LaNi_5$ is a typical AB_5 alloy. Its corresponding hydride, $LaNi_5H_6$, has a high volumetric density (115 kg m^{-3}) and good cycling ability (Schlapbach & Züttel 2001). However, it suffers from a very low gravimetric capacity (1.4 wt.%) due to its heavy transition and rare earth elements, which makes it unsuitable as H_2 storage medium for vehicular applications (Schlapbach & Züttel 2001).

2.5.2 Complex Hydrides

H atoms in the complex hydrides are covalently bonded in a coordination complex compound especially based on light elements, forming anions such as borohydrides ($[BH_4]^-$,), alanates ($[AlH_4]^-$) or amides/imides ($[NH_2]^-$/$[NH]^{2-}$) (Orimo et al. 2007). Metals, especially alkali/alkaline-earth metals or transition metals, are usually combined to compensate the charges that often form solid-state materials. These materials are in general very attractive due to their relatively high H_2 capacity by weight (e.g. 10.5 wt% for $LiAlH_4$ and 18.5 wt.% for $LiBH_4$) and easy to handle as they are in a solid powder form (J. Yang et al. 2010). So far, a large number of complex hydrides as hydrogen storage media have been demonstrated.

For instance, Chen et al. (2002) demonstrated a reversible system using nitrogen-based complex hydrides (e.g. $LiNH_2$-Li_2NH-LiH) that exhibits ~10 wt.% hydrogen release when Li_3N is formed (Chen et al. 2002):

$$\boldsymbol{LiNH_2 + 2LiH \leftrightarrow Li_2NH + LiH + H_2 \leftrightarrow Li_3N + 2H_2} \qquad \textbf{Equation 2.5}$$

However, the kinetics of H_2 sorption processes (both absorption and desorption) involved Li_3N are sluggish even above 320 °C. Thus, a reversible 6.5 wt.% hydrogen content is achieved when Li_2NH and LiH are formed at 255 °C.

Moreover, Züttel et al (2003) firstly introduced the use of metal tetrahydroborates as a potential solid-state H_2 storage media: $LiBH_4$ releases ~9 wt.% hydrogen upon heating to 600 °C in an integrated gas flow (Andreas Züttel et al. 2003).

However, the relatively high thermal stability, low kinetics in H_2 sorptions, poor reversibility and production of gaseous by-products of these types of materials have so far prohibited their practical applications, especially for vehicular hydrogen stores (Li et al. 2011).

2.6 Chemical Hydrogen Storage Systems

The concept of chemical hydrogen storage materials usually indicates the covalently bonded hydrogen in either solid or liquid form that enables high hydrogen density, relatively high stability and safe storability (Yadav & Xu 2012; Callini, Atakli, et al. 2016). The dehydrogenation of stored chemical hydrogen is usually achieved by hydrolysis or thermolysis. Thus, this concept overlaps with the topics of hydrolysis (Section 2.4) and complex hydrides (Section 2.5.2). Typical examples are boron-based compounds (e.g. NH_3BH_3, $N_2H_4BH_3$), anhydrous hydrazine (H_2NNH_2), formic acid (HCOOH) and other liquid organic hydrogen carriers (e.g. n-ethylcarbazole, methyl-cyclopentane) (Umegaki et al. 2009; Jiang et al. 2010; Luo et al. 2011; Yadav & Xu 2012).

Similar to complex hydrides, there are thermodynamic and kinetics drawbacks, which have limited the use of these solid-state materials, especially for mobile vehicular applications. Besides, since some of these chemical hydrogen storage materials works in liquid state, an off-board rehydrogenation for the ‘spent fuel’ is necessary.

2.7 Summary of Hydrogen Storage Methods

The research of safe, efficient and high capacity H_2 storage technology is currently in progress and many approaches have been evaluated over the last two decades. These technologies can be classified into 2 major categories (Figure 2.5): physical storage and material-based storage. However, no single method can fulfil all the technical targets and satisfy the economic demands yet.

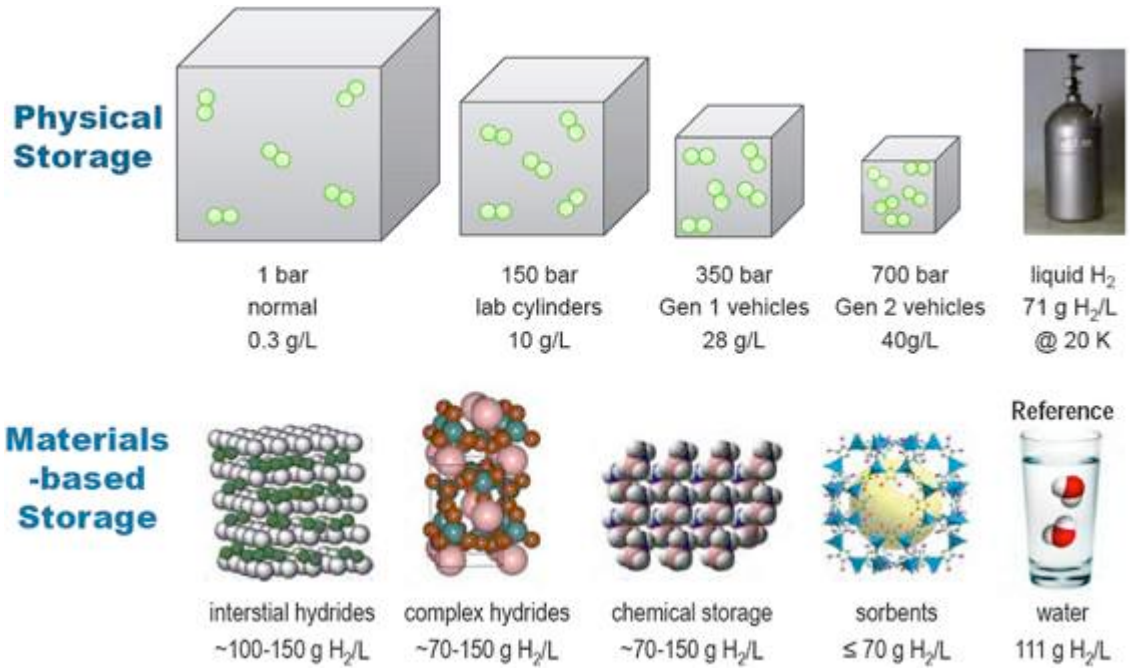

Figure 2.5 Current hydrogen storage technologies (Ren et al. 2017).

For large-scale stationary applications, H_2 is usually stored in a physical state, such as compressed gaseous or cryogenic storage. These options typically require large storage space; however, space is less of an issue compared to cost.

For mobile applications, compressed gaseous H_2 is a near-term solution for initial fuel cell vehicle commercialization into the market. The pressurised cylinders should have strong mechanical strengths as well as a low density, and it is inert in terms of

interaction with H_2 (no reaction or diffusion). Another important aspect of pressurised cylinders is its safety: the design has to ensure the integrity of the cylinder is preserved even during a traffic accident with a strong impact. Thus, the state-of-the-art cylinder design uses carbon composite reinforced tank, but it is suffering from its high cost and relatively large size as a consequence of low volumetric density of H_2. Moreover, cryo-compressed and material-based H_2 storage technologies exhibit high potential to meet the DOE technical targets for vehicles. They are regarded as potential long-term solutions. However, they are facing many technical challenges in practical use.

Figure 2.6 is a comparison of the observed H_2 capacities and their operating temperatures for different material-based H_2 storage materials for mobile application. The capacity of these H_2 storage compounds will reduce significantly when the system hardware mass are counted. It is estimated that the system hardware mass accounts for approximately 50% of the total system mass (Ott 2010); however, it is subject to the material and the design of storage cylinders. In general, to fulfil this DOE targets, the material-based H_2 storage approach needs to have improved system H_2 capacities, accelerated H_2 sorption kinetics within an appropriate temperature and pressure range, and a lower system cost.

This current work focused on the investigation of complex metal hydrides and a detailed introduction of this category compounds will be given in Chapter 3.

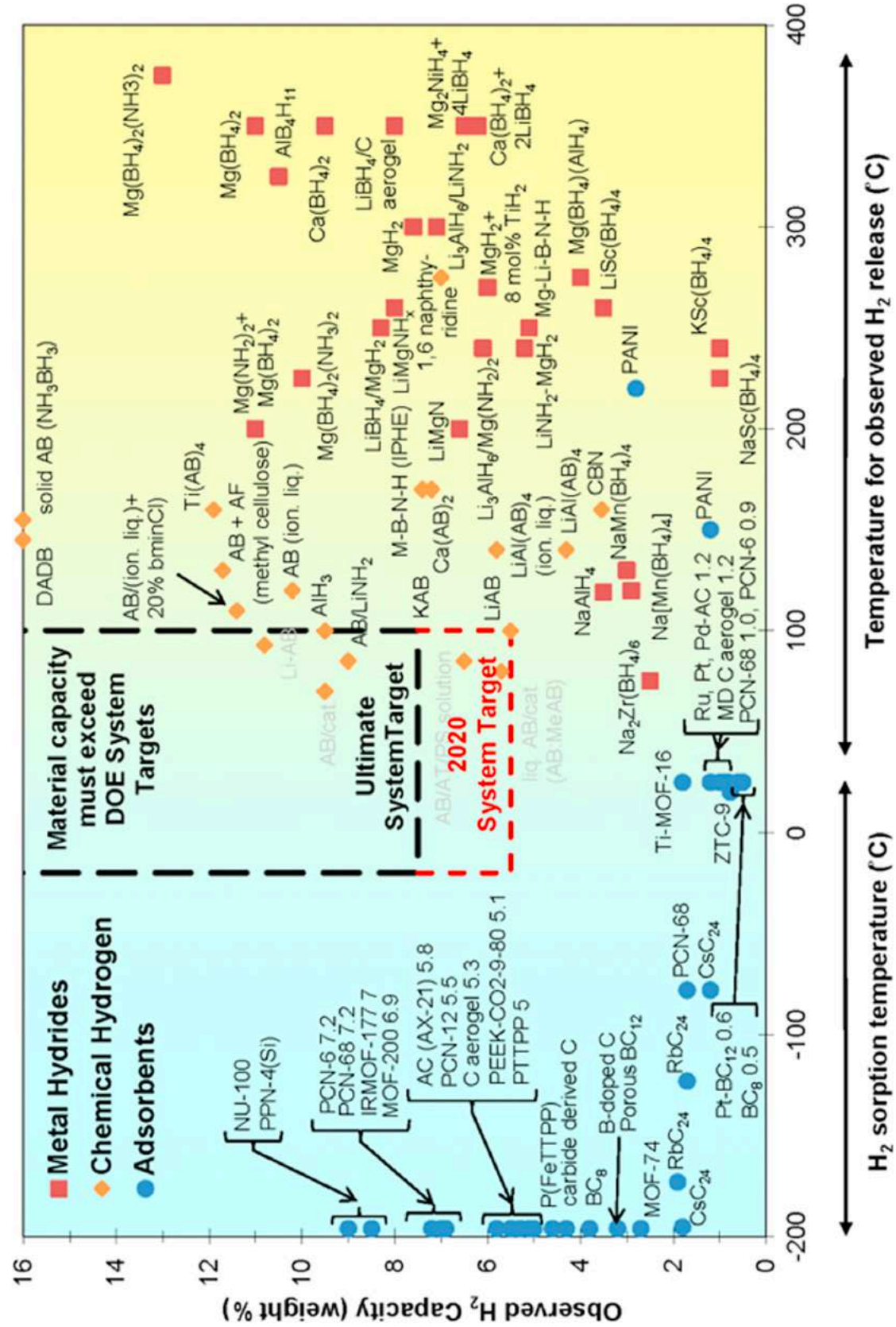

Figure 2.6 Observed H_2 storage capacities of potential H_2 storage materials with corresponding operating temperatures. The DOE system target for 2020 and ultimate goal are marked with dashed lines (Sadhasivam et al. 2017).

CHAPTER 3 COMPLEX METAL BOROHYDRIDES

Metal borohydrides (often noted as $M(BH_4)_n$, where n equals to the valence of metal M), also known as tetrahydroborates, have relatively high H_2 densities and are therefore regarded as one of the most promising groups of solid-state H_2 storage materials for use as a long-term vehicular hydrogen energy solution. Over the past two decades, large varieties of metal borohydrides (and their derivatives) have been discovered and characterized (Paskevicius et al. 2017), revealing a wide range of structures, and chemical and physical properties. Figure 3.1 summarizes the theoretical gravimetric capacities for possible monometallic borohydrides.

1	2											13	14
Li 18.5	Be 20.8												
Na 10.7	Mg 14.9	3	4	5	6	7	8	9	10	11	12	[Al] 16.9	
K 7.5	Ca 11.6	Sc 13.5	Ti III 13.1 IV 15.0	V 12.7	Cr 9.9	[Mn] 9.5	[Fe] 9.4	[Co] 9.1	[Ni] 9.1	[Cu]* 5.1	Zn 4.4	[Ga] 10.6	Ge 12.2
Rb 4.0	Sr 6.9	Y 9.1	Zr 10.7	Nb 8.8						[Ag]* 3.3	[Cd] 2.9	[In] 7.6	[Sn] 9.1
Cs 2.7	Ba 4.8	Ln	Hf 6.8							[Au] 1.9	Hg 1.8	Tl 4.9	
		Ac											

Ln	La 6.6	Ce 6.6		Nd 6.4		Sm 6.2	Eu 6.2	Gd 6.0	Tb 5.9	Dy 5.8	Ho 5.8	Er 5.7	Tm 5.7	Yb 5.6	Lu 5.5
Ac		Th 5.5	Pa 5.6	U III 4.3 IV 5.4	Np 5.4	Pu 5.4									

Figure 3.1 A summary of monometallic borohydrides with theoretical gravimetric capacity in mass fraction. Asterisks indicate compounds stabilized at room temperature by coordination with ligands. Brackets indicate compounds reported to be unstable at room temperature but may be isolated at low temperature (Li et al. 2011).

Apart from monometallic borohydrides, bimetallic and trimetallic borohydrides also exist (Paskevicius et al. 2017). This chapter will only focus on alkali metal borohydrides, such as $LiBH_4$, $NaBH_4$, KBH_4, including their preparations, structures and properties.

3.1 Overview

The metal borohydrides have been known since the 1940s (Schlesinger et al. 1940; Burg & Schlesinger 1940; Schlesinger & Brown 1940; Beach & Bauer 1940). These materials are versatile and suitable for many applications besides H_2 storage. Some of them, such as $LiBH_4$ and $NaBH_4$, are being used as strong reducing agents in industry for organic/inorganic synthesis (Nystrom et al. 1949; Brown & Rao 1956; Bank 1976) as well as for production of various antibiotics (Hensens & Goldberg 1988). Recent research proposes that materials, such as $LiBH_4$ and $Mg(BH_4)_2$, have favourable ionic conductivity that may be attractive for use as solid-state electrolytes in rechargeable batteries (Unemoto et al. 2014).

3.1.1 Structures

In a metal borohydride, H atoms are located at the apices of a tetrahedral ligand and are covalently bonded to the boron atom in the centre (Andreas Züttel et al. 2003). The metal (M) coordinates tetrahydroborates ($[BH_4]^-$) in order to compensate the charges, through either ionic bonding or M-H-B bridges (i.e. covalently bonded with H atoms). Depending on the bonding type and the number (n) of M-H-B bridges, the bonding between a metal and a tetrahedral ligand can be classified into ionic (n=0), monodentate (n=1), bidentate (n=2) or tridentate (n=3) (Figure 3.2).

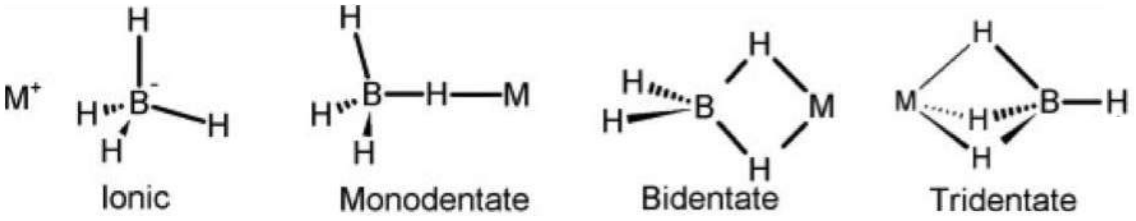

Figure 3.2 Schematic diagrams of typical ionic and covalent bonding configurations between metal (M) and tetrahydroborates (Marks & Kolb 1977).

Usually, metal borohydrides involving alkali metals are ionic compounds (almost complete charge transfer); whilst the rare-earth and transition metals are covalently bonded with borohydride ligand. The alkaline-earth metal borohydrides often have hydride bonds: the bonds exhibit more covalent characters than ionic compounds though they are still bonded ionically (Züttel et al. 2007). These may explain the less stable alkaline-earth and transition metal borohydrides in contrast to the alkali metal borohydrides.

Besides, an ideal isolated $[BH_4]^-$ cluster belongs to T_d symmetry group. It can generate four normal vibration modes depending on the vibrations and symmetry (Figure 3.3).

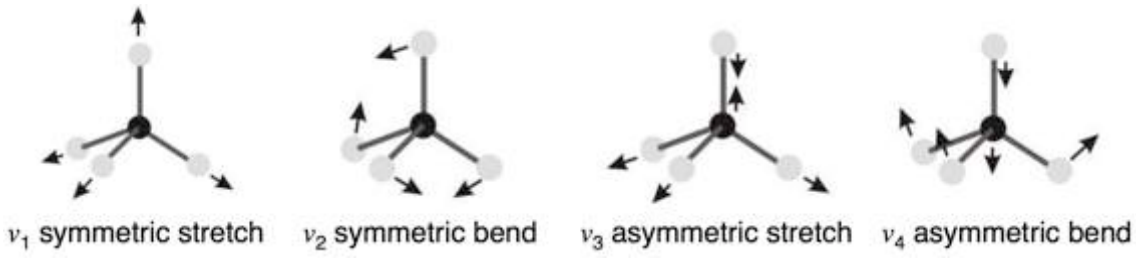

Figure 3.3 Schematic diagrams of typical vibrational modes of a tetrahedral $[BH_4]^-$ cluster (Housecroft & Sharpe 2012).

Usually, the B-H stretching modes, including ν_1 (symmetric, A_1) and ν_3 (asymmetric, T_2), are located in the vibrational region from 2100 to 2500 cm^{-1}; whilst the H-B-H

bending modes, including ν_2 (symmetric, E) and ν_4 (asymmetric, T_2), are observed in a lower vibrational region from 900 to 1200 cm^{-1} (Zavorotynska et al. 2011; D'Anna et al. 2014).

However, coordinated metal in borohydrides may introduce changes in site symmetry as well as in the crystal field that affects the local symmetry of $[BH_4]^-$ cluster and allows the identification of compounds. Usually, the terminal B-H_t and bridging B-H_b stretching modes are common indicators given by their relatively high intensity and distinguishable signal. However, changes of $[BH_4]^-$ cluster can also cause a splitting of vibrations, overtone, Fermi resonance or combination modes, which can make the spectra complicated and difficult to be interpreted (Marks & Kolb 1977; Larkin 2011). The typical ranges of vibrational frequency for common metal borohydrides are illustrated in Figure 3.4 and summarised in Table 3.1.

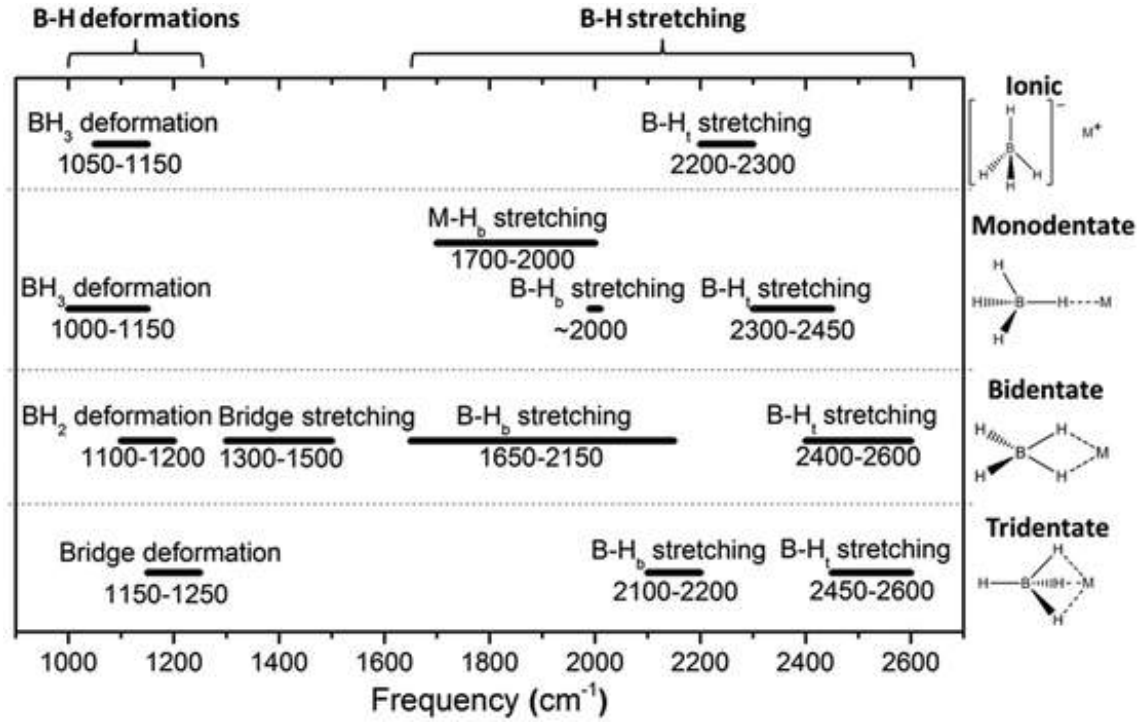

Figure 3.4 The common observed fundamental vibrations for metal borohydrides (Paskevicius et al. 2017).

Table 3.1 A summary of typical vibrational frequency ranges for common $M(BH_4)_n$ (Marks & Kolb 1977; Parker 2010; Guo 2014).

Bonding	Frequency Range cm^{-1}	Internal Modes	Symmetry Type		Relative Intensity and Possible Observations	
			Raman	IR	Raman	IR
Ionic	1050-1150	BH_3 deformation	E	T_2	Weak	Strong, Broad
	2200-2300	B-H_t Stretching	A_1	T_2	Strong, Broad	Strong, Broad
Monodentate	1000-1150	BH_3 deformation	A_1	A_1, E	Strong	Strong, [Extra weaker band]
	1700-2000	M-H_b Stretching	A_1	A_1	[Broad]	[Very Broad]
	~2000	B-H_b Stretching	A_1	A_1		Strong
	2300-2450	B-H_t Stretching	A_1	A_1, E	Strong	Strong, [Doublet]
Bidentate	1100-1200	BH_2 deformation	A_1	B_2	Medium-strong, [Doublet]	Strong
	1300-1500	Bridge Stretching	A_1	A_1	Strong, Broad	Strong, Broad
	1650-2150	B-H_b Stretching	A_1	A_1, B_2	Medium-strong	Strong, [Shoulder]
	2400-2600	B-H_t Stretching	A_1, B_2	A_1, B_1	Strong, Singlet, [Shoulder]	Strong, Doublet, Splitting
Tridentate	1050-1150	BH_2 deformation	A_1	E	Strong, Singlet	Strong
	2100-2200	B-H_b Stretching	A_1	A_1, E	Strong, Singlet, [Shoulder]	Doublet, Splitting
	2450-2600	B-H_t Stretching	A_1	A_1	Strong, Singlet	Strong, Singlet

** The square brackets indicate the possibilities*

3.1.2 Stability and Thermodynamics

One of the common indicators of stability is the enthalpy of borohydrides. For a spontaneous decomposition reaction, the change of Gibbs free energy (ΔG_{Dec}) can be expressed as

$$\boldsymbol{\Delta G_{Dec} = \Delta H_{Dec} - T_{Dec}\Delta S_{Dec}} \qquad \textbf{Equation 3.1}$$

where ΔH_{Dec} is the enthalpy change, ΔS_{Dec} is the entropy change and T_{Dec} is the temperature at which the reaction occurs. Since ΔS_{Dec} is primarily associated with the H_2 dissociation (~130 J K^{-1} mol^{-1} H_2) (Grochala & Edwards 2004), the decomposition

temperature of borohydrides strongly depends on ΔH_{Dec}. For instance, to perform dehydrogenation at ambient conditions (1 bar H_2, ~ 27 °C), the ideal enthalpy change is suggested to be 39.2 kJ mol^{-1} (Züttel 2003).

Another popular indicator of stability for borohydrides is the electronegativity (χ) value of their coordinated metal (Nakamori et al. 2006; Nakamori et al. 2007; Rude et al. 2011).

In material science, the electronegativity describes the tendency of an atom to attract a bonding pair of electrons towards itself (Pauling 1932; Jensen 1996): the more electronegative an element, the stronger its attraction to electrons. When two elements are bonded, the difference of their electronegativity values (Δχ) determines the bond types from nonpolar covalent (Δχ≤0.5), polar covalent (0.5≤Δχ≤1.6) and ionic bonds (Δχ ≥2.0) (for 1.6<Δχ<2.0, the bond type is usually determined to be ionic, especially when a metal is involved).

In a metal borohydride, the B (2.04) and H (2.20) are covalently bonded due to similar electronegativity values. Therefore, the bonding chemistry of M-H-B bridges strongly depends on metal. For instance, the Pauling electronegativity value for Al is 1.61. The relatively small difference (e.g. 0.4-0.6) compared to B and H results in the covalent H-bridges in $Al(BH_4)_3$ (Coe & Nibler 1973) and makes it less stable (e.g. remaining liquid at room temperature) (Hirscher 2010). Moreover, the alkali metals often have small electronegativity values (e.g. 0.98 for Li, 0.93 for Na and 0.82 for K) compared with B or H, leading to ionic bondings.

Besides, the metal electronegativity values are related to the vibration modes and melting temperatures of borohydrides (Nakamori & Orimo 2004):

For monometallic borohydrides (Figure 3.5-a), high electronegative metals lead to weak thermal stability, exhibiting low melting and decomposition temperatures as well as relatively large wavenumbers for B-H stretching and bending modes (particular, the symmetric modes, ν_1 and ν_2) (Nakamori & Orimo 2004; Nakamori et al. 2007). For instance, Na has a higher Pauling electronegativity (0.93) than K (0.82). This agrees with the observations in practice:

- The fusion of $NaBH_4$ occurs at ~505 °C (Urgnani et al. 2008) that is lower than the 625 °C for KBH_4 (M Paskevicius et al. 2013);
- The decomposition temperature of $NaBH_4$ is 565 °C that is lower than the 584 °C for KBH_4 (Orimo et al. 2004);
- The B-H stretching mode ν_1 and bending mode ν_2 of $NaBH_4$ are 2325 cm^{-1} and 1280 cm^{-1} observed in Raman, which are higher compared to the 2305 cm^{-1} and 1240 cm^{-1} for KBH_4 (Orimo et al. 2004).

For bimetallic borohydrides (Figure 3.5-b) that involve two types of metal, the overall property is dominated by the more electronegative metal (Rude et al. 2011). For instance: the Pauling electronegativity for Zn is 1.65, which is higher than the 1.36 and 0.9 for Sc and Na, respectively. Thus, $NaZn(BH_4)_3$ is less thermal stable than $NaSc(BH_4)_4$ (Figure 3.5), exhibiting a irreversible decomposition at ~100 °C (Ravnsbœk et al. 2009), while the later is stable up to 137°C (Černý et al. 2010).

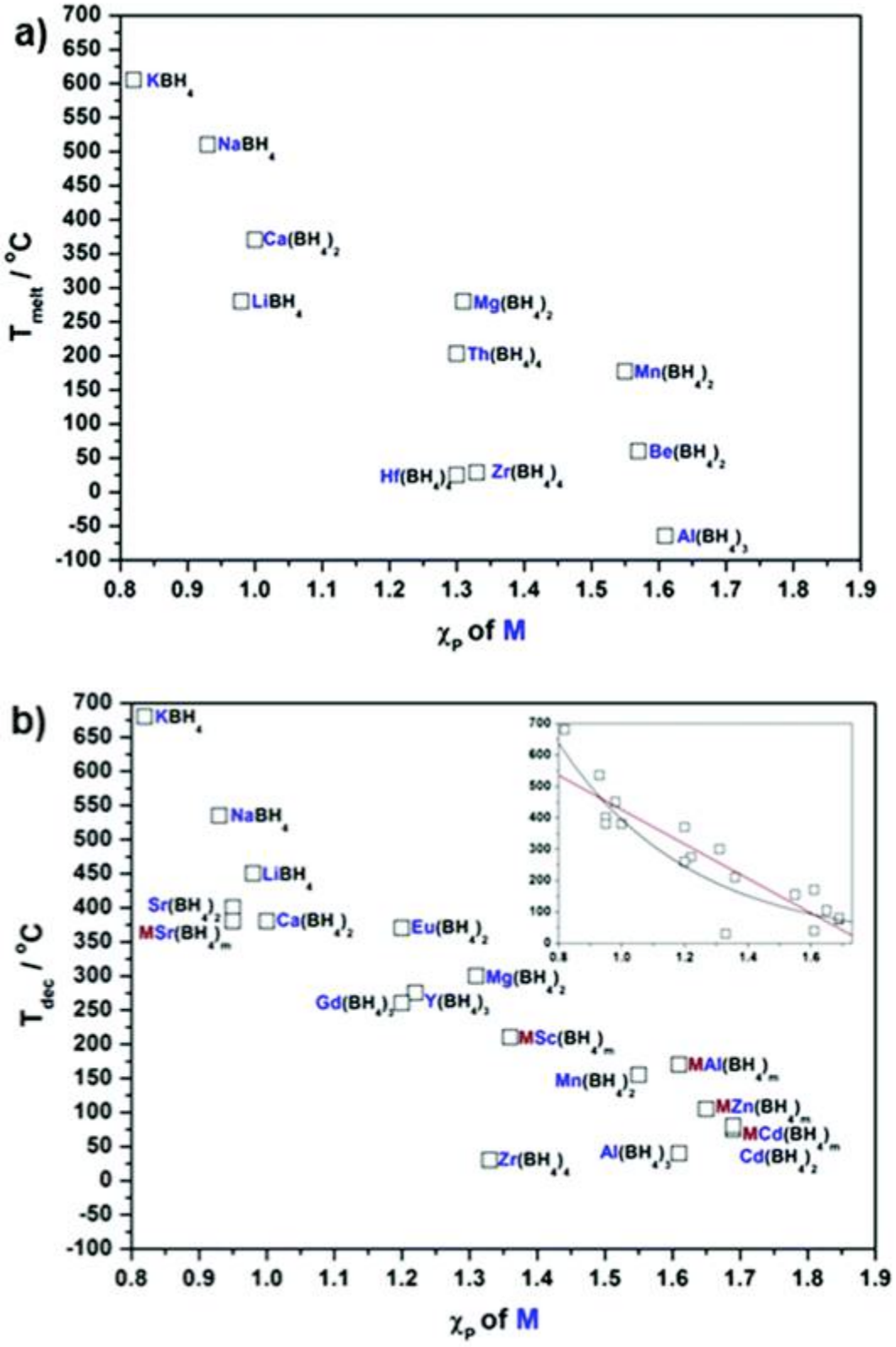

Figure 3.5 A plot of the melting (T_{melt}) and decomposition temperature (T_{dec}) for monometallic ($M'(BH_4)_n$) or bimetallic ($MM'(BH_4)_n$) borohydrides as a function of the Pauling electronegativity (χ_P) of the metal (M') that dominates the overall properties. T_{dec} are measured by *in situ* synchrotron XRD or thermal analysis (TGA/DSC) in an inert atmosphere (Paskevicius et al. 2017).

3.1.3 Decomposition Mechanism

The chemically stored H_2 in metal borohydrides can be simply released by hydrolysis or thermolysis. This work focuses on their thermolysis approach.

In general, dehydrogenation from stable monometallic borohydrides often starts after fusion; whilst, the less stable ones tend to sublime and then start to decompose in the gas phase, as illustrated in Figure 3.5 (Paskevicius et al. 2017).

The decomposition of metal borohydrides is a complex chemical process, which strongly depends on the purity of borohydrides and the temperature and pressure applied (Pendolino et al. 2009; Kato et al. 2010; Price et al. 2011; Yan et al. 2012), and may go through different routes with a number of by-products and/or intermediate phases as a function of temperature and pressure (Shim et al. 2010; Kato et al. 2010; Yan et al. 2012).

Practically, the general decomposition of alkali metal borohydrides to form either metals or metal hydrides can be described as follows (Hirscher 2010):

$$MBH_4 \xrightarrow{\Delta} M + B + 2H_2 \qquad \textbf{Equation 3.2}$$

$$MBH_4 \xrightarrow{\Delta} MH + B + 1.5H_2 \qquad \textbf{Equation 3.3}$$

Similarly, the general decomposition pathways for alkaline-earth borohydrides to form either metal hydrides or metal borides, or a combination of them, are listed as follows (Hirscher 2010):

$$M(BH_4)_2 \xrightarrow{\Delta} MH_2 + 2B + 3H_2 \quad \textbf{Equation 3.4}$$

$$M(BH_4)_2 \xrightarrow{\Delta} MB_2 + 4H_2 \quad \textbf{Equation 3.5}$$

$$M(BH_4)_2 \xrightarrow{\Delta} \frac{2}{3}MH_2 + \frac{1}{3}MB_2 + \frac{4}{3}B + \frac{10}{3}H_2 \quad \textbf{Equation 3.6}$$

In addition, alternative pathways liberating diborane (B_2H_6) (or oven higher homologue) may possibly occur through (Hirscher 2010):

$$M(BH_4)_n \xrightarrow{\Delta} M + \frac{n}{2}B_2H_6 + \frac{n}{2}H_2 \quad \textbf{Equation 3.7}$$

$$M(BH_4)_n \xrightarrow{\Delta} MH_n + \frac{n}{2}B_2H_6 \quad \textbf{Equation 3.8}$$

where n is the charge of metal M.

3.2 Alkali Metal Borohydrides

The alkali metal borohydrides include lithium borohydride ($LiBH_4$), sodium borohydrides ($NaBH_4$), potassium (KBH_4), rubidium borohydrides ($RbBH_4$) and caesium borohydrides ($CsBH_4$). The trend of stability from high to low is $CsBH_4$> $RbBH_4$> KBH_4> $NaBH_4$> $LiBH_4$. In the following section, the structures and properties of alkali metal borohydrides will be discussed using $LiBH_4$, $NaBH_4$ and KBH_4 as examples.

3.2.1 Lithium Borohydrides – $LiBH_4$

$LiBH_4$ is the lightest borohydride. Due to its relatively high theoretical gravimetric (18.5 wt%) and volumetric (121 kg H_2/m^3) hydrogen densities, it became a prime candidate for hydrogen storage (A. Züttel et al. 2003).

3.2.1.1 Synthesis

$LiBH_4$ can be synthesised through a number of chemical approaches, including solvent based or solvent-free methods.

The traditional synthesis methods produce $LiBH_4$ through wet chemistry approaches, where the diborane (B_2H_6) precursor reacts with lithium-based material, such as ethyl-lithium (CH_3CH_2Li) or lithium hydrides solvent (Schlesinger & Brown 1940; Schlesinger, Brown, Abraham, et al. 1953).

Nowadays, the industrial production uses salt metathesis reaction between lithium halides and $NaBH_4$ in solvent of ether or isopropyl amine solution (Brown et al. 1981). The by-products (sodium halides) require extra purification step, and the impurities remained in the final product affect its purity, which becomes a drawback.

$$NaBH_4 + LiCl \rightarrow LiBH_4 + NaCl \qquad \textbf{Equation 3.9}$$

$$NaBH_4 + LiBr \rightarrow LiBH_4 + NaBr \qquad \textbf{Equation 3.10}$$

The more advanced concepts, such as solvent-free or direct approach, in general benefit from circumventing the necessity to remove solvents or unwanted by-products, leading to almost no impurity in the final products (Remhof et al. 2012).

The solvent-free method usually refers to a solid–gas reaction between LiH and B_2H_6, generating $LiBH_4$ at 120 °C at ambient pressure. The rate-limiting step is the formation of the B-H bonds that may be accelerated by using proper catalysts (Friedrichs et al.

2009). This method is also suitable for synthesis of other borohydrides, such as $Mg(BH_4)_2$ or $Ca(BH_4)_2$ (Friedrichs, Remhof, Borgschulte, et al. 2010).

The direct synthesis of $LiBH_4$ from Li, B and H_2 is not thermodynamically encouraging, exhibiting an unfavourable enthalpy of formation of -194.2 kJ (Züttel et al. 2007), and thus requires elevated temperature and high pressure, such as 650-700 °C and 150 bar H_2 (Goerrig 1958; Friedrichs et al. 2008). This reaction also suffers from the kinetic inertness of B that may inhibit the reaction (Züttel et al. 2007). However, the formation of $LiBH_4$ can be improved by Li intercalation into B lattice causing decrepitation of boron particles prior to a subsequent hydrogenation (Remhof et al. 2012). But high concentration of Li may generate lithium borides (LiB, LiB_3, Li_7B_6) (Friedrichs et al. 2008; Çakanyildirim & Gürü 2008b).

3.2.1.2 Crystal and Vibrational Structures

$LiBH_4$ has an orthorhombic (o-$LiBH_4$, space group *Pnma*) structure at room temperature (Figure 3.6-a) where each cation (Li^+) is surrounded by four anions ($[BH_4]^-$) and vice versa. The tetrahedral $[BH_4]^-$ clusters (point group symmetry C_s) are distorted and aligned along two orthogonal directions (A. Züttel et al. 2003). It undergoes a first order phase transition into a hexagonal structure (h-$LiBH_4$, space group $P6_3mc$) at 107-118 °C (Figure 3.6-b) (A. Züttel et al. 2003; Orimo et al. 2007; Filinchuk et al. 2008), where the structure of $[BH_4]^-$ tetrahedron becomes more symmetric and less distorted (point group symmetry C_{3v}). This high temperature phase (h-$LiBH_4$) exhibits high conductivity on the order of 10^{-3} S cm^{-1} (above 117 °C), which is much higher than that

for the low temperature phase (Matsuo et al. 2007). The reported lattice parameters for orthorhombic and hexagonal $LiBH_4$ are summarised in Table 3.2.

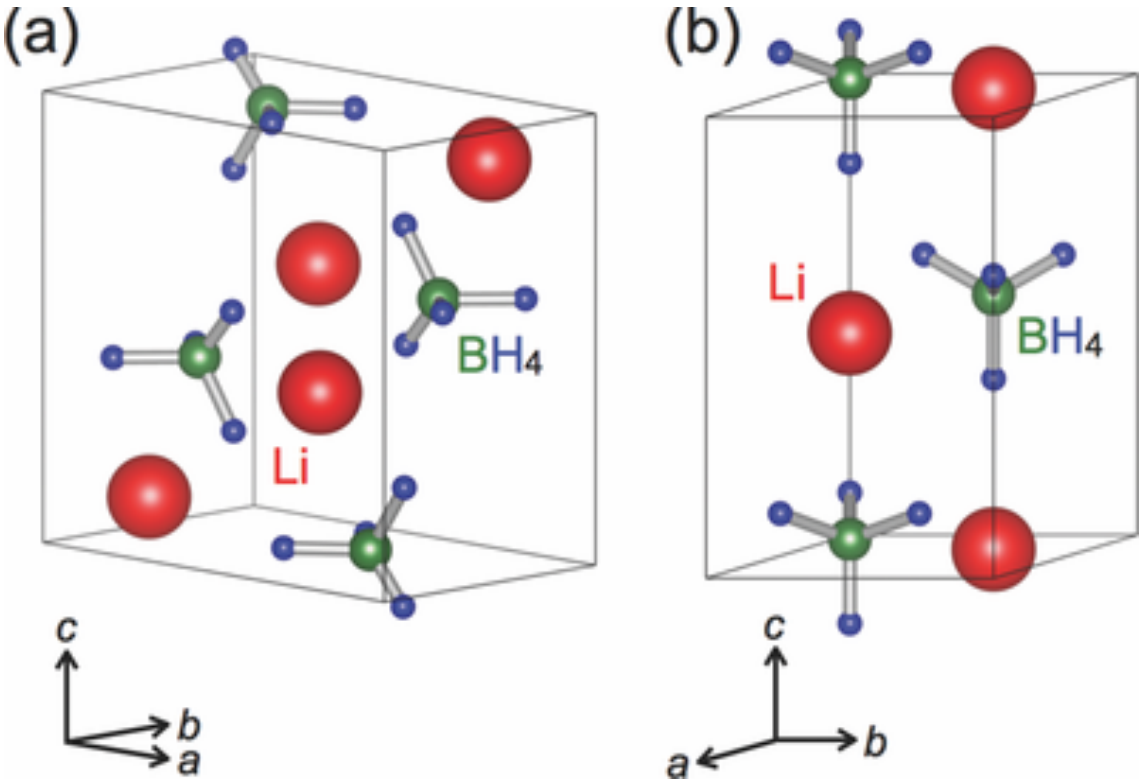

Figure 3.6 Illustration of the crystal structure of a) orthorhombic and b) hexagonal for $LiBH_4$ (Unemoto et al. 2014).

Table 3.2 Lattice parameters of low temperature (orthorhombic) and high temperature (hexagonal structure) phases of $LiBH_4$. All results are measured at atmospheric pressure.

	a Å	b Å	c Å	Volume Å^3	Temp. °C	Radiation Type	Reference
Orthorhombic	7.17858(4)	4.43686(2)	6.80321(4)	216.68	25	Synchrotron	(Soulié et al. 2002)
	7.1730(1)	4.4340(1)	6.7976(1)	216.20	25	Synchrotron	(Züttel 2003)
	7.1900(4)	4.4447(2)	6.8132(4)	217.73	25	Synchrotron	(Filinchuk et al. 2008)
	7.130(2)	4.3978(12)	6.806(2)	213.41	25	Synchrotron	(Roedern et al. 2016)
Hexagonal	4.268270(9)	4.268270(9)	5.931845(3)	109.37	109	Synchrotron	(Filinchuk et al. 2008)
	4.2667(2)	4.2667(2)	6.9223(8)	109.14	127	Neutrons	(Hartman et al. 2007)
	4.27631(5)	4.27631(5)	6.94944(8)	110.04	135	Synchrotron	(Soulié et al. 2002)
	4.3228(10)	4.3228(10)	7.0368(10)	113.88	262	Synchrotron	(Filinchuk et al. 2008)

For the vibrational modes of $LiBH_4$, 36 internal lattice vibrations exist due to the point group symmetry of the o-$LiBH_4$ structure (K B Harvey & McQuaker 1971), describing the bending and stretching modes of $[BH_4]^-$ (Gebert et al. 2011). All of them are Raman active and 15 of them may appear in the infrared (IR) (K B Harvey & McQuaker 1971). A total of 27 modes are identified by Racu et al. (2008) using high resolution Raman in the temperature range from -268 to 27 °C. In addition, the external lattice vibrations include 21 optical translatory modes, 12 optical libratory modes and 3 acoustical translatory modes, describing the motions between Li^+ and $[BH_4]^-$ (K B Harvey & McQuaker 1971). These external modes are often observed in the low wavenumber range.

In practice, the Raman spectrum of o-$LiBH_4$ at room temperature contains 9 fundamental bands that are observed in three major regions, consisting of: external modes (<350 cm^{-1}), B-H bending (1000-1350 cm^{-1}) and B-H stretching (2000-2500 cm^{-1}) (Gomes et al. 2002). It has been revealed that the isolated tetrahedral $[BH_4]^-$ ion has two triply degenerated IR active bands that are usually found at ~ 2300 cm^{-1} for B-H stretching and ~1100 cm^{-1} for B-H bending (D'Anna et al. 2013). In practice, strong Fermi resonances may cause extra bands in B-H stretching region (spread over ~100 cm^{-1}) (D'Anna et al. 2014). When the phase change occurs, the change of point group from C_s (o-$LiBH_4$, anisotropy structure) to the more symmetrical C_{3v} (h-$LiBH_4$, nearly isotropic) results in a simpler spectrum with the disappearance of the splitting modes (such as the bending peaks ν_2 and ν_2') (Gomes et al. 2002; Hagemann et al. 2009). A detailed Raman and FTIR assignment for $LiBH_4$ at room temperature will be given in Section 7.1.1.

3.2.1.3 H_2 Storage Properties

A. Züttel et al. (2003) observed a tiny release of 0.3 wt.% hydrogen during phase transition around 105 °C. However, the dehydrogenation of $LiBH_4$ normally starts after fusion at 270-280 °C. The molten $LiBH_4$ often shows bubbling-frothing effect that the liquid tends to bubble, forth, vaporize, spatter, or climb the containing surface, due to the gas evolution, their relatively low viscosities and high surface tensions (M Paskevicius et al. 2013). The presence of impurities, even in minor quantities, may inhibit the bubbling-frothing during melting (Vines 2016).

The major desorption of $LiBH_4$ occurs above 320 °C, reaching its maximum intensity at around 500 °C (when heated at 2 °C min^{-1} in a integrated gas flow), and results in a total of 9 wt.% of hydrogen release upon heating to 600 °C (A. Züttel et al. 2003). Besides H_2, the major dehydrogenation products are LiH determined by XRD (Orimo et al. 2005), $Li_2B_{12}H_{12}$ and amorphous B observed in *ex situ* and *in situ* Raman (Orimo et al. 2006; Reed & Book 2009) and NMR (Hwang et al. 2008). The desorption reaction can be partially reversed at 600 °C and 350 bar H_2 for 12 h (Orimo et al. 2005).

The formation of $Li_2B_{12}H_{12}$ may be caused by the reaction between $LiBH_4$ and diborane (B_2H_6) at relatively low temperatures (150–200 °C) or further polymerisation between borane species (e.g. B_2H_6 and/or higher boranes) (Friedrichs, Remhof, Hwang, et al. 2010). B_2H_6 is a toxic gas and decreases the hydrogen capacity. It is therefore not preferred in any system, even at an impurity level for $LiBH_4$ (Borgschulte et al. 2011). The evolution of B_2H_6 concurrently with the release of H_2 can be experimentally

observed in ultra-high vacuum (Kato et al. 2010) or within flowing inert gas (Liu et al. 2011).

The well-accepted decomposition pathways for $LiBH_4$ (Figure 3.7) are as follows:

$$LiBH_4 = LiH + B + 3/2H_2 \quad \textbf{13.9 wt. \%} \quad \textbf{Equation 3.11}$$

$$LiBH_4 = 5/6LiH + 1/12Li_2B_{12}H_{12} + 13/12H_2 \quad \textbf{10.0 wt. \%} \quad \textbf{Equation 3.12}$$

which implies that

- The maximum amount of H_2 evolution from $LiBH_4$ is about 13.9 wt%, since LiH is stable until 900 °C (Abbas et al. 2013);
- Reaction forming $Li_2B_{12}H_{12}$ is more thermodynamically favourable (El Kharbachi et al. 2012); however, $Li_2B_{12}H_{12}$ is unfavourable as it reduces the total amount of H_2 released and hinders the reversibility (Yan et al. 2015). .
- Dehydrogenation is temperature and pressure dependent. $Li_2B_{12}H_{12}$ trends to form under high temperature and pressure (Yan et al. 2012) and therefore might be suppressed by limiting the operating temperature as well as adjusting H_2 backpressure (Bösenberg et al. 2010).

It has to be noted that the enthalpy values marked on Figure 3.7 (Yan et al. 2012) are not mathematically matched (e.g. the sum of 61 kJ and 52 kJ equals 113 kJ that is higher than the marked 111 kJ). This is due to the fact that these values are collected from different literature (Smith & Bass 1963; Miwa et al. 2004; Ohba et al. 2006; Mauron et al. 2008) and are determined differently by experimental measurements or by theoretical calculations.

However, the dehydrogenation in practice may occur in multiple stages where different competing routes involving numbers of intermediates are followed simultaneously to construct the complex boron cluster. Thus, it is possible that the decomposition products may contain phases other than $Li_2B_{12}H_{12}$ after dehydrogenation.

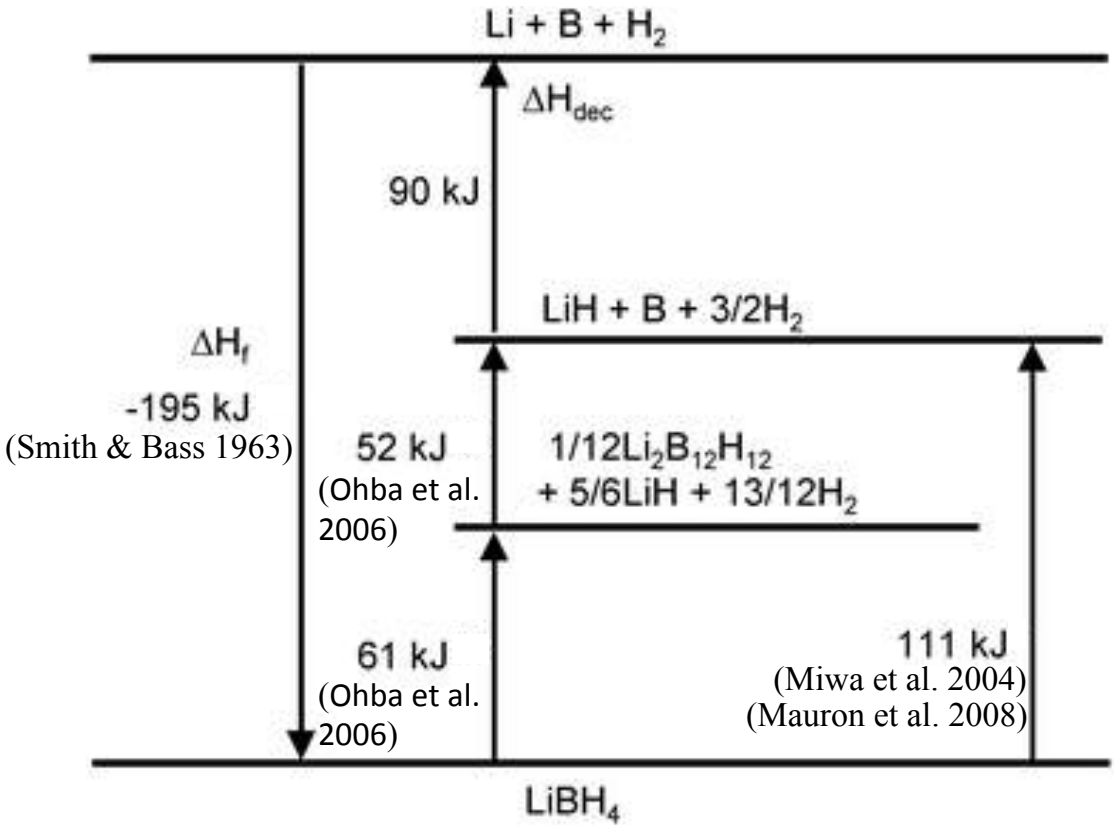

Figure 3.7 A simplified enthalpy diagram for the dehydrogenation of $LiBH_4$, involving the intermediate and neglecting the phase transitions, revised from (Yan et al. 2012).

3.2.1.4 Destabilization and Kinetics Modification

A large number of approaches have been demonstrated for tailoring the thermodynamics and modifying the kinetics of $LiBH_4$, which can be briefly divided into additives/catalyst, reactive hydride composites and nano-engineering (Paskevicius et al. 2017). Only a few of the most prominent candidates will be discussed in this section.

3.2.1.4.1 Additives/Catalyst

In general, additives, such as metals/non-metals, oxides, halides and hydrides, can effectively reduce the dehydrogenation temperatures. And some of them may improve the reversibility as well.

The 1st additive used to destabilize $LiBH_4$ was SiO_2 (A. Züttel et al. 2003): a mixture containing 75 wt.% SiO_2 leads to a significantly reduction in the dehydrogenation temperature of $LiBH_4$ to ~200 °C and allows ~ 9 wt.% hydrogen liberation from $LiBH_4$ when heated to 400 °C in an integrated gas flow. The addition of 30 wt.% TiF_3 into a $LiBH_4$-20 wt.% SiO_2 system can further reduce this onset temperature to 70 °C with a total of 8.3 wt.% hydrogen release below 500 °C (Zhang et al. 2008). However, the reaction products containing Li_2SiO_3 and/or Li_4SiO_4 may prevent the possibility of full reversibility (Mosegaard et al. 2008).

A general redox reaction between $LiBH_4$ and metal oxides ((Yu et al. 2009) can be written as:

$$xLiBH_4 + M_yO_z \xrightarrow{\Delta} Li_xM_yO_z + xB + 2xH_2 \qquad \textbf{Equation 3.13}$$

where M was an element and M_yO_z represented its oxide phase. Nale et al. (2011) proposed a trend of destabilization ability for several oxides: Fe_2O_3 > V_2O_5 > Nb_2O_5 > TiO_2 > SiO_2 (Nale et al. 2011).

Reactions between metals or hydrides and $LiBH_4$ are in general strongly depending on their atomic diffusivity (roughly indicated by melting point) (J. Yang et al. 2007). Additives with high diffusivity (e.g. Mg, Al, MgH_2, CaH_2, $CaNi_5$) normally form their corresponding metal borides, as predicted by thermodynamic calculations (Siegel et al. 2007; Meggouh et al. 2015); whereas the rest may either remain unreacted (e.g.Cr, TiH_2) up to a certain temperature, or form stable metal hydrides (e.g. V, Sc, Ti). Several metal hydrides, such as MgH_2 and CaH_2, can significantly destabilise the $LiBH_4$, forming the so-called Reactive Hydride Composites (RHCs) mixtures (Yuan et al. 2011), and will be discussed in next Section.

Moreover, metal halides, such as TiF_3, $TiCl_3$, $FeCl_2$, $CoCl_2$, $NiCl_2$, ZnF_2 $LaCl_3$ and $CeCl_3$, can effectively reduce the dehydrogenation temperature of $LiBH_4$, through a solid-state cation exchange interaction (Au, Jurgensen, et al. 2008; Zhang & Liu 2010; B. J. Zhang et al. 2011). For example, the $LiBH_4 + 0.2MgCl_2 + 0.1TiCl_3$ system is one of the most promising systems, which has a low dehydrogenation temperature starting at 60 °C through four dehydrogenation steps. This temperature reduction is due to the ion-exchange interactions of $LiBH_4$ with $TiCl_3$ and $MgCl_2$, which form less stable borohydrides, such as $Ti(BH_4)_3$ (dehydrogenation at around 25 °C) and $Mg(BH_4)_2$ (dehydrogenation at 260-280 °C) (Au, Spencer, et al. 2008). This system desorbs 5 wt.% of hydrogen (without releasing B_2H_6) at 400 °C and absorbs 4.5 wt.% of hydrogen at 600 °C and 70 bar (Au, Spencer, et al. 2008).

In fact, due to its strong reduction property, $LiBH_4$ may react with most of the additives, though these additives are sometimes called by ‘catalyst’. Molten $LiBH_4$ can even react

with Au, the noblest metal, forming a Li-Au alloy (Mosegaard et al. 2008). Recently, porous Li_3BO_3 was proposed as a catalyst that facilitates the decomposition and reformation of $[BH_4]^-$, as well as accelerates the kinetics (Ma et al. 2016). This is evidenced by its constant X-ray peak intensity as well as no additional phases are observed by XRD measurements at various stages during cycling.

3.2.1.4.2 Reactive Hydride Composites

The concept of Reactive Hydride Composites (RHCs) is reported independently by Vajo et al. (2005) and Dornheim et al. (2006). It describes the addition of a second hydride to a main hydride matrix (Figure 3.8), in which case, the composite has a more stable dehydrogenation product than that of the original hydrides. So that the primary hydride (or both) is destabilized (Dornheim 2011). However, the issue of sluggish kinetics still remains as one of the major challenges for this novel class of material (Pistidda et al. 2014). And the addition of a second compound may lead to a reduction of the overall H_2 storage capacities due to an increased weight.

Many $LiBH_4$-based RHCs systems have been demonstrated, such as $LiBH_4/MgH_2$ (Vajo et al. 2005), $LiBH_4/CaH_2$ (Pinkerton & Meyer 2008), $LiBH_4/CeH_2$ (Ibikunle et al. 2009), $LiBH_4/YH_3$(Shim et al. 2010), $LiBH_4$-$LiAH_4$ (J. F. Mao, Guo, et al. 2009), $LiBH_4$–Mg_2NiH_4 (Javadian, Zlotea, et al. 2015), etc.

The $2LiBH_4$-MgH_2 RHCs is studied most intensely with a theoretical H_2 capacity of 11.4 wt.% (Price et al. 2010). It possesses a two-stage dehydrogenation (Equation 3.14), in which the formed MgB_2 reduces the overall reaction enthalpy (Figure 3.9) to 40-60

kJ mol^{-1}. This lower enthalpy corresponds to a dehydrogenation temperature of 169 °C at 1 bar H_2 (Vajo et al. 2005; Alapati et al. 2006; Cova et al. 2015), which is much lower than the 370 °C for pure $LiBH_4$ (Mauron et al. 2008).

$$2LiBH_4 + MgH_2 \xrightarrow{\Delta} 2LiBH_4 + Mg + H_2 \xrightarrow{\Delta} 2LiH + MgB_2 + 4H_2 \qquad \textbf{Equation 3.14}$$

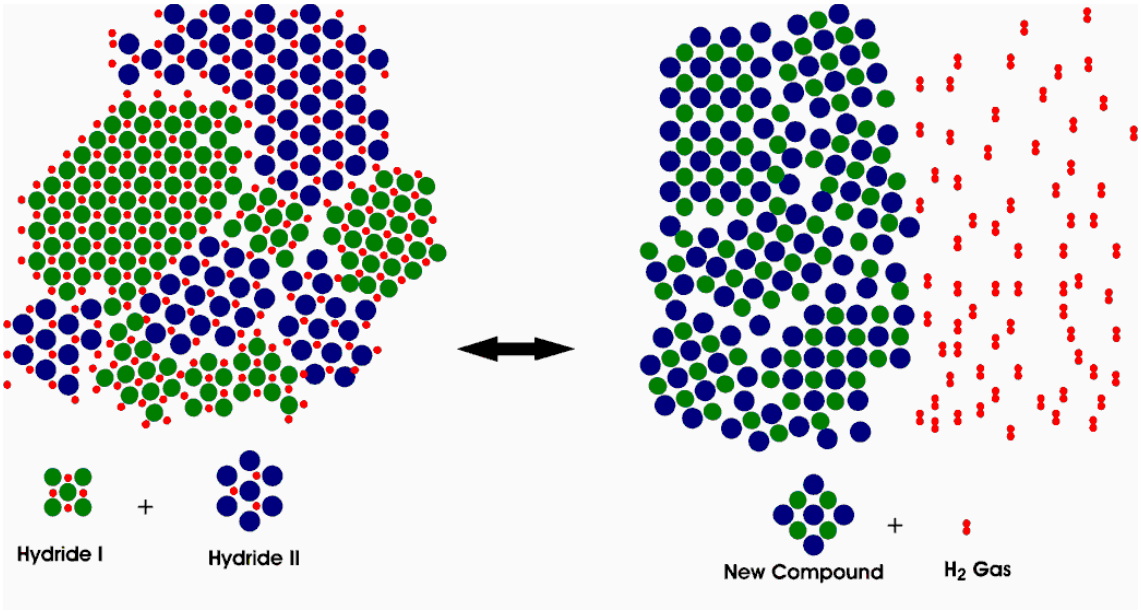

Figure 3.8 A schematic of the reaction mechanism for the Reactive-Hydrides-Composites (RHCs) (Dornheim 2011).

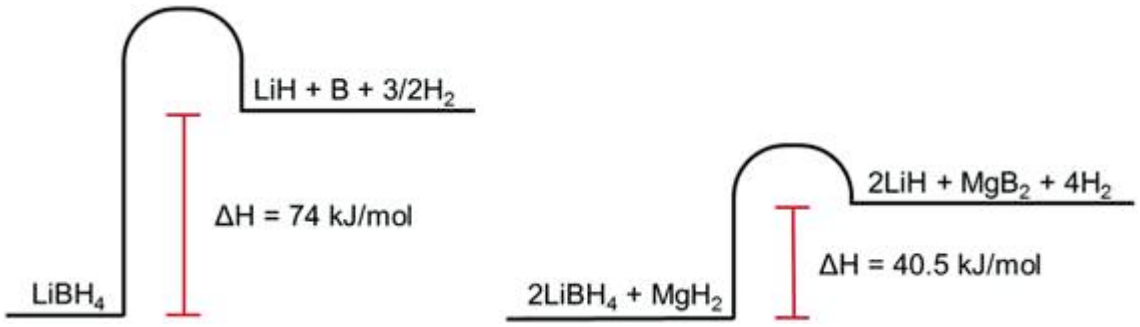

Figure 3.9 A schematic illustration of the overall enthalpy change (ΔH, kJ mol^{-1} H_2) for the $2LiBH_4$-MgH_2 Reactive-Hydride-Composites (RHCs) in contrast to $LiBH_4$ (Paskevicius et al. 2017).

Moreover, MgB_2 also affects the rehydrogenation through its open layered structure and the non-covalent bonding between Mg and B (De la Mora et al. 2002; Paskevicius et al. 2017). As a consequence, the rehydrogenation of $LiBH_4$ from 2LiH-MgB_2 requires more moderate conditions (Vajo et al. 2005; Barkhordarian et al. 2007) than that from LiH, B (Orimo et al. 2005). Nevertheless, due to the long-range diffusion route in a bulk sample, dehydrogenation and rehydrogenation of this RHCs still require relatively high temperatures, such as 250-350 °C (Dornheim 2011). Techniques, such as nano-confinement, can further reduce these temperature requirements as well as enhance the kinetics (Gosalawit-Utke et al. 2011; Hu et al. 2014)

3.2.1.4.3 Nano-engineering

The material properties are size-dependent. They can be significantly changed in nano-scale (10^{-9} m), exhibiting extra-high reactivity because of increased surface area, intimate interaction on contact area, increased numbers of atoms in the grain boundaries and significantly reduced diffusion distance (Berube et al. 2008; C. Liu et al. 2010). For H_2 storage, the nano-scale materials show potential in facilitating hydrogen sorptions and enhancing reaction kinetics (Callini, Aguey-Zinsou, et al. 2016).

3.2.1.4.3.1 Nanoparticles

The nanoparticles added into borohydrides significantly reduce the dehydrogenation temperature and improve reversibility (Li et al. 2014; Zhang et al. 2015; J. Wang et al. 2016; Puszkiel et al. 2017). For instance, the addition of 25 wt.% nano-sized Ni (< 100 nm) to $LiBH_4$, reduces the dehydrogenation peak temperature by 50 °C to 423 °C (when heated by 5 °C min^{-1} in flowing He, Figure 3.10), and improves the reversible hydrogen

content (from 4.3 wt.% for Ni-free sample) to 10.8 wt.% as a consequence of the catalyst effect of Ni_4B_3 (Li et al. 2014). This destabilization effect on dehydrogenation temperature is not observed when bulk Ni (41 μm) is used (Xia et al. 2009).

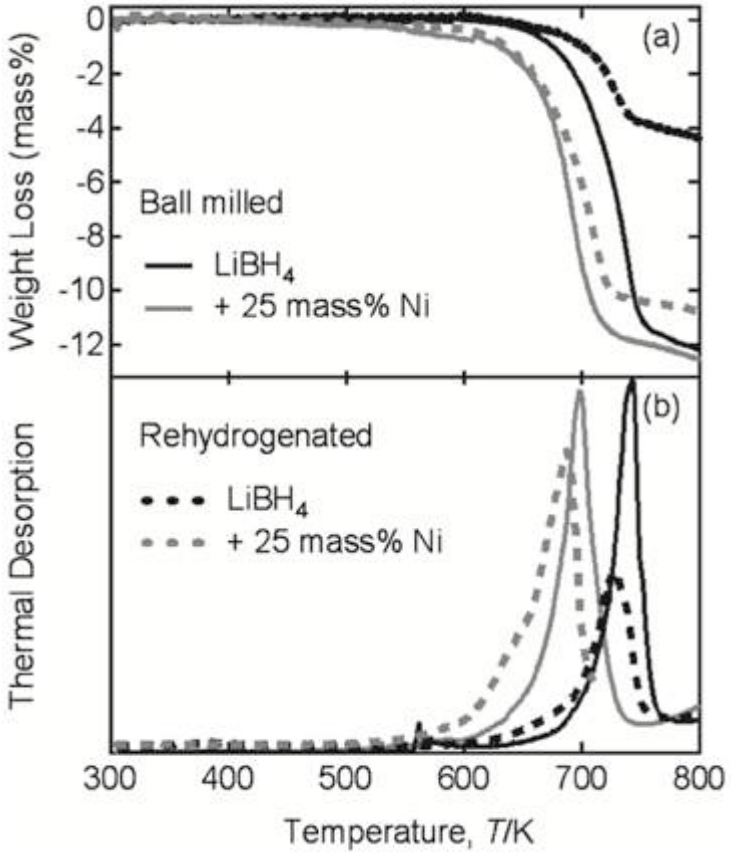

Figure 3.10 H_2 desorption properties exhibited in a) thermogravimetry (TG) and b) quadropole mass spectroscopy for a $LiBH_4$ – 20.wt.% nano-Ni system (Li et al. 2014).

3.2.1.4.3.2 Nano-confinement

Nano-confinement is another popular approach to improve both kinetic and thermodynamic properties of borohydrides. This concept is to use nanoporous materials as scaffolds producing nano-sized hydrides through a melt-infiltration approach (de Jongh & Eggenhuisen 2013). The commonly used scaffolds materials are carbon-based,

silicon-based, and metal-organic-frameworks (MOFs) and metal oxides (MO_x) (Table 3.3) (Nielsen et al. 2011; Gimeno-Fabra et al. 2012; Guo et al. 2017; Xu et al. 2017).

The scaffolds prevent the particle growth and agglomeration for the nano-confined hydride as well as limit the phase segregation of the products after dehydrogenation. In addition, the chemical nature of the scaffolds also affects the properties leading to high hydrogen mobility (Suwarno et al. 2017). However, for most of these composite materials, the system gravimetric and volumetric hydrogen capacities decrease due to the weight and size of the scaffold.

Table 3.3 Common used porous materials utilized for nano-confinement of borohydrides.

Category	Full name	Abbreviation	Avg. diameter nm
Carbon-based	High surface area graphite	HSAG	<4
	Activated carbon	AC	<4
	Ordered Mesoporous Carbon No.3	CMK-3	~5
	Resorcinol-formaldehyde carbon aerogels	RF-CA	7-25
	Resorcinol-formaldehyde carbon cryogels	RF-CC	7-25
	Carbon nanocages	CNCs	~30
Silica-based	Mobil Composition of Matter No.41	MCM-41	1.5-10
	Santa Barbara Amorphous type material No.15	SBA-15	5-30
MOFs	Hong Kong University of Science and Technology No.1	HKUST-1	0.9-1.6
MO_x	Porous ZnO/$ZnCo_2O_4$	ZZCO	7-10
	Porous $NiMnO_3$		~12

The nanoconfinement of $LiBH_4$ by melt-infiltration is usually achieved by heating the $LiBH_4$ in a H_2 backpressure to temperatures just above its melting point. Due to capillary action (Gross et al. 2008), the molten $LiBH_4$ (mainly Li^+ and $[BH_4]^-$) is then drawn into the open porous structures, resulting a confinement within the host material.

The applied H_2 pressure not only suppresses the decomposition of $LiBH_4$ (Pinkerton et al. 2007) but also prevents chemical reactions with the scaffold materials, especially for silica-based materials (e.g. requires ~ 100 bars H_2) (Ngene, Adelhelm, et al. 2010).
The nanoconfined $LiBH_4$ loses its long-range order structure (i.e. reduced crystallinity) and is therefore no longer visible in the XRD pattern (Gross et al. 2008). Thus, a successful loading can often be distinguished from the diffraction results as well as a significant reduction in the measured surface area and pore volume of the scaffold using techniques such as Brunauer–Emmett–Teller (BET) method (Ngene, Adelhelm, et al. 2010; X. Liu et al. 2010; Shao et al. 2014).

The nanoconfined $LiBH_4$ usually has a much lower dehydrogenation temperature and a relatively stable reversibility. For example, after successfully nanoconfined into a highly ordered porous carbon with an average pore size of 2 nm, the $LiBH_4$ becomes highly disordered, exhibiting no signal correlated to phase transition or fusion by Differential Scanning Calorimetry (DSC). The dehydrogenation onset temperature is significantly reduced from 460 °C (bulk $LiBH_4$) to 220 °C (X. Liu et al. 2010).

The pore size of scaffolds is one of the critical parameters that determine the overall performance of nanoconfined $LiBH_4$. For example, the reversible hydrogen content at the 3rd cycle preserves up to 70% of the initial value when nanoconfined in a microporous activated carbon (mean diameter < 2 nm). However, only 40% of the initial content can be achieved when nanoconfined in a carbon aerogel scaffolds (mean diameter ~25 nm) (Gross et al. 2008). Decreasing pore size may also increase the hydrogen release and uptake rate; however, this is more likely caused by a kinetic effect

(Paskevicius et al. 2017). In addition, the unfavourable diborane and closo-boranes may be suppressed using carbon scaffolds with smaller pores (Liu et al. 2011).

3.2.2 Sodium Borohydrides – $NaBH_4$

$NaBH_4$ has relatively large H_2 storage capacities, both gravimetrically (10.7 wt%) and volumetrically (114.5 kg H_2 m^{-3}). It (hydrogen-storage grade: > 98%, £ 5.2 per g) is much less expensive than $LiBH_4$ (hydrogen-storage grade: > 90%, £ 13 per g) (Sigma Aldrich 2018).

3.2.2.1 Synthesis

Several synthesis approaches using different precursors have been investigated for commercial production of $NaBH_4$.

Sodium hydride (NaH) is one of the most common precursors. For instance, it can generate $NaBH_4$ through a combination reaction when it reacts with diborane (B_2H_6) in diglyme (James & Wallbridge 1970):

$$2NaH + B_2H_6 = 2NaBH_4 \qquad \textbf{Equation 3.15}$$

One of the common commercial production routes for $NaBH_4$ is the Schlesinger Process (Schlesinger, Brown & Finholt 1953). It heats NaH and trimethyl borate ($B(OCH_3)_3$) in mineral oil at 225-280 °C. The generated $NaBH_4$ is then extracted from the reaction mixture using organic solvents (ammonia, ethylene diamine or diethylene glycol dimethyl ether) that can be further removed through heat-treatment in vacuum

(Soloveichik 2007; Çakanyildirim & Gürü 2008a). This reaction is also known as Rohm-Haas process performed in an autoclave in an inert atmosphere (Jain, Jain, et al. 2010).

$$4NaH + B(OCH_3)_3 = NaBH_4 + 3NaOCH_3 \qquad \textbf{Equation 3.16}$$

Besides NaH, B_2H_6 can react with the elemental Na or NaOH that yields $NaBH_4$ and by-products. The precipitated $NaBO_2$ in Equation 3.18 can be further recycled as discussed in Section 2.4 (Kojima & Haga 2003).

3.2.2.2 Crystal and Vibrational Structures

At room temperature and under atmospheric pressure, $NaBH_4$ has a NaCl-like Face-Centred Cubic (FCC) structure (space group *Fm-3m*), although it is sometimes described as space group *F-43m*, resulting from the two different orientations of the $[BH_4]^-$ ion (Figure 3.11-a) (Mao & Gregory 2015). A fully disordered *F-43m* model is identical to the space group *Fm-3m* (Davis & Kennard 1985; Fischer & Züttel 2004). Moreover, $NaBH_4$ shows different structures at low temperature or under pressures. For instance, below -86 °C, it undergoes a disorder-order phase transition to a tetragonal phase (space group $P4_2/nmc$) (Figure 3.11-b) (Stockmayer & Stephenson 1953; Abrahams & Kalnajs 1954; Babanova et al. 2010). With increasing pressure, it undergoes a structural transitional into the tetragonal phase at 6.3 GPa (Figure 3.11-b) and further to an orthorhombic phase (space group *Pnma*) above 7.6 GPa (Figure 3.12) (Kumar & Cornelius 2005; Filinchuk et al. 2007).

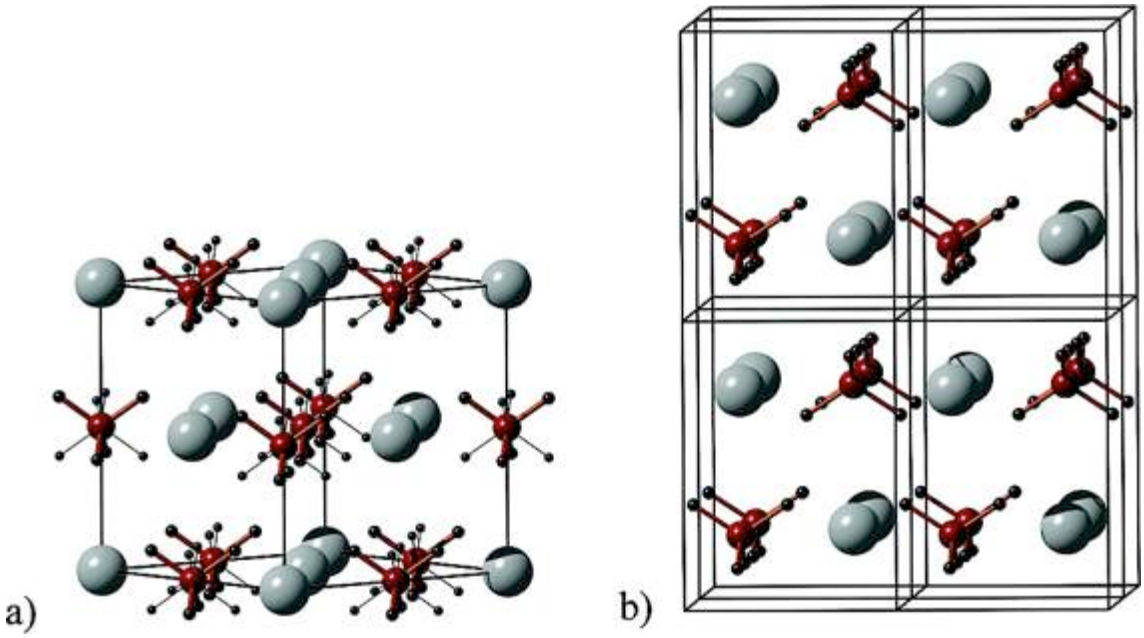

Figure 3.11 Crystal structure of $NaBH_4$ phases: a) cubic, *Fm-3m* and b) tetragonal, *$P4_2/nmc$*. Two orientations of the disordered $[BH_4]^-$ group for the cubic phase are shown by thin and bold lines (Babanova et al. 2010).

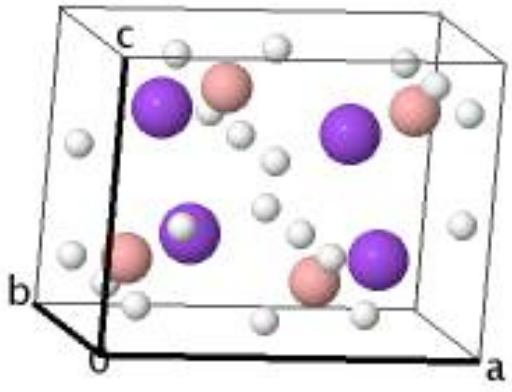

Figure 3.12 Crystal structure of the orthorhombic $NaBH_4$ phase (space group *Pnma*) at room temperature and under 11.2 GPa (Kumar & Cornelius 2005).

The reported lattice parameters for these structures are summarised in Table 3.4.

Table 3.4 Lattice parameters of $NaBH_4$.

	a Å	b Å	c Å	V $Å^3$	T °C	P GPa	Radiation Type	Reference
Cubic		6.13080(10)		230.44	-73	atm	Synchrotron	(Filinchuk & Hagemann 2008)
		6.139(9)		231.36	25	atm	X-ray	(Soldate 1947)
		6.1635(5)		234.14	25	atm	X-ray	(Abrahams & Kalnajs 1954)
		6.1506(3)		232.68	25	atm	Synchrotron	(Kumar & Cornelius 2005)
		6.14357(14)		232.08	25	atm	Synchrotron	(Roedern et al. 2016)
Tetragonal	4.37062(4)		5.95094	113.68	-92	atm	Synchrotron	(Babanova et al. 2010)
Orthorhombic	7.2970(11)	4.1166(5)	5.5692(7)	167.29	25	11.2	Synchrotron	(Filinchuk et al. 2007)

* atm = atmospheric

In theory, depending on the four vibrations modes of $[BH_4]^-$ in $NaBH_4$ at room temperature and atmospheric pressure, 7 internal vibrations (two A_1, B_1, two B_2 and two E symmetries) can produce Raman scattering and only B_2 and E symmetries may be infrared active (K. B. Harvey & McQuaker 1971). Similarly to $LiBH_4$ vibrations, these internal modes are located from 1050-1300 cm^{-1} for $[BH_4]^-$ bending and 2100-2500 cm^{-1} for $[BH_4]^-$ stretching. Moreover, 6 external lattice vibrations are available, including optical translatory (B_2, E symmetries) and libratory (A_2, E symmetries), and acoustical translatory (B_2, E symmetries) origin. In theory, all of them are Raman and IR active, except that A_2 symmetry is IR inactive (K. B. Harvey & McQuaker 1971). Only a limited number of absorption peaks are observed using IR at low temperature by K. B. Harvey & McQuaker (1971). A detailed Raman and FTIR assignment for $NaBH_4$ at room temperature will be given in Section 8.1.1.

3.2.2.3 H_2 Storage Properties

During thermolysis, the solid-state $NaBH_4$ starts to release a small amount of H_2 (~1 wt.%) at around 150 °C (Urgnani et al. 2008). Nevertheless, the major dehydrogenation occurs above 450 °C when heated in an inert atmosphere or at 534 ± 10 °C in 1 bar of H_2 (Martelli et al. 2010). A total of 10.4 wt.% hydrogen is measured when heated up to 600 °C in flowing helium, which is close to the theoretical gravimetric capacity (10.8 wt.%) (Urgnani et al. 2008). Fusion occurs at a temperature slightly higher than 500 °C (Stasinevich & Egorenko 1968; Ley et al. 2014).

First principle calculations suggest that H ions locally convert $NaBH_4$ into NaH and BH_3 molecules during decomposition (Çakır et al. 2011). The BH_3 may decompose immediately, releasing H_2 and leaving B, or it may escape to the gas phase forming B_2H_6. However, in reality, NaH is very unlikely to be observed in the reaction products. This is because it is less thermally stable than $NaBH_4$ (e.g. decomposition temperature: 425 °C for NaH < 450 °C for $NaBH_4$) (Martelli et al. 2010). So any NaH precipitated will simultaneously decompose into its constituent elements. Therefore, for the evidence of a single plateau observed in the isotherms, a one-step decomposition mechanism for $NaBH_4$ has been proposed (Martelli et al. 2010), with an enthalpy and entropy of -108 ± 3 kJ mol^{-1} H_2 and 133 ± 3 J K^{-1} mol^{-1} H_2, respectively:

$$\boldsymbol{NaBH_4 = Na + B + 2H_2} \quad \textbf{10.7 wt.\%} \qquad \textbf{Equation 3.17}$$

However, like other borohydrides, the real decomposition process of $NaBH_4$ may be more complex, and a series of intermediate phases may be involved as a function of temperature and pressure (Mao & Gregory 2015). For instance, the formation of

$Na_2B_{12}H_{12}$ during the decomposition of $NaBH_4$-based systems has been confirmed using Fourier Transformation Infrared Spectroscopy (FTIR) (Mao et al. 2011) and Nuclear Magnetic Resonance (NMR) (Garroni et al. 2011; Ngene, van den Berg, et al. 2011). The formation mechanism of $Na_2B_{12}H_{12}$ is not fully understood, possibly due to the reaction between B_2H_6 released with the remaining $NaBH_4$ (Caputo et al. 2010; Çakır et al. 2011).

3.2.2.4 Destabilization and Kinetics Modification

To address issues such as relatively high thermal stability, slow H_2 exchange kinetics and limited reversibility of thermolysis, several strategies have been demonstrated over the past decade, such as additive destabilization, nano-engineering and chemical modification (Mao et al. 2011).

Ni-containing additives, such as nano-sized Ni (20 nm), NiF_2, $NiCl_2$, Ni_3B, or Ni supported on Si/Al_2O_3, are popular additives used to destabilize the dehydrogenation of $NaBH_4$, exhibiting effective reduction in the dehydrogenation peak temperatures (Humphries et al. 2013). For instance, the nano-sized Ni (2 mol%) decreases the dehydrogenation peak by 27 °C (from 510 °C for pure $NaBH_4$) to 483 °C, whilst the same size Ni (65 wt.%) on Si/Al_2O_3 leads to a 61 °C reduction when heated by 2 °C min^{-1} in dynamic vacuum (Humphries et al. 2013). These reductions are mainly due to the fact that more thermodynamically favourable Ni_xB_y species (such as Ni_3B, Ni_2B and Ni_3B_4) are formed as a consequence of chemical reactions between Ni and $NaBH_4$. Besides, the destabilization effect on the dehydrogenation using a range of selected nano-sized particles, such as Ti (65 nm), Al (80 nm), Pd (25 nm), Cr (30 nm), Fe (25

nm), Ag (30-50 nm), has also been compared. Among these, nano-sized Pd exhibited the best performance, by reducing the peak temperature by 90 °C (from 510 °C for plain $NaBH_4$) to 420 °C (when heated by 2 °C min^{-1} in vacuum) (Humphries et al. 2013).

In addition, other commonly used additives are hydrides and transition metal fluorides.

Metal hydrides dopants, such as MgH_2, CaH_2, TiH_2, $Ca(BH_4)_2$, $LiAlH_4$, Mg_2NiH_4, are demonstrated (J F Mao et al. 2009; Garroni et al. 2010; Mao et al. 2012; Afonso et al. 2013), exhibiting notable reduction in decomposition temperatures. Among these dopants, the $NaBH_4/MgH_2$ is one of the most well-studied RHCs (J. F. Mao, Yu, et al. 2009; Garroni et al. 2009; Kurko et al. 2013).

Fluorides, such as TiF_3, MnF_3, FeF_3, ZnF_2, YF_3, LaF_3, NdF_3, HoF_3 and fluorographite have been demonstrated as additives for $NaBH_4$ (Z. G. Zhang et al. 2011; Zou et al. 2012; Chong et al. 2013; Kalantzopoulos et al. 2014; Chong et al. 2014; Zhang et al. 2014). Due to the similar ionic radius in contrast to H^-, the fluorine substitution may tune the thermodynamic and kinetic properties of the thermolysis for $NaBH_4$. For instance, H-F exchange has been observed at 200-215 °C in the $NaBH_4$-$NaBF_4$ system (Rude et al. 2013). This system decomposes at a lower temperature (300 °C) than pure $NaBH_4$ (476 °C) as observed by thermogravimetric analysis in flowing He.

The nano-engineering approaches include nano-confinement through melt infiltration into scaffolds (such CMK-3, SBA-15) (Ngene, van den Berg, et al. 2011; Ampoumogli et al. 2011; Peru et al. 2013) and encapsulated into core-shell materials (such as Co, Cu,

Fe, Ni, Sn) (Christian & Aguey-Zinsou 2012; Christian & Aguey-Zinsou 2013). Moreover, the chemical modification refers to enhancing the reaction kinetics of H_2 formation using combination of protic- ($H^{\delta+}$) and hydridic- ($H^{\delta-}$) hydrogen atoms such as the $NaBH_4$-$NaNH_2$ system (Chater et al. 2007; Somer et al. 2010; Wu et al. 2012; Pei et al. 2017). These approaches are not the focus of this work.

3.2.3 Potassium Borohydrides – KBH_4

KBH_4 has a relatively large gravimetrical H_2 storage density of 7.4 wt.% in theory. It is very similar to $NaBH_4$ in terms of structure and dehydrogenation properties. But it is less studied than other alkali metal borohydrides, perhaps due to its relatively high thermal stability.

3.2.3.1 Synthesis

KBH_4 was firstly synthesised through reaction of B_2H_6 with potassium tetramethoxyborohydrde $KB(OCH_3)_4$ (Schlesinger, Brown, Hoekstra, et al. 1953):

$$2B_2H_6 + 3KB(OCH_3)_4 = 3KBH_4 + 4B(OCH_3)_3 \qquad \textbf{Equation 3.18}$$

In industry, KBH_4 is often made through chemical reaction between $NaBH_4$ and KOH (Banus & Bragdon 1955):

$$NaBH_4 + KOH = KBH_4 + NaOH \qquad \textbf{Equation 3.19}$$

Alternatively, it can be prepared by a double-replacement reaction whereby $NaBH_4$ react with potassium thiocyanate (KCNS) in an amine or a nitrile solution (Bryant et al. 1961). More recently, a synthesis approach through mechano-chemical reaction of saline hydrides (such as NaH, CaH_2 and MgH_2) with dehydrated borates (KBO_2) at room temperature has been proposed (Li et al. 2003)

3.2.3.2 Crystal and Vibrational Structures

At room temperature, KBH_4 has a face-centred cubic (FCC) structure (space group *Fm-3m*), where the K^+ cation and $[BH_4]^-$ anion form a NaCl-type arrangement (Luck & Schelter 1999). It undergoes a structure transition to a tetragonal phase (space group $P4_2/nmc$) below -203 °C (Renaudin et al. 2004), to tetragonal (space group $P42_1c$) at 3.8 GPa, to orthorhombic (space group *Pnma*) at 6.8 GPa (Kumar et al. 2008). This structural evolution is associated with the rotation and deformation of $[BH_4]^-$ as well as shifts of the ions. The first-principle calculation suggests the structure change leads to a change in electronic mechanism and the material stability (D.-H. Wu et al. 2015). The reported lattice parameters for these structures are summarised Table 3.4.

In theory, the vibrations mode of $[BH_4]^-$ in KBH_4 included 4 internal vibrations (A_1, E, and two F_2 symmetries) that all could produce Raman scattering, but only F_2 vibration symmetry could be viewed in the IR (K. B. Harvey & McQuaker 1971). These internal modes are located from 1050-1300 cm^{-1} for $[BH_4]^-$ bending, and from 2100-2500 cm^{-1} for $[BH_4]^-$ stretching. Moreover, 3 external lattice vibrations are available, including optical translatory (F_2 symmetry) or libratory (F_1 symmetry) and acoustical translatory

(F_2 symmetry) origin. A detailed Raman and FTIR assignment for KBH_4 at room temperature will be given in Section 9.1.1.

Table 3.5 Lattice parameters of KBH_4.

	a Å	b Å	c Å	V Å^3	T °C	P GPa	Radiation Type	Reference
Cubic		6.72556(12)		304.22	20	atm	Synchrotron	(Dovgaliuk et al. 2014)
		6.7272(5)		304.44	25	atm	X-ray	(Abrahams & Kalnajs 1954)
		6.7280(8)		304.55	25	atm	X-ray	(Luck & Schelter 1999)
		6.6897(3)		232.68	25	0.5	X-ray	(Kumar et al. 2008)
Tetragonal	4.4754(2)		6.362(2)	127.45	RT	4	X-ray	(Kumar et al. 2008)
Orthorhombic	6.976(6)	4.933(4)	5.111(3)	175.88	25	20	X-ray	(Kumar et al. 2008)

* atm = atmospheric

3.2.3.3 H_2 Storage Properties

The dehydrogenation of KBH_4 starts from 550 °C (heated by 5 °C min^{-1} in flowing Ar) in solid state as the melting point is 605-625 °C (Orimo et al. 2004; M Paskevicius et al. 2013). The zirconium tetrachloride ($ZrCl_4$) has been demonstrated as one of the promising additives exhibiting synergic effect (Kumar et al. 2017): $ZrCl_4$ decreases the activation energy of dehydrogenation from 274 ± 12 kJ mol^{-1} to 162 ± 6 kJ mol^{-1}, leading to a notable 200 °C decrease to 350 °C in dehydrogenation onset temperature (when heated by 5°C min^{-1} in flowing Ar).

In general, the decomposition of KBH_4 may go through different pathways as follows:

$KBH_4 = K + B + 2H_2$ **7.5 wt.%** **Equation 3.20**

$KBH_4 = KH + B + 1.5H_2$ **5.6 wt.%** **Equation 3.21**

Thermodynamic calculations suggest that dehydrogenation into K, B and H_2 is the most suitable pathway (Figure 3.13) (Kumar et al. 2017). However, the vapour pressure of potassium may be significantly higher at this relatively high temperature where the reaction occurs. The moveable gaseous potassium may be lost, causing contamination in the vessels connected to the storage tank and a poor reversibility. This becomes a big issue for its viable commercial application (Kumar et al. 2017).

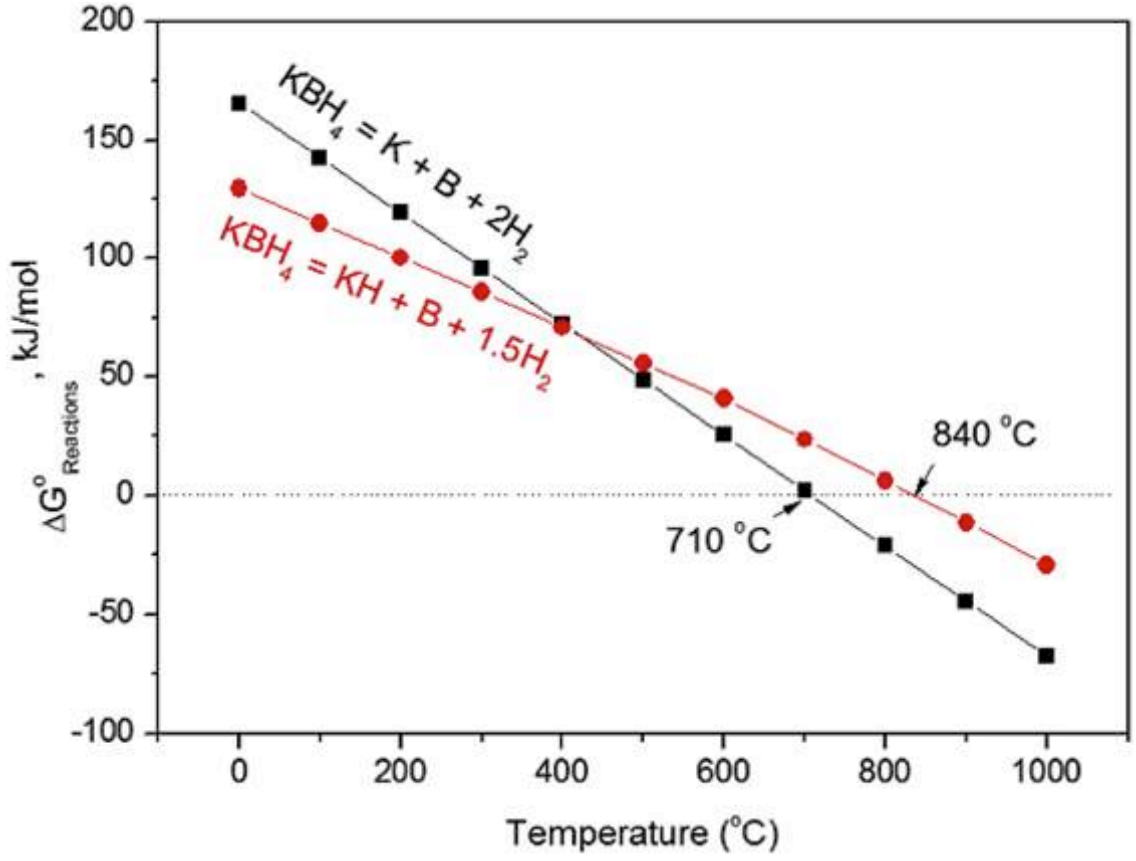

Figure 3.13 The calculated Gibbs free energy of KBH_4 dehydrogenation reactions at 1 bar H_2. The databases used are Enthalpy-Entropy-Capacity (HSC) version 6.0 and Fact-Sage version 6.1 (Kumar et al. 2017).

Nevertheless, similar to other alkali metal borohydrides, the decomposition mechanism of KBH_4 might be more complex. Theoretical calculations suggest $K_2B_{12}H_{12}$ could be one of the intermediate phases during decomposition (Kim & Sholl 2010; Guo et al. 2013).

3.3 Bimetallic Borohydrides

In general, more than 64 different types of bimetallic borohydrides and about 14 trimetallic borohydrides have been experimentally investigated (Paskevicius et al. 2017). Their structure and properties strongly depends on the more electronegative metal, as explained in Section 3.1.2.

$LiK(BH_4)_2$ is the first investigated bimetallic borohydrides (Nickels et al. 2008). At room temperature, it has an orthorhombic (space group *Pnma*) crystal structure (a = 7.91337 Å, b = 4.49067 Å, c = 13.84396 Å, V = 491.96 $Å^3$) and a 10.6 wt.% theoretical H_2 gravimetric capacity (Nickels et al. 2008). It can be synthesised through mechanochemistry using $LiBH_4$ and KBH_4. However, melting or heat treatment does not yield its formation (Ley et al. 2014). Therefore, its formation is pressure-induced. Although Nickels et al. (2008) reported a fusion temperature at 240 °C for the $LiK(BH_4)_2$ and suggested that its dehydrogenation temperature is higher than $LiBH_4$ but lower than KBH_4; the recent research found that it is a metastable phase that dissociates into $LiBH_4$ and KBH_4 above 95 °C (Kim & Sholl 2010; Ley et al. 2014).

3.4 Closo-boranes Structure

A series of boranes were investigated in the 1960s, which can be subdivided into arachno ($[B_nH_{n+5}]^-$), nido- ($[B_nH_{n+3}]^-$) and closo- ($[B_nH_n]^{2-}$, n>5) boranes (Figure 3.13) (Hansen et al. 2016; Sethio et al. 2017). Their stabilities increase with the structural complexity. The Density Functional Theory (DFT) calculations propose that $Li_2B_{10}H_{10}$ and $Li_2B_{12}H_{12}$ are the most stable phase among the $Li_2B_nH_n$ (n=5-12) and $Li_nB_nH_m$ (m≤4n) compounds (Ohba et al. 2006; Huang et al. 2016).

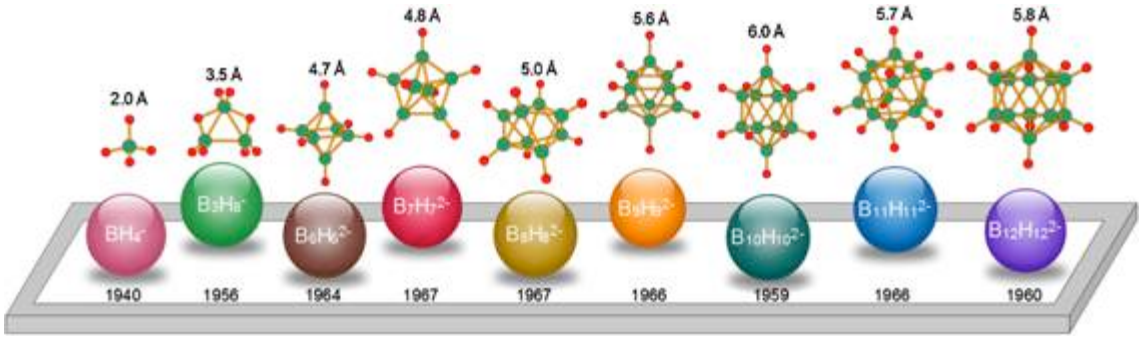

Figure 3.14 A schematic of arachno ($[B_nH_{n+5}]^-$), nido- ($[B_nH_{n+3}]^-$) and closo- ($[B_nH_n]^{2-}$, n>5) borane anions. The year when they are firstly synthesized and the longest distance between their terminal H-atoms are listed (Hansen et al. 2016).

The formation of closo-boranes, $[B_{10}H_{10}]^{2-}$ or $[B_{12}H_{12}]^{2-}$, has been experimentally observed during thermolysis of metal borohydride in the lab; whilst metal borohydrides are used as B-rich precursors to synthesis metal poly-boranes in industry. For instance, several monometallic or bimetallic closo-boranes have been reported and most of them are stable at room temperature (Table 3.6) (White et al. 2016; Sivaev 2017; Paskevicius et al. 2017). And a number of synthesis routes from different B-rich precursors have been demonstrated (Figure 3.15), which usually require relatively high temperatures to initiate the B-B bond building from B-H condensation (Hansen et al. 2016).

Table 3.6 Lattice parameters of selected closo-boranes. All results are measured in atmospheric pressure.

	M^{2+}	Structure		Cell parameters a Å	b Å	c Å	V Å3	T °C	Reference
$[B_{10}H_{10}]^{2-}$	Li_2	Hex.	*$P6_422$*	7.0423	7.0423	14.9313	641.29	22	(H. Wu et al. 2015)
	Na_2	Mono.	*$P12_1/n1$*	10.2828	13.0218	6.6734	891.65	-173	(Hofmann & Albert 2005)
	K_2	Mono.	*$P12_1/n1$*	12.8554	11.1784	6.8227	978.76	25	(Hofmann & Albert 2005)
$[B_{12}H_{12}]^{2-}$	Li_2	Cubic	*Pa-3*	9.57713	9.57713	9.57713	878.43	20	(Her et al. 2008)
				10.0172	10.0172	10.0172	1005.17	25	(Mark Paskevicius et al. 2013)
	Na_2	Mono.	*$P12_1/n1$*	7.03062	10.65399	7.0093	523.28	20	(Her et al. 2009)
	K_2	Cubic	*Fm-3*	10.61	10.61	10.61	1194.39	25	(Wunderlich & Lipscomb 1960)
				10.629	10.629	10.629	1200.82	25	(Tiritiris & Schleid 2003)
	Ca	Mono.	*C12/c1*	7.242	11.971	10.744	931.44	20	(Stavila et al. 2010)
	$Li_{0.76}Na_{1.33}$	Cubic	*Pa-3*	9.9274	9.9274	9.9274	978.38	20	(Tang, Udovic, et al. 2015)
	$Li_{0.94}Na_{1.06}$	Cubic	*Pa-3*	9.82	9.82	9.82	946.97	20	(Tang, Udovic, et al. 2015)
	LiNa	Cubic	*Pa-3*	9.8009	9.8009	9.8009	941.45	25	(He et al. 2015)
	$Li_{1.33}Na_{0.67}$	Cubic	*Pa-3*	9.7248	9.7248	9.7248	919.69	20	(Tang, Udovic, et al. 2015)
	LiK	Ortho.	*Pnma*	7.9134	4.4907	13.8440	491.96	25	(Nickels et al. 2008)

* Hex. = Hexagonal; Mono. = Monoclinic; Ortho. = Orthorhombic

The vibrational structure of isolated $[B_{12}H_{12}]^{2-}$ (symmetry point group I_h) enables 6 Raman-active modes (two A_g and four H_g) and 3 IR-active modes (three F_{1u}) (Muetterties et al. 1962). The $[B_{10}H_{10}]^{2-}$ has a lower symmetry (point group D_{4d}) and therefore has 19 Raman-active modes (six A_1, six E_2 and seven E_3) and 12 IR-active modes (five B_2 and seven E_1) (Leites 1992). In practice, vibrational techniques such as Raman and IR are suitable for the characterization of these closo-boranes (Table 3.7.), especially when they are formed in amorphous structure during dehydrogenation. In addition, due to the different vibration sources, $[B_{10}H_{10}]^{2-}$ and $[B_{12}H_{12}]^{2-}$ have different peak strengths. For instance, The $[B_{12}H_{12}]^{2-}$ has a strong B-H stretching and cage (i.e. B-B breathing) IR adsorption at 2480 cm^{-1} and at 1070 cm^{-1} (Muetterties et al. 1962), as

well as decreasingly weaker peaks at 720 cm^{-1}, and 750 and 1115 cm^{-1} (not listed in Table 3.7) (Muetterties et al. 1964). Whilst, in addition to the strong B-H stretching peak at 2467 cm^{-1}, the $[B_{10}H_{10}]^{2-}$ has a strong cage IR adsorption at 1030 cm^{-1} (Leites 1992), and a much weaker peak at ~ 1070 cm^{-1} (not listed in Table 3.7) (Muetterties et al. 1964).

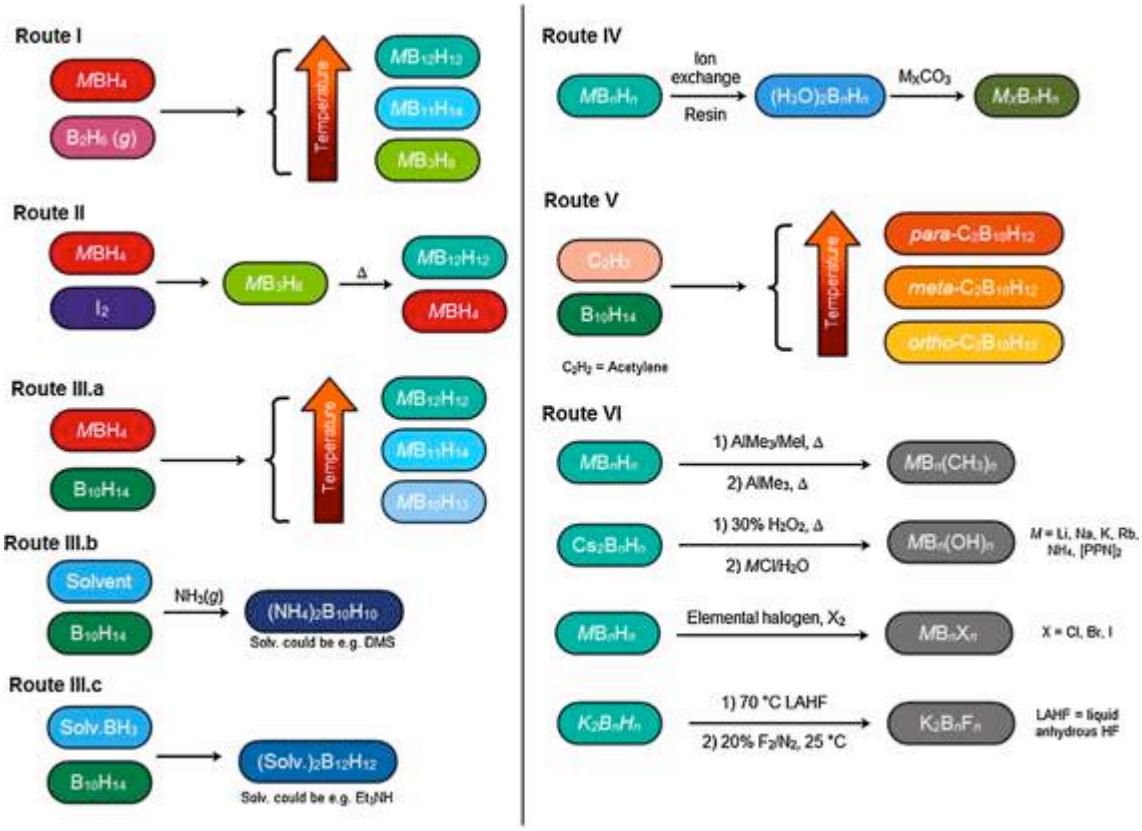

Figure 3.15 Illustration of different poly-boranes synthesis approaches (Hansen et al. 2016).

The complex closo-boranes are thermally stable and inhibit the rehydrogenation of borohydrides, so that they are unfavourable phases for hydrogen storage. However, a partial dehydrogenation from $[B_{12}H_{12}]^{2-}$ to $[B_{12}H_{12-x}]^{-2-x}$ above 250 °C either under vacuum or in H_2 are possible (Pitt et al. 2013; Li et al. 2015; Yan et al. 2018), suggesting a small degradation. Moreover, the Li^+ or Na^+ based closo-boranes become

popular because their ultra high ionic conductivity makes them attractive as potential solid-state electrolytes (Varley et al. 2017).

Table 3.7 Vibrational frequencies of selected closo-boranes.

		$[B_{12}H_{12}]^{2-}$			$[B_{10}H_{10}]^{2-}$	
Raman	ν_1	A_g	2518	ν_1	A_1	2583
	ν_6	H_g	2475	ν_2	A_1	836
	ν_7	H_g	949	ν_5	E_2, E_3	755
	ν_8	H_g	770			
	ν_2	A_g	743			
	ν_9	H_g	584			
IR	ν_3	F_{1u}	2480	ν_7	B_2, E_1	2467
	ν_4	F_{1u}	1070	ν_8	B_2, E1	1030
	ν_6	F_{1u}	720			
Reference	(Muetterties et al. 1962)			(Leites 1992)		

3.5 Summary of Complex Metal Borohydrides

Over last two decades, there has been extensive research into metal borohydrides and their derivatives for H_2 storage as well as other applications (e.g. solid-state batteries); with a large variety of metal borohydrides discovered through solvent-based or mechanochemical reactions and their structures, physical and chemical properties well characterized (Paskevicius et al. 2017).

As one of the most promising solid-state H_2 storage materials, breaking or reforming the B-H bonds during sorption is essential for H_2 storage and cycling using metal borohydrides. However, their relatively high thermal stability, sluggish kinetics and poor reversibility remain as major challenges to meet the DOE targets, especially for mobile application. Novel approaches, such as using additive/catalyst, reactive hydride composites and nano-engineering, have been demonstrated to tailor the

thermodynamics, and to improve the kinetics (Paskevicius et al. 2017). Alternatively, when mixing alkali- and alkaline-earth metal borohydrides, the new compounds may result in a eutectic melting phenomenon (i.e. lower melting point than that for its constituents) and cause H_2 release at a relatively lower temperature than its constitutes as well as improve the H_2 uptake properties. This type of compounds is of great interest and will be discussed in detail in Chapter 4.

CHAPTER 4 EUTECTIC METAL BOROHYDRIDES SYSTEMS

The concept of 'eutectic' in metallurgy indicates the formation of a homogenous liquid mixture from a mixture of substances in fixed composition (i.e. eutectic composition) at a certain temperature (i.e. eutectic temperature) (Callister & Rethwisch 2014). This temperature is the lowest temperature among the melting points of the separate constituents or of any other mixture of them (Figure 4.1).

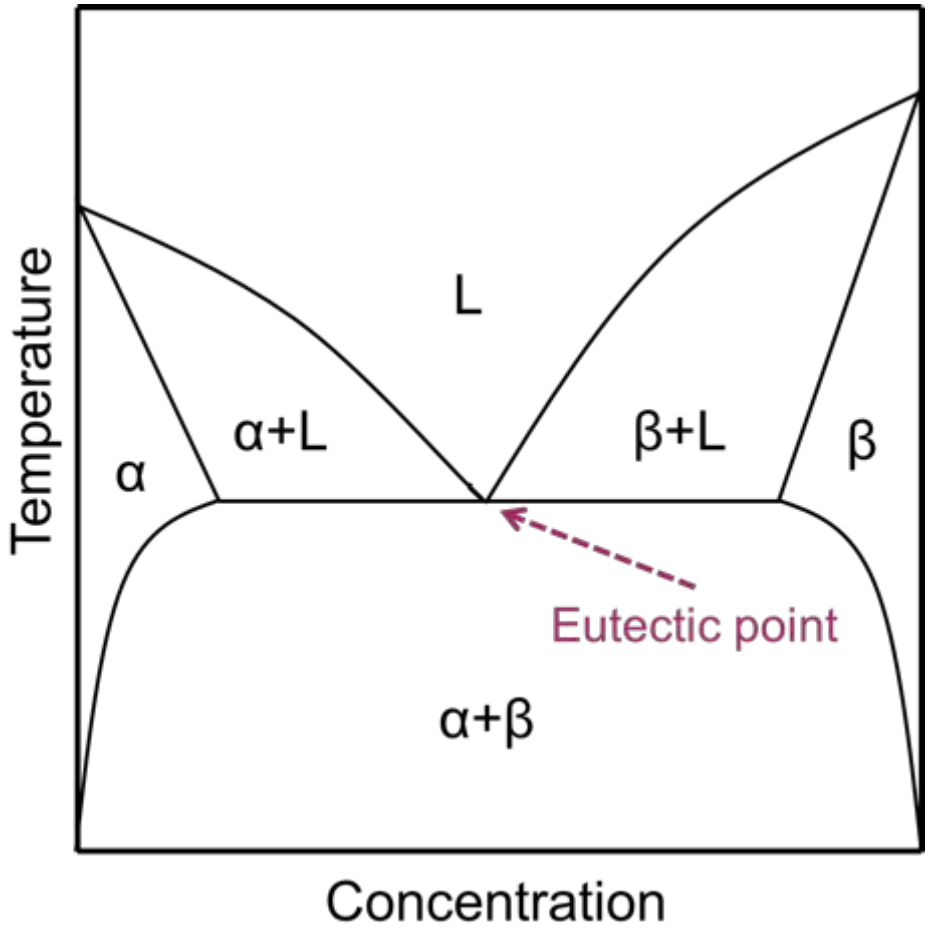

Figure 4.1 A schematic diagram of eutectic melting behaviour, revised from (Imre 2009).

Research interest into molten-salt mixtures dates back to Faraday (1832). These mixtures are usually good conductors for electric current as a consequence of their highly dissociated ionic species in molten status (Blomgren & Artsdalen 1960), and are useful as reaction media (Sundermeyer 1965) or in extractive metallurgy (Habashi 1997). Recently, the utilization of molten-salts mixtures in solar-thermal-energy and H_2 storage has been purposed (Harries et al. 2012; M Paskevicius et al. 2013).

The low-melting-point borohydride mixtures are often noted as "eutectic metal borohydrides" and become a promising route for H_2 storage leading to H_2 desorption at relatively low temperatures (M Paskevicius et al. 2013). These compounds have received intensive attentions since 2009 (Lee et al. 2009). In practice, the nature of molten salts is important in utilizing H_2 release from borohydrides, as some of them (practically alkali-metal borohydrides) often melt before their major H_2 desorption begins. In addition, the dehydrogenation of borohydrides from liquid state (rather than from solid state) may lead to less $[B_{12}H_{12}]^{2-}$ in the reaction products (Yan, Rentsch & Remhof 2017). Moreover, the low melting temperatures of these mixtures are also beneficial for the nanoconfinement-by-infiltration approach, in which molten borohydrides are infiltrated into a porous materials to reduce the decomposition temperature and to improve the reversibility (Liu et al. 2017).

This chapter will summarize the common eutectic borohydride systems between alkali- and alkali- or between alkali- and alkaline earth metal-based borohydrides.

4.1 Alkali-alkali Metal Borohydrides Systems

4.1.1 $LiBH_4$-$NaBH_4$

Research in the 1960s-1970s showed that eutectic melting occurs for $0.62LiBH_4$-$0.38NaBH_4$ between 213 and 224 °C (Adams 1961; Semenenko et al. 1971). Recent research confirms and refines the eutectic point to 210-220 °C (M Paskevicius et al. 2013). No H_2 is released during or directly after fusion. Its major H_2 evolution occurs above 300 °C, and releases ~7 wt.% hydrogen (theoretical gravimetric capacity: 14.5 wt.%) upon heating to 500 °C in Ar without any B_2H_6 detected (M Paskevicius et al. 2013; Javadian, Sheppard, et al. 2015).

This relatively high dehydrogenation temperature can be reduced by nanoconfinement-through-infiltration approach. For instance, 107 °C reduction of dehydrogenation peak temperature while using nanoporous carbon aerogel scaffolds [1] has been studied (Javadian, Sheppard, et al. 2015). In addition, this approach improves the cycling stability during H_2 release and uptake (Figure 4.2). For example, the bulk mixture has poor cycling stability as it drops dramatically from 7.2 wt.% (1st cycle) to 2.1 wt.% (2nd cycle), and remains at 1.6 wt.% (3rd and 4th cycles). However, when this mixture is nanoconfined into a high surface area carbon aerogel scaffold[2], the reversible hydrogen content is still about 70% of the initial capacity after 4 cycles (Javadian, Sheppard, et al. 2015).

[1] Average pore size: 37 ± 0.4 nm; BET surface areas: 690 ± 12 m^2 g^{-1}; Total pore volumes: 1.03 ± 0.14 mL g^{-1}; Materials loading: 32.8 wt.% and 60 vol%.
[2] Average pore size: 38 ± 0.4 nm; BET surface areas: 2358 ± 82 m^2 g^{-1}; Total pore volumes: 2.64 ± 0.33 mL g^{-1}; Materials loading: 55.5 wt.% and 60 vol%.

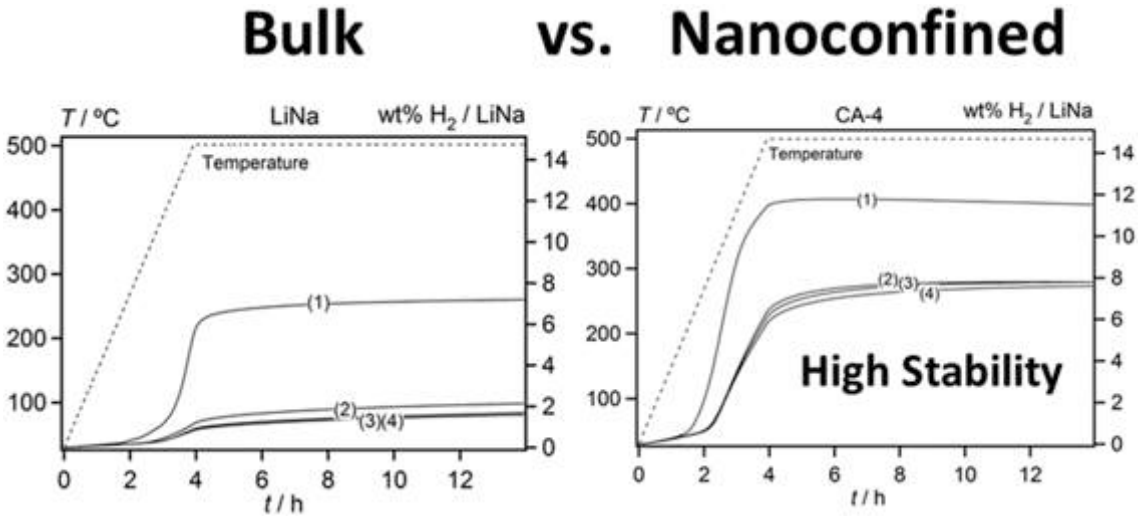

Figure 4.2 A comparison between bulk $0.62LiBH_4$-$0.38NaBH_4$ (LiNa) and nanoconfined mixture in CO_2-actived carbon aerogel scaffold (CA-4). The H_2 release from cycling is measured by Sieverts' measurement using 500 °C for 10 h at 1 bar H_2 for desorption and 400 °C for 10 h at 140 bar H_2 for absorption (Javadian, Sheppard, et al. 2015).

More recently, a new eutectic composition, $0.71LiBH_4$-$0.29NaBH_4$, with a slightly lower melting point (219 °C) was proposed based on thermodynamic calculations (Dematteis et al. 2016). The calculated phase diagram agrees with experiment results, and is illustrated in Figure 4.3.

Apart from eutectic behaviour, the mixture of $LiBH_4$-$NaBH_4$ shows a large solid solution compositional range between $NaBH_4$ and hexagonal-$LiBH_4$ (Semenenko et al. 1971). The recent work calculates the maximum solubility of Na in the hexagonal-$LiBH_4$ as 20 mol%. This is much higher than the 6 mol% for Na into orthorhombic-$LiBH_4$ and 7 mol% for Li into cubic-$NaBH_4$ (Dematteis et al. 2016). In addition, the solid solution stabilizes the high temperature phase of $LiBH_4$ that results in a low phase transition temperature (~97 °C) and a high ionic conductivity (10^{-2} S cm^{-1} above 100 °C) (Xiang et al. 2017).

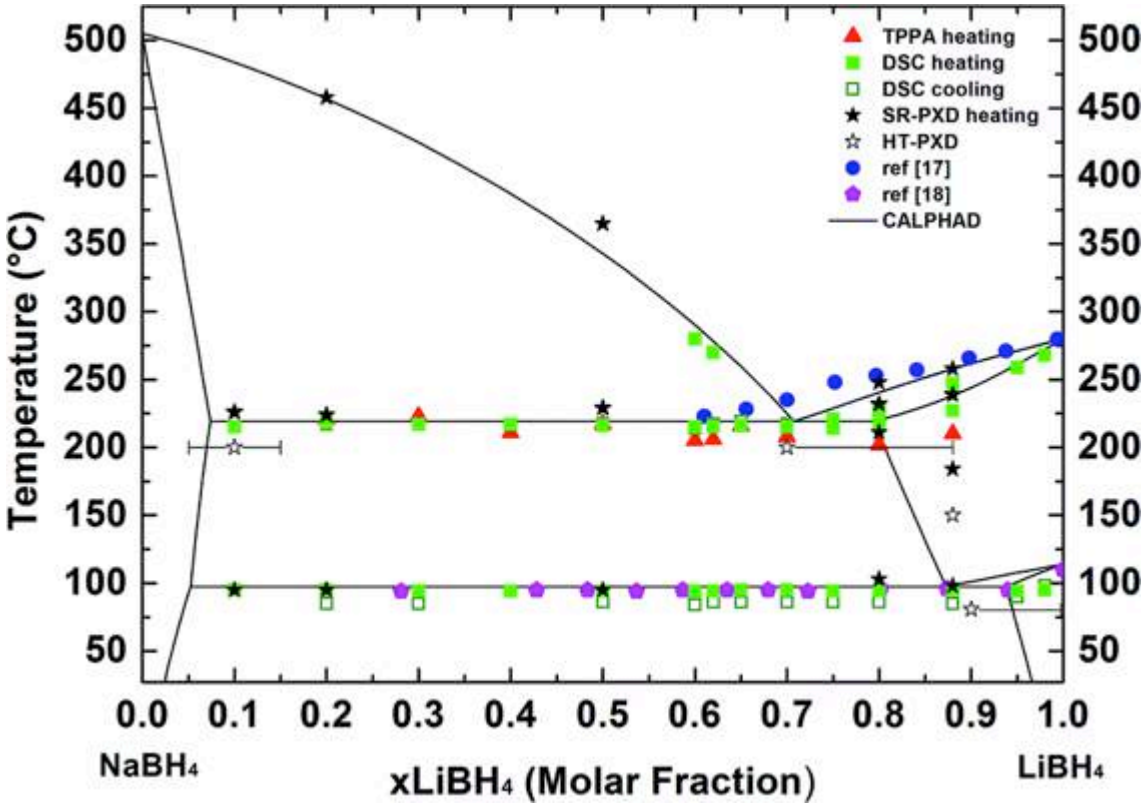

Figure 4.3 A pseudo-binary phase diagram of the $LiBH_4$-$NaBH_4$ system (Dematteis et al. 2016).

4.1.2 $LiBH_4$-KBH_4

The early reach suggests a readily fusible eutectic for $0.46LiBH_4$-$0.53KBH_4$, melting at 103 °C (Adams 1961). The eutectic composition is refined to $0.725LiBH_4$-$0.275KBH_4$ with a eutectic point at 105 °C (Figure 4.4, the lowest fusion temperature among known eutectic metal borohydrides systems) and a theoretical H_2 capacity of 13.2 wt.% (M Paskevicius et al. 2013). This eutectic mixture is usually prepared through ball milling, where a pressure induced metastable phase, $LiK(BH_4)_2$, is formed (Nickels et al. 2008). No H_2 is released at around its fusion temperature; whilst the major dehydrogenation occurs above 400 °C (without B_2H_6), leading to a total of 5.7 wt.% at 500 °C in Ar (Roedern et al. 2015).

Addition of 27 mol% Mg or MgH_2 have been demonstrated to destabilize this system (Roedern et al. 2015), exhibiting noticeable reductions in dehydrogenation temperatures. The major dehydrogenation of $LiBH_4$-KBH_4-Mg system starts from 250 °C (possibly due to the reaction between $LiBH_4$ and Mg) and leads to 3.5 wt.% hydrogen evolution upon heating to 500 °C in Ar. The $LiBH_4$-KBH_4-MgH_2 system has a rapid H_2 release (1.4 wt.%) at 415 °C (possibly due to the dehydrogenation of MgH_2) and can release up to 5.0 wt.% hydrogen at 500 °C in Ar (Roedern et al. 2015).

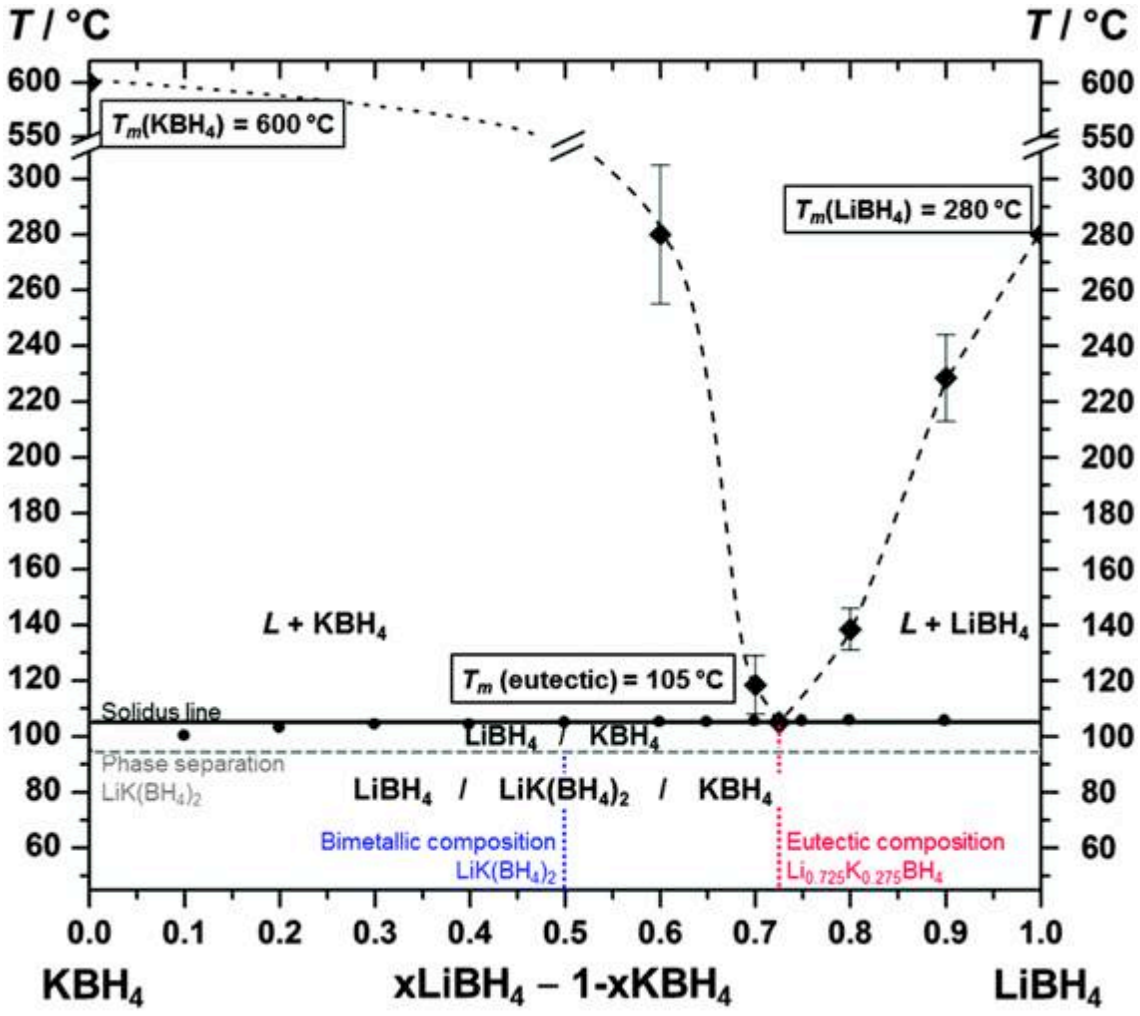

Figure 4.4 Binary phase diagram of $LiBH_4$-KBH_4 system (Ley et al. 2014).

The reversible hydrogen content of $LiBH_4$-KBH_4 during a three-time cycling is found to be 7.3 wt.%, 3.0 wt.% and 3.3 wt.% (500 °C for 4 h at 1 bar H_2 for desorption; 400 °C for 12 h at 100 bar H_2 for absorption). However, nanoconfinement into a CO_2 activated nanoporous carbon scaffold [1] does not further improve the cycling stability. Alternatively, the addition of Mg or MgH_2 can slightly improve the cycling stability, leading to a release of 4.3 wt.% hydrogen at the 3rd cycle (Roedern et al. 2015).

4.1.3 $NaBH_4$-KBH_4

The eutectic $NaBH_4$-KBH_4 mixture is less well studied, possibly due to its relatively stable constituents. The first observation of eutectic behaviour for $0.682NaBH_4$-$0.318KBH_4$ (at 453 °C) was by Semenenko et al. (1971). Its eutectic composition was recently refined to 440 °C for $0.68NaBH_4$-$0.32KBH_4$ with major hydrogen evolution above 460 °C when heated by 5 °C min^{-1} in Ar (M Paskevicius et al. 2013).

In addition, the existence of solid solutions with full solubility over the entire composition range has been reported above 200 °C (Figure 4.5) (Semenenko et al. 1971; Jensen et al. 2015). This is facilitated by thermal expansion as a consequence of the similarity in unit cell volumes between the solid solutions and the reactants (Paskevicius et al. 2017). The solid solutions are metastable and can dissociate to their constituents within 24 h at room temperature (Jensen et al. 2015).

[1] Average pore size: 25 ± 1 nm; BET surface areas: 2142 ± 240 m^2 g^{-1}; Total pore volumes: 2.54 ± 0.27 mL g^{-1}; Materials loading: 62 wt.% and 80 vol%.

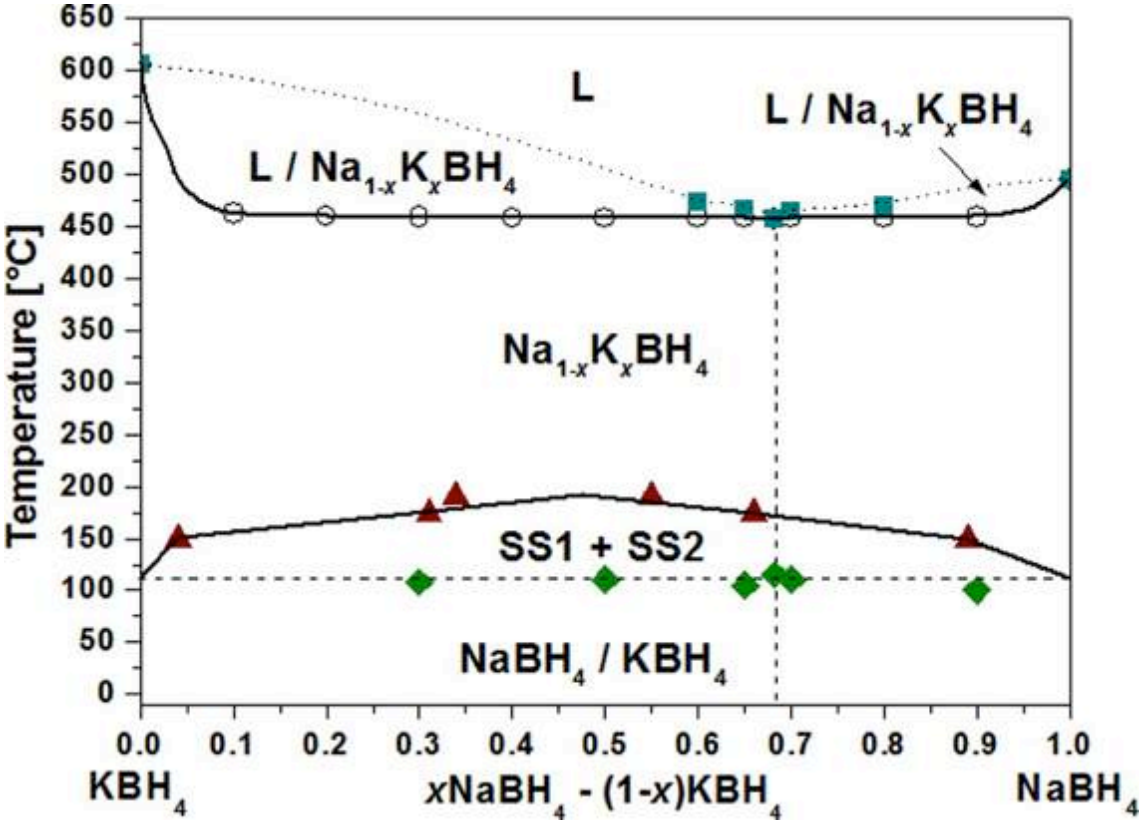

Figure 4.5 Binary phase diagram of $NaBH_4$-KBH_4 system. SS1 and SS2 are two types of solid solutions (Jensen et al. 2015).

4.1.4 $LiBH_4$-$NaBH_4$-KBH_4

The existence of a ternary eutectic of $0.45LiBH_4$-$0.1NaBH_4$-$0.45KBH_4$ at 96 °C was reported by George F (1960). Recent research indicates this is a KBH_4-rich composition (M Paskevicius et al. 2013), and proposes a ternary eutectic composition of $0.66LiBH_4$-$0.11NaBH_4$-$0.23KBH_4$ (Figure 4.6) that melts at 102 °C (Dematteis et al. 2017). So far, the hydrogen storage properties of this system have not been reported.

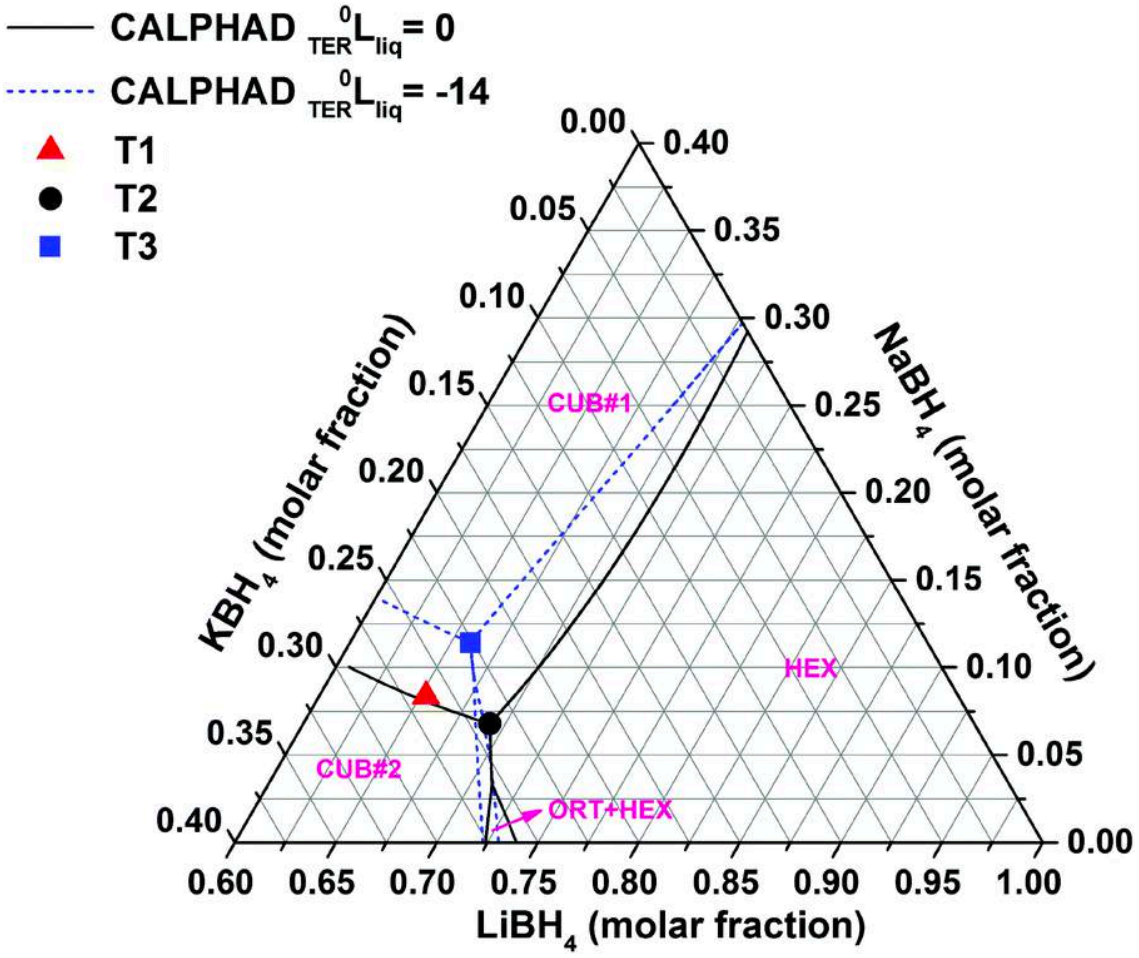

Figure 4.6 Calculated minima of the liquidus surface for $LiBH_4$-$NaBH_4$-KBH_4 system. The calculated eutectic composition is marked with blue-square dot. The black-circle dot is the simple extrapolation from the binary systems without considering a ternary interaction parameter ($_{TER}{}^{0}L_{liq}$) in calculation (ORT=orthorhombic; HEX=hexagonal) (Dematteis et al. 2017).

4.2 Alkali-alkaline Earth Metal Borohydrides Systems

4.2.1 $LiBH_4$-$Mg(BH_4)_2$

The $LiBH_4$-$Mg(BH_4)_2$ is one of the most popular eutectic systems. It has been noted since 2011 with eutectic melting at around 180 °C for a mixture with 40-50 mol% $Mg(BH_4)_2$ (Figure 4.7) (Hagemann et al. 2011; Nale et al. 2011; Bardají et al. 2011). No dual-cation compound has been found after mechanochemical preparation or thermal-treatment.

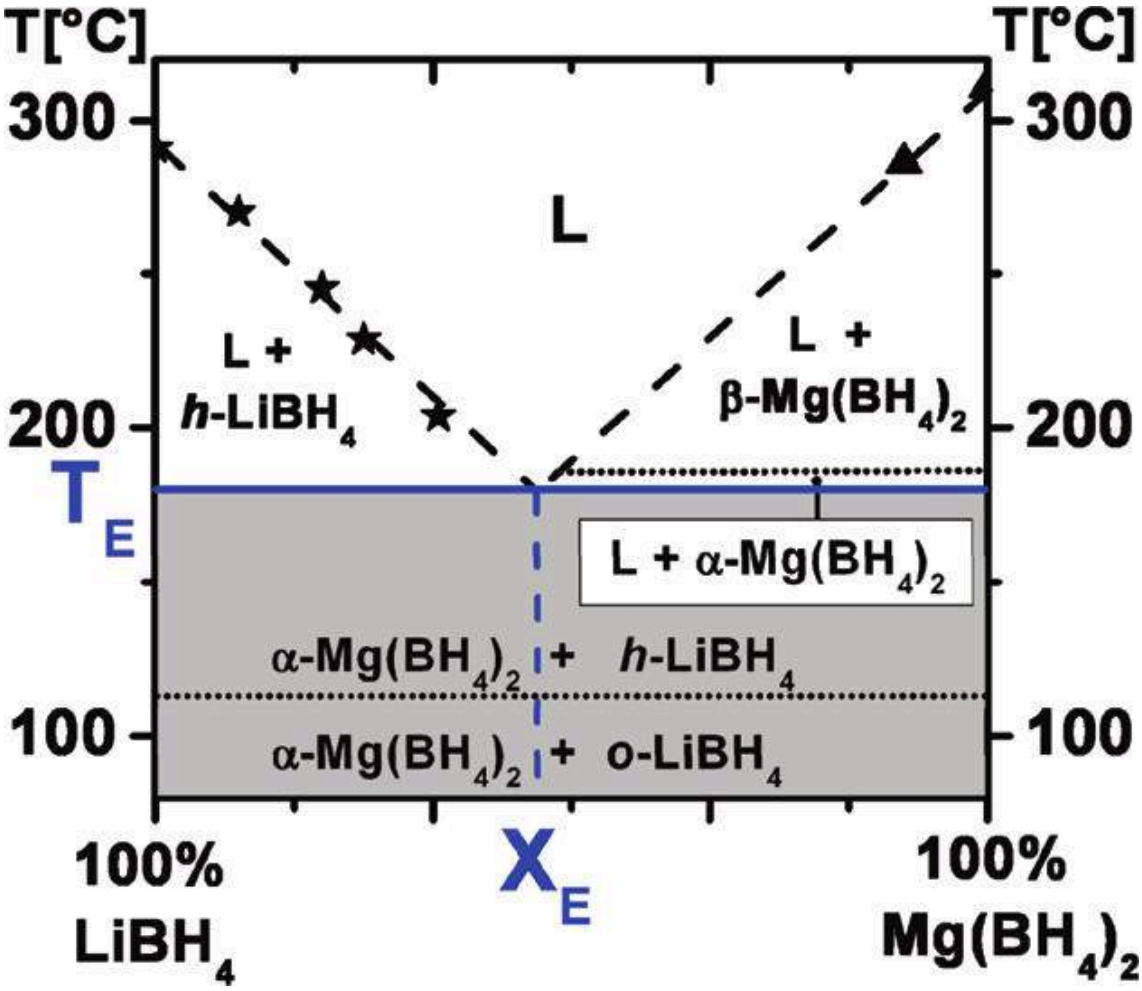

Figure 4.7 Binary phase diagram of the $LiBH_4$-$Mg(BH_4)_2$ system (Bardají et al. 2011).

Under 3 bar H_2, a $0.6LiBH_4$-$0.4Mg(BH_4)_2$ mixture releases a total of 12 wt.% hydrogen up to 550 °C (lower than the theoretical value 14.5 wt.%), through four major steps (Nale et al. 2011):

$$\frac{1}{3}Mg(BH_4)_2 \xrightarrow{235\,^{\circ}C} \frac{1}{3}MgH_2 + \frac{2}{3}B + H_2 \qquad \textbf{Equation 4.1}$$

$$\frac{2}{7}LiBH_4 + \frac{1}{7}Mg(BH_4)_2 \xrightarrow{315\,^{\circ}C} \frac{2}{7}B + \frac{2}{7}LiH + \frac{1}{7}MgB_2 + H_2 \qquad \textbf{Equation 4.2}$$

$$MgH_2 \xrightarrow{365\,^{\circ}C} Mg + H_2 \qquad \textbf{Equation 4.3}$$

$$\frac{2}{3}LiBH_4 \xrightarrow{460\,^{\circ}C} \frac{2}{3}LiH + \frac{2}{3}B + H_2 \; and \; \frac{2}{3}LiBH_4 + \frac{1}{3}Mg \xrightarrow{460\,^{\circ}C} \frac{2}{3}LiH + \frac{1}{3}MgB_2 + H_2 \qquad \textbf{Equation 4.4}$$

The 1st dehydrogenation reaction occurred at 235 °C (Nale et al. 2011), which is significantly lower than that of individual $LiBH_4$ and $Mg(BH_4)_2$ (e.g. ~400 °C and 280 °C, respectively) (Paskevicius et al. 2017).

In addition, nanoconfinement has been used in order to further destabilize this mixture, to improve the cycling stability and to accelerate the H_2 evolution. For instance, when a mixture of $0.5LiBH_4$-$0.5Mg(BH_4)_2$ is loaded into a mesoporous carbon scaffold (IRH33[1]), the nanoconfined sample starts to release H_2 at a much lower temperature (~170 °C) and liberates a total of 8 wt.% hydrogen in 10 hours at 270 °C under 1 bar of H_2; while the bulk material releases only 3 wt.% hydrogen under the same conditions (Zhao-Karger et al. 2013). Moreover, nanoconfinement may alter the decomposition pathway (e.g. changing from a four-step into a two-step reaction mechanism) and inhibit the formation of $[B_{12}H_{12}]^{2-}$ phases (Zhao-Karger et al. 2013). Apart from that, using Co as a catalyst can also reduce the dehydrogenation onset temperatures to 155 °C (when heated by 2 °C min^{-1} in following Ar) (J. Chen et al. 2012).

The reversible hydrogen content for a $0.55LiBH_4$-$0.45Mg(BH_4)_2$ has been investigated. It has a decreasing trend from 8.4, 3.6, 3.1, 3.1 wt.% hydrogen for the 1st to 4th cycle (500 °C for 10 h at 1 bar H_2 for desorption; 400 °C for 10 h at 140-150 bar H_2 for absorption) (Javadian & Jensen 2014). By nanoconfinement into a CO_2-activated carbon aerogel scaffold[2], this mixture shows a significant increase in the H_2 release at the 1st

[1] Average pore size: < 4 nm; BET surface areas: 2587 m^2 g^{-1}; Total pore volumes: 1.17 mL g^{-1}; Materials loading: 27 wt.%.
[2] Average pore size: 29 nm; BET surface areas: 2660 m^2 g^{-1}; Total pore volumes: 3.13 mL g^{-1}; Materials loading: 55.3 wt.% and 51.5 vol%.

cycle (13.3 wt.%) and a better cycling stability (9.1, 8.3 and 8.3 wt.% for the 2nd, 3rd and 4th cycle) (Javadian & Jensen 2014).

4.2.2 $LiBH_4$-$Ca(BH_4)_2$

The eutectic mixture between $LiBH_4$ and $Ca(BH_4)_2$ has been noted since 2009 (Lee et al. 2009), which shows a eutectic melting at ~200 °C for $LiBH_4$-rich (60–80 mol%) samples. The eutectic composition has been refined to $0.68LiBH_4$-$0.32Ca(BH_4)_2$ (Lee et al. 2011; Yan et al. 2013), and in theory can store 14.3 wt.% hydrogen. Upon heating, the phase transitions of orthorhombic-hexagonal $LiBH_4$ and α-/β- to γ- $Ca(BH_4)_2$ occur at 117 °C and 143 °C, respectively (Guo 2014). Then its dehydrogenation starts right above the eutectic point (200 °C). The major H_2 evolution from this system occurs at 310 °C and ends at 400 °C (when heated by 1 °C min^{-1} in 1 bar H_2) with 9.5 wt.% hydrogen liberation, which is much lower than the hydrogen evolution temperature of pure $LiBH_4$ (400 °C) (Yan et al. 2013). The decomposition is a two-step reaction:

- Decomposition of $Ca(BH_4)_2$ (Equation 4.5-4.6): the formations of B-based phases, such as CaB_6 or $CaB_{12}H_{12}$, are competitive and temperature-dependent, where the formation of CaB_6 is more favourable when the dehydrogenation is isothermally controlled at relatively low temperature.
- Reaction between $LiBH_4$ and CaH_2 (Equation 4.7).

$$Ca(BH_4)_2 \rightarrow \frac{1}{3}CaB_6 + \frac{2}{3}CaH_2 + \frac{10}{3}H_2 \qquad \textbf{Equation 4.5}$$

$$Ca(BH_4)_2 \rightarrow \frac{1}{6}CaB_{12}H_{12} + \frac{5}{6}CaH_2 + \frac{13}{6}H_2 \qquad \textbf{Equation 4.6}$$

$$LiBH_4 + \frac{1}{6}CaH_2 \rightarrow LiH + \frac{1}{6}CaB_6 + \frac{5}{3}H_2 \qquad \textbf{Equation 4.7}$$

The $LiBH_4$-$Ca(BH_4)_2$ mixture has a very promising cycling stability (Javadian et al. 2017), exhibiting fully reversible hydrogen content up to 5.6 wt.% from the 2nd to the 5th cycle (500 °C for 10 h at 1 bar H_2 for desorption; 500 °C for 10 h at 134-144 bar H_2 for absorption) corresponding to the fully reversibility of $LiBH_4$ in the system (i.e. 5.43 wt.%), although these values are lower than the 10.5 wt.% hydrogen released from the initial cycle. This reveals that the decomposition products of $Ca(BH_4)_2$, such as CaB_6, play an important role to achieve high reversibility of $LiBH_4$. In addition, nanoconfinement of this mixture in mesoporous carbon scaffolds (CMK-3[1]) leads to at least 50 °C reduction of the major dehydrogenation temperature (Lee et al. 2011; Zhai et al. 2016). However, it does not improve the cycling stability (Javadian et al. 2017). Apart from that, using selected additives, such as $LaMg_3$, can also destabilize the dehydrogenation (e.g. reducing the temperature for main dehydrogenation by 100 °C to ~200 °C when heated by 2 °C min^{-1} in static vacuum) as well as improve the cycling stability (e.g. maintaining 70% of its first H_2 desorption capacity after 5 cycles) (Gu et al. 2015).

4.3 Other Systems

A eutectic behaviour of $xNaBH_4$-$(1-x)Mg(BH_4)_2$ (x=0.4-0.5) at 205 °C has been noticed. The major hydrogen release is observed from 180-300 °C (when heated by 5 °C min^{-1} in flowing Ar). The decomposition products contain MgB_2, MgH_2, and perhaps Mg phases at higher temperature (Ley et al. 2015).

[1] Average pore size: 2.5 nm; BET surface areas: 1229 ± 20 m^2 g^{-1}; Total pore volumes: 1.63 ± 0.05 mL g^{-1}.

In the $xNaBH_4$-$(1-x)Ca(BH_4)_2$ (x=0.335, 0.375, 0.429, 0.445, 0.5 and 0.665) system, eutectic behaviour is not observed, although partial melting occurred in the $0.5NaBH_4$–$0.5Ca(BH_4)_2$ sample above 350 °C during a macroscopic sample observation (Ley et al. 2015).

In the $LiBH_4$-$Mn(BH_4)_2$ system, a partial melting at 150-160 °C for a $0.5LiBH_4$-$0.5Mn(BH_4)_2$ mixture has been reported (M Paskevicius et al. 2013).

4.4 Summary of Eutectic Borohydrides Systems

The formation of eutectic mixture between borohydrides is observed in a number of systems, causing H_2 release at lower temperatures, possibly through a kinetic effect (Paskevicius et al. 2017). The reorganization of crystal structure after fusion may, in principal, lead to a weakening (or strengthening) of chemical bonds as a consequence of changing chemical environments, which can affect decomposition. Interestingly, the constituent with the lowest melting point in a eutectic system usually has the largest concentrations in the eutectic composition (Table 4.1). Some of these eutectic borohydrides, such as $0.68LiBH_4$-$0.32Ca(BH_4)_2$, have relatively low decomposition temperatures and good cycling stabilities. In general, the low melting points of these compounds are beneficial and ideal for the nanoconfinement-by-infiltration approach that has been reported to destabilize the decomposition reaction and to improve hydrogen uptake. However, the dehydrogenation mechanisms for these eutectic systems are not fully understood and therefore needs to be studied, to try to identify suitable reaction routes to lower the temperature of dehydrogenation.

Table 4.1 Eutectic metal borohydride systems, revised from (Paskevicius et al. 2017).

Systems	Constituents			Eutectic mixture			Reference
	T_{mp1} °C	T_{mp2} °C	T_{mp3} °C	T_{mp} °C	T_{dec} °C	ρ_g wt.%	
$0.62LiBH_4$-$0.38NaBH_4$	280	510	-	225	300	14.5	(Javadian, Sheppard, et al. 2015)
$0.71LiBH_4$-$0.29NaBH_4$	280	510	-	219	n.a.	15.2	(Dematteis et al. 2016)
$0.725LiBH_4$-$0.275KBH_4$	280	605	-	105	420	13.2	(Ley et al. 2014)
$0.68NaBH_4$-$0.32KBH_4$	510	605	-	460	465	9.4	(Jensen et al. 2015)
$0.66LiBH_4$-$0.11NaBH_4$-$0.23KBH_4$	280	510	605	102	n.a.	13.0	(Dematteis et al. 2017)
$0.55LiBH_4$-$0.45Mg(BH_4)_2$	280	280	-	180	250	16.1	(Bardají et al. 2011)
$0.68LiBH_4$-$0.32Ca(BH_4)_2$	280	370	-	200	350	14.5	(Lee et al. 2011)
$0.45NaBH_4$-$0.55Mg(BH_4)_2$	510	280	-	205	360	13.4	(Ley et al. 2015)

*: Melting point for individual constituents: T_{mp1}, T_{mp2} and T_{mp3}; Melting point for eutectic mixture: T_{mp}; Decomposition temperature: T_{dec}; Theoretical gravimetric capacity: ρ_g

CHAPTER 5 AIMS OF THIS PROJECT

Hydrogen has been proposed as a potential carbon-free energy vector for the future due to its high energy density. An effective hydrogen storage solution has become one of the main bottlenecks for the widespread introduction of fuel cell and hydrogen technologies (Chapter 1). In general, hydrogen can be stored in a number of different ways (Chapter 2). Among which, metal borohydrides have been considered as one of the most promising solid-state hydrogen storage media due to their relatively high hydrogen storage capacities (especially by volume) and low operating pressures (Chapter 3). However, their high dehydrogenation temperatures and limited hydrogen uptakes during cycling have so far hindered their application, especially in vehicular aspect. Many attempts have been tried in order to tailor the reaction thermodynamics and to improve the reaction kinetics.

A eutectic borohydride mixture exhibits a low melting point that is much lower than its individual constituents. A low-temperature fusion may facilitate the dehydrogenation process at low temperature. In fact, some of these mixtures show low-temperature dehydrogenation and stable reversible hydrogen contents (Chapter 4). In addition, their low-temperature melting points are beneficial for the nano-confinement by melt-infiltration approach, which can further tailor the thermodynamics and improve the cycling stability. So far, a few eutectic borohydrides have been reported (Table 4.1), and most of them are alkali- / alkali- or alkali- / alkaline earth metal borohydride mixtures. In general, the hydrogen sorption properties of these mixtures have been investigated. However, their dehydrogenation mechanisms were in general not well understood (e.g.

only limited numbers of systems have been investigated so far, including $0.68LiBH_4$-$0.32Ca(BH_4)_2$ and $0.6LiBH_4$-$0.4Mg(BH_4)_2$ mixtures), and therefore needs to be studied in order to identify suitable reaction routs towards a better H_2 storage performance.

This work focused on the investigation of the $0.62LiBH_4$-$0.38NaBH_4$ and $0.75LiBH_4$-$0.25KBH_4$ mixtures, because

- These mixtures have relatively large hydrogen storage capacities by weight (Table 4.1) and are relatively cheap;
- Their dehydrogenation mechanisms were not clear, although their hydrogen desoprtions have been investigated in the past;
- The $LiBH_4$-KBH_4 has the lowest eutectic point among known eutectic borohydrides mixtures, which makes it very attractive and beneficial for nano-confinement by infiltration approach;

Besides, additives (such as metal and oxides) are commonly used in the research field of complex hydrides. In general, they (or their reaction products) can destabilise the dehydrogenation and improve the hydrogen reversibility through more thermodynamic favourable chemical reactions or catalytic effects.

This work chose two types of additives, micron-sized SiO_2 and nano-sized Ni, in order 1) to investigate the effect of specific surface areas on the dehydrogenation of $LiBH_4$; 2) to destabilize the dehydrogenation; 3) to improve the hydrogen reversibility of the selected low-melting-point borohydride mixtures. This is because:

- SiO_2 was for the first time used as an additive for $LiBH_4$ that shows a positive destabilization effect (A. Züttel et al. 2003);
- SiO_2 is commercially available with different particle sizes;
- The reaction products of SiO_2 and $LiBH_4$ are well investigated (Zhang et al. 2008; Mosegaard et al. 2008; Opalka et al. 2009; Ngene, Adelhelm, et al. 2010; Chen et al. 2010).
- The reaction between $LiBH_4$ and Ni has low reaction enthalpy values (Li et al. 2014);
- The reaction products of $LiBH_4$ and Ni show promising catalytic effects, especially on hydrogen uptakes (Li et al. 2014).

Therefore, the aims of this project are to gain a greater understanding of the hydrogen desorption mechanisms of lithium based low-melting-point borohydrides mixtures, and to tailor their hydrogen storage property as well as to improve the cycling stability using selected additives. The results from this project can be used to provide guidance for producing a hydrogen storage medium that is feasible for application in vehicular and/or large-scale stationary energy storage in the future.

The major research focuses on aspects as follows:

1. A detailed understanding of the structural and thermal properties of $LiBH_4$, particularly characterization of its structural changes during the phase transition, and any intermediate/product phases formed during thermal decomposition.

Investigate the effect on the decomposition pathways by additive particle size (using a series of micron-sized SiO_2 powders) or by Ni powder.

2. Attempt to modify the dehydrogenation of $LiBH_4$ through forming low-melting-point mixtures ($0.62LiBH_4$-$0.38NaBH_4$ or $0.75LiBH_4$-$0.25KBH_4$). Investigate their dehydrogenation mechanism and rehydrogenation pathways. Attempt to destabilize their dehydrogenation using selected additives (micron-sized SiO_2 or nano-sized Ni) as well as to try to improve their cycling stability.

CHAPTER 6 EXPERIMENTAL METHODS

This Chapter describes the experiment techniques and the methods for data analysis, including:

- Material synthesis methods:
    - Ball milling
    - Hand mixing
- Material characterization methods:
    - X-ray Diffraction
    - Raman and Infrared
    - Difference Scanning Calorimetry
    - Thermal Programmed Composition and Mass Spectrometry
    - Recombination
- Thermodynamic calculation method

6.1 Material Synthesis

All materials in Table 6.1 were received from the chemical manufacturer, stored in an Ar glovebox (O_2 < 0.1 ppm and H_2O < 0.1 ppm) and used under Ar or H_2 during experiments, to try to prevent possible reactions with oxygen or moister in the atmosphere. If necessary, samples were weighted out using an analytical balance (up to ± 0.1 mg accuracy) in the glovebox.

Table 6.1 Table of chemical compounds used in this work.

Compound	Formula	Manufacturer	Purity	Note
Lithium Borohydride	$LiBH_4$	Sigma-Aldrich	95%	
Sodium Borohydride	$NaBH_4$	Sigma-Aldrich	99.99%	
Potassium Borohydride	KBH_4	Sigma-Aldrich	98%	
Silicon dioxide	SiO_2	Alfa Aesar	99.9%	0.5 micron
Silicon dioxide	SiO_2	Alfa Aesar	99.9%	1.0 micron
Silicon dioxide	SiO_2	Alfa Aesar	99.9%	1.5 micron
Nickel	Ni	Sigma-Aldrich	99.7%	3 micron
Nickel	Ni	Sigma-Aldrich	99.9%	~100 nanometre activated, in hexane

6.1.1 Ball Milling

Ball milling is a type of grinders used to crush, grind and blend materials, aiming for physical mixing or size reduction treatments. It is often considered as a mechanochemical synthesis approach, widely applied for synthesising compounds and/or doping with additives.

A Retsch PM400 Planetary Mill was used in this work (Retsch 2017b). It consists of four grinding bowls (pots) positions on one main platform (supporting disc) (Figure 6.1-a). Mixture of compounds and a number of grinding balls are kept in pots that rotate on their own axis. The balanced-weight pots are radial-symmetrically mounted on a counter-rotating platform (Figure 6.1-b). During milling, the balls roll halfway around the pot before falling and impacting the opposite side at high speeds. This causes high-energy collisions between the moving grinding balls, the mixtures, and the inner surface of the pots.

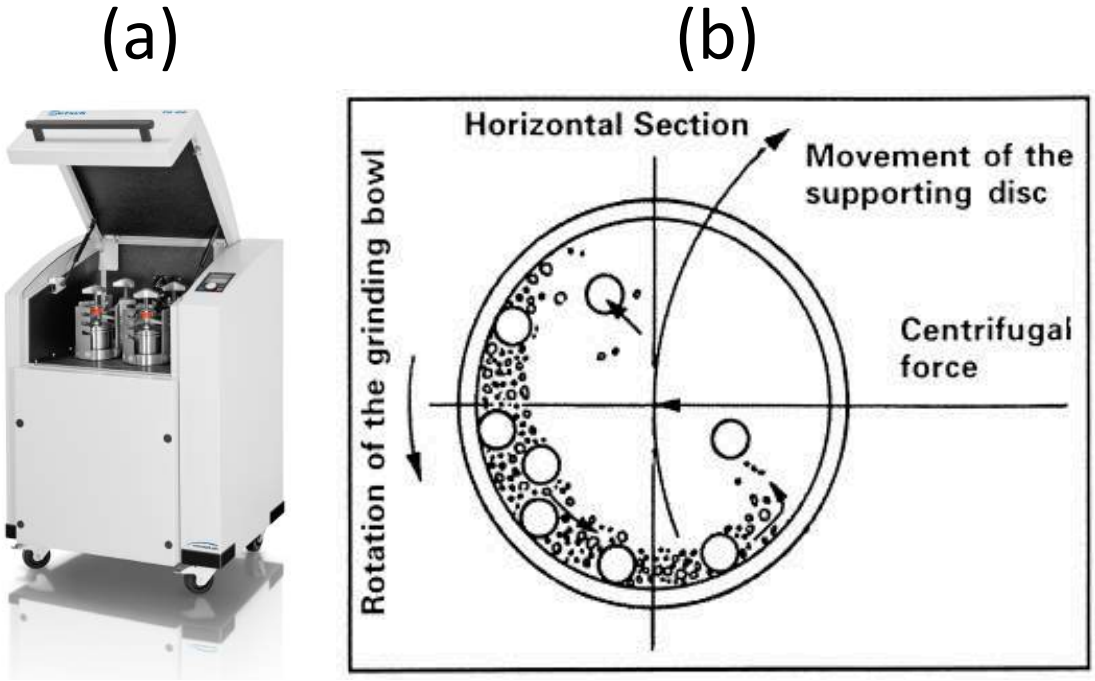

Figure 6.1 (a) A illustration of Retsch PM400 Planetary Mill (Retsch 2017b); (b) A schematic view of the motion of grinding balls during milling (Suryanarayana 2001).

In addition, the high-energy collisions can also lead to slight wear of the milling media (pots and balls), causing the inevitable introduction of very small amounts of impurities into milled compounds, e.g. 1-4 wt.% Fe is usually presented while using steel milling medium (Suryanarayana 2001); 0.2 wt.% Co is found while using WC milling medium that contained a Co binder (Zhang & Book 2013). However, the level of contamination strongly depends on the chosen milling conditions. In this work, the milling pots and balls used are all made of stainless steel (material number 1.4034, designation X46Cr13), containing Fe (≥ 82.9), Cr (12.5-14.5 %), Mn (≤ 1 %), Si (≤ 1 %), C (0.42-0.5 %), S (≤ 0.03%), and P (≤ 0.045 %) (Retsch 2017a). Thus, it is reasonable to assume that a tiny level of Fe and Cr may be present in all the milled samples, although their presence would be difficult to detect by lab-based powder XRD. Magnetic measurements, such as Vibrating Sample Magnetometry (Smith 1956; Foner 1959) and

application of the Honda-Owen method (Soule et al. 1964), could allow ferromagnetic impurities to be quantified.

The key factors that affect the final constitution of as-milled materials are: type of mill, milling container, milling speed, milling time, type/size/size-distribution of the milling balls, ball-to-powder weight ratio, extent of filling of the vial, milling atmosphere, process control agent and temperature of milling (Suryanarayana 2001). In practice, these parameters are not completely independent and need to be optimized in order to obtain the desired product. In this work, the milling conditions (Table 6.2.) are selected based on the optimization for $LiBH_4$-based samples in (Reed 2010).

Table 6.2 Ball milling conditions.

Conditions	Unit	Parameter
Pot volume	ml	250
Ball size	mm	13
Milling time	h	1
Processing time	min	5
Resting time	min	5
Milling speed	rpm	175
Ball-to-powder weight ratio		66:01:00
Atmosphere		1 bar Ar

6.1.2 Hand Mixing

To maintain the size of as-received particles, micron-sized SiO_2 was mixed with borohydrides samples by hand in a glove box. Sample were gently stirred by hand in glass tubes for 5 min and then shaken by hand for 5 min, and repeated for six times.

6.2 Material Characterization and Thermal analysis

6.2.1 Powder X-ray Diffraction

X-ray diffraction is a powerful characterisation technique, used for crystal structure determinations and extensively employed in defining atomic and molecular structures in many scientific fields, such as chemistry, material science and biology (Leng 2008).

6.2.1.1 X-ray Diffraction and Bragg' s Law

X-rays are produced by the collision of electron beams (obtained by heating a tungsten filament) onto a Cu target. The impact of the electrons causes ionisation of Cu that produces primarily Cu K_α and Cu K_β radiation. A monochromatic Cu K_α X-ray beam can therefore be obtained by the removal of unwanted radiation (such as background, and Cu K_β by using a Ni filter) (Leng 2008).

X-rays can be considered as high-energy electromagnetic radiation with short wavelengths. Typically, it has the same order of magnitude (1-100 Å) as the spacing between parallel atomic planes in crystalline materials. Thus, when an X-ray beam strikes a material, the periodical arrangements of atoms scatter X-rays elastically and produce spherical waves. The diffracted beams detected are the constructive interference of these spherical waves at certain directions determined by Bragg's law (Figure 6.2):

$$2d_{hkl} \sin\theta = n\lambda \qquad \textbf{Equation 6.1}$$

where,

d_{hkl} is the separation between two consecutive parallel atomic planes;

θ is the incident angle between X-ray beam and scattering planes;

n is an integer number describing the order of reflection;

λ is the wavelength of the X-ray beam.

Since each crystalline material has a unique set of interplanar distances (d_{hkl}), the pattern obtained with a set of peaks will be unique for a certain material. Based on which, the X-ray diffraction pattern characterises the material.

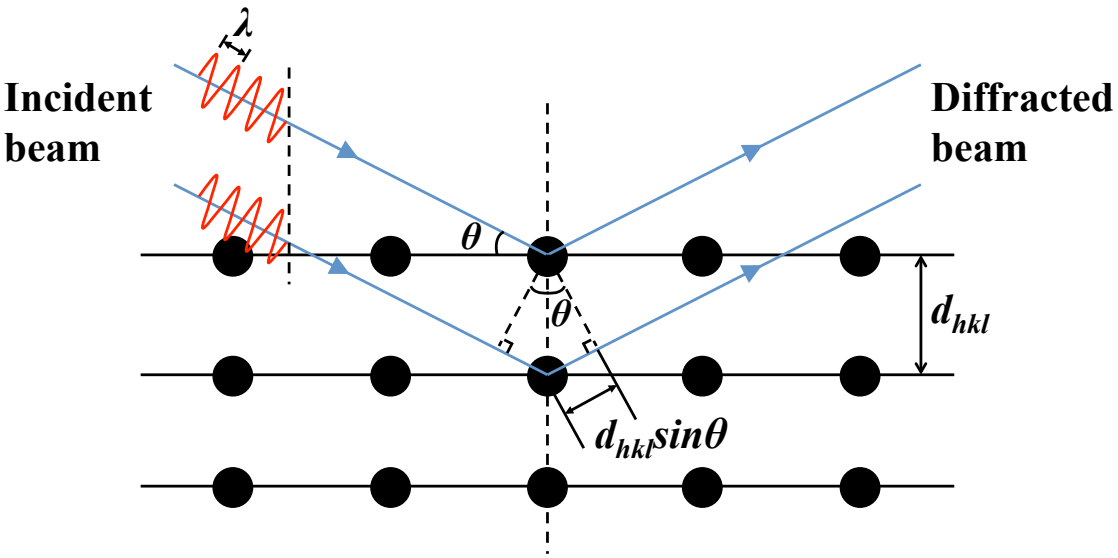

Figure 6.2 Simplified demonstration of Bragg's law.

6.2.1.2 Powder X-ray Diffraction

Materials in powder form usually consist of randomly oriented crystallites. Therefore, their XRD patterns are assumed to be a collection of all possible diffractions at all available crystallographic planes of all crystallites in a given material (David et al. 2006).

In this work, a Bruker D8 Advance X-Ray Diffractometer with Cu K_α radiation (λ = 1.5418 Å) was used for XRD measurements. A 0.2 mm divergence slit was used to limit the divergence of the incident beam and to adjust the peak intensity and shape. A Vantec Position Sensitive Detector (PSD), moving along the circumference of a circle and cutting through diffraction cones at the various diffraction maxima, was used to record the intensity of diffracted X-ray beams as a function of 2θ. The most intensive peak (at 35.149° 2θ) of a standard material (Al_2O_3) was used to check and calibrate detector alignment, before each XRD measurement.

For room temperature measurements, a small amount of powder sample was inertly loaded into a Perspex® airtight dome-shaped sample holder, inside an Ar-filled glovebox. The surface of the powder sample was flattened and smoothed to ensure a well-defined geometry. The measurements were performed in 5–90° 2θ at a scanning rate of 2° min^{-1} using a 9 position multi-changer stage. In case of relatively small amount of powder samples, these samples were loaded into rotating glass capillaries (inner diameter = 0.5 mm) and sealed with silicone grease, then measured in 10-70° 2θ at a scanning rate of 1° min^{-1}.

6.2.1.3 XRD Data Interpretation

XRD patterns were initially analysed using EVA software (equipped with PDF-2 database) for general peak identifications (Bruker 2016). More accurate qualitative and quantitative results for the sample compositions were obtained via a Rietveld refinement method using TOPAS-Academic, jEdit software (Coelho 2007) and published

Crystallographic Information Files (*.cif) from the Inorganic Crystal Systems Database (FIZ Karlsruhe n.d.).

The principle of the Rietveld refinement method – introduced by Hugo Rietveld (Rietveld 1967; Rietveld 1969) – is to fit the entire calculated pattern profile to the experimental data. In theory, a series of variables related to the structure factor and profile function are used in conjunction, to construct a calculated pattern (Young & Wiles 1982). For instance, the calculated intensity (y_i^{calc}) at a point (i) can be simply expressed as:

$$\boldsymbol{y_i^{calc} = s \sum_K L_K |F_K|^2 \phi(2\theta_i - 2\theta_K) P_K A + y_i^{background}} \qquad \textbf{Equation 6.2}$$

where,

s is a scale factor;

L_K is the Lorentz factor and multiplicity, e.g. $1/(\sin\theta \sin 2\theta)$ for powders;

F_K is the structure factor for Bragg's peak K;

$\phi(2\theta_i - 2\theta_K)$ describes the profile function;

P_K describes the preferred orientation;

A describes the absorption;

$y_i^{background}$ is the background profile.

During refinements, these factors are adjusted to minimise the difference between the observed and calculated data through the least-square refinement approach (Wiles & Young 1981). For novel materials, their crystallographic information can be solved

when the predicted profile most closely matches the experimental data. In practice, high quality diffraction data, such as synchrotron X-ray and neutron measurements, would be required to fully refine the structure and atomic composition of XRD phases (Louër 2017).

However, as the structure of materials involved in this work have been solved and their crystallographic information is available online, a pseudo-Rietveld refinement (i.e. quantitative phase analysis) is therefore used for determining unit cell parameters and phase compositions.

6.2.2 Raman and Infrared Spectroscopy

The vibrational spectroscopy techniques, such as Raman and Infrared (IR), are widely used in chemistry and material science to observe the low frequency vibrational modes of chemical bonds, and to provide information (such as symmetry) of chemical structures. These techniques are very efficient and non-destructive.

Different from the X-ray diffraction that can be used only for characterising solid-state crystalline materials, vibrational spectroscopy techniques can examine samples in a range of common physical phases (including solid, liquid, and gas). Thus, samples used can be in the form of powder, solution, vapour or other types (e.g. thin films).

6.2.2.1 Raman Scattering

The Raman scattering effect was discovered by Raman & Krishnan (1928). It requires a monochromatic light source that is usually provided by a laser with wavelengths in near

infrared, visible, or near ultraviolet range. When the laser irradiates at the sample surface, photons can interact with the molecules and polarise their surrounding electron cloud for a short period of time. The molecules are then excited from either the ground rovibronic state (the lowest energy level in the vibrational states, ν = 0) or an excited rovibronic state (the 1st energy level in the vibrational states, ν = 1) to a virtual state (Figure 6.3). The virtual state is unstable and the excited molecules will rapidly collapse back to a more stable (lower energy) state by the emission of photons (Smith & Dent 2005). Depending on the energy difference between the initial energy state of the molecules and the resulting energy state after scattering; the emitted phonons can contain energy that is either equal to (Rayleigh scattering), lower than (Stokes scattering) or higher than (anti-Stokes scattering) the incident phonons (Figure 6.3).

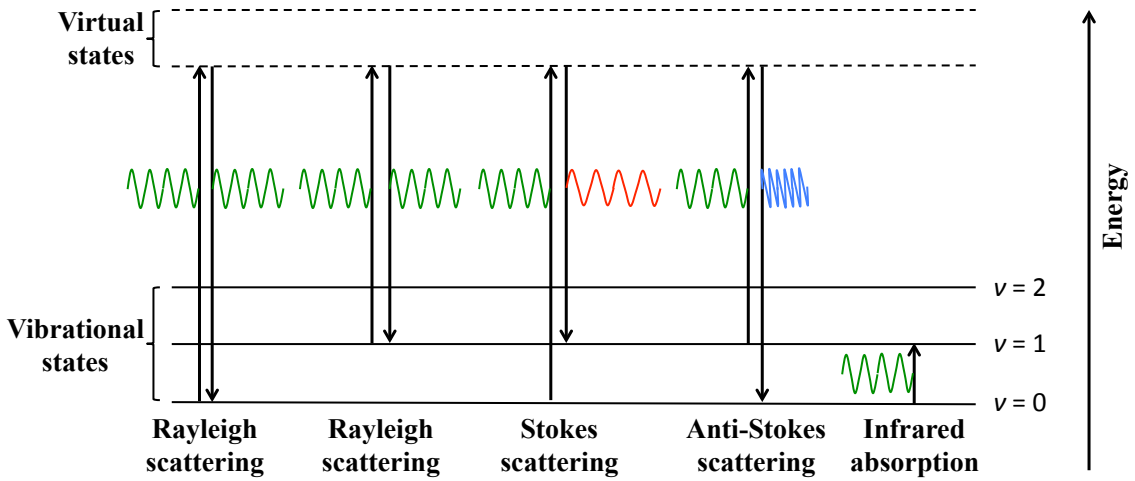

Figure 6.3 A schematic diagram of energy transfer of the Rayleigh scattering, Stokes and Anti-Stokes scatterings, and Infrared absorption.

In fact, the inelastic scattering phenomenon (Stokes and anti-Stokes scatterings) is very rare (e.g. 1 per 10^7 photons) in contrast to the elastic scattering (Rayleigh scatterings). However, they are critical for the Raman technique, as the energy difference between

ground and excited rovibronic states of a certain material is unique. This unique energy difference is often recorded in wavenumbers in a Raman spectrum:

$$\Delta\boldsymbol{\omega} = (\frac{\mathbf{1}}{\boldsymbol{\lambda_0}} - \frac{\mathbf{1}}{\boldsymbol{\lambda_s}})\times\mathbf{10^7} \qquad \textbf{Equation 6.3}$$

where $\Delta\omega$ is the Raman shift (in cm^{-1}), λ_0 and λ_s are the wavelengths (in nm^{-1}) of the incident and scattered phonons, respectively.

Statistically, the numbers of molecules staying at their excited vibrational states are very small (though not zero) at room temperature, so that the anti-Stokes scattering becomes a much weaker effect than the Stokes scattering. Since these two scattering effects describe the same energy gap, only Stokes scattering effects are plotted in common Raman results.

In this work, the Raman measurements were performed using a Renishaw inVia Reflex Raman spectrometer with a confocal microscope (equipped with a ×20 objective) (Figure 6.4-b). The available incident laser sources were 488, 633 nm and 785 nm with a tuneable power of 20-200 mW. The combinations of 488 nm laser with 30 mW powers and 2400 l/mm grating system was used for most of the experiments. However, these parameters will be adjusted in order to obtain the best quality Raman spectra.

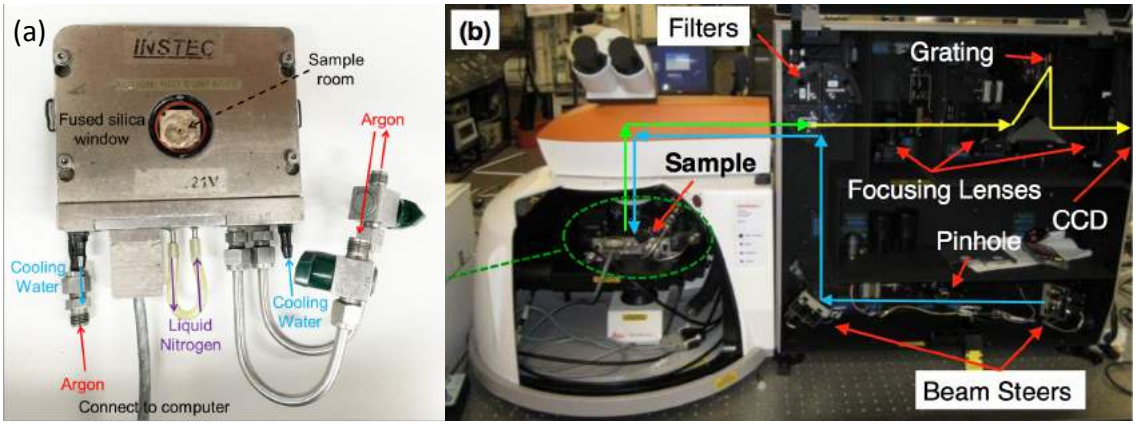

Figure 6.4 (a) INSTEC HCS621V cell. The aluminium crucible with sample is placed on the stage and inside the sample room. Any signal generated due to the fused silica window will be corrected by the calibration. (b) Renishaw inVia Raman Microscope (Guo 2014). The incident laser beam and the scattered are marked in blue and yellow, respectively.

To measure air-sensitive samples, about 5–10 mg of powder sample was loaded in an aluminium crucible, then placed and sealed in the INSTEC HCS621V cell (Figure 6.4-a) inside an Ar glovebox. The INSTEC sample cell is designed to work under 1 bar pressure and between liquid nitrogen temperature (-196 °C) and 600 °C at a heating (or cooling) rate of 1-10 °C/min.

During measurement, the incident laser beam was focused to a ~50 μm diameter spot on the sample's surface in order to preform the Raman scattering effect. The emitted phonons were directed back through a holographic notch filter that removed all photons within ±100 cm^{-1} Raman shifts (including all Rayleigh scatterings). Then the remaining phonons passed through a series of slits and gratings before being channelled to and detected by a Charge-Coupled Device (CCD) (Figure 6.4-b).

The obtained vibrational modes were analysed using Renishaw Wire 4.0 (Renishaw n.d.) and compared with literature data for Raman peak assignments.

6.2.2.2 Fourier Transform Infrared Spectroscopy

The IR measures the energy gap between the ground and excited rovibronic states by matching it with the incident infrared light with a range of different frequencies (Figure 6.3).

The IR and Raman spectroscopy are commonly considered as complementary techniques that provide an overall understanding of the vibrational structure of a given molecule. When the incident light interacts with the sample, Raman measures the polarizability of a molecule; whilst IR tracks the change in the dipole moment of a molecule. Therefore, the symmetry of a molecule is usually considered as a factor that determines the active vibration modes in Raman or IR. Usually, symmetric vibrations lead to intense Raman scattering while asymmetric vibrations cause strong IR absorption and weak (or no) Raman bands (Larkin 2011).

The Fourier transform infrared spectroscopy (FTIR) uses the mathematical process of a Fourier transform to amplify and convert the raw data into actual spectra. In this work, the FTIR measurements were carried out inertly using a BUKER Alpha Platinum-ATR spectrometer in the Institute for Energy Technology (IFE), Norway. The instrument was placed inside an Ar glovebox. A small amount of sample (~2 mg) was placed directly on a diamond disc equipped on the infrared source and then compressed by a one-finger clamp for obtaining intensive signals. The spectra were collected over a wide wavenumber range from 400 to 4000 cm^{-1} with a resolution of 2 cm^{-1} at room temperature. In general, measurements including 32 scans were averaged for each

spectrum and the background. The obtained vibrational results were compared with literature data for assignments.

6.2.3 Differential Scanning Calorimetry

Differential Scanning Calorimetry (DSC) is a powerful thermo-analytical technique, measuring thermodynamic properties of materials, such as the temperature, enthalpy and specific heat of phase transformations.

During measurements, the sample and reference have to be maintaining under the same temperature program. DSC measures the difference in heat flow absorbed by a sample compared to a reference, as a function of temperature. Thus, it is generally divided into power-compensated DSC and heat-flux DSC: the former keeps the power supply as a constant while the later keeps the heat flux as a constant (Brown & Gallagher 1998).

The results of DSC are usually presented in a curve of heat flux as a function of temperature (or time), exhibiting two different conventions, e.g. exothermic or endothermic peaks. For example, fusion often leads to endothermic signals, while crystallisation is linked to exothermic peaks. These curves provide the thermodynamic information, such as the temperature of phase changes, and the enthalpy and specific heat (through integration or differential methods).

Since the DSC is a very sensitive instrument, it requires a multi-point temperature calibration in order to maintaining its high accuracy. The calibration is usually performed using a series of high purity metals (In, Bi, Sn, Pb and Zn) or compounds

(CsCl), whose melting point are well defined. Comparing the measured melting point with the standard at different heating rates makes a calibration curve. This curve is then used to calibrate the experimental measured data for higher accuracy. Apart from that, a measurement of baseline using an empty crucible at certain operating conditions (e.g. heating rate, target temperature and atmosphere) is essential to reduce background noise.

In this work, two types of heat-flux DSC were used: Netzsch 204 Phoenix® High Pressure DSC (HP-DSC) at the University of Turin, Italy (Netzsch n.d.); and Netzsch STA 449 F3 Jupiter® simultaneous Thermogravimetry DSC (TGA-DSC) (Netzsch n.d.) in IFE, Norway. In general, approximately 1 mg of sample was loaded in an Al crucible and sealed with a lid using mechanical pressure. And a clean-empty crucible with lid was used as the reference. The accurate weight of the sample loaded was obtained using an analytical balance (up to ± 0.1 mg accuracy) at the University of Turin, and was measured using the balance system equipped on the TGA-DSC in IFE. However, only the HP-DSC was stored in an Ar glove box. Thus, while using the TGA-DSC, the sample might expose to air for a couple of seconds during transformation. A 2-bar static H_2 was used while using the HP-DSC with the purpose of protecting the instrument; whereas, a 70 mL min^{-1} flowing Ar was applied for the TGA-DSC. The heating/cooling rate used was 5 or 10 °C min^{-1}.

6.2.4 Electron Microscopes

The electron microscopes use a beam of accelerated electrons as their illumination source. The electron has much shorter wavelength than visible light. As a consequence,

the electron microscopes have a much higher resolving power and can reveal the structure and morphology of smaller objects than the common light microscope (Leng 2008). The most common electron microscopes used in materials characterizations are Scanning Electron Microscope (SEM) and Transmission Electron Microscope (TEM).

The SEM images the surface of a specimen through scanning with a focused electron beam. The sample (or at least its surface) must be electrically conductive to avoid scanning faults. The interactions between the electron beam and specimen's surface generate various types of signals (Figure 6.5). These signals carry the characteristic information of the surface, such as its topography and compositions (Leng 2008). The most common captured signal in SEM is the secondary electrons that are emitted very close to the sample surface. In this work, two types of SEM were used to identify the size and morphology of additives: Philips XL-30 (LaB6) with Link Isis EDS and Philips XL-30 FEG Environmental SEM with Oxford Inca EDS.

TEM can usually provide images at a higher resolution than SEM. TEM collects the transmitted electrons from the back of the specimen to produce images (Figure 6.5). As a consequence, it often uses a high voltage electron beam and requires ultrathin (<100 nm) specimen or a suspension of fine powder on a grid. The internal structure and composition information carried by the transmitted electrons are usually magnified by the objective lens system, giving many characteristics, such as morphology, crystallization, stress and magnetic domains (Leng 2008). In this work, a Jeol 2100 200kV LaB6 TEM with Oxford INCA EDS was used to identify the size and morphology of additives.

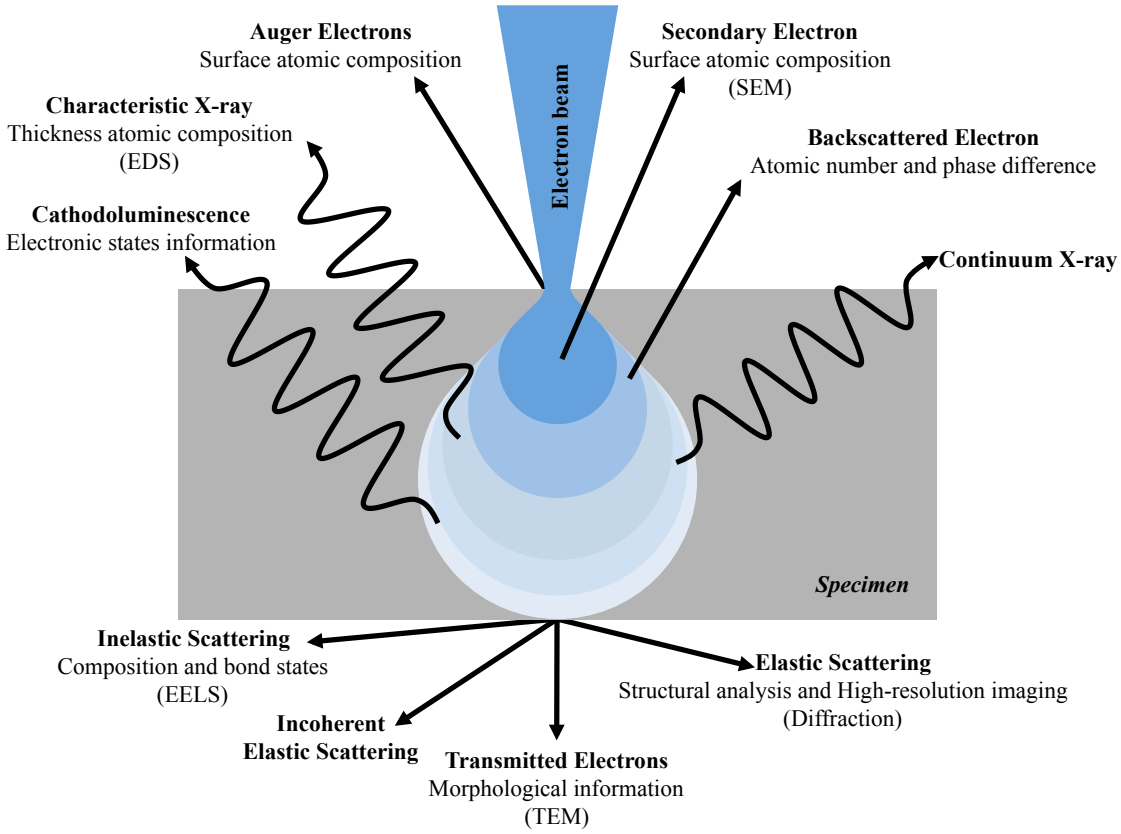

Figure 6.5 A schematic diagram of the interaction with electron beam and a sample, revised from (Claudionico 2013) (EDS = Energy-dispersive X-ray spectroscopy; EELS = Electron Energy Loss Spectroscopy).

6.2.5 Thermal Programmed Decomposition and Mass Spectrometer

6.2.5.1 Thermal Programmed Decomposition

A homemade Thermal Programmed Decomposition (TPD) system was used in this work for thermolysis. Any evolved gases during heating were directed by Ar flow (carrier gas) to a Thermo ProLab Mass Spectrometry (MS) (Figure 6.6).

Around 20 mg of sample was loaded into a stainless steel tube inside an Ar glovebox, and sealed in a T-shape sample holder (T-piece) before being attached to the TPD frame. A thermocouple in contact with the sample was used to obtain the onsite temperature profile during decomposition. Before opening the gate valve that connects

the T-piece to TPD frame, the frame was vacuumed and refilled with Ar for five times. Then a critical leakage check of the entire system was applied, in order to prevent the sample and reaction from oxygen and moisture. The samples was heated at 2 °C min^{-1} to the targeted temperature. The desorbed gases are carried by Ar flowing at 160 mL min^{-1} to the MS via a thermal analysis capillary.

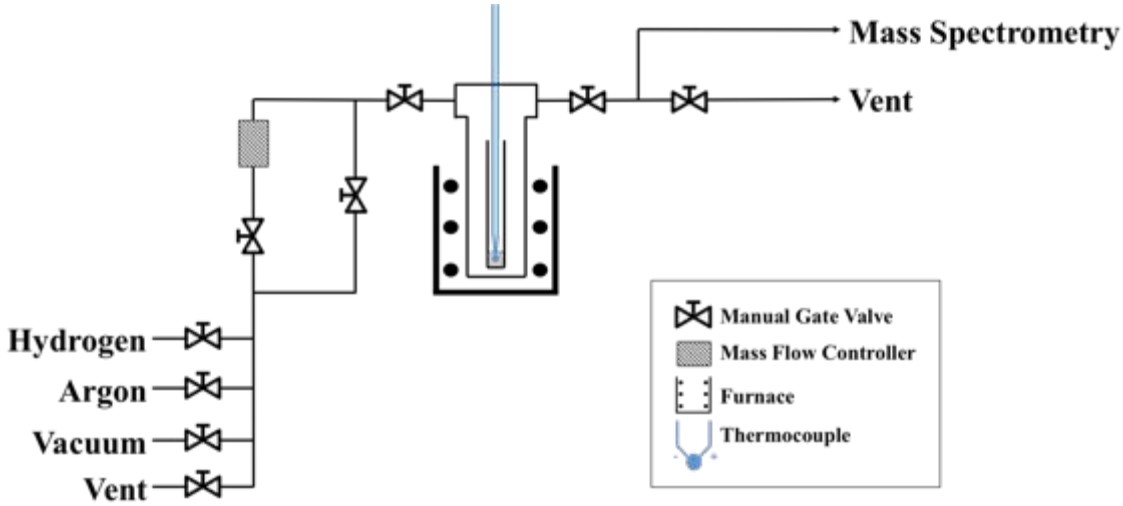

Figure 6.6 A schematic diagram of the homemade Thermal Programmed Decomposition connected to a Mass Spectrometer system, revised from (Guo 2014).

6.2.5.2 Mass Spectrometry

MS is an analytical technique that measures the mass-to-charge (m/z) ratio of ionized chemical species in gaseous phase. A complete MS measurement usually consists three major steps: gas ionization, ions separation and detection (Hoffmann & Stroobant 2007) (Figure 6.7).

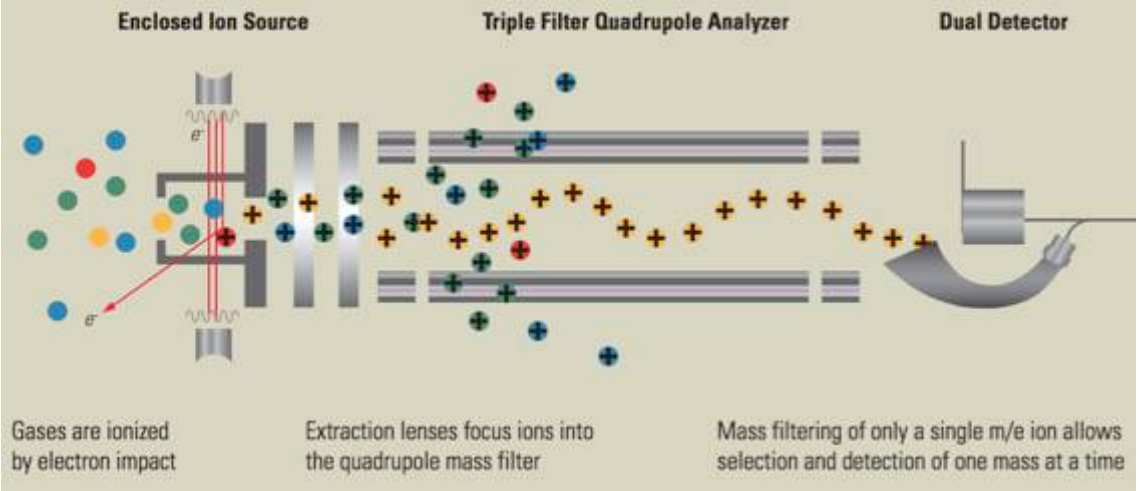

Figure 6.7 A schematic diagram of the analyser architecture for the Thermo ProLab Mass Spectrometry (Thermo Scientific 2011).

The gas ionization is often achieved by high-energy electron impacts, forming the corresponding cations of the analyte. These ions are then extracted from gaseous compounds and directed through the quadropole mass filters (where the ions separation occurs), towards the detector.

The mass filter separates the ions in vacuum according to their m/z ratio. Due to the equation of motion for charged particles (Hoffmann & Stroobant 2007), the location of particle in space and time can be controlled:

$$(\boldsymbol{m/z})\boldsymbol{a} = \boldsymbol{E} + \boldsymbol{v}\times\boldsymbol{B} \qquad \textbf{Equation 6.4}$$

where $\mathrm{m/z}$ is the mass-to-charge ratio, a is the acceleration, E is the electric filed, and $\mathrm{v}\times\mathrm{B}$ is the vector cross product of the ion velocity and the magnetic field.

Thus, only ions with a certain m/z ratio can pass through the filter at a given voltages. All other ions are thrown out of their original path. In practice, the varied voltage applied to the quadropole mass filters consequently brings ions with different m/z ratio to the detector, where a mass spectrum is generated.

Two types of detectors were used in this work: 1) a Faraday cup for monitoring the high concentration gas (carrier gas); and 2) a more sensitive Channeltron® electron multiplier for detecting the low concentration gases (analyte gases). In general, the concentration changes of H_2 (m/z = 2), H_2O (m/z = 18), B_2H_6 (m/z = 26), O_2 (m/z = 32) and Ar (m/z = 40) were record as a function of time.

6.2.5.3 TPD-MS Data Interpretation

The inclusion of a mass flow controller in the TPD-MS system allows the production of pseudo-gravimetric data that provides a relative weight percentage (w_{H_2}) of H_2 release.

$$\boldsymbol{w_{H_2}(t) = \frac{\sum_0^t p_{H_2}(t)\dot{V}_{Ar}V_m^{-1}M_{H_2}}{m_s} \times 100\%} \qquad \textbf{Equation 6.5}$$

In Equation 6.5, the carrier gas (Ar) flows at a constant rate ($\dot{V}_{Ar}$) that is assumed to be unaffected by the gases released from the heated sample.

The partial pressure of H_2 (p_{H_2}) detected experimentally is a function of time (t) and is equivalent to the molar fraction (through an isotherm relation), which provides the volume of H_2 when multiplied with the flow rate.

Because the molar volume of H_2 (V_m) at room temperature and atmosphere pressure is 24.80 L mol^{-1}, an estimate of the number of moles of H_2 released is obtained by multiplying the volume of H_2 with the reciprocal of molar volume.

The number of moles of H_2 multiplied by molecular mass (M_{H_2}) gives the weight of H_2 released. Therefore, the weight loss percentage is calculated by integrating the weight of H_2 released then dividing by the sample mass (m_s).

The TPD-MS system was calibrated using MgH_2 (Goldschmidt, ≥ 95 %) powder, where the relative weight of H_2 released (measured by TPD-MS) from a series of samples with different amount of MgH_2 was linked to the weight losses (6.5 wt.%) measured by a Netzsch TG209 Thermogravimetric Analysis (TGA, cooperated with Dr. Luis Contreras Vasquez) through a linear regression analysis.

6.2.6 Recombination

A homemade Sieverts type Pressure-Composition Isotherms (PCI) apparatus in IFE, Norway (Brinks et al. 2006) was used to dehydrogenate and rehydrogenate samples by subjecting them to suitable conditions (temperature, H_2 pressure or vacuum and processing time).

The PCI setup consists of two reactors on each side of a cupboard, volume tanks, pressure sensors and a number of valves (Figure 6.8). All volumes in reactors, tank, valves, and pipes are precisely calibrated (Nygård 2016). The cupboard is used to

ensure isothermality, and the electric furnace is used to achieve the desired temperature (Bellosta von Colbe 2006).

Figure 6.8 schematically illustrates the left side of the apparatus, in which the reactor side is outside the cupboard and can be detached from the frame for sample loading in the glovebox.

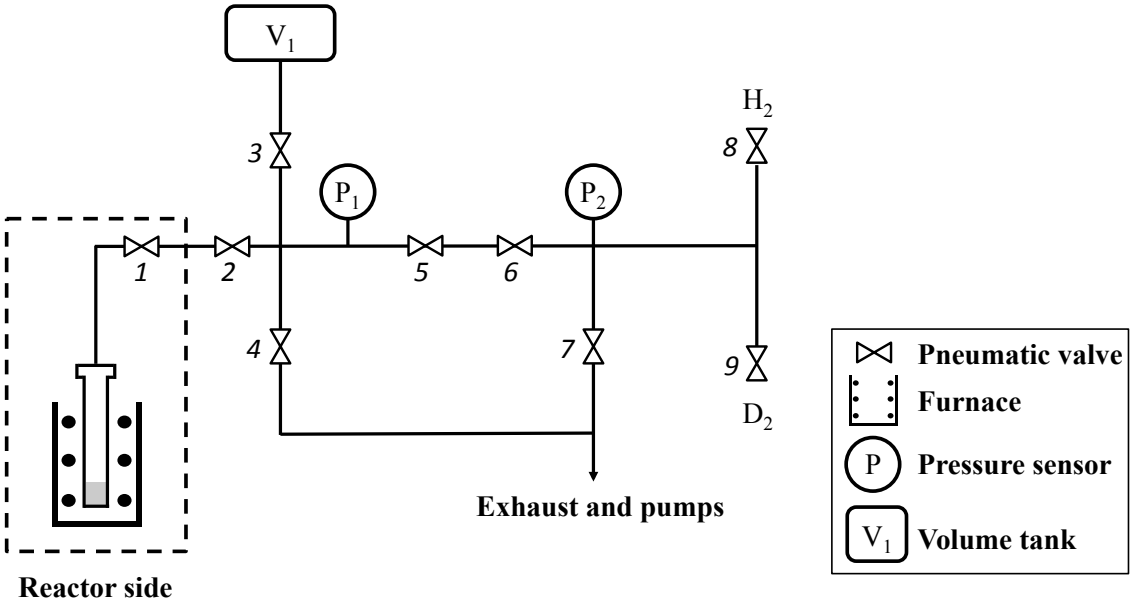

Figure 6.8 A schematic diagram of the left side of the homemade Pressure-Composition Isotherms apparatus in the Institute for Energy Technology, Norway, revised from (Bellosta von Colbe 2006). All valves are pneumatically operated and controlled via computer program.

Approximately 300 mg of sample was loaded into the bottom of the reactor in an Ar glovebox to test the reversible H_2 capacity. The reactor was then sealed, transferred and attached to the PCI rig. In order to avoid air contamination, the PCI rig needed to be fully under vacuum and flushed with a small amount of H_2 several times before opening the pneumatic valves that connected the reactor to the frame. The Ar atmosphere in the reactor was removed and the reactor was kept under vacuum for a leak check

throughout the whole system. Then H_2 or D_2 refilled the reactor until the pressure reached its target.

During measurements, pressure sensor 2 was isolated (by closing value 5, 6, 7, 8 and 9), while the pressure sensor 1 tracked the pressure change in the system. Since H_2 (or D_2) can be treated as an ideal gas, the system pressure (in equilibrium) at a given temperature can be calculated using the Equation 6.6 (Nygård 2016). The pressure difference between this predicted value and the experimental data observed at pressure sensor 1 was converted to the amount of H_2 released from / absorbed by the sample.

$$\boldsymbol{PV = nZRT} \qquad \textbf{Equation 6.6}$$

where P is the pressure, V is the volume, n is the number of moles, Z is the gas compressibility (the empirical model developed by Lemmon et al. (2008) was used), R is the universal gas constant and T is the temperature.

6.3 Thermodynamic Calculation

The Gibbs free energy is a widely used thermodynamic concept that determines the relative stability of a phase or a system (mixture of phases). It can be described as

$$\boldsymbol{G = H - TS} \qquad \textbf{Equation 6.7}$$

where H is the enthalpy, T is the temperature and S in the entropy. A system is defined to be in equilibrium when it is in the most stable state at a constant temperature and

pressure, i.e. a closed system reaches its equilibrium if it has the lowest possible value of Gibbs free energy.

This work used the computing software Thermal-Cal (Thermo-Calc Software 1997) based on the CALPHAD (CALculation of PHAse Diagrams) method (Spencer 2008) to calculate the thermodynamic properties of materials in equilibrium. The key concept is to derive the thermodynamic functions (the Gibbs free energy) of each single phase from all available experimental data and to extrapolate the multi-component phase diagrams through theoretical calculations. This calculation principle is based on the fact that any chemical reaction or phase transformation that results in a negative Gibbs free energy may occur spontaneously (the reaction rate of reaction is dealing with kinetics):

$$\boldsymbol{\Delta G = \left(G_{products} - G_{reactants}\right) = \Delta H - T\Delta S < 0} \qquad \textbf{Equation 6.8}$$

where H is the enthalpy, T is the temperature and S in the entropy.

CALPHAD uses simple models that contain a relatively small number of experimentally optimized variable coefficients to describe the Gibbs free energy of a phase as a function of temperature, pressure and composition. For instance, the Gibbs free energy of a phase can be always described as:

$$\boldsymbol{G^{\varphi} = {}^{ref}G^{\varphi}(T,P) + {}^{id}G^{\varphi}(T,X) + {}^{ex}G^{\varphi}(T,P,X)} \qquad \textbf{Equation 6.9}$$

where ${}^{ref}G^{\varphi}$ is the reference free energy for pure components, ${}^{id}G^{\varphi}$ is the ideal mixing contribution, and ${}^{ex}G^{\varphi}$ is the excess energy of mixing (the non-ideal mixing contribution). In principle, other physical phenomena, such as magnetic, order-disorder transitions that contribute to the Gibbs free energy of a phase should also be considered.

Once the Gibbs free energy function for a phase is assessed, any other thermodynamic quantities can be calculated from it. The equilibrium of a system that consists of multiple phases can be easily calculated by CALPHAD by finding the lowest system Gibbs free energy at a given condition (i.e. temperature, pressure and composition), so that a phase diagram can be predicted.

In this work, the SGTE Substance database V. 4.1 published from the Scientific Group Thermodata Europe (SGTE) (GTT Technologies n.d.) and already published thermodynamic functions (Baricco et al. 2010; Dematteis et al. 2016) were collected in cooperation with Dr. Pinatel Eugenio Riccardo and used as input data. For instance, the thermodynamic functions for elements (such as H_2, Li, B, Na, Si, K) and simple compounds (LiH, NaH, KH, SiO_2) are well demonstrated in the SGTE substance database (GTT Technologies n.d.) that can be used for calculation directly. Besides, the Gibbs free energy function for borohydrides in a format of CALPHAD database are collected from literature and summarised in Table 6.3 and the expressions of macros are summarised in Table 6.4.

Table 6.3 Assessment of Gibbs free energy function of complex compound.

Compound	Phase	Temp. range K		Gibbs free energy assessment
$LiBH_4$	Solid_Orth.	1	386.6	+GORTHEIN#
		386.6	2000	-9638.04924+20.0828437*T+1.61605129E+25*T**(-9)+GLIBH4L#
	Solid_Hex.	1	386.6	+GORTHEIN#+6082.44225-16.1564515*T+1.29142131E-16*T**7
		386.6	553	-2.11122558E+05+3.29071660E+02*T-5.65296358E+01*T*LN(T)-5.77796403E-02*T**2+4.30390228E-06*T**3+7.66385129E+05*T**-1
		553	2000	-9234.71833+16.5249828*T+5.10393987E+26*T**(-9)+GLIBH4L#
	Liquid	1	533	+GORTHEIN#+10413.8671-22.0351513*T+2.73911433E-17*T**7
		533	2000	+GLIBH4L#
$NaBH_4$	Solid	298.15	500	+GNABH4S#
	Liquid	298.15	6000	-2.08097940E+05+6.80119082E+02*T-1.19233000E+02*T*LN(T)
KBH_4	Solid	298.15	6000	+GB1H4K1#
	Liquid	298.15	6000	+GB1H4K1#+20000-22.4*T
$Li_2B_{10}H_{10}$	Solid	298.15	6000	+10*GHSERBB+4*GH2GAST+2*GLIHS-348000+480*T
$Li_2B_{12}H_{12}$	Solid	298.15	6000	+12*GHSERBB+6*GH2GAST+2*GHSERLI-7.833E5+702*T
$Na_2B_{12}H_{12}$	Solid	298.15	6000	+12*GHSERBB+6*GH2GAST+2*GHSERNA-8.68E5+750*T
Li_2SiO_3	Solid	298.15	6000	+F12491T#+28032.8-19.0181818*T
	Liquid	298.15	6000	+F12491T#
Li_4SiO_4	Solid	298.15	6000	+F12536T#+31129-20.3723822*T
	Liquid	298.15	6000	+F12536T#

"T" stands for temperature;
"T**n" means T to the power of n, e.g. T^n; "LN" is the natural logarithm;
Macros are summarised in Table 6.4;

Table 6.4 Macros used in the assessment of Gibbs free energy function for complex compounds (Table 6.3).

Marcos	For	Temp. range K		Gibbs free energy assessment
GORTHEIN	$LiBH_4$	1	6000	-2.0643880E+05+GEIN#-7.0568714E-02*T**2-3.0118631E-05*T**3
GEIN	$LiBH_4$	1	6000	+3.1284347E+02*GEIN15R#+GEIN3RT#*LN(GEINEXP#)
GEIN15R	$LiBH_4$	1	6000	12.4716
GEIN3RT	$LiBH_4$	1	6000	+24.9432*T
GEINEXP	$LiBH_4$	1	6000	+1-1*EXP(-RATIOEIN#)
RATIOEIN	$LiBH_4$	1	6000	+312.84347*T**(-1)
GLIBH4L	$LiBH_4$	1	6000	-2.2165569E+5+7.5049266E+02*T-1.2470000E+02*T*LN(T)
GNABH4S	$NaBH_4$	298.15	600	-215396.375+362.347799*T-65.62694*T*LN(T)-.039943205*T**2+2.0758E-06*T**3+82445.5*T**(-1)
		600	900	-246176.6+712.133426*T-116.5235*T*LN(T)-.00822906*T**2-2.133325E-07*T**3+3283588.5*T**(-1)
		900	1200	-156907.445-242.126185*T+22.42824*T*LN(T)-.10502305*T**2+1.25379417E-05*T**3-7527375*T**(-1)
		1200	1500	-320118.497+1285.22558*T-194.8747*T*LN(T)+.02314327*T**2-1.5941835E-06*T**3+15372465*T**(-1)
		1500	1800	-244558.461+776.868137*T-126.3704*T*LN(T)-.0038875*T**2+3.504385E-07*T**3
		1800	2000	-255664.881+909.819332*T-145.458*T*LN(T)+.007037235*T**2-6.90789333E-07*T**3
GB1H4K1	KBH4	298.15	600	-293231.57+1332.6103*T-226.809*T*LN(T)+.19700505*T**2-5.85629833E-05*T**3+1955620*T**(-1)
		600	800	-488023.684+3356.66883*T-514.005*T*LN(T)+.32279125*T**2-5.04640167E-05*T**3+23332510*T**(-1)
		800	2000	-288613.971+822.480344*T-134.187*T*LN(T)+.00330155*T**2-3.85736667E-07*T**3+3833085*T**(-1)
GHSERBB	$Li_2B_{10}H_{10}$ $Li_2B_{12}H_{12}$ $Na_2B_{12}H_{12}$	298.15	1100	-7735.28368+107.111863*T-15.6641*T*LN(T)-.006864515*T**2+6.188775E-07*T**3+370843*T**(-1)
		1100	2348	-16649.4743+184.801744*T-26.6047*T*LN(T)-7.9809E-04*T**2-2.55601667E-08*T**3+1748269.5*T**(-1)
		2348	6000	-21357.9884+222.327208*T-31.4*T*LN(T)
GH2GAST	$Li_2B_{10}H_{10}$ $Li_2B_{12}H_{12}$ $Na_2B_{12}H_{12}$	298.15	1000	-9522.97393+78.5273873*T-31.35707*T*LN(T)+.0027589925*T**2-7.46390667E-07*T**3+56582.3*T**(-1)
		1000	2100	+180.10884-15.6128262*T-17.84857*T*LN(T)-.00584168*T**2+3.14618667E-07*T**3-1280036*T**(-1)
		2100	6000	-18840.1661+92.3120249*T-32.05082*T*LN(T)-.0010728235*T**2+1.14281783E-08*T**3+3561002.5*T**(-1)
GLIHS	$Li_2B_{10}H_{10}$	298.15	965	-100373.458+135.665823*T-21.00559*T*LN(T)-.021857085*T**2-1.651466E-09*T**3+226236.7*T**(-1)
		965	2000	-112352.348+360.842441*T-55*T*LN(T)
GHSERLI	$Li_2B_{12}H_{12}$	200	453.6	-10583.8178+217.637496*T-38.94049*T*LN(T)+.03546693*T**2-1.98698167E-05*T**3+159994.05*T**(-1)
		453.6	3000	-9057.23628+179.265766*T-31.22837*T*LN(T)+.0026332215*T**2-4.38057833E-07*T**3-102386.85*T**(-1)

Continued

GHSERNA	$Na_2B_{12}H_{12}$	200	370.8	-11989.4321+260.548717*T-51.03936*T*LN(T)+.07230665*T**2-4.36382833E-05*T**3+132153.75*T**(-1)
		370.8	2300	-10997.4281+199.589765*T-38.11988*T*LN(T)+.009745855*T**2-1.70664E-06*T**3+34342.48*T**(-1)
F12491T	Li_2SiO_3	298.15	500	-1679374.59+328.194552*T-48.08504*T*LN(T)-.15307455*T**2+4.545045E-05*T**3+646942.5*T**(-1)
		500	800	-1696427.94+770.523352*T-123.582*T*LN(T)-.01324715*T**2-9.76545667E-07*T**3+1310686*T**(-1)
		800	1100	-1674386.81+495.861422*T-82.42647*T*LN(T)-.048431055*T**2+4.820645E-06*T**3-968548*T**(-1)
		1100	1474	-1771098.58+1402.07621*T-211.5054*T*LN(T)+.02874868*T**2-3.90406333E-06*T**3+12719445*T**(-1)
		1474	4000	-1726225.71+1089.30771*T-167.36*T*LN(T)
F12536	Li_4SiO_4	298.15	1528	-2377346.24+824.272069*T-137.3189*T*LN(T)-.03416236*T**2+491620*T**(-1)
		1528	2200	-2525687.98+1966.94823*T-287.0224*T*LN(T)

"T" stands for temperature;
"T**n" means T to the power n, e.g. T^n; "LN" is the natural logarithm;
"EXP" is the exponential function

CHAPTER 7 LITHIUM BOROHYDRIDE

The focus of this chapter is:

- To characterise the crystal structure, vibrational frequencies, thermodynamic property of $LiBH_4$;
- To investigate the thermal decomposition mechanism of $LiBH_4$ in Ar;
- To study the effect of the additives (SiO_2 and Ni) on the dehydrogenation of $LiBH_4$ in Ar.

7.1 Lithium Borohydride

7.1.1 Sample Characterisations

7.1.1.1 As-received $LiBH_4$

Figure 7.1 shows the XRD pattern and Raman & FTIR spectra of the as-received $LiBH_4$ (Sigma-Aldrich, > 95%) at room temperature. Peaks were caused by the orthorhombic $LiBH_4$ phase.

The pseudo-Rietveld refinement results (Figure 7.2) showed that the as-received $LiBH_4$ had a high purity. Although the manufacturer suggests less than 5 wt.% impurities (e.g. sodium halide) were possible, they were not detectable by the lab-based XRD (Dutrow & Clark n.d.). The refined lattice parameters of as-received $LiBH_4$ are summarised in Table 7.1. They were in good agreement with the range of published data (Soulié et al. 2002; Züttel 2003; Filinchuk et al. 2008; Roedern et al. 2016).

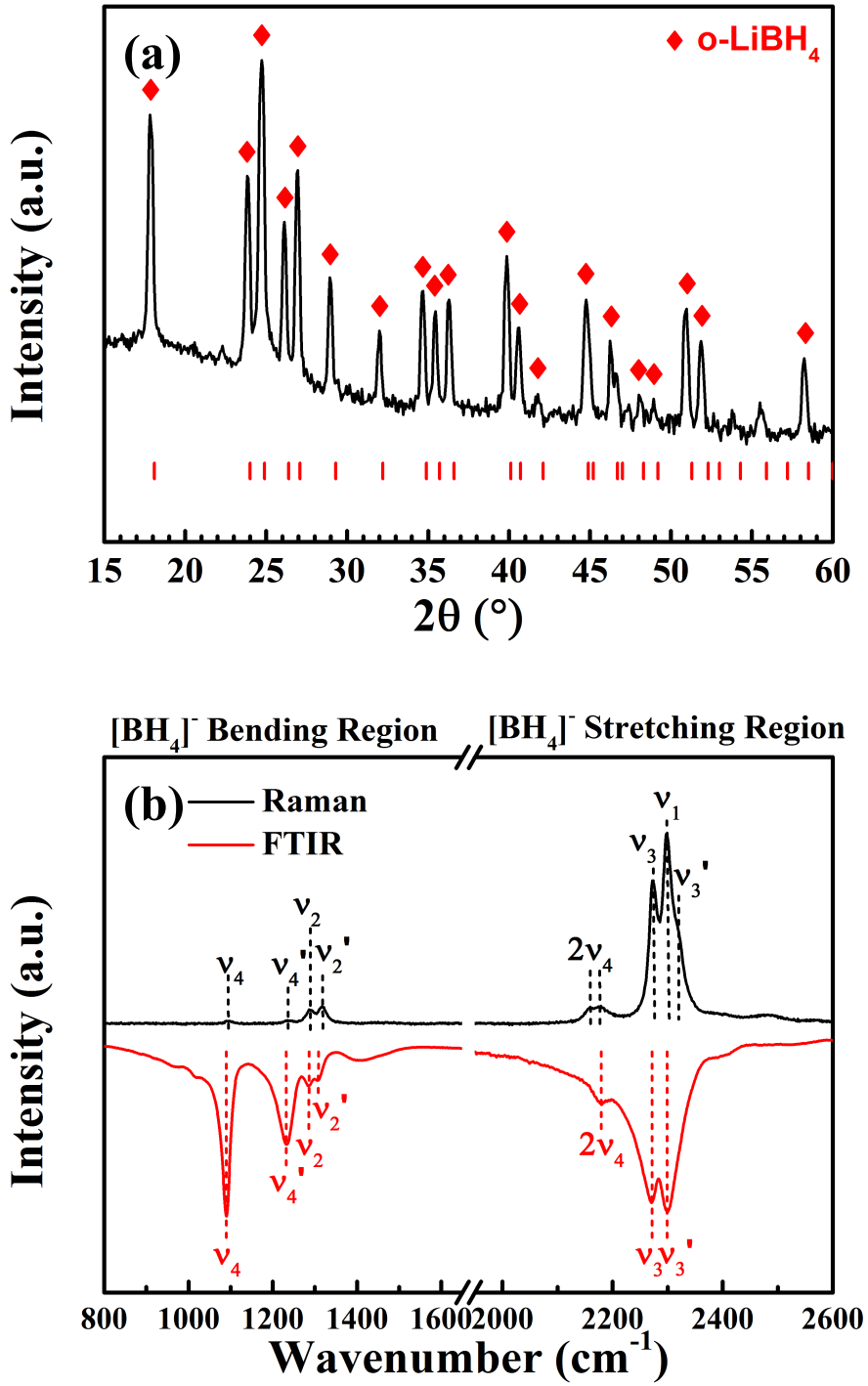

Figure 7.1 (a) XRD (Cu K_α radiation, λ = 1.5418 Å) pattern (intensity in log scale) of as-received $LiBH_4$ at room temperature compared to an experimental data (red vertical lines) from literature (Filinchuk et al. 2008). The weak peaks in the 2θ regions of 20-23°, 30-31°, 47-48°, 53-57° are noise, which appear larger due to log-scale plotting. (b) Raman (measured with 488 nm laser and 2400 l/mm grating system) and FTIR spectra of as-received $LiBH_4$ at room temperature. A horizontal break was used to divide the spectra into $[BH_4]^-$ bending and stretching regions. Dashed lines are guides for the eye.

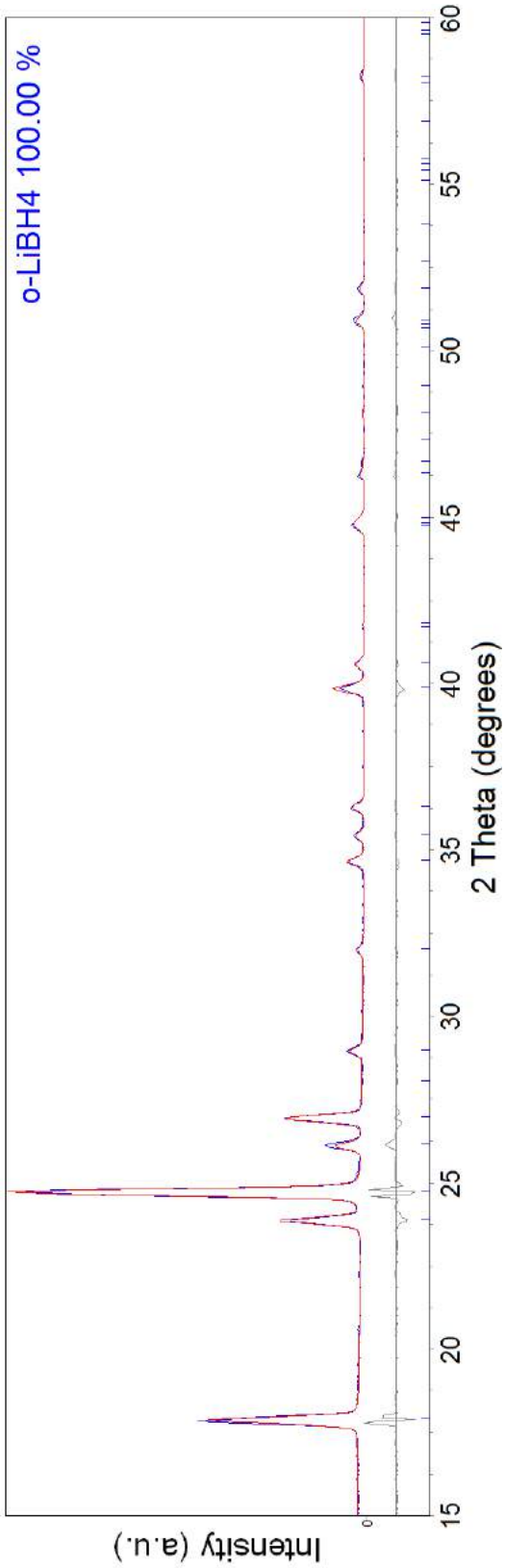

Figure 7.2 Pseudo-Rietveld refinement result of the as-received $LiBH_4$, including the observed XRD (Cu K_α radiation, λ = 1.5418 Å) profile (blue), the calculated profile (red, used to fit the observed profile) and the difference profile (grey). The goodness-of-fit was 2.215.

Table 7.1 Refined lattice parameters (Å) of as-received and as-milled $LiBH_4$ compared to literature data.

	As-received	As-milled	Literature
a	7.199 ± 0.003	7.179 ± 0.002	7.130 – 7.190
b	4.438 ± 0.002	4.438 ± 0.001	4.398 – 4.445
c	6.798 ± 0.003	6.806 ± 0.002	6.798 – 6.813

Depending on the vibration modes, the spectroscopy results can be divided into two ranges:

- Peaks in 1000-1350 cm^{-1} were $[BH_4]^-$ bending modes, consisting of symmetric ν_2 and asymmetric ν_4 modes (together with their splitting modes ν_2' and ν_4');

- Peaks in 2000-2500 cm^{-1} were $[BH_4]^-$ stretching modes, including the symmetric ν_1 and asymmetric ν_3 (with its splitting mode ν_3') modes, and a combination mode $2\nu_4$. The symmetric ν_1 mode was not observed in FTIR, because there is no change in dipole moment for a symmetric stretching mode.

The observed wavenumbers (cm^{-1}) of as-received $LiBH_4$ are summarised in Table 7.2. Results agreed well with the literature data (K. B. Harvey & McQuaker 1971; Gomes et al. 2002; Racu et al. 2008).

Table 7.2 Experiment Raman and FTIR frequencies (cm^{-1}) of as-received and as-milled $LiBH_4$ compared to literature values.

Mode			Raman			FTIR	
			Experiment		Literature	Experiment	Literature
			As-received	As-milled		As-received	
			188	193	189	-	-
External vibrations			252	250	255	-	-
			n.a.	n.a.	285	-	-
Internal bending	ν_4	A_g	1099	1096	1090	1089	1089
	ν_4'	A_g	1237	n.a.	1235	1233	1254
	ν_2	B_{1g}	1288	1290	1286	1285	1284
	ν_2'	A_g	1318	1319	1316	1307	1323
Internal stretching	$2\nu_4$		2159	2163	2156		
	$2\nu_4'$		2179	2180	2177	2180	2176
	ν_3	A_g	2274	2273	2275	2271	2277
	ν_1	A_g	2298	2299	2301	-	-
	ν_3'	A_g	2321 (sh)	2318	2321 (sh)	2300	2307
	ν_3''		-	-	-	n.a.	2350
	$\nu_2+\nu_4$		-	-	-	n.a.	2387 (sh)
	Com.		2402	2396	2391	-	-
	$\nu_2'+\nu_4$		-	-	-	2410	2423
	Com.		2489	2488	2491	-	-
	Com.		2575	2574	2572	-	-

* sh = shoulder
* Com. = Combination bands

7.1.1.2 As-milled $LiBH_4$

The as-milled sample was prepared using ball milling under the conditions described in Section 6.1.1. Its room temperature XRD, Raman and refinement results are shown in Figure 7.3-7.4.

The crystal structure and vibrational modes remained unchanged after ball milling. However, the most intensive peak in XRD was changed from (200) to (101).

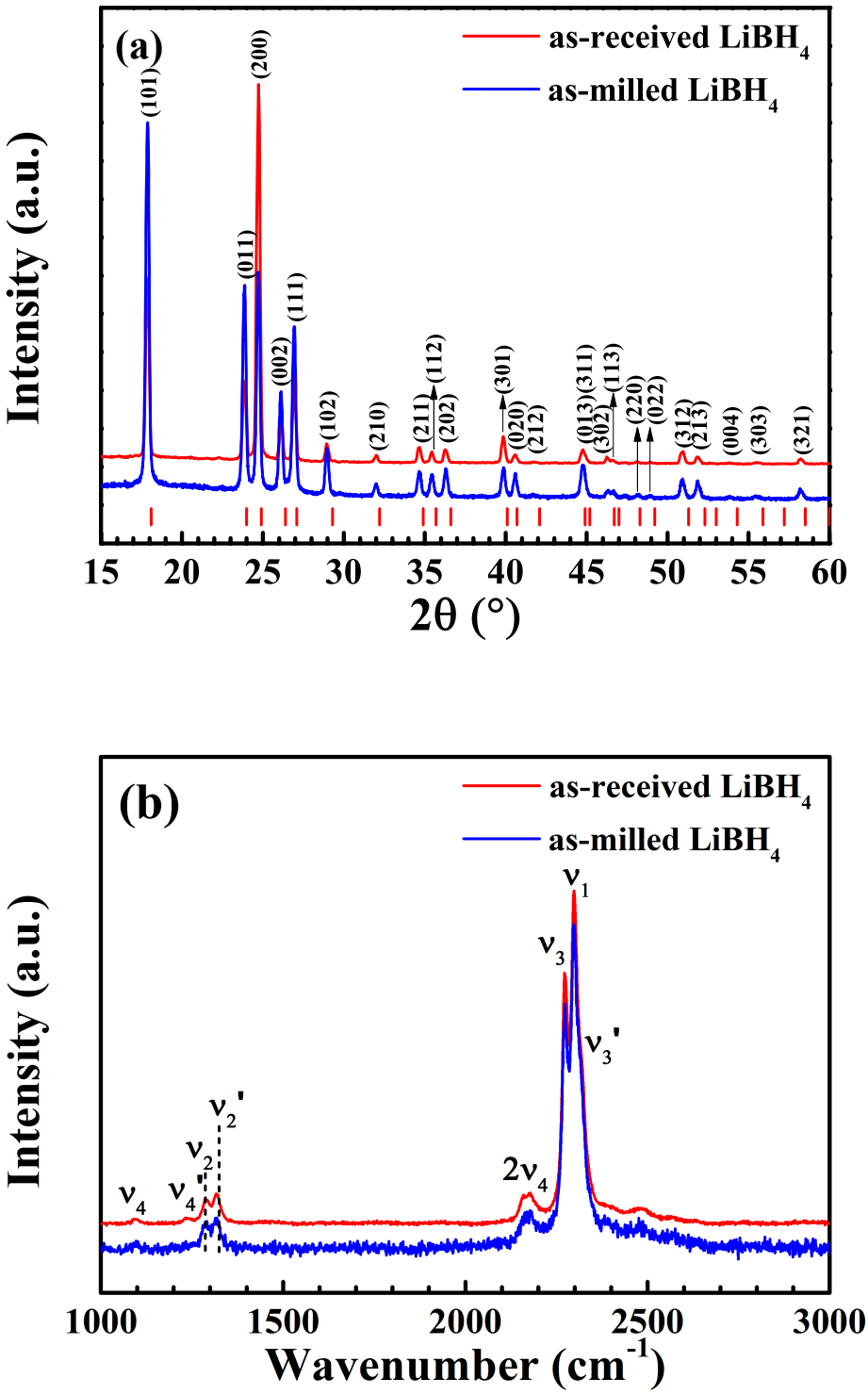

Figure 7.3 (a) XRD patterns (Cu K_α radiation, λ = 1.5418 Å) of as-received and as-milled $LiBH_4$ at room temperature compared to experimental data (red vertical lines) from the literature (Filinchuk et al. 2008). (b) Raman spectra (measured with 488 nm laser and 2400 l/mm grating system) of as-received and as-milled $LiBH_4$ at room temperature. Peak intensities were normalized to make spectra easier to compare. Dashed lines are guides for the eye.

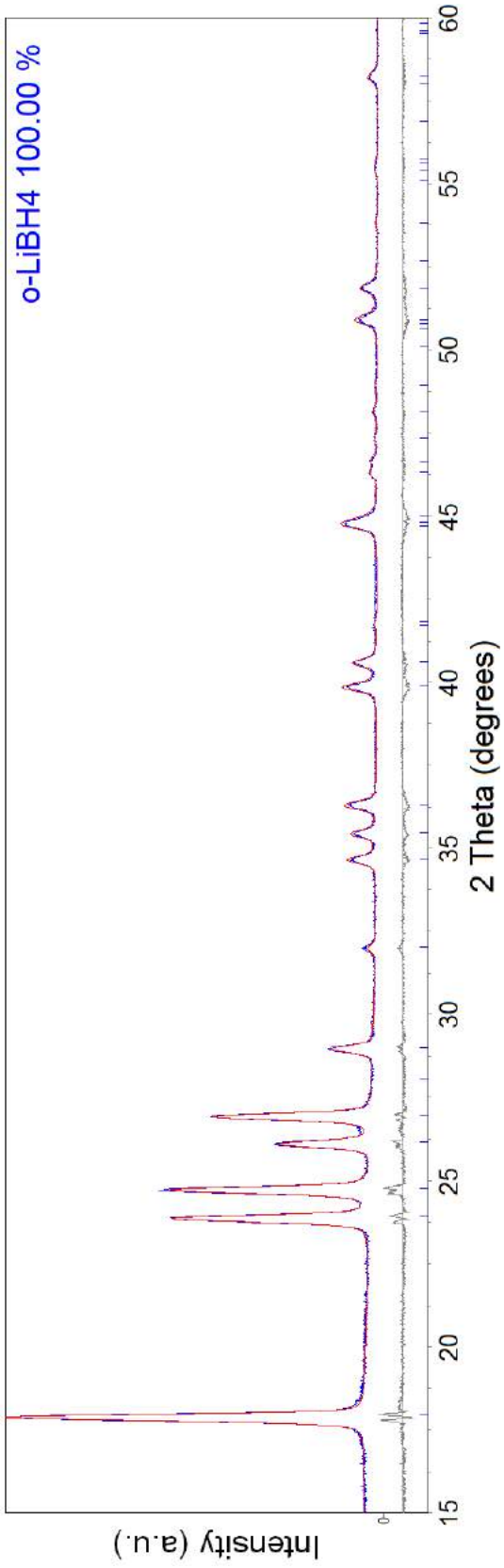

Figure 7.4 Pseudo-Rietveld refinement of as-milled $LiBH_4$, including the observed XRD (Cu K_α radiation, λ = 1.5418 Å) profile (blue), the calculated profile (red, used to fit the observed profile) and the difference profile (grey). The goodness-of-fit was 1.549.

For the as-milled $LiBH_4$, all X-ray peaks were fitted to the orthorhombic phase in the pseudo-Rietveld refinement (Figure 7.4), indicating a high purity. The refined lattice parameters of as-milled $LiBH_4$ (Table 7.1) are close to those of as-received sample; however, synchrotron XRD data suggested that the milling process can reduce the lattice parameters (<1%) due to induced strains as a function of milling temperature (Lang et al. 2012).

7.1.2 Thermal Analysis

Figure 7.5 shows the DSC trace of as-milled $LiBH_4$ heated in 2 bar static H_2, where three main endothermic features (2 sharp peaks and a broad area) were observed.

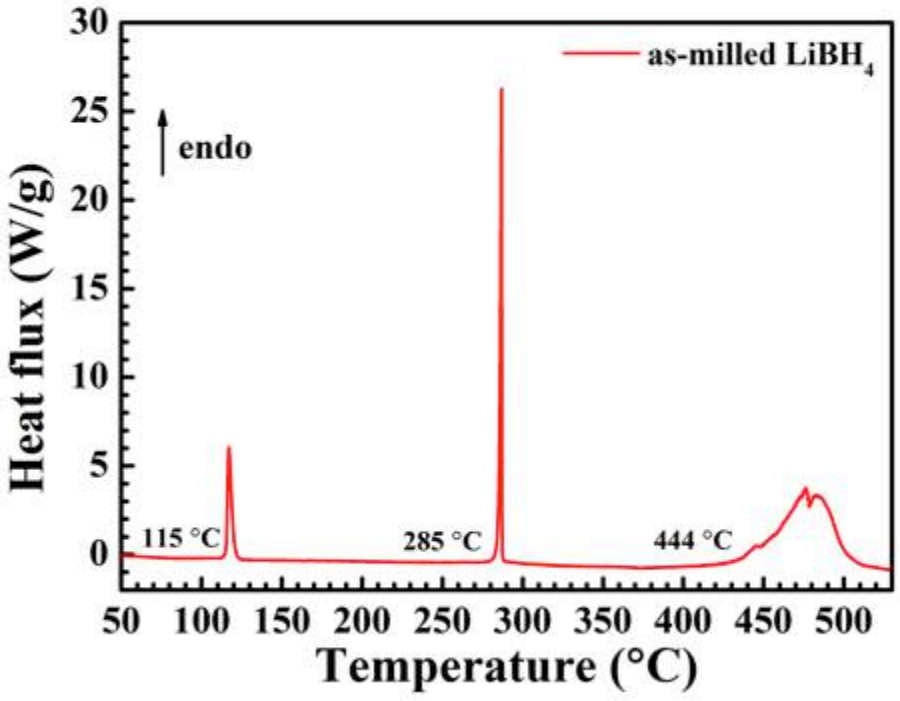

Figure 7.5 DSC trace of the as-milled $LiBH_4$ heated up to 530 °C in 2 bar static H_2 at a heating rate of 5 °C min^{-1}.

The 1st endothermic peak at 115 °C corresponded to the orthorhombic-hexagonal polymorphic transformation of $LiBH_4$. The calculated enthalpy was 5.11 ± 0.26 kJ mol^{-1} $LiBH_4$, which agreed with the reported value of 5.32 ± 0.90 kJ mol^{-1} $LiBH_4$ (El Kharbachi et al. 2012).

The 2nd endothermic peak at 285 °C was the fusion of $LiBH_4$, and is in good agreement with literature (El Kharbachi et al. 2011). The enthalpy of melting was 8.27 ± 0.41 kJ mol^{-1} $LiBH_4$ that was similar to the 8.18 ± 0.30 kJ mol^{-1} $LiBH_4$ reported.

DSC results suggested that thermal decomposition of $LiBH_4$ in 2 bar static H_2 occurred from 444 °C with a broad endothermic signal. This broadening was caused by the complicated decomposition pathways, passing through multiple steps as a function of conditions (Yan et al. 2012). The integration of DSC curves from 444 °C to 530 °C gave the enthalpy of dehydrogenation of 47.02 ± 2.40 kJ mol^{-1} $LiBH_4$, which was far below the reported 84 to 111 kJ mol^{-1} $LiBH_4$ (Pendolino 2013). This is likely due to the different techniques used, as these literature values were obtained from theoretical calculations (such as first-principles calculations and calculation through standard enthalpy of formation for $LiBH_4$ and LiH) and different experimental measurements (such as Pressure-Concentration-Isothermal method, Thermal gravimetric analysis and etc.).

7.1.3 Thermodynamic Simulation

The thermal decomposition of $LiBH_4$ is complicated. Depending on temperatures and pressures applied, the possible products include $(Li)_n$, $(B)_n$, $(LiB)_n$, $(LiH)_n$, $Li_2B_nH_n$ (or

$Li_nB_nH_m$, $m \leq 4n$) (Huang et al. 2016). In reality, $Li_2B_{10}H_{10}$ and $Li_2B_{12}H_{12}$ were experimentally observed above 150 °C in inert gas or H_2 (Orimo et al. 2006; Hwang et al. 2008; Friedrichs, Remhof, Hwang, et al. 2010; Pitt et al. 2013). Because of their complex structures, a series of intermediate metastable polyborane complexes were expected during the formation process.

Figure 7.6 shows the calculated phase diagram of $LiBH_4$ using Thermo-Cal software (Thermo-Calc Software 1997) considering Equations 7.1 – 7.5.

$\boldsymbol{LiBH_4 = Li + B + 2H_2}$	**18.5 wt. %**	**Equation 7.1**
$\boldsymbol{LiBH_4 = LiH + B + 3/2H_2}$	**13.9 wt. %**	**Equation 7.2**
$\boldsymbol{LiBH_4 = 5/6LiH + 1/12Li_2B_{12}H_{12} + 13/12H_2}$	**10.0 wt. %**	**Equation 7.3**
$\boldsymbol{LiBH_4 = 4/5LiH + 1/10Li_2B_{10}H_{10} + 11/10H_2}$	**10.2 wt. %**	**Equation 7.4**
$\boldsymbol{2LiH = 2Li + H_2}$	**12.7 wt. %**	**Equation 7.5**

Calculations suggested the decomposition of $LiBH_4$ through LiH, $Li_2B_{12}H_{12}$ and H_2 (Blue triangle) was more thermodynamically favourable due to the high stability of $Li_2B_{12}H_{12}$. From a thermodynamic point of view, solid-state dehydrogenation through LiH, $Li_2B_{12}H_{12}$ and H_2 around room temperature is possible when the H_2 backpressure is very small (e.g. smaller than 10^{-3} bar). However, this reaction was not experimentally observed at such low temperatures, because the formation of $Li_2B_{12}H_{12}$ is kinetically hindered (El Kharbachi et al. 2012).

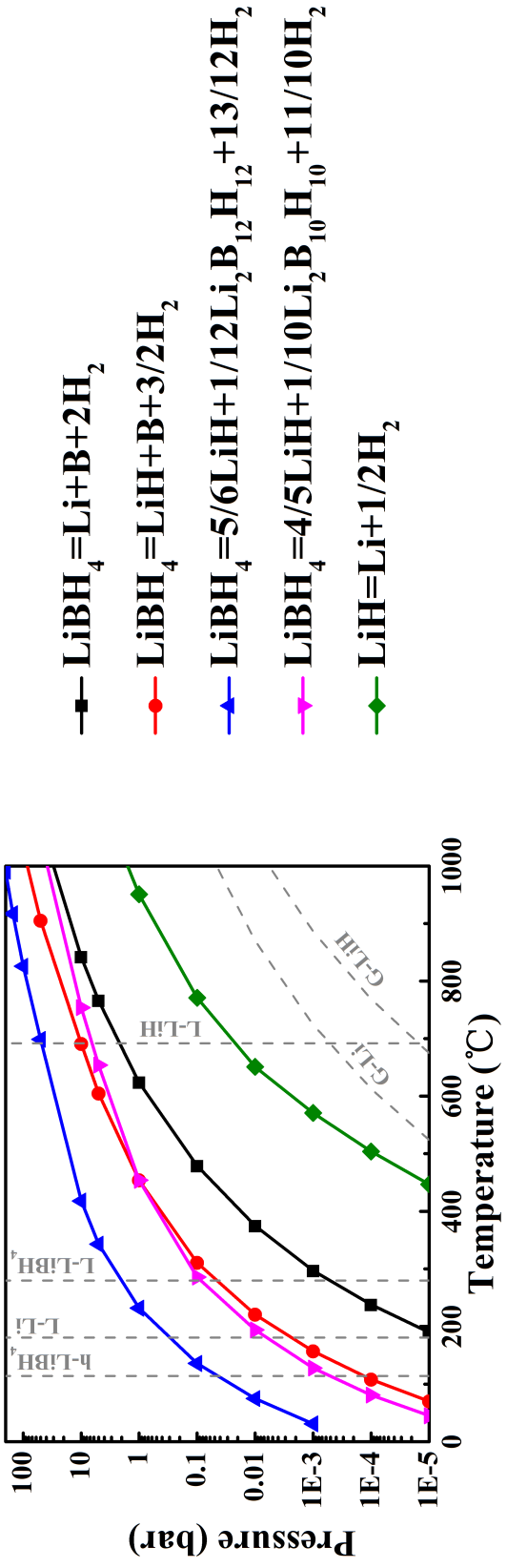

Figure 7.6 CALPHAD calculated phase diagram of $LiBH_4$. The dashed lines indicate the phase transition and fusion of $LiBH_4$, fusion of Li and LiH, gasification of Li and LiH as a function of temperature and pressure.

The decomposition pathway across LiH, $Li_2B_{10}H_{10}$ and H_2 (Pink inverted triangle) had a similar trend with the pathway through LiH, B and H_2 (Red dot). When the pressure was higher than 1 bar H_2, $LiBH_4$ preferred to decompose into LiH, B and H_2. Otherwise, the formation of LiH, $Li_2B_{10}H_{10}$ and H_2 was more favourable. However, similar to $Li_2B_{12}H_{12}$, the formation of $Li_2B_{10}H_{10}$ might be kinetically hindered (El Kharbachi et al. 2012).

The decomposition into Li, B and H_2 (Black square) was less favoured compared with other reactions. In practice, metallic Li has not yet been observed as a decomposition product of $LiBH_4$. This might be because LiH has a high thermal stability (Green square) and will not decompose below 450 °C even under high vacuum conditions (i.e. H_2 pressure = 10^{-5} bar).

7.1.4 Thermo-decomposition

7.1.4.1 *In situ* Raman spectroscopy

Figure 7.7 shows a line-stacked figure of *in situ* Raman spectra at selected temperatures with peaks assigned (e.g. room temperature, 112 °C for phase transition, 275 °C for fusion and 324 °C decomposition onset temperature).

At room temperature, $LiBH_4$ had an orthorhombic structure (o-$LiBH_4$). It changed into a hexagonal structure (h-$LiBH_4$) when heated to 112 °C. The h-$LiBH_4$ had broad peaks corresponding to $[BH_4]^-$ bending (ν_2) and stretching (ν_1) modes observed at 1303 and 2295 cm^{-1}, respectively, and agreed with Gomes et al. (2002). This spectrum

simplification was because of the increase in point group symmetry of $[BH_4]^-$ from C_s to C_{3v} (Hagemann et al. 2009).

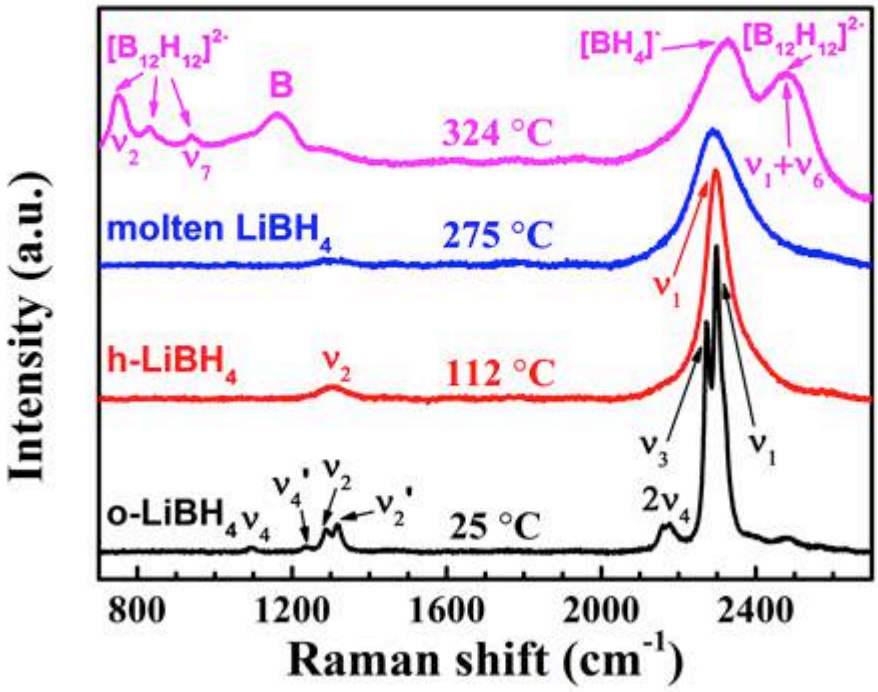

Figure 7.7 *In situ* Raman spectra (measured with 488 nm laser and 2400 l/mm grating system) of as-received $LiBH_4$ at 25, 112, 275 and 324 °C. The sample was heated at 2 °C min^{-1} in Ar flowing at 100 mL min^{-1}.

When fusion occurred, the molten $LiBH_4$ had similar peak positions compared to h-$LiBH_4$. But the two peaks corresponding to $[BH_4]^-$ bending (ν_2) and stretching (ν_1) modes became much broader and the peak intensities reduced as a result of losing crystallinity.

During decomposition, amorphous boron was identified around 1100 cm^{-1} (B-B skeletal vibration) and several vibration modes of $Li_2B_{12}H_{12}$ were detected at 752 cm^{-1} (boron breathing mode, ν_2), 832 cm^{-1}, 940 cm^{-1} (ν_7) and around 2500 cm^{-1} (the equatorial and

apical breathing modes, ν_1 and ν_6) (Muetterties et al. 1962; He et al. 2015). The signals for boron and $Li_2B_{12}H_{12}$ indicated that the reactions described in Equation 7.2 and Equation 7.3 occurred simultaneously.

Figure 7.8 provides an overview of the decomposition process of as-received $LiBH_4$ by two surface plots of *in situ* Raman spectra (if viewed from above). Due to the fact that the signal intensity of $[BH_4]^-$ bending modes (1000 to 1350 cm^{-1}) were much weaker than those of $[BH_4]^-$ stretching modes (2000 to 2500 cm^{-1}), spectra of $[BH_4]^-$ bending modes were hardly visible in Figure 7.8-a. Therefore, the bending region was measured solely as shown in Figure 7.8-b.

The temperatures of phase change, fusion and decomposition in Figure 7.8 were determined by manually checking the change of peaks (intensity and peak width) in every spectrum in the *in situ* results. For instance:

- The phase transition temperature was assigned according to the temperature at which peaks of hexagonal structure were first shown in the spectra. The polymorphic transformation temperatures were therefore found between 100 and 112 °C, which agreed with the DSC result (Figure 7.5).

- In addition, the fusion temperatures (~280 °C) were found, when the peak intensity decreased and only the baseline was presented. The *in situ* Raman suggested a slightly lower (~ 5 °C) fusion temperature than the DSC. However, the later was more accurate in determining temperature during phase changing.

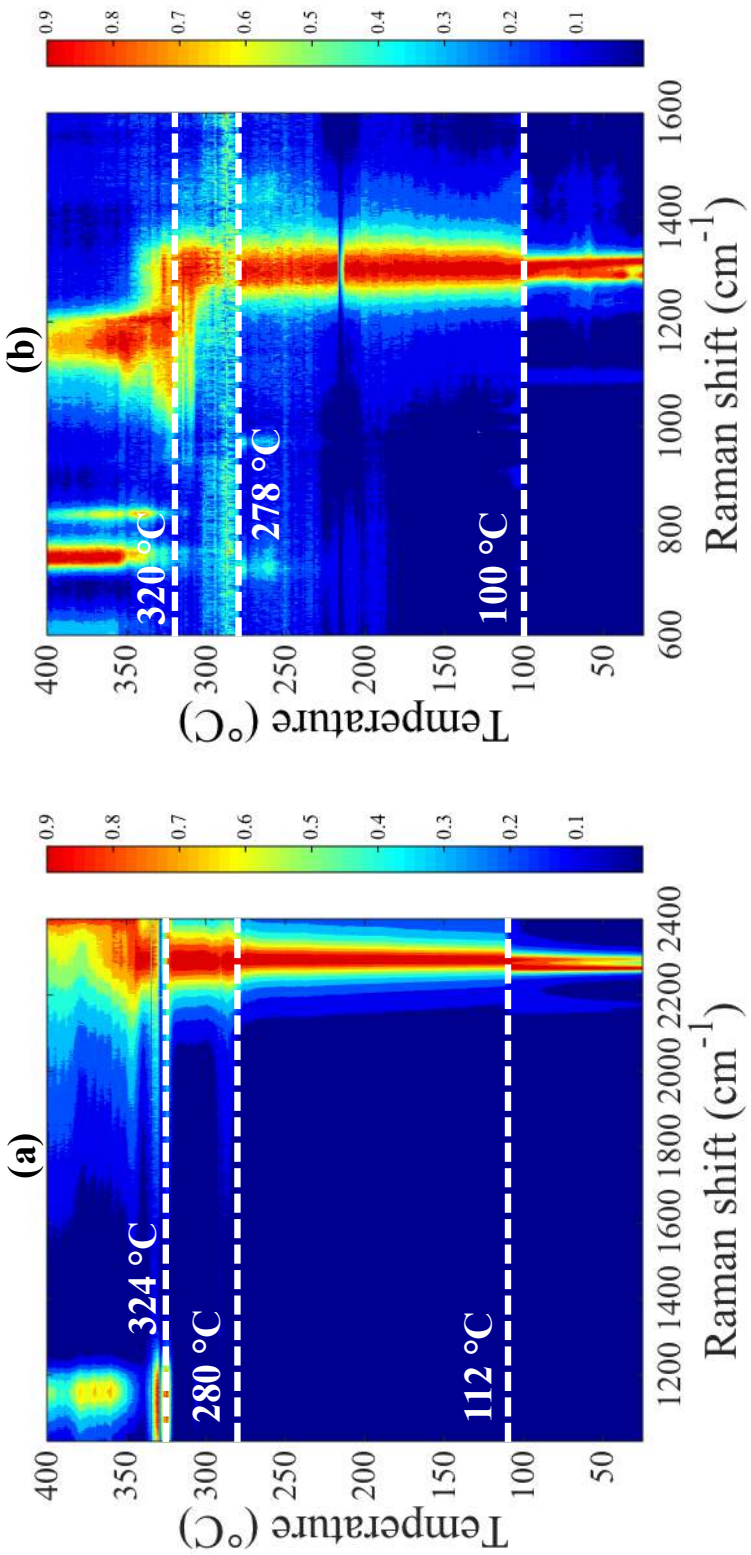

Figure 7.8 Surface plots of *in situ* Raman spectra (measured with 488 nm laser and 2400 l/mm grating system) of as-received $LiBH_4$ heated at 2 °C min^{-1} in Ar flowing at 100 mL min^{-1}. Figure (a) shows the in situ Raman results in a larger range from 1100 to 2400 cm^{-1}. Figure (b) shows the spectra change as a function of temperature in the $[BH_4]^-$ bending region from 600 to 1600 cm^{-1}. The dashed line indicates the occurrence of phase polymorphic transformations, fusion and decomposition.

Moreover, the decomposition onset temperatures (~320 °C) were allocated when new phases (amorphous boron and/or $Li_2B_{12}H_{12}$) started to appear. The signal for amorphous boron (around 1100 cm^{-1}) was only detected discontinuously in Figure 7.8-a. This was possibly due to the weak signal of this phase.

Some background noises appeared during the fusion and decomposition processes. This was due to a loss of focus. The measurements were made using an auto-focus setting, which means that the in Via Raman microscope was always focused on the top surface of the sample. When fusion occurred, the solid phase melted and tended to foam. This caused a decrease in focus height and blurred the measurement. The measurement might become inaccurate in this case and these background noises were therefore generated. However, the phases precipitated during decomposition re-enabled the auto-focus function, leading to less noisy spectra again.

7.1.4.2 TPD-MS

Figure 7.9 shows the thermal dehydrogenation of as-milled $LiBH_4$ in Ar.

No H_2 was detected between 100 and 120 °C, which corresponds to the polymorphic transformation temperature range. This observation conflicted with the reported 0.3 wt.% of hydrogen released between 100-200 °C for $LiBH_4$ (> 95%) heated in vacuum by 2 °C min^{-1} (A. Züttel et al. 2003). It is likely due to that fact that such a small H_2 evolution (e.g. 0.06 mg for a 20 mg $LiBH_4$ sample = a peak height of ~ 0.08×10^{-9} mbar g^{-1}) was below the detection limit of the current TPD-MS set-up.

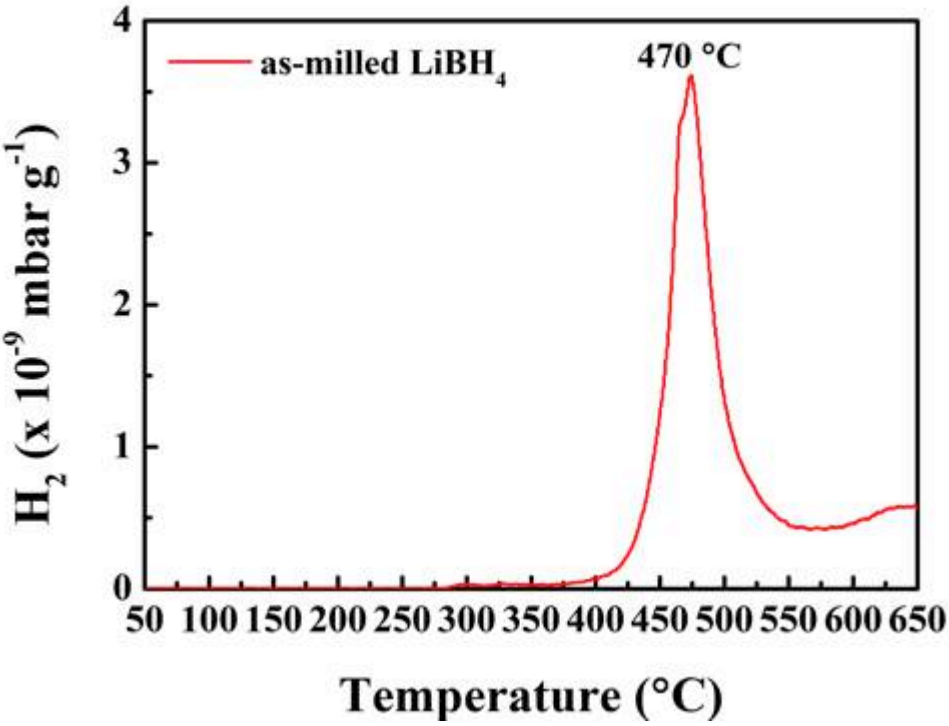

Figure 7.9 TPD-MS results of as-milled $LiBH_4$ in the range 50 – 650 °C heated at 2 °C min^{-1} in TPD. Desorbed H_2 was carried by Ar flowing at 160 mL min^{-1} to be detected in MS. No B_2H_6 was detected.

The onset of H_2 release was at 285 °C. It was the same as the melting temperature measured by DSC, indicating $LiBH_4$ released H_2 along with fusion. The major dehydrogenation event occurred above 400 °C and reached its maximum intensity at 470 °C. A total of 10.0 wt. % hydrogen was released upon heating to 650 °C. However, the dehydrogenation process was continued even beyond 650 °C.

Table 7.3 shows the summarised decomposition temperatures of $LiBH_4$ compared with literature values.

Table 7.3 Decomposition temperatures (onset and peak) of $LiBH_4$.

	Temperatures (°C)		Conditions			Technique
	Onset	Peak	Purity (%)	Rate °C/min	Atmosphere	
This work	285	470	95	2	Ar	TPD-MS
(Andreas Züttel et al. 2003)	320	~500	95	2	Inert gas	Mass Flow controller
(Orimo et al. 2005)	327	460	95	10	1 bar H_2	DSC
(Orimo et al. 2006)	290	450	95	5	He	TG-MS
(Yu et al. 2007)	300	440	95	10	Ar	TG-MS
(J. Yang et al. 2007)	300	445	95	5	Ar	TPD-MS
(Fang et al. 2008)	280	460	95	2	Ar	TG-MS
(Yu et al. 2008)	290	450	95	10	Ar	TG-MS
(Au, Jurgensen, et al. 2008)	300	478	95	5	Ar	TG-RGA
(Pendolino et al. 2009)	360	490-500	95	11	1 bar H_2	DSC
(Au & Walters 2010)	285	>500	95	5	Ar	TG-RGA
(M Paskevicius et al. 2013)	290	450	90	5 or 10	Ar	TG-DSC-MS
(Li et al. 2014)	280	470	95	5	He	TG-MS
(Zhao et al. 2014)	290	442	n.a.	2	Ar	TPD-MS

The kinetic of dehydrogenation for a borohydride is very sensitive to the purity of the starting material (especially surface oxidation) and the conditions used (such as heating rate and H_2 backpressure applied):

- a small fraction of surface oxidation can kinetically promote the dehydrogenation process by reducing the activation energy (Kato et al. 2010);
- a slower heating rate leads to a lower dehydrogenation peak temperature (Pendolino et al. 2009).
- a higher H_2 backpressure will postpone the release of H_2 from borohydrides (Hanada et al. 2008) as well as change the reaction route (Yan et al. 2012).

Therefore, although similar temperature ranges were reported previously, it was difficult to compare kinetic of dehydrogenation directly if they were measured using different experimental set-ups and conditions.

In this work, no B_2H_6 (m/z = 26) was detected by MS during the dehydrogenation, though studies suggested concurrent releases of H_2 and B_2H_6 at low temperature (100 – 200 °C) when $LiBH_4$ was heated under ultra-high vacuum condition and the detector was directly above the sample (Friedrichs, Remhof, Hwang, et al. 2010). This was due to the experimental set-up used in this work, whereby the mass spectrometer is connected to the TPD frame via a heated capillary, through which the amount of evolved gas reaching the detector was limited. Thus, small desorption of reactive gases, such as B_2H_6, were very difficult to detect. Therefore, its presence should not be fully ruled out.

Although the decomposition of $LiBH_4$ is complicated and may go through the formation of a series of metastable polyborane complexes as a function of temperature and pressures, it was assumed that only Equations 7.2 and 7.3 occurred during dehydrogenation, based on the *in situ* Raman results. In theory, a completed decomposition forming LiH and B released 13.9 wt.% hydrogen (Equation 7.2); while the dehydrogenation via the LiH and $Li_2B_{12}H_{12}$ route liberated 10.0 wt.% hydrogen (Equation 7.3). The overall H_2 evolution (including both heating and cooling) of as-milled $LiBH_4$ was 12.3 wt.% which lies between those two values. It was assumed that this experimental value was a linear combination of the hydrogen releases from Equation 7.2 and Equation 7.3, meaning 60% of hydrogen came from the former and 40% from the later. Therefore the overall decomposition mechanism of $LiBH_4$ in Ar was

$$\boldsymbol{LiBH_4 = 0.94LiH + 0.64B + 0.03Li_2B_{12}H_{12} + 1.35H_2} \qquad \textbf{Equation 7.6.}$$

7.2 Decomposition with the Addition of 5 mol% of SiO_2

SiO_2 powder showed interesting destabilization behaviour when added to $LiBH_4$. For example, it decreased the onset dehydrogenation temperature by 200 °C (Andreas Züttel et al. 2003) and increased the conductivity to 10^{-4} Ω^{-1} at room temperature (Choi et al. 2016). However, the amount of SiO_2, 75 wt.%, used by Andreas Züttel et al. (2003) significantly affected the systematic gravimetric density as the molar weight of SiO_2 (60.08 g mol^{-1}) was about 3 times heavier than $LiBH_4$ (21.784 g mol^{-1}). To compensate the gravimetric density loss, a small amount of SiO_2 (5 mol%) was mixed with as-received $LiBH_4$ in this work. The decomposition of $LiBH_4$ influenced by SiO_2 with a series of different sizes was studied, revealing how specific surface area affected the dehydrogenation reactions.

7.2.1 Characterisation of the as-received SiO_2

The as-received SiO_2 powders (99.9%) with different partial sizes (diameter = 0.5, 1.0, 1.5 μm) were examined by XRD, Raman, SEM and TEM for characterizing their purity, structure and surface morphologies, as shown in Figure 7.10-11.

Two broad peaks at around 10° and 23° 2θ were observed for the as-received SiO_2 particles in XRD (Figure 7.10-a). The peak at around 10° 2θ was the background; whilst the broad peak centred at 23° 2θ was assigned as fine SiO_2 particle that agreed with literature for SiO_2 aerogel (K. Chen et al. 2012).

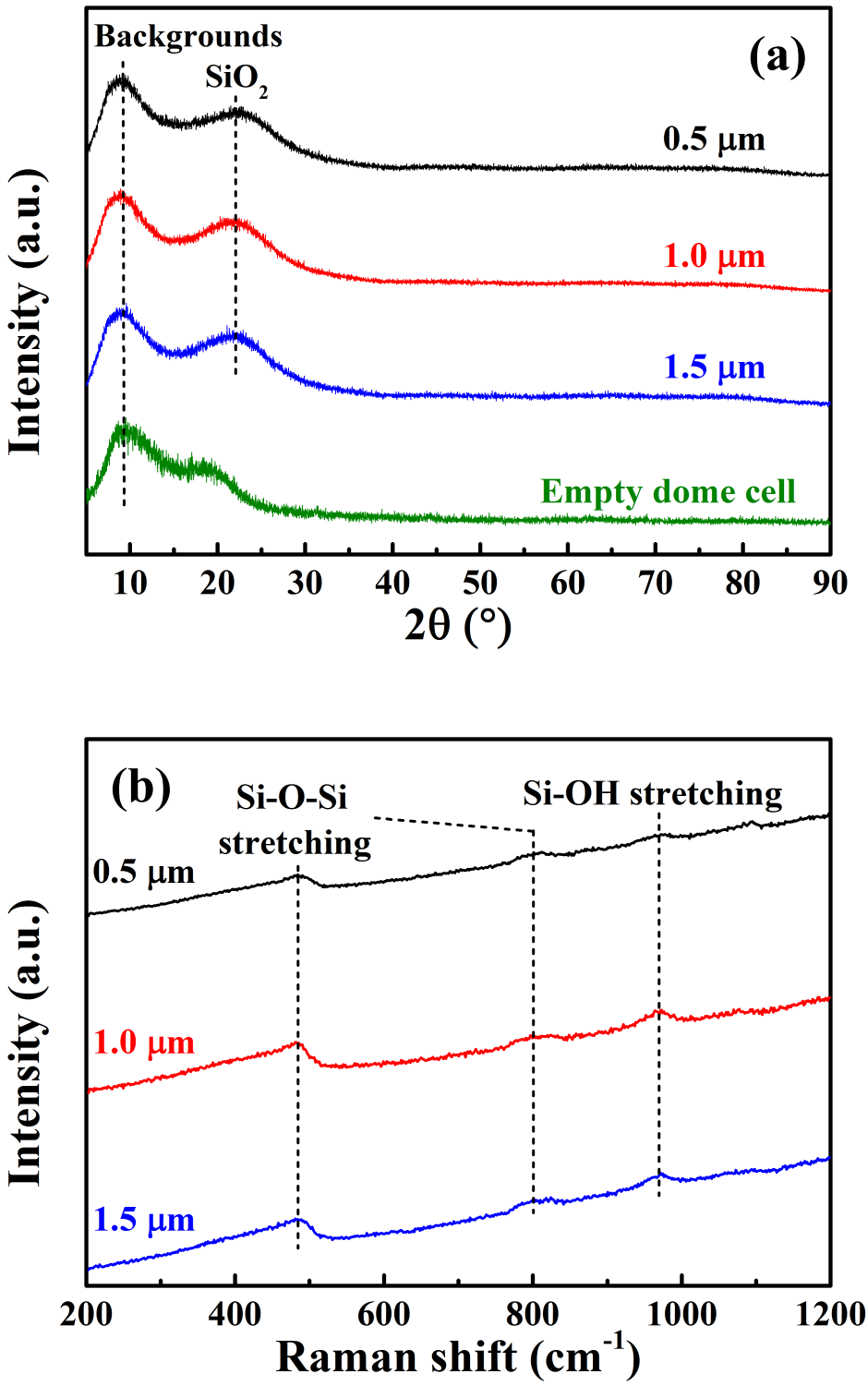

Figure 7.10 (a) XRD (Cu K_α radiation, λ = 1.5418 Å) patterns of as-received SiO_2 at room temperature compared to an XRD result of an empty sample holder (dome cell). (b) Raman spectra (measured with 488 nm laser and 2400 l/mm grating system) of as-received SiO_2 at room temperature. Dashed lines are guides for the eye.

Peaks centred at 480 cm^{-1}, 820 cm^{-1}, and 960 cm^{-1} were observed in Raman (Figure 7.10-b) and were assigned to the Si-O-Si bending (Chligui et al. 2010) and Si–OH stretching. The Si–OH stretching (960 cm^{-1}) was not expected and remained after the sample was kept at 250 °C under vacuum for 24 hours. This was probably due to strong dangling bonds at the surface (Lemke & Haneman 1978), and could be passivated using H_2 deposited in a remote microwave hydrogen-plasma system at 250 mTorr (i.e. 3.3×10^{-4} bar) (Cartier et al. 1993).

The as-received particles were non-porous spherical solid material with smooth outer surfaces (Figure 7.11). The particle sizes were measured by fitting the diameter using the scale bar and were in good agreement with the diameter values suggested by the manufacture (i.e. 0.5, 1.0, 1.5 μm).

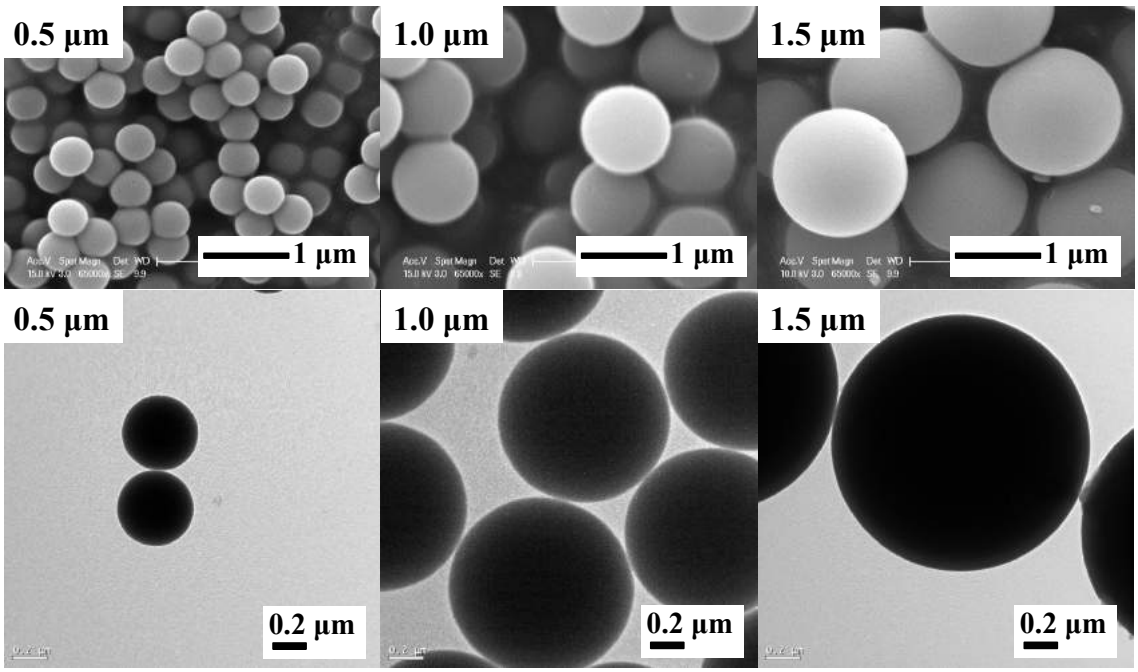

Figure 7.11 SEM (top) and TEM (bottom) images of as-received SiO_2 (suggested diameters 0.5, 1.0, 1.5 μm) at room temperature.

7.2.2 Characterisation of the as-prepared $LiBH_4$-SiO_2 Mixture

The $0.95LiBH_4$-$0.05SiO_2$ mixture was prepared by hand mixing 0.8732 ± 0.001 g of as-received $LiBH_4$ and 0.1268 ± 0.001 g of as-received SiO_2. The characterisation results of XRD and Raman for the as-prepared mixture are shown in Figure 7.12.

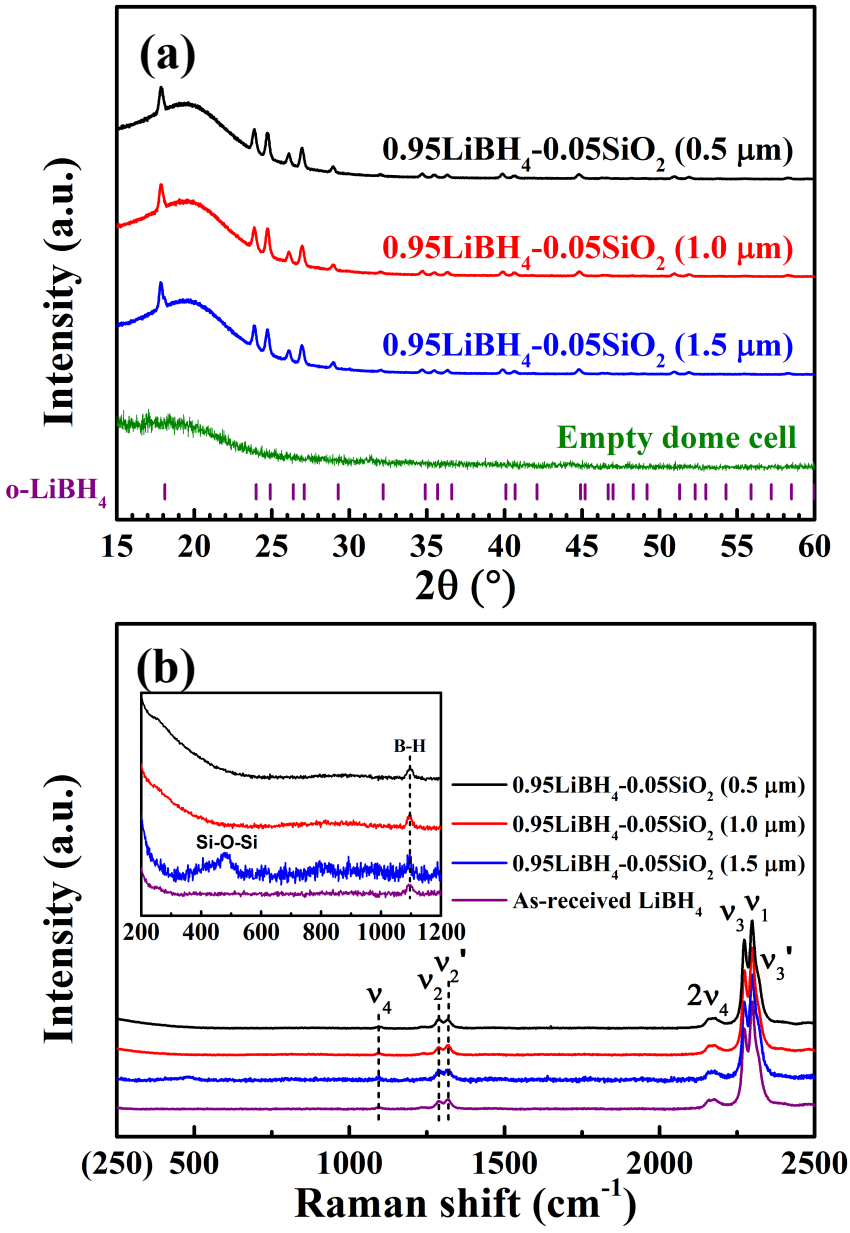

Figure 7.12 (a) XRD (Cu K_α radiation, λ = 1.5418 Å) patterns of as-prepared $LiBH_4$-SiO_2 (diameter = 0.5, 1.0, 1.5 μm) at room temperature compared to experimental $LiBH_4$ data (purple vertical lines) from (Filinchuk et al. 2008) and the XRD result for an empty dome cell. (b) Raman spectra (measured with 488 nm laser and 2400 l/mm grating system) of as-prepared $0.95LiBH_4$-$0.05SiO_2$ (diameter = 0.5, 1.0, 1.5 μm) at room temperature. An embedded spectra figure focused the data in the range from 200 to 1200 cm^{-1}.

All XRD peaks for the as-prepared $0.95LiBH_4$-$0.05SiO_2$ (diameter = 0.5, 1.0, 1.5 μm) samples were assigned to orthorhombic $LiBH_4$ (no Bragg peaks for SiO_2 were observed). The Raman spectrum of as-prepared $0.95LiBH_4$-$0.05SiO_2$ (diameter = 1.5 μm) showed a broad peak at 481 cm^{-1} (Si-O-Si stretching), indicating the presence of SiO_2. However, this was not seen in other samples. Since the majority of Raman scatterings occurred on top of the sample surface where the laser spot (diameter: ~ 50 μm) was focused (possible interaction depth: ~ 1 μm), detecting the SiO_2 particles underneath the surface might be difficult.

Figure 7.13 shows the DSC trace of the as-prepared $0.95LiBH_4$-$0.05SiO_2$ (diameter = 0.5 μm) in flowing Ar.

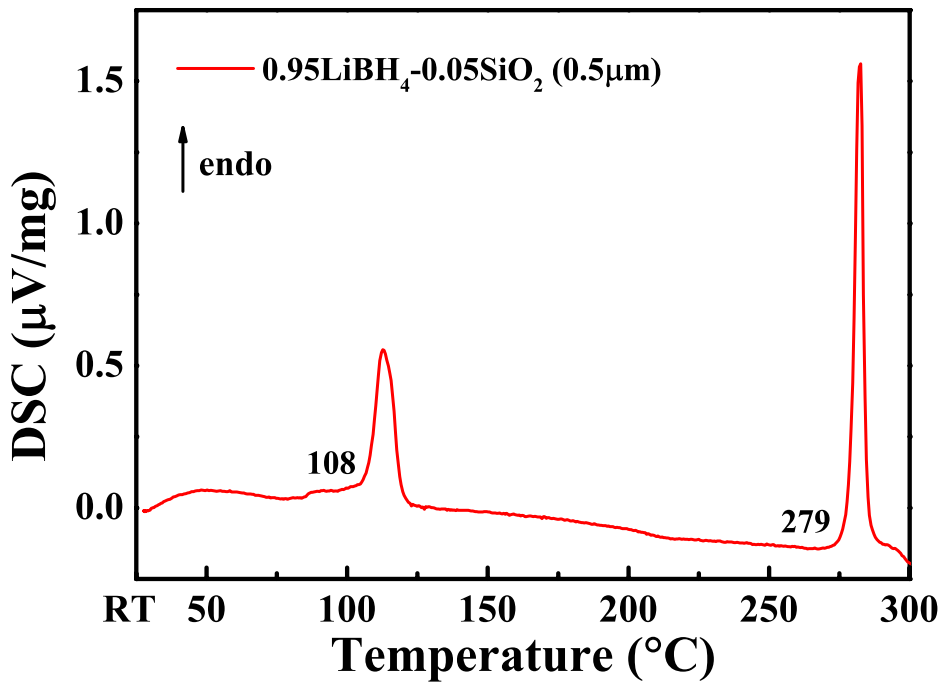

Figure 7.13 DSC trace of the as-prepared $0.95LiBH_4$-$0.05SiO_2$ (diameter = 0.5 μm) heated up to 300 °C at a heating rate of 5 °C/min in Ar flowing at 70 mL min^{-1}.

Two endothermic peaks were observed during heating: 108 °C for polymorphic transformation and 279 °C for fusion of $LiBH_4$, respectively. Although these values were slightly lower than the 115 and 285 °C measured for as-received $LiBH_4$, they were still in agreement with literature (Andreas Züttel et al. 2003; Fakioğlu et al. 2004; Orimo et al. 2005; Li et al. 2011; El Kharbachi et al. 2012).

7.2.3 Thermal Decomposition

7.2.3.1 Low Temperature Dehydrogenation

The thermal desorption of as-prepared $0.95LiBH_4$-$0.05SiO_2$ (diameter = 0.5, 1.0, 1.5 μm) samples in Ar were investigated using TPD-MS, as shown in Figure 7.14.

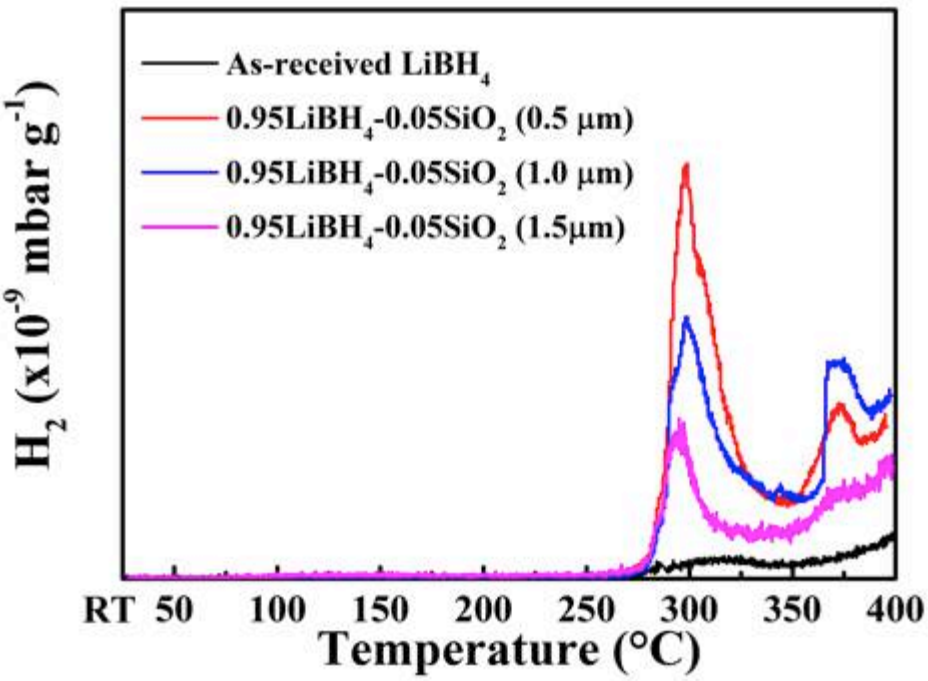

Figure 7.14 TPD-MS results of as-prepared $LiBH_4$-SiO_2 (diameter = 0.5, 1.0, 1.5 μm) in the range of 25-400°C heated at 2 °C min^{-1} in TPD in contrast to as-received $LiBH_4$. The desorbed H_2 was carried by Ar flowing at 160 mL min^{-1} and measured by MS. No B_2H_6 was detected.

For all samples, no H_2 signal was detected before 280 °C. Since the major dehydrogenation of $LiBH_4$ occurred at higher temperature range (400-500 °C), only 0.2 wt.% of hydrogen was released from the as-received $LiBH_4$ sample when heated to 400 °C.

When 5 mol% SiO_2 was added, two dehydrogenation peaks were observed at 300 °C and 370 °C, indicating 2 separate reactions. The total amounts of H_2 released from as-prepared $0.95LiBH_4$-$0.05SiO_2$ mixtures were: 1.5, 1.3 and 0.7 wt.%, for samples containing 0.5, 1.0, 1.5 μm SiO_2, respectively. After fitting the curve areas using Origin-Lab, the ratio between peak 1 and peak 2 were found to be: 58:42, 57:43 and 54:46, for samples containing 0.5, 1.0, 1.5 μm SiO_2, respectively. Therefore, the amount of H_2 released at each step was obtained by multiplying the relative area percentage with the total H_2 release and summarised in Table 7.4.

Table 7.4 Hydrogen desorption (wt.%) for as-prepared $0.95LiBH_4$-$0.05SiO_2$ (diameter = 0.5, 1.0, 1.5 μm) in contrast to as-received $LiBH_4$.

Additive	Diameter	Specific surface area[1]	H desorption Step 1	H desorption Step 2	H desorption Total
	μm	m^2/g	wt.%	wt.%	wt.%
None	-	-	0.13	0.07	0.2
SiO_2	0.5	4.5	0.87	0.63	1.5
SiO_2	1.0	2.3	0.75	0.57	1.3
SiO_2	1.5	1.5	0.39	0.34	0.7

[1] The specific surface areas are calculated by:

$$A_{SiO_2}^{SS} = \frac{m}{\rho_{SiO_2} V_{SiO_2}} \times \frac{A_{SiO_2}}{m},$$

where m, ρ_{SiO_2}, V_{SiO_2} and A_{SiO_2} are the mass, density, volume and surface area of SiO_2, respectively.

These results implied that the total amount of H_2 released increased, when the specific surface area rose. For example, the specific surface area of the smallest SiO_2 particle (diameter = 0.5 μm) was 3 times larger than that of the biggest particles (1.5 μm), as a consequence it led to more than 100 % excess H_2 release under the same conditions.

To investigate the reactions happening at each step, the as-prepared $0.95LiBH_4$-$0.05SiO_2$ (diameter = 0.5 μm) sample was heated to 300, 370 and 400 °C at 2 °C min^{-1} in Ar. The heat-treated sample was then measured by XRD after cooling to room temperature (Figure 7.15).

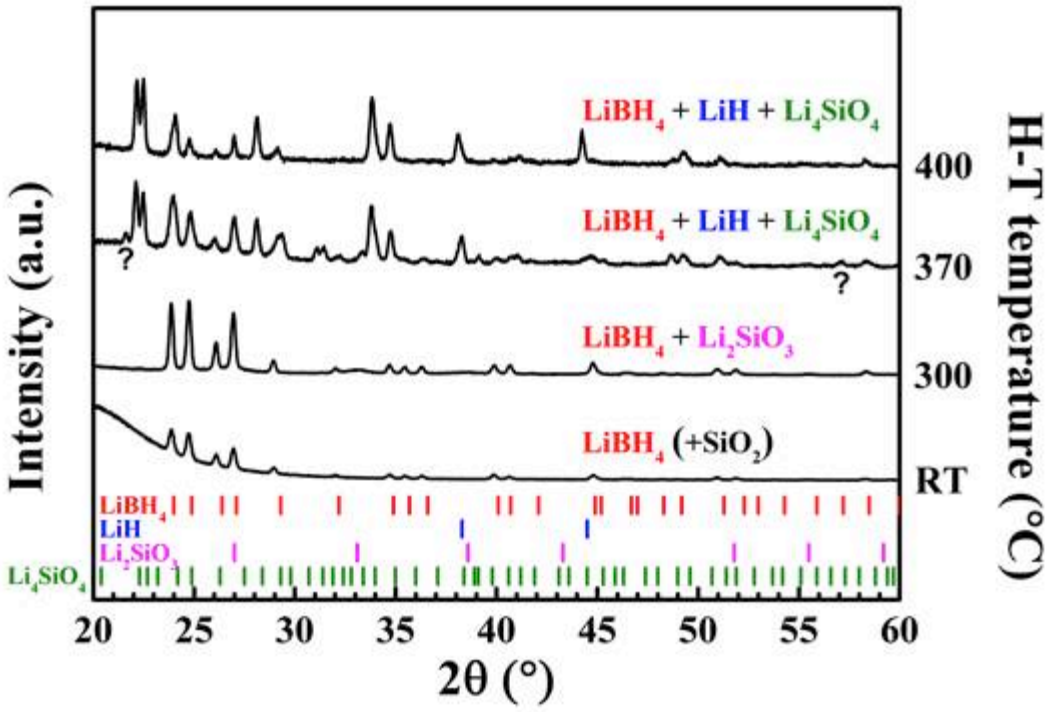

Figure 7.15 XRD patterns (Cu K_α radiation, λ = 1.5418 Å) of as-prepared $0.95LiBH_4$-$0.05SiO_2$ (diameter = 0.5 μm). The samples were heated to 300 °C, 370 °C and 400 °C by 2 C min^{-1} in Ar flowing at 160 mL min^{-1}. The intensities were normalized.

When the mixture was heat-treated to 300 °C in Ar, a broad, weak peak at 33° 2θ was observed and was assigned to Li_2SiO_3, a known reaction product of $LiBH_4$ and SiO_2 (Opalka et al. 2009; Chen et al. 2010; Ngene, Adelhelm, et al. 2010). It was not stable and disappeared when the sample was heated to 370 °C.

$$4LiBH_4 + 3SiO_2 = 2Li_2SiO_3 + Si + 4B + 8H_2 \qquad \textbf{6.0 wt.\%} \qquad \textbf{Equation 7.7}$$

Besides the Bragg peaks of $LiBH_4$, multiple new peaks were observed in the heat-treated sample at 370 °C and 400 °C that were assigned to Li_4SiO_4, an oxidation product of Li_2SiO_3 (Zhang et al. 2008; Mosegaard et al. 2008; Ngene, Adelhelm, et al. 2010).

$$4LiBH_4 + 4Li_2SiO_3 = 3Li_4SiO_4 + Si + 4B + 8H_2 \qquad \textbf{3.6 wt.\%} \qquad \textbf{Equation 7.8.}$$

The X-ray peaks at 21.6 ° 2θ and 57 ° 2θ ("?" marked in Figure 7.15) were unknown, but might be oxides or intermediate phases. Silicon (Si), silicon borides (SiB_4, SiB_6), other lithium silicates ($Li_2Si_2O_5$, $Li_2Si_3O_7$, $Li_6Si_2O_7$ and Li_8SiO_6) and other possible reaction products ($LiBO_2$, H_3BO_3) have been ruled out (Brosset & Magnusson 1960; Zachariasen 1964; Voellenkle et al. 1969; Vlasse et al. 1986; Hofmann & Hoppe 1987; Smith et al. 1990; Krüger et al. 2007; Opalka et al. 2009)

Figure 7.16 shows the *in situ* Raman results of as-prepared $0.95LiBH_4$-$0.05SiO_2$ (diameter = 0.5 μm) sample heated from room temperature to 400 °C by 2 °C min^{-1} in Ar.

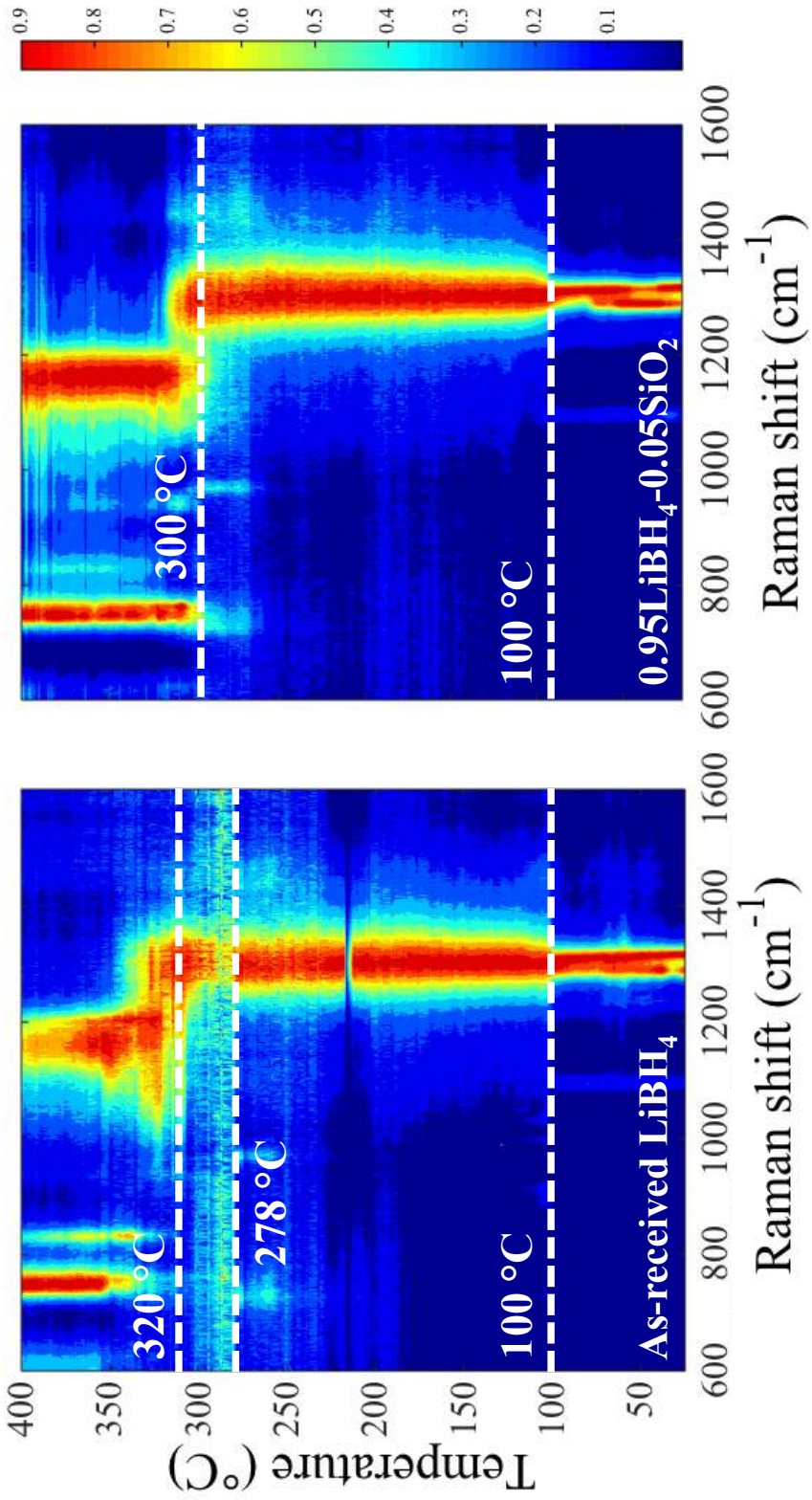

Figure 7.16 *In situ* Raman spectra (measured with 488 nm laser and 2400 l/mm grating system) of as-prepared $0.95LiBH_4$-$0.05SiO_2$ (diameter = 0.5 μm) in contrast to the as-received $LiBH_4$. Samples were heated up to 400 °C at 2 °C min^{-1} in Ar flowing at 100 mL min^{-1}. The temperatures of phase transition, fusion and decomposition were determined by manually checking the change of peaks in every spectrum.

The $0.95LiBH_4$-$0.05SiO_2$ mixture had the same orthorhombic to hexagonal phase transition temperature (100 °C) as that for $LiBH_4$.

Although the fusion of the mixture occurred at 279 °C (DSC, Figure 7.13), it could not be labelled in the *in situ* Raman result. This was because the melting temperature in an *in-situ* Raman surface plot was usually determined when the peak intensities decreased and only baseline was presented. This led to a dramatic reduction in focus height (tracked during measurement using an auto focus setting) for transparent liquids. For example, the molten $LiBH_4$ phase was a colourless and transparent material. The laser would automatically focus on the bottom of the sample pan causing a reduction in focus height. However, when SiO_2 was reacted with $LiBH_4$, the non-transparent reaction products (Figure 7.17) reduced the overall transmission leading to a non-significant change in focus height. Therefore, the fusion behaviour could not be traced and it was challenging to determine this during manually screening. In addition, reaction between SiO_2 and $LiBH_4$ inhibited the bubbling-frothing effect often observed for molten $LiBH_4$ (Figure 7.17), possibly by increasing the viscosity and/or reducing the surface tension of the system (M Paskevicius et al. 2013).

The major decomposition of this mixture occurred at 300 °C, forming $Li_2B_{12}H_{12}$ (around 750 cm^{-1}, boron breathing mode, ν_2) and B (around 1100 cm^{-1}, B-B skeletal vibration). This temperature was about 20 °C lower than the 320 °C for as-received $LiBH_4$, denoting a lower temperature decomposition occurred, probably through a reduction in activation energy as a consequence of the presence of oxide materials (Kato et al. 2010).

Figure 7.17 Photo of decomposed $LiBH_4$ sample (flake like) and $0.95LiBH_4$-$0.05SiO_2$ sample (compact). The inner diameter of the red circle is 2.5 cm.

7.2.3.2 High Temperature Dehydrogenation

Figure 7.18 shows the thermal dehydrogenation of as-prepared $0.95LiBH_4$-$0.05SiO_2$ (diameter = 0.5 μm) in the range of 50-550 °C heated at 2 °C min^{-1} in Ar.

A total of 3 desorption peaks were observed for the as-prepared $LiBH_4$-SiO_2 (diameter = 0.5 μm) sample at 303 °C, 375 °C and 467 °C.

These low-temperature desorption peaks (303 and 375 °C) agree well with the data presented in Figure 7.14, and were not observed for as-milled $LiBH_4$. About 0.8 wt.% and 0.6 wt.% of hydrogen was released at these two steps, respectively. These results are in very good agreement with the data presented in Table 7.4.

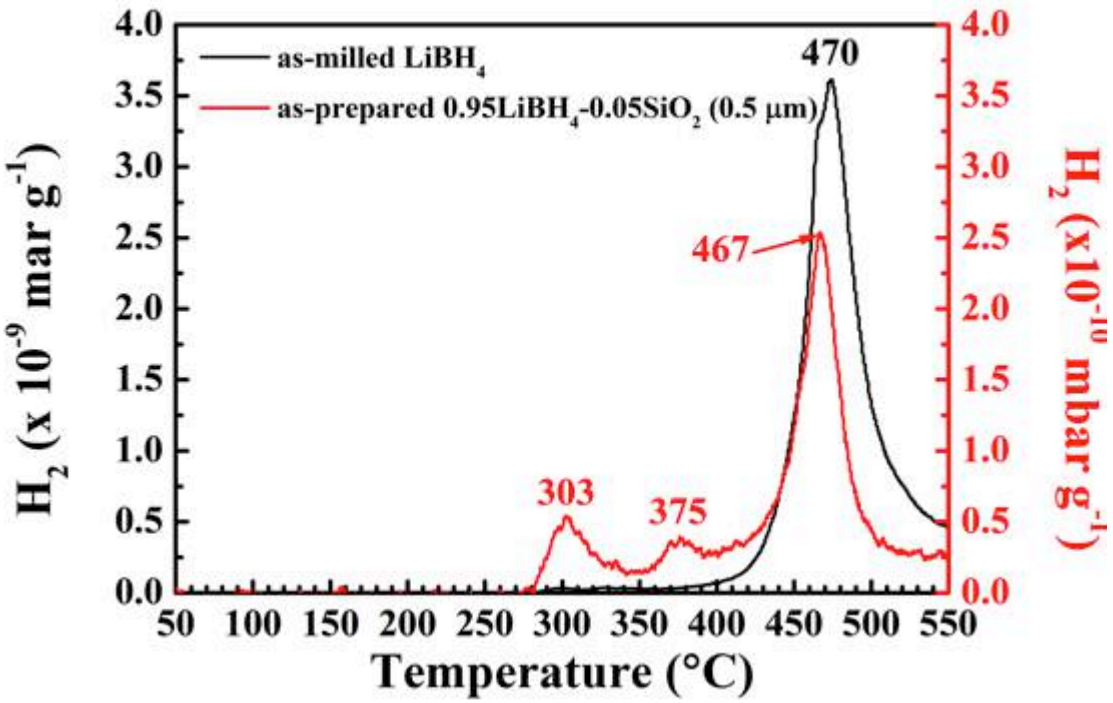

Figure 7.18 TPD-MS results of as-prepared $LiBH_4$-SiO_2 (diameter = 0.5,μm) in the range of 50-550°C heated at 2 °C min^{-1} in TPD in contrast to as-milled $LiBH_4$. The desorbed H_2 was carried by Ar flowing at 160 mL min^{-1} and measured by MS. Since the experiments were performed at different time period and different calibration files were used, the measured signal intensities of as-prepared $LiBH_4$-SiO_2 were about one order of magnitude lower than those of as-milled $LiBH_4$.

The major desorption peak at 467 °C for $LiBH_4$-SiO_2 sample was close to the 470 °C for the as-milled $LiBH_4$, suggesting the SiO_2 additive (and its reaction products) did not significantly influence the decomposition kinetics of $LiBH_4$. A total of 5.1 wt.% hydrogen was released upon heating to 550 °C, and was 38 % lower than the 8.2 wt.% for the as-milled $LiBH_4$. This reduction was possibly due to SiO_2 consumed $LiBH_4$ and/or the lithium silicates formed enhanced the precipitating $Li_2B_{12}H_{12}$.

7.2.4 Effect of additive SiO_2

Adding SiO_2 particles with a larger specific surface area led to a larger H_2 release at

relatively low temperatures (< 400°C). The small amount (5 mol%) of micron-sized SiO_2 additive destabilised $LiBH_4$ through chemical reactions happened at 300 °C and 370 °C, forming stable Li_2SiO_3 and Li_4SiO_4, respectively. Reaction between LiH and SiO_2 was more thermodynamically favourable than that between $LiBH_4$ and SiO_2, and both were more favourable than the dehydrogenation of $LiBH_4$ (Appendix C).

Figure 7.19 shows the decomposition pathway of the $0.95LiBH_4$-$0.05SiO_2$ system in a flow chart. The high stability of Li_2SiO_3 and Li_4SiO_4 led to irreversible hydrogen loss (Zhang et al. 2008; Ngene, Adelhelm, et al. 2010).

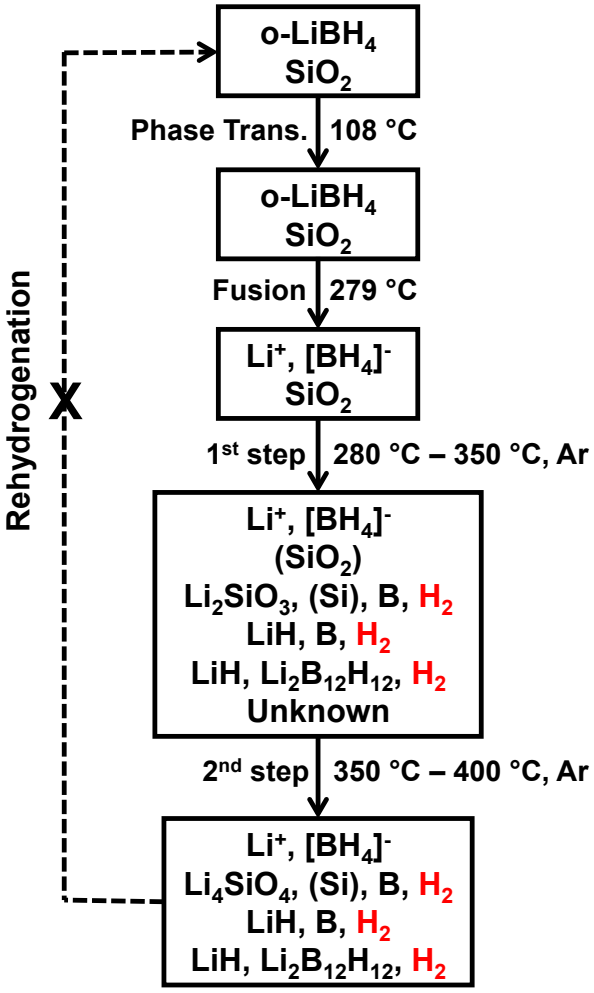

Figure 7.19 A flow chart of decomposition for $0.95LiBH_4$-$0.05SiO_2$ in Ar from 25 to 400 °C.

7.3 Decomposition with the Addition of 14 wt% of Ni

The $LiBH_4$-Ni system was expected to be a good candidate for solid-state H_2 storage. The addition of a small amount of nano-sized Ni could effectively affect the decomposition and recombination process of $LiBH_4$. The 25, 30, 40 and 47 wt.% addition of Ni into $LiBH_4$ have been studied in the past (Xia et al. 2009; Li et al. 2014). Since Ni (58.693 g mol^{-1}) is much heavier than $LiBH_4$ (21.784 g mol^{-1}), it decreases the system hydrogen capacity subject to its composition. Nevertheless, the catalytic effect given by the reaction product between Ni and $LiBH_4$ is more important and interesting in destabilizing the dehydrogenation. Thus, a lower amount of Ni was used in this work, i.e. 14 wt.% of Ni was mixed with $LiBH_4$ to destabilize the decomposition pathways. However, further optimisation of the Ni concentration is required.

7.3.1 Characterisation of the As-received Ni

Two types of Ni powder (bulk: average size 3 μm, 99.7%; nano-sized: average size <100 nm, 99.9%) were purchased from Sigma-Aldrich, Theses commercial Ni powders were examined by XRD for their purity and structure, and by SEM for morphology.

Figure 7.20 shows the XRD pattern of the as-received Ni at room temperature. Peaks were mainly caused by the cubic Ni phase. For the nano-sized Ni, peaks associated to NiO were also observed as the impurity in the as-received sample. The amount of NiO was estimated by a pseudo-Rietveld refinement to be 6.4 ± 0.2 wt.% (Figure 7.21).

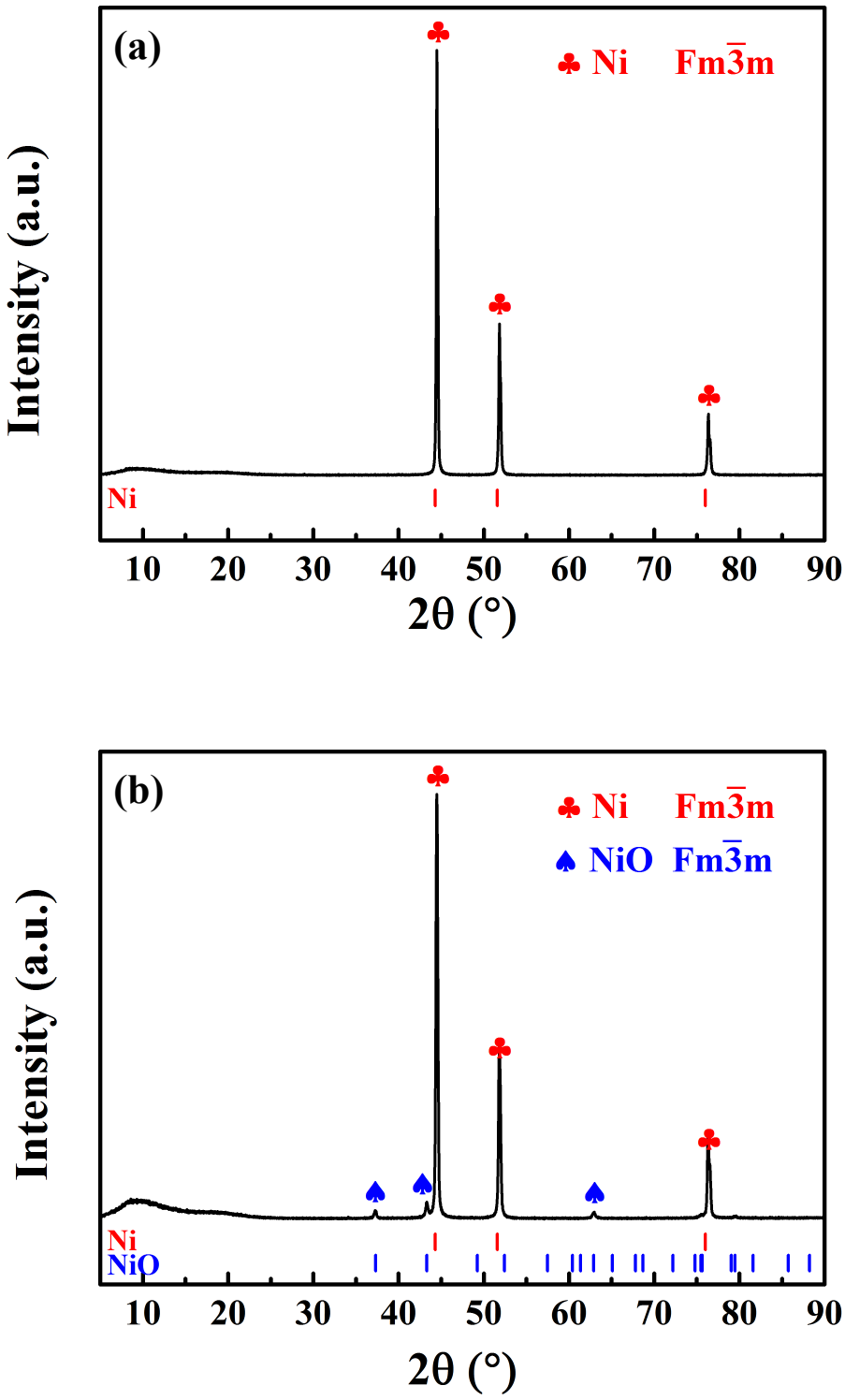

Figure 7.20 XRD patterns (Cu K_α radiation, λ = 1.5418 Å) of as-received Ni (a – 3 μm; b - 100 nm) at room temperature compared to experimental data (vertical lines) from literature (Hull 1917; Sasaki et al. 1971).

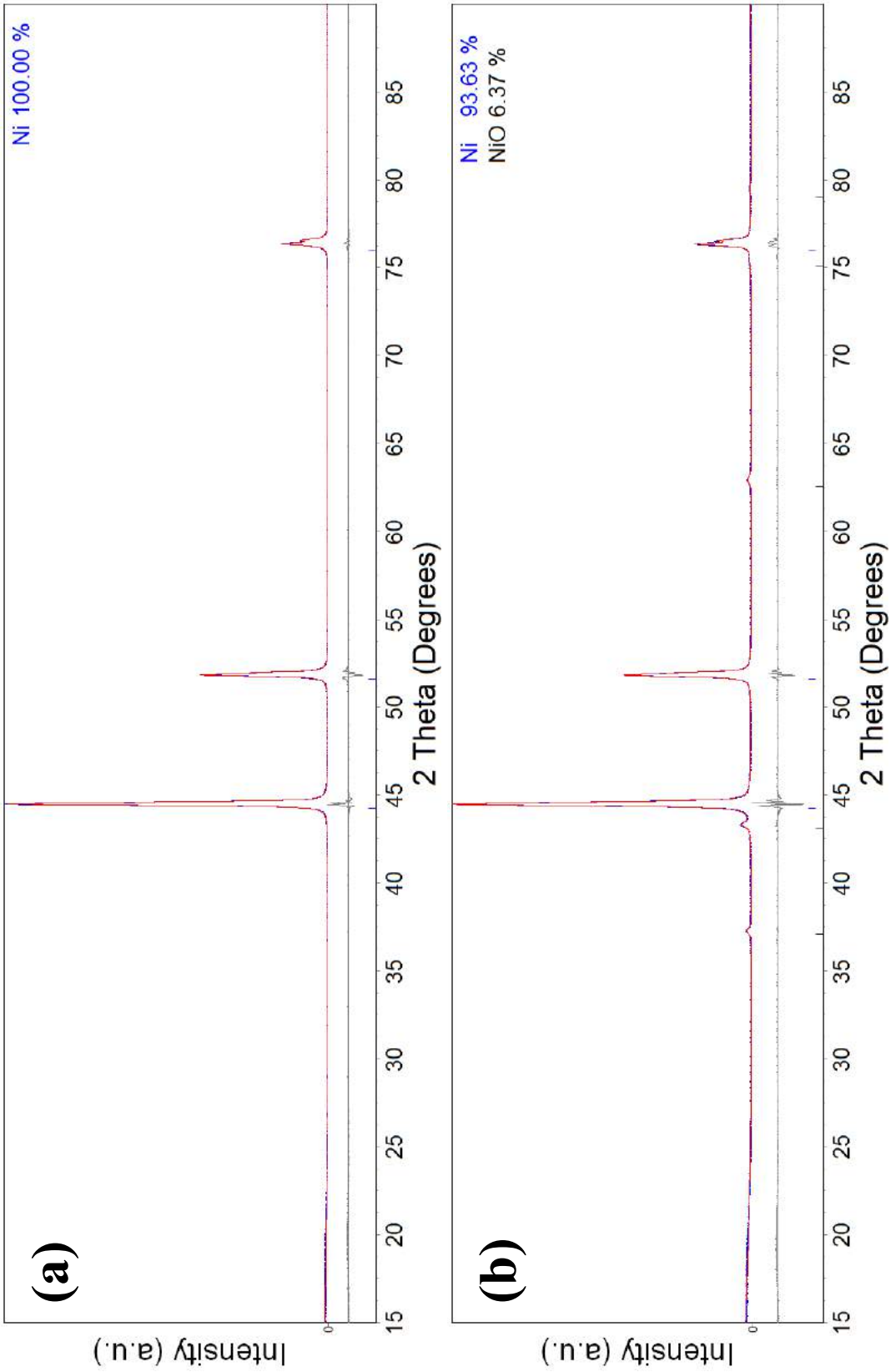

Figure 7.21 Pseudo-Rietveld refinement results of as-received Ni (a – 3 µm; b- 100 nm), including the observed XRD (Cu K_α radiation, λ = 1.5418 Å) profile (blue), the calculated profile (red, used to fit the observed profile) and the difference profile (grey). The goodness-of-fit were 1.344 for (a) and 1.483 for (b).

Table 7.5 summarizes the refined lattice parameters of as-received Ni samples. These parameters are in good agreement with the literature (Hull 1917).

Table 7.5 Refined lattice parameters of as-received Ni, comparing to a published literature data (Hull 1917).

Ni bulk	Ni nano	Literature
3.5400 ± 0.0003	3.5403 ± 0.0009	3.54

Figure 7.22 shows the morphology of the as-received Ni samples using SEM. The bulk-Ni particles had distinct micron-scale sizes and irregular shapes, possibly due to agglomerations. The nano-sized Ni particles were nearly spherical and were around 100 nm. However, the agglomeration was still a big issue.

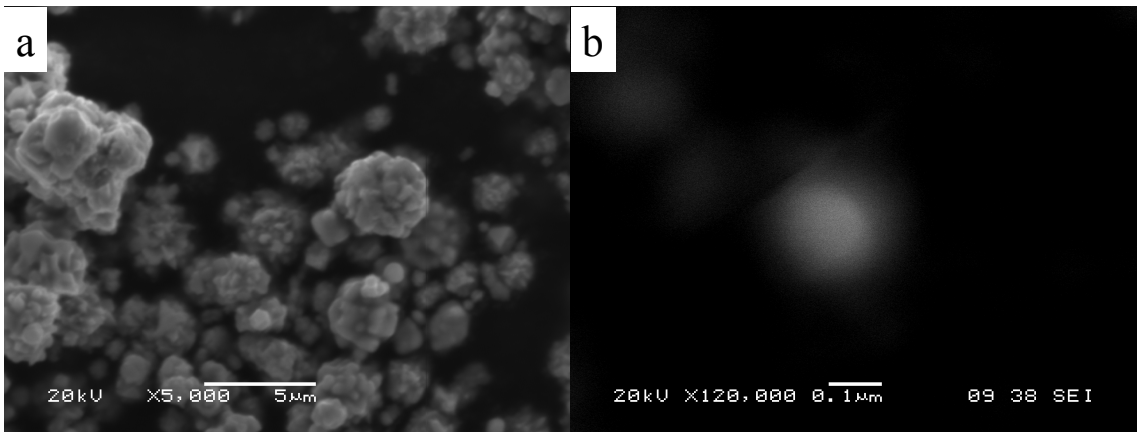

Figure 7.22 SEM of as-received Ni samples (a – bulk; b - nano-sized) at room temperature.

7.3.2 Characterisation of the As-prepared $LiBH_4$-Ni Mixture

The $LiBH_4$-Ni mixture was prepared by mixing 0.8 g of as-received $LiBH_4$ (Sigma-Aldrich, ≥95.0%) and 0.2 g as-received Ni using ball milling under the conditions described in Section 6.1.1. Their room temperature XRD, Raman and FTIR and the pseudo-Rietveld refinement results are shown in Figure 7.23 and Figure 7.24.

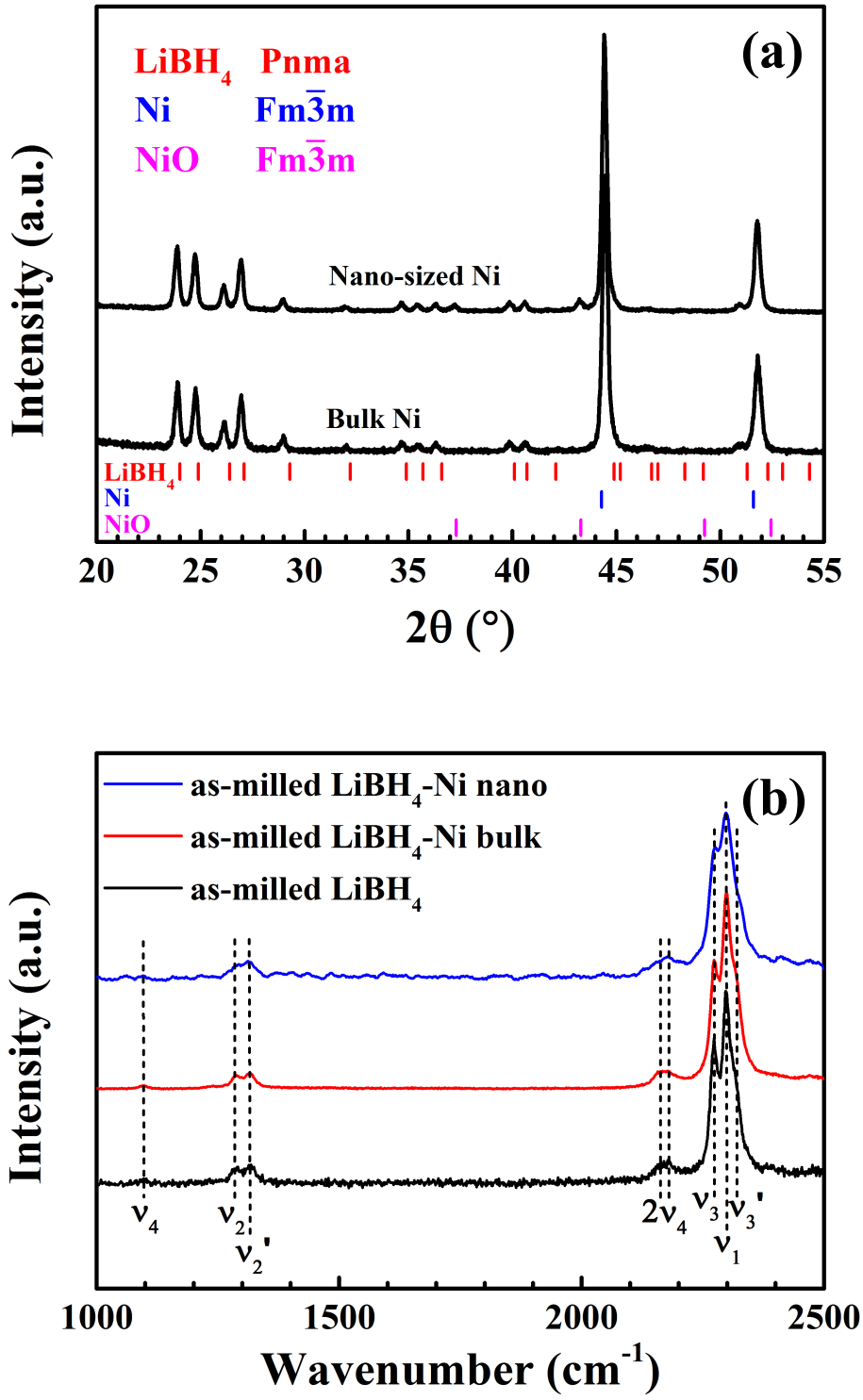

Figure 7.23 (a) XRD patterns (Cu K_α radiation, $\lambda = 1.5418$ Å) of as-milled $LiBH_4$ with 14 wt.% Ni (bulk; nano-sized) at room temperature compared to experimental data (vertical lines) from literature (Hull 1917; Sasaki et al. 1971; Filinchuk et al. 2008). (b) Raman spectra (measured with 488 nm laser and 2400 l/mm grating system) of as-milled $LiBH_4$-Ni (bulk and nano-sized) in contrast to as-milled $LiBH_4$ at room temperature. Dashed lines are guides for the eye.

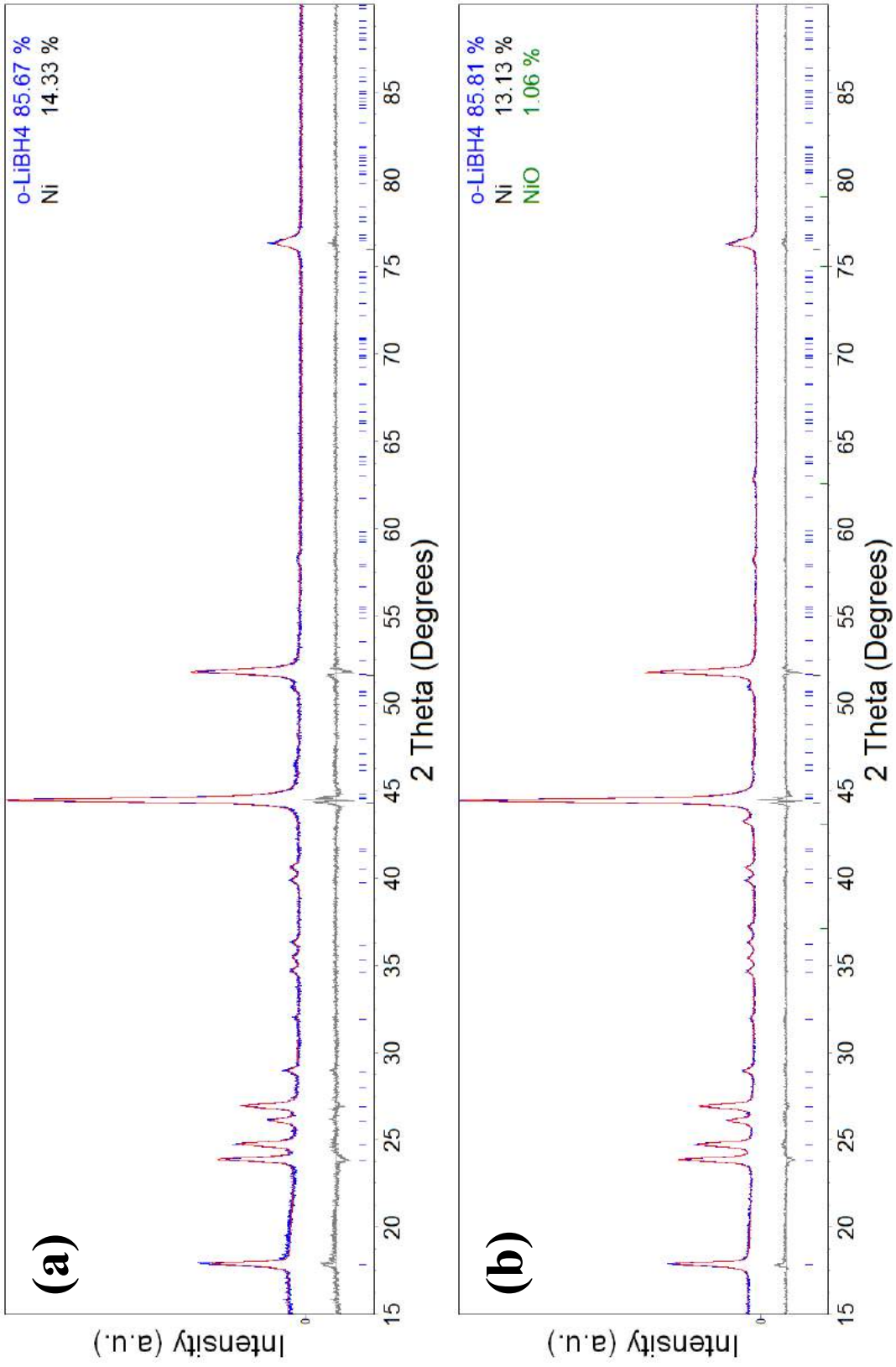

Figure 7.24 Pseudo-Rietveld refinement results of as-milled $LiBH_4$-Ni (14 wt.%) (a – bulk; b - nano-sized), including the observed XRD (Cu K_α radiation, λ = 1.5418 Å) profile (blue), the calculated profile (red, used to fit the observed profile) and the difference profile (grey). The goodness-of-fit are 1.197 for (a) and 1.258 for (b).

Peaks observed in Figure 7.23-a were assigned to orthorhombic $LiBH_4$, and cubic Ni and NiO (impurity in as-received sample) phases. Due to its metallic bonds, Ni could not be detected using vibrational spectroscopy techniques (such as Raman and FTIR). Therefore, no peaks other than $LiBH_4$ were observed in the Raman spectra (Figure 7.23-b). The pseudo-Rietveld refinement results (Figure 7.24) of as-milled $LiBH_4$-Ni samples are summarized in Table 7.6.

Table 7.6 Quantitative phase analysis (wt.%) for as-milled $LiBH_4$-Ni (bulk and nano).

Phase	Sample with bulk Ni	Sample with nano-sized Ni
$LiBH_4$	85.7 ± 0.3	85.8 ± 0.2
Ni	14.3 ± 0.3	13.1 ± 0.2
NiO	n.a.	1.1 ± 0.1

Though 0.2 g of Ni sample was weighed out during preparation, the refined composition of Ni in the as-milled sample was about 14 wt.% for both samples. This discrepancy in the Ni amount is likely due to loss of Ni during sample preparation, such as the attachment of Ni to weight boat and/or mill balls/pot. In addition, a 14 wt.% Ni additive was identical to 5.7 mol% in $LiBH_4$-Ni. Therefore, the as-milled $LiBH_4$-Ni (14 wt.%) samples were referred to $0.943LiBH_4$-0.057Ni (bulk or nano).

7.3.3 Thermal Decomposition

The temperature-dependent desorption of as-milled $LiBH_4$-Ni (14 wt.%) samples from 50 to 600 °C was investigated using TPD-MS in flowing Ar. The results are shown in Figure 7.25, where signals were normalized to the highest peak for ease of comparison.

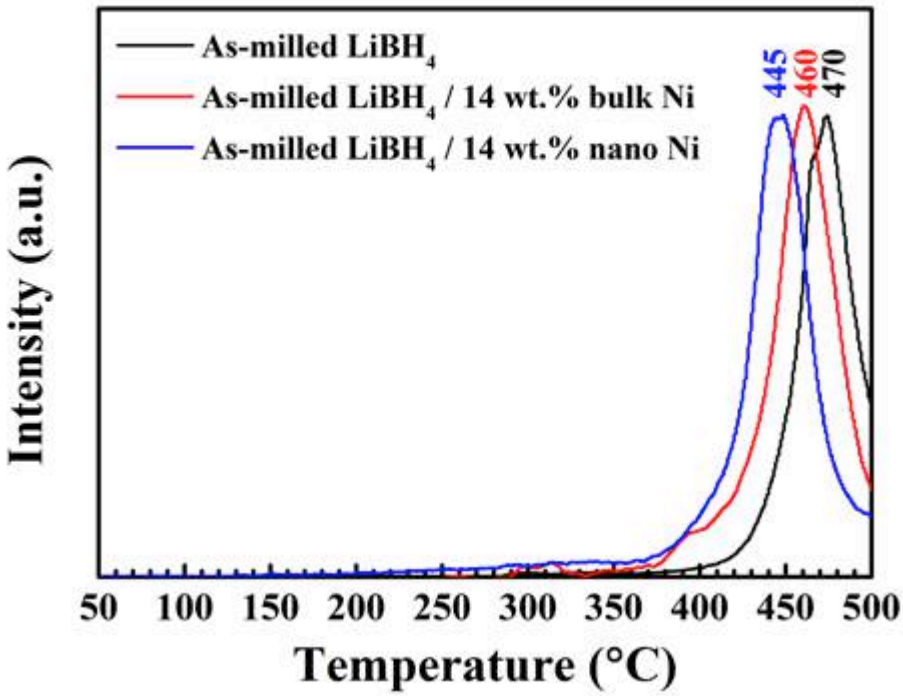

Figure 7.25 TPD-MS results of as-milled $LiBH_4$-Ni (14 wt.%) samples in the range of 50-500°C heated at 2 °C min^{-1} in contrast to as-milled $LiBH_4$. The desorbed H_2 was carried by Ar flowing at 160 mL min^{-1} and measured by MS. Signals were normalized for comparison. No B_2H_6 was detected.

The $LiBH_4$-Ni (bulk) sample started dehydrogenation at 287 °C that was very close to 285 °C for the as-milled $LiBH_4$. Thus, the added 14 wt.% bulk Ni did not decrease the decomposition onset temperature. However, it reduced the peak temperature by 10 °C (to 460 °C) compared with the 470 °C for the as-milled $LiBH_4$. Upon heating to 500 °C, the amount of H_2 released from the $LiBH_4$-Ni (bulk) sample was 5.2 wt.%. If the weight of Ni is excluded, $LiBH_4$ content released 6.0 wt.% of hydrogen, which was slightly smaller than the 6.7 wt.% for the as-milled $LiBH_4$.

The nano-sized Ni not only decreased the decomposition onset temperature (from 285 °C for as-milled $LiBH_4$) to 187 °C, but also reduced the peak temperature by 25 °C (to 445 °C) compared with the 470 °C for Ni-free sample. In contrast to the bulk Ni

sample, this peak temperature was also 15 °C lower. In fact, the decrease of onset temperature was possibly due to the NiO presented; whilst the reduction in peak temperature was caused by the nano-sized Ni additive and enhanced by its nano-scale effect when compared with the bulk Ni sample. The H_2 release from nano-sized Ni sample was 5.5 wt.% when heated to 500 °C. This value was close to the 5.2 wt.% for bulk Ni sample. They were about half of the 12.3 wt.% reported by Li et al. (2014) for a $LiBH_4$-Ni (25 wt.%) sample when heated to 527 °C using a Thermo-Gravimetric Analysis (TGA) apparatus. Since this work used different experimental conditions (such as size and amount of nano-sized Ni, sample preparation methods, equipment and decomposition conditions) when compared with (Li et al. 2014), it is difficult to determine the reason for this difference in observed H_2 evolutions. Moreover, considering the available composition of $LiBH_4$ in the nano-sized Ni sample, about 6.4 wt.% of hydrogen was released from the $LiBH_4$ content, which was slightly larger than the 6.0 wt.% for the bulk Ni sample but was still smaller than the 6.7 wt.% for Ni-free sample.

Thus, in general, the addition of Ni destabilized the decomposition. This was achieved by changing the reaction pathways (Xia et al. 2009; Li et al. 2014). For example, Ni_4B_3 phase was identified in XRD results for heat-treated samples at 445 °C or 460 °C (Figure 7.26). An unknown peak at 29.5° 2θ was observed in both XRD patterns. For which, other possible nickel borides, such as Ni_2B and Ni_3B (Xia et al. 2009; Li et al. 2014), had been ruled out. However, the addition of Ni did not enhance the amount of H_2 liberated from $LiBH_4$.

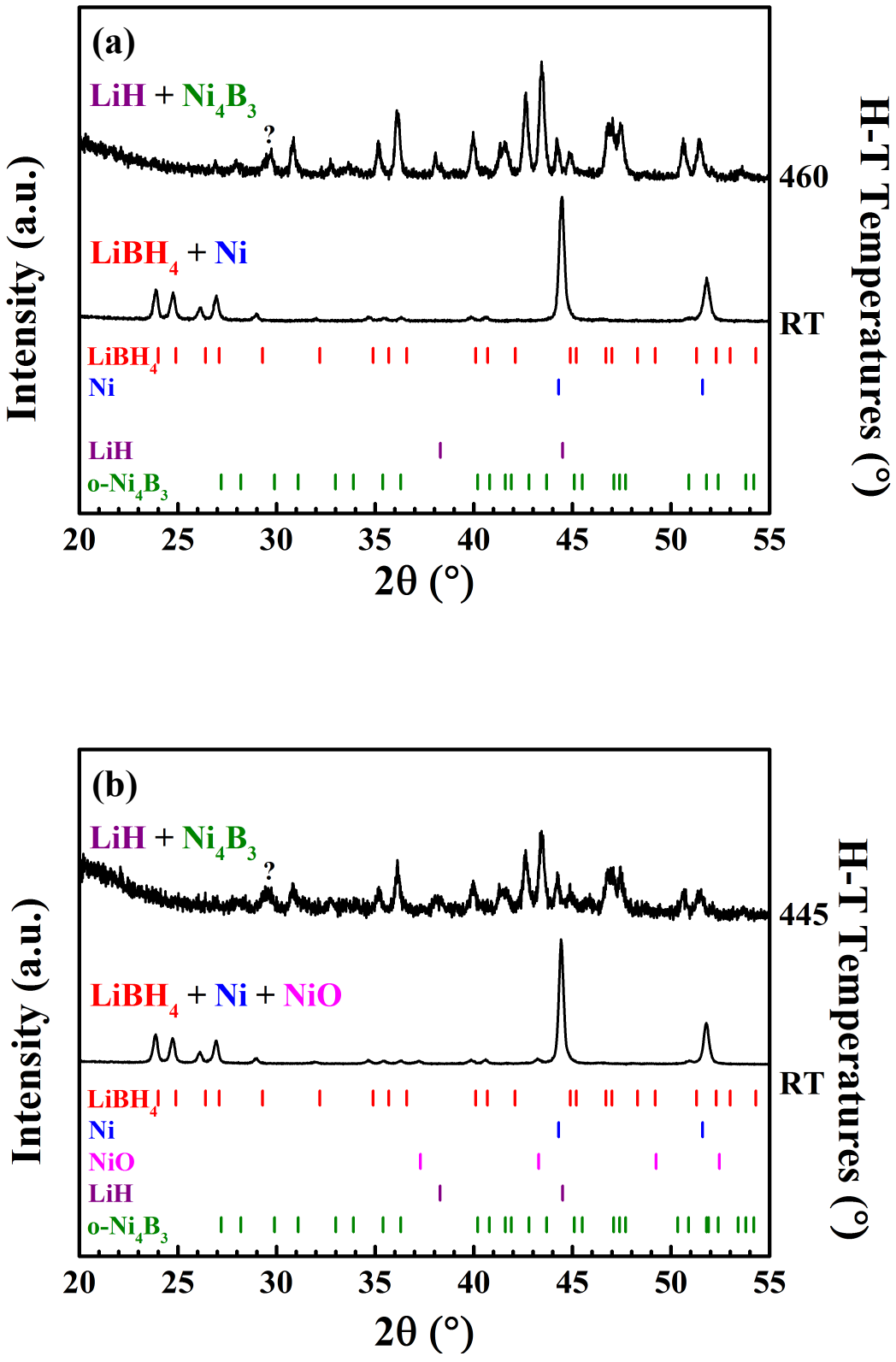

Figure 7.26 Room temperature XRD patterns (Cu K_α radiation, $\lambda = 1.5418$ Å) of as-milled $LiBH_4$-Ni (14. wt%) samples (a-bulk; b-nano-sized) heated treated at their peak temperature (445 °C or 460 °C) by 2 C min^{-1} in Ar flowing at 160 mL min^{-1}. The intensities were normalized.

Besides, $Li_2B_{12}H_{12}$ and B peaks were shown in the Raman spectra (Figure 7.27) of the heat-treated sample of $LiBH_4$-Ni (bulk) at 460 °C, confirming the simultaneously dehydrogenation of $LiBH_4$. However, due to extensive fluorescence effects, Raman spectra for $LiBH_4$-Ni (nano-sized) could not be observed.

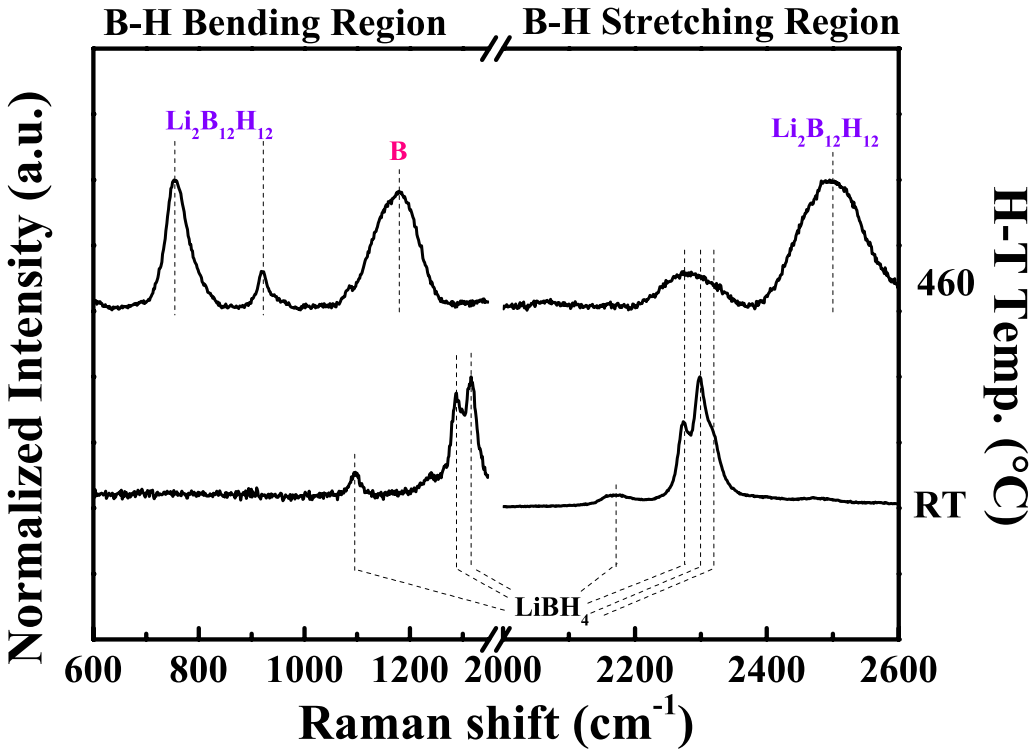

Figure 7.27 Room temperature Raman spectra (measured with 488 nm laser and 2400 l/mm grating system) of heat-treated $LiBH_4$-bulk Ni (14 wt.%) at 460 °C. A horizontal break is used to divide the spectra into $[BH_4]^-$ bending and stretching regions. Dashed lines are guides for the eye

Since the nano-sized Ni had a better destabilization performance, understanding its decomposition mechanism was of great interest. The simultaneous dehydrogenation of $LiBH_4$ in the $LiBH_4$-Ni (nano) sample could be quantitatively assessed if the following assumptions were made:

1) All nano-sized Ni reacted with $LiBH_4$ through:

$$6LiBH_4 + 8Ni = 2Ni_4B_3 + 6LiH + 9H_2 \qquad 3.0\ wt.\% \qquad \text{Equation 7.9}$$

2) $LiBH_4$ decomposed through Equation 7.2 and 7.3.

Since the overall H_2 release from $LiBH_4$-Ni (nano-sized) including heating and cooling was 9 wt.%, the decomposition reaction of its $LiBH_4$ content was calculated to be:

$$\boldsymbol{LiBH_4 = 0.86LiH + 0.16B + 0.07Li_2B_{12}H_{12} + 1.15H_2} \qquad \textbf{Equation 7.10}$$

Compared with Equation 7.6, where only 0.03 mole of $Li_2B_{12}H_{12}$ was generated from 1 mole of pure $LiBH_4$, adding nano-sized Ni increased the formation of $Li_2B_{12}H_{12}$ by more than two times. This would be a significant drawback for this system in real use, as $Li_2B_{12}H_{12}$ inhibited the reversibility. However, the nickel borides (reaction products) played an important role in the improvement effect on the rehydrogenation of $LiBH_4$ (Ngene, van Zwienen, et al. 2010; Li et al. 2014), which may compensate the drawback given by $Li_2B_{12}H_{12}$.

Thus, the overall reaction of the $0.943LiBH_4$-0.057Ni (nano) sample was:

$$\boldsymbol{0.943LiBH_4 + 0.057Ni = 0.817LiH + 0.144B + 0.063Li_2B_{12}H_{12} + 0.014Ni_4B_3 + 1.099H_2} \qquad \textbf{Equation 7.11}$$

7.3.4 Effect of Additive Ni

The addition of Ni (14 mol%) destabilized $LiBH_4$ through chemical reactions in the range 400-500 °C, forming Ni_4B_3. The addition of nano-sized Ni led to a 5.5 wt.% hydrogen release at a lower temperature: 25 °C reduction in peak temperature compared to Ni-free sample. However, the nano-sized Ni facilitated the formation of $Li_2B_{12}H_{12}$.

Figure 7.28 shows the decomposition pathway of $LiBH_4$-Ni (nano) (14 wt.%) system in a flow chart.

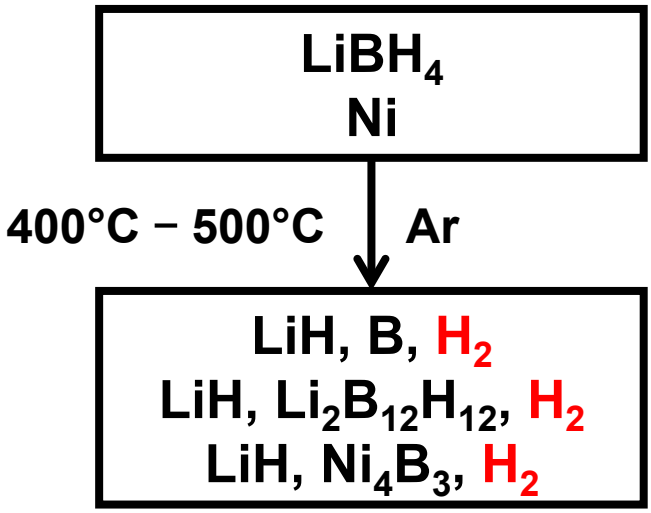

Figure 7.28 A flow chart of decomposition pathways for $LiBH_4$-Ni (nano) (14 wt.%).

7.4 Summary

In this work, the crystal structure and vibrational modes of as-received $LiBH_4$ were detected using XRD, Raman and FTIR spectroscopy at room temperature. Signals were caused by the orthorhombic phase (space group: *Pnma*) and was confirmed to be consistent with the literatures (Filinchuk et al. 2008), exhibiting lattice parameters of a = 7.199 (3) Å, b = 4.438 (2) Å, c = 6.789 (3) Å. Though the as-received $LiBH_4$ was in powder form, it was highly orientated towards (200) lattice plane that disagreed with the most common highest peak (011) or (101) in the literature (Gomes et al. 2002; A. Züttel et al. 2003; Filinchuk et al. 2008; Hartman et al. 2007; Roedern et al. 2016). After ball milling, its unit cell volume slightly decreased from 217.2 (1) $Å^3$ to 216. 8 (1) $Å^3$ corresponding to the reduction caused by ball-milling effect (Lang et al. 2012), and the highest peak changed to (101). The observed B-H stretching and bending modes in Raman spectra for as-received and as-milled samples were in good agreement with the

assignments proposed in the literature (K. B. Harvey & McQuaker 1971; Gomes et al. 2002; Racu et al. 2008).

Upon heating, $LiBH_4$ underwent a polymorphic structure transformation (from orthorhombic to hexagonal) observed at 115 °C by DSC. This high temperature phase caused a much simpler Raman spectrum (where only ν_1 and ν_2 were shown) due to the increase in point group symmetry of $[BH_4]^-$ from C_s to C_{3v} (Gomes et al. 2002; Hagemann et al. 2004). The fusion occurred at 285 °C (determined by DSC) and the decomposition simultaneously started at this temperature (indicated by the H_2 liberation in TPD-MS).

The thermal dehydrogenation of $LiBH_4$ was carried out by TPD-MS in Ar. A total of 10.0 wt.% hydrogen was detected upon heating to 650 °C. By calculating from the overall H_2 release (including heating and cooling), 60 wt.% of $LiBH_4$ decomposed through Equation 7.2 (forming LiH, B and H_2) and the rest went through Equation 7.3 (forming LiH, $Li_2BH_{12}H_{12}$ and H_2). The overall decomposition mechanism was shown in Equation 7.6 and summarised in Table 7.7.

Table 7.7 Comparison of decomposition mechanism of as-milled $LiBH_4$ vs. 0.943$LiBH_4$-0.057Ni (nano-sized) in Ar.

Reactant		Product				
$LiBH_4$	Ni	LiH	$Li_2B_{12}H_{12}$	B	H_2	Ni_4B_3
1	-	0.94	0.03	0.64	1.35	-
1	0.060	0.866	0.067	0.153	1.166	0.015

Using additives could tailor the energy required for dehydrogenation, leading to destabilization of decomposition. With a better understanding of the thermal

decomposition mechanism, H_2 evolution might be controlled and products from which subsequently facilitate rehydrogenation (i.e. improve reversibility).

In this work, a small amount of SiO_2 (5 mol%) and Ni (5.7 mol%) were used to destabilize $LiBH_4$ due to their interesting reported behaviour (Zhang et al. 2008; Mosegaard et al. 2008; Xia et al. 2009; Ngene, Adelhelm, et al. 2010; Ngene, van Zwienen, et al. 2010; Ngene, Verkuijlen, et al. 2011; Li et al. 2014).

In general, both additives destabilised dehydrogenation, exhibiting lower peak temperatures for H_2 desorption, as summarised in Table 7.8

Table 7.8 Effect of additives on the dehydrogenation of $LiBH_4$.

Sample	Temperature (°C)			H_2 release (wt.%) 500 °C, Ar
	Onset	Early peak(s)	Major Peak	
$LiBH_4$	285	-	470	6.7
$0.95LiBH_4$-$0.05SiO_2$ (0.5 μm)	281	303, 375	467	4.7
$0.943LiBH_4$-0.057Ni (bulk)	287	-	460	5.2
$0.943LiBH_4$-0.057Ni (nano)	187	-	445	5.5

Adding SiO_2 to $LiBH_4$ resulted in early dehydrogenation (not observed for Ni samples) that released up to 1.5 wt.% hydrogen before 400 °C, due to chemical reactions. The literature proposed Equation 7.7 and 7.8 (Ngene, Adelhelm, et al. 2010). However, actual reactions might be more complex suggested by thermodynamic calculations (Appendix C). At 500 °C in Ar, this system had the lowest amount of H_2 evolution among all the studied additives in this Chapter.

The nano-sized Ni (containing ~6 wt.% NiO impurity) significantly decreased the dehydrogenation onset temperature by ~100 °C, likely through a reaction between NiO and $LiBH_4$ (Ngene, van Zwienen, et al. 2010). In addition, a small amount of Ni additive (14 wt.%) reduced the major dehydrogenation peak (from 470 °C for pure $LiBH_4$) to 445 °C by changing the reaction pathways, forming Ni_4B_3. By adding more nano-sized Ni (25 wt.%), the major dehydrogenation peak temperature could be further decreased to 423 °C (Li et al. 2014).

The major decomposition products of $LiBH_4$-Ni (nano-sized) system were LiH, B, Ni_4B_3, $Li_2B_{12}H_{12}$ and H_2 (Table 7.7). Compared with that of pure $LiBH_4$, the amount of $Li_2B_{12}H_{12}$ was increased by 2.2 times when nano-sized Ni was added, indicating that Ni_4B_3 not only played a catalytic role in the decomposition of $LiBH_4$ (Li et al. 2014) but also affected the phase evolution of the boron-based materials. Such a change in the formation of $Li_2B_{12}H_{12}$ had also been reported for nano-confined $LiBH_4$-Ni in carbon scaffolds by Ngene, van Zwienen, et al. (2010). Moreover, since additives are usually much heavier than $LiBH_4$; their addition often reduces the overall intrinsic H_2 capacity by weight. Therefore, the amount of additive used, the desorption temperature obtained, and the amount of H_2 released needs to be optimised in the future. Further investigation into changes in the chemical bonding states and microstructures of the reaction products should also be considered for future work.

CHAPTER 8 LITHIUM AND SODIUM BOROHYDRIDES MIXTURE

The focus of this chapter is:

- To characterise the crystal structure, vibrational frequencies, thermodynamic property of the low-melting-point $0.62LiBH_4$-$0.38NaBH_4$ mixture;
- To investigate its dehydrogenation mechanism and recombination behaviour;
- To modify its dehydrogenation and recombination properties using selected additives, such as micron-sized SiO_2 (diameter = 0.5 μm) and nano-sized Ni (~100 nm), and to investigate the modified reaction pathways.

8.1 Sodium Borohydride

8.1.1 Sample Characterisations

8.1.1.1 As-received $NaBH_4$

Figure 8.1-a shows the room temperature phase structure of as-received $NaBH_4$ (Sigma-Aldrich, > 99.99%). The Bragg peaks were caused by a cubic structure (space group *Fm-3m*).

The pseudo-Rietveld refinement result in Figure 8.2 shows the as-received $NaBH_4$ has high purity; the refined lattice parameters was slightly (< 1%) higher than the published values (Table 8.1) (Soldate 1947; Abrahams & Kalnajs 1954; Kumar & Cornelius 2005; Filinchuk & Hagemann 2008; Roedern et al. 2016).

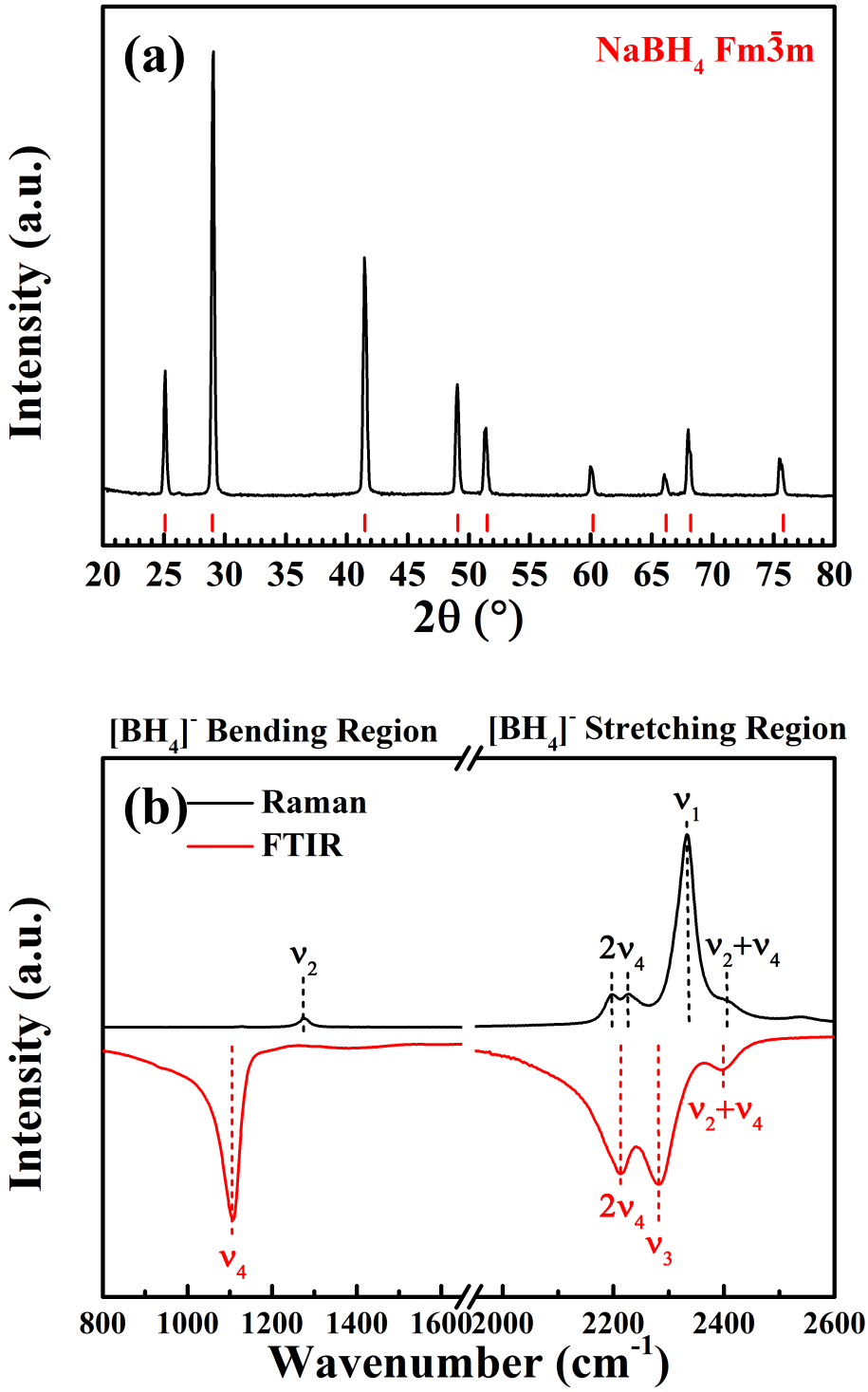

Figure 8.1 (a) XRD pattern (Cu K_α radiation, λ = 1.5418 Å) of as-received $NaBH_4$ at room temperature compared to an synchrotron XRD data (red vertical lines) from the literature (Kumar & Cornelius 2005). (b) Raman (measured with 488 nm laser and 2400 l/mm grating system) and FTIR spectra of as-received $NaBH_4$ at room temperature. A horizontal break was used to divide the spectra into $[BH_4]^-$ bending and stretching regions. Dashed lines are guides for the eye.

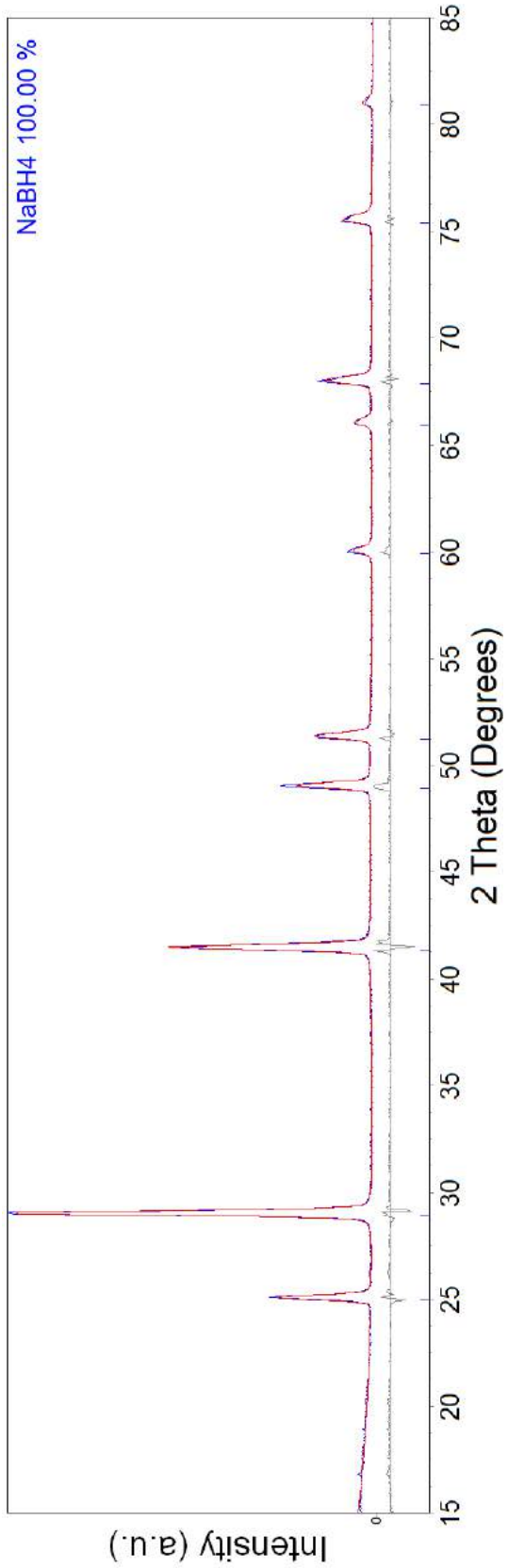

Figure 8.2 Pseudo-Rietveld refinement result of as-received $NaBH_4$, including the observed XRD (Cu K_α radiation, λ = 1.5418 Å) profile (blue), the calculated profile (red, used to fit the observed profile) and the difference profile (grey). The goodness-of-fit was 1.891.

Table 8.1 Refined lattice parameter of as-received and as-milled $NaBH_4$, comparing to literature values.

As-received	As-milled	Literature
6.180 ± 0.002	6.169 ± 0.002	6.131 – 6.164

The wavenumbers (cm^{-1}) of Raman and FTIR results (Figure 8.1-b) are summarised in Table 8.2. In theory, depending on the four vibrations modes of $[BH_4]^-$ in $NaBH_4$, 7 internal vibrations could produce Raman scattering and only 4 of them might be infrared active (K. B. Harvey & McQuaker 1971). In this work, 5 internal vibrations were observed in Raman and their wavenumbers were in good agreement with literature values (K. B. Harvey & McQuaker 1971). In addition, though all infrared active modes were observed, their wavenumbers were slightly lower than the reported values (K. B. Harvey & McQuaker 1971).

Table 8.2 Experiment frequencies (cm^{-1}) of as-received and as-milled $NaBH_4$ observed in Raman and FTIR compared to literature values.

Mode			Raman			FTIR	
			Experiment		Literature	Experiment	Literature
			As-received	As-milled		As-received	
	ν_4	B_2	-	-	-	1107	1119
	ν_2	A_1	1276	1277	1278	-	-
	$2\nu_4$		2198	2195	2198	-	-
Internal	$2\nu_4$		2228	2227	2229	2213	2222
	ν_3	B_2	-	-	-	2282	2297
	ν_1	A_1	2334	2331	2335	-	-
	$\nu_2+\nu_4$	E	2408	2401	2403	2399	2393

8.1.1.2 As-milled $NaBH_4$

The as-milled sample was prepared using ball milling under the conditions described in Section 6.1.1. Its room temperature XRD, Raman and refinement results are shown in Figure 8.3-8.4.

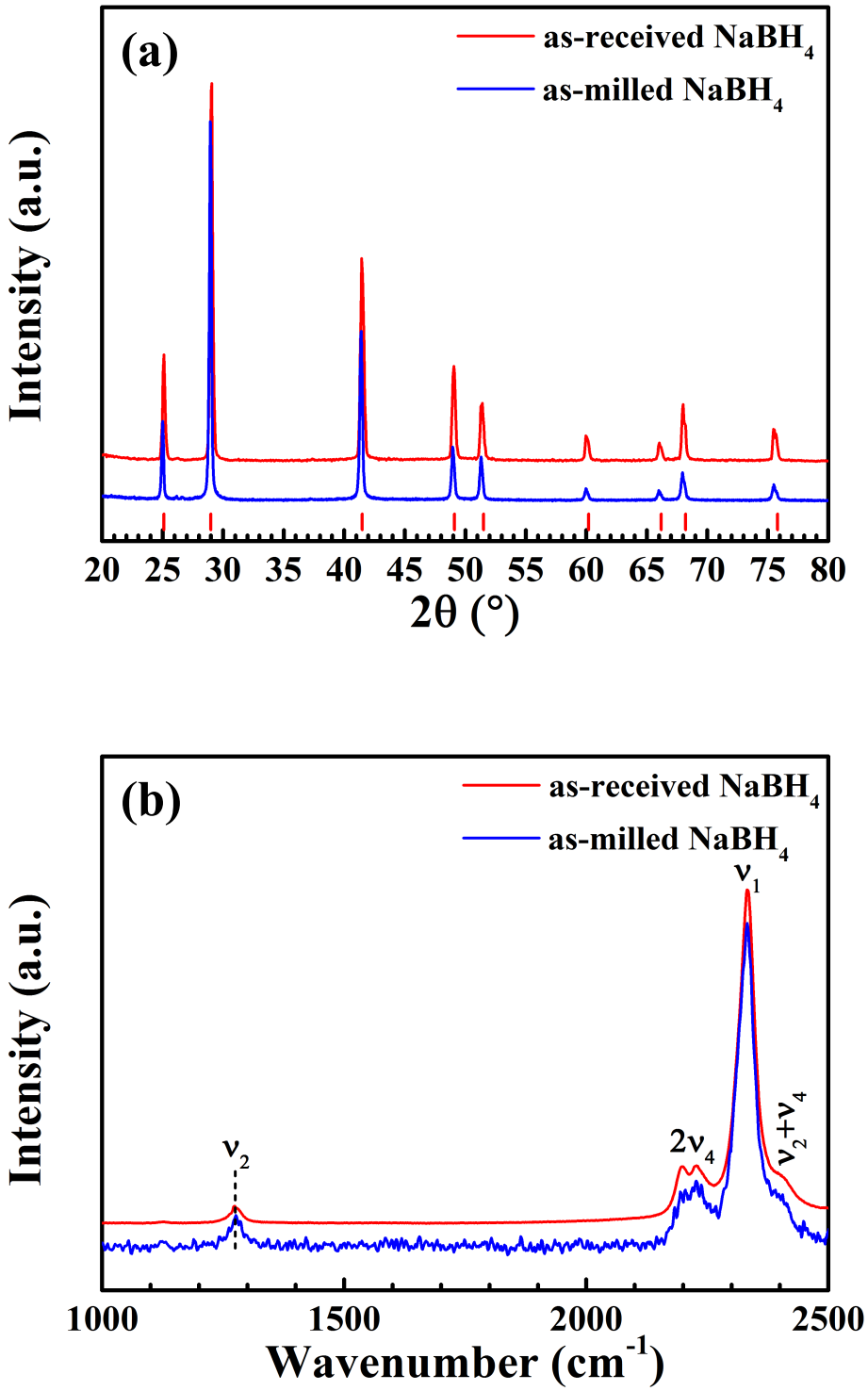

Figure 8.3 (a) XRD patterns (Cu K_α radiation, λ = 1.5418 Å) of as-milled $NaBH_4$ at room temperature compared to the as-received material and an synchrotron XRD data (red vertical lines) from the literature (Kumar & Cornelius 2005). (b) Raman (measured with 488 nm laser and 2400 l/mm grating system) spectra of as-received and as-milled $NaBH_4$ at room temperature. Peaks were normalized for comparison. Dashed lines are guides for the eye.

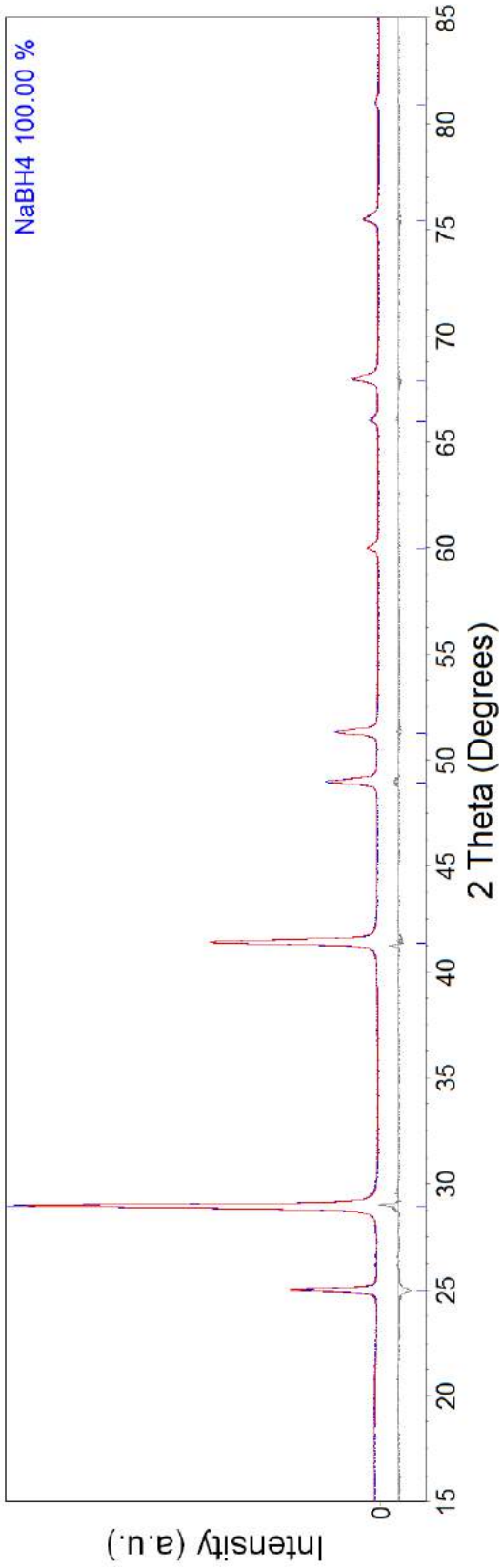

Figure 8.4 Pseudo-Rietveld refinement result of as-milled $NaBH_4$, including the observed XRD (Cu K_α radiation, λ = 1.5418 Å) profile (blue), the calculated profile (red, used to fit the observed profile) and the difference profile (grey). The goodness-of-fit was 1.494.

The crystal structure and vibrational modes remained unchanged after ball milling. But the refined lattice parameter (Table 8.1) was about 0.17% smaller caused by ball milling effect (Lang et al. 2012), which was in agreement with the 0.15% (ball milled for 50 h at 75-175 rpm) observed by Varin & Chiu (2005).

8.1.2 Thermal Decomposition

Figure 8.5 shows the TPD-MS results of the as-milled $NaBH_4$ heated to 650 °C by 2 °C min^{-1} in Ar.

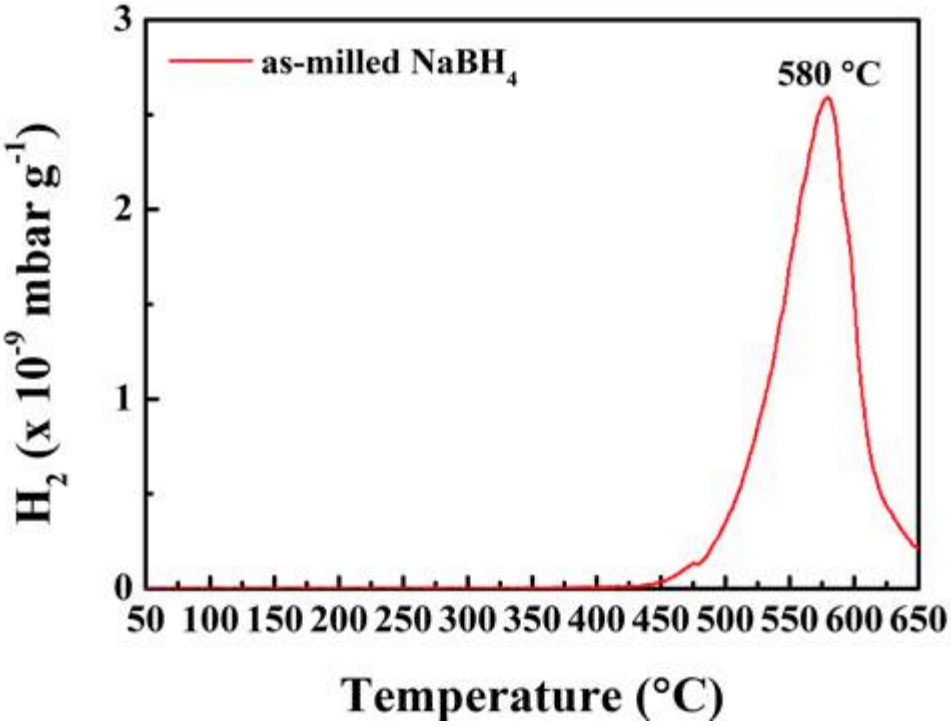

Figure 8.5 TPD-MS results of as-milled $NaBH_4$ in the range 50 – 650 °C heated at 2 °C min^{-1} in TPD. The desorbed H_2 was carried by Ar flowing at 160 mL min^{-1} to MS. No B_2H_6 was detected.

The dehydrogenation began at 450 °C, followed by a peak at 580 °C (without B_2H_6). Although Urgnani et al. (2008) suggests that the H_2 release from $NaBH_4$ starts at a

lower temperature (~150 °C) than its melting point (~505 °C), such a solid-state H_2 desorption was not observed in this work. A total of 7.8 wt. % hydrogen was released after heating to 650 °C.

Figure 8.6 shows the room temperature XRD pattern of the decomposition products of $NaBH_4$. Diffraction peaks related to elemental Na were observed that agreed with the proposed decomposition reaction (Urgnani et al. 2008; Martelli et al. 2010; Mao & Gregory 2015):

$$NaBH_4 = Na + B + 2H_2 \quad \textbf{10.7 wt.\%} \qquad \textbf{Equation 8.1}$$

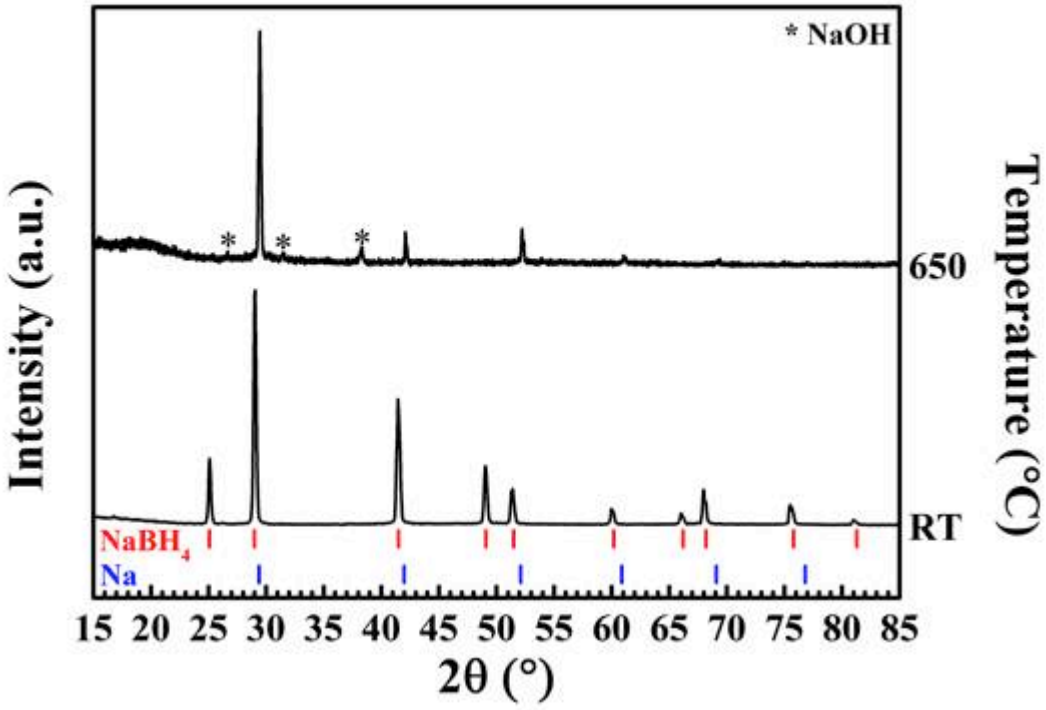

Figure 8.6 XRD patterns (Cu K_α radiation, λ = 1.5418 Å) of decomposed $NaBH_4$ through heat treatment to 650 °C by 2 C min^{-1} in Ar flowing at 160 mL min^{-1}.

In addition, some low-intensity peaks of NaOH were found, due to oxidation of Na. Peaks assigned to B were often not detectable using XRD, possibly due to its low scattering factor to X-rays and thus became 'XRD amorphous'. In theory, Raman spectroscopy could help with B identification. However, in practice, it was not possible due to the high fluorescence effect caused by Na.

In theory, $NaBH_4$ contained 10.7 wt.% hydrogen, which was about 40% higher than the 7.8 wt.% measured by TPD-MS. This was because:

1) The $NaBH_4$ loaded was not fully decomposed due to its high stability and the experiment set-up (e.g. limited heat zone range);
2) Formation of intermediate phases (or bi-products), such as $Na_2B_{12}H_{12}$ (Mao & Gregory 2015). However, $Na_2B_{12}H_{12}$ was not observed in XRD or Raman (due to high fluorescence background caused by Na) results. Nuclear Magnetic Resonance (NMR) spectroscopy might be able to determine if $Na_2B_{12}H_{12}$ was present (Geis et al. 2009; Hanumantha Rao & Muralidharan 2013).

The CALPHAD method was used to calculate the thermodynamic properties of possible decomposition reactions of $NaBH_4$, including Equation 8.1-8.5. Because the thermodynamic database of $Na_2B_{10}H_{10}$ was not available, decomposition involving this product could not be calculated. The calculated phase diagram is shown in Figure 8.7.

$\mathbf{2NaBH_4 = 2NaH + 2B + 3H_2}$	**8.0 wt.%**	**Equation 8.2**
$\mathbf{12NaBH_4 = 10Na + Na_2B_{12}H_{12} + 18H_2}$	**8.0 wt.%**	**Equation 8.3**
$\mathbf{12NaBH_4 = 10NaH + Na_2B_{12}H_{12} + 13H_2}$	**5.8 wt.%**	**Equation 8.4**
$\mathbf{2NaH = 2Na + H_2}$	**4.2 wt.%**	**Equation 8.5**

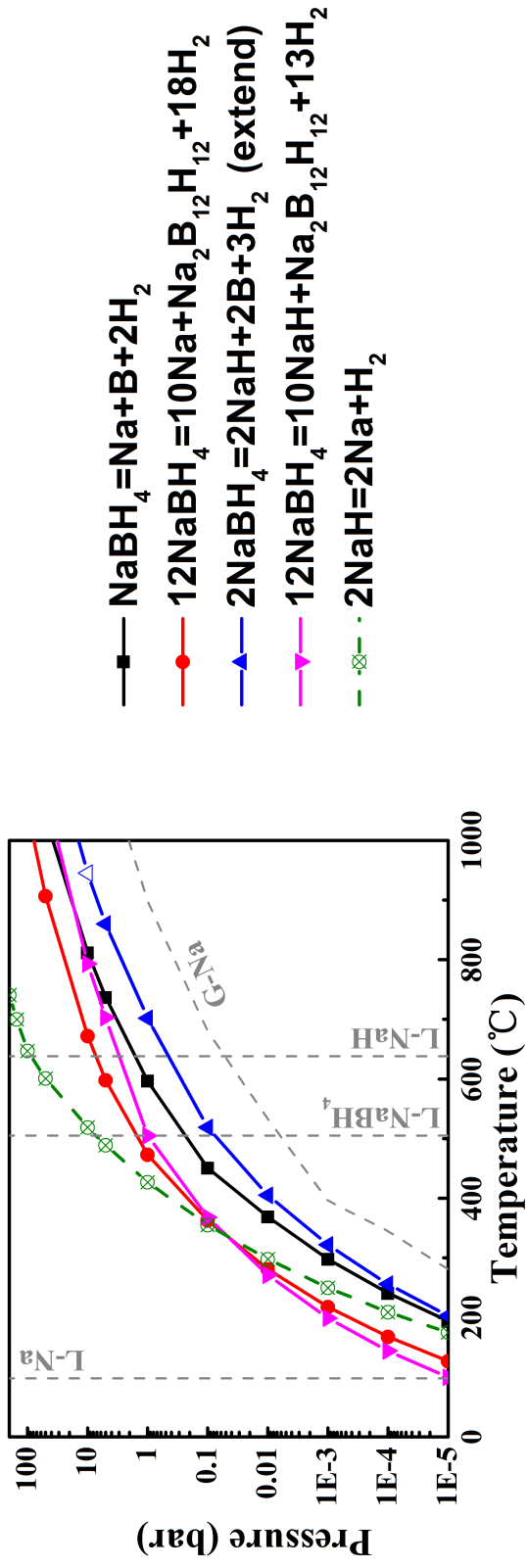

Figure 8.7 CALPHAD calculated phase diagram of $NaBH_4$. The dashed lines indicated the fusion of Na, $NaBH_4$ and NaH as a function of pressure, and the gasification of Na as a function of temperature and pressure. Because the Gibbs free energy functions for NaH was only available till 1200K (963 °C), an extension was made for reaction involved NaH. The extension dots were marked in hollow dots.

The calculation results suggested that decomposition reactions involving $Na_2B_{12}H_{12}$ (Red spot and Pink inverted triangle) were more thermodynamically favourable than any other reactions. When the pressure was lower than 0.1 bar H_2, the formation of NaH, $Na_2B_{12}H_{12}$ and H_2 (Pink inverted triangle) was more favourable than forming Na, $Na_2B_{12}H_{12}$ and H_2 (Red dot). Otherwise, the later became more promising. However, due to the complex structure of $Na_2B_{12}H_{12}$, its formation was not kinetically favourable.

In addition, the decomposition pathway into Na, B and H_2 (Black square) was always more thermodynamically favourable compared to the formation of NaH, B and H_2 (Blue triangle). Because NaH was not stable when the temperature was higher than 175 °C (when H_2 pressure = 10^{-5} bar) and decomposed into Na and H_2 (Green crossed hollow dots), even if some NaH precipitated during dehydrogenation, it should further decompose into Na and H_2 immediately, which agreed with the fact that no NaH was found experimentally in inert atmospheres.

8.2 Low-melting-point $0.62LiBH_4$-$0.38NaBH_4$ Mixture

8.2.1 Sample Characterisations

The $0.62LiBH_4$-$0.38NaBH_4$ mixture was prepared using ball milling under the conditions described in Section 6.1.1. Figure 8.8 show room temperature phases and vibrational structures of as-milled and recrystallized $0.62LiBH_4$-$0.38NaBH_4$ mixtures. The recrystallized sample was prepared by a heat-treatment to 250 °C by 2 °C min^{-1} in Ar flowing at 160 mL min^{-1} and then freely cooled down to room temperature. This target temperature was chosen due to its low melting temperature (~220 °C) (M Paskevicius et al. 2013; Javadian, Sheppard, et al. 2015; Dematteis et al. 2016).

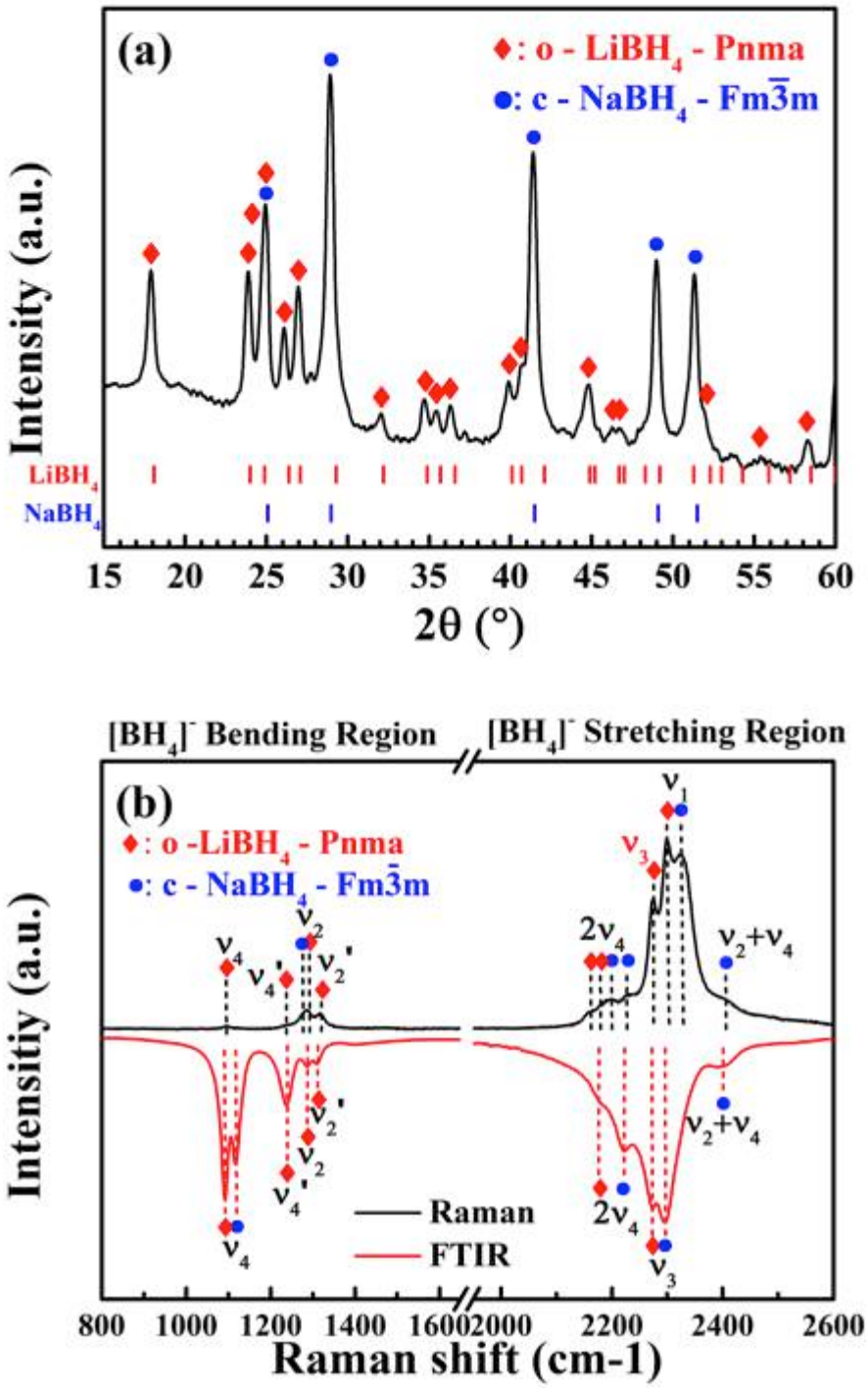

Figure 8.8 (a) room temperature XRD pattern (Cu K_α radiation, λ = 1.5418 Å) (intensity in log scale) for as-milled $0.62LiBH_4$-$0.38NaBH_4$ mixture; (b) room temperature Raman (measured with 488 nm laser and 2400 l/mm grating system) and FTIR spectra for as-milled $0.62LiBH_4$-$0.38NaBH_4$ mixture; (c) room temperature XRD pattern (Cu K_α radiation, λ = 1.5418 Å) (intensity in log scale) for recrystallized $0.62LiBH_4$-$0.38NaBH_4$ mixture; (d) room temperature Raman (measured with 488 nm laser and 2400 l/mm grating system) spectrum for recrystallized $0.62LiBH_4$-$0.38NaBH_4$ mixture. The recrystallized sample is heat-treated to 250 °C in flowing Ar at 160 mL min^{-1}. Dashed lines are guides for the eye.

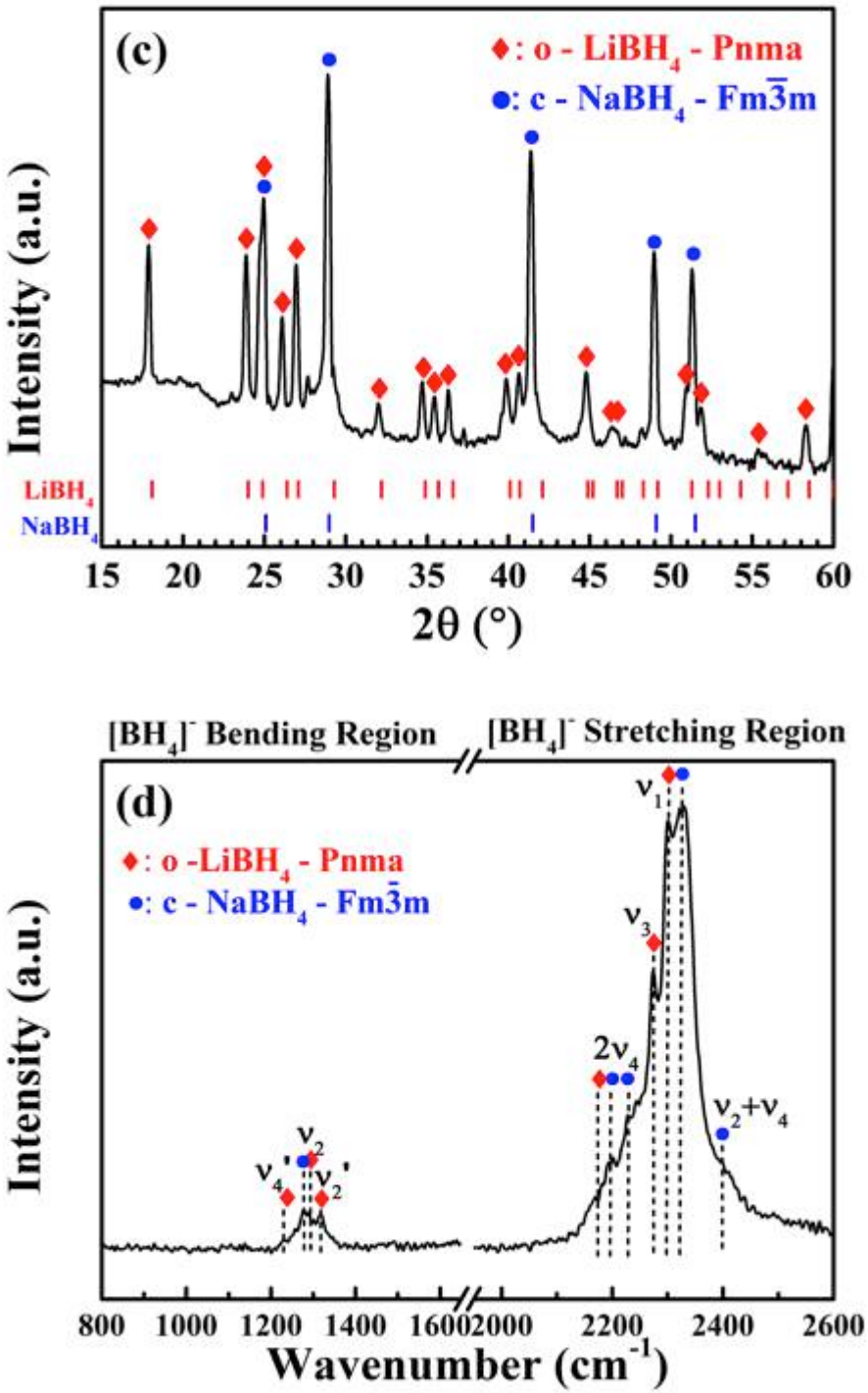

Figure 8.8 (a) room temperature XRD pattern (Cu K_α radiation, λ = 1.5418 Å) (intensity in log scale) for as-milled $0.62LiBH_4$-$0.38NaBH_4$ mixture; (b) room temperature Raman (measured with 488 nm laser and 2400 l/mm grating system) and FTIR spectra for as-milled $0.62LiBH_4$-$0.38NaBH_4$ mixture; (c) room temperature XRD pattern (Cu K_α radiation, λ = 1.5418 Å) (intensity in log scale) for recrystallized $0.62LiBH_4$-$0.38NaBH_4$ mixture; (d) room temperature Raman (measured with 488 nm laser and 2400 l/mm grating system) spectrum for recrystallized $0.62LiBH_4$-$0.38NaBH_4$ mixture. The recrystallized sample is heat-treated to 250 °C in flowing Ar at 160 mL min^{-1}. Dashed lines are guides for the eye.

For the as-milled sample, only $LiBH_4$ and $NaBH_4$ phases were detected and no new peaks were observed. For the recrystallized structure, the phases and structures detected were unchanged after the heat treatment, whilst the crystallinity was improved as the Bragg peaks had narrower widths (e.g. 30-60% reduction of full width at half maximum).

Table 8.3 and Table 8.4 show the summarised Raman and FTIR frequencies for as-milled and recrystallized $0.62LiBH_4$-$0.38NaBH_4$ mixtures, compared with literature values (K B Harvey & McQuaker 1971; K. B. Harvey & McQuaker 1971; Gomes et al. 2002; Racu et al. 2008).

Table 8.3 Experiment frequencies (cm^{-1}) of as-milled and recrystallized $0.62LiBH_4$-$0.38NaBH_4$ observed in Raman compared to literature values.

Mode		$LiBH_4$		$NaBH_4$		$0.62LiBH_4$-$0.38NaBH_4$	
		As-milled	Literature	As-milled	Literature	As-milled	Recrystallized
ν_4	A_g	1096	1090	-	-	1097	n.a.
ν_4'	A_g	n.a.	1235	-	-	1242	1233
ν_2	A_1	-	-	1277	1278	1282	1277
ν_2	B_{1g}	1290	1286	-	-	1290	1286
ν_2'	A_g	1319	1316	-	-	1317	1318
$2\nu_4$		2163	2156	-	-	2159	n.a.
$2\nu_4'$		2180	2177	-	-	2167	2170
$2\nu_4$		-	-	2195	2198	2198	2200
$2\nu_4$		-	-	2227	2229	2229	2229
ν_3	A_g	2273	2275	-	-	2275	2273
ν_1	A_g	2299	2301	-	-	2300	2301
ν_1	A_1	-	-	2331	2335	2323	2326
$\nu_2+\nu_4$	E	-	-	2401	2403	2404	2399

Table 8.4 Experiment frequencies (cm^{-1}) of as-milled and recrystallized $0.62LiBH_4$-$0.38NaBH_4$ observed in FTIR compared to literature values.

Mode		$LiBH_4$		$NaBH_4$		$0.62LiBH_4$-$0.38NaBH_4$
		As-received	Literature	As-received	Literature	As-milled
ν_4	A_g	1089	1089	-	-	1092
ν_4	B_2	-	-	1107	1119	1117
ν_4'	A_g	1233	1254	-	-	1237
ν_2	B_{1g}	1285	1284	-	-	1286
ν_2'	A_g	1307	1323	-	-	1310
$2\nu_4'$		2180	2176	-	-	2180
$2\nu_4$		-	-	2213	2222	2221
ν_3	A_g	2271	2277	-	-	2274
ν_3	B_2	-	-	2282	2297	2295
ν_3'	A_g	2300	2307	-	-	n.a.
$\nu_2+\nu_4$	E			2399	2393	2400

The molar ratio of $LiBH_4$ to $NaBH_4$ in the as-milled sample was 62 ± 1 mol% $LiBH_4$ with 38 ± 1 mol% $NaBH_4$, which were achieved from the weight percentage (45.2 ± 0.4 wt. % for $LiBH_4$ and 54.8 ± 0.4 wt. % for $NaBH_4$) obtained from pseudo-Rietveld refinement result (Figure 8.9-a). The molar ratio of the recrystallized $0.62LiBH_4$-$0.38NaBH_4$ mixture was within errors for the as-milled sample.

The refined crystal structure parameters of $LiBH_4$ and $NaBH_4$ components in the as-milled $0.62LiBH_4$-$0.38NaBH_4$ mixture were summarised in Table 8.5, compared with those parameters of as-milled pure compounds.

Table 8.5 Refined crystal structure parameters (Å) of $LiBH_4$ and $NaBH_4$ components in as-milled and recrystallized $0.62LiBH_4$-$0.38NaBH_4$ mixture in contrast to those parameters of as-milled pure compounds.

	o-$LiBH_4$			c-$NaBH_4$		
	Pure	Mixture		Pure	Mixture	
	As-milled	As-milled	Recrystallized	As-milled	As-milled	Recrystallized
a (Å)	7.199 ± 0.003	7.179 ± 0.002	7.180 ± 0.002	6.169 ± 0.002	6.163 ± 0.002	6.161 ± 0.002
b (Å)	4.438 ± 0.002	4.438 ± 0.001	4.434 ± 0.001	-	-	-
c (Å)	6.798 ± 0.002	6.806 ± 0.002	6.812 ± 0.003	-	-	-

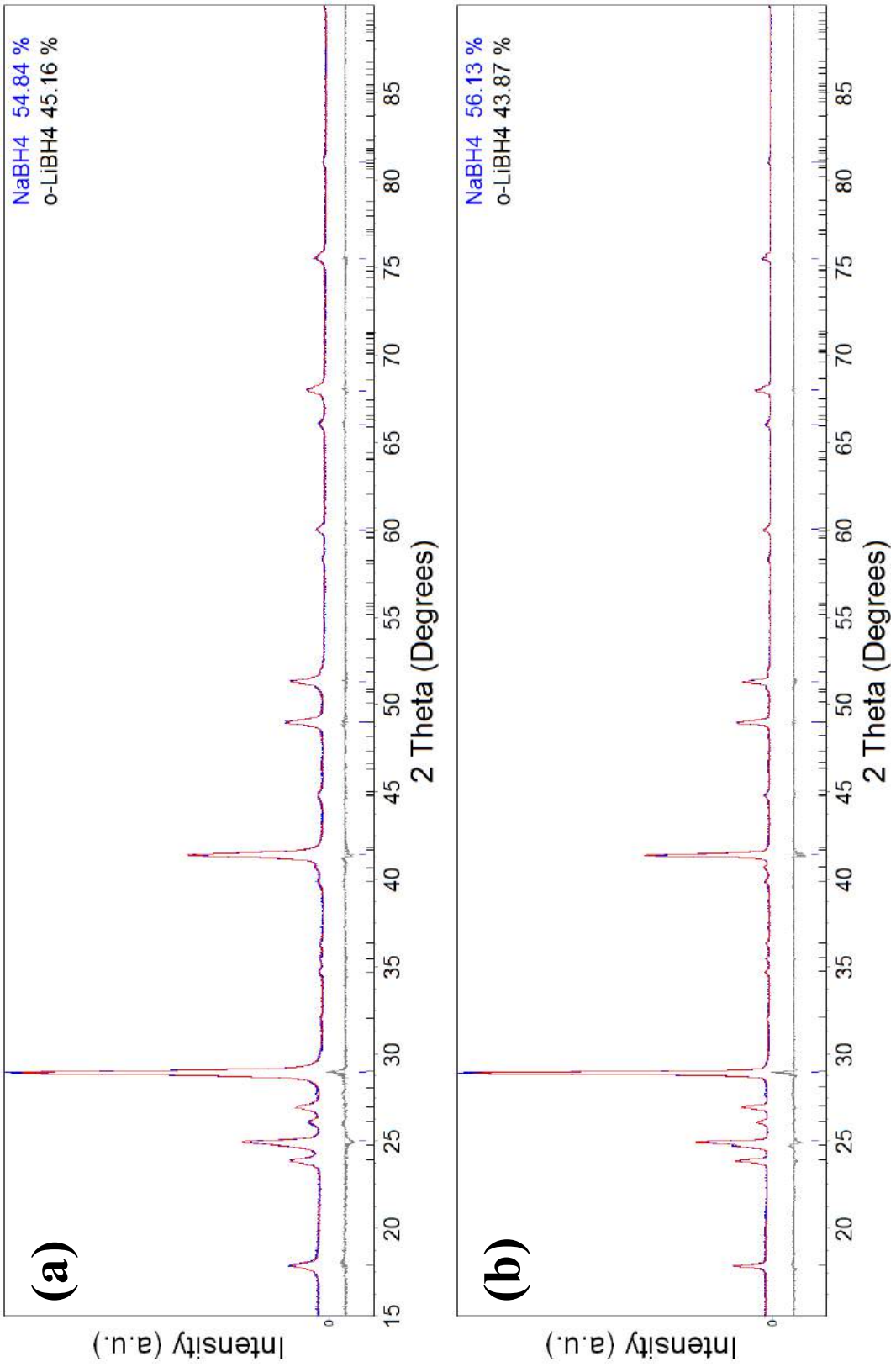

Figure 8.9 Pseudo-Rietveld refinement results of (a) as-milled and (b) recrystallized $0.62LiBH_4$-$0.38NaBH_4$ mixtures, including the observed XRD (Cu K_α radiation, λ = 1.5418 Å) profile (blue), the calculated profile (red, used to fit the observed profile) and the difference profile (grey) in each figure. The goodness-of-fit values for (a) and (b) were 1.208 and 1.343, respectively.

In fact, the refinement results showed different unit cell volumes for $LiBH_4$ and $NaBH_4$ components in as-milled $0.62LiBH_4$-$0.38NaBH_4$ mixture compared to as-milled $LiBH_4$ and as-milled $NaBH_4$, as shown in Figure 8.10.

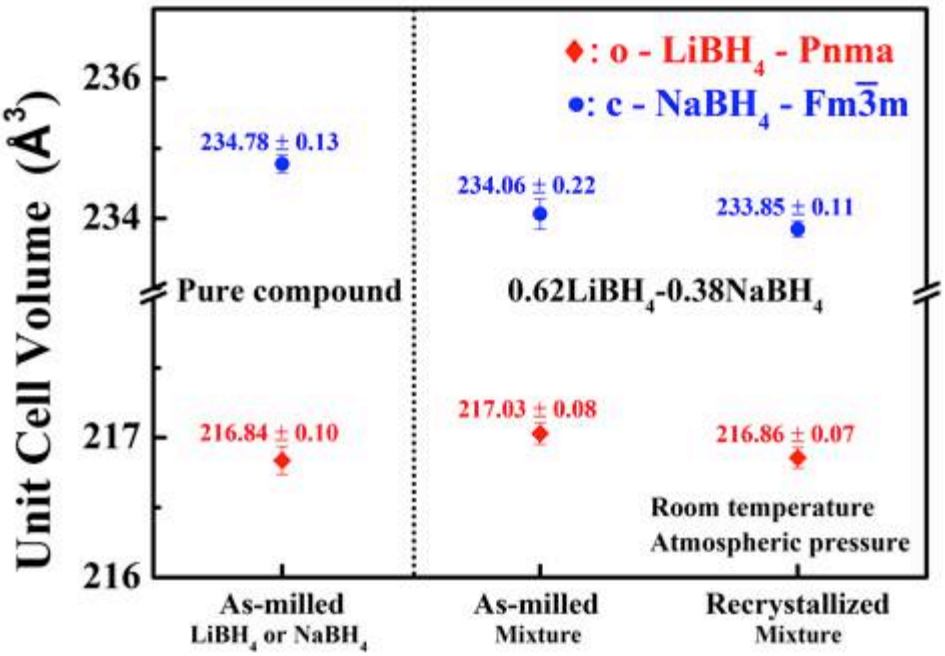

Figure 8.10 Comparison of unit cell volumes ($Å^3$) of: as-milled $LiBH_4$, as-milled $NaBH_4$, as-milled $0.62LiBH_4$-$0.38NaBH_4$ mixture, and recrystallized $0.62LiBH_4$-$0.38NaBH_4$ mixture.

At room temperature, The $LiBH_4$ lattice in the $0.62LiBH_4$-$0.38NaBH_4$ mixture slightly expanded and the $NaBH_4$ lattice slightly shrank:

- 217.03 ± 0.08 $Å^3$ ($LiBH_4$ in mixture) > 216.84 ± 0.10 $Å^3$ (as-milled $LiBH_4$);
- 234.06 ± 0.22 $Å^3$ ($NaBH_4$ in mixture) < 234.78 ± 0.13 $Å^3$ (as-milled $NaBH_4$).

Although $LiBH_4$ and $NaBH_4$ had different structures and coordination preferences of Li^+ and Na^+ (A. Züttel et al. 2003; Kumar & Cornelius 2005), the *in situ* synchrotron

XRD data in (Dematteis et al. 2016) showed changes in lattice parameters for orthorhombic (expansion), hexagonal (expansion) and cubic (shrinkage) phases in the $LiBH_4$-$NaBH_4$ mixture that indicated the existence of solid solutions - Li(Na)BH_4 and Na(Li)BH_4. Therefore, the enlargement and shrinkage of the lattices observed in the refinement results were due to the substitution of Li^+ (into $NaBH_4$) and Na^+ (into $LiBH_4$).

In addition, at room temperature, the total symmetric stretching mode (ν_1) of the $NaBH_4$ in as-milled 0.62$LiBH_4$-0.38$NaBH_4$ mixture was 2323 cm^{-1}, which was smaller than the 2331 cm^{-1} for the as-milled $NaBH_4$ (Table 8.3). According to Badger's rule (Badger 1934; Renaudin et al. 2004), which described a linear inverse relationship between the bond lengths and the Raman shift of stretching modes, this decrease in wavenumbers indicates an expansion of the bond length of the $NaBH_4$ in as-milled 0.62$LiBH_4$-0.38$NaBH_4$ mixture and was proposed due to the substitution of Li^+ into $NaBH_4$. However, this wavenumber of $LiBH_4$ in the as-milled 0.62$LiBH_4$-0.38$NaBH_4$ mixture (2300 cm^{-1}) was the same as that for as-milled $LiBH_4$ (2299 cm^{-1}), indicating that the solubility of Na^+ (in $LiBH_4$) was limited so that the change was not obvious in the Raman spectra.

The unit cell volume of $LiBH_4$ component in the recrystallized 0.62$LiBH_4$-0.38$NaBH_4$ mixture was 216.86 ± 0.07 $Å^3$. This value was slightly smaller than the 217.03 ± 0.08 $Å^3$ for the as-milled mixture unexpectedly. This suggested that the Li(Na)BH_4 in the as-milled mixture was a supersaturated solid solution, in which case the solubility of Na^+ (in $LiBH_4$) reduced after recrystallization.

Though the unit cell volume of $NaBH_4$ component in the recrystallized $0.62LiBH_4$-$0.38NaBH_4$ mixture (233.85 ± 0.11 Å) and the one in the as-milled mixture (234.06 ± 0.22 Å) were within errors, the former value was still smaller than the 234.78 ± 0.13 Å for as-milled $NaBH_4$, suggesting the substitution of Li^+ into $NaBH_4$ remained after recrystallization and indicating the formation of $Na(Li)BH_4$ was relatively stable.

8.2.2 Thermal Analysis

Figure 8.11 shows the DSC traces of as-milled $0.62LiBH_4$-$0.38NaBH_4$ mixture compared with that for as-milled $LiBH_4$. The as-milled $NaBH_4$ was not tested due to its relatively high stability (Mao & Gregory 2015).

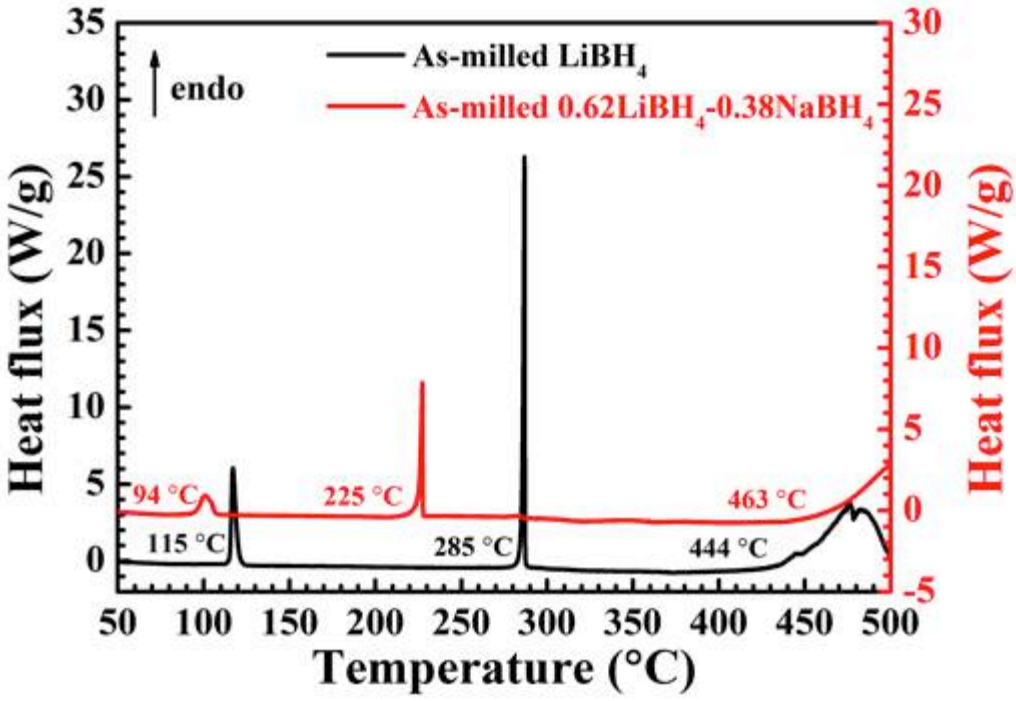

Figure 8.11 DSC results of as-milled $0.62LiBH_4$-$0.38NaBH_4$ mixture, compared to as-milled $LiBH_4$. Samples were heated at 5 °C min^{-1}. To protect the instrument, the maximum operating temperature was set at 500 °C and a 2 bar static H_2 was applied.

The melting point of as-milled $0.62LiBH_4$-$0.38NaBH_4$ mixture was 225 ± 1 °C (that was much lower than the 285 ± 1 °C for as-milled $LiBH_4$) with an enthalpy of fusion of 4.99 ± 0.25 kJ mol^{-1}, which agreed with values calculated by CALPHAD method (Dematteis et al. 2016).

Figure 8.12 shows a continuous DSC trace of the as-milled $0.62LiBH_4$-$0.38NaBH_4$ mixture heated from 50 °C to 250 °C and cooled back to 50 °C by 10 °C min^{-1} in 2 bar static H_2 for 3 times. The endothermic and exothermic signals corresponded to melting and solidification were exactly the same (overlapped) during cycling, indicating this low-temperature fusion behaviour was stable against cycling.

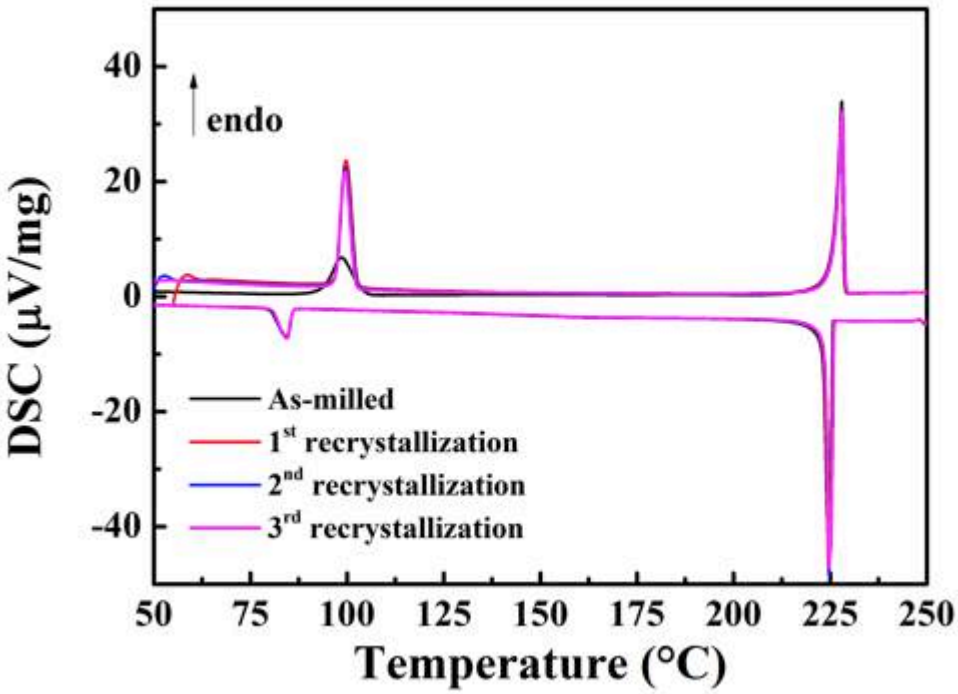

Figure 8.12 DSC traces of as-milled $0.62LiBH_4$-$0.38NaBH_4$ mixture when recrystallized 3 times. Samples were heated/cooled at 10 °C min^{-1} in 2 bar static H_2.

In addition, the Li(Na)BH_4 in as-milled 0.62$LiBH_4$-0.38$NaBH_4$ mixture exhibited an orthorhombic to hexagonal phase transition at 94 °C (onset) with an enthalpy of 3.14 ± 0.16 kJ mol^{-1} (Figure 8.11). This temperature was about 20 °C lower than the phase transition for as-milled $LiBH_4$ (115 °C) measured under the same conditions. This reduction of temperature was due to Na^+ substitution and the solubility increased as function of temperature (Dematteis et al. 2016). Because of the higher solubility of Na^+ in hexagonal $LiBH_4$ (max. 20 mol%) than that in orthorhombic $LiBH_4$ (max. 6 mol%) (Dematteis et al. 2016), a small fraction of cubic $NaBH_4$ dissolved (into hexagonal $LiBH_4$) immediately after the phase transition. Therefore, the enthalpy of the 1st peak in DSC (for as-milled 0.62$LiBH_4$-0.38$NaBH_4$ mixture) was contributed by 3 factors:

1) The orthorhombic to hexagonal phase transition of Li(Na)BH_4;
2) The vanishing of a small amount of cubic Na(Li)BH_4;
3) The substitution of Na^+ into h-$LiBH_4$.

This early phase transition was constantly observed (at 97 °C) for those recrystallized samples during cycling (Figure 8.12), although their peak shapes were slightly different and the peak area was about 10% higher. These changes in peak shape and area are possibly due to the defects induced from ball milling that lowered the energy required for phase transition at the 1st cycle. Once the defects were recovered, the curve shape and area became identical.

8.2.3 Thermal Decomposition

The TPD-MS trace for the dehydrogenation of the as-milled $0.62LiBH_4$-$0.38NaBH_4$ mixture was compared with those of as-milled $LiBH_4$ and as-milled $NaBH_4$ in Figure 8.13.

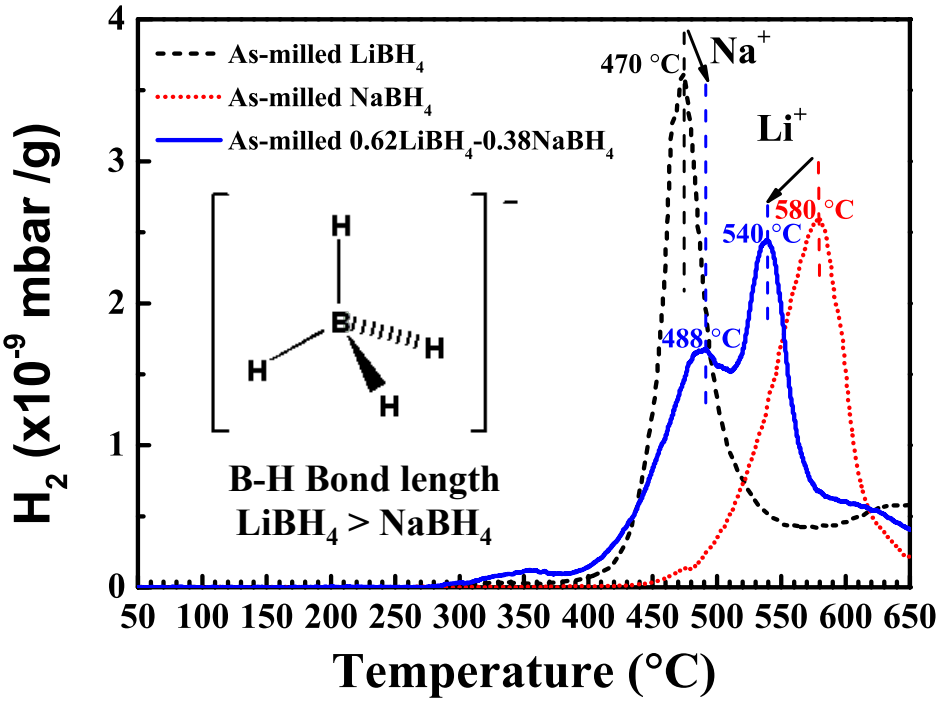

Figure 8.13 TPD-MS hydrogen desorption traces of as-milled $0.62LiBH_4$-$0.38NaBH_4$ mixture, compared with as-milled $LiBH_4$ and as-milled $NaBH_4$. Samples were heated at 2 °C min^{-1} in flowing Ar at 160 mL min^{-1}. No B_2H_6 was detected during the decomposition of any sample.

The dehydrogenation of as-milled $LiBH_4$ (black dash line) started immediately after melting at 285 °C. It reached the highest intensity at 470 °C. A total of 10.0 wt. % of hydrogen was released after heating to 650 °C.

The dehydrogenation of as-milled $NaBH_4$ (red dot line) began at 450 °C, with a peak at 580 °C. A total of 7.8 wt. % of hydrogen was released after heating to 650 °C.

The as-milled 0.62$LiBH_4$-0.38$NaBH_4$ mixture (blue solid line) did not release H_2 directly after melting as no H_2 was detected when temperature was lower than 287 °C. This onset temperature was very close to the 285 °C for the as-milled $LiBH_4$, indicating the presence of Na^+ did not have a significant effect on the start of the dehydrogenation reactions. Two H_2 release peaks were observed at 488 °C and 540 °C, respectively, which suggested the occurrence of two separated decomposition steps. A total of 10.8 wt. % hydrogen was released upon heating up to 650 °C, which corresponds to 74.5 % of the available H_2 in the sample content. This was about 8 % and 38 % higher than the amount of H_2 released from as-milled $LiBH_4$ and as-milled $NaBH_4$, respectively.

An expected H_2 release of 8.9 wt. % for the as-milled 0.62$LiBH_4$-0.38$NaBH_4$ mixture ($m_{H_2}^{LiNa}$) was calculated via a weighted average method (Equation 8.6). This value described the estimated H_2 release from a simple mixture of $LiBH_4$ and $NaBH_4$ (without interaction).

$$\boldsymbol{m_{H_2}^{LiNa} = (m_{H_2}^{Li} w_{Li} + m_{H_2}^{Na} w_{Na})/(w_{Li} + w_{Na})} \qquad \textbf{Equation 8.6}$$

where w_{Li}, w_{Na} are the mass fraction of $LiBH_4$ and $NaBH_4$ gained from the refinement results and $m_{H_2}^{Li}, m_{H_2}^{Na}$ are the amount of H_2 released experimentally measured by TPD-MS for as-milled $LiBH_4$ and $NaBH_4$.

The amount of hydrogen released from the as-milled 0.62$LiBH_4$-0.38$NaBH_4$ mixture experimentally was 10.8 wt.%, which was 21% higher than the estimated value (8.9 wt. %), suggesting the existence of a cation interaction in the liquid phase (M Paskevicius et

al. 2013). Though the decomposition of $LiBH_4$ was complex where different metastable polyborane complexes may possibly formed as a function of conditions (Hwang et al. 2008; Yan et al. 2012; El Kharbachi et al. 2012; Huang et al. 2016), only $Li_2B_{12}H_{12}$ was observed by Raman in this work. The decomposition mechanism of $LiBH_4$ was assumed as a combination of Equation 7.2 (into LiH, B, H_2) and 7.3 (into LiH, $Li_2B_{12}H_{12}$, H_2). Thus, the presence of Na^+ increased the fraction of $LiBH_4$ decomposed through Equation 7.2. This leads to extra H_2 release and partially inhibits the formation of metal dodecarborate. In addition, the dodecaborate was known as a boron sink that obstructed the rehydrogenation (Yan et al. 2015). A system with less metal dodecaborate may, therefore, exhibit improved reversibility.

Figure 8.14 shows the room temperature XRD and Raman results of decomposition products of as-milled $0.62LiBH_4$-$0.38NaBH_4$ after heat treatment at 250 °C, 490 °C, 540 °C and 600 °C in Ar. They suggested that 1) the 1st decomposition route, from 287 °C to 520 °C, was the precipitation of LiH, $Li_2B_{12}H_{12}$ and B as well as the release of H_2; 2) the 2nd decomposition route involved the formation of Na, B as well as the release of H_2, at the temperatures above 520 °C. In Figure 8.14-b, although the Raman shifts of B-B breathing mode (753 cm^{-1}) for the $[B_{12}H_{12}]^{2-}$ cluster remained unchanged when the heat-treatment temperature increased from 490°C, to 540 °C and to 600 °C, the wavenumber of the B-H stretching mode for the $[B_{12}H_{12}]^{2-}$ cluster decreased from 2500 cm^{-1}, to 2482 cm^{-1} and to 2437 cm^{-1} over the temperature range. A reduction in Raman shift indicated an elongation of the B-H bond of the $[B_{12}H_{12}]^{2-}$ cluster (Smith & Dent 2005), but the reason was not clear. It might due to the thermal degradation of $[B_{12}H_{12}]^{2-}$ cluster as observed by Pitt et al. (2013) and Yan et al. (2018).

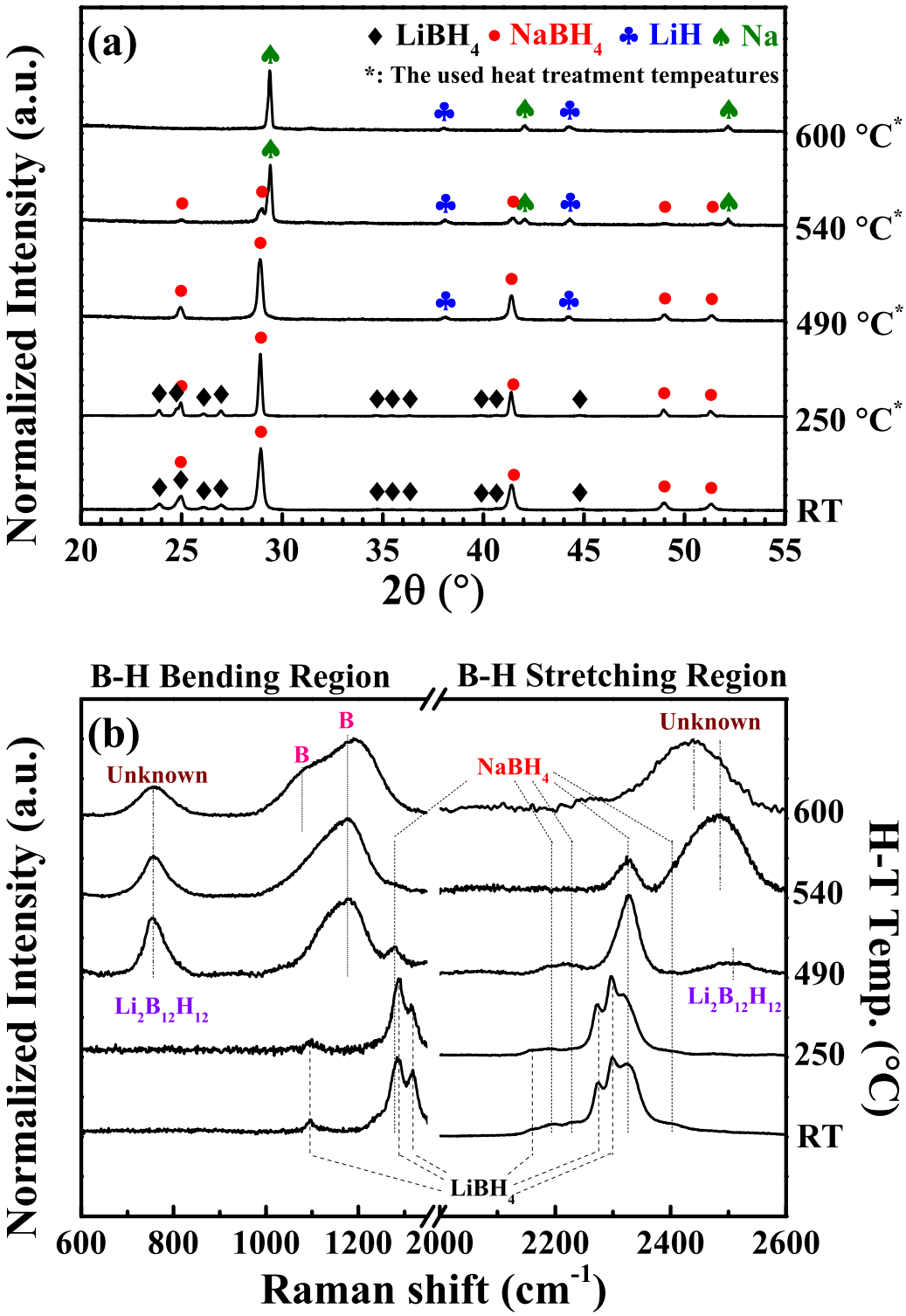

Figure 8.14 Room temperature (a) XRD patterns (Cu K_α radiation, λ = 1.5418 Å) and (b) Raman (measured with 488 nm laser and 2400 l/mm grating system) spectra of $0.62LiBH_4$-$0.38NaBH_4$ mixture, which had been heat-treated at 250 °C, 490 °C, 550 °C and 600 °C by 2 °C min^{-1} in Ar flowing at 160 mL min^{-1}. The intensities of the XRD and Raman peaks were normalized. A horizontal break was used to divide the Raman spectra (b) into B-H bending and B-H stretching regions of $[BH_4]^-$ (normalized separately). Dashed lines are guides for the eye.

The hydrogen desorption peaks observed for the as-milled $0.62LiBH_4$-$0.38NaBH_4$ mixture in Figure 8.13 (488 °C and 540 °C) were higher than the 470 °C for as-milled $LiBH_4$ and lower than the 580 °C for as-milled $NaBH_4$. The shifts in hydrogen desorption peak temperatures were due to the mixing of cations with different electronegativities (Nakamori & Orimo 2004; Nakamori et al. 2006; Nakamori et al. 2007; Harrison & Thonhauser 2016), where Na^+ had a lower electronegativity (0.93) than Li^+ (0.98). For instance, at the 1st step, the presence of Na^+ increased the decomposition peak temperature by 18 °C, through a local change (reduction) in B-H bond length around Na^+ (from a $LiBH_4$ like status to a $NaBH_4$ like status) that required a higher decomposition temperature. At the 2nd step, although most of Li^+ had been consumed by precipitation into LiH or $Li_2B_{12}H_{12}$, the remaining Li^+ destabilized the mixture by a local change (elongation) of B-H bond length (from a $NaBH_4$ like status to a $LiBH_4$ like status) and reduced the decomposition temperature by 40 °C at the 2nd peak.

The entire amount of hydrogen released from $0.62LiBH_4$-$0.38NaBH_4$ mixture (including heating and cooling) was 12.2 wt.%. Calculated from which, the decomposition mechanism of $0.62LiBH_4$-$0.38NaBH_4$ mixture (in Ar) was given:

$$\mathbf{0.62}LiBH_4 - \mathbf{0.38}NaBH_4 \rightarrow \mathbf{0.6}LiH + \mathbf{0.88}B + \mathbf{0.01}Li_2B_{12}H_{12} + \mathbf{0.38}Na + \mathbf{1.64}H_2 \qquad \textbf{Equation 8.7.}$$

Figure 8.15 schematically shows the decomposition (in a non-equilibrium condition) of the $0.62LiBH_4$-$0.38NaBH_4$ mixture in the range of 25-650 °C.

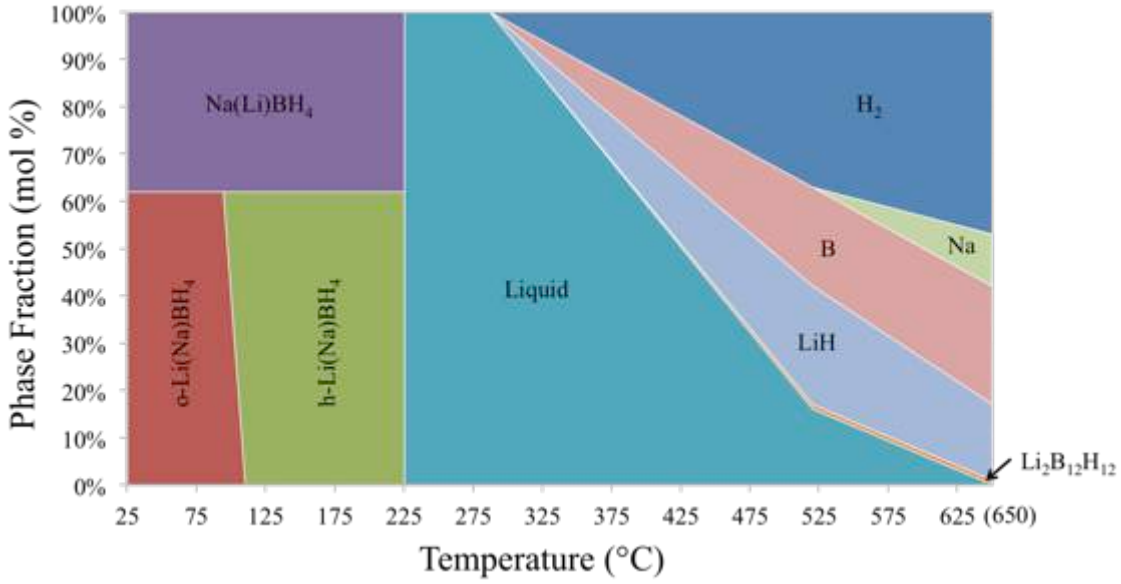

Figure 8.15 Phase fractions (non-equilibrium) present in the $0.62LiBH_4$-$0.38NaBH_4$ mixture from room temperature to 650 °C. Data points were obtained from DSC (T < 287 °C) and TPD-MS (T > 287 °C). The conditions used for DSC and TPD-MS were 5 °C min^{-1} in 2 bar static H_2 and 2 °C min^{-1} in flowing Ar at 160 mL min^{-1}, respectively.

8.2.4 Recombination

The reversibility of the as-milled $0.62LiBH_4$-$0.38NaBH_4$ mixture was carried out using a Sieverts type apparatus as described in Section 6.2.6. The reaction conditions used were: 500 °C, 1 bar H_2 and 10 h for desorption; and 400 °C, 130 bar H_2 and 12 h for absorption.

Figure 8.16 shows the reversible H_2 content of $0.62LiBH_4$-$0.38NaBH_4$ mixture during cycling.

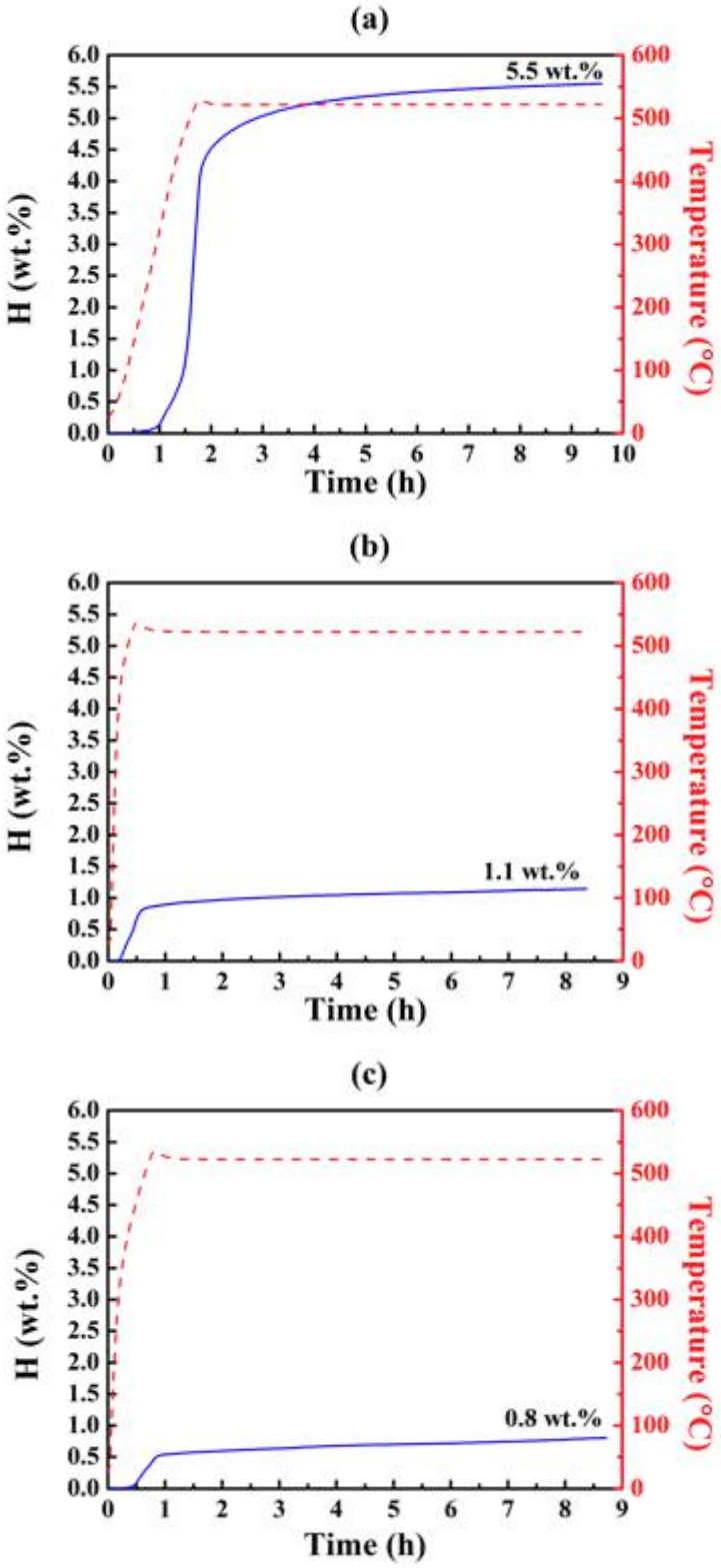

Figure 8.16 Sievert's measurements showing hydrogen release (in wt.%) while keeping the 0.62$LiBH_4$-0.38$NaBH_4$ under 1 bar H_2 at 500 °C ($\Delta T/\Delta t$ = 5 °C min^{-1}) for 10 h for desorption and under 130 bar H_2 at 400 °C for 12 h for rehydrogenation. (a) 1st cycle, (b) 2nd cycle (c) 3rd cycle. The different heating rate was because the furnace had not completely cooled down to room temperature.

The $0.62LiBH_4$-$0.38NaBH_4$ mixture released 5.5 wt.% of hydrogen during the 1st dehydrogenation. The amount of hydrogen desorbed under the same conditions after reabsorption reduced dramatically to 1.1 wt.% at the 2nd cycle and further to 0.8 wt.% at the 3rd cycle. This poor cycling stability agreed with Javadian, Sheppard, et al. (2015), where the reversible hydrogen contents from a three-cycle sorption (using PCT Pro 2000 Sieverts' apparatus; 500 °C, 1 bar H_2 and 10 h for desorption; 400 °C, 140-150 bar H_2 and 10 h for absorption) were found to be 7.2, 2.1 and 1.6 wt.%. But the reversible hydrogen contents obtained in this work were slightly lower; this is likely because a lower H_2 pressure for absorption was used.

Figure 8.17 shows the XRD and FTIR results for the $0.62LiBH_4$-$0.38NaBH_4$ mixture in its reabsorbed states after being cycled three times.

The rehydrogenated $0.62LiBH_4$-$0.38NaBH_4$ mixture contained LiH (XRD) and $NaBH_4$ (XRD, FTIR), indicating the $NaBH_4$ component was stable during cycling and the $LiBH_4$ component was not reversible under the applied conditions. The $LiBH_4$ was not fully decomposed after being kept at 500 °C in 1 bar H_2 for 10 h. Thus, the small amount reabsorbed hydrogen contents at the 2nd and 3rd cycle were likely due to the dehydrogenation of the remaining $LiBH_4$. In addition, no $LiBH_4$ was reformed using the current sorption conditions. To partially reform $LiBH_4$, a stronger condition might needed, such as 600°C, 350 bar H_2, 12 h (Orimo et al. 2005).

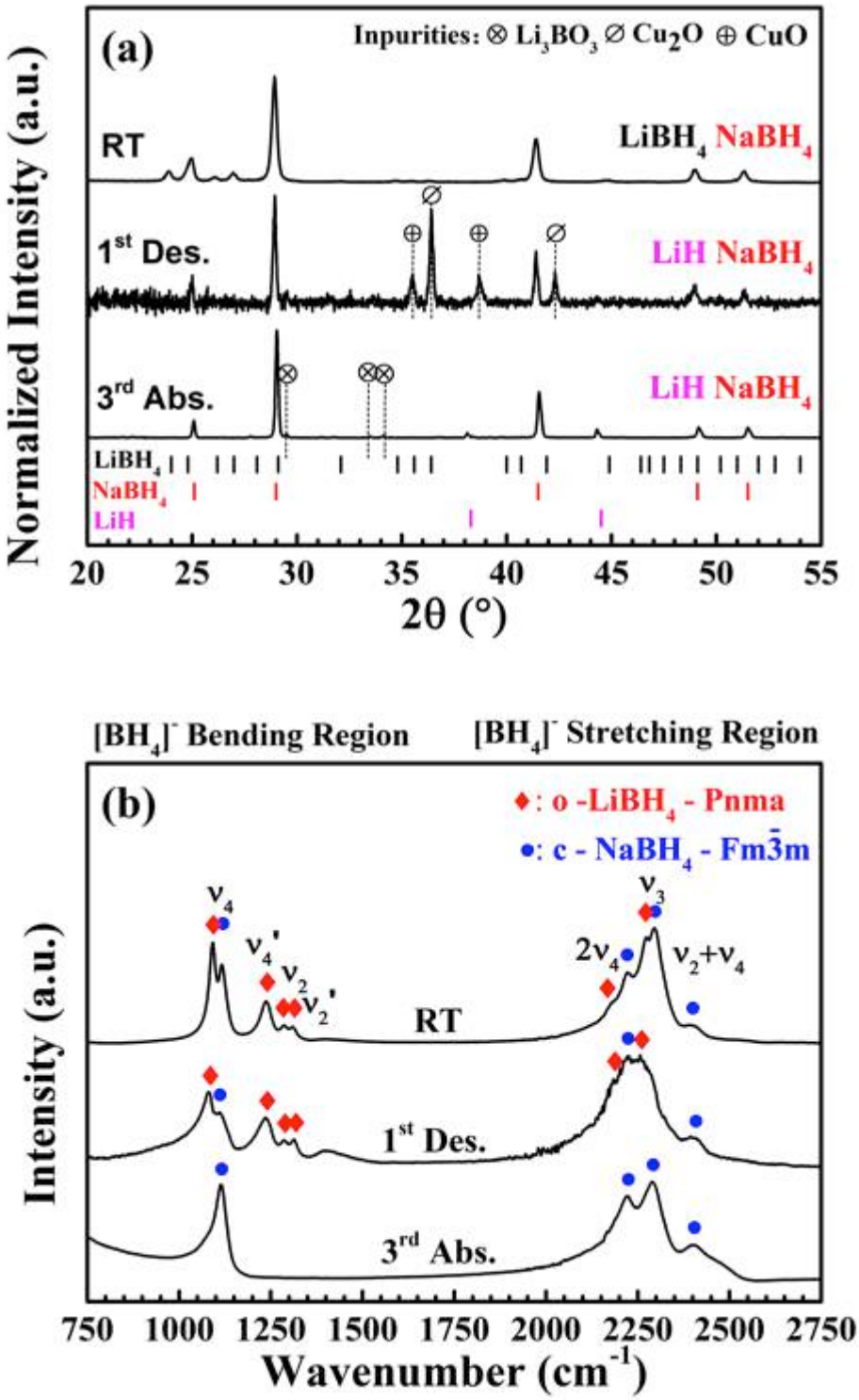

Figure 8.17 (a) XRD patterns Cu K_α radiation, λ = 1.5418 Å) and (b) FTIR spectra for the as-milled $0.62LiBH_4$-$0.38NaBH_4$ mixtures decomposed at 500 °C in 1 bar static H_2 for 10 h (denoted as 1st Des.) and recombined with 130 bar H_2, 400 °C for 12 h at the 3rd cycle (denoted as 3rd Abs.). The Cu based impurities (Cu_2O and CuO) observed in XRD pattern was introduced from the outer surface of sample holder during operation (not participated in dehydrogenation).

In fact, there are reports of reversibility of $LiBH_4$ in other eutectic borohydrides systems. For example, J. Y. Lee et al. (2009) reported the reformation of o-$LiBH_4$ using XRD for the rehydrogenated 0.4$LiBH_4$-0.6$Ca(BH_4)_2$ mixture under relatively moderate conditions (desorption: 400°C, static vacuum, 2 h; absorption: 400°C, 90 bar H_2, 20 h). More recently, a fully reversible $LiBH_4$ was achieved for the same mixture using different conditions (desorption: 500°C, 1 bar H_2, 10 h; absorption: 500°C, 134-144 bar H_2, 10 h) (Javadian et al. 2017). The precipitation of CaH_2 phases was considered as an important factor leading to reversible $LiBH_4$.

8.3 Decomposition with the Addition of 5 mol% SiO_2

Adding a small amount of SiO_2 enhanced the H_2 desorption from $LiBH_4$ in low temperature range (300 - 400 °C) by altering the reaction pathways (Section 7.2). Due to the presence of Na^+, the major dehydrogenation of 0.62$LiBH_4$-0.38$NaBH_4$ mixture occurred at a temperature slightly higher that of $LiBH_4$. To try to destabilize this dehydrogenation, 5 mol% of micron-sized SiO_2 (diameter = 0.5 μm) was added into 0.62$LiBH_4$-0.38$NaBH_4$. Its influence on the decomposition was studied.

8.3.1 Sample Characterisations

The 0.95(0.62$LiBH_4$-0.38$NaBH_4$)-0.05SiO_2 mixture was prepared by hand mixing, where 0.1019 g micron-sized SiO_2 (Alfa Aesar, 99.9%, 0.5 μm) was added to 0.8981 g as-milled 0.62$LiBH_4$-0.38$NaBH_4$. The as-prepared sample was then characterized using XRD and Raman for the structure, shown in Figure 8.18.

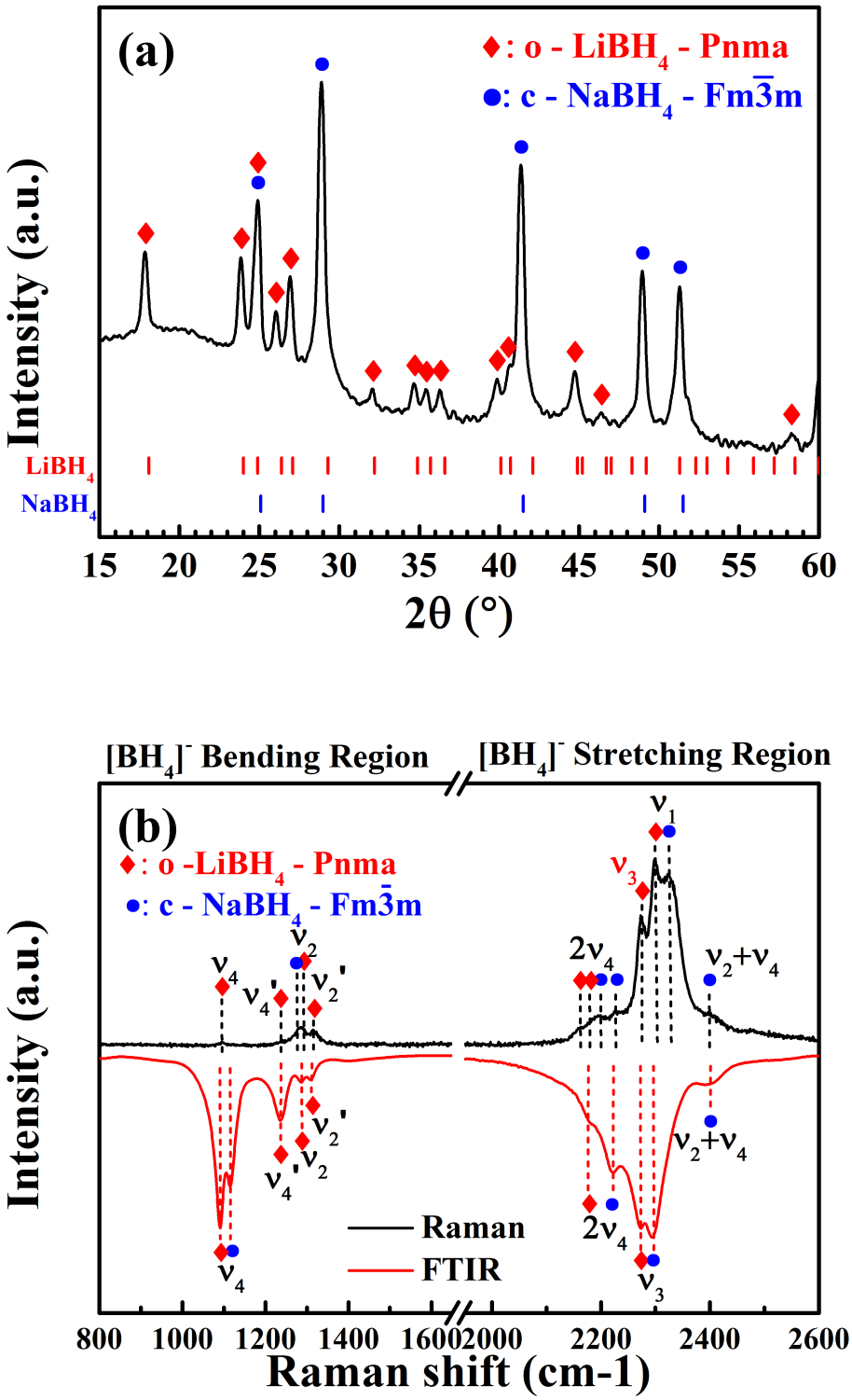

Figure 8.18 (a) XRD patterns (Cu K_α radiation, λ = 1.5418 Å) (intensity in log scale) and (b) Raman (measured with 488 nm laser and 2400 l/mm grating system) and FTIR spectra for the as-prepared 0.95(0.62$LiBH_4$-0.38$NaBH_4$)-0.05SiO_2 mixture, measured at room temperature.

The XRD peaks were caused by orthorhombic $LiBH_4$ and cubic $NaBH_4$. The SiO_2 used was not detectable using XRD as discussed in Section 7.2.1. Though Si-O-Si and Si-O-H bonds peaks were able to show in Raman for the as-received SiO_2, these peaks were not observed for the as-prepared $0.95(0.62LiBH_4\text{-}0.38NaBH_4)\text{-}0.05SiO_2$ mixture, due to their weak intensities.

8.3.2 Thermal Analysis

Figure 8.19 shows the DSC trace of as-prepared $0.95(0.62LiBH_4\text{-}0.38NaBH_4)\text{-}0.05SiO_2$ mixture, compared with the SiO_2-free mixture. These measurements were preformed from 50 to 250 °C at 5 °C min^{-1} in Ar flowing at 70 mL min^{-1}.

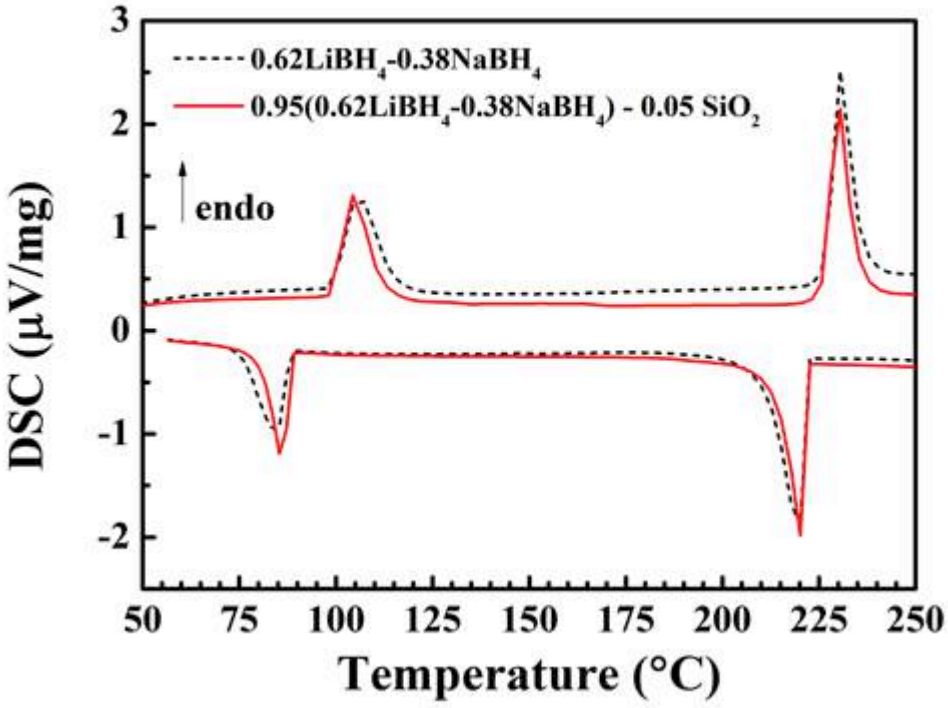

Figure 8.19 DSC results of as-prepared $0.95(0.62LiBH_4\text{-}0.38NaBH_4)\text{-}0.05SiO_2$ mixture (red solid line), compared with the as-milled $0.62LiBH_4\text{-}0.38NaBH_4$ (black dash line). Samples were heated from 50 to 250 °C at 5 °C min^{-1} in Ar flowing at 70 mL min^{-1}.

The phase transition of $LiBH_4$ component in the $0.95(0.62LiBH_4\text{-}0.38NaBH_4)\text{-}0.05SiO_2$ mixture occurred at 99 ± 1 °C during heating and at 89 ± 1 °C during cooling. These temperatures were the same as that of SiO_2-free sample, though the curve shapes were slightly different.

The fusion and solidification onset temperatures of the $0.95(0.62LiBH_4\text{-}0.38NaBH_4)\text{-}0.05SiO_2$ mixture were 226 ± 1 °C and 222 ± 1 °C, respectively, suggesting a small over-cooling effect. These temperatures were the same as that of SiO_2-free sample.

Though the DSC used in IFE, Norway was not completed calibrated for determining the accurate enthalpy, the area under the DSC curve was proportional to this enthalpy that provided a guide for comparison, as shown in Table 8.6.

Table 8.6 DSC curve areas for as-prepared $0.95(0.62LiBH_4\text{-}0.38NaBH_4)\text{-}0.05SiO_2$ compared with as-milled $0.62LiBH_4\text{-}0.38NaBH_4$ (noted as LiNa).

	Sample	Energy			
		Heating		Cooling	
		Phase change	Fusion	Phase change	Solidification
		μV mg^{-1} $LiBH_4$	μV mg^{-1} LiNa	μV mg^{-1} $LiBH_4$	μV mg^{-1} LiNa
1	$0.62LiBH_4\text{-}0.38NaBH_4$	18.9 ± 1.0	12.7 ± 0.6	13.2 ± 0.7	12.8 ± 0.6
2	$0.95(0.62LiBH_4\text{-}0.38NaBH_4)\text{-}0.05SiO_2$	19.3 ± 1.0	13.0 ± 0.7	11.8 ± 0.6	11.1 ± 0.6

It has been found that the energy required for phase changes of the $0.95(0.62LiBH_4\text{-}0.38NaBH_4)\text{-}0.05SiO_2$ mixture was close to that of SiO_2-free mixture, suggesting the additive SiO_2 did not affect the phase change and fusion of the $0.95(0.62LiBH_4\text{-}0.38NaBH_4)\text{-}0.05SiO_2$ mixture.

8.3.3 Thermal Decomposition

The TPD-MS trace for the dehydrogenation of the as-prepared 0.95(0.62$LiBH_4$-0.38$NaBH_4$)-0.05SiO_2 mixture was compared with that of SiO_2-free mixture in Figure 8.20. These samples were heated to 650 °C by 2°C min^{-1} in Ar flowing at 160 mL min^{-1}. No B_2H_6 was detected.

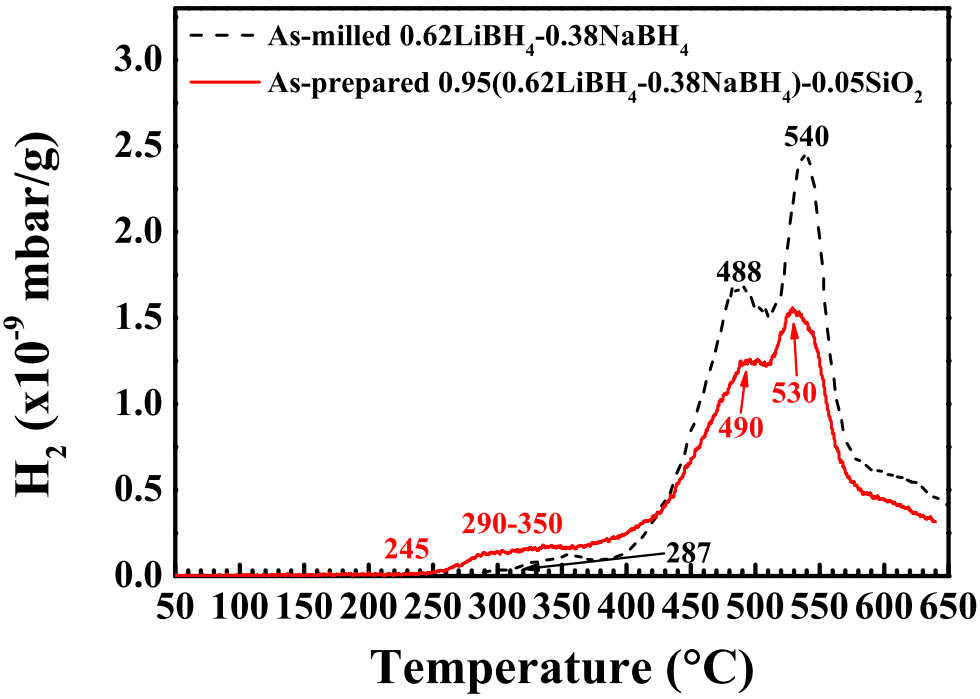

Figure 8.20 TPD-MS hydrogen desorption traces of as-prepared 0.95(0.62$LiBH_4$-0.38$NaBH_4$)-0.05SiO_2 mixture, compared with as-milled 0.62$LiBH_4$-0.38$NaBH_4$. Samples were heated at 2 °C min^{-1} in flowing Ar at 160 mL min^{-1}. No B_2H_6 was detected.

Due to the addition of SiO_2, the H_2 release from the as-prepared 0.95(0.62$LiBH_4$-0.38$NaBH_4$)-0.05SiO_2 mixture started from 245 °C, which is 42 °C lower than the 287 °C for the SiO_2-free sample. This dehydrogenation progress could be divided into 3 parts: a broad peak around 290-350 °C, and 2 major peaks at 490 °C and 530 °C. The broad peak was located in the similar temperature range with $LiBH_4$-SiO_2 system (Section 7.2.3). The 1st major peak at 490 °C was close to the 488 °C for the SiO_2-free

sample, whilst the 2nd main peak at 530 °C was 10 °C lower than the 540 °C for the SiO_2-free sample.

The $0.95(0.62LiBH_4\text{-}0.38NaBH_4)\text{-}0.05SiO_2$ mixture released ~1.0 wt.% hydrogen when heated up to 400 °C that was lower than the 1.5 wt.% released from $0.95LiBH_4\text{-}0.05SiO_2$ sample (Section 7.2.3). The difference was likely caused by 2 possible reasons (or a combination of them):

- The SiO_2 composition was slightly different. For a mixture weighted 1 g, 0.1267 g SiO_2 was available in the $0.95LiBH_4\text{-}0.05SiO_2$ mixture. However, there was 0.1019 g SiO_2 mixed in the $0.95(0.62LiBH_4\text{-}0.38NaBH_4)\text{-}0.05SiO_2$ mixture, which was slightly less.
- The presence of Na^+ in the molten phase may hinder the diffusion routes of Li^+ and degrade the kinetics.

A total of 7.3 wt.% hydrogen was released from the $0.95(0.62LiBH_4\text{-}0.38NaBH_4)\text{-}0.05SiO_2$ mixture upon heating to 650 °C. This amount was 33% less than the 10.8 wt.% for the SiO_2-free sample. Even when the amount of SiO_2 (~10.2 wt.%) was excluded, the calculated 8.1 wt.% was still lower than that for the SiO_2-free sample. This reduction in the H_2 liberation values was likely due to a change in reaction pathway caused by the SiO_2 additives. To investigate the changed decomposition pathway, the as-prepared $0.95(0.62LiBH_4\text{-}0.38NaBH_4)\text{-}0.05SiO_2$ mixture was heat-treated at 2 °C min^{-1} to 290, 490, 530 and 650 °C in flowing Ar. These heat-treated samples, were measured at room temperature by XRD and Raman, as shown in Figure 8.21.

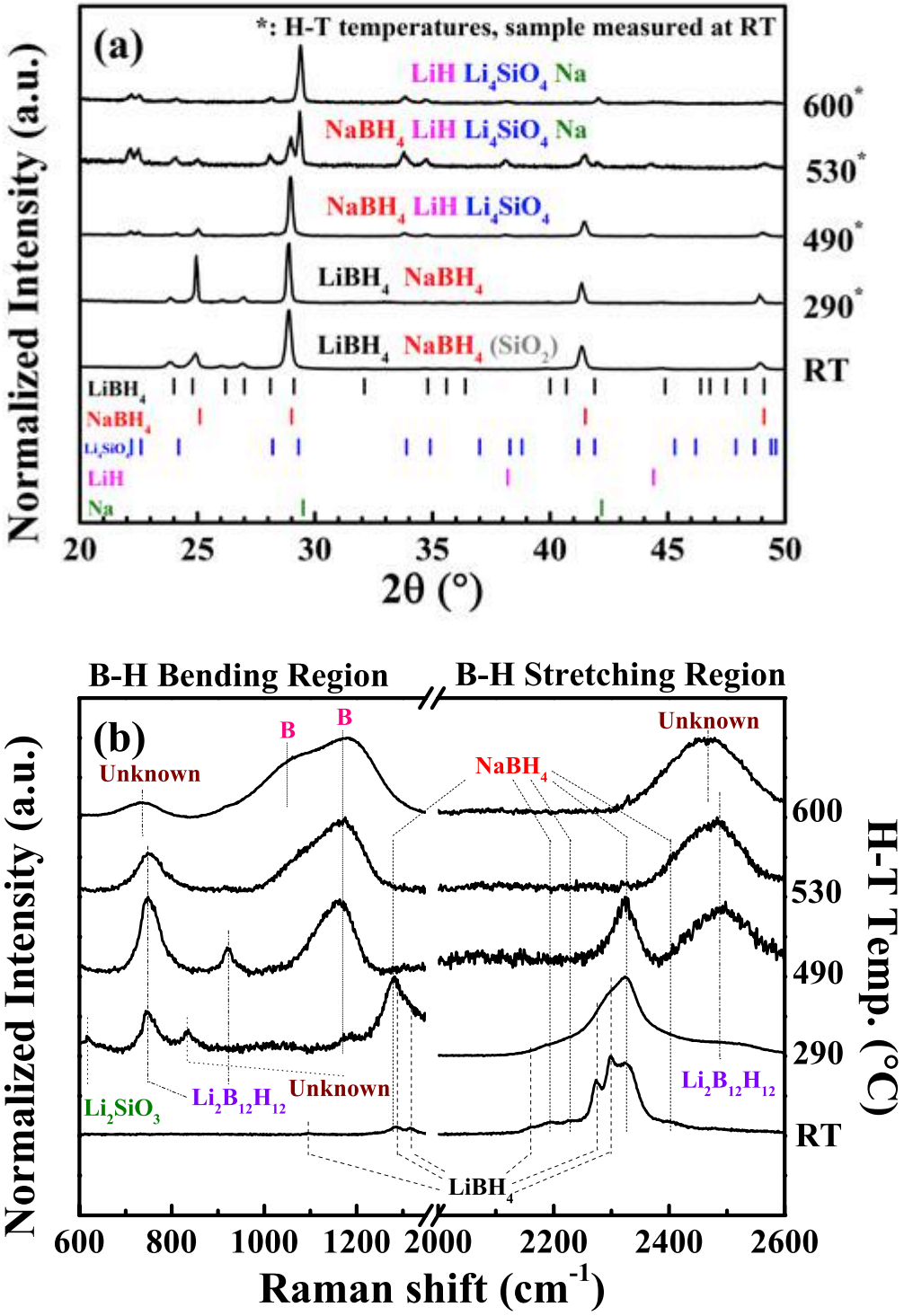

Figure 8.21 Room temperature (a) XRD patterns (Cu K_α radiation, λ = 1.5418 Å) and (b) Raman spectra (measured with 488 nm laser and 2400 l/mm grating system) of as-prepared 0.95(0.62$LiBH_4$-0.38$NaBH_4$)-0.05SiO_2 mixture, which had been heat-treated at 290 °C, 490 °C, 530 °C and 600 °C by 2 °C min^{-1} in Ar flowing at 160 mL min^{-1}. The intensities of the XRD and Raman peaks were normalized. A horizontal break was used to divide the Raman spectra into B-H bending and B-H stretching regions of $[BH_4]^-$ (normalized separately). Dashed lines are guides for the eye.

According to the results in Section 7.2.3, the formations of lithium silicates (Li_2SiO_3, Li_4SiO_4) were expected as the reaction products of $LiBH_4$ and SiO_2. However, due to its small quantity and lack of diffraction, the Li_2SiO_3 was not observed in the heat-treated sample at 290 °C. But when the as-prepared sample was kept at 290 °C in flowing Ar for 10 h, weak peaks of Li_2SiO_3 were displayed on the XRD pattern as shown in Figure 8.22. The corresponding Raman spectrum at this temperature showed $Li_2B_{12}H_{12}$, suggesting a small amount of $LiBH_4$ was decomposed in parallel with the reaction between $LiBH_4$ and SiO_2. In addition, the peak observed at 615 cm^{-1} was a mixed vibration of Si-O-Si bending and Si-Si stretching (Richet et al. 1996), confirming the formation of Li_2SiO_3. An unknown peak was observed at 835 cm^{-1} and lithium silicates (Li_2SiO_3, Li_4SiO_4) have been ruled out (Takahashi et al. 1989; Richet et al. 1996).

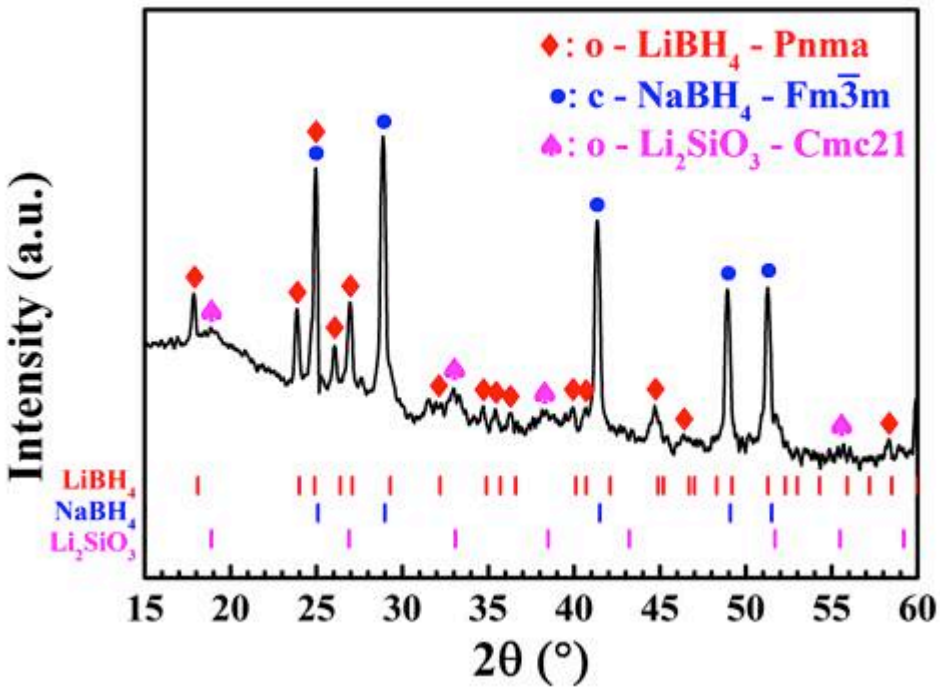

Figure 8.22 Room temperature XRD pattern (Cu K_α radiation, λ = 1.5418 Å) (intensity in log scale) of as-prepared $0.95(0.62LiBH_4\text{-}0.38NaBH_4)\text{-}0.05SiO_2$ mixture heat-treated at 290 °C in flowing Ar for 10 h.

In addition, although Bragg peaks for Li_4SiO_4 were observed for the sample heat-treated at 490 °C, the formation of Li_4SiO_4 (i.e. oxidation product of Li_2SiO_3) occurred at a lower temperature around 300 °C (Section7.2.3). Thus, the H_2 release from 290 to 350 °C was mainly due to the reaction between $LiBH_4$ and SiO_2.

At 490 °C, the $LiBH_4$ peaks disappeared, while LiH peaks appeared in XRD pattern and a strong B peak showed in Raman spectrum. No direct evidence (such as element Na) was detected, showing that the decomposition of $NaBH_4$ component had not yet occurred. These observations are similar to the SiO_2-free sample (Section 8.2.3). Thus, the major H_2 release at 1st step was associated to the precipitation of LiH, $Li_2B_{12}H_{12}$ and B.

At 530 °C, peaks of Na were presented in XRD pattern and the peaks of $NaBH_4$ became relatively less intense, indicating the occurrence of the decomposition of $NaBH_4$. In the corresponding Raman spectra, the B-H stretching peak for $NaBH_4$ (at 2322 cm^{-1}) became very weak which agreed with the XRD results. The peaks corresponding to $NaBH_4$ completely eliminated at 600 °C, leaving LiH, Li_4SiO_4 and Na in the XRD pattern. Besides, red shifts of B-B breathing and B-H stretching modes of the $[B_{12}H_{12}]^{2-}$ cluster occurred at 600 °C, which might because of the formation of $Na_2B_{12}H_{12}$ (or even $LiNaB_{12}H_{12}$). Although the wavenumbers of B-B breathing and B-H stretching modes for $Na_2B_{12}H_{12}$ and $LiNaB_{12}H_{12}$ are often slightly lower than that for $Li_2B_{12}H_{12}$ (Mao & Gregory 2015), it is hard to distinguish them if they overlap (Figure 8.23). Techniques, such as solid-state Nuclear Magnetic Resonance (NMR) spectroscopy, may be helpful to distinguish them. Therefore, the formation of $Na_2B_{12}H_{12}$ cannot be fully ruled out.

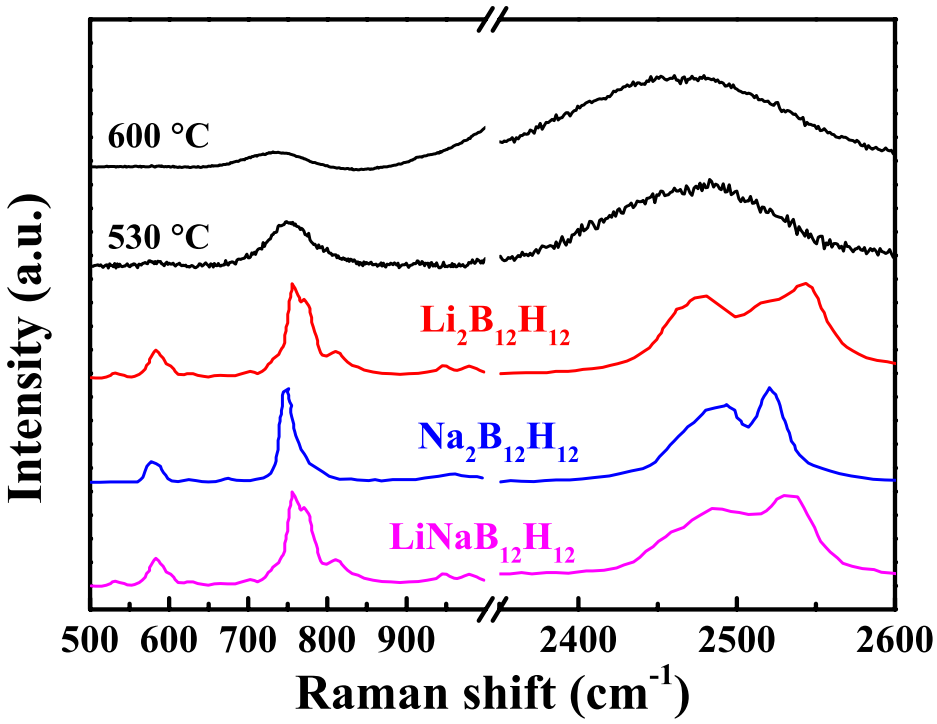

Figure 8.23 Comparisons of the B-B breathing and B-H stretching modes of $[B_{12}H_{12}]^{2-}$ cluster among experimental Raman spectra (measured with 488 nm laser and 2400 l/mm grating system) of heat-treated $0.95(0.62LiBH_4\text{-}0.38NaBH_4)\text{-}0.05SiO_2$ mixture at 530 °C and 600 °C, $Li_2B_{12}H_{12}$, $Na_2B_{12}H_{12}$ and $LiNaB_{12}H_{12}$. The data for these closo-boranes are obtained by He et al. (2015).

The entire amount of H_2 released (in Ar) from the $0.95(0.62LiBH_4\text{-}0.38NaBH_4)\text{-}0.05SiO_2$ mixture (including heating and cooling) was 8.6 wt.%. Since the reaction between SiO_2 and $LiBH_4$ was complex and hard to determine (Appendix C), with limited information, the reactions occurring below 350 °C were not possible to fully work out. The reaction pathways for the main peaks above 350°C could possibly be calculated if the following assumptions were made:

1) All SiO_2 reacted with $LiBH_4$ before 350 °C through Equation 7.7 (forming Li_2SiO_3, Si, B and H_2) and 7.8 (forming Li_4SiO_4, Si, B and H_2). Calculated from which, 5 mol% SiO_2 consumed 10 mol% $LiBH_4$ at this step that changed the composition to $0.49LiBH_4\text{-}0.36NaBH_4$;

2) All activities below 350 °C are excluded. Thus, the 0.7 wt.% hydrogen for sample heated up to 350 °C was removed (from the total H_2 release – 8.6 wt.%) and the dehydrogenation of $LiBH_4$ decomposed below 350 °C was ignored;
3) The area ratio from a Gaussian fitting of the TPD-MS curve was related to the amount of H_2 released at the main peaks via a linear function (63% and 37% for $LiBH_4$ and $NaBH_4$ dominated peaks, respectively)
4) $LiBH_4$ decomposed through 2 reactions, via Equation 7.2 (forming LiH, B, H_2) and 7.3 (forming LiH, $Li_2B_{12}H_{12}$, H_2);
5) $NaBH_4$ decomposed via 2 reactions, through Equation 8.1 (forming Na, B, H_2) and 8.3 (forming Na, $Na_2B_{12}H_{12}$, H_2), though no direct evidence shows $Na_2B_{12}H_{12}$ was formed.

Based on these assumptions, the decomposition mechanism (in Ar) of the $0.62LiBH_4$-$0.38NaBH_4$ component in the $0.95(0.62LiBH_4$-$0.38NaBH_4)$-$0.05SiO_2$ mixture was calculated to be:

$$\mathbf{0.49}LiBH_4 - \mathbf{0.36}NaBH_4 \xrightarrow{>350\,^{\circ}C} \mathbf{0.412}LiH + \mathbf{0.034}B + \mathbf{0.039}Li_2B_{12}H_{12} + \mathbf{0.302}Na + \mathbf{0.029}Na_2B_{12}H_{12} + \mathbf{1.086}H_2$$

Equation 8. 8

The ratio 0.49 $LiBH_4$: 0.36 $NaBH_4$ could be normalized to 0.58 $LiBH_4$: 0.42 $NaBH_4$. The normalized results are summarised in Table 8.7. Compared with the SiO_2-free sample (Equation 8.7), more $Li_2B_{12}H_{12}$ and $Na_2B_{12}H_{12}$ were formed during the decomposition. This could be relevant to the enhanced precipitation of $Li_2B_{12}H_{12}$ seen in the $LiBH_4$-SiO_2 system (Section 7.2). Thus, the additive SiO_2 enhanced the fraction of $LiBH_4$ and $NaBH_4$ that decomposed into $Li_2B_{12}H_{12}$ and $Na_2B_{12}H_{12}$.

Table 8.7 The decomposition mechanism (Ar) of $0.95(0.62LiBH_4\text{-}0.38NaBH_4)\text{-}0.05SiO_2$ compared with $0.62LiBH_4\text{-}0.38NaBH_4$.

	Sample	Equation	Reactant		Product					
			$LiBH_4$	$NaBH_4$	LiH	B	$Li_2B_{12}H_{12}$	Na	$Na_2B_{12}H_{12}$	H_2
1	$LiBH_4$-$NaBH_4$	8.7	0.62	0.38	0.60	0.88	0.01	0.38	n.a.	1.64
2	$LiBH_4$-$NaBH_4$-SiO_2	8.8	0.58	0.42	0.48	0.04	0.05	0.36	0.03	1.28

8.3.4 Effect of Additive: SiO_2

The early phase transition (o→h) of the $LiBH_4$ content and low-temperature fusion of $0.95(0.62LiBH_4\text{-}0.38NaBH_4)\text{-}0.05SiO_2$, occurring at 99 °C and 226 °C respectively, were not affected by the addition of 5 mol% micron-size SiO_2.

In flowing Ar, the added SiO_2 in the $0.62LiBH_4\text{-}0.38NaBH_4$ mixture leads to an earlier dehydrogenation starting at 245 °C (about 40 °C lower than the 287 °C for SiO_2-free sample), through chemical reactions between the $LiBH_4$ and SiO_2 that were more thermodynamically favourable. As a consequence, Li_2SiO_3 and Li_4SiO_4 were formed in the temperature range 245-350 °C. A small quaintly of $LiBH_4$ was decomposed simultaneously.

A total of 7.3 wt.% hydrogen was released from $0.95(0.62LiBH_4\text{-}0.38NaBH_4)\text{-}0.05SiO_2$ upon heating to 650 °C. The major dehydrogenation occurred above 350 °C, exhibiting two peaks at 490 °C and 530 °C. The 1st major peak temperature was similar to the 488 °C for SiO_2-free mixture, whilst the 2nd major peak temperature was 10 °C lower. Similarly to the SiO_2-free sample, the H_2 release at the 1st peak was associated with the precipitation of LiH, $Li_2B_{12}H_{12}$ and B, whilst the 2nd peak was mainly due to the formation of Na, $Na_2B_{12}H_{12}$ and B (though no direct evidence showed the formation of

$Na_2B_{12}H_{12}$, the calculation from the weight of H_2 release suggested it was possibly formed, as shown in Equation 8.8).

Figure 8.24 schematically summaries the decomposition process (in Ar) of $0.95(0.62LiBH_4\text{-}0.38NaBH_4)\text{-}0.05SiO_2$.

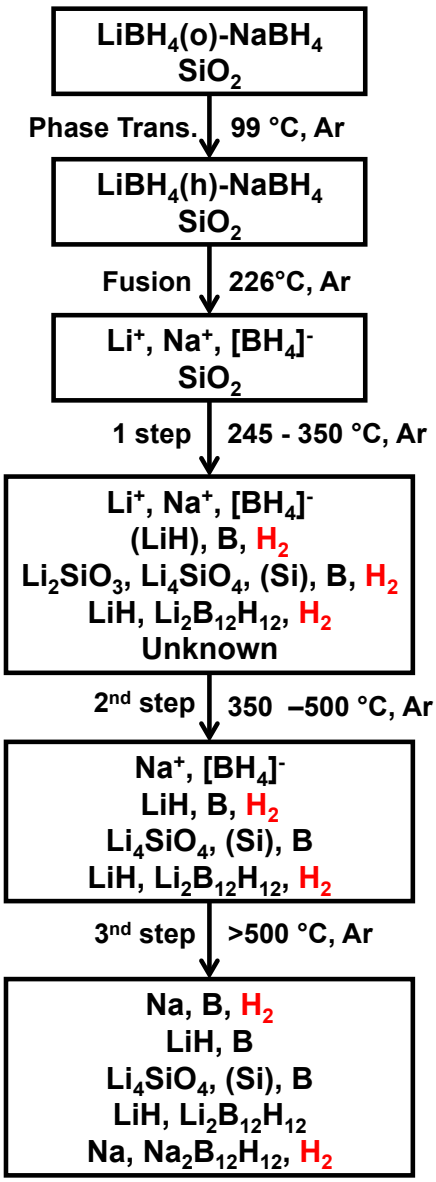

Figure 8.24 A flow chart of decomposition pathways of the as-prepared $0.95(0.62LiBH_4\text{-}0.38NaBH_4)\text{-}0.05SiO_2$ in Ar.

8.4 Decomposition and Recombination with the Addition of 14 wt.% nano-sized Ni

Nano-Ni showed an interesting destabilization effect on the decomposition of $LiBH_4$ that reduced the dehydrogenation peak temperature by 25 °C and formed Ni_4B_3 (Section 7.3). In this section, nano-sized Ni was used to destabilize the $0.62LiBH_4$-$0.38NaBH_4$ and its influence on the decomposition reactions was investigated.

8.4.1 Sample Characterisations

0.2 g nano-sized Ni (Sigma-Aldrich, 99.9%), 0.3875 g $LiBH_4$ (Sigma-Aldrich, 95.0 %) and 0.4125 g $NaBH_4$ (Sigma-Aldrich, 99.99 %) were mixed using ball milling under the conditions described in Section 6.1.1. Figure 8.25 shows the XRD and Raman results of the as-milled sample at room temperature. Due to high fluorescence effect caused by the Ni additive, the quality of Raman spectra became worse; however, FTIR results were not affected.

The XRD pattern of the as-milled sample shows Bragg peaks for $LiBH_4$, $NaBH_4$, Ni and NiO phases, suggesting no reaction between the parent borohydrides and additive has occurred during the milling process. The Pseudo-Rietveld refinement (Figure 8.26) suggests the following composition: 40.1(7) wt.% of $LiBH_4$, 42.1(5) wt.% of $NaBH_4$, 16.5(3) wt.% of Ni and 1.3(3) wt.% of NiO, respectively. This small amount of NiO was neglected for simplicity in phase composition reported below. The refined composition of the as-milled sample was $0.91(0.62LiBH_4$-$0.38NaBH_4)$-0.09Ni. Due to the addition of nano-sized Ni, the nominal phase composition of the $0.91(0.62LiBH_4$-$0.38NaBH_4)$-0.09Ni mixture was different from that of $0.62LiBH_4$-$0.38NaBH_4$. However, the molar ratios of $LiBH_4$ to $NaBH_4$ for these two mixtures were identical.

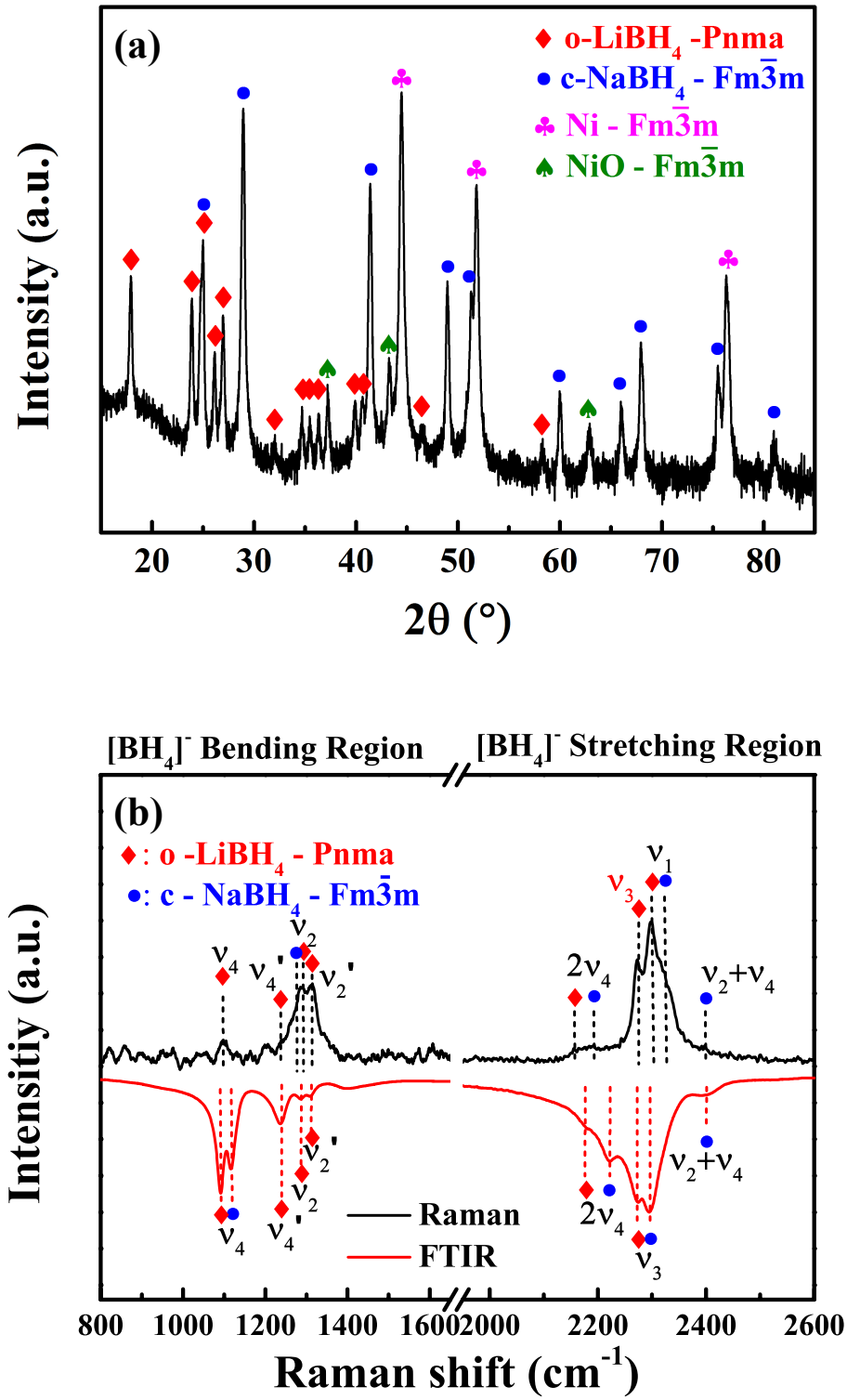

Figure 8.25 (a) XRD pattern (Cu K_α radiation, λ = 1.5418 Å) (intensity in log scale) and (b) Raman (measured with 488 nm laser and 2400 l/mm grating system) and FTIR spectra for the as-milled 0.91(0.62$LiBH_4$-0.38$NaBH_4$)-0.09Ni mixture, measured at room temperature. The Raman spectra were normalized separately at different regions.. Dashed lines are guides for the eye. As a metal, Ni cannot be detected by Raman or FTIR.

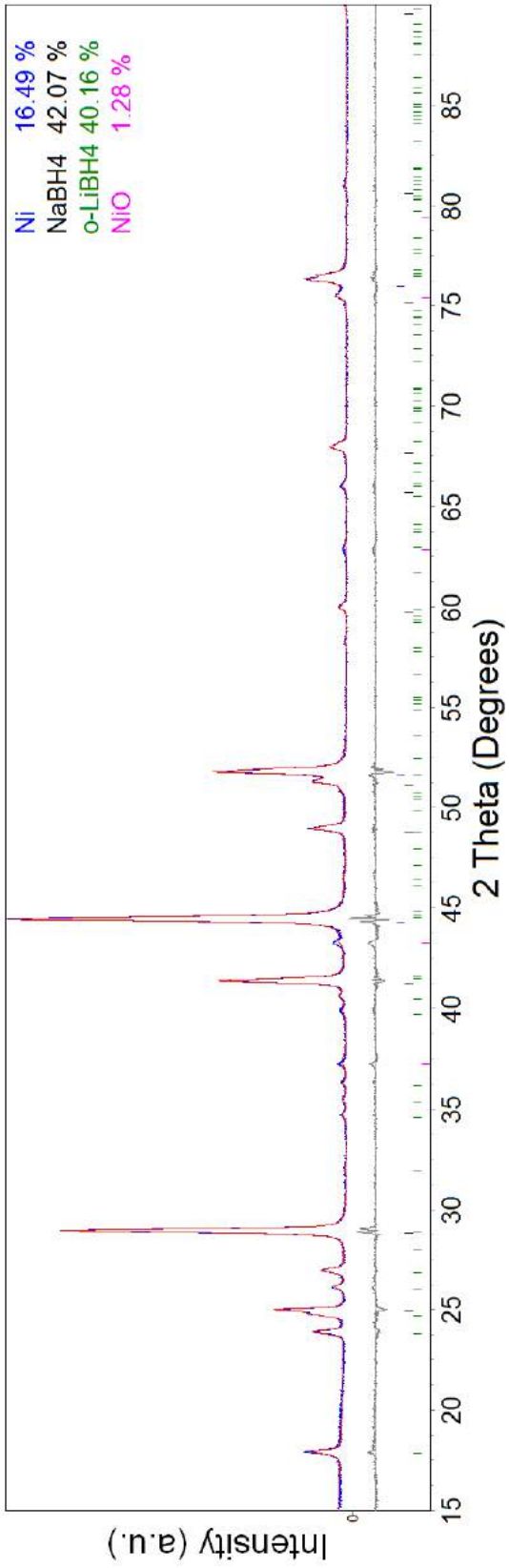

Figure 8.26 Pseudo-Rietveld refinement result of as-milled 0.91(0.62LiBH$_4$-0.38NaBH$_4$)-0.09Ni, including the observed XRD (Cu K$_\alpha$ radiation, λ = 1.5418 Å) profile (blue), the calculated profile (red, used to fit the observed profile) and the difference profile (grey) in each figure. The goodness-of-fit value was 1.459.

The refined lattice parameters of the 0.91(0.62$LiBH_4$-0.38$NaBH_4$)-0.09Ni mixture are summarised in Table 8.8. The addition of nano-sized Ni enlarged the refined unit cell volumes for the $LiBH_4$ and $NaBH_4$ constituents in the 0.91(0.62$LiBH_4$-0.38$NaBH_4$)-0.09Ni mixture. These values were both larger than that for the $LiBH_4$ and $NaBH_4$ constituents in the 0.62$LiBH_4$-0.38$NaBH_4$ mixture and for as-milled $LiBH_4$ and $NaBH_4$.

Table 8.8 Refined crystal structure parameters of $LiBH_4$, $NaBH_4$ components in as-milled 0.91(0.62$LiBH_4$-0.38$NaBH_4$)-0.09Ni in contrast to that of as-milled pure compound and in as-milled 0.62$LiBH_4$-0.38$NaBH_4$ mixture.

		As-milled Pure		As-milled Mixture	
		$LiBH_4$	**$NaBH_4$**	**$LiBH_4$-$NaBH_4$**	**$LiBH_4$-$NaBH_4$-Ni**
o-$LiBH_4$	a (Å)	7.199 ± 0.003	-	7.179 ± 0.002	7.211 ± 0.001
	b (Å)	4.438 ± 0.002	-	4.438 ± 0.001	4.456 ± 0.001
	c (Å)	6.798 ± 0.002	-	6.806 ± 0.002	6.837 ± 0.002
	Volume ($Å^3$)	*216.84 ± 0.01*	-	*217.03 ± 0.08*	*219.71 ± 0.08*
c-$NaBH_4$	a (Å)	-	6.169 ± 0.002	6.163 ± 0.002	6.188 ± 0.001
	Volume ($Å^3$)	-	*234.8 ± 0.013*	*234.06 ± 0.022*	*236.91 ± 0.11*

Table 8.9 and Table 8.10 summarised the Raman and FTIR frequencies for the 0.91(0.62$LiBH_4$-0.38$NaBH_4$)-0.09Ni mixture compared with Ni-free sample, where a good agreement was found. The measured wavenumbers of the total symmetric stretching mode (ν_1) for $NaBH_4$ in the as-milled 0.91(0.62$LiBH_4$-0.38$NaBH_4$)-0.09Ni and 0.62$LiBH_4$-0.38$NaBH_4$ mixtures were found to be 2323 cm^{-1} and 2324 cm^{-1}, respectively. These wavenumbers were 7-8 cm^{-1} lower than the 2331 cm^{-1} measured for as-milled pure $NaBH_4$ (Table 8.2), suggesting again the volume expansion via an increase in B-H bond length according to Badger's rule (Badger 1934; Renaudin et al. 2004). This expansion was proposed due to the substitution of Li^+ into $NaBH_4$, suggesting the formation of a Na(Li)BH_4 solid solution in the as-milled 0.91(0.62$LiBH_4$-0.38$NaBH_4$)-0.09Ni mixture. However, no shift in wavenumbers was

found for the $LiBH_4$ peaks, possibly due to the limited solubility of Na^+ in orthorhombic $LiBH_4$ (Dematteis et al. 2016).

Table 8.9 Experiment frequencies (cm^{-1}) of as-milled 0.91(0.62$LiBH_4$-0.38$NaBH_4$)-0.09Ni observed in Raman compared as-milled 0.62$LiBH_4$-0.38$NaBH_4$.

Mode		$LiBH_4$-$NaBH_4$ As-milled	$LiBH_4$-$NaBH_4$-Ni As-milled	Assignment
ν_4	A_g	1097	1097	$LiBH_4$
ν_4'	A_g	1242	1239	$LiBH_4$
ν_2	A_1	1282	1285	$NaBH_4$
ν_2	B_{1g}	1290	1291	$LiBH_4$
ν_2'	A_g	1317	1314	$LiBH_4$
$2\nu_4$		2159	2156	$LiBH_4$
$2\nu_4'$		2167	-	$LiBH_4$
$2\nu_4$		2198	2194	$NaBH_4$
$2\nu_4$		2229	-	$NaBH_4$
ν_3	A_g	2275	2273	$LiBH_4$
ν_1	A_g	2300	2298	$LiBH_4$
ν_1	A_1	2323	2324	$NaBH_4$
$\nu_2+\nu_4$	E	2404	2399	$NaBH_4$

Table 8.10 Experiment frequencies (cm^{-1}) of as-milled 0.91(0.62$LiBH_4$-0.38$NaBH_4$)-0.09Ni observed in FTIR compared as-milled 0.62$LiBH_4$-0.38$NaBH_4$.

Mode		$LiBH_4$-$NaBH_4$ As-milled	$LiBH_4$-$NaBH_4$-Ni As-milled	Assignment
ν_4	A_g	1092	1092	$LiBH_4$
ν_4	B_2	1117	1116	$NaBH_4$
ν_4'	A_g	1237	1236	$LiBH_4$
ν_2	B_{1g}	1286	1286	$LiBH_4$
ν_2'	A_g	1310	1309	$LiBH_4$
$2\nu_4'$		2180	2179	$LiBH_4$
$2\nu_4$		2221	2222	$NaBH_4$
ν_3	A_g	2274	2275	$LiBH_4$
ν_3	B_2	2297	2295	$NaBH_4$
$\nu_2+\nu_4$	E	2400	2400	$NaBH_4$

8.4.2 Thermal Analysis

Figure 8.27 shows the DSC trace of the 0.91(0.62$LiBH_4$-0.38$NaBH_4$)-0.09Ni mixture compared with the Ni-free sample. The DSC measurements were performed between 50 and 250 °C heated at 5 °C min^{-1} in Ar flowing at 70 mL min^{-1}.

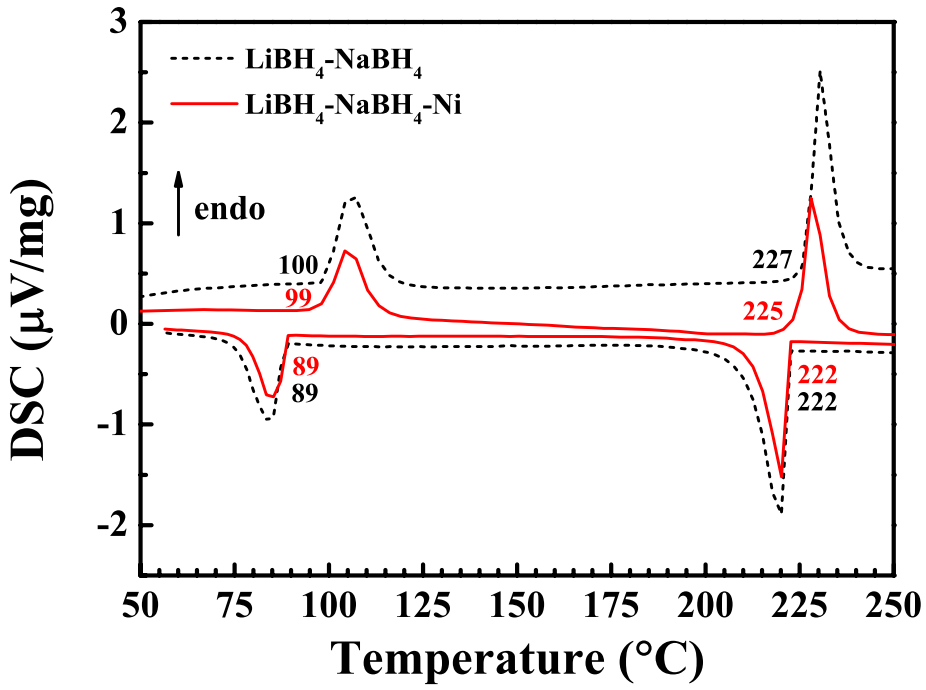

Figure 8.27 DSC results of as-milled 0.91(0.62$LiBH_4$-0.38$NaBH_4$)-0.09Ni (red solid line), compared with the as-milled 0.62$LiBH_4$-0.38$NaBH_4$ (black dash line). Samples were heated from 50 to 250 °C at 5 °C min^{-1} in Ar flowing at 70 mL min^{-1}.

The orthorhombic to hexagonal phase transition of the $LiBH_4$ content in the 0.91(0.62$LiBH_4$-0.38$NaBH_4$)-0.09Ni mixture occurred at an onset temperature of 99 ± 1 °C during heating. This was in agreement with the Ni-free sample within standard deviation, and about 16 °C lower than the common phase transition temperature of pure $LiBH_4$ (~115 °C). This temperature reduction is proposed due to the existence of Li(Na)BH_4 (Dematteis et al. 2016). Therefore, the Li(Na)BH_4 solid solution was formed

in the as-milled 0.91(0.62$LiBH_4$-0.38$NaBH_4$)-0.09Ni mixture even though it was not observed in the XRD and Raman data. The corresponding phase transition temperatures during cooling of the 0.91(0.62$LiBH_4$-0.38$NaBH_4$)-0.09Ni and Ni-free mixtures were both 89 ± 1 °C. This temperature was lower than that during heating as a consequence of under-cooling (Dematteis et al. 2016).

The fusion and solidification onset temperatures of the as-milled 0.91(0.62$LiBH_4$-0.38$NaBH_4$)-0.09Ni mixture were determined to be 225 ± 1 °C and 222 ± 1 °C, respectively, influenced by a minor under-cooling effect. These temperatures were similar to those for the Ni-free sample (227 ± 1 °C and 222 ± 1 °C, respectively); suggesting the addition of 9 mol% nano-sized Ni did not change the melting point of its 0.62$LiBH_4$-0.38$NaBH_4$ component. However, by analysing the area of those events, it was found that the phase transition areas were reduced by 10-20 % (Table 8.11). These areas were linearly proportional to the enthalpy.

Table 8.11 DSC curve areas for as-milled 0.91(0.62$LiBH_4$-0.38$NaBH_4$)-0.09Ni compared with as-milled 0.62$LiBH_4$-0.38$NaBH_4$.

	Sample	Energy			
		Heating		Cooling	
		Phase change	Fusion	Phase change	Solidification
		μV mg^{-1} $LiBH_4$	μV mg^{-1} LiNa	μV mg^{-1} $LiBH_4$	μV mg^{-1} LiNa
1	0.62$LiBH_4$-0.38$NaBH_4$	18.9 ± 1.0	12.7 ± 0.6	13.2 ± 0.7	12.8 ± 0.6
2	0.91(0.62$LiBH_4$-0.38$NaBH_4$)-0.09Ni	15.5 ± 0.7	11.1 ± 0.6	11.8 ± 0.6	10.4 ± 0.6

8.4.3 Thermal Decomposition

The thermal dehydrogenation of the 0.91(0.62$LiBH_4$-0.38$NaBH_4$)-0.09Ni mixture was carried out in Ar flowing at 160 mL min^{-1} and heated to 650 °C by 2 °C min^{-1}, as shown in Figure 8.28. No B_2H_6 was detected during decomposition.

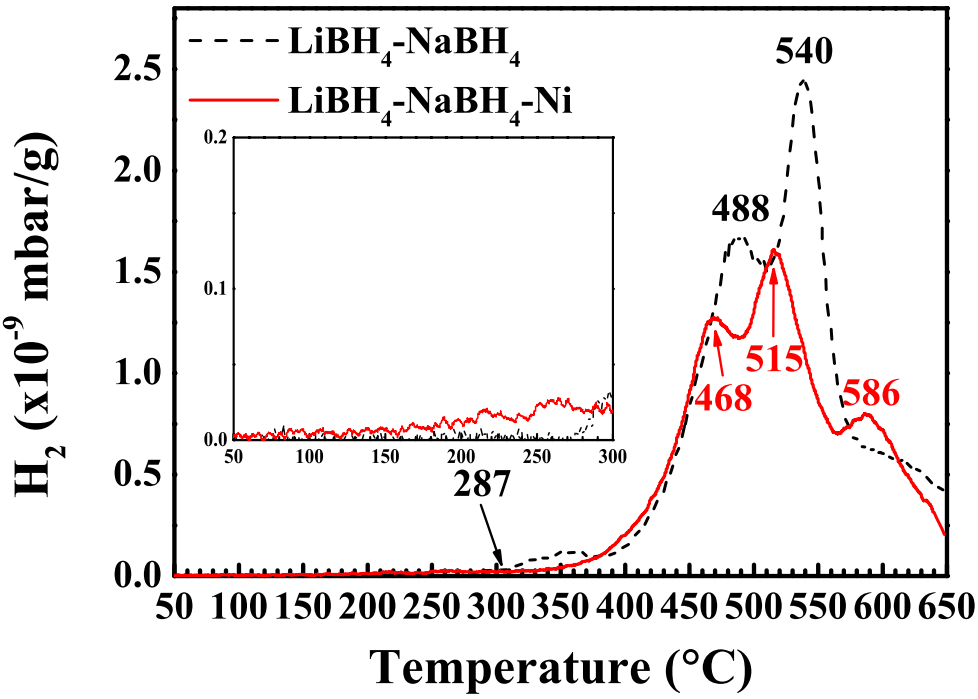

Figure 8.28 TPD-MS results of as-milled 0.91(0.62$LiBH_4$-0.38$NaBH_4$)-0.09Ni, compared with as-milled 0.62$LiBH_4$-0.38$NaBH_4$. Samples were heated at 2 °C min^{-1} in flowing Ar at 160 mL min^{-1}. No B_2H_6 was detected. An embedded figure focused on the hydrogen desorption in the temperature from 50 to 300 °C.

The 0.91(0.62$LiBH_4$-0.38$NaBH_4$)-0.09Ni mixture started to released H_2 from a relatively low temperature between 150-200 °C (exhibiting as a small deviation form the baseline), which was about 50 °C lower than its melting point (225 °C) and about 100 °C lower than the dehydrogenation onset temperature (287 °C) for the Ni-free sample. This low temperature dehydrogenation was also observed when adding this nano-sized Ni to $LiBH_4$ that the destabilized dehydrogenation started from 187 °C

(Section 7.3.3). However, a very limited amount of H_2 is released in this low temperature range.

The major dehydrogenation of the 0.91(0.62$LiBH_4$-0.38$NaBH_4$)-0.09Ni mixture began above 350 °C, which was much lower than the 400 °C for the Ni-free sample. During decomposition, three peaks corresponding to three different dehydrogenation steps were observed at 468 °C, 515 °C and 586 °C. The peak temperatures for the 1st and 2nd peaks were 20 °C and 25 °C lower than the peaks 488 °C and 540 °C for the Ni-free mixture. The 3rd peak at 586 °C was not observed in the Ni-free sample, suggesting a different decomposition pathway.

A total of 8.1 wt.% hydrogen was released from the 0.91(0.62$LiBH_4$-0.38$NaBH_4$)-0.09Ni mixture upon heating to 650 °C in Ar. When the weight of additive (17.8 wt%) was excluded, the $LiBH_4$-$NaBH_4$ content liberated 9.9 wt.% of hydrogen. Nevertheless, the later value was 9% less than the 10.9 wt.% for the Ni-free sample, as the addition of nano-sized Ni changed the reaction pathways

To investigate its decomposition pathways, the 0.91(0.62$LiBH_4$-0.38$NaBH_4$)-0.09Ni mixture was heat treated by 2 °C min^{-1} to 250 °C, 468 °C, 515 °C, 586 °C and 650 °C in flowing Ar. These heat-treated samples were measured by XRD and Raman at room temperature, as shown in Figure 8.29. Due to a high fluorescence effect, Raman data in the B-H stretching region were not available.

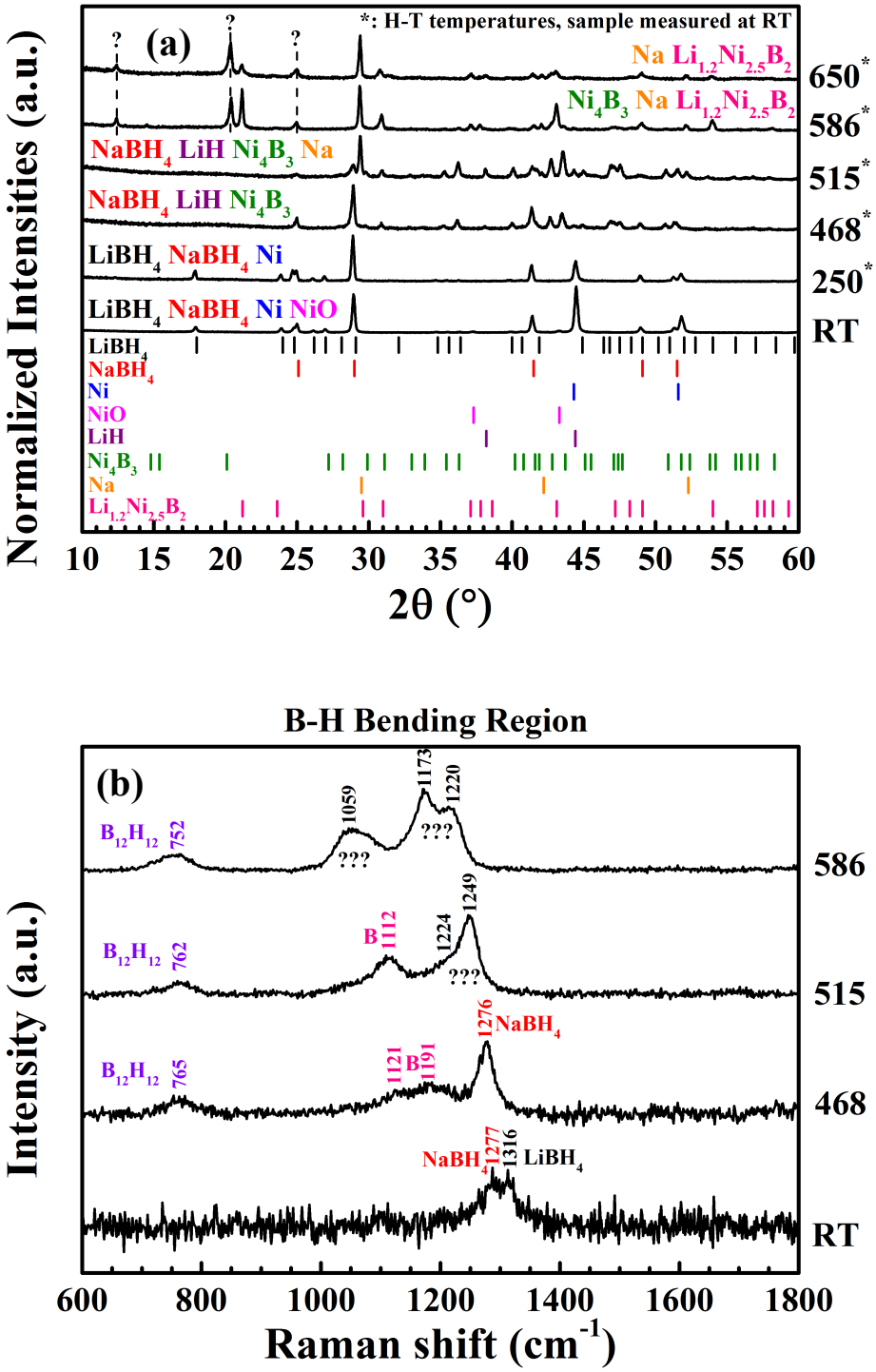

Figure 8.29 Room temperature (a) XRD patterns (Cu K_α radiation, λ = 1.5418 Å) and (b) Raman spectra (measured with 488 nm laser and 2400 l/mm grating system) of as-milled 0.91(0.62$LiBH_4$-0.38$NaBH_4$)-0.09Ni, which had been heat-treated at 250 °C, 468 °C, 515 °C, 586 °C and 650 °C in flowing Ar. The intensities of the XRD and Raman peaks were normalized. Dashed lines are guides for the eye.

In order to investigate reactions occurring in the low temperature range (150-250 °C), the as-milled 0.91(0.62$LiBH_4$-0.38$NaBH_4$)-0.09Ni mixture was heated to 250 °C; this was below the temperature where major dehydrogenation started in Ar. After heat-treatment, Bragg peaks of NiO disappeared, indicating reactions between the parent borohydrides (very likely $LiBH_4$) and NiO. According to Yu et al. (2009), $LiMO_x$ (M = transition metals) is observed as the main reaction product in a reaction involving metal oxide (MO_x) and $LiBH_4$. Thus, the formation of $Li_xNi_yO_z$ (e.g. Li_xNiO_2, x =0.25, 0.33, 04, 0.75, 1 (Arroyo y de Dompablo & Ceder 2003)) was expected. However, no Bragg peaks of a possible reaction product $Li_xNi_yO_z$ were observed by XRD.

The XRD pattern for heat-treated sample at 468 °C showed LiH, Ni_4B_3 and $NaBH_4$ phases. The formation of Ni_4B_3 was caused by the reaction between $LiBH_4$ and nano-sized Ni (forming Ni_4B_3, LiH and H_2, Equation 7.9) that caused a 20 °C reduction of dehydrogenation peak temperature compared with the Ni-free sample (Figure 8.28). This destabilization agreed with $LiBH_4$-Ni system discussed in Section 7.3.3 where a 25 °C decrease was achieved. The former temperature reduction was slightly lower than the later, possibly due to the presence of Na^+ that postponed the dehydrogenation. The corresponding Raman spectrum at this temperature presented signals of remaining $NaBH_4$ (at 1276 cm^{-1}), B (at 1121 cm cm^{-1} and 1191 cm cm^{-1}), and $Li_2B_{12}H_{12}$ (at 765 cm^{-1}). The identification of LiH from XRD, as well as B and $Li_2B_{12}H_{12}$ from Raman spectroscopy confirmed the decomposition of $LiBH_4$ via two competing decomposition pathways as suggested in Equation 7.2 and 7.3. There was no evidence of the decomposition of $NaBH_4$ so far, which was in good agreement with the Ni-free sample. Thus the 1st dehydrogenation route (300-490 °C) was associated with the reaction

between $LiBH_4$ and nano-sized Ni along with the dehydrogenation of the $LiBH_4$ component in the mixture.

At 515 °C, Bragg peaks of elemental Na, LiH and Ni_4B_3, along with weak peaks from $NaBH_4$, were observed in the XRD pattern. This indicated that H_2 release mainly due to dehydrogenation of $NaBH_4$ for the 2nd dehydrogenation step (490-565 °C). The corresponding Raman spectra at this temperature showed $[B_{12}H_{12}]^{2-}$ (762 cm^{-1}), B (1112 cm^{-1}), and 2 unknown peaks at 1249 cm^{-1} and 1224 cm^{-1} (shoulder). In contrast to the heat-treated sample at 468 °C, the wavenumber of amorphous boron at which it centred was decreased slightly that might be due to the formation of a rhombohedral boron, whose peaks were suggested at 1083 cm^{-1}, 1113 cm^{-1} and at 1223 cm^{-1} in the literature (Kudlmann & Roberg 1994).

At 586 °C, where the 3rd dehydrogenation step occurred, phases such as $Li_{1.2}Ni_{2.5}B_2$, Ni_4B_3 and Na were present in the XRD pattern, but the Bragg peaks of LiH disappeared. $Li_{1.2}Ni_{2.5}B_2$ had not been observed in any other sample heat-treated at lower temperatures. Its existence was in agreement with the formation of $Li_{1.2}Ni_{2.5}B_2$ at 600 °C for $2LiBH_4$-Ni (micro-size Ni ~ 41 μm) (Xia et al. 2009). $Li_{1.2}Ni_{2.5}B_2$ was stable and it was observed in the XRD pattern of the sample heat-treated at 650 °C, where Ni_4B_3 disappeared. The corresponding Raman spectra at 586 °C showed $[B_{12}H_{12}]^{2-}$ (752 cm^{-1}), and 3 unknown peaks at 1059 cm^{-1}, 1173 cm^{-1} and 1220 cm^{-1}. The signals of B were not observed. Thus the dehydrogenation reaction occurring at this temperature was proposed to a chemical reaction between LiH, B and Ni_4B_3 that formed $Li_{1.2}Ni_{2.5}B_2$, H_2 and unknown phase(s).

Furthermore, the position of the boron-breathing mode (ν_2) of the $[B_{12}H_{12}]^{2-}$ red shifted with increasing heat-treatment temperature. This reduction in wavenumber was possibly due to the formation of $Na_2B_{12}H_{12}$ or a solid solution: $Li_xNa_{1-x}B_{12}H_{12}$, since the Raman shift of $Na_2B_{12}H_{12}$ was about 20 cm^{-1} lower than that of $Li_2B_{12}H_{12}$ (Figure 8.30) (He et al. 2015), and the addition of Ni facilitated the formation of metal dodecaborates (Ngene, van Zwienen, et al. 2010). Besides, a degradation of the boron skeleton of $[B_{12}H_{12}]^{2-}$ might cause such a shift of wavenumbers in theory, but it was unlikely to occur due to the strong B-B bonds of the cluster (Glockler 1963; Li et al. 2015). Moreover, lithium borates (such as LiB_3O_5, Li_2BO_2, $Li_2B_4O_7$, $Li_4B_2O_5$) were ruled out as contributing towards the unknown Raman peaks in the heat-treated samples at 515 and 586 °C (Kowada et al. 1989; Xiong et al. 1993; Jiang et al. 1996; Voronko et al. 2013; Moiseenko et al. 2000).

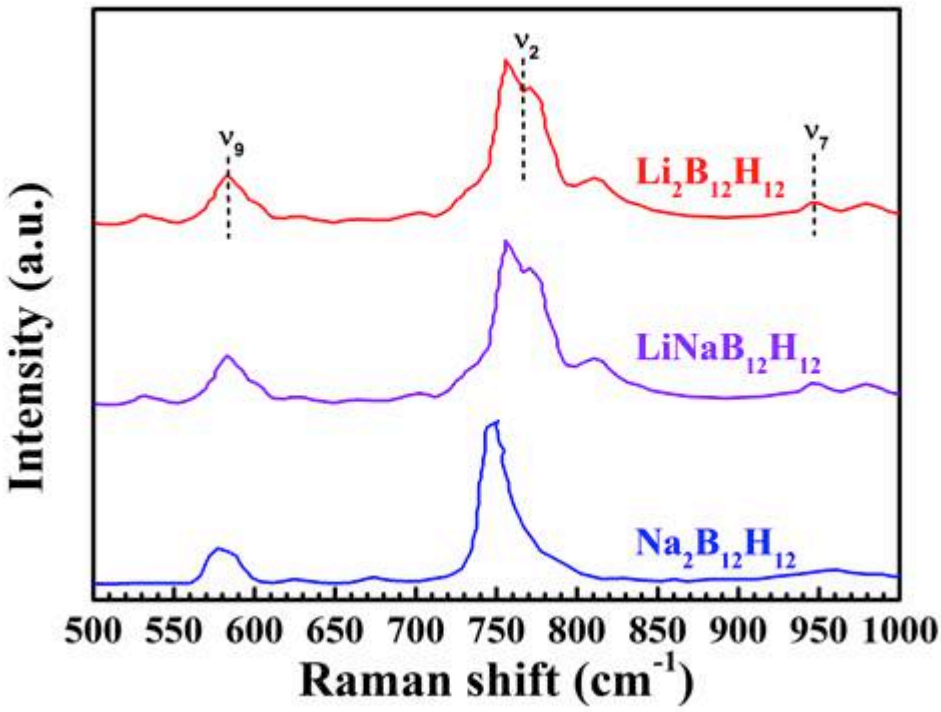

Figure 8.30 Room temperature Raman spectra of $Li_2B_{12}H_{12}$, $LiNaB_{12}H_{12}$ and $Na_2B_{12}H_{12}$, revised from (He et al. 2015).

A theoretical range of H_2 release for the 0.91(0.62$LiBH_4$-0.38$NaBH_4$)-0.09Ni mixture could be calculated as follows:

- The maximum theoretical value was 10.1 wt.%, corresponding to a combination of dehydrogenation reactions involving Equation 7.2 ($LiBH_4$ into LiH, B and H_2), Equation 8.1 ($NaBH_4$ into Na, B and H_2) and Equation 7.9 ($LiBH_4$ into LiH, Ni_4B_3 and H_2);
- The minimum value was found to be 6.5 wt.% that was calculated based on Equation 7.3 ($LiBH_4$ into LiH, $Li_2B_{12}H_{12}$, H_2), Equation 8.3 ($NaBH_4$ into Na, $Na_2B_{12}H_{12}$ and H_2) and Equation 7.9 ($LiBH_4$ into LiH, Ni_4B_3 and H_2).

The experimental H_2 release from the 0.91(0.62$LiBH_4$-0.38$NaBH_4$)-0.09Ni mixture (including heating and cooling) using TPD-MS was found to be 9.5 wt.%, which was in this theoretical range (6.5-10.1 wt.%). However, it should be noted that this experimental decomposition routes is different from that in the theoretical calculations: the 3rd dehydrogenation route where LiH reacted with Ni_4B_3 has not been considered in these theoretical calculations.

The area ratio from a Gaussian fitting (R^2 = 0.983) of the TPD-MS curve was assumed to be linearly related to the amount of H_2 released at the main peaks (47.4%, 25.3 % and 27.3 % for the 1st, 2nd and 3rd peak, respectively), so that the 3rd peak contributed 2.6 wt.% hydrogen (calculated by multiplying the curve area, 27.3%, with the total H_2 release, 9.5 wt.%). Once this 2.6 wt. % was deducted from the total value (9.5 wt.%), the remaining 6.9 wt.% was still in the calculated range (6.5-10.1 wt.%). However, it became very close to the lower limit (minimum value), suggesting the dehydrogenation

through forming $[B_{12}H_{12}]^{2-}$ (Equation 7.3 and 8.3) dominated the overall decomposition. The enhanced formation of $[B_{12}H_{12}]^{2-}$ compounds agreed with the finding in $LiBH_4$-Ni (nano-sized) system (Section 7.3) and in a nano-confined $LiBH_4$-Ni at carbon scaffold system (Ngene, van Zwienen, et al. 2010).

In addition, in order to find a possible stoichiometric ratio for an overall dehydrogenation reaction of the $0.91(0.62LiBH_4\text{-}0.38NaBH_4)$-0.09Ni mixture, a further calculation based on the H_2 evolution has been tried to balance the ratios between the following decomposition reactions: Equation 7.2 ($LiBH_4$ into LiH, B and H_2), Equation 7.3 ($LiBH_4$ into LiH, $Li_2B_{12}H_{12}$, H_2), Equation 7.9 ($LiBH_4$ into LiH, Ni_4B_3 and H_2), Equation 8.1 ($NaBH_4$ into Na, B and H_2) and Equation 8.3 ($NaBH_4$ into Na, $Na_2B_{12}H_{12}$ and H_2). However, the results are not available, suggesting that, in practice, dehydrogenation might be more complex.

In an attempt to understand the effect of additives on the dehydrogenation rate, the activation energies of $0.62LiBH_4\text{-}0.38NaBH_4$ (with or without additives) samples were calculated through Kissinger's equation (Kissinger 1957):

$$\ln\left(\frac{T_P^2}{\beta}\right) = \frac{E_a}{RT_P} - k \qquad \textbf{Equation 8.9}$$

where T_P was the temperature at the maximum of the decomposition rate (i.e. peak temperature), β was the heating rate, R was the gas constant (i.e. 8.314 J K^{-1} mol^{-1}) and k was a constant. Though this method was only valid for simple one-step chemical reactions, it can be generalized in practice use to fit complex multistep reactions by

adopting rate-controlling step concept: the slowest chemical reaction happened in a serial of reactions determined the speed for the overall reaction proceeded (Wellen & Canedo 2014).

To obtain the activation energies of reactions, the temperature at the maximum of the decomposition rate for each reaction was obtained by performing multiple TPD-MS measurements in Ar where different heating rates were applied (i.e. 0.5, 2, 5 and 10 °C min^{-1}). Though more than one reaction happened at each step and the peak temperatures detected by TPD-MS was not as accurate as the data determined by DSC, the results in Figure 8.31 and Table 8.12 provided a general guide, suggesting the additives did not significantly affect the activation energies (the rate of the reactions). However, these data might be not comparable to literature values.

Table 8.12 Activation energies of chemical reactions of $LiBH_4$, $NaBH_4$, and the $LiBH_4$-$NaBH_4$ systems, calculated using Kissinger's method.

Sample	E_a (kJ)		
	1st peak	2nd peak	3rd peak
$LiBH_4$	264 ± 6	n.a.	n.a.
$NaBH_4$	n.a.	147 ± 2	n.a.
LiNa	112 ± 1	126 ± 1	n.a.
LiNa-Si	134 ± 5	127 ± 5	n.a.
LiNa-Ni	140 ± 2	148 ± 2	194 ± 3

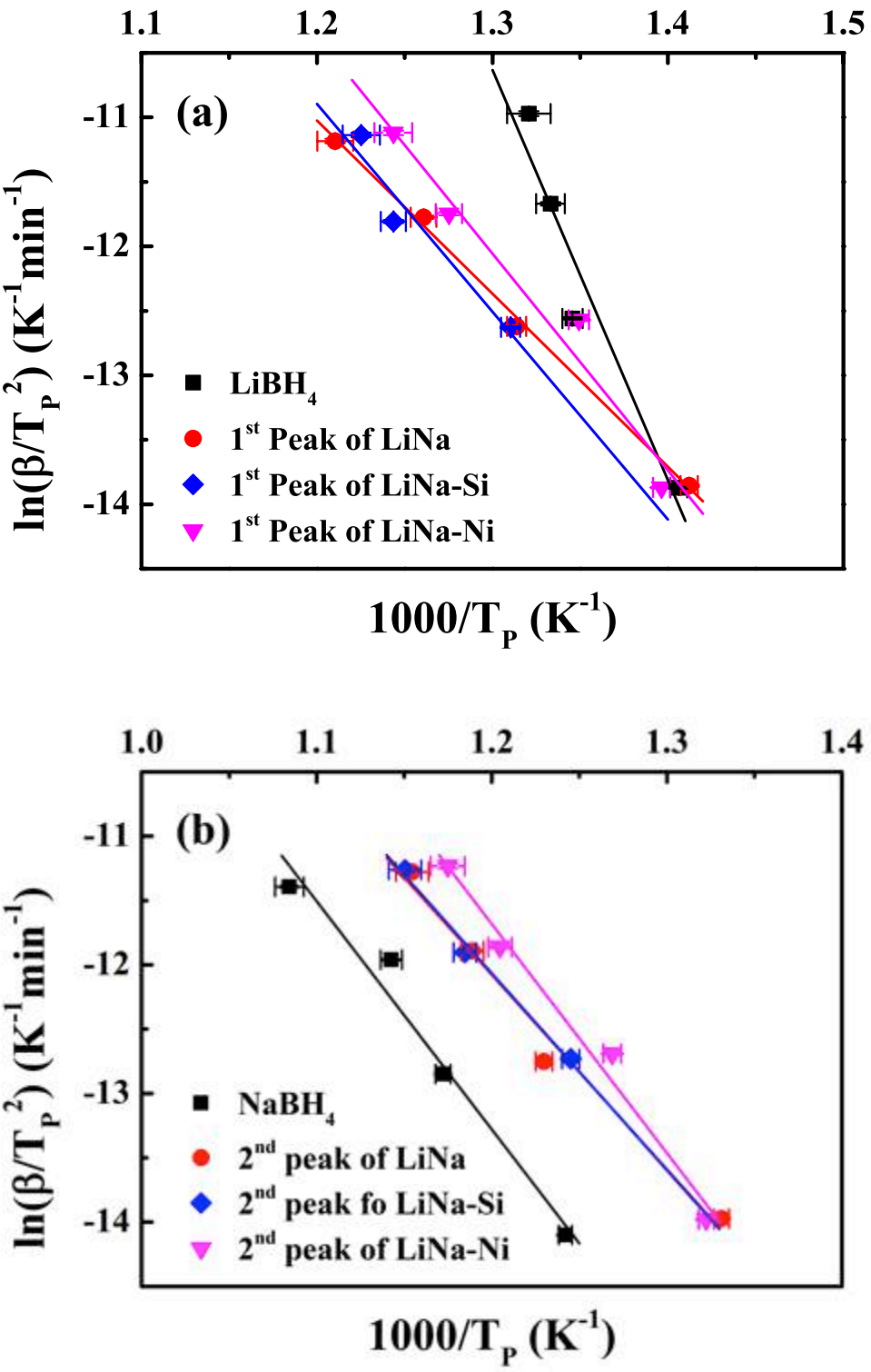

Figure 8.31 Kissinger plot for the major decomposition reactions in as-milled $0.62LiBH_4$-$0.38NaBH_4$ (noted as LiNa), as-prepared $0.95(0.62LiBH_4$-$0.38NaBH_4)$-$0.05SiO_2$ (0.5 µm, noted as LiNa-Si) and as-milled $0.91(0.62LiBH_4$-$0.38NaBH_4)$-0.09Ni (nano-sized Ni, noted as LiNa-Ni), compared with as-milled $LiBH_4$ and $NaBH_4$. The activation energies were calculated from the slope of trend-lines. Some error bars are very small.

8.4.4 Recombination

The reversibility of the 0.91(0.62$LiBH_4$-0.38$NaBH_4$)-0.09Ni mixture was carried out using a Sieverts type apparatus as described in Section 6.2.6. The reaction conditions were: 500 °C, 1 bar H_2 and 10 h for desorption; and 400 °C, 130 bar H_2 and 12 h for absorption.

Figure 8.32 shows the H_2 releases of each desorption process during cycling and the measured H_2 release during cycling were summarized in Table 8.13. The corrected values (Corr.) excluded the weight of additive.

Table 8.13 H_2 release (wt.%) of 0.91(0.62$LiBH_4$-0.38$NaBH_4$)-0.09Ni during cycling compared with 0.62$LiBH_4$-0.38$NaBH_4$. The corrected (Corr.) value excludes the weight of additive from the measured (Meas.) results.

H (wt.%)	$LiBH_4$-$NaBH_4$	$LiBH_4$-$NaBH_4$-Ni		
	Meas.	Meas.		Corr.
1st cycle	5.5	5.1	→	6.2
2nd cycle	1.1	1.1	→	1.3
3rd cycle	0.8	0.6	→	0.7

In general, the 0.91(0.62$LiBH_4$-0.38$NaBH_4$)-0.09Ni mixture had a poor system (i.e. including additives) reversibility that was similar to the Ni-free sample. Once the weight of additives was excluded (corrected values): the 0.91(0.62$LiBH_4$-0.38$NaBH_4$)-0.09Ni mixture released 6.2 wt.% of hydrogen during the 1st dehydrogenation, which was 13 % higher than the 5.5 wt.% for the Ni-free sample, due to the destabilization effect of the nano-sized Ni additive. After rehydrogenation, the 0.91(0.62$LiBH_4$-0.38$NaBH_4$)-0.09Ni mixture absorbed 1.3 wt.% of hydrogen at the 2nd cycle, which was slightly higher than the 1.1 wt.% for the Ni-free sample. In addition, the reversible hydrogen content at the 3rd cycle for the 0.91(0.62$LiBH_4$-0.38$NaBH_4$)-0.09Ni mixture was 0.7 wt.%, which was

close to the 0.8 wt.% for the Ni-free sample. Nevertheless, the reversible hydrogen contents of the 0.91(0.62$LiBH_4$-0.38$NaBH_4$)-0.09Ni mixture at the 2nd and 3rd cycles were significantly reduced in contrast to that for the 1st cycle, which was not expected due to the Ni-induced high reabsorption capacity of $LiBH_4$ (Li et al. 2014). This may be caused by the use of much harsher rehydrogenation conditions (350 bar, 550 °C, 24 h) by Li et al. (2014).

Figure 8.33 shows the XRD and FTIR results for the 0.91(0.62$LiBH_4$-0.38$NaBH_4$)-0.09Ni mixture during cycling.

The XRD pattern of the three-time rehydrogenated 0.91(0.62$LiBH_4$-0.38$NaBH_4$)-0.09Ni mixture shows Bragg peaks of $NaBH_4$, LiH, NaH, Ni_4B_3, Ni_3B and Ni_2B phases, indicating the occurrence of: reactions of $LiBH_4$ with Ni, decomposition of $LiBH_4$, and partial decomposition of $NaBH_4$ during the cycling.

Due to the addition of nano-sized Ni, $LiBH_4$ was found to be fully decomposed after the first dehydrogenation process as no $LiBH_4$ signal was observed in either XRD or FTIR result. A broad shoulder peak at around 2470 cm^{-1} was found in the FTIR data for the reaction product of the 0.91(0.62$LiBH_4$-0.38$NaBH_4$)-0.09Ni mixture at the 1st dehydrogenated state, which was due to the formation of closo-boranes ($[B_{10}H_{10}]^{2-}$ at ~2467 cm^{-1} or $[B_{12}H_{12}]^{2-}$ at ~2480 cm^{-1}) (Leites 1992; Muetterties et al. 1962). This broad peak was not seen by FTIR for the dehydrogenation product of the Ni-free sample at the same state (Figure 8.17), confirming again the addition of Ni facilitated the formation of metal dodecaborates (Ngene, van Zwienen, et al. 2010).

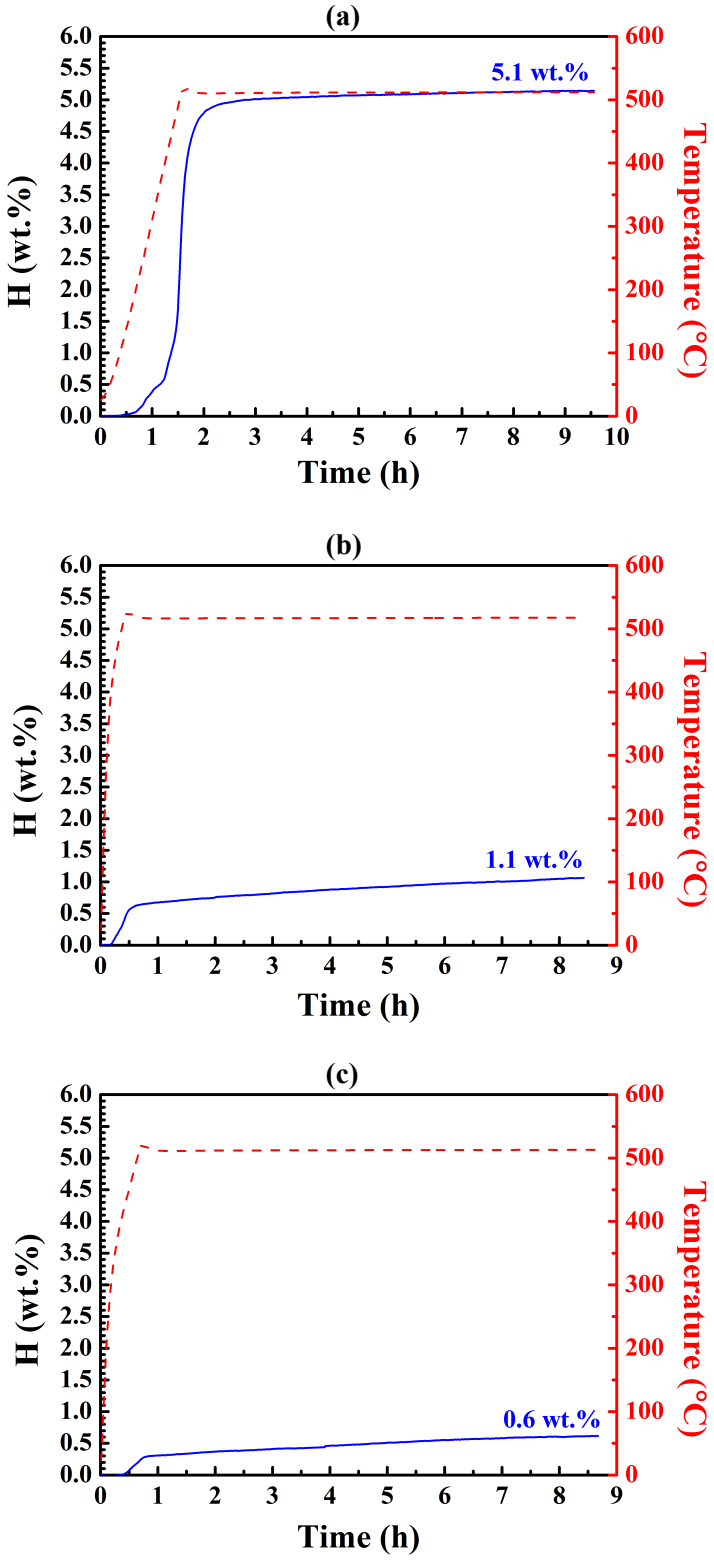

Figure 8.32 Sievert's measurements showing hydrogen release (in wt.%) while keeping the 0.91(0.62$LiBH_4$-0.38$NaBH_4$)-0.09Ni under 1 bar H_2 at 500 °C ($\Delta T/\Delta t$ = 5 °C min^{-1}) for 10 h for desorption and under 130 bar H_2 at 400 °C for 12 h for rehydrogenation. (a) 1st cycle, (b) 2nd cycle (c) 3rd cycle. The different heating rate was because the furnace had not completely cooled down to room temperature.

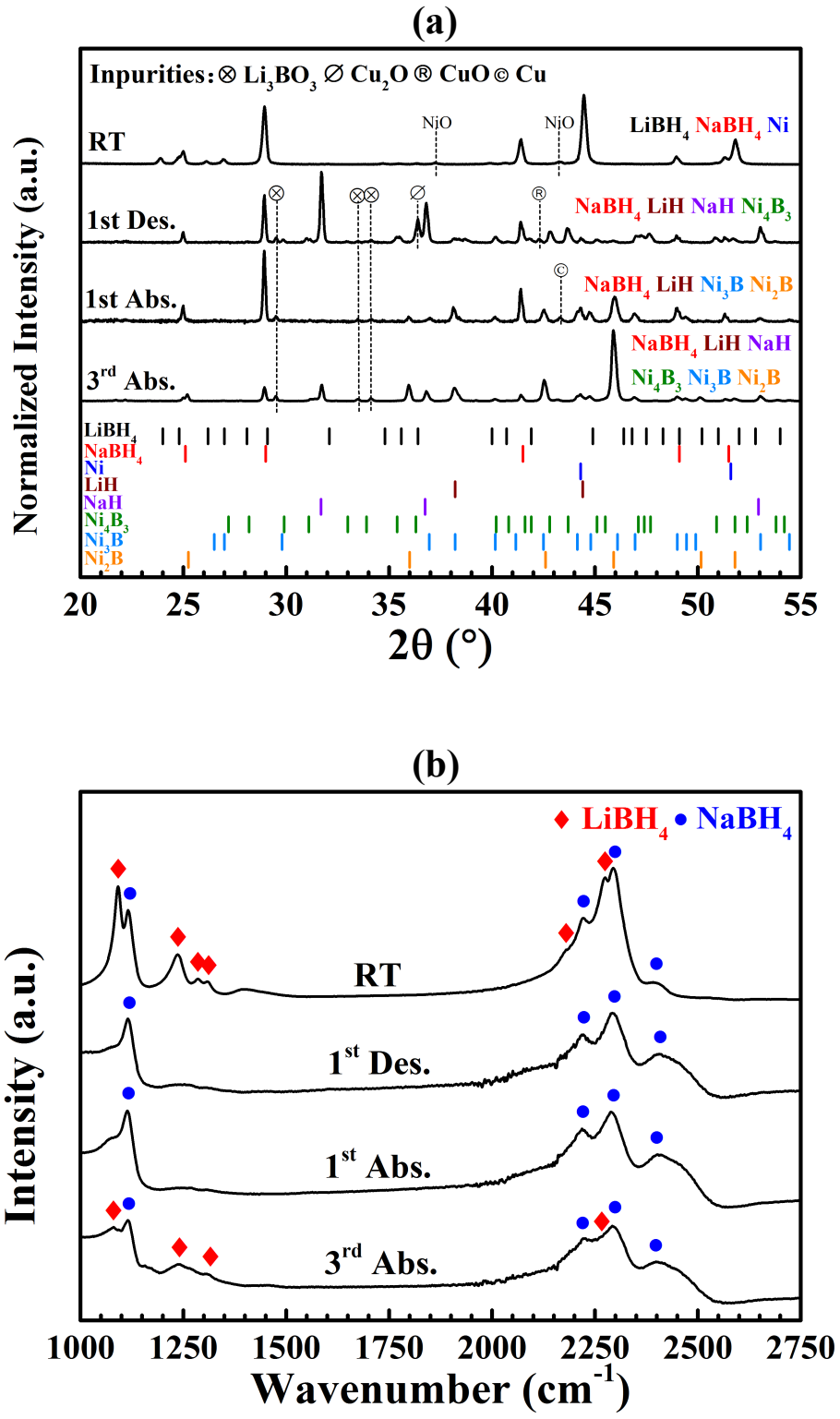

Figure 8.33 (a) XRD patterns (Cu K_α radiation, λ = 1.5418 Å) and (b) FTIR spectrum of 0.91(0.62$LiBH_4$-0.38$NaBH_4$)-0.09Ni decomposed at 500 °C in 1 bar static H_2 for 10 h (denoted as 1st Des.) and recombined in 130 bar H_2, 400 °C for 12 h at the 1st and 3rd cycle (denoted as 1st Abs. and 3rd Abs., respectively). The Cu based impurities (Cu_2O and CuO) observed in XRD patterns were introduced from the outer surface of sample holder during operation (not participated in dehydrogenation).

The Bragg peaks of NaH were first found in the XRD pattern for the dehydrogenation product of the 0.91(0.62$LiBH_4$-0.38$NaBH_4$)-0.09Ni mixture after being kept at 500 °C in 1 bar H_2 for 10 h and its observation were explained as follows (Humphries et al. 2013): due to the low boiling point of Na (281 °C at 10^{-5} bar of Na gas, as shown in Figure 8.7), any precipitated Na vaporized immediately. The gaseous Na could condense when it reached the cold part outside the hot zone (might further solidify, subject to temperature). The escaped Na reacted in an exothermic reaction with gaseous H_2 to form NaH, leading to a physical segregation of decomposition products as observed in Figure E.4 (Appendix E). Thus, when the decomposition occurs in Ar, NaH was not observed. To prevent such eventualities, Na could be physically or chemically confined using nano-scaffolds (nanoconfinement) or metal fluorides (Mao & Gregory 2015) or closed containers (Sheppard et al. 2016).

In addition, Ni_4B_3 was one of the major dehydrogenation products of the 0.91(0.62$LiBH_4$-0.38$NaBH_4$)-0.09Ni mixture after being kept at 500 °C in 1 bar H_2 for 10 h. It could convert to Ni_3B after rehydrogenation, and Ni_3B could be further oxidized by B to Ni_2B (Humphries et al. 2013). Since the Bragg peaks for NaH disappeared after the first rehydrogenation step, it is therefore proposed that NaH reacted with Ni_4B_3 under H_2 and consequently formed $NaBH_4$ and Ni_3B during H_2 absorption, via:

$$\boldsymbol{2NaH + 3Ni_4B_3 + 3H_2 \rightarrow 2NaBH_4 + 4Ni_3B + 3B} \qquad \textbf{Equation 8.10}$$

$$\boldsymbol{2Ni_3B + B \rightarrow 3Ni_2B} \qquad \textbf{Equation 8.11}$$

After being cycled for three times, the FTIR result for the rehydrogenated 0.91(0.62$LiBH_4$-0.38$NaBH_4$)-0.09Ni mixture shows peaks at 1079 cm^{-1}, 1238 cm^{-1},

1308 cm^{-1} and a shoulder peak around 2270 cm^{-1}. These peaks were similar to $LiBH_4$ (1092 cm^{-1}, 1236 cm^{-1}, 1309 cm^{-1} and a 2275 cm^{-1} in the as-milled mixture), suggesting an amorphous $LiBH_4$ phase was reformed, which could be attributed to the catalytic effect of Ni_4B_3 on rehydrogenation (Li et al. 2014). The reformation of $LiBH_4$ occurred under much milder conditions (lower temperature and pressure) than reported before (Li et al. 2014). Since no $LiBH_4$ was reformed immediately after the 1st rehydrogenation process, the possible reasons were:

1) Quality accumulation

A small shoulder peak was shown around 1070 cm^{-1} in FTIR after the 1st rehydrogenation, suggesting a small amount of $LiBH_4$ might be formed at this stage. But, the lab-scale FTIR used in this work was not able to confirm the reformation of $LiBH_4$ based on such a very small amount of phase. However, during further cycling, the quantity of $LiBH_4$ accumulated and became detectable.

2) Induced impurities

Due to the sample holder being opened after the 1st dehydrogenation for collecting XRD samples, a small quantity of impurities (such as CuO, Cu_2O) might have been introduced before performing the 1st rehydrogenation. These impurities might have hindered reformation of $LiBH_4$ during hydrogenation. However, the 3rd rehydrogenated sample was obtained from a non-stop measurement in which case such impurities were not introduced.

Broad signals around 2400-2500 cm^{-1} were noticed in the FTIR data for the rehydrogenated $0.62LiBH_4$-$0.38NaBH_4$ (Figure 8.17) and $0.91(0.62LiBH_4$-$0.38NaBH_4)$-0.09Ni (Figure 8.33) mixtures, indicating the formation of $[B_{10}H_{10}]^{2-}$ (~2467 cm^{-1}) (Leites 1992) or $[B_{12}H_{12}]^{2-}$ (~2480 cm^{-1}) (Muetterties et al. 1962). However, none of these dodecaborates could be identified from the corresponding XRD data, where Bragg peaks in the low 2θ range were expected (15-20 2θ°) (H. Wu et al. 2015; Her et al. 2008), thus indicating that they could be present in an amorphous or nano-crystalline state.

8.4.5 Effect of Additive: nano-sized Ni

The dehydrogenation mechanism of the $0.91(0.62LiBH_4$-$0.38NaBH_4)$-0.09Ni mixture was systematically studied between 25 °C and 650 °C in flowing Ar. The addition of 9 mol% nano-sized Ni powder did not affect the low orthorhombic to hexagonal $LiBH_4$ phase transition temperature (99 °C) and the low melting temperature (225 °C), whilst it reduced the dehydrogenation peak temperatures by 20-25 °C, leading to three major decomposition routes:

- 300 °C to 490 °C, H_2 release was associated with a reaction between $LiBH_4$ and nano-sized Ni (forming LiH and Ni_4B_3), along with the dehydrogenation of the $LiBH_4$ component in the mixture, forming LiH, B, $Li_2B_{12}H_{12}$;
- 490 °C to 565 °C, the dehydrogenation was mainly due to the decomposition of the $NaBH_4$ component, forming Na, B, and possibly $Na_2B_{12}H_{12}$;
- 565 °C to 650 °C, H_2 liberation was due to a reaction between LiH, B and Ni_4B_3, forming $Li_{1.2}Ni_{2.5}B_2$ and unknown phases.

A total of 8.1 wt.% of hydrogen was released upon heating to 650 °C in Ar, which was lower than the 10.8 wt.% for that of the Ni-free mixture. This 0.91(0.62$LiBH_4$-0.38$NaBH_4$)-0.09Ni mixture had a poor cycling stability as its reversible hydrogen content reduced from 5.1 wt.% to 1.1 wt.% to 0.6 wt.% during three complete desorption-absorption-cycles. However, it was suggested that its $LiBH_4$ content was partially reversible under much milder conditions than reported before (Li et al. 2014).

Figure 8.34 shows the dehydrogenation and rehydrogenation pathways of the 0.91(0.62$LiBH_4$-0.38$NaBH_4$)-0.9Ni mixture in a flow chart.

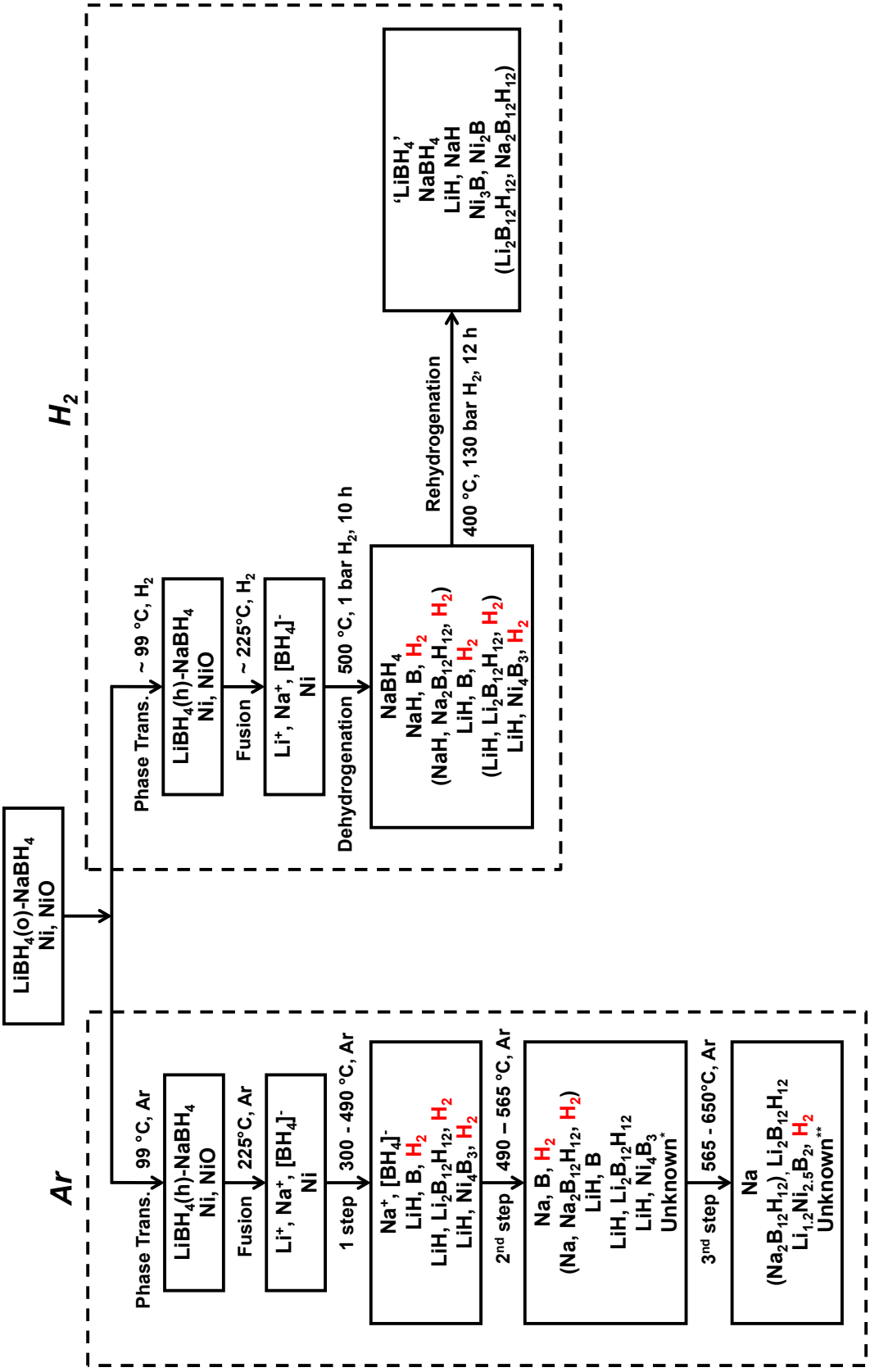

Figure 8.34 A flow chart of decomposition pathways (in Ar and H_2) and the rehydrogenation (H_2) of the as-milled 0.91(0.62$LiBH_4$-0.38$NaBH_4$)-0.9Ni.

8.5 Summary

The eutectic $LiBH_4$-$NaBH_4$ mixture had a relatively low cost among the known eutectic borohydrides mixtures and a high theoretical gravimetric hydrogen storage capacity (e.g. approximately 15 wt. %). Therefore, this mixture has attracted significant research attention. Two eutectic composition based on experiments and thermodynamic modelling have been reported before, which were $0.62LiBH_4$-$0.38NaBH_4$ (melting point 224 °C) (M Paskevicius et al. 2013; Javadian, Sheppard, et al. 2015) and $0.71LiBH_4$-$0.29NaBH_4$ (melting point 216 °C) (Dematteis et al. 2016), respectively. This work focused on studying the decomposition and recombination pathways of a $0.62LiBH_4$-$0.38NaBH_4$ mixture.

The dehydrogenation mechanisms of the $0.62LiBH_4$-$0.38NaBH_4$ mixture were systematically studied between 25 °C and 650 °C in flowing Ar. Solid solutions ($Li(Na)BH_4$ and $Na(Li)BH_4$) were formed during ball milling and the substitution of Na^+ was responsible for a decrease in the orthorhombic to hexagonal $LiBH_4$ phase transition temperature by 21 °C to 94 °C. The melting started from 225 °C with an enthalpy of 4.99 ± 0.25 kJ mol^{-1}. No H_2 release was detected upon heating to 287 °C and two major decomposition routes were found: 1) the dehydrogenation from 287 °C to 520 °C was accompanied by the precipitation of LiH, $Li_2B_{12}H_{12}$ and B; and 2) from 520 °C to 650 °C, the dehydrogenation was dominated by the formation of Na and B. The presence of two cations with different Pauling electronegativity values affected the dehydrogenation temperatures so that the measured desorption peak temperatures (488 and 540 °C) for as-milled $0.62LiBH_4$-$0.38NaBH_4$ mixture were shifted: higher than that for as-milled $LiBH_4$ (470 °C) and lower than that for as-milled $NaBH_4$ (580 °C). A total

of 10.8 wt. % hydrogen was released after heating to 650 °C, that exceeded the estimated amount (8.9 wt. %) suggesting less metal dodecaborate (than that of as-milled $LiBH_4$) was formed during decomposition.

The rehydrogenation of the $0.62LiBH_4$-$0.38NaBH_4$ mixture was carried out at 500 °C in 1 bar H_2 for 10 h for desorption and at 400 °C in 130 bar H_2 for 12 h for absorption. The reversible hydrogen content decreased dramatically from 5.5 wt.% to 1.1 wt.% and to 0.8 wt.%. This poor cyclic stability was also observed by Javadian, Sheppard, et al. (2015) and could improved by nano-confinement. Unfortunately, No $LiBH_4$ was reformed during cycling.

Since Chapter 7 has studied the destabilization effects of micron-sized SiO_2 (0.5 μm) and nano-sized Ni on the decomposition of $LiBH_4$, exhibiting lower onset and peak temperatures. These additives were then used to try to tailor the energy required for dehydrogenation in order to destabilise the decomposition of the $0.62LiBH_4$-$0.38NaBH_4$ mixture (noted as LiNa). Therefore, $0.95(0.62LiBH_4$-$0.38NaBH_4)$-$0.05SiO_2$ (noted as LiNa-Si) and $0.91(0.62LiBH_4$-$0.38NaBH_4)$-0.09Ni (noted as LiNa-Ni) mixtures were prepared and the additive effect on the ‘eutectic behaviour’ and their dehydrogenation was investigated.

In general, these additives did not significantly affect the low-temperature phase transition of $LiBH_4$ and the melting, as the onset temperatures and energies required for these phase changes were similar (Table 8.14).

Table 8.14 Summary of DSC data for $0.62LiBH_4$-$0.38NaBH_4$ (LiNa), $0.95(0.62LiBH_4$-$0.38NaBH_4)$-$0.05SiO_2$ (LiNa-Si) and $0.91(0.62LiBH_4$-$0.38NaBH_4)$-0.09Ni (LiNa-Ni) in Ar.

Sample	Heating				Cooling			
	Phase change		Fusion		Phase change		Solidification	
	Temp. °C	Energy μV mg^{-1} $LiBH_4$	Temp. °C	Energy μV mg^{-1} LiNa	Temp. °C	Energy μV mg^{-1} $LiBH_4$	Temp. °C	Energy μV mg^{-1} LiNa
LiNa	100 ± 1	18.9 ± 1.0	227 ± 1	12.7 ± 0.6	88 ± 1	13.2 ± 0.7	222 ± 1	12.8 ± 0.6
LiNa-Si	99 ± 1	19.3 ± 1.0	226 ± 1	13.0 ± 0.7	89 ± 1	11.8 ± 0.6	222 ± 1	11.1 ± 0.6
LiNa-Ni	99 ± 1	15.5 ± 0.7	225 ± 1	11.1 ± 0.6	89 ± 1	11.8 ± 0.6	222 ± 1	10.4 ± 0.6

The effect of additives on the dehydrogenations is summarised in Table 8.15.

Table 8.15 Improvement effect of additives on the dehydrogenation of $0.62LiBH_4$-$0.38NaBH_4$ systems.

Sample	Temperature (°C)			H_2 release (wt.%)
	Onset	Early Peak(s)	Major Peak(s)	650 °C, Ar
$LiBH_4$	285		470	10.0
$NaBH_4$	450		580	7.8
LiNa	287		488, 540	10.8
LiNa-Si	245	290-350	490, 530	7.3
LiNa-Ni	150-200		468, 515, 586	8.1

LiNa-Si and LiNa-Ni started to release H_2 at much lower temperatures than LiNa, indicating even a small amount of oxides (SiO_2, NiO) in the additive reduced the decomposition onset temperature dramatically.

Upon heating to 650 °C, LiNa released 10.8 wt.% of hydrogen that was higher than the 7.3 wt.% for LiNa-Si and 8.1 wt.% for LiNa-Ni. But these additives changed the dehydrogenation peak temperatures (Figure 8.35) and also alerted the reaction mechanisms (Table 8.7).

The difference of peak temperatures between the $LiBH_4$ (470 °C) and the $LiBH_4$ dominated peak (1st peak) of LiNa (488 °C) was affected by Na^+ (whose Pauling electronegativity value was lower than Li^+). Though adding additives led to a lower or similar 1st peak temperatures (468 °C for LiNa-Ni < 488 °C for LiNa ≈ 490 °C for LiNa-Si), these destabilized peak temperatures were still higher in contrast to those destabilised $LiBH_4$ samples using the same additives (467 °C for $LiBH_4$-Si system and 445 °C for $LiBH_4$-Ni system) studied in Chapter 7, due to the cation interaction of Na^+ in the LiNa-Si and LiNa-Ni samples.

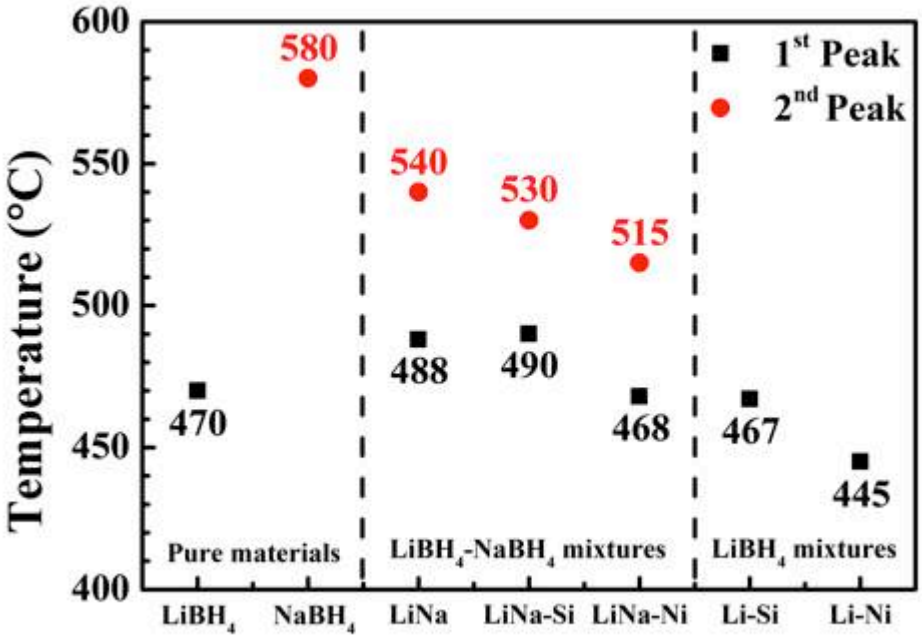

Figure 8.35 A comparison of dehydrogenation peak temperatures of as-milled $LiBH_4$, as-milled $NaBH_4$, as-milled $0.62LiBH_4$-$0.38NaBH_4$ (noted as LiNa), as-prepared $0.95(0.62LiBH_4$-$0.38NaBH_4)$-$0.05SiO_2$ (0.5 µm, noted as LiNa-Si) and as-milled $0.91(0.62LiBH_4$-$0.38NaBH_4)$-0.09Ni (nano-sized, noted as LiNa-Ni). Sample were heated by 2 °C min^{-1} in Ar flowing at 160 mL min^{-1}.

The decomposition mechanism of the $0.62LiBH_4$-$0.38NaBH_4$ component in LiNa-Si and LiNa-Ni mixtures were different in contrast to that of LiNa. Since the additives consumed parts of $LiBH_4$ during dehydrogenation, the molar ratio of remained $LiBH_4$ to $NaBH_4$ was slightly moved from the reported eutectic composition (62:38) into $NaBH_4$-rich statuses (58:42 for LiNa-Si, and 59:41 for LiNa-Ni): the excess molar percentage for LiNa-Si and LiNa-Ni were 4 mol% and 3 mol%, respectively. These changes of compositions became one of the possible reasons that changed the decomposition mechanism. In addition, the intermediate phases during decomposition and reaction products of $LiBH_4$ (such as Li_2SiO_3, Li_4SiO_4, Ni_4B_3) might also strongly influence the overall reactions and change the mechanisms.

In general, adding additives, such as micron-sized SiO_2 and nano-sized Ni, facilitated the formation of $[B_{12}H_{12}]^{2-}$. This enhancement of $Li_2B_{12}H_{12}$ was also seen in $LiBH_4$-Ni (nano-sized) system (Section 7.3) and in a nano-confined $LiBH_4$-Ni at carbon scaffold system (Ngene, van Zwienen, et al. 2010). Besides, the formation of $Na_2B_{12}H_{12}$ was also enhanced, as no $Na_2B_{12}H_{12}$ existed in the reaction products of LiNa, but LiNa-Si contained 0.04 mole of $Na_2B_{12}H_{12}$. Since, the decomposition reaction of $NaBH_4$ into Na, $Na_2B_{12}H_{12}$ and H_2 (82 kJ mol^{-1} H_2, Equation 8.3) had a lower reaction enthalpy than the pathway into Na, B and H_2 (93 kJ mol^{-1} H_2, Equation 8.1). The former reaction occurred at a relatively lower temperature than the later from a thermodynamic point of view (Figure 8.7). Thus, the promoted formation of $Na_2B_{12}H_{12}$ might be one reason for the reduction of $NaBH_4$-domainated dehydrogenation temperatures (2^{nd} peak in Figure 8.35) when additives were used.

Though $LiBH_4$ showed an enhanced cyclic stability with addition of 25 wt.% nano-sized Ni in (Li et al. 2014), the cyclic stability of LiNa-Ni sample was not improved in this work, exhibiting a similar amount of reversibly H_2 content compared to the Ni-free mixture (Table 8.13). However, FTIR showed several vibrational modes similar to $LiBH_4$ after absorption at the 3rd cycle, suggesting a small amount of $LiBH_4$ was reformed. This was indeed different from the Ni-free sample where no $LiBH_4$ was found after rehydrogenation.

In addition, the XRD results showed the synchronous appearance of Ni_3B and Ni_2B and the disappearance of NaH and Ni_4B_3 in LiNa-Ni sample during cycling, suggesting that $NaBH_4$ was decomposed and may be regenerated through Equation 8.10. In fact, as the reaction conditions used in this work were not suitable to achieve full decomposition of $NaBH_4$, only a limited amount of NaH was formed during decomposition. The formation of NaH was due to light gaseous Na escaping the heating zone (i.e. the bottom of the sample holder) and then subsequently reacting with H_2. So that the major NaH was physically segregated from major decomposition products (containing Ni_4B_3) sit at the bottom of the sample holder. Due to these two reasons, the rehydrogenation of $NaBH_4$ was limited, leading to a minor change in reversible H_2 content. Using a specially designed sample container to confining the Na, it could be possible to prohibit sample segregation and perhaps improve cyclic stability.

The future work should consider destabilizing the decomposition and improving the rehydrogenation of LiNa-Ni using nano-confinement, as well as further understanding the possible reaction mechanisms.

CHAPTER 9 LITHIUM AND POTASSIUM BOROHYDRIDES MIXTURE

The focus of this chapter is:

- To characterise the crystal structure, vibrational frequencies, thermodynamic property of the low-melting-point $0.75LiBH_4$-$0.25KBH_4$ mixture;
- To investigate its dehydrogenation mechanism and recombination behaviour;
- To modify its dehydrogenation and recombination properties using selected additives, such as micron-sized SiO_2 (0.5 μm) and nano-sized Ni (~ 100 nm), and to investigate the modified reaction pathways.

9.1 Potassium Borohydride

9.1.1 Sample Characterisations

9.1.1.1 As-received KBH_4

Figure 9.1-a shows room temperature crystal structure of as-received KBH_4 (Sigma-Aldrich, ≥ 98.0%). The Bragg peaks were caused by a cubic structure (space group *Fm-3m*). The pseudo-Rietveld refinement result (Figure 9.2) shows that the as-received KBH_4 has high purity. The refined lattice parameters (Table 9.1) were slightly higher (~ 1%) than the published values (Abrahams & Kalnajs 1954; Luck & Schelter 1999; Kumar et al. 2008; Dovgaliuk et al. 2014).

Figure 9.1-b shows the vibrational structures of as-received KBH_4. The wavenumbers (cm^{-1}) of Raman and FTIR results were summarised in Table 9.2.

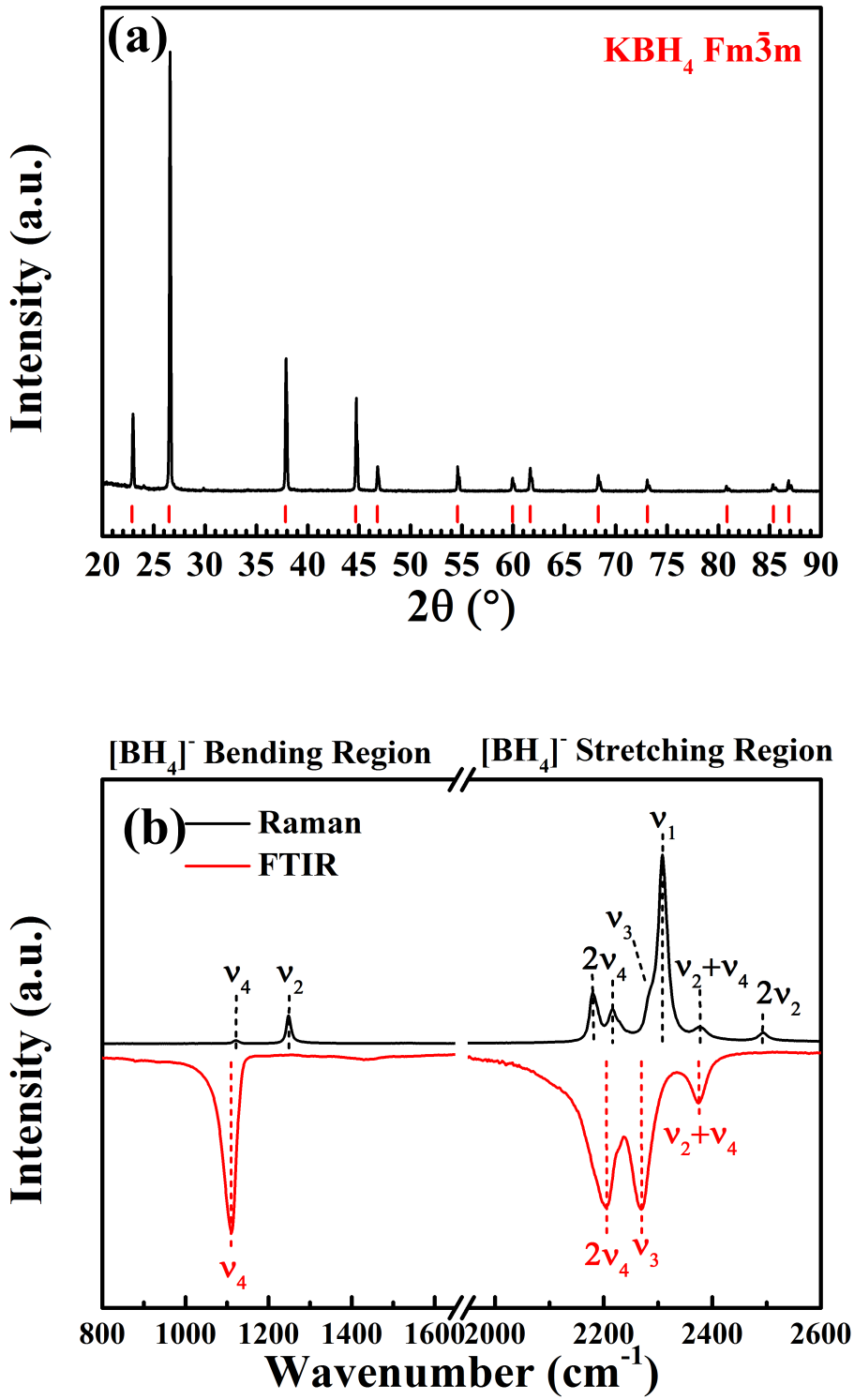

Figure 9.1 (a) XRD pattern (Cu K_α radiation, λ = 1.5418 Å) of as-received KBH_4 at room temperature compared to an synchrotron XRD data (red vertical lines) from the literature (Dovgaliuk et al. 2014). (b) Raman (measured with 488 nm laser and 2400 l/mm grating system) and FTIR spectra of as-received KBH_4 at room temperature. A horizontal break was used to divide the spectra into $[BH_4]^-$ bending and stretching regions. Dashed lines are guides for the eye.

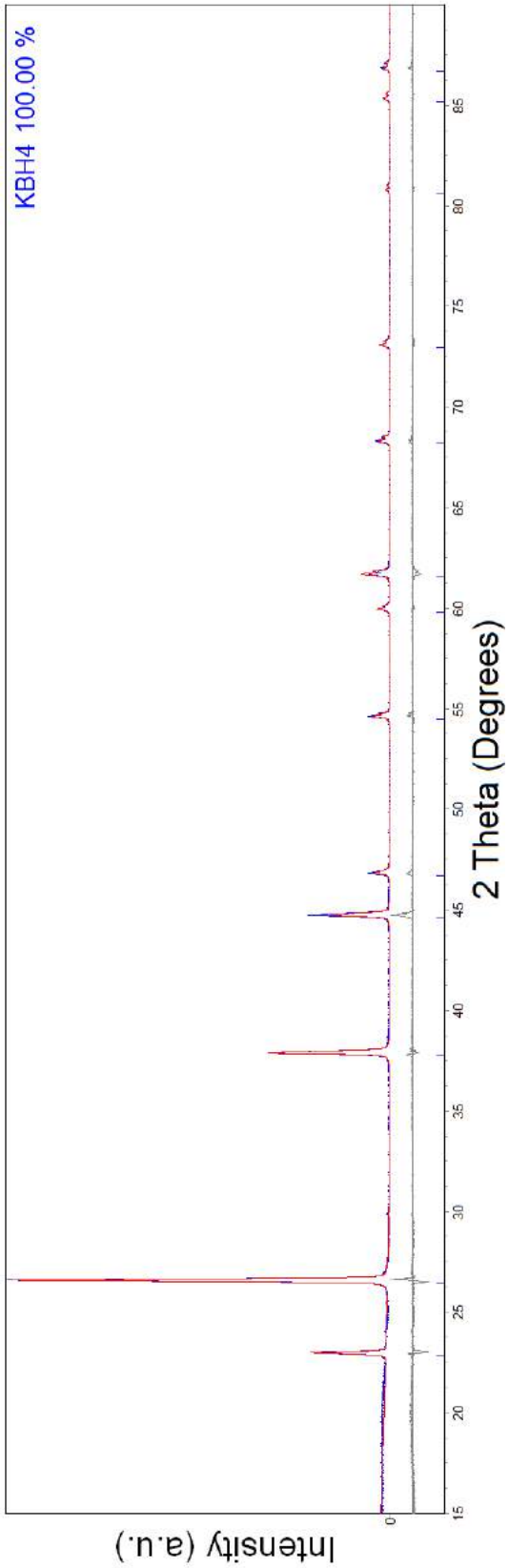

Figure 9.2 Pseudo-Rietveld refinement result of as-received KBH_4, including the observed XRD (Cu K_α radiation, λ = 1.5418 Å) profile (blue), the calculated profile (red, used to fit the observed profile) and the difference profile (grey). The goodness-of-fit was 1.809.

Table 9.1 Refined lattice parameter of as-received and as-milled KBH_4, comparing to literature values.

As-received	As-milled	Literature
6.733 ± 0.001	6.732 ± 0.002	6.7256 – 6.7280

In theory, the vibrations mode of $[BH_4]^-$ in KBH_4 included 4 internal vibrations (A_1, E, and two F_2 symmetries) that all could produce Raman scattering and only F_2 vibration symmetry could be viewed in the FTIR (K. B. Harvey & McQuaker 1971). In this work, all internal vibrations were observed in Raman and their wavenumbers are in good agreement with values in the literature (K. B. Harvey & McQuaker 1971; Zavorotynska et al. 2011). However, though all infrared active modes were observed, their wavenumbers were slightly lower than the values reported.

Table 9.2 Experiment frequencies (cm^{-1}) of as-received and as-milled KBH_4 observed in Raman and FRIT compared to literature values.

Mode			Raman			FTIR	
			Experiment		Literature	Experiment	Literature
			As-received	As-milled		As-received	
Internal	ν_4	F_2	1122	1122	1122	1111	1117
	ν_2	E	1250	1248	1249	-	-
	$2\nu_4$	A_1	2179	2180	2181	-	-
	$2\nu_4$	F_2	2216	2216	2217	2205	2213
	ν_3	F_2	2285	2286	2285	2269	2279
	ν_1	A_1	2308	2306	2310	-	-
	$\nu_2+\nu_4$	F_2	2377	2378	2380	2374	2377
	$2V_2$	A_1+E	2493	2495	2495	-	-

9.1.1.2 As-milled KBH_4

The as-milled sample was prepared using ball milling under the conditions described in Section 6.1.1. Its room temperature XRD, Raman and refinement results are shown in Figure 9.3-9.4.

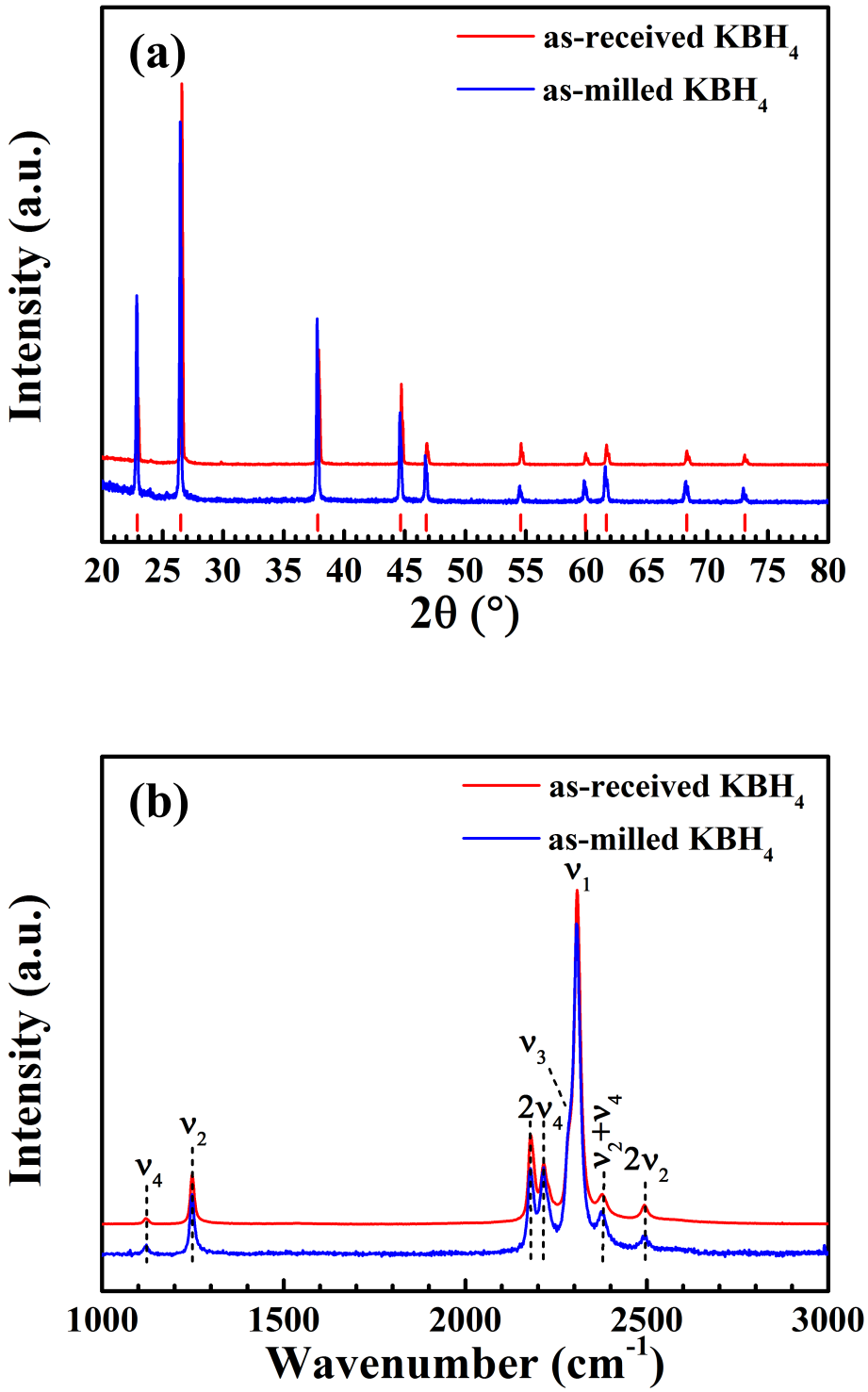

Figure 9.3 (a) XRD patterns (Cu K_α radiation, λ = 1.5418 Å) of as-milled KBH_4 at room temperature compared to the as-received material and an synchrotron XRD data (red vertical lines) from the literature (Dovgaliuk et al. 2014). (b) Raman spectra (measured with 488 nm laser and 2400 l/mm grating system) of as-received and as-milled KBH_4 at room temperature. Peaks were normalized for comparison. Dashed lines are guides for the eye.

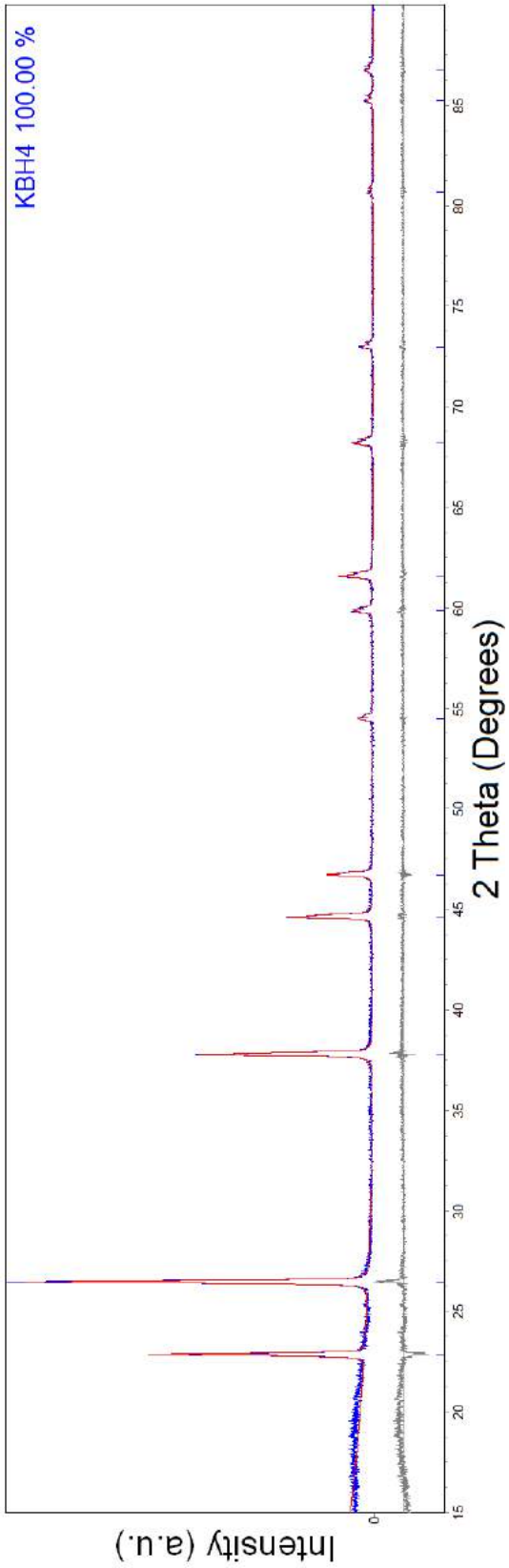

Figure 9.4 Pseudo-Rietveld refinement result of as-milled KBH_4, including the observed XRD (Cu K_α radiation, λ = 1.5418 Å) profile (blue), the calculated profile (red, used to fit the observed profile) and the difference profile (grey). The goodness-of-fit was 1.279.

The crystal structure and vibrational modes remained unchanged after ball milling. Although the milling process may reduce the lattice parameters (Lang et al. 2012), the refined lattice parameters for the as-milled sample were the same as for the as-received sample (Table 9.1).

9.1.2 Thermal Decomposition

Figure 9.5 shows the TPD-MS trace of as-milled KBH_4 heated up to 800 °C by 2 °C min^{-1} in Ar.

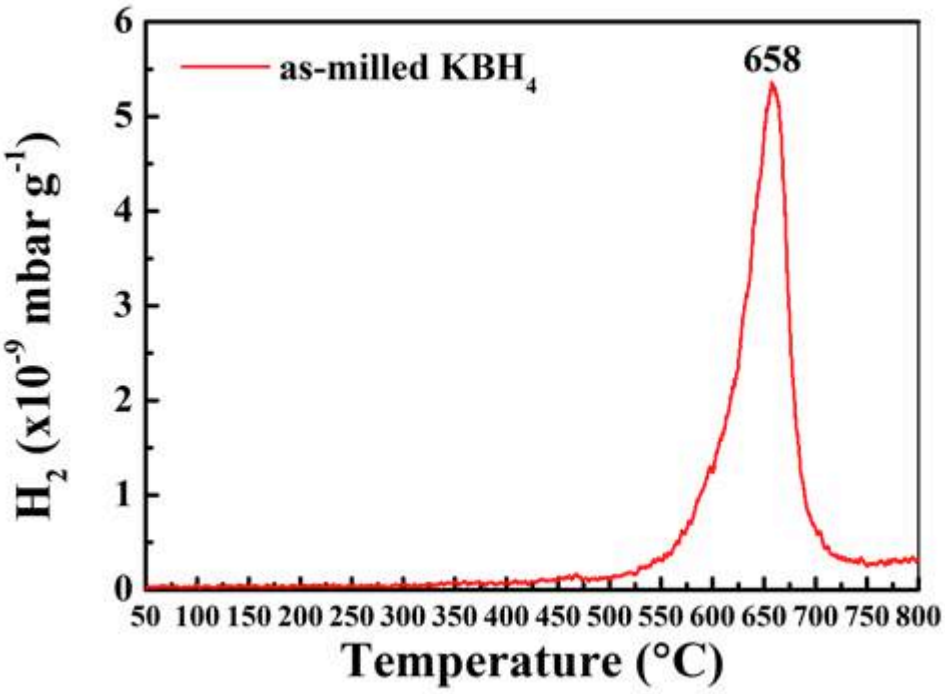

Figure 9.5 TPD-MS result of as-milled KBH_4 in the range 50–800 °C heated at 2 °C min^{-1} in TPD. The desorbed H_2 was carried by Ar flowing at 160 mL min^{-1}, measured by MS. No B_2H_6 was detected.

The KBH_4 had a better thermal stability than $LiBH_4$ and $NaBH_4$ (Nakamori & Orimo 2004; Nakamori et al. 2006; Nakamori et al. 2007; Harrison & Thonhauser 2016). Its

major dehydrogenation began at 550 °C followed by a peak at 658 °C. A total of 6.6 wt. % of hydrogen was released after heating to 800 °C (without B_2H_6). Because the melting point of KBH_4 was 625 °C (M Paskevicius et al. 2013), dehydrogenation lower than 625 °C (~2.1 wt.% of hydrogen) occurred from a solid-state sample. Figure 9.6 shows the room temperature XRD pattern of the decomposition products of KBH_4 heat-treated at 660 °C.

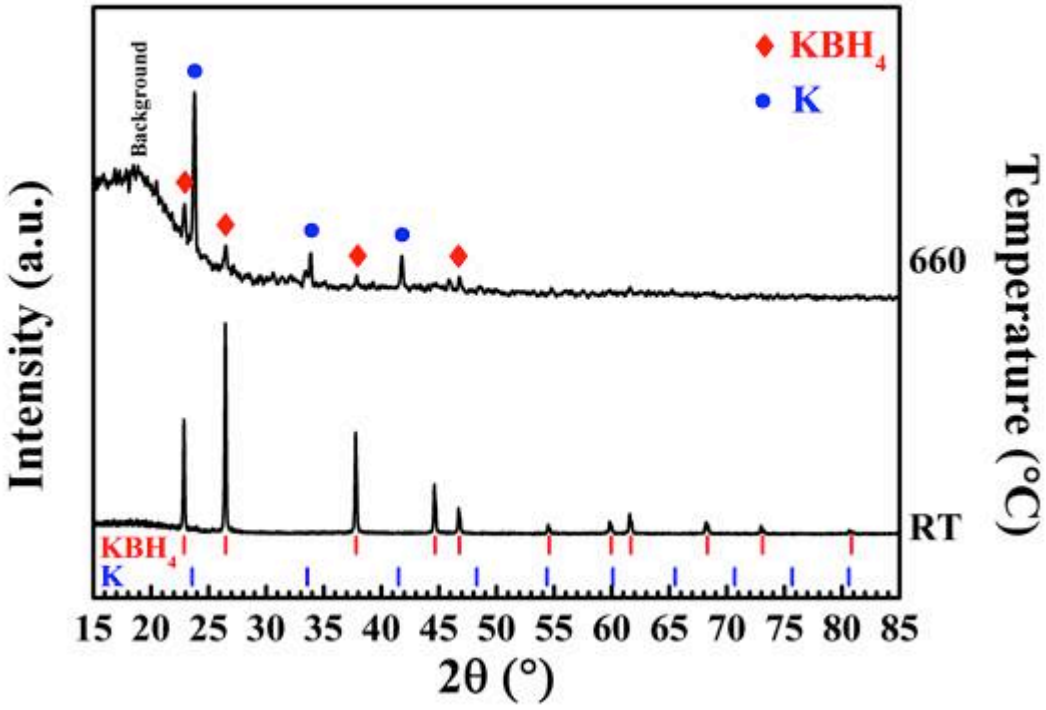

Figure 9.6 XRD pattern (Cu K_α radiation, λ = 1.5418 Å) of decomposed KBH_4 heat-treated to 800 °C by 2 C min^{-1} in Ar flowing at 160 mL min^{-1}, compared with the as-received KBH_4.

Signals associated to K were observed with the remained KBH_4, indicating the major dehydrogenation reaction was:

$$KBH_4 = K + B + 2H_2 \qquad \textbf{7.5 wt.\%} \qquad \textbf{Equation 9.1.}$$

However, the decomposition of KBH_4 might be similar to other borohydrides that went through different pathways and generated different metastable polyborane complexes (as a function of conditions), though these materials were not observed in this work. The remaining KBH_4 was possibly due to the sample outside hot zone caused by the bubbling-frothing effect (M Paskevicius et al. 2013).

In theory, about 7.5 wt.% hydrogen could be released from Equation 9.1 that was about 14% higher than the 6.6 wt.% measured in TPD-MS, possibly due to:

1) The KBH_4 loaded was not fully decomposed (Figure 9.6) as a consequence of its high thermal stability (Orimo et al. 2004; M Paskevicius et al. 2013) and/or the possibility of escaping the hot zone;
2) Other (XRD amorphous) intermediate phase(s) (KH or bi-products) might be formed.

9.2 Low-melting-point $0.75LiBH_4$-$0.25KBH_4$ Mixture

9.2.1 Sample Characterisations

The $0.75LiBH_4$-$0.25KBH_4$ mixture containing 0.5156 g $LiBH_4$ and 0.4844 g KBH_4 was prepared using ball milling under the conditions described in Section 6.1.1. Figure 9.7 shows the room temperature phases and vibration structures of as-milled and recrystallized $0.75LiBH_4$-$0.25LiBH_4$ mixtures. The recrystallized sample was prepared by a heat-treatment to 150 °C by 2 °C min^{-1} in Ar flowing at 160 mL min^{-1} and then freely cooled down to room temperature. This target temperature was chosen due to its low melting temperature (~105 °C) (M Paskevicius et al. 2013; Ley et al. 2014; Roedern et al. 2015).

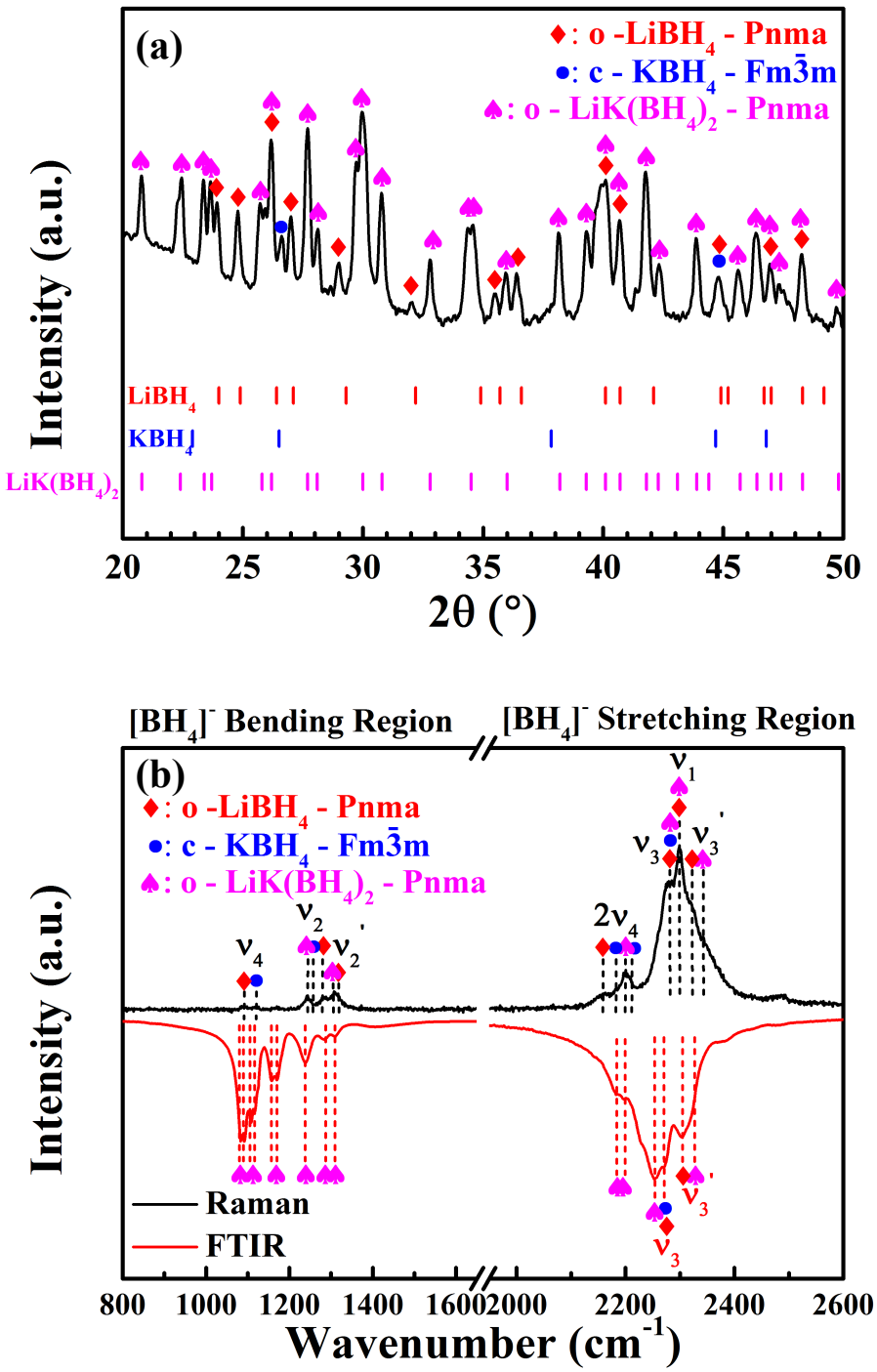

Figure 9.7 (a) Room temperature XRD pattern (Cu K_α radiation, λ = 1.5418 Å) (intensity in log scale) for as-milled $0.75LiBH_4$-$0.25KBH_4$ mixture; (b) room temperature Raman (measured with 488 nm laser and 2400 l/mm grating system) and FTIR spectra for as-milled $0.75LiBH_4$-$0.25KBH_4$ mixture; (c) room temperature XRD pattern (Cu K_α radiation, λ = 1.5418 Å) (intensity in log scale) for recrystallized $0.75LiBH_4$-$0.25KBH_4$ mixture; (d) room temperature Raman spectrum (measured with 488 nm laser and 2400 l/mm grating system) for recrystallized $0.75LiBH_4$-$0.25KBH_4$ mixture. The recrystallized sample was prepared by heat-treatment to 150 °C by 2 °C min^{-1} in Ar flowing at 160 mL min^{-1}.

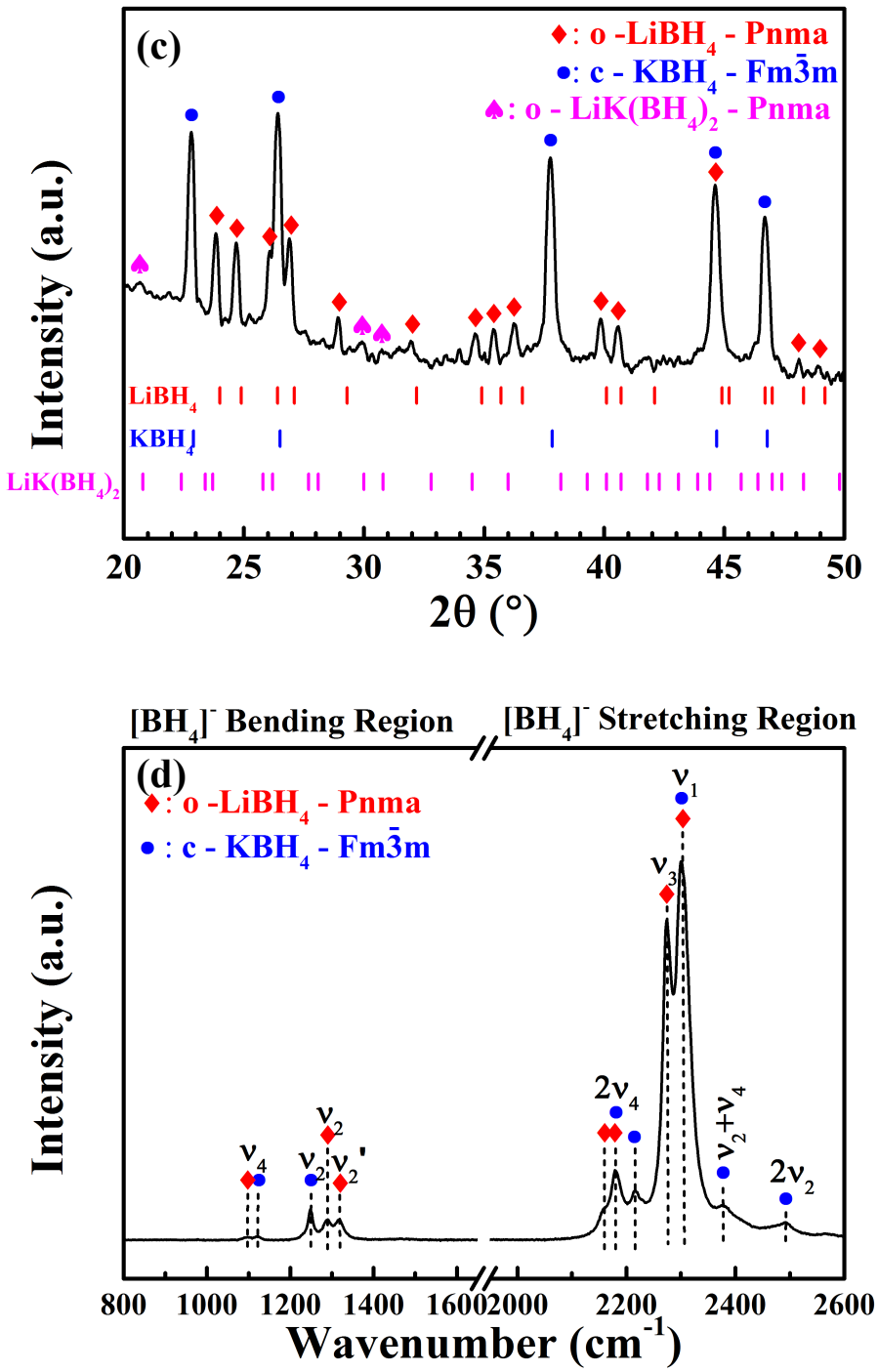

Figure 9.7 (a) Room temperature XRD pattern (Cu K_α radiation, λ = 1.5418 Å) (intensity in log scale) for as-milled $0.75LiBH_4$-$0.25KBH_4$ mixture; (b) room temperature Raman (measured with 488 nm laser and 2400 l/mm grating system) and FTIR spectra for as-milled $0.75LiBH_4$-$0.25KBH_4$ mixture; (c) room temperature XRD pattern (Cu K_α radiation, λ = 1.5418 Å) (intensity in log scale) for recrystallized $0.75LiBH_4$-$0.25KBH_4$ mixture; (d) room temperature Raman spectrum (measured with 488 nm laser and 2400 l/mm grating system) for recrystallized $0.75LiBH_4$-$0.25KBH_4$ mixture. The recrystallized sample was prepared by heat-treatment to 150 °C by 2 °C min^{-1} in Ar flowing at 160 mL min^{-1}.

The XRD and Raman results confirmed the formation of $LiK(BH_4)_2$ caused by pressure due to ball-milling (Kim & Sholl 2010; Tuan et al. 2014; Ley et al. 2014), via:

$$LiBH_4 + LiBH_4 \xrightarrow{Ball-milling} LiK(BH_4)_2 \qquad \textbf{Equation 9.2}$$

This is a metastable phase that will decompose into its constituents above 95 °C (Ley et al. 2014). In this work, its XRD intensity became significantly weak and its vibrational modes were not observed in the Raman in the recrystallized sample.

Table 9.3 summarized the observed Raman shifts of the as-milled and recrystallized $0.75LiBH_4$-$0.25KBH_4$ mixtures compared to literature (K B Harvey & McQuaker 1971; K. B. Harvey & McQuaker 1971; Gomes et al. 2002; Racu et al. 2008; Nickels 2010; Zavorotynska et al. 2011).

Figure 9.8 shows the pseudo-Rietveld refinement results of the as-milled and recrystallized $0.75LiBH_4$-$0.25KBH_4$ mixtures. The molar percentage of $LiBH_4$ and KBH_4 in the as-milled sample was 75 ± 2 mol% for $LiBH_4$ and 25 ± 2 mol% for KBH_4, which were achieved from the refined weight percentage (36.3 ± 0.9 wt. % for $LiBH_4$, 0.6 ± 0.1 wt. % for KBH_4 and 63.1 ± 0.9 wt. % for $LiK(BH_4)_2$) (Table 9.4). This molar ratio (75:25) was slightly different from the reported eutectic composition (0.725:0.275), yielding a $LiBH_4$-rich compound. The recrystallized sample mixture contained 72 ± 2 mol% $LiBH_4$ with 28 ± 2 mol% KBH_4 that was similar to the as-milled sample.

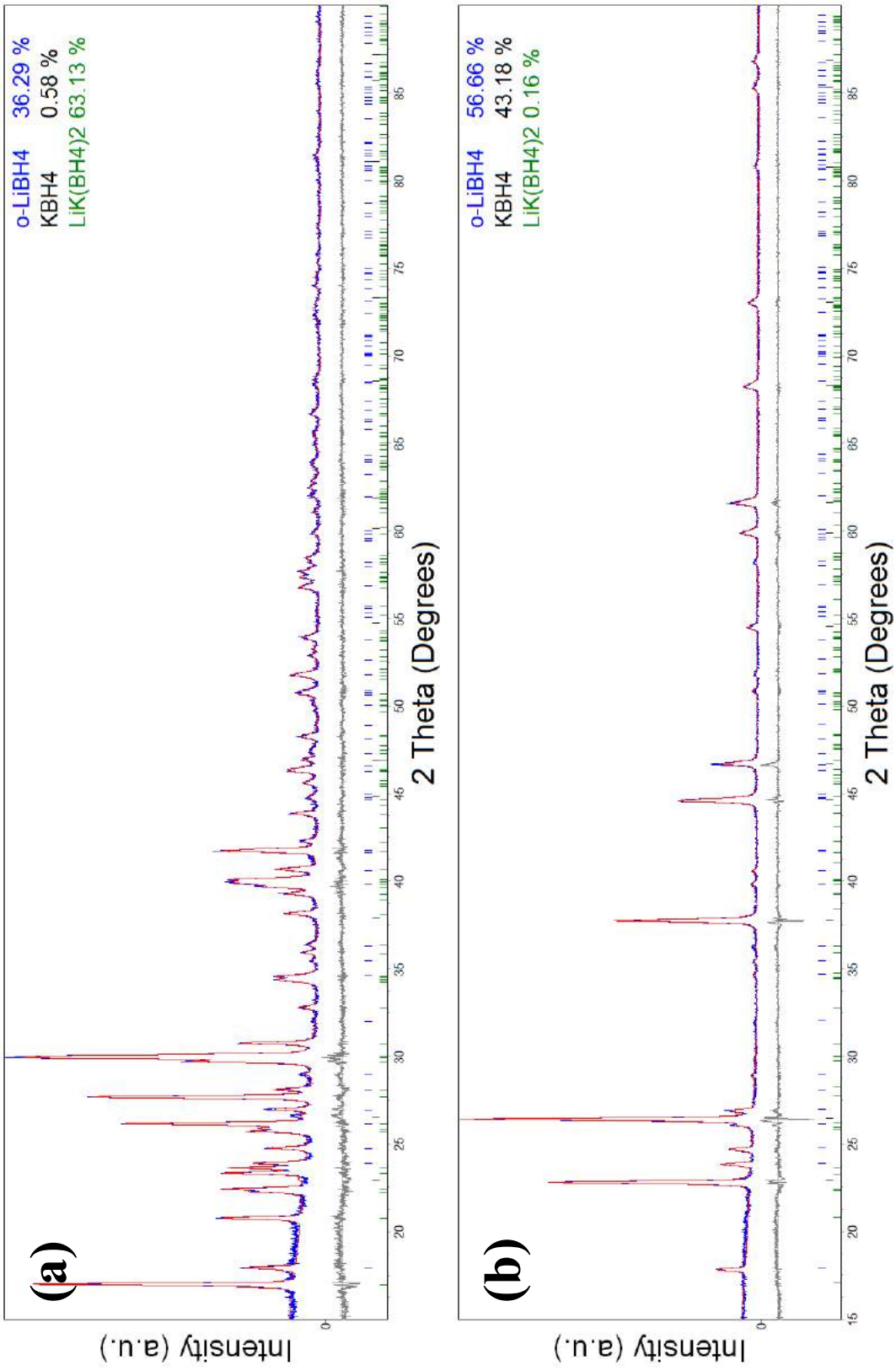

Figure 9.8 Pseudo-Rietveld refinement results of (a) as-milled and (b) recrystallized $0.75LiBH_4$-$0.25KBH_4$ mixtures, including the observed XRD (Cu K_α radiation, λ = 1.5418 Å) profile (blue), the calculated profile (red, used to fit the observed profile) and the difference profile (grey) in each figure. The goodness-of-fit values for (a) and (b) were 1.216 and 1.327, respectively.

Table 9.3 Experiment frequencies (cm^{-1}) of as-milled and recrystallized $0.75LiBH_4$-$0.25KBH_4$ mixtures observed in Raman compared to literature values.

Mode		$LiBH_4$		KBH_4		$LiK(BH_4)_2$	$0.75LiBH_4$-$0.25KBH_4$	
		As-milled	Literature	As-milled	Literature	Literature	As-milled	Recrystallized
ν_4	A_g	1096	1090	-	-	-	1092	1097
ν_4		-	-	-	-	1106	n.a.	n.a.
ν_4	F_2	-	-	1122	1122	-	1122	1123
ν_4'	A_g	n.a.	1235	-	-	-	n.a.	n.a.
ν_2		-	-	-	-	1242	1243	n.a.
ν_2	E	-	-	1248	1249		1252	1248
ν_2	B_{1g}	1290	1286	-	-	-	1284	1286
ν_2'		-	-	-	-	1311	1309	n.a.
ν_2'	A_g	1319	1316	-	-	-	1319	1319
$2\nu_4$		2163	2156	-	-	-	2159	2158
$2\nu_4'$		2180	2177	-	-	-	n.a.	2179
$2\nu_4$	A_1	-	-	2180	2181	-	2181	2180
$2\nu_4$		-	-	-	-	2200	2200	n.a.
$2\nu_4$	F_2	-	-	2216	2217	-	2211	2217
ν_3	A_g	2273	2275	-	-	-	2273	2274
ν_3		-	-	-	-	2282	2279	n.a.
ν_3	F_2	-	-	2286	2285		2285	n.a.
ν_1		-	-	-	-	2298	2299	n.a.
ν_1	A_g	2299	2301	-	-	-	2299	2301
ν_1	A_1	-	-	2306	2310	-	n.a.	n.a.
ν_3'	A_g	2318	2321	-	-	-	2322	n.a.
$\nu_2+\nu_4$	F_2	-	-	2378	2380		n.a.	2377
$2V_2$	A_1+E	-	-	2495	2495		n.a.	2493

Table 9.4 Summary of Pseudo-Rietveld refined weight percentages and their equivalent molar percentage in eutectic form for as-milled and recrystallized $0.75LiBH_4$-$0.25KBH_4$.

	As-milled		Recrystallized	
Component	Refined wt. %	Equivalent mol%	Refined wt. %	Equivalent mol%
$LiBH_4$	36.3 ± 0.9	75 ± 2	56.6 ± 1.0	72 ± 2
KBH_4	0.6 ± 0.1	25 ± 2	43.2 ± 1.0	28 ± 2
$LiK(BH_4)_2$	63.1 ± 0.9	-	0.2 ± 0.1	-

The refined crystal structure parameters of $LiBH_4$ and KBH_4 components in the as-milled and recrystallized $0.75LiBH_4$-$0.25KBH_4$ mixtures are summarised in Table 9.5, compared with those parameters of as-milled pure compounds.

Table 9.5 Refined crystal structure parameters of $LiBH_4$ and KBH_4 components in as-milled and recrystallized $075LiBH_4$-$0.25NaBH_4$ mixture in contrast to those parameters of as-milled pure compounds.

	o-$LiBH_4$			c-KBH_4		
	Pure	Mixture		Pure	Mixture	
	As-milled	As-milled	Recrystallized	As-milled	As-milled	Recrystallized
a (Å)	7.199 ± 0.003	7.187 ± 0.001	7.184 ± 0.002	6.732 ± 0.002	6.702 ± 0.003	6.724 ± 0.001
b (Å)	4.438 ± 0.002	4.442 ± 0.001	4.438 ± 0.001	-	-	-
c (Å)	6.798 ± 0.002	6.817 ± 0.002	6.813 ± 0.002	-	-	-
V (Å^3)	*216.84 ± 0.10*	*217.64 ± 0.07*	*217.21 ± 0.08*	*305.15 ± 0.06*	*300.99 ± 0.35*	*304.04 ± 0.15*

Since the majority of KBH_4 reacted with $LiBH_4$ and was consumed during ball milling, its XRD intensity became very weak (Figure 9.7-a) that lowered the refinement accuracy. Therefore, the unit cell volume of KBH_4 in the as-milled $0.75LiBH_4$-$0.25KBH_4$ mixture (300.99 ± 0.35 Å^3) was significantly reduced compared with as-milled pure KBH_4 (305.15 ± 0.06 Å^3). After heat treatment, the XRD peaks of KBH_4 became obvious in the recrystallized sample (Figure 9.7-c). The refined lattice parameter after recrystallization was similar to that for pure KBH_4.

As Dematteis et al. (2017) suggests there is no solubility of Li^+ in c-KBH_4 or K^+ in o-$LiBH_4$, the formation of solid solutions between $LiBH_4$ and KBH_4 became impossible, which was different from the $0.62LiBH_4$-$0.38NaBH_4$ mixture.

9.2.2 Thermal Analysis

Figure 9.9 shows the DSC traces of the as-milled $0.75LiBH_4$-$0.25KBH_4$ mixture compared with that for as-milled $LiBH_4$. The as-milled KBH_4 was not tested due to its relatively high stability (M Paskevicius et al. 2013).

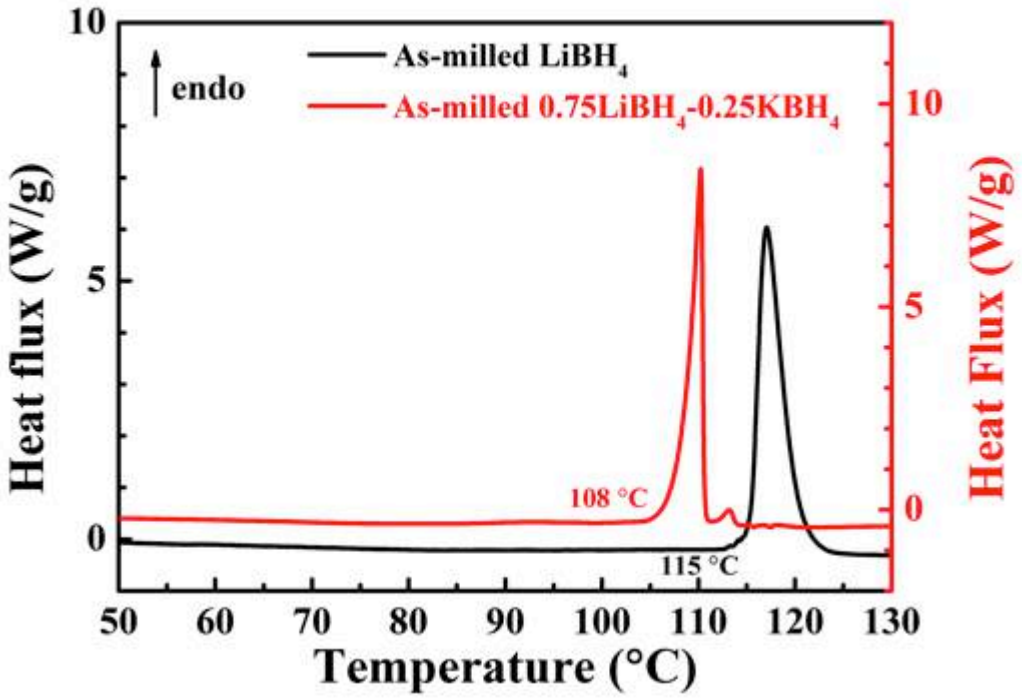

Figure 9.9 DSC results of as-milled $0.75LiBH_4$-$0.25KBH_4$ mixture, compared to as-milled $LiBH_4$. Samples were heated at 5 °C min^{-1}. To protect the instrument, the measurement was operated under a 2 bar static H_2.

The melting point of as-milled $0.75LiBH_4$-$0.25KBH_4$ mixture was 108 ± 1 °C. It was even lower than the 115 ± 1°C for the orthorhombic to hexagonal phase transition of $LiBH_4$, and much lower than the melting points for as-milled $LiBH_4$ (285 ± 1 °C, Figure 7.5) and KBH_4 (625 °C) (M Paskevicius et al. 2013). The enthalpy of fusion was 5.3 ± 0.3 kJ mol^{-1} and was lower than the 10.7 kJ mol^{-1} reported by Ley et al. (2014). A small peak at 113 °C (0.3 kJ mol^{-1}) was observed following the major peak for an unknown reason. This disagreed with Ley et al. (2014), where this 2nd endothermic peak was not presented. It may be because of the phase transformation of $LiBH_4$ as the as-milled sample contained excess $LiBH_4$ compared with the suggested eutectic composition.

9.2.3 Thermal Decomposition

Figure 9.10 shows the TPD-MS trace for the as-milled $0.75LiBH_4$-$0.25KBH_4$ mixture in contrast to the as-milled $LiBH_4$ and as-milled KBH_4, when heated to 700 °C at 2 °C min^{-1} in Ar. Since these data were measured at different time periods that required different calibration files, their intensities were normalized for a fair comparison.

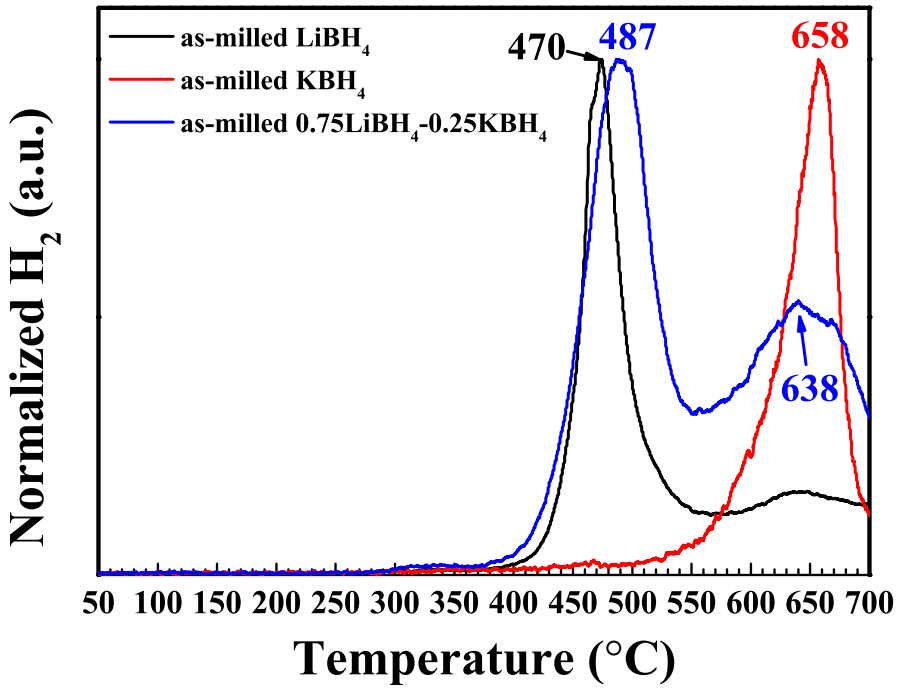

Figure 9.10 TPD-MS hydrogen desorption traces of as-milled $0.75LiBH_4$-$0.25KBH_4$ mixture, compared with as-milled $LiBH_4$ and as-milled KBH_4. Samples were heated at 2 °C min^{-1} in flowing Ar at 160 mL min^{-1}. No B_2H_6 was detected.

The dehydrogenation of as-milled $LiBH_4$ (black line) started at 285 °C followed by a peak at 470 °C. A total of 10.9 wt. % hydrogen was released after heating to 700 °C.

The major dehydrogenation of as-milled KBH_4 (red line) began above 550 °C, with a peak at 658 °C. A total of 6.1 wt. % hydrogen was released after heating to 700 °C.

The as-milled $0.75LiBH_4$-$0.25KBH_4$ mixture had a similar onset desorption temperature (290 °C) in contrast to the as-milled $LiBH_4$ (285 °C), indicating that the presence of K^+ did not significantly affect the initiation of dehydrogenation. Two H_2 desorption peaks were observed at 487 °C and 638 °C, which were higher than the 470 °C for as-milled $LiBH_4$ and lower than the 658 °C for as-milled KBH_4. Similar temperature shifts have been observed in $0.62LiBH_4$-$0.38NaBH_4$ system (Section 8.2.3) as a consequence of mixing of cations with different electronegativities. A total of 8.9 wt.% hydrogen was released upon heating to 700 °C. This was 18% less than the 10.9 wt.% from as-milled $LiBH_4$, but was 46% higher than the 6.1 wt.% released from as-milled KBH_4.

Figure 9.11 shows the room temperature XRD and Raman results of decomposition products of as-milled $0.75LiBH_4$-$0.25KBH_4$ after heat treatment at 150 °C, 490 °C, 640 °C and 700 °C in Ar.

For the heat-treated sample at 490 °C, the presence of LiH in XRD and B and $Li_2B_{12}H_{12}$ in Raman suggested that the 1st dehydrogenation route (290-550 °C) was due to the decomposition of $LiBH_4$.

Moreover, KH, K and remaining KBH_4 phases in XRD sample at 640 °C confirmed the dehydrogenation of KBH_4 content during the 2nd decomposition route (> 550 °C). The formation of KH was due to reaction between the H_2 desorbed from the reactant and the K outside the heating zone. The escaped K could be caused by the bubbling-frothing effect (M Paskevicius et al. 2013) or the moveable gaseous potassium (Kumar et al. 2017).

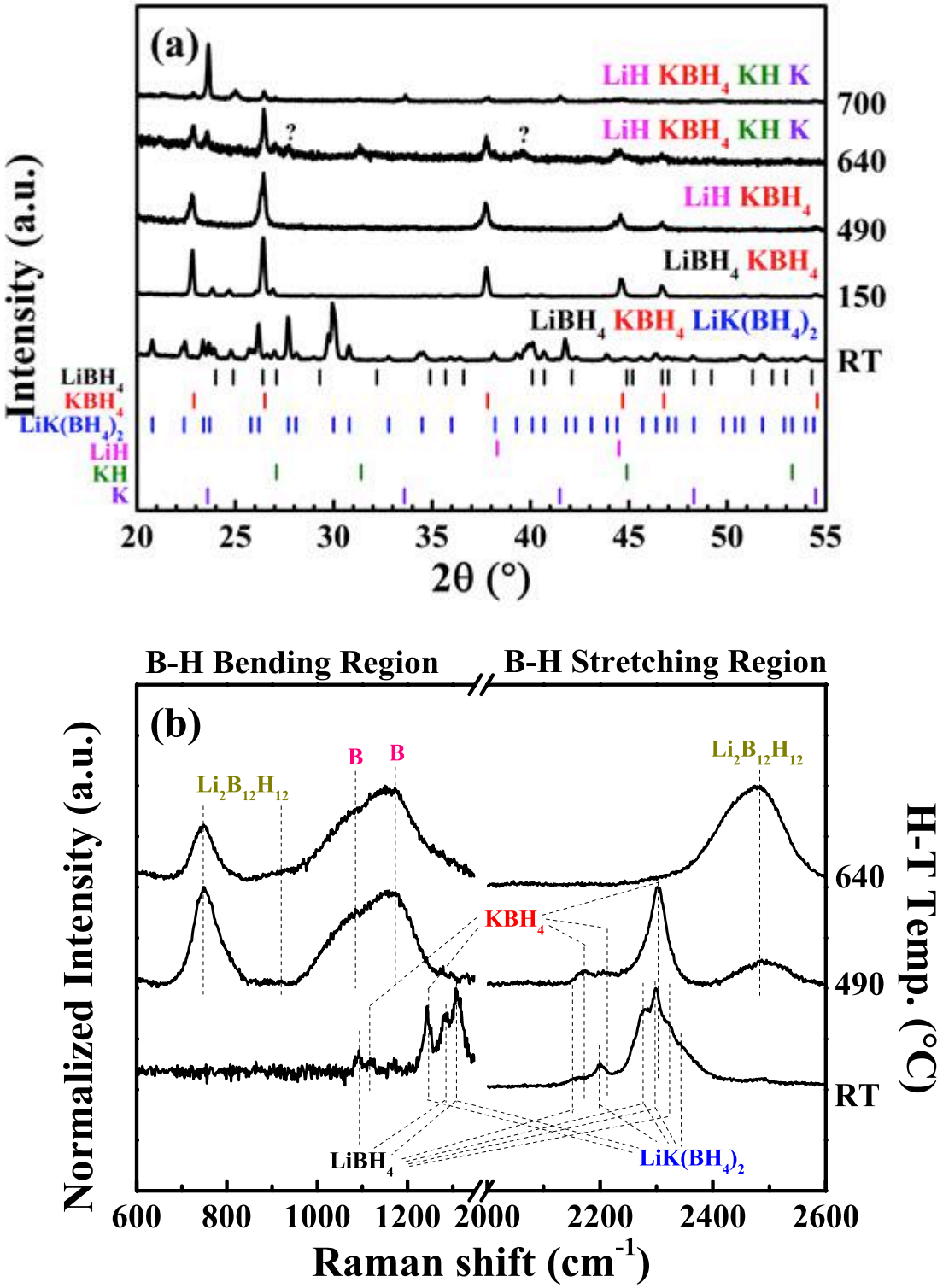

Figure 9.11 Room temperature (a) XRD patterns (Cu K_α radiation, λ = 1.5418 Å) and (b) Raman spectra (measured with 488 nm laser and 2400 l/mm grating system) of as-milled $0.75LiBH_4$-$0.25KBH_4$ mixture, which had been heat-treated at 150 °C, 490 °C, 640 °C and 700 °C by 2 °C min^{-1} in Ar flowing at 160 mL min^{-1}. The intensities of the XRD and Raman peaks were normalized. A horizontal break was used to divide the Raman spectra (b) into B-H bending and B-H stretching regions of $[BH_4]^-$ (normalized separately). Dashed lines are guides for the eye.

Two unknown X-ray peaks were observed at 27.8 °and 39.6 ° for the sample heat-treated at 640 °C. They were very likely caused by the oxidation of products, such as K_2O (Carter et al. 1952).

The entire amount of H_2 release (including heating and cooling) from the as-milled $0.75LiBH_4$-$0.25KBH_4$ mixture was 10.0 wt.%. The curve area ratio of the two-dehydrogenation peaks in Figure 9.10 was 48:52 (obtained by a Gaussian peak fitting, $R^2 = 0.9957$) that was very close to 1:1, indicating that the quantity of H_2 release from each reaction step was similar (e.g. 4.8 wt.% for the 1st step and 5.2 wt.% for the 2nd step). However, these experimental values disagreed with the expected ranges in principle: 7.5-10.4 wt.% dehydrogenated from 0.75 moles of $LiBH_4$ (through Equation 7.2 forming LiH, B, H_2 or via Equation 7.3 forming LiH, $Li_2B_{12}H_{12}$, H_2); and 1.4-1.9 wt.% from 0.25 moles of KBH_4 (via Equation 9.1 forming K, B, H_2 or through Equation 3.23 forming KH, B H_2). These disagreements indicate a strong cation interaction that affects the dehydrogenation of $LiBH_4$, suggesting that at least 3.3 wt.% of hydrogen release from the 2nd step is due to the precipitation of LiH, B and/or $Li_2B_{12}H_{12}$.

Figure 9.12 schematically summaries the decomposition process (in Ar) of $0.75LiBH_4$-$0.25KBH_4$.

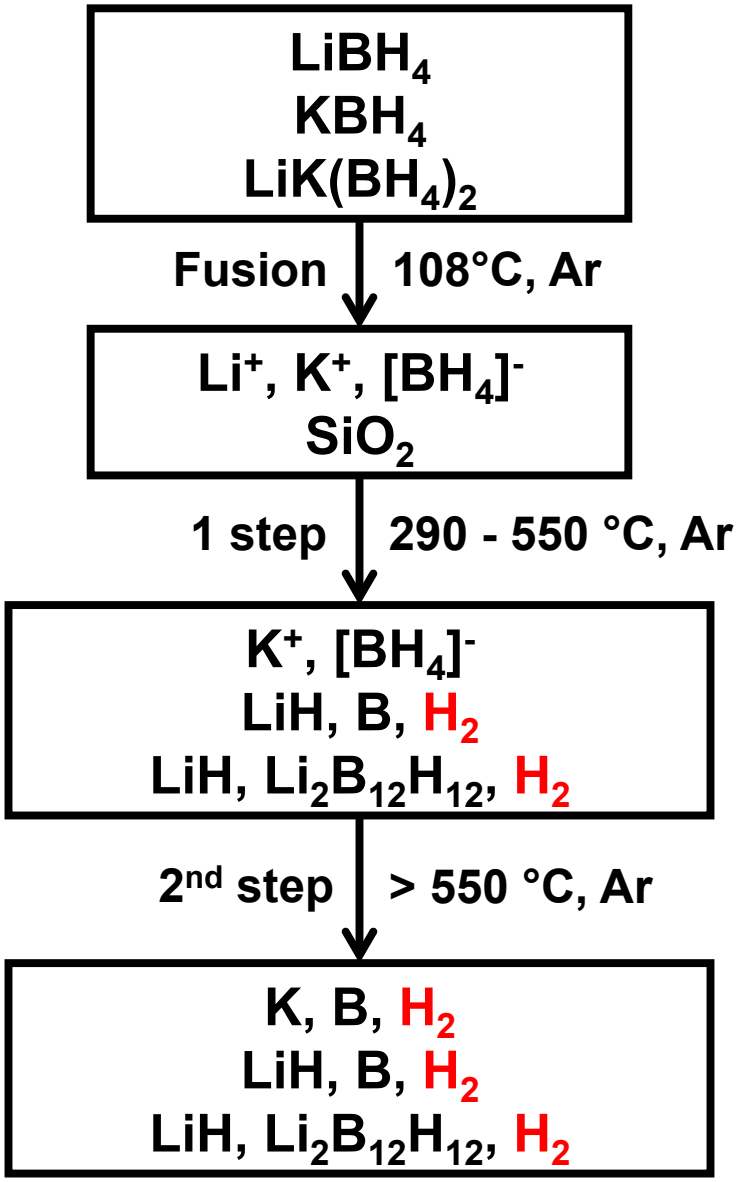

Figure 9.12 A flow chart of decomposition pathways of the as-milled 0.75$LiBH_4$-0.25KBH_4 in Ar.

9.2.4 Recombination

The reversibility test of the as-milled 0.75$LiBH_4$-0.25KBH_4 mixture was carried out using a Sieverts type apparatus as described in Section 6.2.6. The reaction conditions were: 500 °C, 1 bar H_2 and 10 h for desorption; and 400 °C, 130 bar H_2 and 12 h for absorption. The PCI results are shown in Figure 9.13. The XRD and FTIR results in its reabsorbed states after being cycled three times are shown in Figure 9.14.

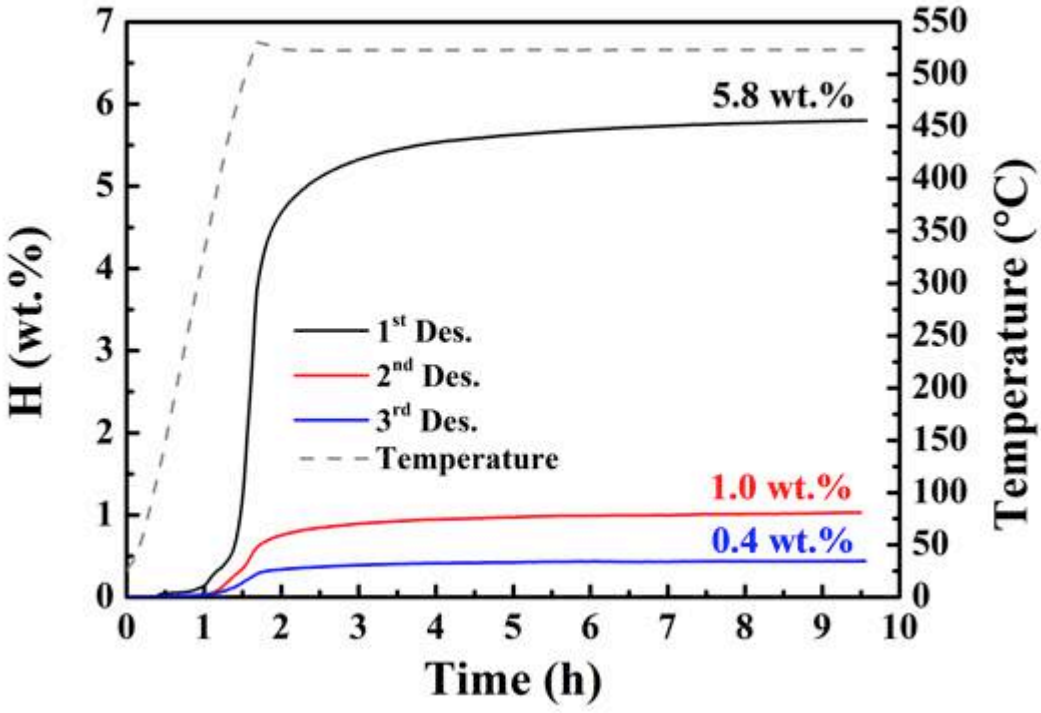

Figure 9.13 Sievert's measurements showing hydrogen release (in wt.%) while keeping the $0.75LiBH_4$-$0.25KBH_4$ mixture under 1 bar H_2 at 500 °C ($\Delta T/\Delta t$ = 5 °C min^{-1}) for 10 h for desorption and under 130 bar H_2 at 400 °C for 12 h for rehydrogenation.

The as-milled $0.75LiBH_4$-$0.25KBH_4$ sample desorbed a total of 5.8 wt.% hydrogen during the 1st dehydrogenation in 1 bar H_2. This value was about 20% lower than the reported 7.3 wt.% from a $0.725LiBH_4$-$0.275KBH_4$ mixture using a PCT Pro 2000 Sieverts' apparatus (500 °C by 3 °C min^{-1} in 1 bar H_2 for 4 h) (Roedern et al. 2015). In general, this mixture had a poor cycling stability as the reversible hydrogen content reduced dramatically to 1.0 wt.% and 0.4 wt.% at the 2nd cycle and the 3rd cycle, respectively. This reduction of hydrogen uptake has also been observed for the $0.725LiBH_4$-$0.275KBH_4$ mixture by Roedern et al. (2015), where the material reabsorbed ~ 3.0 wt.% at both the 2nd cycle and the 3rd cycle (400 °C in 100 bar H_2 for 12 h for absorption).

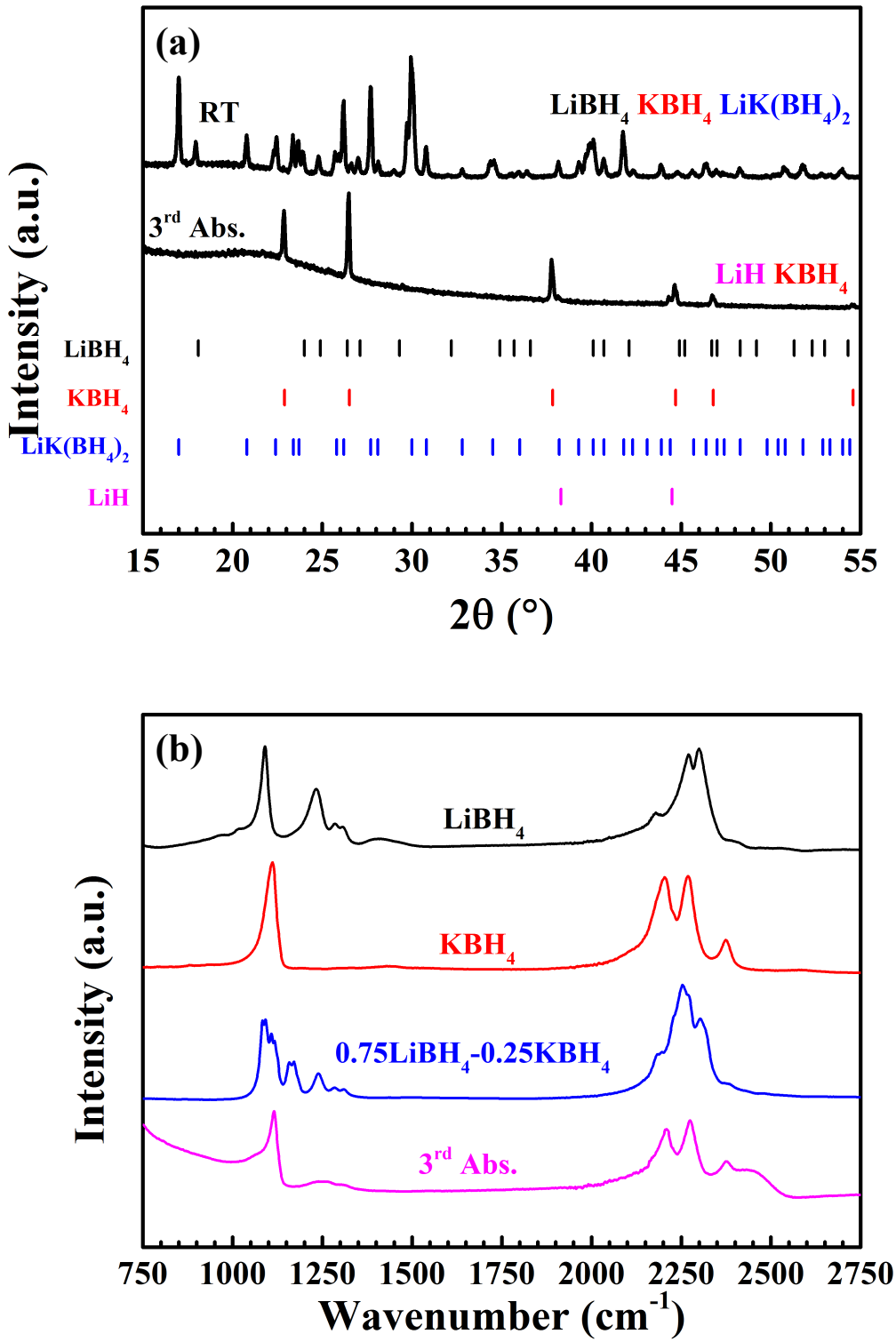

Figure 9.14 (a) XRD pattern (Cu K_α radiation, λ = 1.5418 Å) and (b) FTIR spectrum for the as-milled $0.75LiBH_4$-$0.25KBH_4$ mixture decomposed at 500 °C in 1 bar static H_2 for 10 h (denoted as 1st Des.) and recombined with 130 bar H_2, 400 °C for 12 h at the 3rd cycle (denoted as 3rd Abs.).

The rehydrogenated $0.75LiBH_4$-$0.25KBH_4$ mixture (Figure 9.14) contained LiH (XRD) and KBH_4 (XRD, FTIR), indicating stable KBH_4 component during cycling due to its high thermal stability. Besides, the $LiBH_4$ component was not reversible under the applied conditions. Roedern et al. (2015) suggests that the poor reversibility of $LiBH_4$ in this type low-melting-point borohydride mixture cannot be improved by using nano-confinement under the applied conditions as follows: 500 °C, 1 bar H_2 and 4 h for desorption; and 400 °C, 100 bar H_2 and 12 h for absorption. Thus, to partially reform $LiBH_4$, a stronger conditions might be required, such as: 600°C, 350 bar H_2, 12 h (Orimo et al. 2005).

9.3 Decomposition with the addition of 5 mol% SiO_2

An addition of 5 mol% micron-sized SiO_2 could destabilize the decomposition of $LiBH_4$, especially in the low temperature range (Section 7.2). This additive was used to try to destabilize the $0.75LiBH_4$-$0.25KBH_4$ mixture, and the modified dehydrogenation pathways were studied.

9.3.1 Sample Characterisations

The $0.95(0.75LiBH_4$-$0.25KBH_4)$-$0.05SiO_2$ mixture was prepared by hand mixing, where 0.0936 g micron-sized SiO_2 (Alfa Aesar, 99.9%, 0.5 μm) was added to 0.9064 g as-milled $0.75LiBH_4$-$0.25KBH_4$. The as-prepared sample was characterized using XRD and Raman (Figure 9.15), where only $LiBH_4$, KBH_4 and $LiK(BH_4)_2$ were shown. Due to its low quantity, SiO_2 signals were not observed.

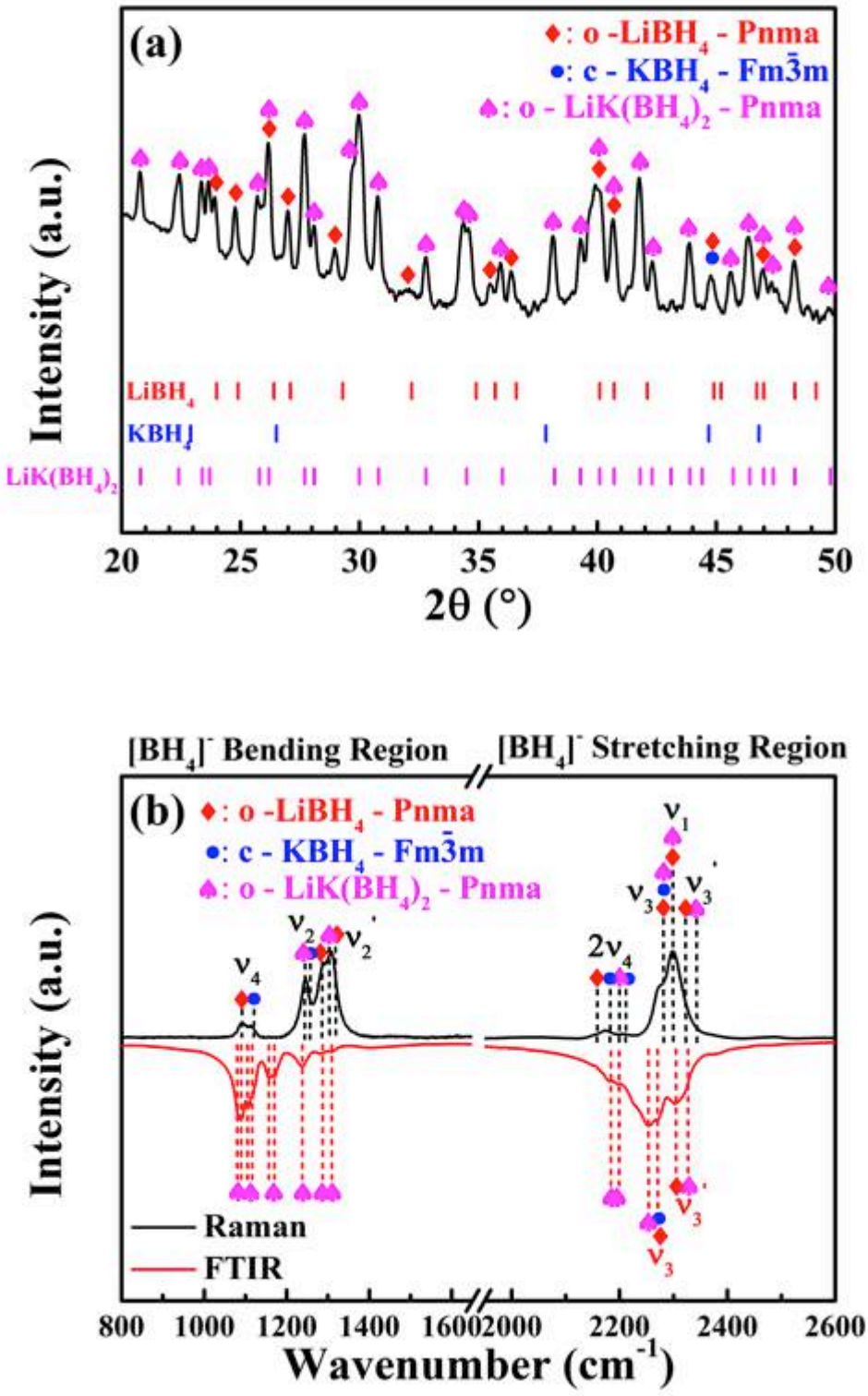

Figure 9.15 (a) XRD pattern (Cu K_α radiation, λ = 1.5418 Å) (intensity in log scale) and (b) Raman and (measured with 488 nm laser and 2400 l/mm grating system) FTIR spectra for the as-prepared $0.95(0.75LiBH_4\text{-}0.25KBH_4)\text{-}0.05SiO_2$ mixture, measured at room temperature.

9.3.2 Thermal Analysis

Figure 9.16 shows the DSC trace of the as-prepared $0.95(0.75LiBH_4\text{-}0.25KBH_4)\text{-}0.05SiO_2$ mixture, compared with the SiO_2-free mixture. These measurements were performed from 50 to 150 °C at 5 °C min^{-1} in Ar flowing at 70 mL min^{-1}.

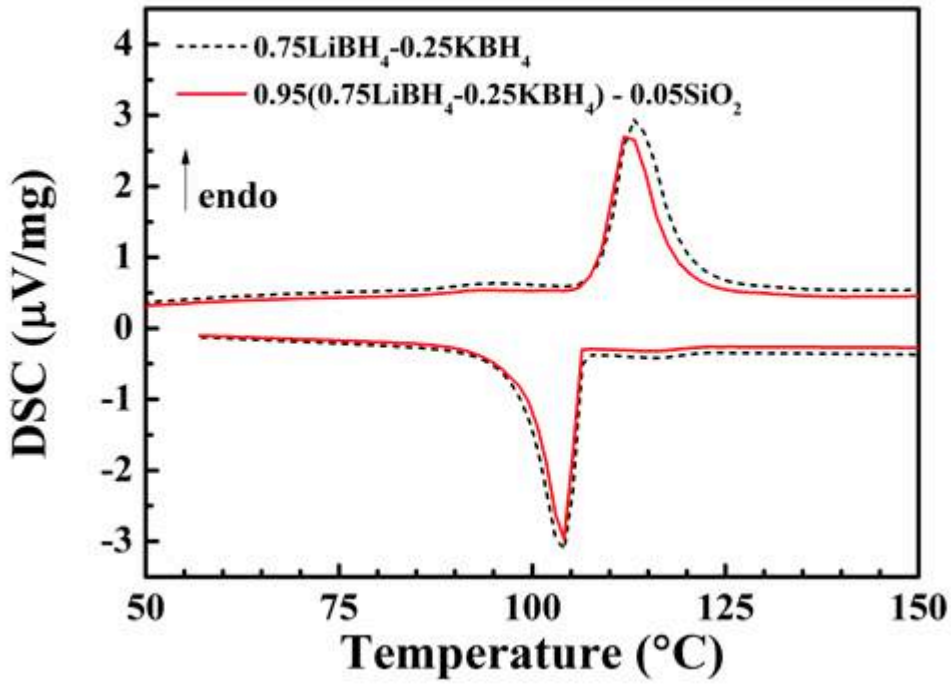

Figure 9.16 DSC results of as-prepared $0.95(0.75LiBH_4\text{-}0.25KBH_4)\text{-}0.05SiO_2$ mixture (red solid line), compared with the as-milled $0.75LiBH_4\text{-}0.25KBH_4$ (black dash line). Samples were heated from 50 to 150 °C at 5 °C min^{-1} in Ar flowing at 70 mL min^{-1}.

In general, the addition of SiO_2 did not affect the melting behaviour of $0.95(0.75LiBH_4\text{-}0.25KBH_4)\text{-}0.05SiO_2$ mixture. Compared with the SiO_2-free sample, the $0.95(0.75LiBH_4\text{-}0.25KBH_4)\text{-}0.05SiO_2$ mixture had the same fusion (108 ± 1 °C) and solidification temperatures (106 ± 1 °C), and similar curve areas (Table 9.6). These curve areas were linearly linked to enthalpy of phase change.

Table 9.6 DSC curve areas for as-prepared 0.95(0.75$LiBH_4$-0.25KBH_4)-0.05SiO_2 compared with as-milled 0.75$LiBH_4$-0.25KBH_4.

	Sample	Energy	
		Heating	Cooling
		Fusion	Solidification
		μV mg^{-1} LiK	μV mg^{-1} LiK
1	0.75$LiBH_4$-0.25KBH_4	20.8 ± 1.0	17.9 ± 0.9
2	0.95(0.75$LiBH_4$-0.25KBH_4)-0.05SiO_2	20.5 ± 1.0	17.1 ± 0.9

9.3.3 Thermal Decomposition

Figure 9.17 shows the TPD-MS trace for the as-prepared 0.95(0.75$LiBH_4$-0.25KBH_4)-0.05SiO_2 mixture compared with SiO_2-free mixture. These samples were heated to 700 °C by 2°C min^{-1} in Ar. No B_2H_6 was observed.

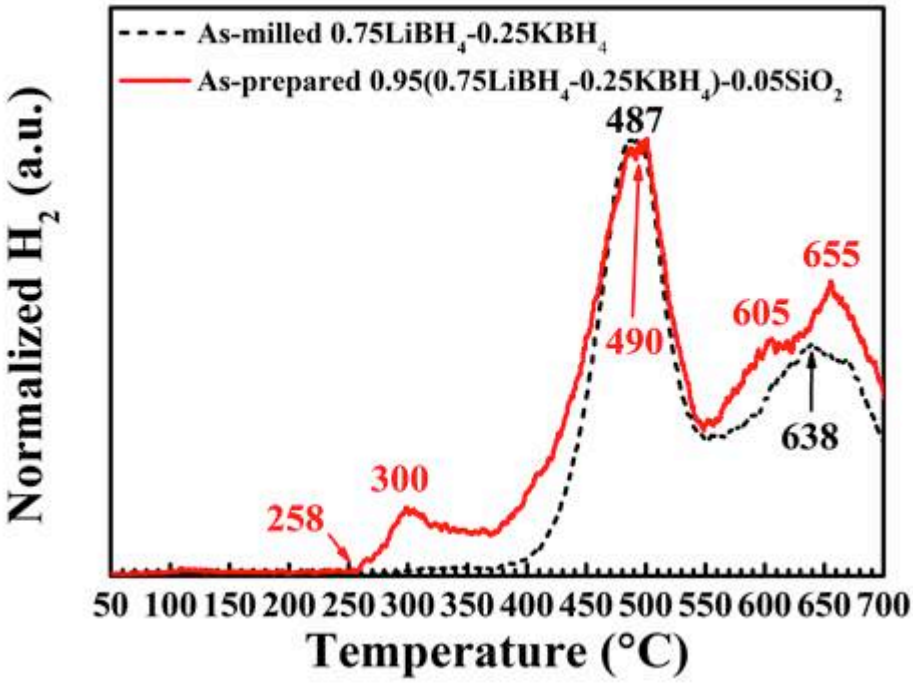

Figure 9.17 TPD-MS hydrogen desorption traces of as-prepared 0.95(0.75$LiBH_4$-0.25KBH_4)-0.05SiO_2 mixture, compared with as-milled 0.75$LiBH_4$-0.25KBH_4. Samples were heated at 2 °C min^{-1} in flowing Ar at 160 mL min^{-1}. Peak intensities were normalized due to different TPD-MS calibration files were used. No B_2H_6 was detected.

Due to the addition of SiO_2, the H_2 release from the $0.95(0.75LiBH_4\text{-}0.25KBH_4)\text{-}0.05SiO_2$ mixture started from 258 °C, which was 32 °C lower than the 290 °C for the SiO_2-free sample. The dehydrogenation of the $0.95(0.75LiBH_4\text{-}0.25KBH_4)\text{-}0.05SiO_2$ mixture could be divided into 3 parts: a small peak at 300 °C, a major peak at 490 °C, and a broad area consisting of peaks at 605 °C (shoulder) and 655 °C. The major peak at 490 °C was very close to the 488 °C for the SiO_2-free sample, whilst the broad area overlapped with the 2nd dehydrogenation peak (638 °C) of the SiO_2-free sample, suggesting that the SiO_2 additive did not provide any significant destabilization effect on dehydrogenation peak temperatures.

About 1.1 wt.% of hydrogen was released from the $0.95(0.75LiBH_4\text{-}0.25KBH_4)\text{-}0.05SiO_2$ mixture when heated up to 400 °C. This was lower than the 1.5 wt.% released from the $0.95LiBH_4\text{-}0.05SiO_2$ sample (Section 7.2.3) due to similar reasons explained for the $LiBH_4\text{-}NaBH_4$-Si mixture (Section 8.3.3).

A total of 9.6 wt.% hydrogen was released from the $0.95(0.75LiBH_4\text{-}0.25KBH_4)\text{-}0.05SiO_2$ mixture upon heating to 700 °C. When the amount of SiO_2 (9 wt.%) was excluded, about 10.6 wt.% of hydrogen was released from the materials contained hydrogen atoms in this mixture. These amounts were higher than the 8.9 wt.% for the SiO_2-free sample, possibly due to the change of reaction pathways caused by SiO_2 additives.

Figure 9.18 shows room temperature XRD and Raman results of the heat-treated $0.95(0.75LiBH_4\text{-}0.25KBH_4)\text{-}0.05SiO_2$ mixtures at 300, 490 and 655 °C.

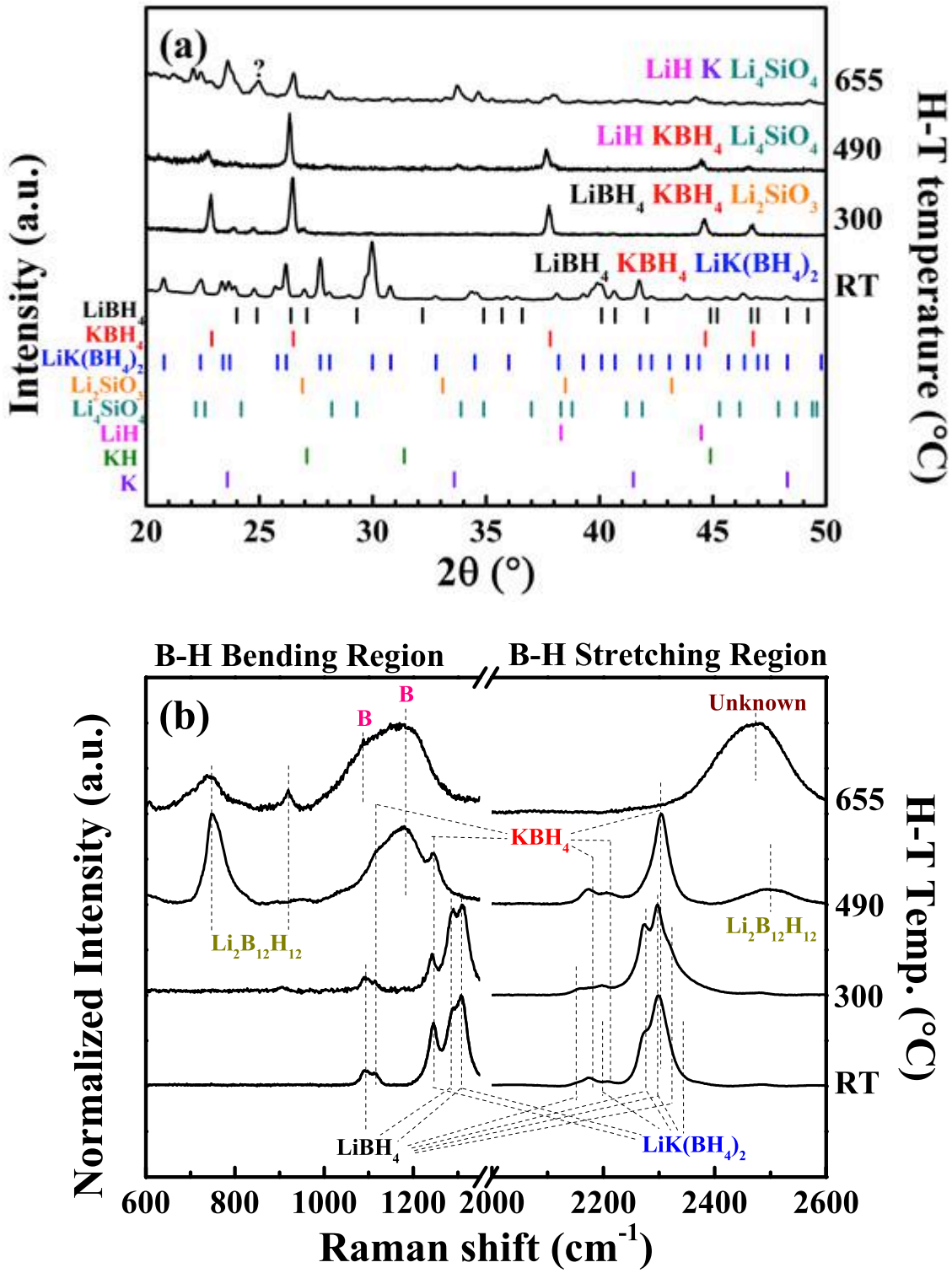

Figure 9.18 Room temperature (a) XRD patterns (Cu K_α radiation, λ = 1.5418 Å) and (b) Raman spectra (measured with 488 nm laser and 2400 l/mm grating system) of as-prepared $0.95(0.75LiBH_4\text{-}0.25KBH_4)\text{-}0.05SiO_2$ mixture, which had been heat-treated at 300 °C, 490 °C and 655 °C by 2 °C min^{-1} in Ar flowing at 160 mL min^{-1}. The intensities of the XRD and Raman peaks were normalized. A horizontal break was used to divide the Raman spectra (b) into B-H bending and B-H stretching regions of $[BH_4]^-$ (normalized separately). Dashed lines are guides for the eye.

For the heat-treated $0.95(0.75LiBH_4\text{-}0.25KBH_4)\text{-}0.05SiO_2$ sample at 300 °C, phases of $LiBH_4$, KBH_4 and Li_2SiO_3 were observed. Although several $K_xSi_yO_z$ type materials were present at room temperature and under atmospheric pressure (such as $K_2Si_4O_9$ (Swanson & Prewitt 1983), K_4SiO_4 (Bernet & Hoppe 1990), $K_6Si_3O_9$ (Werthmann & Hoppe 1981), $K_6Si_7O_7$ (Jansen 1982), etc.), none of them was observed in this work using XRD or Raman, This showed that the reaction between KBH_4 and SiO_2 was unlikely happened, which was possibly because the reaction between $LiBH_4$ and SiO_2 was more thermodynamically favourable. The Bragg peaks of Li_4SiO_4 were observed in the heat-treated sample at 490 °C. It was an oxidation product of Li_2SiO_3. Therefore the H_2 release in the temperature range 258-375 °C was mainly due to a reaction between $LiBH_4$ and SiO_2. Besides, though the signal of $Li_2B_{12}H_{12}$ and B were weak and difficult to be clearly seen in the corresponding Raman spectrum, the previous results (Section 7.2.3 and 8.3.3) have confirmed the simultaneous dehydrogenation of a small amount of $LiBH_4$ in this temperature range.

At 490 °C, phases of LiH, KBH_4 and Li_4SiO_4 were seen in XRD pattern, whilst $Li_2B_{12}H_{12}$, B and KBH_4 were presented in the Raman spectra. KBH_4 was stable at this temperature and was not decomposed yet. The disappearance of $LiBH_4$ together with formations of LiH, $Li_2B_{12}H_{12}$ and B indicated that the dehydrogenation of $LiBH_4$ caused the major H_2 release in the temperature range of 375-550 °C.

At 655 °C, signals of KBH_4 became very weak in XRD pattern and were disappeared in Raman spectra, suggesting it dehydrogenated leaving K and B. KH was not seen in this decomposition product, which was different from the SiO_2-free sample. This might be

due to the addition of SiO_2 inhibited the frothing effect and reduced the amount of K that escaped from the hot zone. A red shift of the B-H stretching mode for the $[B_{12}H_{12}]^{2-}$ cluster was again observed, which may be caused by the formation of $K_2B_{12}H_{12}$ (Li et al. 2015) or a partial dehydrogenation of the $[B_{12}H_{12}]^{2-}$ cluster (Pitt et al. 2013).

The entire amount of H_2 release (including heating and cooling) for the $0.95(0.75LiBH_4\text{-}0.25KBH_4)\text{-}0.05SiO_2$ sample mixture was 11.0 wt.%, which was higher than the 10.0 wt.% for the SiO_2-free sample. The dehydrogenation peak area ratio for these 3 steps was 8.6 : 46.8 : 44.6 (obtained by a Gaussian peak fitting, R^2 = 0.9936). The area ratio was assumed to be linearly related to the amount of H_2 released from each step. Thus, the associated H_2 release from each step was 1.0 wt.%, 5.1 wt.% and 4.9 wt.%, respectively.

Assuming all added SiO_2 (5 mol%) reacted with $LiBH_4$ via Equation 7.7 (forming Li_2SiO_3, Si, B and H_2) and 7.8 (forming Li_4SiO_4, Si, B and H_2), it then consumed 10 mol% $LiBH_4$ in the 1st step and released 1 wt.% hydrogen. The simultaneous dehydrogenation of $LiBH_4$ was neglected due to its tiny amount. Then the remaining sample could be written as $0.61LiBH_4\text{-}0.24KBH_4$, corresponding to the 5.1 wt.% and 4.9 wt.% from the 2nd and 3rd peaks. However, these hydrogen releases from $LiBH_4$ or KBH_4 dominated peaks disagreed with their theoretical ranges, for instance, 6.1-8.5 wt.% for the 0.61 moles of $LiBH_4$ (through Equation 7.2 forming LiH, B, H_2 or via 7.3 forming LiH, $Li_2B_{12}H_{12}$, H_2) and 1.3-1.8 wt.% from 0.24 moles of KBH_4 (via Equation 9.1 forming K, B, H_2 or through Equation 3.23 forming KH, B H_2). These mismatches

suggest a strong cation interaction that affected the dehydrogenation process, postponing the dehydrogenation of the $LiBH_4$ towards a higher temperature.

9.3.4 Effect of Additive SiO_2

In general, the addition of 5 mol% micron-sized SiO_2 did not affect the low melting point of the $0.75LiBH_4$-$0.25KBH_4$ mixture at 108 °C.

In flowing Ar, the added SiO_2 in the $0.75LiBH_4$-$0.25KBH_4$ mixture led to lower temperature dehydrogenation starting at 258 °C, through chemical reactions between the $LiBH_4$ and SiO_2 that were more thermodynamically favourable than the dehydrogenation of the borohydrides constituents. As a consequence, Li_2SiO_3 and Li_4SiO_4 were formed in the temperature range 258-375 °C at the 1st step. Besides these reactions, a small quaintly of $LiBH_4$ was decomposed simultaneously. The total H_2 release in this temperature range was found to be ~1.0 wt.% hydrogen.

A total of 9.6 wt.% hydrogen was released from the $0.95(0.75LiBH_4$-$0.25KBH_4)$-$0.05SiO_2$ mixture upon heating to 700 °C in Ar. The major dehydrogenation occurred above 375 °C, exhibiting one major peak at 490 °C and one broad peak at 655 °C (with a shoulder at 605 °C). Both peak temperatures were similar to that for the SiO_2-free sample. The major H_2 release at the 2nd step was associated with the precipitation of LiH, $Li_2B_{12}H_{12}$ and B, whilst the 3rd step was due to the formation of K and B, and the postponed dehydrogenation of $LiBH_4$.

Figure 9.19 schematically summarizes the decomposition process (in Ar) of $0.95(0.75LiBH_4\text{-}0.25KBH_4)\text{-}0.05SiO_2$. Phases marked in brackets were not observed in either XRD patterns or Raman spectra.

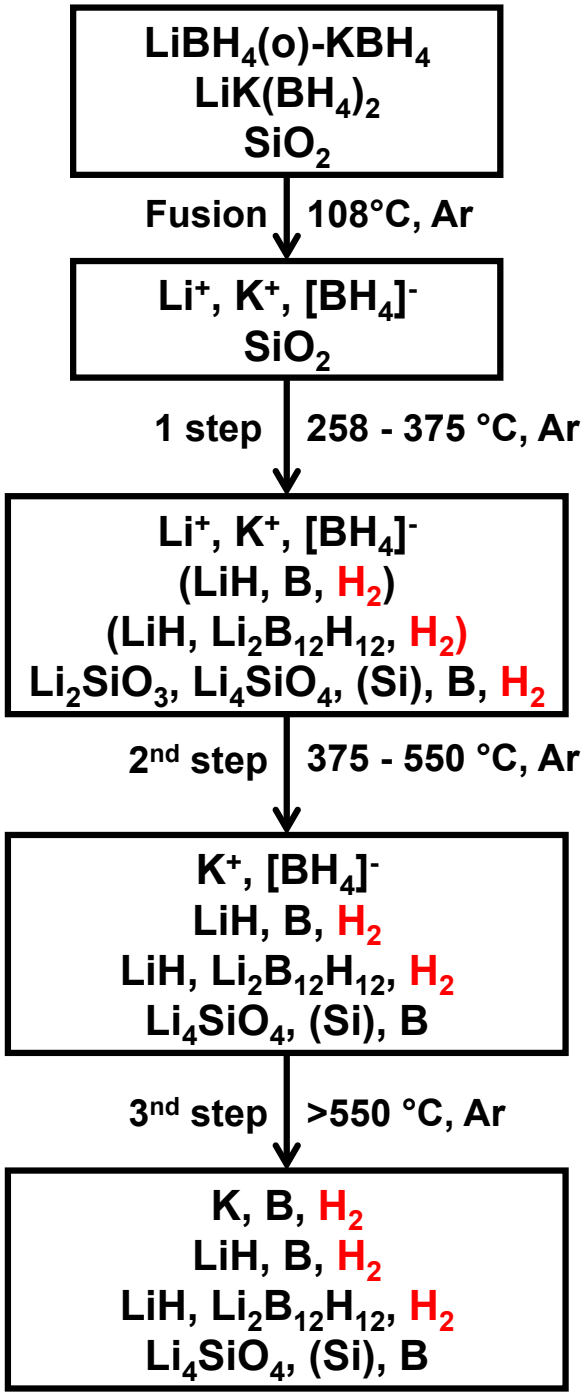

Figure 9.19 A flow chart of decomposition pathways of the as-prepared $0.95(0.75LiBH_4\text{-}0.25KBH_4)\text{-}0.05SiO_2$ in Ar.

9.4 Decomposition and Recombination with the Addition of 19 wt.% nano-sized Ni

The nano-sized Ni used in Section 7.3 showed an interesting destabilization effect on the decomposition of $LiBH_4$. In this section, it was used in order to destabilize the $0.75LiBH_4$-$0.25NaBH_4$ mixture, and the influence on the decomposition reactions was investigated.

9.4.1 Characterisation of the As-prepared $LiBH_4$-KBH_4-Ni Mixture

0.2 g nano-sized Ni (Sigma-Aldrich, 99.9%), 0.3300 g $LiBH_4$ (Sigma-Aldrich, 95.0 %) and 0.3100 g KBH_4 (Sigma-Aldrich, 98.0 %) were mixed using ball milling under the conditions described in Section 6.1.1.

Figure 9.20 shows the XRD and FTIR results of the as-milled mixture at room temperature. The Raman results were not available due to the high fluorescence effect caused by Ni.

In general, the peaks in the XRD pattern were caused by orthorhombic $LiBH_4$, KBH_4, $LiK(BH_4)_2$, Ni and NiO. The presence of NiO was due to the impurity in the as-received nano-sized Ni (Section 7.3.1). The Pseudo-Rietveld refinement (Figure 9.21) suggested that their compositions were 30.5 ± 3.3 wt.%, 0.0 ± 0.1 wt.%, 50.0 ± 2.4 wt.%, 17.8 ± 0.9 wt.% and 1.6 ± 0.2 wt.%, respectively. Calculated from which, the equivalent molar percentage of $LiBH_4$ and KBH_4 in the as-milled sample was 76 ± 1 mol% and 24 ± 1 mol%, respectively. They were in agreement with the 75 ± 1 mol% and 25 ± 1 mol% measured for the Ni-free sample. Thus, the as-milled sample was referred as $0.86(0.75LiBH_4$-$0.25KBH_4)$-0.14Ni.

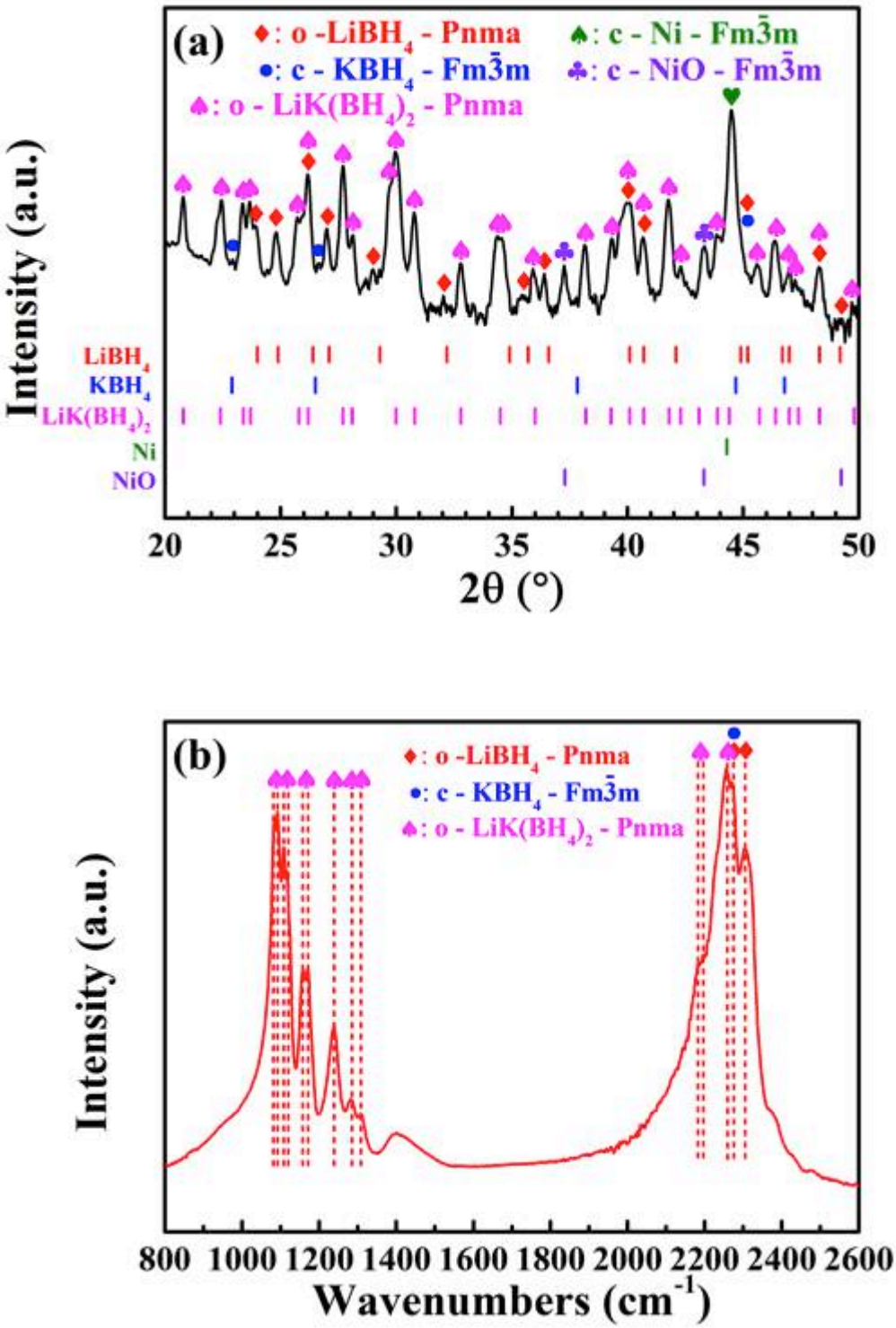

Figure 9.20 (a) XRD pattern (Cu K_α radiation, λ = 1.5418 Å) (intensity in log scale) and (b) FTIR spectra for the as-milled 0.86(0.75$LiBH_4$-0.25KBH_4)-0.14Ni mixture, measured at room temperature. Dashed lines are guides for the eye. The FTIR results are in good agreement with Anna et al. (2014).

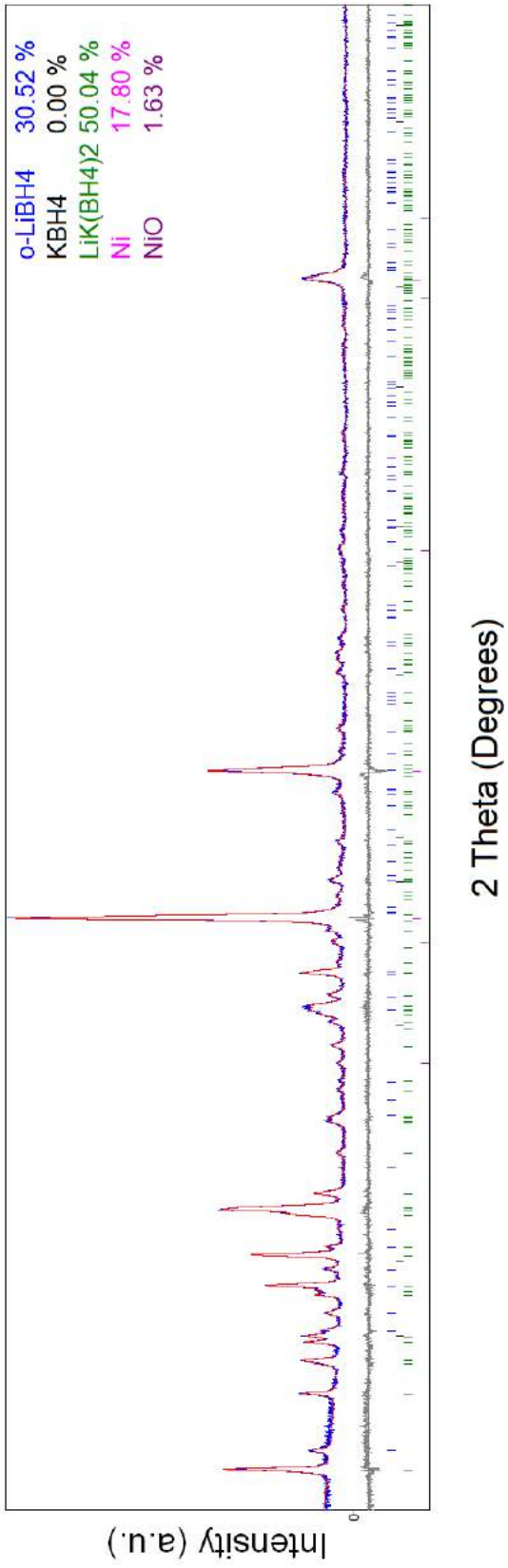

Figure 9.21 Pseudo-Rietveld refinement result of as-milled 0.86(0.75$LiBH_4$-0.25KBH_4)-0.14Ni, including the observed XRD (Cu K_α radiation, λ = 1.5418 Å) profile (blue), the calculated profile (red, used to fit the observed profile) and the difference profile (grey) in each figure. The goodness-of-fit value was 1.127.

The refined lattice parameters of the $LiBH_4$ and KBH_4 phases presented in the as-milled sample was summarised in Table 9.7.

Table 9.7 Refined crystal structure parameters of $LiBH_4$, KBH_4 components in as-milled 0.86(0.75$LiBH_4$-0.25KBH_4)-0.14Ni in contrast to that of as-milled pure compound and in as-milled 0.75$LiBH_4$-0.25KBH_4 mixture.

		As-milled Pure		As-milled Mixture	
		$LiBH_4$	**KBH_4**	**$LiBH_4$-KBH_4**	**$LiBH_4$-KBH_4-Ni**
o-$LiBH_4$	a (Å)	7.199 ± 0.003	-	7.187 ± 0.001	7.180 ± 0.002
	b (Å)	4.438 ± 0.002	-	4.442 ± 0.001	4.444 ± 0.001
	c (Å)	6.798 ± 0.002	-	6.817 ± 0.002	6.818 ± 0.003
	Volume ($Å^3$)	*216.84 ± 0.01*	-	*217.64 ± 0.07*	*217.57 ± 0.14*
c-KBH_4	a (Å)	-	6.732 ± 0.002	6.702 ± 0.003	6.503 ± 0.098
	Volume ($Å^3$)	-	*305.15 ± 0.06*	*300.99 ± 0.35*	*275.018* ± 12.44

The unit cell volume of the $LiBH_4$ component in the as-milled 0.86(0.75$LiBH_4$-0.25KBH_4)-0.14Ni mixture (217.57 ± 0.14 $Å^3$) was the same as that of the Ni-free sample (217.64 ± 0.07 $Å^3$) but higher than that of pure $LiBH_4$ after ball-milling (216.84 ± 0.01 $Å^3$). A large reduction of the unit cell volume KBH_4 in the as-milled 0.86(0.75$LiBH_4$-0.25KBH_4)-0.14Ni mixture was noticed, due to its very low XRD intensity, as explain in Section 9.2.1.

9.4.2 Thermal Analysis

Figure 9.22 shows the DSC trace of the 0.86(0.75$LiBH_4$-0.25KBH_4)-0.14Ni mixture compared with the Ni-free sample, preformed in 50-150 °C by 5 °C min^{-1} in Ar flowing at 70 mL min^{-1}. The fusion and solidification onset temperatures of this mixture were 109 ± 1 °C and 106 ± 1 °C, respectively, suggesting a small over-cooling effect. These temperatures were the same as that for Ni-free sample, suggesting this additive did not

affect fusion temperature. However, the curve areas were reduced by 10 – 20 % (Table 9.8). These reductions were also observed for $LiBH_4$-$NaBH_4$-Ni sample (Section 8.4.2), likely because the added nano-sized Ni (NiO) particles played a catalytic role.

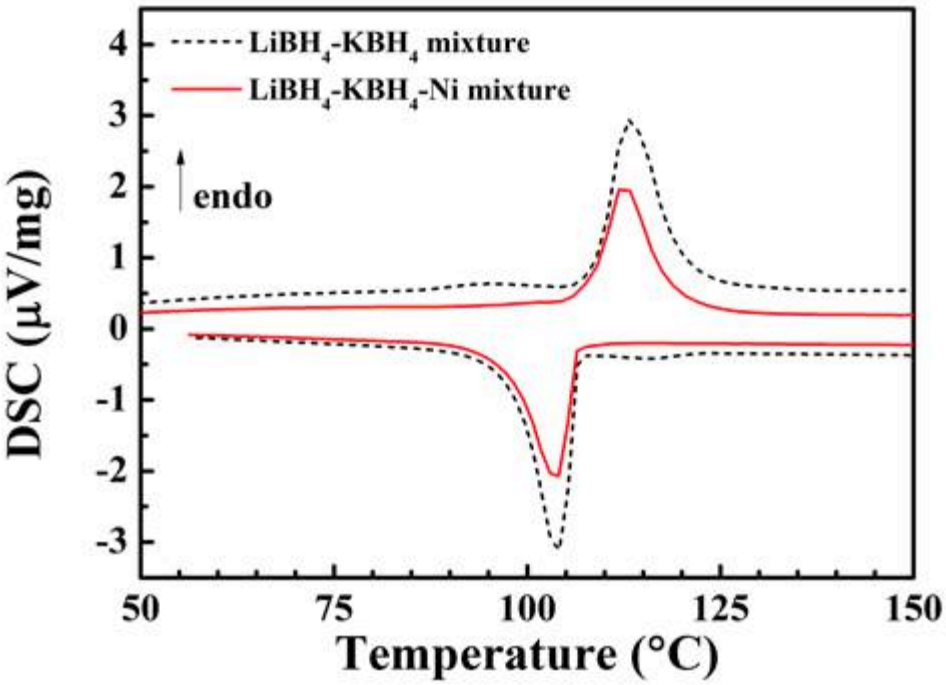

Figure 9.22 DSC results of as-milled 0.86(0.75$LiBH_4$-0.25KBH_4)-0.14Ni, compared with the as-milled 0.75$LiBH_4$-0.25KBH_4 (black dash line). Samples were heated from 50 to 150 °C at 5 °C min^{-1} in Ar flowing at 70 mL min^{-1}.

Table 9.8 DSC curve areas for as-milled 0.86(0.75$LiBH_4$-0.25KBH_4)-0.14Ni compared with as-milled 0.75$LiBH_4$-0.25KBH_4.

	Sample	Energy	
		Heating	Cooling
		Fusion	Solidification
		μV mg^{-1} LiK	μV mg^{-1} LiK
1	0.75$LiBH_4$-0.25KBH_4	20.8 ± 1.0	17.9 ± 0.9
2	0.86(0.75$LiBH_4$-0.25KBH_4)-0.14Ni	18.0 ± 0.9	15.2 ± 0.8

9.4.3 Thermal Decomposition

The thermal dehydrogenation of the 0.86(0.75$LiBH_4$-0.25KBH_4)-0.14Ni mixture was carried out in Ar flowing at 160 mL min^{-1} while heated to 700 °C by 2 °C min^{-1}, showing in Figure 9.23. No B_2H_6 was detected during the decomposition.

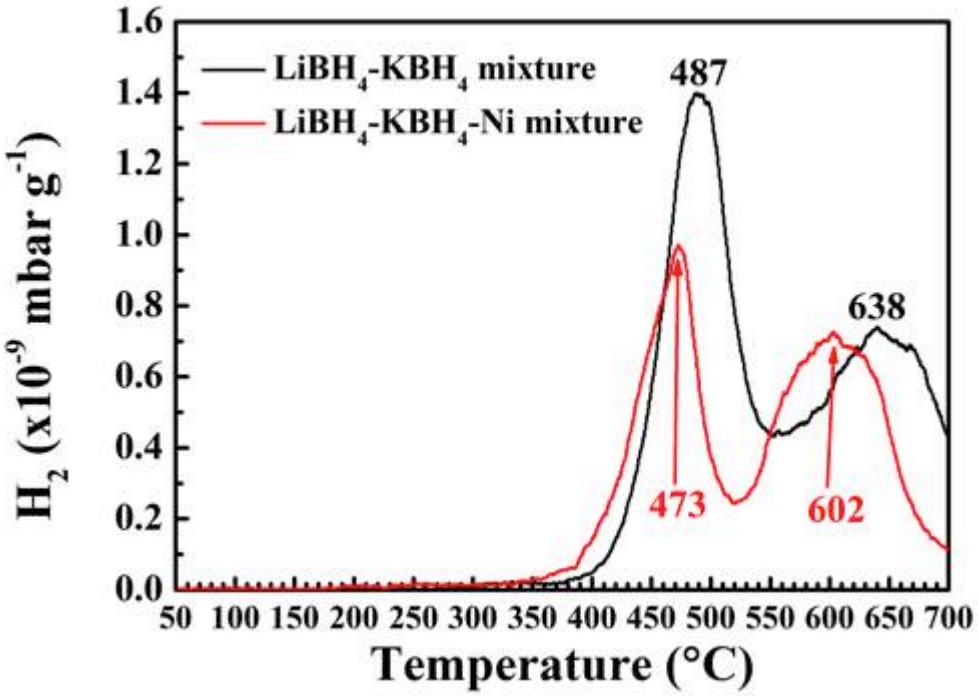

Figure 9.23 TPD-MS hydrogen desorption of as-milled 0.86(0.75$LiBH_4$-0.25KBH_4)-0.14Ni, compared with as-milled 0.75$LiBH_4$-0.25KBH_4. Samples were heated at 2 °C min^{-1} in flowing Ar at 160 mL min^{-1}. No B_2H_6 was detected.

Similar to the $LiBH_4$-$NaBH_4$-Ni system in Section 8.4.3, an early dehydrogenation (exhibiting as a small deviation form the baseline) from 180 °C was noticed for the 0.86(0.75$LiBH_4$-0.25KBH_4)-0.14Ni mixture due to the reaction between $LiBH_4$ and NiO.

The major dehydrogenation of the 0.86(0.75$LiBH_4$-0.25KBH_4)-0.14Ni mixture started above 375 °C that was slightly lower than the Ni-free sample. During decomposition, two peaks, corresponding to two dehydrogenation reactions, were observed at 473 °C and 602 °C, respectively. Compared with the Ni-free sample, the 1st peak temperature was 14 °C lower, and the 2nd was 36 °C lower. No extra peak was observed upon heating to 700 °C, which was different from the dehydrogenation of the $LiBH_4$-$NaBH_4$-Ni mixture in Section 8.4.3, where a 3rd peak was observed at 586 °C due to the formation of $Li_{1.2}Ni_{2.5}B_2$ and an unknown phase(s).

A total of 7.1 wt.% hydrogen was released from the 0.86(0.75$LiBH_4$-0.25KBH_4)-0.14Ni mixture upon heating to 700 °C in Ar. This amount was lower than the 8.9 wt.% for the Ni-free sample. However, when the weight of additive (19.4 wt%) was excluded, the remained $LiBH_4$-KBH_4 content liberated 8.8 wt.% of hydrogen, which was similar to the Ni-free sample.

To investigate its decomposition pathways, the 0.86(0.75$LiBH_4$-0.25KBH_4)-0.14Ni sample was heat treated by 2 °C min^{-1} to 470 °C, 600 °C and 700 °C in flowing Ar. These heat-treated samples were measured by XRD and Raman, as shown in Figure 9.24.

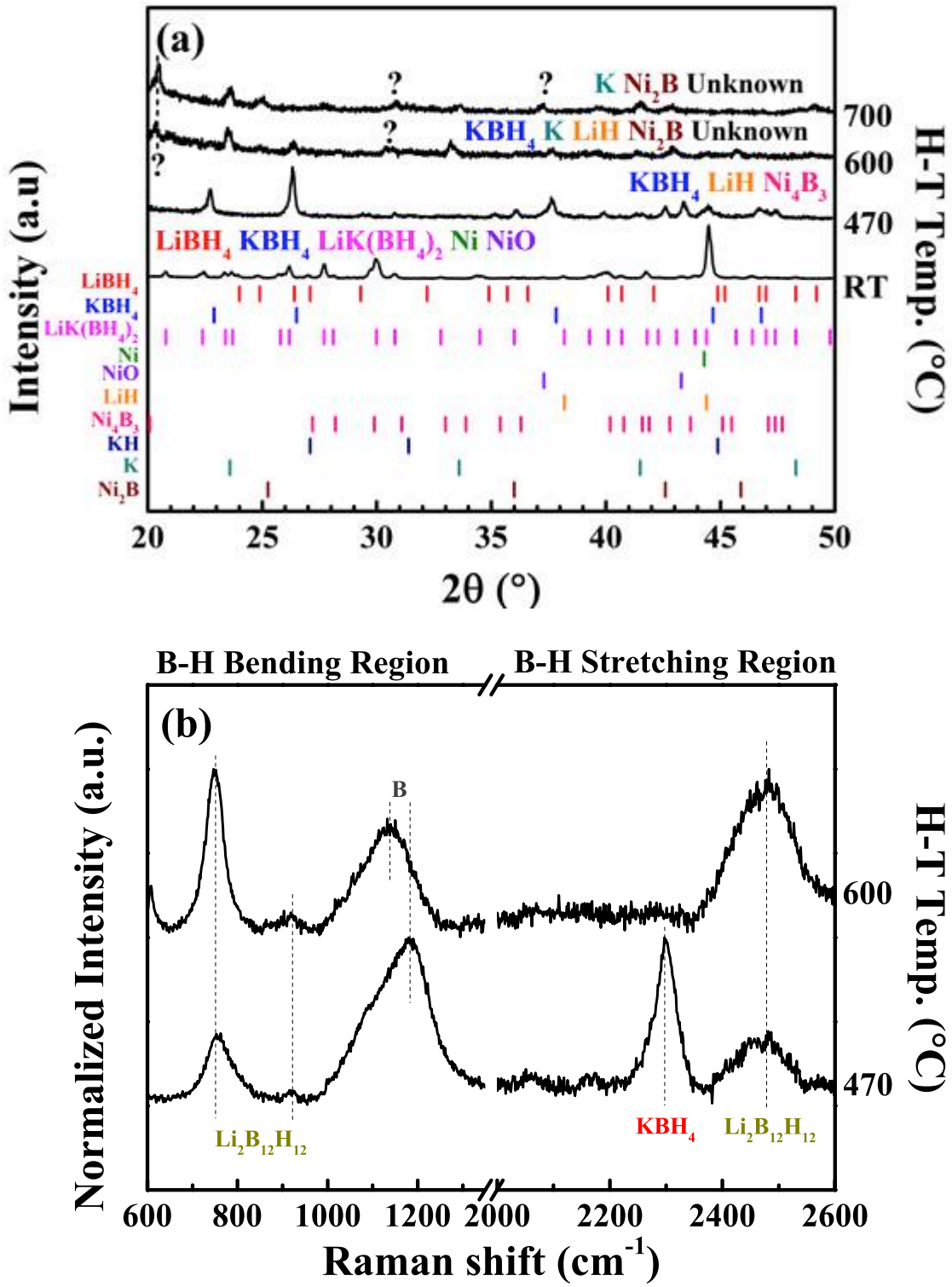

Figure 9.24 Room temperature (a) XRD patterns (Cu K_α radiation, λ = 1.5418 Å) and (b) Raman spectra (measured with 488 nm laser and 2400 l/mm grating system) of as-prepared 0.86(0.75$LiBH_4$-0.25KBH_4)-0.14Ni mixture, which had been heat-treated at 470 °C, 600 °C and 700 °C by 2 °C min^{-1} in Ar flowing at 160 mL min^{-1}. The intensities of the XRD and Raman peaks were normalized. A horizontal break was used to divide the Raman spectra (b) into B-H bending and B-H stretching regions of $[BH_4]^-$ (normalized separately). Dashed lines are guides for the eye.

Upon heating to 470 °C (1st dehydrogenation peak), the XRD results showed KBH_4, LiH and Ni_4B_3. The presence of Ni_4B_3 confirmed the reaction between $LiBH_4$ and the nano-sized Ni through Equation 7.9 (forming Ni_4B_3, LiH and H_2). This chemical reaction also caused a 14 °C reduction of dehydrogenation peak temperature (Figure 9.23), that agreed with the $LiBH_4$-Ni system (Section 7.3.3) where a 25 °C reduction was observed. The former temperature reduction was slightly lower than the later, possibly due to the presence K^+ that affected and postponed the dehydrogenation. Similar to the Ni-free sample, no evidence suggested the decomposition of KBH_4 had occurred so far. The corresponding Raman spectra presented signals of remaining KBH_4 (2300 cm^{-1}), B (around 1180 cm cm^{-1}), and $Li_2B_{12}H_{12}$ (at 754 cm^{-1}, 920 cm^{-1}, around 2473 cm^{-1}). The occurrence of LiH, B and $Li_2B_{12}H_{12}$ confirmed the decomposition of $LiBH_4$ through Equation 7.2 and 7.3.

At 600 °C where the 2nd dehydrogenation happened, peaks of element K, KBH_4 (low intensity), LiH (low intensity), Ni_2B and an unknown phase(s) (located at 20.4°, 30.7°) were observed in XRD pattern. The $Li_xNi_yB_z$ was ruled out for these unknown peaks (Jung 1977; Jung 1980). A transformation from Ni_4B_3 to Ni_2B was occurred during reactions.

At a higher temperature (700 °C), the remaining KBH_4 and LiH phases were not shown and a new unknown peak at 37.2° was observed. This indicates that the hydrogen released at high temperature was due to: 1) dehydrogenation of the KBH_4 component; and 2) chemical reaction that at least consumed LiH and Ni_3B_4, forming Ni_2B and

unknown phase(s). The corresponding Raman showed $Li_2B_{12}H_{12}$ (at 750 cm^{-1}, 918 cm^{-1} and around 2480 cm^{-1}) and B (around 1138 cm^{-1}).

The entire amount of H_2 release (including heating and cooling) for the $0.86(0.75LiBH_4\text{-}0.25KBH_4)\text{-}0.14Ni$ mixture was 7.6 wt.% that was lower than the 10.0 wt.% for the Ni-free sample. The dehydrogenation peak area ratio for the 2 steps was 48:52 (obtained by a Gaussian peak fitting, $R^2 = 0.9863$). This area ratio was assumed linearly related to the amount of H_2 released from each step. Therefore, multiplying the relatively curve area percentage with the amount of H_2 release, about 3.6 wt.% was contributed from the 1st reaction step and about 4.0 wt.% was from the 2nd reaction step.

Assuming the addition of 14 mol% Ni reacted with $LiBH_4$ through Equation 7.9 (forming Ni_4B_3, LiH and H_2), it would consume 10.5 mol% $LiBH_4$ at the 1st step and released 0.8 wt.% of hydrogen. Deducting the $LiBH_4$ consumed at this step, the remaining mole amount of $LiBH_4$ in the mixture was 54 mol%. Thus, the remaining composition was $0.54LiBH_4\text{-}0.215KBH_4$, which released 2.8 wt.% at 1st reaction step and 4.0 wt.% at the 2nd step. These values again mismatched their theoretical range, for instance, 5.4-7.5 wt.% for dehydrogenation of 0.54 moles of $LiBH_4$ (through Equation 7.2 forming LiH, B, H_2 or via 7.3 forming LiH, $Li_2B_{12}H_{12}$, H_2) and 1.2-1.6 wt.% from 0.215 moles of KBH_4 (via Equation 9.1 forming K, B, H_2 or through Equation 3.23 forming KH, B H_2). These disagreements were possibly due to the strong cation interactions that postponed the release of H_2 from $LiBH_4$.

The activation energies for the two-step dehydrogenation for the $LiBH_4\text{-}KBH_4$ system

were estimated using the Kissinger equation (Equation 8.9), which provides general concepts for comparison, as most of these dehydrogenation steps contained more than one chemical reaction. The results are illustrated in Figure 9.25 and summarised in Table 9.9.

Table 9.9 Activation energies of chemical reactions of $LiBH_4$, KBH_4, and the $LiBH_4$-KBH_4 systems with added SiO_2 and nano-sized Ni, calculated using Kissinger's method.

Sample	E_a (kJ)	
	1st peak	2nd peak
$LiBH_4$	264 ± 6	
KBH_4		191 ± 5
LiK	110 ± 2	163 ± 5
LiK-Si	87 ± 2	181 ± 3
LiK-Ni	120 ± 3	131 ± 3

In general, the activation energies for the 1st dehydrogenation peak in the $LiBH_4$-KBH_4 systems (including LiK, LiK-Si and LiK-Ni samples) were more than 50% lower than that for pure $LiBH_4$ and the one for LiK-Si mixture is much lower than the others, which may due to insufficient data points (three points in this work) for obtaining activation energies from the slope of Kissinger plot.

The activation energies for the 2nd dehydrogenation peak of the LiK and LiK-Si systems were similar to that for the pure KBH_4. However, the one of LiK-Ni was much lower. This was possibly due to its complex reaction mechanisms (for instance, the unknown reaction forming Ni_2B and unknown phases) that were different from the case for LiK and LiK-Si samples.

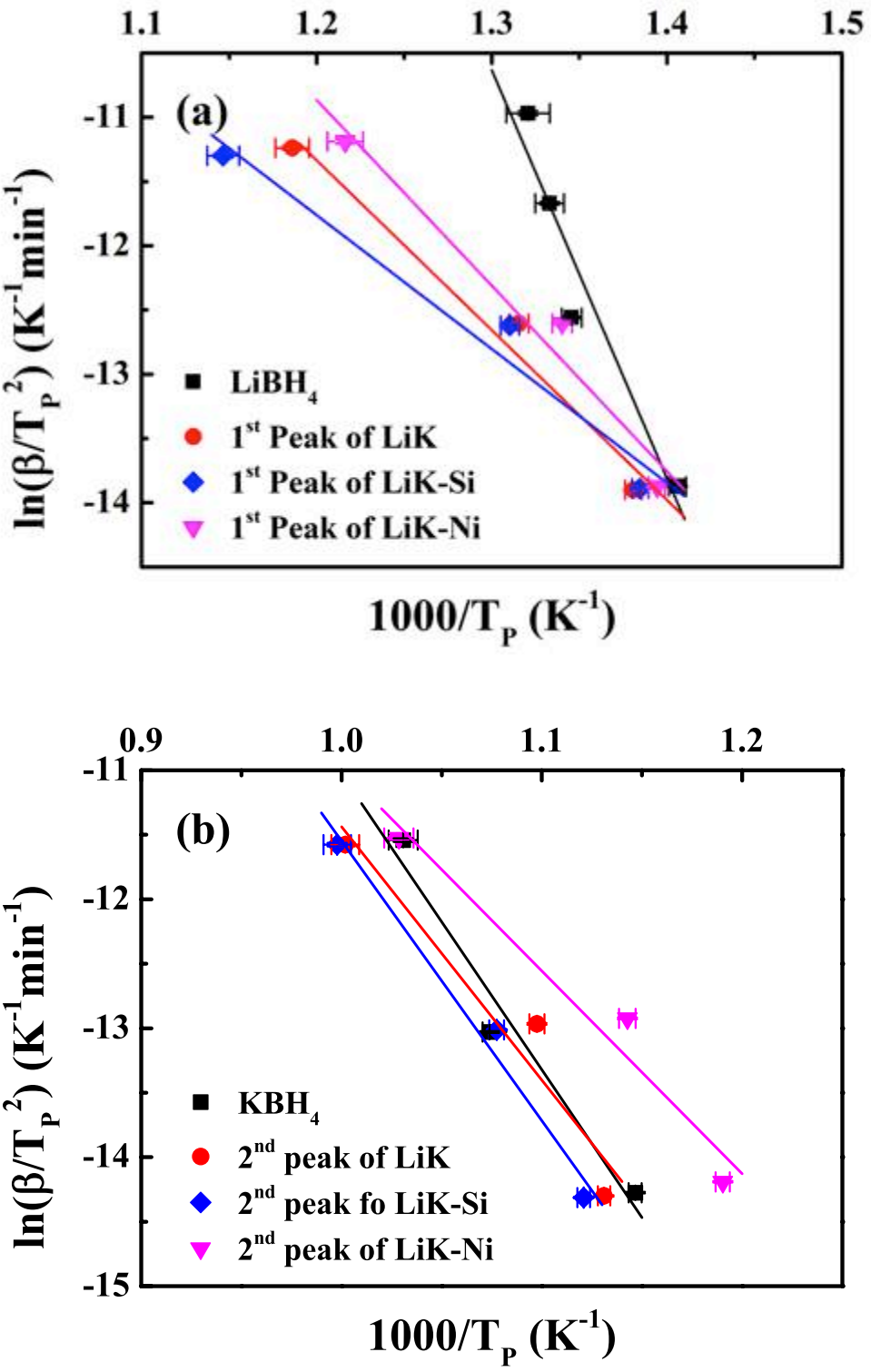

Figure 9.25 Kissinger plot for the major decomposition reactions in as-milled $0.75LiBH_4$-$0.25KBH_4$ (noted as LiK), as-prepared $0.95(0.75LiBH_4$-$0.25KBH_4)$-$0.05SiO_2$ (0.5 µm, noted as LiK-Si) and as-milled $0.86(0.75LiBH_4$-$0.25KBH_4)$-0.14Ni (nano-sized, noted as LiK-Ni), compared with as-milled $LiBH_4$ and KBH_4. The activation energies were calculated from the slope of trend-lines. Some error bars are very small.

9.4.4 Recombination

The reversibility of the 0.86(0.75$LiBH_4$-0.25KBH_4)-0.14Ni mixture was carried out using a Sieverts type apparatus as described in Section 6.2.6. The reaction conditions were: 500 °C, 1 bar H_2 and 10 h for desorption; and 400 °C, 130 bar H_2 and 12 h for absorption. The results are shown in Figure 9.26 and summarized in Table 9.10.

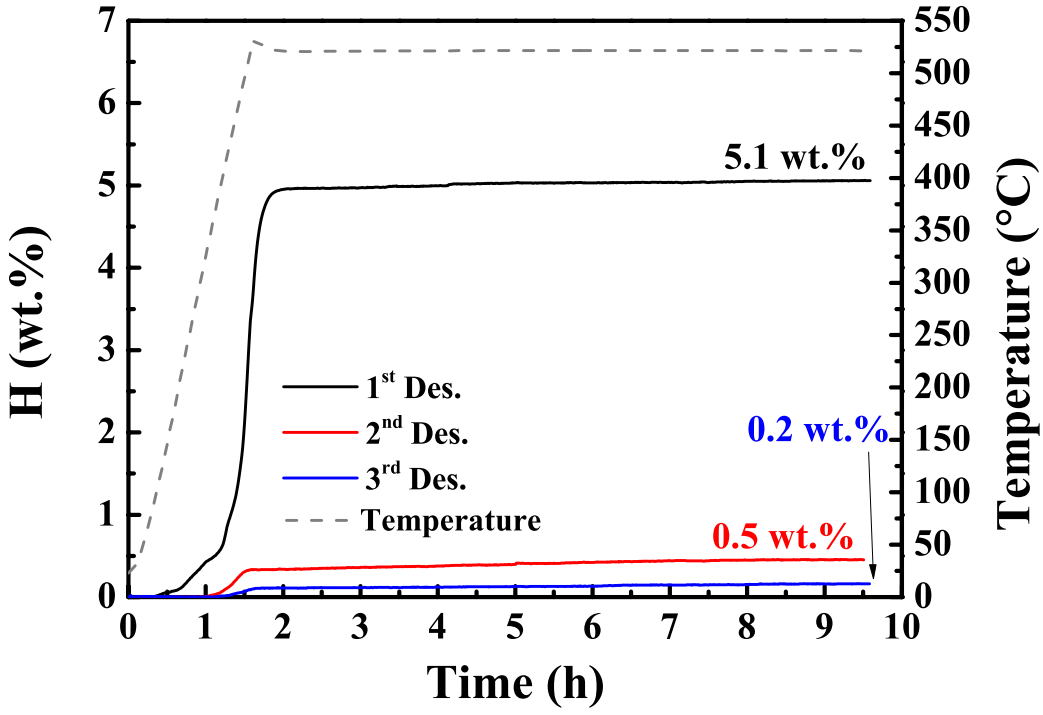

Figure 9.26 Sievert's measurements showing hydrogen release (in wt.%) while keeping the 0.86(0.75$LiBH_4$-0.25KBH_4)-0.14Ni mixture under 1 bar H_2 at 500 °C ($\Delta T/\Delta t$ = 5 °C min^{-1}) for 10 h for desorption and under 130 bar H_2 at 400 °C for 12 h for rehydrogenation.

Table 9.10 H_2 release (wt.%) of 0.86(0.75$LiBH_4$-0.25KBH_4)-0.14Ni during cycling compared with 0.75$LiBH_4$-0.25KBH_4. The corrected values (Corr.) excluded the weight of additive from the measured (Meas.) results.

	H_2 (wt.%)			
Sample	**$LiBH_4$-KBH_4**	**$LiBH_4$-KBH_4-Ni**		
	Meas.	Meas.		**Corr.**
1st cycle	5.8	5.1	→	6.3
2nd cycle	1.0	0.5	→	0.6
3rd cycle	0.4	0.2	→	0.3

In general, the 0.86(0.75$LiBH_4$-0.25KBH_4)-0.14Ni mixture had a poor cycling stability as its reversible hydrogen content decreased dramatically. After correction, this mixture released 6.3 wt.% of hydrogen at 1st cycle, which was 9% higher than the 5.8 wt.% for Ni-free sample due to the destabilization effect of Ni. After rehydrogenation, it restored a total of 0.6 wt.% and 0.3 wt.% hydrogen at the 2nd and 3rd cycle that were both lower than those of Ni-free sample. This large reduction in reversible H_2 content was not expected and different with the Ni-induced high reversibility of $LiBH_4$ (Li et al. 2014). However, (Li et al. 2014) used 350 bar H_2, 550 °C, 24 h for rehydrogenation that was stronger than the conditions used in this work (130 bar H_2, 400 °C, 12 h). Thus, to improve the reversible H_2 content, stronger conditions might be needed.

Figure 9.27 shows the XRD and FTIR results for the 0.86(0.75$LiBH_4$-0.25KBH_4)-0.14Ni mixture in its reabsorbed states after being cycled three times.

The XRD for dehydrogenated product at the 3rd cycle were KBH_4, LiH and Ni_2B, which disagreed with the decomposition products in Ar, where Ni_4B_3 was the major reaction product and Ni_2B was formed at higher temperatures. A broad peak at around 2400-2500 cm^{-1} was seen in FTIR results, suggesting the formation of closo-boranes structures. Since no K or KH was observed, KBH_4 was stable during cycling. In addition, the FTIR confirmed that no $LiBH_4$ was reformed during cycling, which was different from the results for the $LiBH_4$-$NaBH_4$-Ni system (Section 8.4.4) where some signals of $LiBH_4$ were observed by FTIR after the 3rd cycle using the same hydrogen sorption conditions.

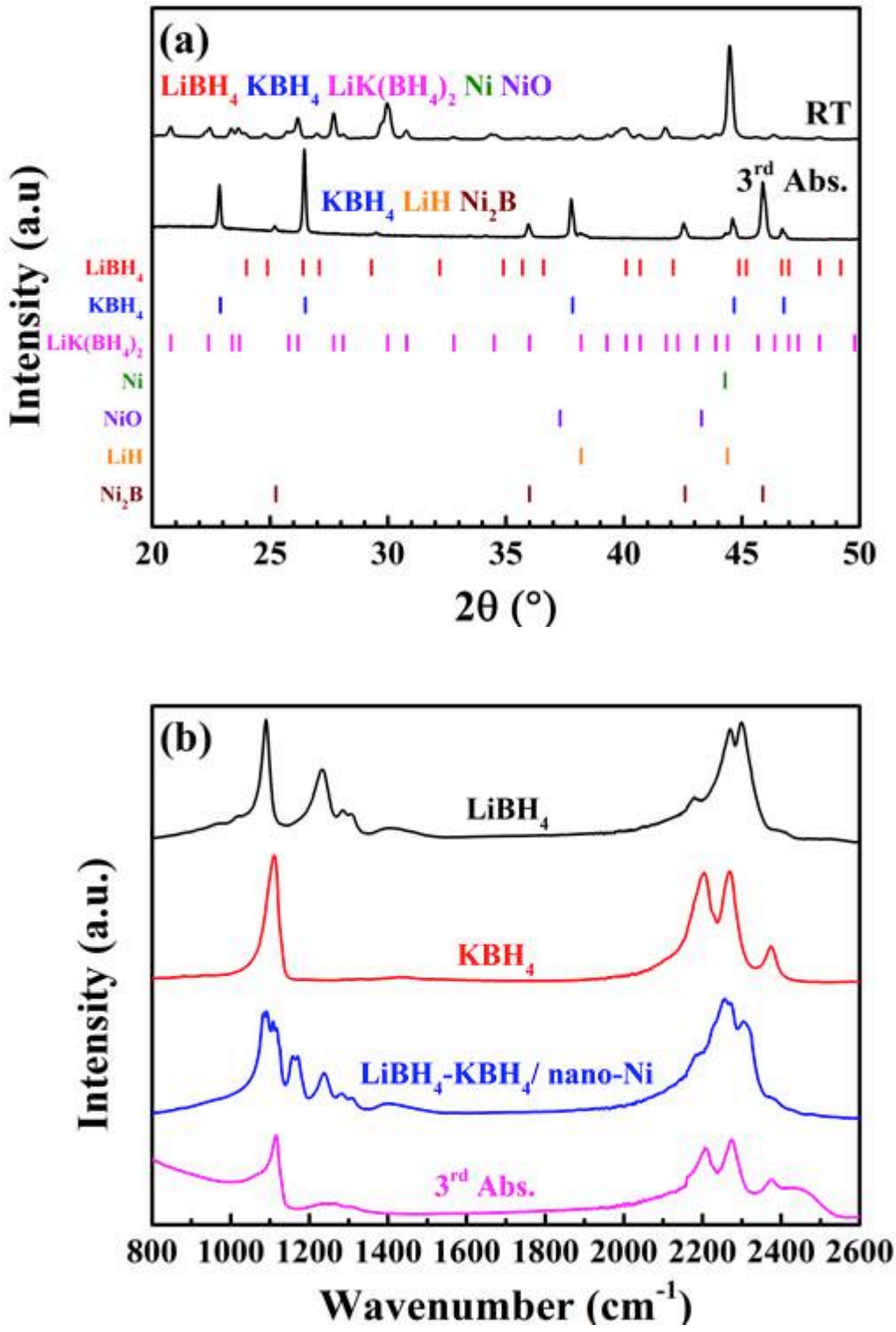

Figure 9.27 (a) XRD pattern (Cu K_α radiation, λ = 1.5418 Å) and (b) FTIR spectrum for the as-milled 0.86(0.75$LiBH_4$-0.25KBH_4)-0.14Ni decomposed at 500 °C in 1 bar static H_2 for 10 h and recombined with 130 bar H_2, 400 °C for 12 h at the 3rd cycle (denoted as 3rd Abs.).

9.4.5 Effect of Additive nano-sized Ni

Figure 9.28 shows the dehydrogenation pathway (in Ar) of the 0.86(0.75$LiBH_4$-0.25KBH_4)-0.14Ni mixture in a flow chart.

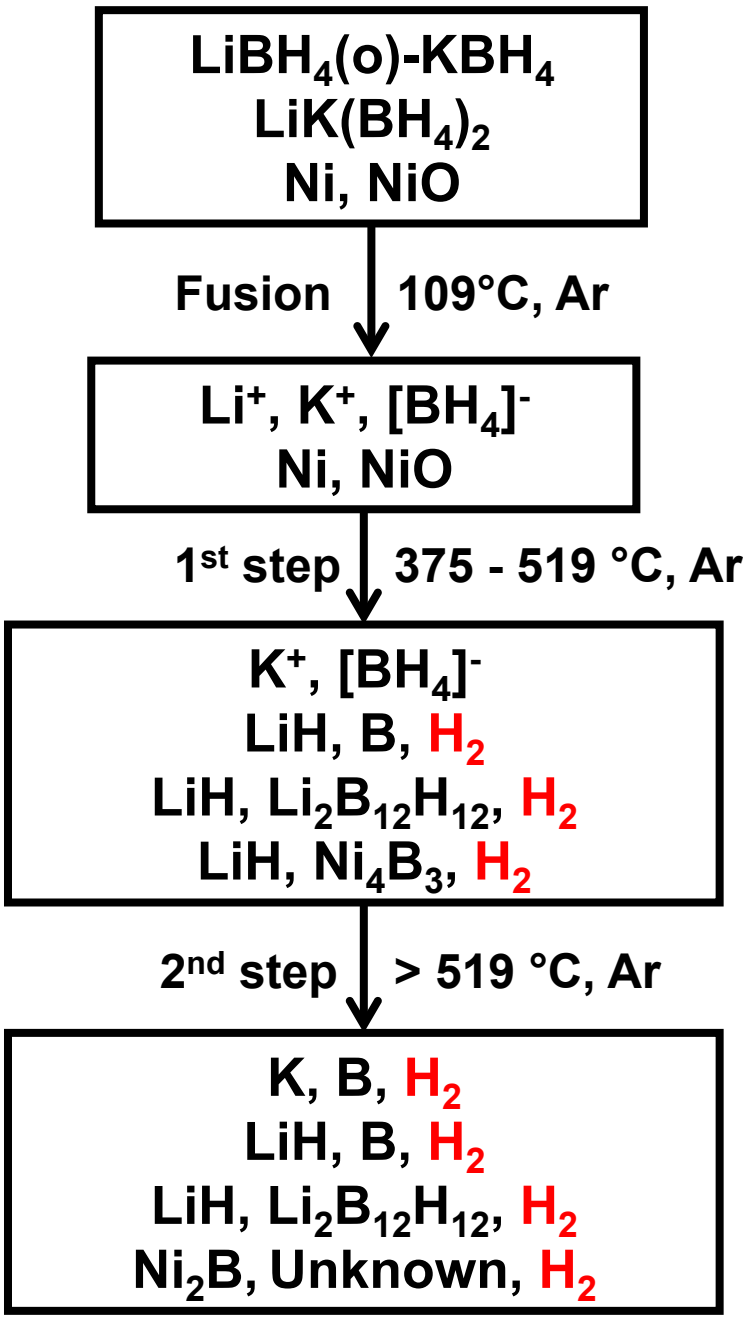

Figure 9.28 A flow chart of decomposition pathways (in Ar) of the as-milled 0.86(0.75$LiBH_4$-0.25KBH_4)-0.14Ni.

In general, the addition of nano-sized Ni did not affect the low-temperature fusion; however, it destabilized the decomposition. The major dehydrogenation of $0.86(0.75LiBH_4\text{-}0.25KBH_4)\text{-}0.14Ni$ started above 375 °C with 2 peaks at 473 °C (~14 °C lower than Ni-free mixture) and 602 °C (~36 °C lower than Ni-free mixture), indicating 2 different decomposition routes. Ni_4B_3 and Ni_2B were found as one of the major dehydrogenation products in step 1 and 2, respectively. A total of 7.1 wt. % of hydrogen was released upon heating to 700 °C in Ar (lower than the 8.9 wt.% for the Ni-free mixture). The reversible H_2 content reduced from 5.1 wt.% to 0.5 wt.% to 0.2 wt.%. No $LiBH_4$ reformed during cycling.

9.5 Summary

In this work, the decomposition and recombination of a $0.75LiBH_4\text{-}0.25KBH_4$ mixture were investigated. This mixture was prepared using ball milling. $LiK(BH_4)_2$, the reaction product of $LiBH_4$ and KBH_4 caused by pressure (Kim & Sholl 2010; Tuan et al. 2014; Ley et al. 2014), was the major phase in the as-milled mixture.

It melted at 108 ± 1 °C (measured in flowing Ar or under 2 bar static H_2) with an enthalpy of 5.3 ± 0.3 kJ mol^{-1} (measured under 2 bar static H_2). This onset temperature agreed with Ley et al. (2014); however, the enthalpy value was lower than the 10.7 kJ mol^{-1} reported. No H_2 release was detected upon heating to 290 °C and two major dehydrogenation routes were found: 1) from 290 °C to 700 °C, by the precipitation of LiH, $Li_2B_{12}H_{12}$ and B; and 2) from 550 °C to 700 °C, accompanied by the formation of K, KH and B as well. The presence of two cations with different Pauling electronegativity values affected the dehydrogenation temperatures, so that the

measured desorption peak temperatures (487 °C and 638 °C) were shifted, compared with as-milled $LiBH_4$ (470 °C) and as-milled KBH_4 (658 °C). A total of 8.9 wt. % hydrogen was released upon heating to 700 °C. A strong cation interaction effect caused a postponed dehydrogenation of parts of $LiBH_4$ (2.4 wt.%) to a higher temperature (> 550 °C).

The rehydrogenation of $0.75LiBH_4$-$0.25KBH_4$ mixture was carried out at 500 °C in 1 bar H_2 for 10 h for desorption and at 400 °C in 130 bar H_2 for 12 h for absorption. No $LiBH_4$ was reformed during cycling. The reversible H_2 content decreased dramatically from 5.8 wt.% to 1.0 wt.% and to 0.4 wt.%. This poor cyclic stability was also observed by Roedern et al. (2015) and it could not be significantly improved by using nano-confinement.

Unlike other eutectic borohydrides systems (e.g. $LiBH_4$-$Ca(BH_4)_2$ (Lee et al. 2009) and $LiBH_4$-$Mg(BH_4)_2$ (Bardají et al. 2011)), the $LiBH_4$-KBH_4 had a relatively high dehydrogenation temperature (and limited reversibility). To destabilize the dehydrogenation of 0.75 $LiBH_4$-$0.25KBH_4$ (noted as LiK) mixture, the micron-sized SiO_2 (0.5 μm) and nano-sized Ni were used as additives since they reduced the dehydrogenation temperatures of $LiBH_4$ (Chapter 7), leading to relatively lower onset and peak temperatures. Therefore, the $0.95(0.75LiBH_4$-$0.25KBH_4)$-$0.05SiO_2$ (noted as LiK-Si) and $0.86(0.75LiBH_4$-$0.25KBH_4)$-0.14Ni (noted as LiK-Ni) mixtures were prepared and the effect of additives on the low-temperature fusion behaviour and their dehydrogenation were investigated.

In general, these additives did not significantly affect the low-temperature fusion of LiK as the onset temperature and energies required for these phase changes were similar (Table 9.11).

Table 9.11 Summary of DSC data for $0.75LiBH_4$-$0.25KBH_4$ (LiK), $0.95(0.75LiBH_4$-$0.25KBH_4)$-$0.05SiO_2$ (LiK-Si) and $0.86(0.75LiBH_4$-$0.25KBH_4)$-0.14Ni (LiK-Ni) in Ar.

Sample	Fusion		Solidification	
	Temp. °C	Energy $\mu V\ mg^{-1}$ LiK	Temp. °C	Energy $\mu V\ mg^{-1}$ LiK
LiK	109 ± 1	20.8 ± 1.0	106 ± 1	17.9 ± 0.9
LiK-Si	108 ± 1	20.5 ± 1.0	106 ± 1	17.1 ± 0.9
LiK-Ni	109 ± 1	18.0 ± 0.9	106 ± 1	15.2 ± 0.8

The effect of additives on the dehydrogenations are summarised in Table 9.12.

Table 9.12 Improvement effect of additives on the dehydrogenation of $0.75LiBH_4$-$0.25KBH_4$ systems.

Sample	Temperature (°C)			H_2 release (wt.%)
	Onset	Early Peak(s)	Major Peak(s)	700 °C, Ar
$LiBH_4$	285		470	10.9
KBH_4	325		658	6.1
LiK	290		487, 638	8.9
LiK-Si	258	300	490, (605), 655	9.6
LiK-Ni	150-200		473, 602	7.1

Due to the additives used, LiK-Si and LiK-Ni started to release H_2 at lower temperatures than LiK. The presence of K^+ (with a lower Pauling electronegativity value than Li^+) always increases the dehydrogenation peak temperatures for those $LiBH_4$-dominated peaks (1^{st} peak). For instance, the $LiBH_4$-dominated peak temperature of LiK (487 °C) is higher than that for pure $LiBH_4$ (470 °C). And the temperatures for the $LiBH_4$-dominated peaks in LiK-Si (490 °C) and LiK-Ni (473 °C) are higher than those for Li-Si (467 °C) and Li-Ni (445 °C), as illustrated in Figure 9.29. In addition,

the total amount of H_2 released upon heating to 700 °C for LiK-Si (9.6 wt.%) and LiK-Ni (7.1 wt.%) samples were different from that for LiK (8.9 wt.%) sample (Table 9.12).

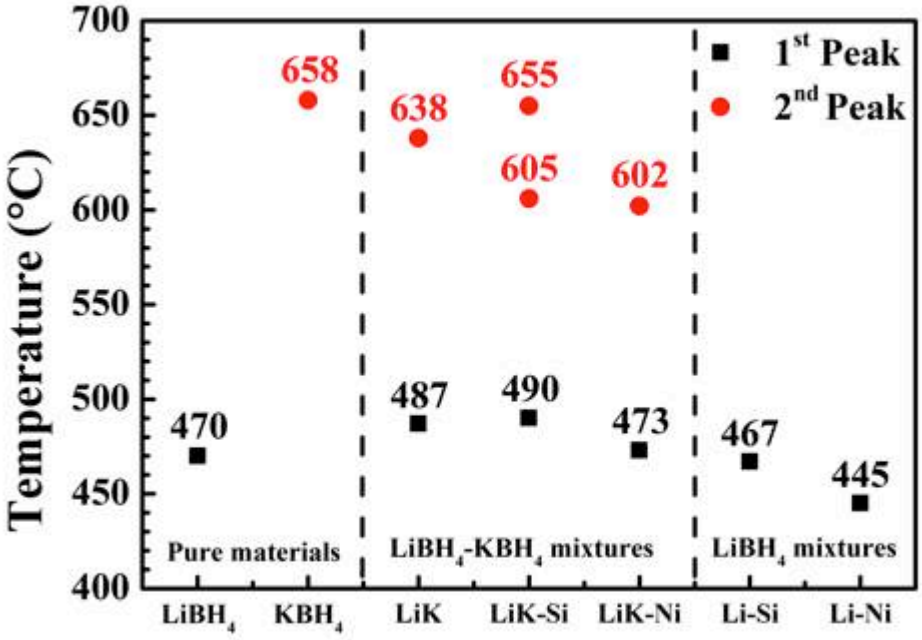

Figure 9.29 A comparison of peak dehydrogenation temperatures of as-milled $LiBH_4$, as-milled KBH_4, as-milled $0.75LiBH_4$-$0.25KBH_4$ (noted as LiK), as-prepared $0.95(0.75LiBH_4$-$0.25KBH_4)$-$0.05SiO_2$ (0.5 µm, noted as LiK-Si) and as-milled $0.86(0.75LiBH_4$-$0.25KBH_4)$-0.14Ni (nano-sized, noted as LiK-Ni). Sample were heated by 2 °C min^{-1} in Ar flowing at 160 mL min^{-1}.

Using additives not only caused these changes but also altered the dehydrogenation pathways. To calculate these decomposition reactions, it was assumed the amount of H_2 released from each step was linearly related to the curve area (fitted using Gaussian function) in the TPD-MS plots. Table 9.13 summarizes the calculated H_2 released from each reaction step.

Table 9.13 Summarised theoretical and experimental H_2 released from each chemical reaction step in the $0.75LiBH_4$-$0.25KBH_4$, $0.95(0.75LiBH_4$-$0.25KBH_4)$-$0.05SiO_2$ and $0.86(0.75LiBH_4$-$0.25KBH_4)$-0.14Ni in Ar.

Sample	Theoretical				Experimental			
	Molar ratio		Associated H_2 release (wt.%)		Peak area (%)		Associated H_2 release (wt.%)	
	$LiBH_4$: KBH_4		$LiBH_4$	KBH_4	1st Peak	2nd Peak	1st Peak	2nd Peak
LiK	0.75	0.25	7.5 – 10.4	1.4 – 1.9	48	52	4.8	5.2
LiK-Si	0.61	0.24	6.1 – 8.5	1.3 – 1.8	51	49	5.1	4.9
LiK-Ni	0.54	0.22	5.4 – 7.5	1.2 – 1.6	48	52	2.8	4.0

In general, the amount of H_2 experimentally released from the $LiBH_4$ content (1^{st} peak) in these samples was much lower than the estimated theoretical ranges; whilst the experimentally measured H_2 release from the KBH_4 content (2^{nd} peak) was higher than these theoretical values. It revealed that due to the presence of K^+, $LiBH_4$ contents were not fully dehydrogenated at the 1^{st} step and at least 2.4 wt.% of hydrogen released from 2^{nd} step was due to the dehydrogenation of $LiBH_4$. This postponed dehydrogenation of borohydride has not been reported in the literature and its reason was unclear, possibly due to a strong cation interaction.

CHAPTER 10 GENERAL DISCUSSION

This thesis has been focussed on investigation on the H_2 sorption mechanisms for $LiBH_4$, $LiBH_4$-based low-melting-point borohydride systems ($0.62LiBH_4$-$0.38NaBH_4$, $0.75LiBH_4$-$0.25KBH_4$), as well as their destabilized systems using selected additives (micron-sized SiO_2, nano-sized Ni).

All decomposition products presented in XRD, Raman and FTIR results were measured at room temperature. Thus, these data only indicate the stable phases at room temperature. Unstable or intermediate phases are therefore not represented but cannot be ruled out. In addition, most of decomposition products have higher melting points than the heat-treatment temperatures used (Appendix F), they were in crystalline structures once formed. The exceptions are metallic Na and K, which stayed in their liquid state.

10.1 Dehydrogenation of $LiBH_4$ and $LiBH_4$-based Low-melting-point Borohydride Systems

$LiBH_4$, the lightest borohydride, has been considered as one of the most promising solid-state H_2 storage candidates since 2003 (A. Züttel et al. 2003), due to its relatively high theoretical gravimetric (18.5 wt%) and volumetric (121 kgH_2/m^3) H_2 densities. It starts to release H_2 immediately after fusion at 270-280 °C, but the major dehydrogenation often starts above 350 °C through partial reversible reactions (Orimo et al. 2005). The high thermal stability and limited reversibility have so far hindered its applications as a H_2 storage material, particularly for mobile application. There have

been many efforts in trying to find suitable approaches to destabilize the dehydrogenation process, as well as to improve the cycling properties (i.e. the ability to rapidly reabsorb hydrogen).

In fact, the dehydrogenation of $LiBH_4$ involves complex chemical reactions, which vary as a function of temperature and pressure. A series of boranes may be present during this process as intermediate phases and/or by-products (Ohba et al. 2006; Huang et al. 2016; Hansen et al. 2016; Sethio et al. 2017). Among which, the most stable phases are $Li_2B_{10}H_{10}$ and $Li_2B_{12}H_{12}$. These two phases have been experimentally observed during the dehydrogenation of $LiBH_4$ (Friedrichs, Remhof, Hwang, et al. 2010), as a consequence of the chemical reactions between B_2H_6 with the excess $LiBH_4$ at temperatures (~150 °C) lower than the major decomposition reactions (> 350 °C).

However, the well-accepted decomposition pathways for $LiBH_4$ are:

$$\boldsymbol{LiBH_4 = LiH + B + 3/2H_2} \qquad \textbf{13.9 wt. \%} \qquad \textbf{Equation 10.1}$$

$$\boldsymbol{LiBH_4 = 5/6LiH + 1/12Li_2B_{12}H_{12} + 13/12H_2} \qquad \textbf{10.0 wt. \%} \qquad \textbf{Equation 10.2}$$

In this work, LiH, B, $Li_2B_{12}H_{12}$ have been observed using XRD and Raman. Although some reports claim that $Li_2B_{10}H_{10}$ is present during the dehydrogenation and rehydrogenation of $LiBH_4$ (Friedrichs, Remhof, Hwang, et al. 2010; Xu et al. 2013), this phase was not observed throughout this work using XRD, Raman or FTIR. This was possibly due to its relatively low composition (6 mol%) in the product in contrast to $Li_2B_{12}H_{12}$ (94 mol%) (Yan, Rentsch, Battaglia, et al. 2017). In general, since breaking and forming B-H bonds is critical for reversible H_2 sorption in borohydrides, these closo-boranes are therefore not favourable due to their strong thermal stability.

Assuming all $LiBH_4$ has been completely decomposed in the TPD-MS measurement, this work found around 60 % of H_2 release was associated with the formation of LiH and B, and the rest were contributed from the precipitation of LiH, $Li_2B_{12}H_{12}$.

Recently, the low-melting-point borohydride systems (often noted as "eutectic borohydrides") have been proposed as one of the promising approaches to achieve destabilization of borohydrides and to improve reversibility (M Paskevicius et al. 2013). Several systems have been reported, as introduced in Chapter 4. However, only a limited number of them have been fully studied, especially on their dehydrogenation and recombination mechanisms. This work focused on investigating the $0.62LiBH_4$-$0.38NaBH_4$ (Chapter 8) and $0.75LiBH_4$-$0.25KBH_4$ (Chapter 9) systems. These mixtures were synthesized using ball milling.

For the $0.62LiBH_4$-$0.38NaBH_4$ mixture (noted as LiNa), the expansion and shrinkage of unit cell volumes for $LiBH_4$ and $NaBH_4$ in the as-milled mixture were observed, respectively. They indicate the existence of solid solutions: $Li(Na)BH_4$ and $Na(Li)BH_4$ although the $LiBH_4$ and $NaBH_4$ had different structures and coordination preferences of Li^+ and Na^+ (A. Züttel et al. 2003; Kumar & Cornelius 2005). These changes in unit cell volumes agreed well with the *in situ* synchrotron XRD data reported by Dematteis et al. (2016). The solid solution $Li(Na)BH_4$ was considered as the major reaction that caused an early orthorhombic-hexagonal phase transition of the $LiBH_4$ content in the mixture (e.g. 94 °C for LiNa < 115 °C for $LiBH_4$), leading to an enhanced Li^+ conductivity (Xiang et al. 2017). In addition, the additives used in this work, i.e. micron-sized SiO_2

and nano-sized Ni, did not affect this low phase transition temperature of $LiBH_4$, indicating that the solid solutions were relatively stable.

For the $0.75LiBH_4$-$0.25KBH_4$ mixture (noted as LiK), a binary stoichiometric compound, $LiK(BH_4)_2$, was found in the as-milled mixture as a reaction product of $LiBH_4$ and KBH_4 by compression (Nickels et al. 2008). This was not a stable phase that disappeared in the recrystallized sample (after annealing at 150 °C in Ar) through dissociating into $LiBH_4$ and KBH_4. This agreed with the observation by Ley et al. (2014) where this phase was not present above 95 °C.

As a low-melting-point borohydride system, the LiNa or LiK mixture exhibited a much lower melting temperature (225 °C for LiNa, 108 °C for LiK) than their pure constituents (285 °C for $LiBH_4$, 510 °C for $NaBH_4$ and 605 °C for KBH_4) (Table 10.1). Although LiNa or LiK synthesized in this work did not match the suggested eutectic composition precisely, their melting points agreed well with the literature (Ley et al. 2014; Javadian, Sheppard, et al. 2015). In fact, the eutectic behaviour of borohydride mixtures was due to the fact that the stable liquid phase of borohydrides mixture has the lowest Gibbs free energy among all possible phases in an equilibrium system above the melting point.

In Table 10.1, the amount of H_2 released from each system was investigated using TPD-MS in Ar. In general, none of these systems reached their maximum theoretical gravimetric capacity. This is a common phenomenon in the research field of borohydrides for H_2 storage applications, possibly due to: 1) uncompleted

dehydrogenation of reactants as a consequence of relatively high thermal stability or leaving heating zone by bubbling-frothing effect; 2) products (e.g. LiH, NaH, KH) or by-products (e.g. $Li_2B_{12}H_{12}$, $Na_2B_{12}H_{12}$, $K_2B_{12}H_{12}$) formed during dehydrogenation that held the available H_2 content.

Table 10.1 Summary of the melting temperature (Tm), gravimetric capacity (ρ_g), H_2 released at the target temperature (T_t) in Ar, the dehydrogenation onset (T_{onset}) and peak (T_{peak}) temperatures when heating at 2 °C min^{-1} in Ar for systems of $LiBH_4$; $NaBH_4$; KBH_4 and their low-melting-point mixtures (0.62$LiBH_4$-0.38$NaBH_4$ (LiNa), 0.75$LiBH_4$-0.27KBH_4 (LiK)).

System	T_m	ρ_g	H_2 (T_t) in Ar	T_{onset}	T_{peak} (2 °C min^{-1}, Ar)
	°C	wt.%	wt.%	°C	°C
$LiBH_4$	285	18.5	10.0 (650) 10.9 (700)	285	470
$NaBH_4$	510*	10.7	7.8 (650)	450	580
KBH_4	605*	7.5	6.1 (700)	325	658
LiNa	225	14.5	10.8 (650)	287	488, 540
LiK	108	13.5	8.9 (700)	290	487, 638

** the melting point of $NaBH_4$ and KBH_4 are not measured in this work, obtained from (Paskevicius et al. 2017)*

The bubbling-frothing effect implies that the molten phase of several borohydrides (or their mixtures) tends to bubble, forth, vaporize, spatter, or climb the containing surface, due to the gas evolution and their relatively low viscosities combined with high surface tensions (M Paskevicius et al. 2013). The presence of impurities, even in minor quantities, may effectively inhibit the bubbling-frothing during melting (Vines 2016). This work found that bubbling-frothing effect can be significantly reduced through adding 5 mol% of micron-sized SiO_2 (Figure 7.17).

In addition, the dehydrogenation peak temperatures for each system are also compared in Table 10.1. The peak temperature indicates the moment when the kinetic of chemical reaction(s) reaches the maximum. The LiNa and LiK mixtures consisted of two constituents (e.g. $LiBH_4$ and $NaBH_4$ for LiNa; $LiBH_4$ and KBH_4 for LiK) and had two

major dehydrogenation peaks. Although the overall dehydrogenation progress of LiNa and LiK mixtures could be seen as a combination of their constituents, the temperatures of these dehydrogenation peaks for LiNa and LiK mixtures were shifted and lay between that for their constituents. For example,

- 470 °C for $LiBH_4$ < 488, 540 °C for LiNa < 580 °C for $NaBH_4$;
- 470 °C for $LiBH_4$ < 487, 638 °C for LiK < 658 °C for KBH_4.

These shifts were due to cation interactions, where cations with different Pauling electronegativity (Pauling 1932; Jensen 1996) (0.98 for Li^+ > 0.93 for Na^+ > 0.92 for K^+) simultaneously existed in the molten phase. Electronegativity of metal has been found strongly related to the thermal stability of the corresponded borohydrides (Nakamori et al. 2006; Nakamori et al. 2007; Rude et al. 2011): the high electronegative metal leads to weak thermal-stable borohydride. For a molten borohydrides mixture, the dual cations may locally change the B-H bond length and thus affected the overall dehydrogenation.

The cation interaction concept could explain the changes of dehydrogenation peak temperatures in LiNa and LiK systems. However, it could not explain the relatively lower dehydrogenation temperatures observed in $0.55LiBH_4$-$0.45Mg(BH_4)_2$ (noted as LiMg) or $0.68LiBH_4$-$0.32Ca(BH_4)_2$ (noted as noted as LiCa) system than their pure constituents (Yan et al. 2013; Paskevicius et al. 2017), since these destabilization phenomenon were likely caused by a kinetic effect according to Paskevicius et al. (2017).

Besides H_2 storage properties, this work also studied the decomposition mechanisms of the $LiBH_4$, LiNa and LiK systems. The dehydrogenation reactions (in Ar) for $LiBH_4$ and LiNa could be written in chemical equations (Equation 7.6 and 8.7) and are thus compared in Table 10.2.

Table 10.2 The decomposition mechanism of $LiBH_4$ compared with $0.62LiBH_4$-$0.38NaBH_4$ whose composition is normalized to 1 mole of $LiBH_4$.

Reactants		Product				
$LiBH_4$	$NaBH_4$	LiH	B	$Li_2B_{12}H_{12}$	Na	H_2
1		0.94	0.64	0.03		1.35
1	0.61	0.97	1.42	0.02	0.61	2.65

It has been noted that less $Li_2B_{12}H_{12}$ was formed from the LiNa mixture. This agrees with more H_2 being released from LiNa (10.8 wt.%) than for the theoretical expectation (8.9 wt.%, calculated via a weighted average method using the mass fraction and experimental H_2 release from $LiBH_4$ and $NaBH_4$). Due to its high thermal stability, the $Li_2B_{12}H_{12}$ phase was often considered as a boron-sink (Yan et al. 2012) that hindered the rehydrogenation. And it was therefore not preferred in any H_2 storage system. Thus, reducing the composition of $[B_{12}H_{12}]^{2-}$ phase in the decomposition product is critical at achieving a highly reversible-H_2 storage system.

Besides, LiK had more complicated dehydrogenation behaviour and thus its decomposition reactions could not be numerically expressed. For instance, due to the presence of K^+, the $LiBH_4$ content in LiK was not fully dehydrogenated at the 1st dehydrogenation step and released at least 3.3 wt.% hydrogen at the 2nd dehydrogenation step. This phenomenon has not been reported for other borohydrides

mixtures. The major dehydrogenation products at each step were found to be 1) LiH, B, $Li_2B_{12}H_{12}$, H_2 and 2) K, B, H_2.

Compared with other known eutectic borohydrides systems (e.g. LiMg or LiCa), the decomposition mechanisms of LiNa and LiK are relatively simpler. In general, the LiMg and LiCa systems have multistep decomposition mechanisms (Bardají et al. 2011; Lee et al. 2011): the less stable borohydrides ($Mg(BH_4)_2$ or $Ca(BH_4)_2$) often dehydrogenate first at low temperatures, and then their decomposition products (Mg, MgH_2 or CaH_2) (or sometimes themself) can intensively react with $LiBH_4$ at relatively higher temperatures (Nale et al. 2011; Yan et al. 2013). In fact, $LiBH_4$-MgH_2 or $LiBH_4$-CaH_2 is a recognized reactive hydride composites (RHCs) system that significantly destabilizes the dehydrogenation of $LiBH_4$ by forming a more stable compound (MgB_2 or CaB_6) (Pinkerton & Meyer 2008). However, the formation of a RHCs is not possible in LiNa and LiK systems, as $LiBH_4$ is the less stable borohydride and any of its major decomposition products (Li, LiH, B) (or itself) cannot react with $NaBH_4$ or KBH_4 in a destabilization way. Thus, the destabilization effect through forming RHCs during dehydrogenation was not possible for LiNa and LiK systems (M Paskevicius et al. 2013).

10.2 Effect of Micron-size SiO_2 Additives

As a strong reducing agent, $LiBH_4$ can react with almost all kinds of additives, which affects its common decomposition pathways. In some cases, adding additives can destabilize the dehydrogenation of $LiBH_4$ causing lower onset or peak temperatures; and the reaction products may improve the cycling stability.

The 1st studied additive for $LiBH_4$ was SiO_2 (A. Züttel et al. 2003). It significantly reduces the dehydrogenation onset temperatures by 200 °C (25 wt.% $LiBH_4$ with 75 wt.% SiO_2), although the reactions are non-reversible due to the stable reaction products: Li_2SiO_3 and/or Li_4SiO_4 (Mosegaard et al. 2008).

In this work, a series of 5 mol% SiO_2 particles with different sizes (diameters: 0.5, 1.0 and 1.5 μm) were gently mixed with $LiBH_4$ by hand. Their destabilization effects on the dehydrogenation of $LiBH_4$ (e.g. up to 1.5 wt.% H_2 release for $LiBH_4$-SiO_2 before 400 °C > 0.2 wt.% for pristine $LiBH_4$) and the formation of Li_2SiO_3 and Li_4SiO_4 agreed with the literature (Opalka et al. 2009; Chen et al. 2010; Ngene, Adelhelm, et al. 2010). The formation of Li_4SiO_4 was usually observed at high temperatures (450-500 °C) (Zhang et al. 2008; Mosegaard et al. 2008; Ngene, Adelhelm, et al. 2010). However, in this work, it was observed at a much lower temperature, e.g. above 350 °C. Thermodynamic calculations (Appendix C) suggest that reactions between $LiBH_4$ and SiO_2 may go through different pathways than those reported equations (Ngene, Adelhelm, et al. 2010). In addition, this work found that the total amount of H_2 released from $0.95LiBH_4$-$0.05SiO_2$ (noted as Li-Si) upon heating to 400 °C in Ar increased when the specific surface area of SiO_2 rose. This suggests that the additives with a smaller particle size had a greater destabilization effect than for larger particles.

To try to destabilize the low-melting-point borohydride mixtures studied in this work, the SiO_2 particles (0.5 μm) were added to the LiNa and LiK mixtures by hand mixing. The as-prepared samples are $0.95(0.62LiBH_4$-$0.38NaBH_4)$-$0.05SiO_2$ (noted as LiNa-Si)

and $0.95(0.75LiBH_4\text{-}0.25KBH_4)\text{-}0.05SiO_2$ (noted as LiK-Si), and their dehydrogenation properties are compared in Table 10.3.

Table 10.3 Summary of the melting temperature (Tm), gravimetric capacity (ρ_g), H_2 released at the target temperature (T_t) in Ar, the dehydrogenation onset (T_{onset}) and peak (T_{peak}) temperatures while heating at 2 °C min-1 in Ar for systems of $LiBH_4$; $NaBH_4$; KBH_4; their low-melting-point mixtures ($0.62LiBH_4\text{-}0.38NaBH_4$ (LiNa), $0.75LiBH_4\text{-}0.27KBH_4$ (LiK)) and systems containing 5 mol% SiO_2 (0.5 µm) ($0.95LiBH_4\text{-}0.05SiO_2$ (Li-Si), $0.95(0.62LiBH_4\text{-}0.38NaBH_4)\text{-}0.05SiO_2$ (LiNa-Si), $0.95(0.75LiBH_4\text{-}0.25KBH_4)\text{-}0.05SiO_2$ (LiK-Si)).

System		T_m	ρ_g	H_2 (T_t) in Ar	T_{onset}	T_{peak} (2 °C min^{-1}, Ar)
		°C	wt.%	wt.%	°C	°C
Pure	$LiBH_4$	285	18.5	6.7 (500) 10.0 (650) 10.9 (700)	285	470
	$NaBH_4$	510*	10.7	7.8 (650)	450	580
	KBH_4	605*	7.5	6.1 (700)	325	658
Mixture	LiNa	225	14.5	10.8 (650)	287	488, 540
	LiK	108	13.5	8.9 (700)	290	487, 638
with Si	Li-Si	n.a.	17.6	4.7 (500) 5.1 (550)	281	303, 375, 467
	LiNa-Si	226	13.7	7.3 (650)	245	(290-350), 490, 530
	LiK-Si	108	12.8	9.6 (700)	258	300, 490, 655(605, sh)

* *sh = shoulder peak*

In general, adding SiO_2 did not affect the low-temperature melting behaviours of LiNa-Si and LiK-Si systems. However, it destabilized these systems, exhibiting reductions of dehydrogenation onset temperatures by 32-42 °C and allowing ~1 wt.% hydrogen release at 400 °C in Ar. These early H_2 releases below 400 °C were due to reactions between $LiBH_4$ and SiO_2 forming Li_2SiO_3 and Li_4SiO_4, which were in agreement with the case of Li-Si. Although reactions between $NaBH_4$ or KBH_4 and SiO_2 might be possible as the stable sodium- or potassium- silicate existed (McDonald & Cruickshank 1967; Baur et al. 1986; Bernet & Hoppe 1990; Kahlenberg et al. 1999), these silicate compounds were not observed in this work; likely due to the fact that formation of Li_2SiO_3 and Li_4SiO_4 were more thermodynamically stable than them.

Besides, due to the change of reaction pathways (Table 10.4), the total amount of H_2 released from LiNa-Si was lower than that of LiNa. Comparing with the SiO_2-free samples, SiO_2 facilitated the formation of $[B_{12}H_{12}]^{2-}$ phases, as the amount of $Li_2B_{12}H_{12}$ was significantly higher and the existence of $Na_2B_{12}H_{12}$ was suggested by calculations (under several assumptions).

Table 10.4 The decomposition mechanism of $LiBH_4$ compared with $0.62LiBH_4$-$0.38NaBH_4$ (LiNa) and $0.95(0.62LiBH_4$-$0.38NaBH_4)$-$0.05SiO_2$ (LiNa-Si). The reaction between $LiBH_4$ and SiO_2 are not shown.

System	Reactants		Product					
	$LiBH_4$	$NaBH_4$	LiH	B	$Li_2B_{12}H_{12}$	Na	$Na_2B_{12}H_{12}$	H_2
$LiBH_4$	1		0.94	0.64	0.03			1.35
LiNa	1	0.61	0.97	1.42	0.02	0.61		2.65
LiNa-Si	1	0.72	0.83	0.07	0.09	0.62	0.05	2.21

Moreover, the LiK-Si released more H_2 in contrast to LiK (Table 10.3). A peak with a shoulder at 655 °C was found for LiK-Si. This peak has not been observed in other systems studied in this work and its corresponded reaction was under investigation. Similarly to LiK, the $LiBH_4$ content in LiK-Si was not fully dehydrogenated at the first dehydrogenation step. Some parts of $LiBH_4$ decomposed at higher temperature along with the decomposition of KBH_4, releasing at least 3.1 wt.% of hydrogen.

10.3 Effect of Nano-sized Ni Additives

The results of adding SiO_2 suggested that the particle size plays an important role in destabilization of dehydrogenation: the small-size particles usually lead a better destabilization results. From the engineering aspects, the smallest manufacturable solid particle is in nano-size (<100 nm). These ultra-small particles have significantly improved specific surface areas, leading to more extensive intimate interactions at the

contacts with other materials, and can finally results in ultra-high reactivity. This effect is usually noted as “nano-size effect” (Berube et al. 2008; C. Liu et al. 2010).

Many nano-sized particles have been used to destabilize borohydrides, and some of them can improve the cycling stability at the same time (Li et al. 2014; Zhang et al. 2015; J. Wang et al. 2016; Puszkiel et al. 2017). This work was interested in the destabilization effect of Ni on the dehydrogenation of $LiBH_4$. This metal has been used in the past: the addition of 25 wt.% nano-sized Ni into $LiBH_4$ can reduce the dehydrogenation peak temperature by 50 °C and improve the reversible H_2 content (from 4.3 wt.% for Ni-free sample) to 10.8 wt.% (Li et al. 2014).

In this work, 14 mol% Ni (nano-sized: ~100 nm; bulk: ~ 3 μm) was added to $LiBH_4$ using ball milling. The major dehydrogenation of the as-milled samples started around 350-450 °C and their peak temperatures (445 °C for nano-sized Ni, and 460 °C for bulk Ni) were much lower than that for the Ni-free sample (470 °C). These destabilization effects were due to the change of reaction pathway whereby Ni_4B_3 was formed, which agreed with the literature (Li et al. 2014). Other nickel borides, such as Ni_2B and Ni_3B, have been suggested as reaction products (Xia et al. 2009; Li et al. 2014); however, they were not found in this work. This was possibly because the formation of nickel borides (from $LiBH_4$ and Ni) was a function of composition, temperature, pressure and other conditions. In addition, the nano-sized Ni additive facilitated the formation of $Li_2B_{12}H_{12}$, as the amount of $Li_2B_{12}H_{12}$ generated from $0.943LiBH_4$-0.057Ni (noted as Li-Ni) was found to be three times higher than that from the Ni-free sample (Table 10.4).

To attempt to reduce the dehydrogenation temperatures and to improve the cycling stability, the same nano-sized Ni was added to the LiNa and LiK mixtures. The as-milled samples were $0.91(0.62LiBH_4\text{-}0.38NaBH_4)\text{-}0.09Ni$ (noted as LiNa-Ni) and $0.86(0.75LiBH_4\text{-}0.25KBH_4)\text{-}0.14Ni$ (noted as LiK-Ni). Their dehydrogenation properties are compared in Table 10.5.

Table 10.5 Summary of the melting temperature (Tm), gravimetric capacity (ρ_g), H_2 released at the target temperature (T_t) in Ar, the dehydrogenation onset (T_{onset}) and peak (T_{peak}) temperatures while heating at 2 °C min-1 in Ar for systems of $LiBH_4$; $NaBH_4$; KBH_4; their low-melting-point mixtures ($0.62LiBH_4\text{-}0.38NaBH_4$ (LiNa), $0.75LiBH_4\text{-}0.27KBH_4$ (LiK)); systems containing 5 mol% SiO_2 (0.5 µm) ($0.95LiBH_4\text{-}0.05SiO_2$ (Li-Si), $0.95(0.62LiBH_4\text{-}0.38NaBH_4)\text{-}0.05SiO_2$ (LiNa-Si), $0.95(0.75LiBH_4\text{-}0.25KBH_4)\text{-}0.05SiO_2$ (LiK-Si)) and system containing nano-sized Ni (~100 nm) ($0.943LiBH_4\text{-}0.057Ni$ (Li-Ni), $0.91(0.62LiBH_4\text{-}0.38NaBH_4)\text{-}0.09Ni$ (LiNa-Ni), $0.86(0.75LiBH_4\text{-}0.25KBH_4)\text{-}0.14Ni$ (LiK-Ni)).

System		T_m	ρ_g	H_2 (T_t) in Ar	T_{onset}	T_{peak} (2 °C min^{-1} Ar)
		°C	wt.%	wt.%	°C	°C
Pure	$LiBH_4$	285	18.5	6.7 (500) 10.0 (650) 10.9 (700)	285	470
	$NaBH_4$	510*	10.7	7.8 (650)	450	580
	KBH_4	605*	7.5	6.1 (700)	325	658
Mixture	LiNa	225	14.5	10.8 (650)	287	488, 540
	LiK	108	13.5	8.9 (700)	290	487,638
with Si	Li-Si	n.a.	17.6	4.7 (500)	281	303, 375, 467
	LiNa-Si	226	13.7	7.3 (650)	245	(290-350), 490, 530
	LiK-Si	108	12.8	9.6 (700)	258	300, 490, 655(605, sh)
with Ni	Li-Ni	n.a.	17.5	5.5 (500)	187	445
	LiNa-Ni	225	13.2	8.1 (650)	150-200	468, 515, 586
	LiK-Ni	109	11.6	7.1 (700)	150-200	473, 602

The low dehydrogenation onset temperatures observed in LiNa-Ni and LiK-Ni systems were due to the NiO presented in the as-received nano-sized Ni. These onset temperatures were much lower than that of Si-contained samples; perhaps due to the fact that the transition-metal oxides have much better destabilization performances than that of SiO_2 as observed by Nale et al. (2011).

Compared with the Ni-free mixtures, the nano-sized Ni did not affect the low melting points of LiNa-Ni and LiK-Ni systems. In addition, it caused slight lower gravimetrical H_2 releases from these systems as the price for using Ni, a relatively heavy transition metal. However, using nano-sized Ni destabilized the dehydrogenations of these low-melting-point mixtures, causing lower dehydrogenation peak temperatures for all major peaks. This was different from the case of SiO_2, possibly due to the strong catalyst effect of Ni_4B_3 (Li et al. 2014). A 3rd dehydrogenation peak at 586 °C was observed in LiNa-Ni mixture, this was due to the formation of $Li_{1.2}Ni_{2.5}B_2$ and unknown phase(s). The former phase has been seen in the past as one of the reaction products of $LiBH_4$ and Ni powder (~ 41 μm) at 600 °C (Xia et al. 2009). The XRD results in this work proposed that its formation was due to the reaction between LiH, B, and Ni_4B_3.

In the past, Mg or MgH_2 (27 mol%) have been used to destabilize the dehydrogenation of LiK mixture (Roedern et al. 2015), causing reductions in dehydrogenation onset temperatures (e.g. hydrogen release since melting at 105 °C) and the major dehydrogenation temperatures (by ~25 °C), and a total of 2.5 wt.% or 5.0 wt.% H_2 release at 500 °C in Ar, respectively. Compared with MgH_2, the addition of 5 mol% SiO_2 or 14 mol% nano-sized Ni to LiK released less H_2 upon heating to the same temperature in Ar, e.g. 4.0 wt.% or 3.2 wt.%, respectively. Since the amount of these additives were different, it was hard to determine which additive had the greatest destabilization effect.

Similar to other LiK-based systems, the $LiBH_4$ content in LiK-Ni was not fully dehydrogenated at one step, and some parts of $LiBH_4$ decomposed at higher temperature

along with the decomposition of KBH_4, releasing at least 2.4 wt.% H_2. In addition, the formation of Ni_2B and unknown phase(s) above 519 °C together with the disappearance of Ni_4B_3 at the 2nd step was noticed. This was different from the case of LiNa-Ni where $Li_{1.2}Ni_{2.5}B_2$ was formed and from the case of Li-Ni where only Ni_4B_3 was observed in the reaction products. Thus, the addition of different alkali metal cations may lead to different Ni-based reaction products.

Similar to the case of SiO_2, the addition of nano-sized Ni caused more $[B_{12}H_{12}]^{2-}$ phases in the products. This may due to the external surface areas provided by the stable reaction products (Li_2SiO_3, Li_4SiO_4, or Ni_4B_3) in molten $LiBH_4$; since Appendix B revealed that the rough surface facilitated the formation of $[B_{12}H_{12}]^{2-}$ phase during decomposition of $LiBH_4$.

Because nano-sized Ni could significantly improve the reversibility of $LiBH_4$ suggested by Li et al. (2014), the rehydrogenation of LiNa, LiNa-Ni, LiK and LiK-Ni were studied using a Sieverts type apparatus as described in Section 6.2.6. The reaction conditions were: 500 °C, 1 bar H_2 and 10 h for desorption; and 400 °C, 130 bar H_2 and 12 h for absorption. The contents of reversible H_2 in these systems are compared in Table 10.6.

Table 10.6 Reversible H_2 contents (wt.%) of $0.62LiBH_4$-$0.38NaBH_4$ (LiNa), $0.75LiBH_4$-$0.27KBH_4$ (LiK), and system containing nano-sized Ni (~100 nm): $0.943LiBH_4$-0.057Ni (Li-Ni), $0.86(0.75LiBH_4$-$0.25KBH_4)$-0.14Ni (LiK-Ni). The corrected value that excluded the weight of additives is list in brackets.

H_2 (wt.%)	LiNa	LiNa-Ni	LiK	LiK-Ni
1st cycle	5.5	5.1 (6.2)	5.8	5.1 (6.3)
2nd cycle	1.1	1.1 (1.3)	1	0.5 (0.6)
3rd cycle	0.8	0.6 (0.7)	0.4	0.2 (0.3)

As a consequence of using nano-sized Ni, more H_2 was released from LiNa-Ni (6.2 wt.%) and LiK-Ni (6.3 wt.%) samples at the 1st cycle compared with their Ni-free samples (5.5 and 5.8 wt.%, respectively). This was due to the destabilization effect of nano-sized Ni with $LiBH_4$, as Ni_4B_3 was observed in their decomposition products.

Although the samples were kept at 500 °C that was not favourable for the major dehydrogenation of $NaBH_4$ or KBH_4 to occur, NaH was found in the dehydrogenation products of LiNa-Ni, whilst no K or KH was seen. This disagreed with the LiNa sample, where pure Na was often formed. Since Na has a low vaporization temperature, it can leave the heating zone as a gas phase and further react with H_2 forming NaH. This phenomenon has been noticed in the $NaBH_4$-Ni system as well and caused a physical segregation, leading to poor cycling stability (Humphries et al. 2013). Thus, physically controlling the contacts of reaction products became important for achieving high reversibility of borohydrides. This might be achieved via the confinement of reactants in scaffolds, i.e. nanoconfinement.

In addition, physically mixing the segregated dehydrogenation products of LiNa-Ni at 1st cycle (Figure E.4), the XRD signals of NaH and Ni_4B_3 disappeared after rehydrogenation treatment. Instead, peaks of Ni_4B and Ni_2B were observed. Since Ni_2B is the oxidation product of Ni_3B (Humphries et al. 2013), a possible rehydrogenation reaction of $NaBH_4$ was proposed:

$$2NaH + 3Ni_4B_3 + 3H_2 \rightarrow 2NaBH_4 + 4Ni_3B + 3B \qquad \textbf{Equation 10.3}$$

However, the thermodynamic calculations cooperated with Mrs. Erika Michela Dematteis (University of Turin) have not found a negative Gibbs free energy of reaction for this chemical equation yet. This is likely because that the currently Gibbs free energy function in the database for the phases involved in this equation needed to be optimised.

Moreover, all samples studied in this work showed poor cycling stability as the reversible H_2 content reduced dramatically starting from the 2nd cycle, maintaining 4-15% of initial H_2 capacity after three-complete hydrogen release and uptake cycles. The poor cycling stability for LiNa and LiK agreed with the literature (Javadian, Sheppard, et al. 2015; Roedern et al. 2015), though different condition were applied for H_2 sorption measurements. However, this was not expected for the LiNa-Ni and LiK-Ni systems, and disagreed with the high reversibility of $LiBH_4$ achieved by adding nano-sized Ni in (Li et al. 2014). This may be because much stronger rehydrogenation conditions (350 bar H_2, 550 °C, 24 h) were used by Li et al. (2014) than in this work (130 bar H_2, 400 °C, 12 h). Since the recombination of $LiBH_4$ from LiH, B and H_2 often required strong conditions (350 bar H_2, 600 °C, 12 h) (Orimo et al. 2005), a stronger combination of conditions might be needed in order to improve the cycling stability. Alternatively, nanoconfinement into the high surface area carbon aerogel scaffold could significantly stabilize the H_2 cycling capacities of LiNa (Javadian, Sheppard, et al. 2015). Combining using additives and nanoconfinement techniques may become another approach that has the potential to provide a better cycling stability.

Different from $0.4LiBH_4$-$0.6Ca(BH_4)_2$ system where $LiBH_4$ is fully reversible starting from the 2nd cycle (Javadian et al. 2017), no direct evidence showing $LiBH_4$ was reformed in LiNa or LiK using XRD or FTIR. Interestingly, some FTIR signals related to $LiBH_4$ were observed for LiNa-Ni after absorbing H_2 at the 3rd cycle, indicating that a partial reversible $LiBH_4$ was formed in an amorphous state. As this was not seen in its corresponding Ni-free sample, this partial reversible $LiBH_4$ content might be induced with the help of other reaction products, such as Ni_3B_4 (Li et al. 2014). In addition, this partial reversibility of $LiBH_4$ was not observed in the LiK-Ni sample, suggesting that the reaction products of $NaBH_4$ in LiNa-Ni may also play a role in reforming amorphous $LiBH_4$.

10.4 Summary

This thesis is a detailed and thorough investigation into $LiBH_4$-based pseudo eutectic borohydride mixtures ($0.62LiBH_4$-$0.38NaBH_4$ and $0.725LiBH_4$-$0.275KBH_4$) for hydrogen storage. Although these low-melting-point borohydride systems have been studied (for their hydrogen storage properties) in the past, this work presents a detailed study investigating the reaction pathways, which is important for further understanding of these borohydride systems.

In general, these mixtures are able to release up to 10.8 wt.% of hydrogen at high temperatures (> 650 °C) (Table 10.5). These gravimetric hydrogen capacities are far above the DOE technical system targets for 2020 (Table 2.1) and are still competitive when system hardware mass are counted by a rule of thumb (Ott 2010). However, this work suggested these materials are not feasible as hydrogen storage materials for

mobile applications because of their very high dehydrogenation temperature and limited reversibility. Nanoconfinement is therefore recommended in order to improve the hydrogen desorption and uptake.

Moreover, the dehydrogenations of these low-melting-point borohydride mixtures occur at higher temperatures than their melting points (Table 10.5). As a consequence, the composition ratio between the parent borohydrides will change during dehydrogenation as a function of temperature and pressure and result in $NaBH_4$-rich or KBH_4-rich mixtures. According to their binary phase diagrams (Figure 4.3 and 4.4), the mixture crosses the liquidus line and precipitates the parent borohydride ($NaBH_4$ or KBH_4) when the concentration of $LiBH_4$ reduces. However, this precipitation is doubtful and was not observed in the DSC data of a $0.725LiBH_4$-$0.275KBH_4$ mixture reported by Roedern et al. (2015). Thus, *in situ* measurements using high-temperature XRD are recommended in order to identify this solidification of parent borohydride at high temperature. Apart from that, this work identified the dehydrogenation products (in Ar) in a wide temperature range. Most of the decomposition phases are solid and have not been included in the previously reported phase diagrams. Therefore, the results of this work are helpful to construct the detailed phase diagram for these systems in the future.

In addition, the effect of micron-sized silica and nano-sized nickel additions to these systems and the resulting influence on the reaction pathways has been investigated for the first time. It needs to be noticed that use of these additives facilitates the formation of unfavourable phases (dodecaborates) for hydrogen storage, although the dehydrogenations are destabilized thermodynamically. This facilitation is very likely

caused by the roughness of the surface of the reaction products and may be a general situation when additives are used to destabilize the dehydrogenation of borohydrides. Optimizations of the composition of additives are also needed.

In summary, before practical application of a low-melting-point alkali metal borohydride mixture, further compositional optimization with respect to the rehydrogenation conditions is required, in parallel with the use of nano-confinement of the mixture via an infiltration approach.

CHAPTER 11 CONCLUSIONS AND FUTURE WORK

Metal borohydride is one of the most promising solid-state H_2 storage materials, and consequently has been intensively investigated since 2003. However, much research is still needed to gain better understandings of their structural evolution during the dehydrogenation and rehydrogenation processes, as well as to further tailor their properties to obtain novel systems suitable for mobile H_2 storage applications. With a greater understanding of the H_2 sorption mechanisms, it may be possible to "tune" a more favourable reaction pathway, as well as to lower the conditions (i.e. reduce temperature and/or H_2 pressure) required to achieve reversibility (i.e. reabsorption of hydrogen).

The aims of this project were to gain a greater understanding of the H_2 desorption mechanisms of $LiBH_4$ and $LiBH_4$-based low-melting-point borohydride systems, and to tailor their H_2 storage property using selected additives, as well as to improve the cycling stability.

11.1 Conclusions

In this thesis, $LiBH_4$ and two low-melting-point borohydride systems ($0.62LiBH_4$-$0.38NaBH_4$, $0.75LiBH_4$-$0.25KBH_4$) have been systematically investigated mainly by XRD, Raman, FTIR, DSC, TPD-MS, Sieverts-type PCI measurements with particular attentions given to their crystal and vibrational structures, hydrogenation and dehydrogenation pathways:

- $LiBH_4$ has two polymorphs. It has an orthorhombic structure (space group *Pnma*) at room temperature and undergoes a first order phase transition to hexagonal structure (space group $P6_3mc$) at 115 °C. It starts to release H_2 immediately after fusion at 285 °C with a total of 10 wt.% hydrogen release upon heating to 650 °C in Ar, through:

$$\boldsymbol{LiBH_4 = 0.94LiH + 0.64B + 0.03Li_2B_{12}H_{12} + 1.35H_2} \qquad \textbf{Equation 11.1}$$

- The $0.62LiBH_4$-$0.38NaBH_4$ mixture exhibits a low melting point at 225 °C. In the as-milled mixture, solid solutions ($Li(Na)BH_4$ and $Na(Li)BH_4$) exist that affect the unit cell volume of $LiBH_4$ (expansion) and $NaBH_4$ (shrinkage). The substitution of Na^+ is responsible for a decrease in the orthorhombic to hexagonal $LiBH_4$ phase transition temperature by 21 °C to 94 °C. This mixture starts to release H_2 at 287 °C with a total of 10.8 wt.% hydrogen evolution upon heating to 650 °C in Ar, forming less $Li_2B_{12}H_{12}$ via:

$$\boldsymbol{0.62LiBH_4 - 0.38NaBH_4 \rightarrow 0.6LiH + 0.88B + 0.01Li_2B_{12}H_{12} + 0.38Na + 1.64H_2} \qquad \textbf{Equation 11.2}$$

- In the $0.75LiBH_4$-$0.25KBH_4$ mixture, $LiK(BH_4)_2$ becomes the major phase. It forms from reaction between $LiBH_4$ and KBH_4 under compression during sample preparation using ball milling. It is not a thermally stable phase and will dissociate after heating to 150 °C. The fusion temperature of this system is 108 °C, which is even lower than the phase transition temperature of pure $LiBH_4$ (115 °C). The H_2 evolution starts above 290 °C with a total of 8.9 wt.% hydrogen upon heating to 700 °C, following two routes: 1) H_2 release

accompanied by the precipitation of LiH, $Li_2B_{12}H_{12}$ and B in whole dehydrogenation temperature range (290 - 700 °C); and 2) above 550 °C, dehydrogenation is also accompanied by the formation of K, KH and B.

- Due to the presence of different metal cations with different Pauling electronegativity values, the dehydrogenation peaks temperatures for these low-melting-point borohydride mixtures shift so they are located between the peaks for their pure constituents; possibly through local changes of the B-H bond lengths around the metal cations.

- The low-melting-point borohydride mixtures have poor cycling stabilities under the conditions used for H_2 sorptions (500 °C, 1 bar H_2, 10 h for desorption, and 400 °C 130 bar H_2, 12 h for reabsorption). The reversible H_2 contents are reduced dramatically by 80% starting from the 2nd cycle, maintaining 4-15% of the initial H_2 capacity at the 3rd cycle.

In addition, attempts to use small amount of additives (micron-sized SiO_2, nano-sized Ni) to affect the dehydrogenation of $LiBH_4$ and these low-melting-point borohydride systems ($0.62LiBH_4$-$0.38NaBH_4$, $0.75LiBH_4$-$0.25KBH_4$) have been demonstrated:

- The addition of 5 mol% micron-size SiO_2 destabilizes $LiBH_4$, leading to 0.7-1.5 wt.% hydrogen evolution (depending on the particle size of SiO_2) before 400 °C. This is achieved by two chemical reactions, forming Li_2SiO_3 or Li_4SiO_4 at

around 300 °C or 370 °C, respectively. The amount of H_2 released increases with increasing specific surface area.

- The addition of 14 mol% nano-sized Ni (~100 nm) reduces the dehydrogenation onset and peak temperatures of $LiBH_4$ (by 98 °C and 25 °C) to 187 °C and 445 °C, respectively. It also changes the reaction pathway, producing N_4B_3 and generating more $Li_2B_{12}H_{12}$:

$$\mathbf{0.943LiBH_4 + 0.057Ni = 0.817LiH + 0.144B + 0.063Li_2B_{12}H_{12} + 0.014Ni_4B_3 + 1.099H_2}$$

Equation 11.3

- In general, the addition of micron-sized SiO_2 (diameter = 0.5 μm) into $0.62LiBH_4$-$0.38NaBH_4$ and $0.75LiBH_4$-$0.25KBH_4$ mixtures destabilizes dehydrogenation, resulting in a reduction of 32-42 °C in the dehydrogenation onset temperatures and leading to ~1 wt.% hydrogen release below 400 °C due to the formation of lithium silicates.

The $0.95(0.62LiBH_4$-$0.38NaBH_4)$-$0.05SiO_2$ mixture starts to release H_2 at 245 °C with a total of 7.3 wt.% hydrogen upon heating to 650 °C in Ar (3.5 wt.% lower than SiO_2-free mixture). Excluding the reaction between $LiBH_4$ and SiO_2, the decomposition can be expressed as:

$$\mathbf{0.49LiBH_4 - 0.36NaBH_4 \xrightarrow{>350\ ^\circ C} 0.412LiH + 0.034B + 0.039Li_2B_{12}H_{12} + 0.302Na + 0.029Na_2B_{12}H_{12} + 1.086H_2}$$

Equation 11.4

The dehydrogenation of $0.95(0.75LiBH_4\text{-}0.25KBH_4)\text{-}0.05SiO_2$ starts at 258 °C with a total of 9.6 wt.% hydrogen released at 700 °C in Ar (0.7 wt.% higher than the SiO_2-free mixture). The H_2 release is associated with the precipitation (or formation) of 1) Li_2SiO_3, Li_3SiO_4, Si and B from 258 to 375 °C; 2) K and B above 550 °C and 3) LiH, B and $Li_2B_{12}H_{12}$ through the whole dehydrogenation temperature range (258 – 700 °C).

- In general, the addition of nano-sized Ni into $0.62LiBH_4\text{-}0.38NaBH_4$ and $0.75LiBH_4\text{-}0.25KBH_4$ mixtures destabilizes dehydrogenation, resulting in a much lower dehydrogenation onset temperature at 150-200 °C as a consequence of a reaction between NiO (impurity in the as-received Ni) and $LiBH_4$. It also causes lower dehydrogenation peak temperatures for all major peaks. But unfortunately, it does not significantly improve the cycling stability of these mixtures, although partially reversible $LiBH_4$ was observed in $0.91(0.62LiBH_4\text{-}0.38NaBH_4)\text{-}0.09Ni$ at the 3rd rehydrogenation cycle.

  The $0.91(0.62LiBH_4\text{-}0.38NaBH_4)\text{-}0.09Ni$ releases a total of 8.1 wt.% hydrogen upon heating to 650 °C in Ar (2.7 wt.% lower than the Ni-free mixture), the H_2 evolution is associated with the precipitation (or formation) of 1) LiH, Ni_4B_3, $Li_2B_{12}H_{12}$ in 300-490°C; 2) Na, B in 490-565 °C and 3) $Li_{1.2}Ni_{2.5}B_2$ above 565 °C.

  The $0.86(0.75LiBH_4\text{-}0.25KBH_4)\text{-}0.14Ni$ mixture releases 7.1 wt.% hydrogen upon heating to 700 °C in Ar (1.8 wt.% lower than the Ni-free sample). The H_2

release is associated with the precipitation (or formation) of 1) LiH, Ni_4B_3 in 375-519 °C; 2) K, B, Ni_2B above 519 °C and 3) LiH, B, $Li_2B_{12}H_{12}$ through the whole dehydrogenation temperature range (375-700 °C).

- These additives do not change the low melting points. But they facilitate the formation of metal dodecaborate compounds. This is possibly due to their reaction products (Li_2SiO_3, Li_4SiO_4, Ni_3B_4) providing extra contact surface for the molten borohydrides that helps nucleation and growth of metal dodecaborates.

11.2 Future Work

This work is a fundamental study of the hydrogenation and dehydrogenation mechanisms of the low-melting-point $0.62LiBH_4$-$0.38NaBH_4$ and $0.75LiBH_4$-$0.25KBH_4$ mixtures, and in an attempt to tailor their dehydrogenation using selective additives. However, different from the $0.4LiBH_4$-$0.6Ca(BH_4)_2$ system, for which a fully reversible $LiBH_4$ starting from the 2nd cycle has been recently noticed (Javadian et al. 2017), systems studied in this work had poor cycling stabilities and none of them could meet the ultimate targets for vehicular or large-scale stationary application advised by the United States DOE .

The future work should focus on:

- Identifying the impurities introduced by ball milling. This can be achieved through magnetic measurements, e.g. Vibrating Sample Magnetometry (VSM)

(Smith 1956; Foner 1959) and application of the Honda-Owen method (Soule et al. 1964).

- Investigating on the changes in chemical bonding states and microstructures of the reaction products. Quantitative analysis of the species containing boron in the reaction products, since reforming B-H bonds is critical for achieving reversibility. This can be done using *in situ* Nuclear Magnetic Resonance Spectroscopy (NMR) (Nöth & Wrackmeyer 1978). Besides, identifying the intermediate phases at high temperature range using high temperature XRD, *in situ* Raman or NMR is necessary.

- Studying the reaction products between $LiBH_4$ and NiO, and understanding the influence of NiO on dehydrogenation.

- Using isotopes to track and to determine the hydrogen release from the $LiBH_4$-KBH_4 system, for a better understanding of the postponed dehydrogenation phenomena of its $LiBH_4$ component.

- Applying nano-confinement to suitable low-melting-point borohydride systems, and screening and optimising suitable additives to tailor the H_2 storage properties and achieve relatively high cycling stability.

APPENDIX

A Calibration of TPD-MS

Due to the maintenance of the TPD apparatus (e.g. replace components) or restarted the MS, the calibration coefficient for the TPD-MS varied in different time period. The used calibration coefficient and their valid dates are as follows:

- 5.5475, valid from 7 July 2014 to 9 October 2016;
- 29.451, valid from 10 October 2016 to 25 January 2017;
- 1.64, valid from 26 January 2017 to 25 May 2017;
- 0.3725, valid from 26 May 2017 to present.

B Decomposition with Different Contact Surfaces

To continually supply H_2 using complex hydrides (e.g. to a fuel cell), a specially designed container will be required. Many material properties should be taken into consideration when constructing this container. A parameter that might play an important role in controlling the decomposition of borohydrides is the surface condition of the container where it is in contact with the reactants (i.e. complex hydride powders). Ideally, a rougher surface may provide more nucleation sites and in this way the decomposition reaction might be affected. Thus, a preliminary study of surface roughness effect on the decomposition of $LiBH_4$ was carried out using *in situ* Raman spectroscopy. Moreover, this study can be helpful for understanding whether or not the *in situ* Raman measurements were going to be affected by the choice of sample container.

B.1 Confocal Laser Microscopes

The confocal laser microscope is an optical imaging technique using a spatial pinhole to block the out-of-focus light in image formation. As a consequence, the optical resolution and contrast of a micrograph are increased (Pawley 2006). By capturing a serial of two-dimensional images at different depths, the morphology of a sample can be viewed in three-dimensional.

In this work, an Olympus LEXT 3100 laser confocal microscope (Olympus 2007) was used to examine the surface profiles (roughness) of a number of roughened NETZSCH DSC crucibles. The crucibles were placed under a ×5 objective lens and their average plane roughness values were measured in confocal model using ultraviolet light. The

depth information of their surface morphology was analysed with LEXT OLS software to obtain the roughness values.

B.2 Characterization of Surface Roughness

In order to study the influence of surface container roughness on the decomposition of as-received $LiBH_4$ (as a function of temperature and pressure), three sample containers (pans) with different surface profiles were prepared (Figure B.1):

(a) As-received pan was the commercial DSC-Crucibles (Al, 25 μL) obtained from NETZSCH without any modification;

(b) Line-scratched pan was prepared by gently scratching the centre of the as-received pans using tweezers. Cuts on the edges were used to mark the position of scratch;

(c) The ground pan was prepared by gently grinding the as-received pan using 120 SiC sandpaper.

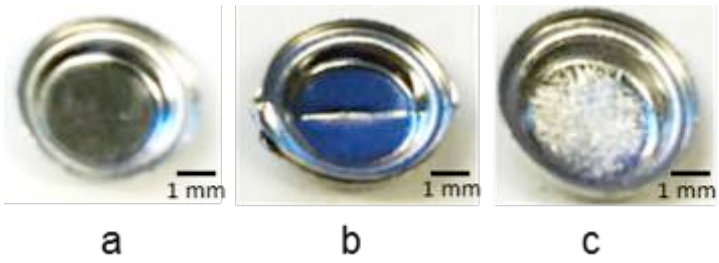

Figure B.1 Pans with different surface profiles: a) As-received pan; b) Line-scratched pan; c) Ground pan.

All pans were cleaned in an ultrasonic bath with distilled water for 5 minutes (repeated 3 times), and washed with Industrial Methylated Spirit (IMS) between each ultrasonic cleaning process to remove dust and contaminations. A hot air dryer was used

afterwards to remove moisture from the surface. All cleaned pans were stored in an Ar glove box to avoid moisture contamination.

The roughness values of each sample pan were measured by the confocal microscopy using an ultraviolet laser. The arithmetical mean deviations of the assessed profile, Ra values, are used to describe the overall surface roughness. This value can be calculated by the absolute arithmetic mean of contour deviated distance of a surface profile measured experimentally (Olympus 2007):

$$\boldsymbol{Ra} = \frac{\mathbf{1}}{\boldsymbol{n}}\sum_{\boldsymbol{i}=\mathbf{1}}^{\boldsymbol{n}}|\boldsymbol{y}_{\boldsymbol{i}}| \qquad \textbf{Equation B.1}$$

where y was the distance between each point of the contour surface and the base line.

Figure B.2 shows the obtained average Ra values of as-received, line-scratched and ground pans. The measured surface roughness of the line-scratched pans was 12.5 ± 1.9 μm, which was the same as the as-received pans. However, a line defect had been introduced so that the only influence was expected at the line defect area. The Ra value of the ground pans was 22.2 ± 2.7 μm. It was about 78% higher in contrast to that of the as-received pans. This increase of roughness was expected and it was due to a higher surface area.

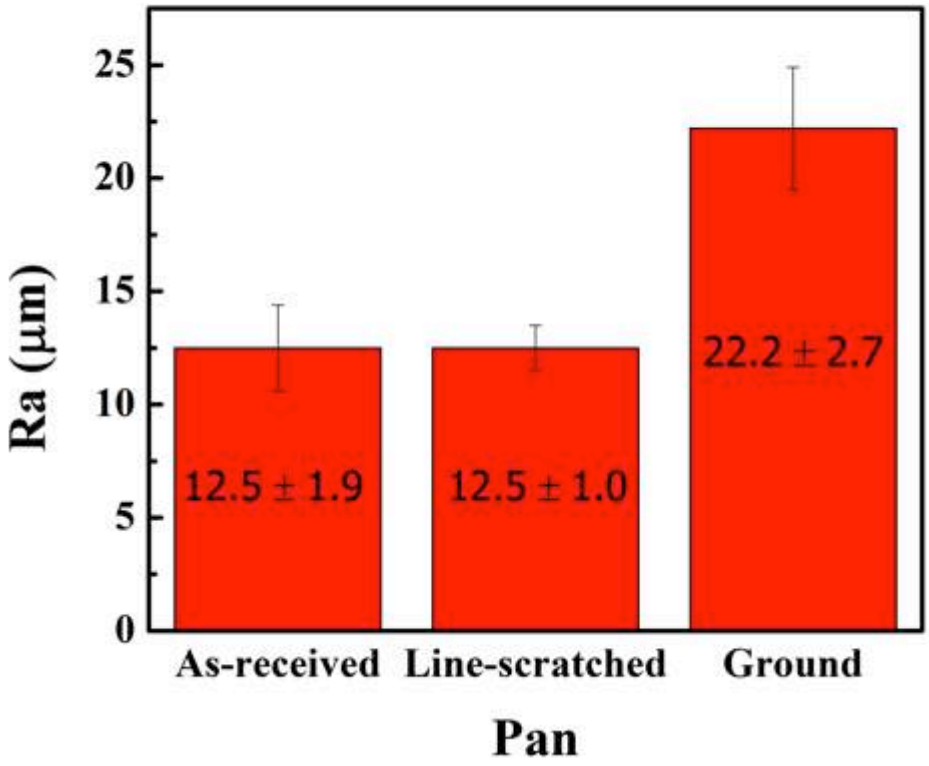

Figure B.2 Roughness vales of each pan measured by confocal microscopy.

B.3 Thermal Decomposition

Figure B.3 shows the overall *in situ* Raman results of as-received $LiBH_4$ decomposed in sample pans with different surface areas.

Temperatures were determined by manually checking the change of peaks in every spectrum in the *in situ* results. The measured temperatures of the phase transition, fusion and formation of B and $Li_2B_{12}H_{12}$ from *in situ* Raman were summarised in Table B. 1. The decomposition temperatures marked in Figure B.3 were the formation temperatures of B (lower than that of $Li_2B_{12}H_{12}$).

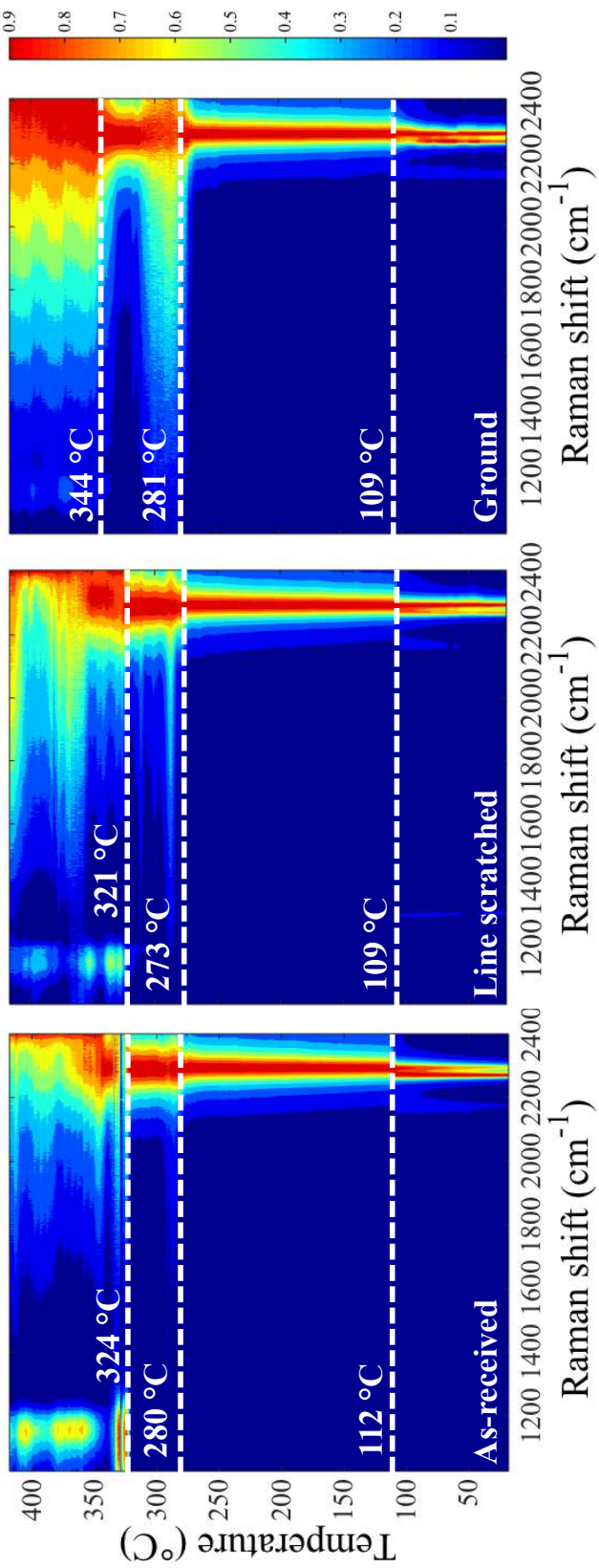

Figure B.3 *In situ* Raman spectra of $LiBH_4$ loaded on pans with different surface roughness heated to 400 °C by 2 °C min^{-1} in Ar flowing at 100 mL min^{-1}.

Table B. 1 Measured Temperatures (°C) from *in situ* Raman results of as-received $LiBH_4$ decomposed on pans with different surface roughness.

Pan conditions	Roughness	Phases transition	Melting	Formation of B	Formation of $Li_2B_{12}H_{12}$
As-received	12.5 ± 1.9	112	280	324	344
Line-scratched	12.5 ± 1.0	109	273	321	326
Ground	22.2 ± 2.7	109	281	344	349

Since no modification was made on the as-received pan, the *in situ* Raman result of the as-received $LiBH_4$ was the same data discussed in Section 7.1.4.1. It showed that the phase transition, fusion and decomposition occurred at 112, 280 and 324 °C, respectively, which were in the range of 108-115 °C for phase transition, 270-280 °C for fusion and 320-330 °C for decomposition reported in literature (Andreas Züttel et al. 2003; Fakioğlu et al. 2004; Orimo et al. 2005; Li et al. 2011; El Kharbachi et al. 2012).

For the line-scratched pan, the phase transition, fusion and decomposition reaction of $LiBH_4$ occurred at 109, 273 and 321 °C, respectively. Compared to those for as-received pan, they were slightly changed, but these changes were within errors. However, a relatively weaker signal of amorphous boron was observed for this sample, suggesting that introducing a line scratch may change the decomposition mechanism by inhibiting the reaction pathway through LiH, B and H_2 (Equation 7.2).

Using the ground pan, the phase transition temperature of $LiBH_4$ was 109 °C. It was close to that observed using the as-received pan and it was the same as the line-scratched pan. Fusion occurred at 281 °C. However, the measured decomposition temperature increased by 20 °C (to 344 °C). It disagreed with the idea that the increased surface area introduced extra nucleation sites and enhanced the possibility of the nucleation for the decomposition products, leading to a lower decomposition temperature. A much weaker signal of amorphous boron was observed. This indicates

that the decomposition pathway had been affected and the reaction pathway through LiH, B and H_2 was further inhibited.

B.4 Effect of Contact-Surface Roughness

The decomposition pathway of $LiBH_4$ was changed with an increase of contact surface roughness, showing as weaker B signals and simultaneously enhanced $Li_2B_{12}H_{12}$ signals where the $[B_{12}H_{12}]^{2-}$ to B ratio increased with roughness from as-received to line-scratched to ground. In addition, the decomposition temperature was increased slightly with the increase of contact surface roughness.

In reality, the high thermal stability of the $Li_2B_{12}H_{12}$ phase (up to 900 °C) formed during decomposition reduced the amount of H_2 evolved (e.g. 10.0 wt.% for dehydrogenation through LiH, $Li_2B_{12}H_{12}$ < 13.9 wt.% for dehydrogenation through LiH, B). The closo-borate was known as a boron sink, which will obstruct rehydrogenation (Yan et al. 2012). Therefore, the design of a smooth inner surface for the fuel container becomes necessary in order to inhibit the formation of $[B_{12}H_{12}]^{2-}$ phases.

B.5 Summary

A preliminary study of surface roughness effect on the decomposition of $LiBH_4$ was carried out using *in situ* Raman spectroscopy. The different surface roughnesses were achieved by roughening DSC crucibles using sandpapers. The *in situ* Raman results proposed an increase of $[B_{12}H_{12}]^{2-}$ to B ratio along with roughness growth, suggesting the formation of $Li_2B_{12}H_{12}$ phase was enhanced when contacting with rough surroundings. Since the dehydrogenation of $LiBH_4$ via forming LiH, $Li_2B_{12}H_{12}$ is more

thermodynamically favourable (Section 7.2.3) but is often hindered due to kinetics reasons (El Kharbachi et al. 2012), the rougher surface may reduce the activation energy for the $Li_2B_{12}H_{12}$ formation by providing more nucleation sites. So that this dehydrogenation reaction pathway becomes dominant. Because $Li_2B_{12}H_{12}$ had a high thermal stability and hindered the rehydrogenation by holding the boron (Friedrichs, Remhof, Hwang, et al. 2010; Pitt et al. 2013), its formation was not favourable for H_2 storage applications. However, thanks to its relatively high ionic conductivity (He et al. 2015; Varley et al. 2017), it was suitable for solid-state electrolyte in Li^+ batteries or to be used as luminescent down-conversion dye (Tang, Unemoto, et al. 2015; Teprovich et al. 2015). Knowing rough surface enhanced the precipitation of $Li_2B_{12}H_{12}$ might provide a new/advanced route for its industry production.

C Thermodynamic Calculations for $0.95LiBH_4$-$0.05SiO_2$

For a better understanding of the reaction mechanism from the thermodynamic aspect, the Gibbs free energies of possible reactions between $LiBH_4$ and SiO_2 (Equation C.1-12) were calculated using the CALPHAD method in the 1 bar H_2 scenario (Figure C.1, a – reaction forms Li_2SiO_3, b – reaction forms Li_4SiO_4). As an indicator of the spontaneity ($\Delta G<0$), reaction with lower Gibbs free energy is generally more thermodynamic favourable. Other aspects, such as kinetics and activation energy, will not be discussed here.

$\mathbf{4LiBH_4 + 3SiO_2 = 2Li_2SiO_3 + Si + 4B + 8H_2}$	**6.0 wt.%**	**Equation C.1**
$\mathbf{4LiH + 3SiO_2 = 2Li_2SiO_3 + Si + 2H_2}$	**1.9 wt.%**	**Equation C.2**
$\mathbf{2Li_2B_{10}H_{10} + 3SiO_2 = 2Li_2SiO_3 + Si + 20B + 10H_2}$	**4.5 wt.%**	**Equation C.3**
$\mathbf{2Li_2B_{12}H_{12} + 3SiO_2 = 2Li_2SiO_3 + Si + 24B + 12H_2}$	**4.9 wt.%**	**Equation C.4**
$\mathbf{8LiBH_4 + 2Li_2SiO_3 + 3SiO_2 = 3Li_4SiO_4 + 2Si + 8B + 16H_2}$	**6.0 wt.%**	**Equation C.5**
$\mathbf{4LiBH_4 + 4Li_2SiO_3 = 3Li_4SiO_4 + Si + 4B + 8H_2}$	**3.6 wt.%**	**Equation C.6**
$\mathbf{4LiH + 4Li_2SiO_3 = 3Li_4SiO_4 + Si + 2H_2}$	**1.0 wt.%**	**Equation C.7**
$\mathbf{8LiH + 2Li_2SiO_3 + 3SiO_2 = 3Li_4SiO_4 + 2Si + 4H_2}$	**1.9 wt.%**	**Equation C.8**
$\mathbf{2Li_2B_{10}H_{10} + 4Li_2SiO_3 = 3Li_4SiO_4 + Si + 20B + 10H_2}$	**3.2 wt.%**	**Equation C.9**
$\mathbf{4Li_2B_{10}H_{10} + 2Li_2SiO_3 + 3SiO_2 = 3Li_4SiO_4 + 2Si + 40B + 20H_2}$	**4.5 wt.%**	**Equation C.10**
$\mathbf{2Li_2B_{12}H_{12} + 4Li_2SiO_3 = 3Li_4SiO_4 + Si + 24B + 12H_2}$	**3.6 wt.%**	**Equation C.11**
$\mathbf{4Li_2B_{12}H_{12} + 2Li_2SiO_3 + 3SiO_2 = 3Li_4SiO_4 + 2Si + 48B + 24H_2}$	**4.9 wt.%**	**Equation C.12**

In general, the reactions involving SiO_2 and/or Li_2SiO_3 (Figure C.1-a&b) were much more thermodynamically favourable than the decomposition of $LiBH_4$ (Figure C.1-c).

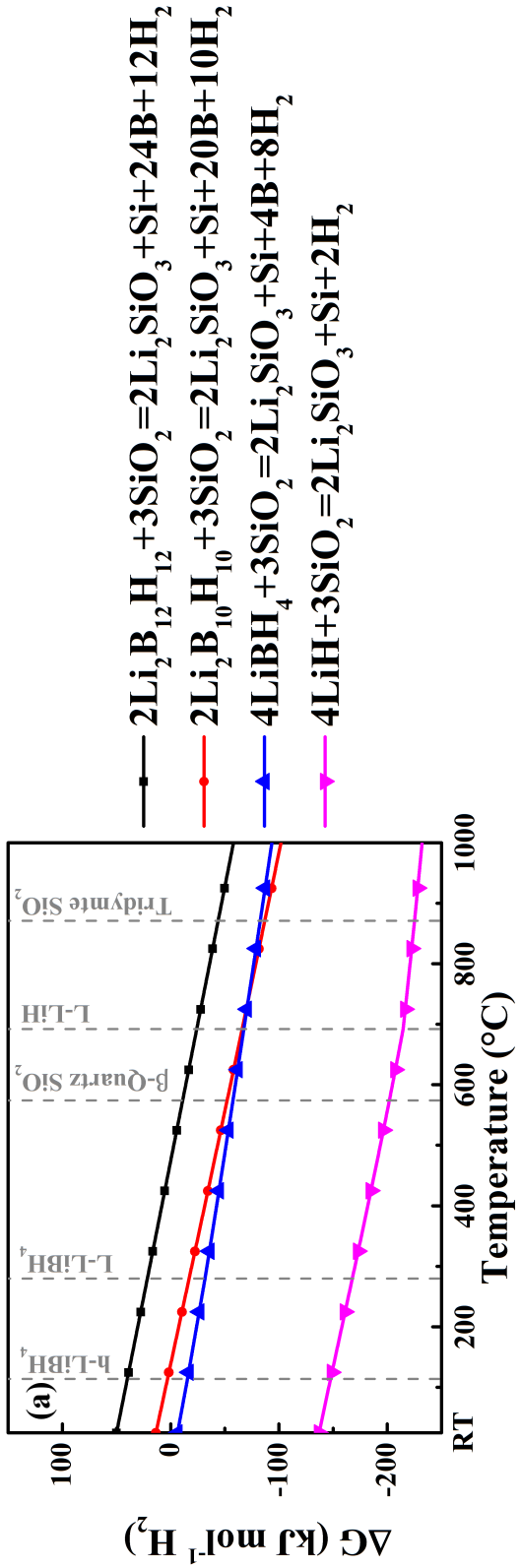

Figure C.1 CALPHAD calculated Gibbs Free Energy (ΔG, kJ mol^{-1} H_2) of reaction in an isobaric system (1 bar H_2) of reactions between $LiBH_4$ and SiO_2 that forms (a) Li_2SiO_3 and (b) Li_4SiO_4. The calculation reactions of $LiBH_4$ in (c) are plotted for comparison.

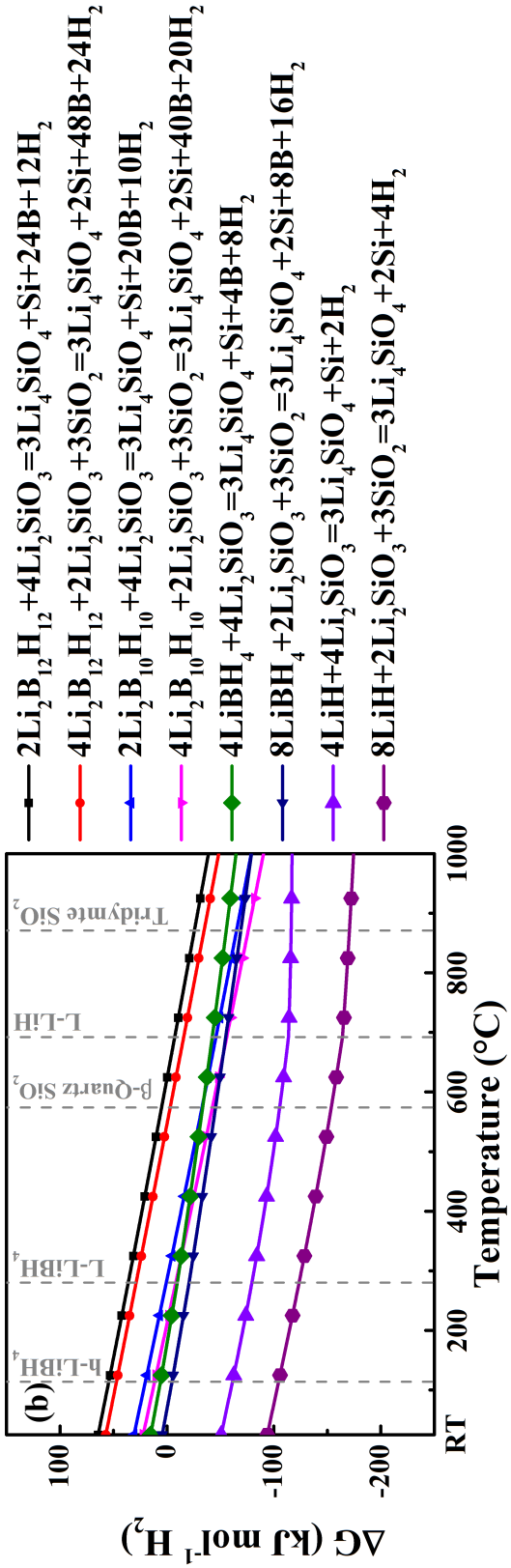

Figure C.1 CALPHAD calculated Gibbs Free Energy (ΔG, kJ mol^{-1} H_2) of reaction in an isobaric system (1 bar H_2) of reactions between $LiBH_4$ and SiO_2 that forms (a) Li_2SiO_3 and (b) Li_4SiO_4. The calculation reactions of $LiBH_4$ in (c) are plotted for comparison.

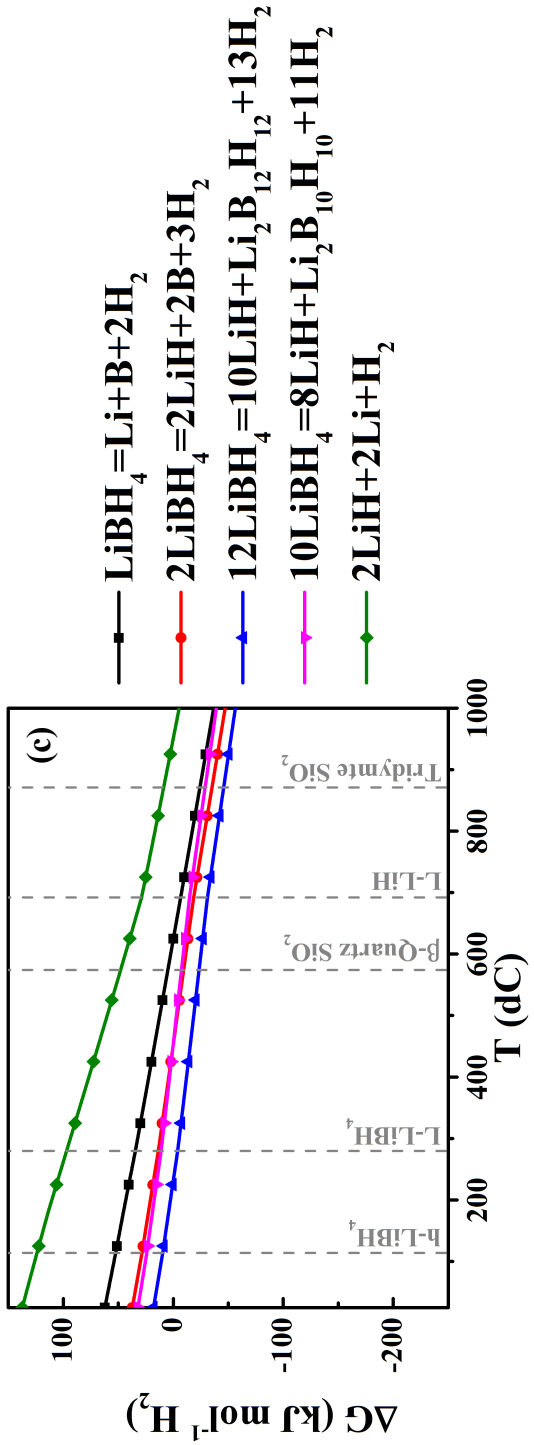

Figure C.1 CALPHAD calculated Gibbs Free Energy (ΔG, kJ mol^{-1} H_2) of reaction in an isobaric system (1 bar H_2) of reactions between $LiBH_4$ and SiO_2 that forms (a) Li_2SiO_3 and (b) Li_4SiO_4. The calculation reactions of $LiBH_4$ in (c) are plotted for comparison.

Among all the calculated reactions forming Li_2SiO_3 (Figure C.1-a), the reaction between LiH and SiO_2 (Equation C.2) was the most favourable one. At 300 °C, its Gibbs free energy of reaction was -170 kJ mol^{-1} H_2, which was much smaller than the -35 kJ mol^{-1} for the Equation C.1 suggested in literature. Thus, from the thermodynamic point of view, any LiH formed during dehydrogenation may react with SiO_2 (if any) immediately. This might explain no LiH was observed in XRD for heat-treated sample at 300 °C (Figure 7.15), although the B signal in *in situ* Raman spectra (Figure 7.16) confirmed that the dehydrogenation of $LiBH_4$ have occurred.

In an attempt to investigate the decomposition pathway for the 1st reaction step (i.e. forming Li_2SiO_3), the amount of H_2 released from 1g $0.95LiBH_4$-$0.05SiO_2$ sample experimentally (0.0039–0.0087 g, Table 7.4) was much lower than the theoretical values (0.0109-0.0113 g) calculated as below:

- If all SiO_2 reacted with $LiBH_4$ (Equation C.1), the total amount of H_2 generated was 0.0113 g;
- If all SiO_2 reacted with LiH (Equation C.2) that generated from the decomposition of $LiBH_4$, the total amount of H_2 released was 0.0109g.

This mismatch suggested that the SiO_2 was not fully reacted. Perhaps, its outer surface reacted first, then the generated Li_2SiO_3 reduced the reaction kinetics by limiting the diffusion rate of Li^+ or SiO_2. Therefore, the core of the particles remained as SiO_2 and could not be detected by XRD or Raman. As the specific area of SiO_2 was proportionally associated to its reactivity (Borgwardt & Bruce 1986), the approximate percentages of SiO_2 remained unreacted were estimated to be: 34 %, 44 % and 77 % for

samples with SiO_2 diameters equal to 0.5, 1.0 and 1.5 μm (specific area are summarised in Table 7.4), respectively.

Among all the reactions producing Li_4SiO_4 (Figure C.1-b), the reactions between LiH and Li_2SiO_3 (Equation C.7 and C.8) were the most favourable ones. The Gibbs Free Energy values of reaction them were -87 and -133 kJ mol^{-1} H_2 at 370 °C, respectively. Both of them were much lower than the -17 kJ mol^{-1} H_2 for Equation C.6 suggested in the literature.

Although it was difficult to directly determine the nature of the decomposition process, an attempt has been made to analysis the reaction mechanism by comparing the theoretical H_2 release with the experimental values.

Since a small portion of SiO_2 remained unreacted after Step 1, the following assumptions were made:

1) All remained SiO_2 reacted with Li_2SiO_3 through Equation C.8;
2) The excess Li_2SiO_3 was reacted via Equation C.6 or Equation C.7.

Under the above assumptions, a 1g $0.95LiBH_4$-$0.05SiO_2$ sample releases 0.0094-0.0096 g of hydrogen. This range was again much higher than the experiment data (0.0034-0.0063 g), indicating this reaction sequence was unlikely to occur.

If all the Li_2SiO_3 reacted in the 2nd step, the calculated H_2 release for a 1g $0.95LiBH_4$-$0.05SiO_2$ sample via Equation C.6 or C.7 would be 0.0057 g or 0.0055 g, respectively.

These values are closer to the experimental results. However, the real situation might be more complex and require future study.

Thus, due to the formation of stable lithium silicates (such as Li_2SiO_3 and Li_4SiO_4), the dehydrogenation reactions of $LiBH_4$ through reacting with SiO_2 became more thermodynamically favourable than its common dehydrogenation pathways. The CALPHAD calculation suggested the reactions between $LiBH_4$ and SiO_2 could be more complex than that reported in the literature (Ngene, Adelhelm, et al. 2010). This was because SiO_2 and Li_2SiO_3 preferred to react with LiH once it formed during dehydrogenation, from the thermodynamic aspect. However, other aspects, such as kinetics and activation energy, should be considered as well in order to determine the real reaction pathways in the future.

D Crystallite Sizes of as-received Ni

The crystallite size of the nano-sized powder was estimated using Scherrer's equation (Scherrer 1918; Dinnebier & Billinge, Simon 2008):

$$\tau = K\lambda/\beta cos\,\theta \qquad \textbf{Equation D. 1}$$

where

τ is the size of sub-micrometre particles (or crystallites);

K is dimension-less shape factor usually regarded as the Scherrer constant;

β os the line broadening at the full width at half maximum (FWHM);

λ is the X-ray wavelength and equals 1.5418 Å for Cu K_α radiation;

θ is the Bragg angle in degrees.

Normally, 0.94 is a good approximation if the FWHM is used. However, if β is integral height to width of the diffraction peak, a unity value should be applied.

In this work, the peak position and FWHM were obtained by a Gaussian peak fitting using Origin-Lab. Thus, a relative comparison between estimated crystallite sizes was possible: the calculated value for the as-received (nano-sized) Ni was 33.6 nm. It was relatively smaller than the 40.5 nm for as-received (bulk) Ni. After ball milled with $LiBH_4$, these values reduced to 26.3 nm and 29.4 nm, respectively.

E Thermal Decomposition in H_2

Because solid-state H_2 storage materials are most likely to work under a relatively low H_2 pressures (< 12 bar for vehicular applications) (Fakioğlu et al. 2004; Renewable n.d.), and the dehydrogenation of borohydrides (especially the kinetics and reaction products) is strongly influenced by the atmosphere (Hanada et al. 2008; Yan et al. 2012); study of the thermal decomposition of in H_2 atmosphere was therefore necessary.

It was very challenging to interpret the poor quality MS data when H_2 was used as carrier gas in the TPD-MS system. Alternatively, since the cycling stability was preformed in H_2 using a Sieverts type apparatus (Section 6.2.6); the dehydrogenation trace in H_2 could be therefore obtained by calculating the derivative of H_2 pressure with respect to time.

E.1 $0.62LiBH_4$-$0.38NaBH_4$

Figure E.1 shows H_2 desorption traces for the as-milled $0.62LiBH_4$-0.38NaBH4 mixture decomposed in flowing Ar at 160 mL min^{-1} versus in 1 bar static H_2, while keeping the same heating rate (5 °C min^{-1}).

In both atmospheres, the as-milled $0.62LiBH_4$-0.38NaBH4 mixtures started to decompose around 300 °C. Under 1 bar static H_2, the major dehydrogenation occurred above 450 °C that was slightly higher than that in flowing Ar case, suggesting the applied H_2 backpressure could kinetically hinder the decomposition reaction without dramatically changing the onset temperatures.

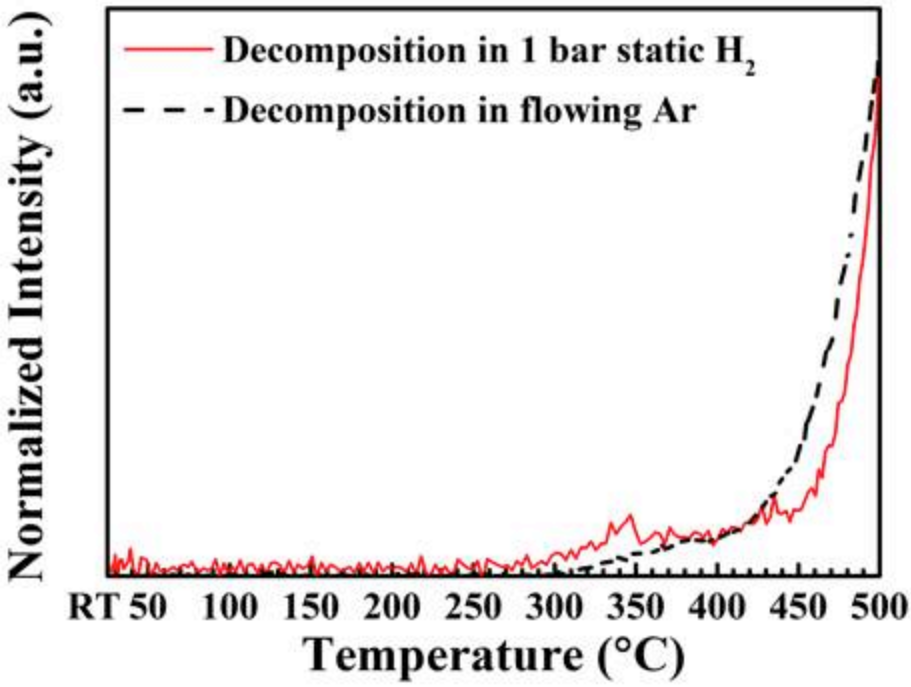

Figure E.1 H_2 desorption traces for as-milled $0.62LiBH_4$-$0.38NaBH_4$ decomposed in Ar (black dots) using TPD-MS in University of Birmingham, the U.K. vs. in 1 bar static H_2 (red line) using PCT in IFE, Norway. Sample were heated at 5 °C min^{-1}. Signals were normalized for comparison.

Figure E.2 shows the XRD and FTIR results for the $0.62LiBH_4$-$0.38NaBH_4$ sample decomposed at 500 °C in 1 bar static H_2.

The Cu-based impurities (Cu_2O and CuO) in XRD pattern were introduced from the outer surface of sample holder during operation and not involved in dehydrogenation. Both XRD and FTIR suggested that the $LiBH_4$ component was not fully decomposed, although the sample had been kept at relatively high temperature for 10 h. This was different from the decomposition in flowing Ar where no $LiBH_4$ signals was observed in XRD above 490 °C (Figure 8.14). The remaining $LiBH_4$ was very likely caused by the applied H_2 backpressure that postponed decomposition. Thus, a higher temperature might be needed to fully decompose this phase in practical use.

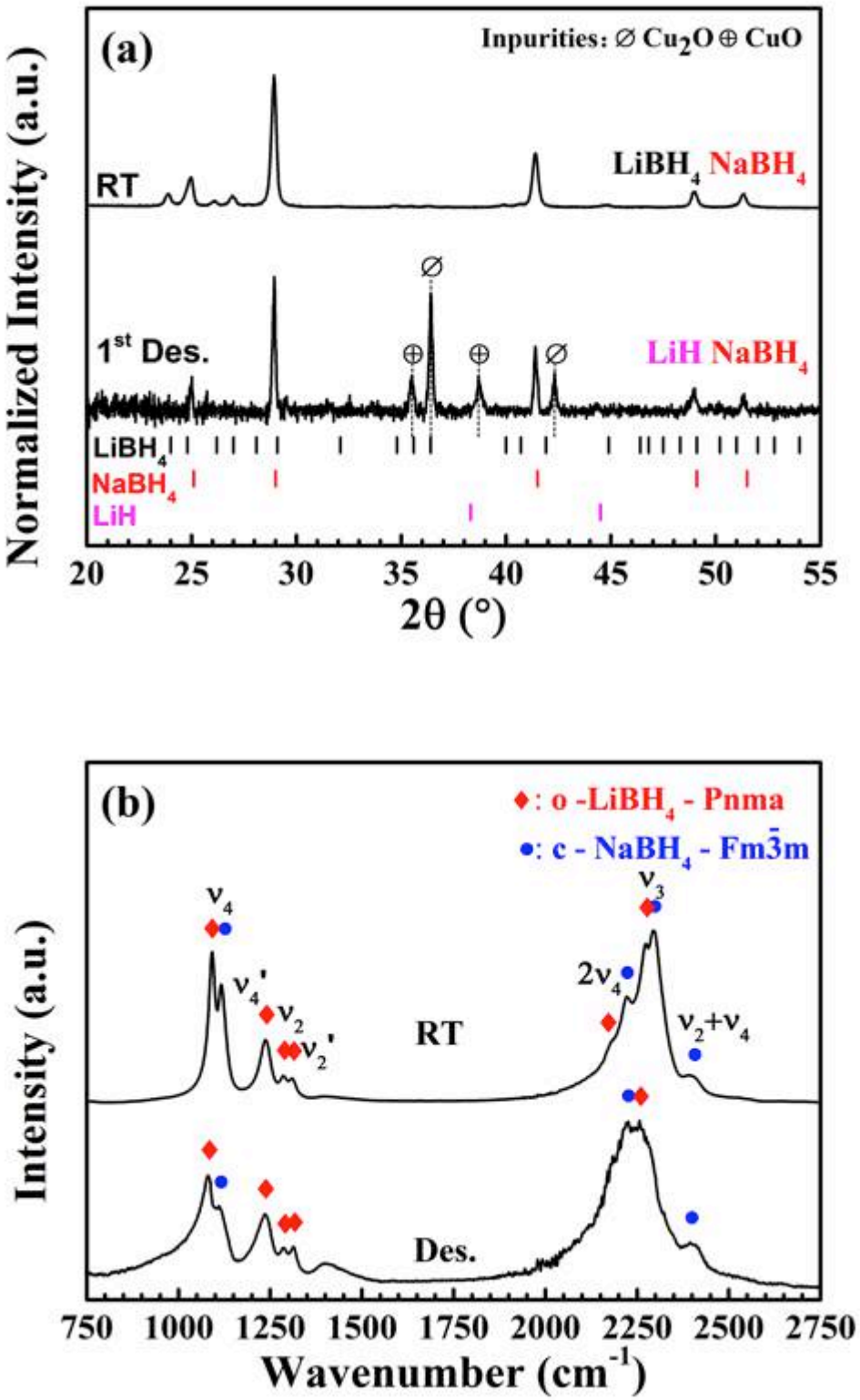

Figure E.2 (a) XRD (Cu K_α radiation, λ = 1.5418 Å) pattern and (b) FTIR spectrum for the as-milled $0.62LiBH_4$-$0.38NaBH_4$ mixtures decomposed at 500 °C in 1 bar static H_2 for 10 h (denoted as 1st Des. or Des.).

E.2 0.91(0.62LiBH$_4$-0.38NaBH$_4$)-0.09Ni

In 1 bar static H_2, the 0.91(0.62LiBH$_4$-0.38NaBH$_4$)-0.09Ni mixture started to release H_2 at around 200 °C (Figure E.3) that was similar to its decomposition performance in Ar (Section 8.4.3) (where a small deviation was observed between 150 - 200 °C due to reaction of LiBH$_4$ with NiO). However, the major dehydrogenation occurred above 450 °C in 1 bar static H_2 that was higher than the 400 °C for that in flowing Ar case. Thus, the dehydrogenation was postponed caused by the H_2 backpressure, similar to what has also been in other borohydride systems (Hanada et al. 2008; Yan et al. 2012).

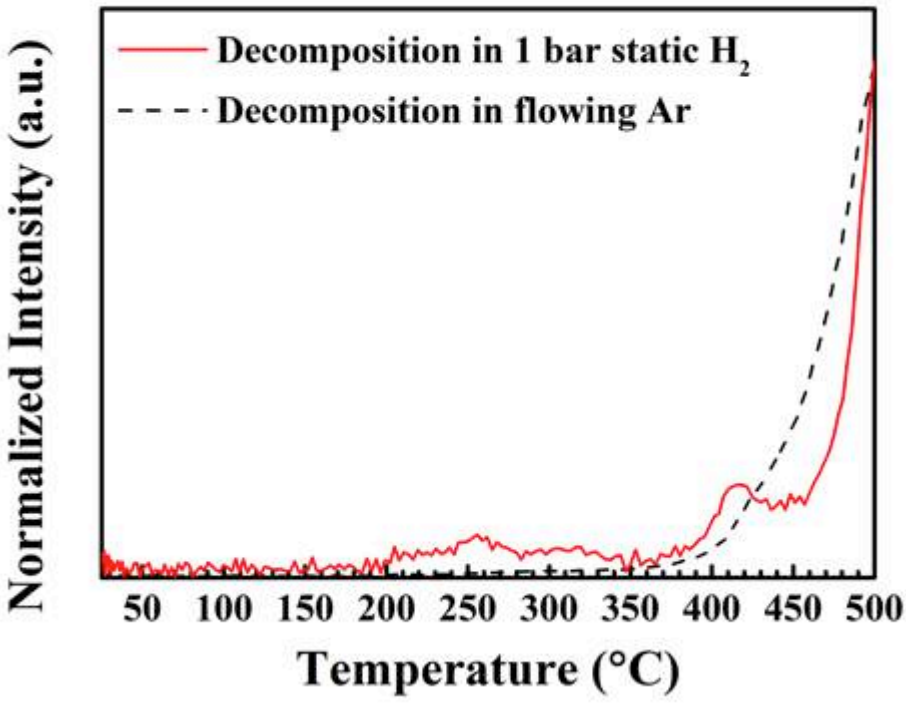

Figure E.3 H_2 desorption traces for 0.91(0.62LiBH$_4$-0.38NaBH$_4$)-0.09Ni decomposed in Ar (black dots) using TPD-MS in University of Birmingham, the U.K. vs. in 1 bar static H_2 (red line) using PCT in IFE, Norway. Samples were heated at 5 °C min^{-1}.

After dehydrogenation in H_2, the decomposition products showed phase segregations (Figure E.4), where two different solid materials were observed: black powders and

white soft flakes. Terry D Humphries et al. (2013) also observed this kind of phase segregation in a $NaBH_4$-Ni system (when decomposed in H_2) and proposed that the white part was mainly NaH and Na, whilst the black part was Ni_3B_4.

To investigate these decomposition products, the reaction products were generally ground using a mortar and a pestle before loading into a capillary container for XRD. Figure E.5 shows the corresponding XRD and FTIR results. The Cu-based impurities (Cu_2O and CuO) observed in XRD pattern were introduced from the outer surface of sample holder during operation (not involved during dehydrogenation).

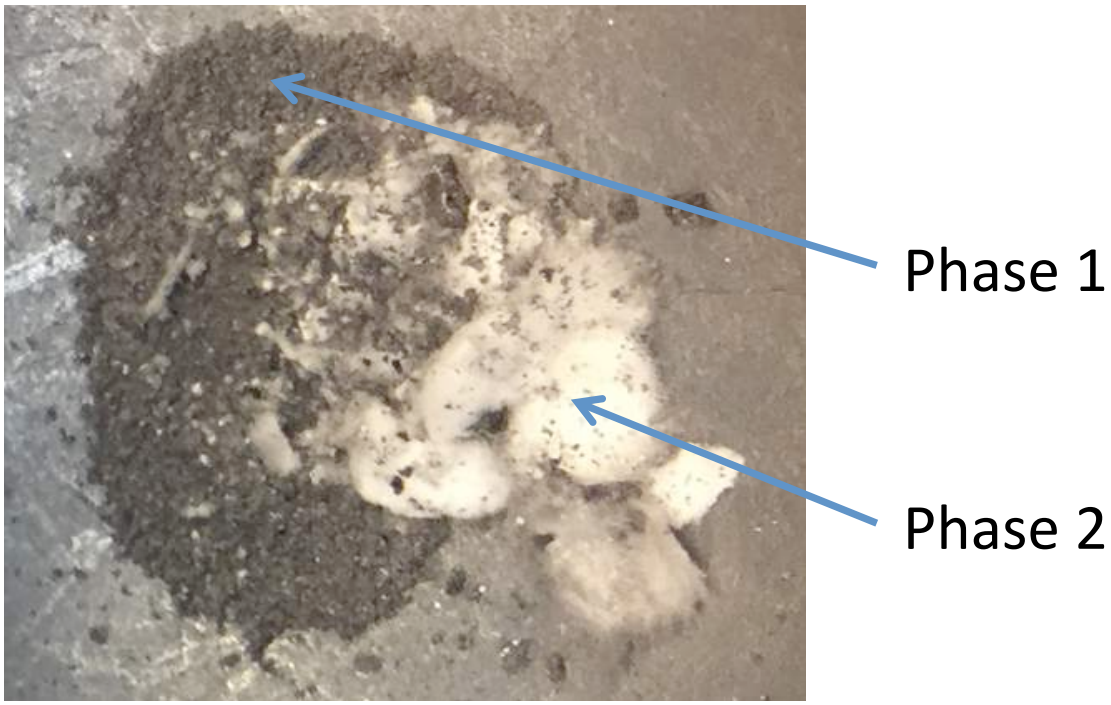

Figure E.4 Photo of the decomposition products of 0.91(0.62LiBH$_4$-0.38NaBH$_4$)-0.09Ni decomposed at 500 °C in 1 bar static H_2 for 10 h. The diameter of the sample area is ~ 1 cm.

After keeping at 500 °C in 1 bar static H_2 for 10 h, LiH, NaH, $NaBH_4$ and orthorhombic Ni_4B_3 were shown in XRD (Figure E.5) that agreed with Humphries et al. (2013).

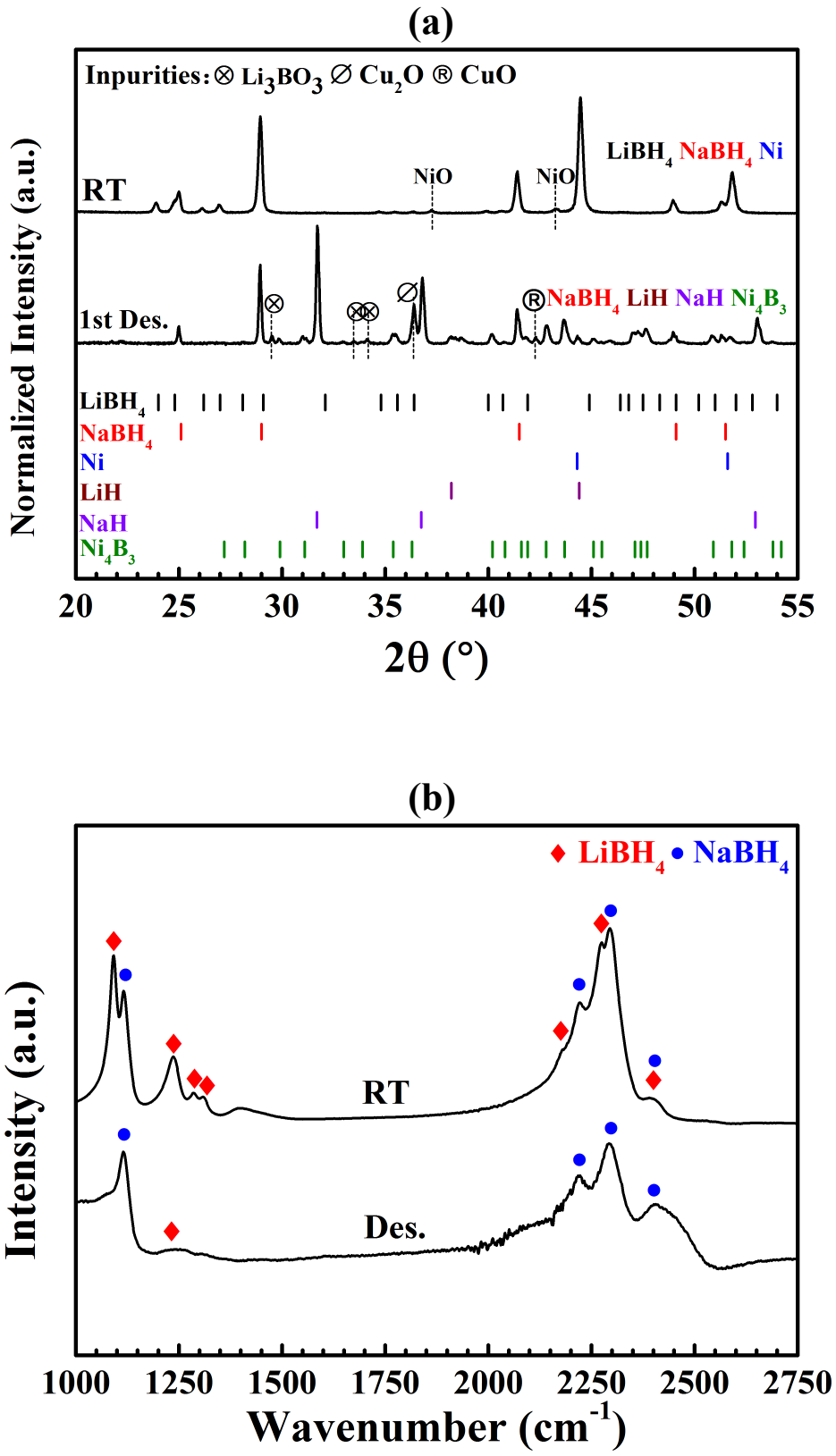

Figure E.5 (a) XRD (Cu K_α radiation, λ = 1.5418 Å) pattern and (b) FTIR spectrum for 0.91(0.62$LiBH_4$-0.38$NaBH_4$)-0.09Ni decomposed at 500 °C in 1 bar static H_2 for 10 h.

The existence of NaH rather than Na was inconsistent with the XRD results for the same sample when decomposed in an Ar atmosphere. According to the thermodynamic calculations, NaH was unstable under the current used conditions (500 °C, 1 bar H_2; marked as a red cross in Figure E.6). However, due to the low melting point of Na (281 °C at 10^{-5} bar of Na gas), any precipitated Na (liquid) vaporized immediately. Due to the heating, the Na gas was moveable inside the container. It was condensed (might be further solidified, subject to its temperature) when reached cooler area outside the hot zone. This part of Na could react with H_2 forming NaH leading to a physical segregation of decomposition products as observed in Figure E.4. To prevent such eventualities, Na could be physically or chemically confined using in nano-scaffolds (nanoconfinement) or metal fluorides (Mao & Gregory 2015).

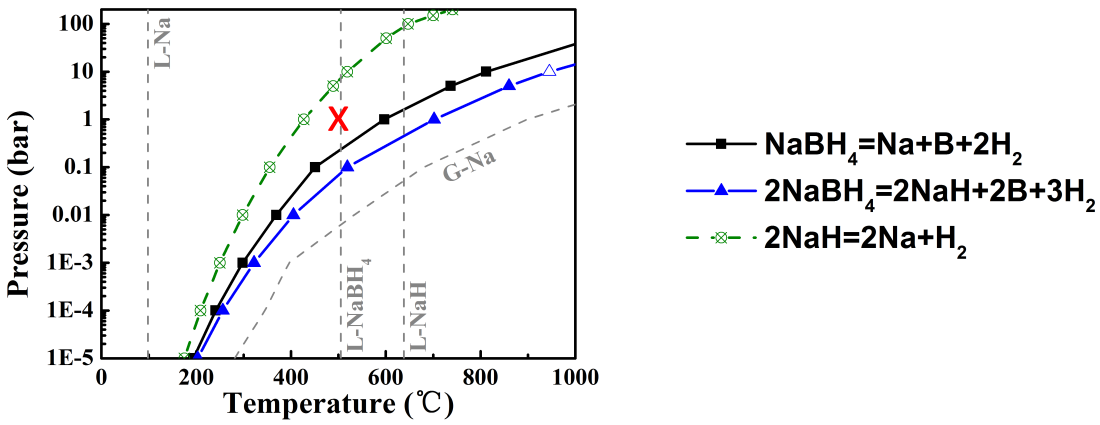

Figure E.6 CALPHAD calculated phase diagram of NaH. The dashed lines indicated the fusion of Na, $NaBH_4$ and NaH as a function of pressure, and the gasification of Na as a function of temperature and pressure. Conditions (500 °C, 1 bar H_2) for dehydrogenation was marked with a red cross.

The FTIR results (Figure E.5-b) showed that all $LiBH_4$ was reacted. This was different from the case of Ni-free sample, where vibration modes of $LiBH_4$ were still presented even after being kept at 500 °C for 10 h (Figure 8.17).

F List of Melting Points of Materials

Due to their high melting points, most of the products in the heat-treated samples observed in XRD and Raman are in their crystalline structures. The exceptions are Na and K, which stay in their liquid form.

Table F 1 Summary of melting points (at atmospheric condition) for products found in this work in room temperature XRD and Raman.

	Phases	Melting point (°C)	Note	Reference
Reactants	$LiBH_4$	285(1)	-	This work
	$NaBH_4$	510	-	(Paskevicius et al. 2017)
	KBH_4	605	-	(Paskevicius et al. 2017)
	$LiK(BH_4)_2$	Unknown	Metastable: dissociates above 95 °C	(Ley et al. 2014)
	SiO_2	1710	-	(Alfa Aesar 2015)
	Ni	1452(2)		(DETHERM n.d.)
	NiO	1955		(DETHERM n.d.)
Products	LiH	688(1)		(DETHERM n.d.)
	B	2052(21)		(DETHERM n.d.)
	$Li_2B_{12}H_{12}$	Unknown	No melting/fusion/frothing up to 600 °C	(Pitt et al. 2013)
	Na	98(1)		(DETHERM n.d.)
	NaH	638	Formed outside hot-zone	(GTT Technologies n.d.)
	$Na_2B_{12}H_{12}$	Unknown	Might be in a similar case as $Li_2B_{12}H_{12}$	(Li et al. 2015)
	K	64(1)		(DETHERM n.d.)
	KH	n.a.	Formed outside hot-zone	
	$K_2B_{12}H_{12}$	Unknown	Might be in a similar case as $Li_2B_{12}H_{12}$	(Li et al. 2015)
	Si	1421(11)		(DETHERM n.d.)
	Li_2SiO_3	1209		(Claus et al. 1996)
	Li_4SiO_4	1258		(Claus et al. 1996)
	Ni_2B	1125		(Bondar 2007)
	Ni_3B	1156		(Bondar 2007)
	Ni_4B_3	1008		(Franke & Neuschütz n.d.)
	$Li_{1.2}Ni_{2.5}B_2$	Unknown	Stable in crystalline structure till 760 °C	(Jung 1977)

LIST OF REFERENCES

Abbas, M.A. et al., 2013. Reducing the dehydrogenation temperature of lithium hydride through alloying with germanium. *Physical Chemistry Chemical Physics*, 15(29), p.12139. Available at: http://xlink.rsc.org/?DOI=c3cp51330k.

Abrahams, S.C. & Kalnajs, J., 1954. The Lattice Constants of the Alkali Borohydrides and the Low-Temperature Phase of Sodium Borohydride. *The Journal of Chemical Physics*, 22(3), pp.434–436.

Acosta, B. et al., 2014. JRC reference data from experiments of on-board hydrogen tanks fast filling. *International Journal of Hydrogen Energy*, 39(35), pp.20531–20537. Available at: http://dx.doi.org/10.1016/j.ijhydene.2014.03.227.

Adams, B.D. & Chen, A., 2011. The role of palladium in a hydrogen economy. *Materials Today*, 14(6), pp.282–289. Available at: http://dx.doi.org/10.1016/S1369-7021(11)70143-2.

Adams, R.M., 1961. Preparation of Diborane. In pp. 60–68. Available at: http://pubs.acs.org/doi/abs/10.1021/ba-1961-0032.ch008.

Afonso, G., Bonakdarpour, A. & Wilkinson, D.P., 2013. Hydrogen storage properties of the destabilized 4NaBH4/5Mg2NiH4 composite system. *Journal of Physical Chemistry C*, 117(41), pp.21105–21111.

Agarwal, V. & Saxena, R., 2014. An Introduction to Fuel Cell Electric Vehicles : State of Art. , 4(1), pp.35–38.

Ahluwalia, R.K. et al., 2010. Technical assessment of cryo-compressed hydrogen storage tank systems for automotive applications. *International Journal of Hydrogen Energy*, 35(9), pp.4171–4184. Available at: http://dx.doi.org/10.1016/j.ijhydene.2010.02.074.

Ahmad, H. et al., 2015. Hydrogen from photo-catalytic water splitting process: A review. *Renewable and Sustainable Energy Reviews*, 43, pp.599–610. Available at:

http://dx.doi.org/10.1016/j.rser.2014.10.101.

Alapati, S. V., Johnson, J.K. & Sholl, D.S., 2006. Identification of destabilized metal hydrides for hydrogen storage using first principles calculations. *Journal of Physical Chemistry B*, 110(17), pp.8769–8776.

Alfa Aesar, 2015. *Safety Date Sheet for Silicon(IV) oxide*,

Amendola, S.C. et al., 2000. A Safe, portable, hydrogen gas generator using aqueous borohydride solution and Ru catalyst. *International Journal of Hydrogen Energy*, 25(10), pp.969–975.

Amendola, S.C. et al., 1999. An ultrasafe hydrogen generator: Aqueous, alkaline borohydride solutions and Ru catalyst. *ACS Division of Fuel Chemistry, Preprints*, 44(4), pp.864–866.

Ampoumogli, A. et al., 2011. Nanostructured composites of mesoporous carbons and boranates as hydrogen storage materials. *Journal of Alloys and Compounds*, 509(SUPPL. 2), pp.S705–S708. Available at: http://dx.doi.org/10.1016/j.jallcom.2010.10.098.

Andújar, J.M. & Segura, F., 2009. Fuel cells: History and updating. A walk along two centuries. *Renewable and Sustainable Energy Reviews*, 13(9), pp.2309–2322.

Arroyo y de Dompablo, M.E. & Ceder, G., 2003. First-principles calculations on LixNiO2: phase stability and monoclinic distortion. *Journal of Power Sources*, 119–121(January), pp.654–657. Available at: http://linkinghub.elsevier.com/retrieve/pii/S037877530300199X.

Au, M., Spencer, W., et al., 2008. Hydrogen storage properties of modified lithium borohydrides. *Journal of Alloys and Compounds*, 462(1–2), pp.303–309.

Au, M., Jurgensen, A.R., et al., 2008. Stability and reversibility of lithium borohydrides doped by metal halides and hydrides. *Journal of Physical Chemistry C*, 112(47), pp.18661–18671.

Au, M. & Walters, R.T., 2010. Reversibility aspect of lithium borohydrides.

International Journal of Hydrogen Energy, 35(19), pp.10311–10316. Available at: http://dx.doi.org/10.1016/j.ijhydene.2010.07.130.

Babanova, O. a. et al., 2010. Structural and Dynamical Properties of NaBH4 and KBH4 : NMR and Synchrotron X-ray Diffraction Studies. *The Journal of Physical Chemistry C*, 114(8), pp.3712–3718. Available at: http://dx.doi.org/10.1021/jp9119606%5Cnhttp://pubs.acs.org/doi/full/10.1021/jp9119606%5Cnhttp://pubs.acs.org/doi/abs/10.1021/jp9119606.

Baburin, I.A. et al., 2015. Hydrogen adsorption by perforated graphene. *International Journal of Hydrogen Energy*, 40(20), pp.6594–6599. Available at: http://dx.doi.org/10.1016/j.ijhydene.2015.03.139.

Badger, R.M., 1934. A Relation Between Internuclear Distances and Bond Force Constants. *The Journal of Chemical Physics*, 2(3), pp.128–131. Available at: http://aip.scitation.org/doi/10.1063/1.1749433.

Bank, S., 1976. Organic syntheses via boranes (Brown, Herbert C.). *Journal of Chemical Education*, 53(5), p.A274. Available at: http://pubs.acs.org/doi/abs/10.1021/ed053pA274.1.

Banus, M.D. & Bragdon, R.W., 1955. Method for preparing borohydrides of alkali metals.

Bardají, E.G. et al., 2011. LiBH4−Mg(BH4)2 : A Physical Mixture of Metal Borohydrides as Hydrogen Storage Material. *The Journal of Physical Chemistry C*, 115(13), pp.6095–6101.

Baricco, M. et al., 2010. Thermodynamic Database for Hydrogen Storage Materials. *Advances in Science and Technology*, 72, pp.213–218. Available at: http://www.scientific.net/AST.72.213.

Barkhordarian, G. et al., 2007. Unexpected kinetic effect of MgB2 in reactive hydride composites containing complex borohydrides. *Journal of Alloys and Compounds*, 440(1–2), pp.18–21.

Barthelemy, H., Weber, M. & Barbier, F., 2017. Hydrogen storage: Recent

improvements and industrial perspectives. *International Journal of Hydrogen Energy*, 42(11), pp.7254–7262. Available at: http://dx.doi.org/10.1016/j.ijhydene.2016.03.178.

Baur, W.H., Halwax, E. & Völlenkle, H., 1986. Comparison of the crystal structures of sodium orthosilicate, Na4SiO4, and sodium orthogermanate, Na4GeO4. *Monatshefte for Chemie Chemical Monthly*, 117(6–7), pp.793–797. Available at: http://link.springer.com/10.1007/BF00810070.

Beach, J.Y. & Bauer, S.H., 1940. The Structure of the Hydrides of Boron. VI. AlB3H12. *Journal of the American Chemical Society*, 62(12), pp.3440–3442. Available at: http://pubs.acs.org/doi/abs/10.1021/ja01869a041.

Bell, M. et al., 2016. *UK climate change following the Paris Agreement*, Available at: https://www.theccc.org.uk/wp-content/uploads/2016/10/UK-climate-action-following-the-Paris-Agreement-Committee-on-Climate-Change-October-2016.pdf.

Bellosta von Colbe, J.M., 2006. *Instructions for the PCT 2*,

Bénard, P. & Chahine, R., 2001. Determination of the adsorption isotherms of hydrogen on activated carbons above the critical temperature of the adsorbate over wide temperature and pressure ranges. *Langmuir*, 17(6), pp.1950–1955.

Bénard, P. & Chahine, R., 2007. Storage of hydrogen by physisorption on carbon and nanostructured materials. *Scripta Materialia*, 56(10), pp.803–808.

Bernet, K. & Hoppe, R., 1990. Zur Kristallstruktur von K4(SiO4). *Zeitschrift fuer Anorganische und Allgemeine Chemie*, 589, pp.129–138.

Berube, V., Chen, G. & Dresselhaus, M.S., 2008. Impact of nanostructuring on the enthalpy of formation of metal hydrides. *International Journal of Hydrogen Energy*, 33(15), pp.4122–4131.

Blomgren, B.G.E. & Artsdalen, E.R.V.A.N., 1960. Fused Salts. *Annual Review of Physical Chemistry*, 11, pp.273–306.

Bondar, A., 2007. B-Cr-Ni (Boron-Chromium-Nickel). In *Non-Ferrous Metal Systems.*

Part 3. Berlin, Heidelberg: Springer Berlin Heidelberg, pp. 153–167. Available at: http://materials.springer.com/lb/docs/sm_lbs_978-3-540-47004-5_19.

Borgschulte, A. et al., 2011. Impurity gas analysis of the decomposition of complex hydrides. *Journal of Physical Chemistry C*, 115(34), pp.17220–17226.

Borgwardt, R.H. & Bruce, K.R., 1986. Effect of specific surface area on the reactivity of CaO with SO2. *AIChE Journal*, 32(2), pp.239–246. Available at: http://doi.wiley.com/10.1002/aic.690320210.

Bösenberg, U. et al., 2010. Role of additives in LiBH4-MgH2 reactive hydride composites for sorption kinetics. *Acta Materialia*, 58(9), pp.3381–3389.

Boudghene Stambouli, A. & Traversa, E., 2002. Fuel cells, an alternative to standard sources of energy. *Renewable and Sustainable Energy Reviews*, 6(3), pp.297–306.

Brinks, H.W. et al., 2006. Pressure–composition isotherms of TbNiAlHx. *Journal of Alloys and Compounds*, 417(1–2), pp.92–95. Available at: http://linkinghub.elsevier.com/retrieve/pii/S0925838805014192.

Brosset, C. & Magnusson, B., 1960. The Silicon-Boron System. *Nature*, 187(4731), pp.54–55. Available at: http://www.nature.com/doifinder/10.1038/187054a0.

Brown, H.C., Moon Choi, Y. & Narasimhan, S., 1981. Convenient Procedure for the Conversion of Sodium Borohydride into Lithium Borohydride in Simple Ether Solvents. *Inorganic Chemistry*, 20(12), pp.4454–4456.

Brown, H.C. & Rao, B.C.S., 1956. A New Powerful Reducing Agent—Sodium Borohydride in the Presence of Aluminum Chloride and Other Polyvalent Metal Halides 1,2. *Journal of the American Chemical Society*, 78(11), pp.2582–2588. Available at: http://pubs.acs.org/doi/abs/10.1021/ja01592a070.

Brown, M.E. & Gallagher, P.K. eds., 1998. *Handbook of Thermal Analysis and Calorimetry*, Principles and Practice.

Bruker, 2016. EVA Software - The next era in phase analysis. Available at: https://www.bruker.com/products/x-ray-diffraction-and-elemental-analysis/x-ray-

diffraction/xrd-software/eva/overview.html [Accessed October 10, 2016].

Bryant, J.M., Cunningham, G.L. & Gause, E.M., 1961. Preparation of potassium borohydride.

Burg, A.B. & Schlesinger, H.I., 1940. Metallo Borohydrides. II. Beryllium Borohydride. *Journal of the American Chemical Society*, 62(12), pp.3425–3429. Available at: http://pubs.acs.org/doi/abs/10.1021/ja01869a038.

Çakanyildirim, Ç. & Gürü, M., 2008a. Hydrogen cycle with sodium borohydride. *International Journal of Hydrogen Energy*, 33(17), pp.4634–4639.

Çakanyildirim, Ç. & Gürü, M., 2008b. Processing of LiBH4 from its elements by ball milling method. *Renewable Energy*, 33(11), pp.2388–2392.

Çakır, D., de Wijs, G.A. & Brocks, G., 2011. Native Defects and the Dehydrogenation of NaBH4. *The Journal of Physical Chemistry C*, 115(49), pp.24429–24434. Available at: http://pubs.acs.org/doi/10.1021/jp208642g.

Callini, E., Atakli, Z.Ö.K., et al., 2016. Complex and liquid hydrides for energy storage. *Applied Physics A*, 122(4), p.353. Available at: http://link.springer.com/10.1007/s00339-016-9881-5.

Callini, E., Aguey-Zinsou, K.F., et al., 2016. Nanostructured materials for solid-state hydrogen storage: A review of the achievement of COST Action MP1103. *International Journal of Hydrogen Energy*, 41(32), pp.14404–14428.

Callister, W.D.J. & Rethwisch, D.G., 2014. *Materials Science and Engineering: An Introduction* 1st ed., John Wiley & Sons.

Cao, Z. et al., 2015. Composition design of Ti-Cr-Mn-Fe alloys for hybrid high-pressure metal hydride tanks. *Journal of Alloys and Compounds*, 639, pp.452–457. Available at: http://dx.doi.org/10.1016/j.jallcom.2015.03.196.

Cao, Z. et al., 2016. Development of Zr-Fe-V alloys for hybrid hydrogen storage system. *International Journal of Hydrogen Energy*, 41(26), pp.11242–11253. Available at: http://dx.doi.org/10.1016/j.ijhydene.2016.04.083.

Caputo, R. et al., 2010. Can Na2[B12H12] be a decomposition product of NaBH4? *Physical Chemistry Chemical Physics*, 12(45), p.15093. Available at: http://xlink.rsc.org/?DOI=c0cp00877j.

Carter, G.F., Margrave, J.L. & Templeton, D.H., 1952. A high-temperature crystal modification of K2O. *Acta Crystallographica*, p.851.

Cartier, E., Stathis, J.H. & Buchanan, D.A., 1993. Passivation and depassivation of silicon dangling bonds at the Si/SiO2 interface by atomic hydrogen. *Applied Physics Letters*, 63(11), pp.1510–1512. Available at: http://aip.scitation.org/doi/10.1063/1.110758.

Černý, R. et al., 2010. NaSc(BH4)4: A novel scandium-based borohydride. *Journal of Physical Chemistry C*, 114(2), pp.1357–1364. Available at: http://pubs.acs.org/doi/abs/10.1021/jp908397w.

Chater, P.A. et al., 2007. Synthesis and characterization of amide-borohydrides: New complex light hydrides for potential hydrogen storage. *Journal of Alloys and Compounds*, 446–447, pp.350–354.

Chen, J. et al., 2012. Enhanced hydrogen desorption from the Co-catalyzed LiBH4–Mg(BH4)2 eutectic composite. *International Journal of Hydrogen Energy*, 37(17), pp.12425–12431. Available at: http://dx.doi.org/10.1016/j.ijhydene.2012.06.057.

Chen, K. et al., 2012. Freestanding monolithic silicon aerogels. *Journal of Materials Chemistry*, 22, pp.16196–16200.

Chen, P. et al., 2002. Interaction of hydrogen with metal nitrides and imides. *Nature*, 420(6913), pp.302–304. Available at: http://www.nature.com/doifinder/10.1038/nature01210.

Chen, X.Y. et al., 2013. A Review on the Metal Hydride Based Hydrogen Purification and Separation Technology. *Applied Mechanics and Materials*, 448–453(October), pp.3027–3036. Available at: http://www.scientific.net/AMM.448-453.3027.

Chen, X.Y. et al., 2010. Improved dehydrogenation of LiBH4 supported on nanoscale SiO2 via liquid phase method. *Journal of Materials Research*, 25(12), pp.2415–

2421.

Chligui, M. et al., 2010. New features in the Raman spectrum of Silica : Key-points in the improvement on structure knowledge. *Physics Revue B*, (September), pp.1–5.

Choi, Y.S. et al., 2016. Interface-enhanced Li ion conduction in a LiBH4–SiO4 solid electrolyte. *Physical Chemistry Chemical Physics*, 18(32), pp.22540–22547. Available at: http://xlink.rsc.org/?DOI=C6CP03563A.

Chong, L. et al., 2013. Mechanisms of reversible hydrogen storage in NaBH4 through NdF3 addition. *Journal of Materials Chemistry A*, 4, pp.3983–3991.

Chong, L. et al., 2014. Study on reversible hydrogen sorption behaviors of a 3NaBH4/HoF3 composite. *International Journal of Hydrogen Energy*, 39(26), pp.14275–14281. Available at: http://xlink.rsc.org/?DOI=C4TA00715H.

Christian, M. & Aguey-Zinsou, K.-F., 2013. Synthesis of core–shell NaBH4@M (M = Co, Cu, Fe, Ni, Sn) nanoparticles leading to various morphologies and hydrogen storage properties. *Chemical Communications*, 49(60), p.6794. Available at: http://xlink.rsc.org/?DOI=c3cc42815j.

Christian, M.L. & Aguey-Zinsou, K.F., 2012. Core-shell strategy leading to high reversible hydrogen storage capacity for NaBH 4. *ACS Nano*, 6(9), pp.7739–7751.

Claudionico, C., 2013. Signals emitted from different parts of the interaction volume. *Wikipedia*. Available at: https://en.wikipedia.org/wiki/Scanning_electron_microscope#/media/File:Electron_Interaction_with_Matter.svg [Accessed March 25, 2018].

Claus, S., Kleykamp, H. & Smykatz-Kloss, W., 1996. Phase equilibria in the Li4SiO4-Li2SiO3 region of the pseudobinary Li2O-SiO2 system. *Journal of Nuclear Materials*, 230(1), pp.8–11. Available at: http://linkinghub.elsevier.com/retrieve/pii/0022311596000220.

Coe, D.A. & Nibler, J.W., 1973. Infrared and Raman spectra of aluminum borohydride, Al(BH4)3. *Spectrochimica Acta Part A: Molecular Spectroscopy*, 29(10), pp.1789–1804. Available at:

http://linkinghub.elsevier.com/retrieve/pii/0584853973801655.

Coelho, A., 2007. TOPAS Academic Version 4.1.

Cova, F.H. et al., 2015. New Insights Into the Thermodynamic Behavior of 2LiBH4-MgH2 Composite for Hydrogen Storage. *The Journal of Physical Chemistry C*, 119(28), pp.15816–15822. Available at: http://www.scopus.com/inward/record.url?eid=2-s2.0-84937128024&partnerID=tZOtx3y1%5Cnhttp://pubs.acs.org/doi/abs/10.1021/acs.jpcc.5b02047.

D'Anna, V. et al., 2014. FT-IR spectra of inorganic borohydrides. *Spectrochimica Acta Part A: Molecular and Biomolecular Spectroscopy*, 128, pp.902–906. Available at: http://dx.doi.org/10.1016/j.saa.2014.02.130.

D'Anna, V., Lawson Daku, L.M. & Hagemann, H., 2013. Vibrational spectra and structure of borohydrides. *Journal of Alloys and Compounds*, 580, pp.S122–S124. Available at: http://dx.doi.org/10.1016/j.jallcom.2013.01.112.

David, W.I.F. et al. eds., 2006. *Structure Determination from Powder Diffraction Data*, Oxford University Press. Available at: http://www.oxfordscholarship.com/view/10.1093/acprof:oso/9780199205530.001.0001/acprof-9780199205530.

Davis, R.L. & Kennard, C.H.L., 1985. Structure of Sodium Tetradeuteroborate, NaBD4. *Journal of Solid State Chemistry*, 59, pp.393–396. Available at: http://linkinghub.elsevier.com/retrieve/pii/0022459685903081.

Dekock, R.L. & Gray, H.B., 1989. *Chemical Structure and Bonding* 2nd ed., University Science Books.

Dematteis, E.M. et al., 2016. A thermodynamic investigation of the LiBH4-NaBH4 system. *RSC Adv.*, 6(65), pp.60101–60108. Available at: http://xlink.rsc.org/?DOI=C6RA09301A.

Dematteis, E.M. et al., 2017. Phase diagrams of the LiBH4–NaBH4–KBH4 system. *Physical Chemistry Chemical Physics*, 19(36), pp.25071–25079. Available at:

http://pubs.rsc.org/en/Content/ArticleLanding/2017/CP/C7CP03816J%0Ahttp://xlink.rsc.org/?DOI=C7CP03816J.

DETHERM, DETHERM database. *Gesellschaft für Chemische Technik und Biotechnologie e.V.* Available at: http://dechema.de/en/detherm.html [Accessed April 11, 2018].

Dinnebier, R.E. & Billinge, Simon, J.L., 2008. *Powder Diffraction Theory and Practice* R. E. Dinnebier & J. L. Billinge, Simon, eds., The Royal Society of Chemistry.

Dornheim, M. et al., 2006. Tailoring hydrogen storage materials towards application. *Advanced Engineering Materials*, 8(5), pp.377–385.

Dornheim, M., 2011. Thermodynamics of Metal Hydrides: Tailoring Reaction Enthalpies of Hydrogen Storage Materials. In *Thermodynamics - Interaction Studies - Solids, Liquids and Gases*. InTech. Available at: http://www.intechopen.com/books/thermodynamics-interaction-studies-solids-liquids-and-gases/thermodynamics-of-metal-hydrides-tailoring-reaction-enthalpies-of-hydrogen-storage-materials.

Dovgaliuk, I. et al., 2014. The first halide-free bimetallic aluminum borohydride: synthesis, structure, stability, and decomposition pathway. *Journal of Physical Chemistry C*, 118, pp.145–153.

Durbin, D.J. & Malardier-Jugroot, C., 2013. Review of hydrogen storage techniques for on board vehicle applications. *International Journal of Hydrogen Energy*, 38(34), pp.14595–14617.

Dutrow, B.L. & Clark, C.M., X-ray Powder Diffraction (XRD). *The Science Education Resource Center at Carleton College*. Available at: https://serc.carleton.edu/research_education/geochemsheets/techniques/XRD.html [Accessed March 27, 2018].

elementenergy, 2015. *Installing accessible hydrogen refuelling stations - A best practice guide*,

Fakioğlu, E., Yürüm, Y. & Veziroğlu, T.N., 2004. A review of hydrogen storage

systems based on boron and its compounds. *International Journal of Hydrogen Energy*, 29(13), pp.1371–1376.

Fang, Z.Z. et al., 2008. Kinetic- and thermodynamic-based improvements of lithium borohydride incorporated into activated carbon. *Acta Materialia*, 56(20), pp.6257–6263. Available at: http://dx.doi.org/10.1016/j.actamat.2008.08.033.

Faraday, M., 1832. Experimental Researches in Electricity. *Philosophical Transactions of the Royal Society of London*, 122(0), pp.125–162. Available at: http://rstl.royalsocietypublishing.org/cgi/doi/10.1098/rstl.1832.0006.

Felderhoff, M. & Bogdanović, B., 2009. High temperature metal hydrides as heat storage materials for solar and related applications. *International journal of molecular sciences*, 10(1), pp.325–344.

Filinchuk, Y. et al., 2007. High-pressure phase of NaBH4: Crystal structure from synchrotron powder diffraction data. *Physical Review B - Condensed Matter and Materials Physics*, 76(9), pp.7–10.

Filinchuk, Y., Chernyshov, D. & Cerny, R., 2008. Lightest Borohydride Probed by Synchrotron X-ray Diffraction: Experiment Calls for a New Theoretical Revision. *Journal of Physical Chemistry C*, 112, pp.10579–10584.

Filinchuk, Y. & Hagemann, H., 2008. Structure and properties of NaBH4·2H2O and NaBH4. *European Journal of Inorganic Chemistry*, (20), pp.3127–3133.

Fischer, P. & Züttel, A., 2004. Order-Disorder Phase Transition in NaBD4. *Materials Science Forum*, 443–444, pp.287–290. Available at: http://www.scientific.net/MSF.443-444.287.

FIZ Karlsruhe, Inorganic Crystal Structure Databas (ICSD). *2017*. Available at: http://icsd.cds.rsc.org/ [Accessed February 16, 2017].

Flynn, T., 2004. *Cryogenic Engineering, Second Edition, Revised and Expanded* 2nd ed.,

Foner, S., 1959. Versatile and Sensitive Vibrating‐Sample Magnetometer. *Review of*

Scientific Instruments, 30(7), pp.548–557. Available at: http://aip.scitation.org/doi/10.1063/1.1716679.

Franke, P. & Neuschütz, D., B-Ni. In *Binary systems. Part 2: Elements and Binary Systems from B – C to Cr – Zr*. Berlin/Heidelberg: Springer-Verlag, pp. 1–4. Available at: http://materials.springer.com/lb/docs/sm_lbs_978-3-540-45201-0_11.

Friedrichs, O., Remhof, A., Borgschulte, A., et al., 2010. Breaking the passivation—the road to a solvent free borohydride synthesis. *Physical Chemistry Chemical Physics*, 12(36), p.10919. Available at: http://xlink.rsc.org/?DOI=c0cp00022a.

Friedrichs, O. et al., 2008. Direct synthesis of Li[BH4] and Li[BD4] from the elements. *Acta Materialia*, 56(5), pp.949–954. Available at: http://linkinghub.elsevier.com/retrieve/pii/S135964540700746X.

Friedrichs, O. et al., 2009. Low-temperature synthesis of LiBH4 by gas-solid reaction. *Chemistry - A European Journal*, 15(22), pp.5531–5534.

Friedrichs, O., Remhof, A., Hwang, S.J., et al., 2010. Role of Li2B12H12 for the formation and decomposition of LiBH4. *Chemistry of Materials*, 22(10), pp.3265–3268.

Garroni, S. et al., 2011. Experimental evidence of Na2[B12H12] and Na formation in the desorption pathway of the 2NaBH4 + MgH 2 system. *Journal of Physical Chemistry C*, 115(33), pp.16664–16671.

Garroni, S. et al., 2009. Hydrogen desorption mechanism of 2NaBH4+MgH2 composite prepared by high-energy ball milling. *Scripta Materialia*, 60(12), pp.1129–1132. Available at: http://linkinghub.elsevier.com/retrieve/pii/S1359646209001559.

Garroni, S. et al., 2010. Sorption properties of NaBH4/MH2 (M = Mg, Ti) powder systems. *International Journal of Hydrogen Energy*, 35(11), pp.5434–5441.

Gebert, F. et al., 2011. Polarization-dependent Raman spectroscopy of LiBH4 single crystals and Mg(BH4)2 powders. *Journal of Raman Spectroscopy*, 42(9), pp.1796–1801.

Geis, V. et al., 2009. Synthesis and characterization of synthetically useful salts of the weakly-coordinating dianion [B12Cl12]2−. *Dalton Transactions*, (15), p.2687. Available at: http://xlink.rsc.org/?DOI=b821030f.

George F, H., 1960. Method and composition for subjecting metals to reducing conditions.

Gilman, E.L. et al., 2008. Threats to mangroves from climate change and adaptation options: A review. *Aquatic Botany*, 89(2), pp.237–250.

Gimeno-Fabra, M. et al., 2012. Instant MOFs: continuous synthesis of metal–organic frameworks by rapid solvent mixing. *Chemical Communications*, 48(86), p.10642. Available at: http://xlink.rsc.org/?DOI=c2cc34493a.

Gkanas, E.I. et al., 2016. Efficient hydrogen storage in up-scale metal hydride tanks as possible metal hydride compression agents equipped with aluminium extended surfaces. *International Journal of Hydrogen Energy*, 41(25), pp.10795–10810. Available at: http://dx.doi.org/10.1016/j.ijhydene.2016.04.035.

Glockler, G., 1963. Bond energies and bond distances of boron hydrides. *Transactions of the Faraday Society*, 59, p.1080. Available at: http://xlink.rsc.org/?DOI=tf9635901080.

Goddard, W.A. et al., 2008. Covalent Organic Frameworks as Exceptional Hydrogen Storage Materials. , 105(November 2016), pp.76–78.

Goerrig, D., 1958. Verfahren zur herstellung von boranaten.

Gogotsi, Y. et al., 2005. Tailoring of nanoscale porosity in carbide-derived carbons for hydrogen storage. *Journal of the American Chemical Society*, 127(46), pp.16006–16007.

Gomes, S., Hagemann, H. & Yvon, K., 2002. Lithium boro-hydride LiBH4. *Journal of Alloys and Compounds*, 346(1–2), pp.206–210. Available at: http://linkinghub.elsevier.com/retrieve/pii/S0925838802006680.

Gosalawit-Utke, R. et al., 2011. Nanoconfined 2LiBH4-MgH2 prepared by direct melt

infiltration into nanoporous materials. *Journal of Physical Chemistry C*, 115(21), pp.10903–10910.

Grochala, W. & Edwards, P.P., 2004. Thermal decomposition of the non-interstitial hydrides for the storage and production of hydrogen. *Chemical Reviews*, 104(3), pp.1283–1315.

Gross, A.F. et al., 2008. Enhanced Hydrogen Storage Kinetics of LiBH4 in Nanoporous Carbon Scaffolds. *The Journal of Physical Chemistry C*, 112(14), pp.5651–5657. Available at: http://pubs.acs.org/doi/abs/10.1021/jp711066t.

GTT Technologies, SGTE Subst. database V 4.1. Available at: http://www.gtt-technologies.de/data/sgte-databases.

Gu, J. et al., 2015. Improved hydrogen storage properties of combined Ca(BH4)2 and LiBH4 system motivated by addition of LaMg3 assisted with ball milling in H2. *International Journal of Hydrogen Energy*, 40(36), pp.12325–12335. Available at: http://dx.doi.org/10.1016/j.ijhydene.2015.07.089.

Guo, L. et al., 2017. Enhanced hydrogen storage capacity and reversibility of LiBH4 encapsulated in carbon nanocages. *International Journal of Hydrogen Energy*, 42(4), pp.2215–2222. Available at: http://dx.doi.org/10.1016/j.ijhydene.2016.11.184.

Guo, S., 2014. *Light Metal Borohdyride and Mg-Based Hydrides For Hydrogen Stroage*. Univerisity of Birmingham.

Guo, Y. et al., 2013. Prediction of thermodynamically reversible hydrogen storage reactions in the KBH4/M(M=Li, Na, Ca)(BH4)n(n=1,2) system from first-principles calculation. *Chemical Physics*, 418, pp.22–27. Available at: http://linkinghub.elsevier.com/retrieve/pii/S0301010413001638.

Habashi, F., 1997. *Handbook of Extractive Metallurgy* F. Habashi, ed., Heidelberg, Germany: Wiley VCH.

Hagemann, H. et al., 2009. Lattice anharmonicity and structural evolution of LiBH4 : an insight from Raman and X-ray diffraction experiments. *Phase Transitions*, 82(4),

pp.344–355. Available at: http://apps.webofknowledge.com/full_record.do?product=UA&search_mode=GeneralSearch&qid=1&SID=3DP6O5fYqeucZcfUuIJ&page=1&doc=1.

Hagemann, H. et al., 2011. New fundamental experimental studies on α-Mg(BH4)2 and other borohydrides. *Journal of Alloys and Compounds*, 509(SUPPL. 2), pp.S688–S690. Available at: http://linkinghub.elsevier.com/retrieve/pii/S0925838810025776.

Hagemann, H. et al., 2004. Raman studies of reorientation motions of [BH4]- anionsin alkali borohydrides. *Journal of Alloys and Compounds*, 363(1–2), pp.126–129.

Hanada, N. et al., 2008. Thermal decomposition of Mg(BH4)2 under He flow and H2 pressure. *Journal of Materials Chemistry*, 18(22), p.2611. Available at: http://pubs.rsc.org/en/content/articlehtml/2008/jm/b801049h.

Hansen, B.R.S. et al., 2016. Metal boranes: Progress and applications. *Coordination Chemistry Reviews*, 323, pp.60–70. Available at: http://dx.doi.org/10.1016/j.ccr.2015.12.003.

Hanumantha Rao, M. & Muralidharan, K., 2013. Syntheses, characterization and energetic properties of closo-(B12H12)2− salts of imidazolium derivatives. *Dalton Transactions*, 42(24), p.8854. Available at: http://xlink.rsc.org/?DOI=c3dt32834a.

Harries, D.N. et al., 2012. Concentrating Solar Thermal Heat Storage Using Metal Hydrides. *Proceedings of the IEEE*, 100(2), pp.539–549. Available at: http://ieeexplore.ieee.org/ielx5/5/6132586/05955063.pdf?tp=&arnumber=5955063&isnumber=6132586%5Cnhttp://ieeexplore.ieee.org/xpls/abs_all.jsp?arnumber=5955063&tag=1.

Harrison, D. & Thonhauser, T., 2016. Suppressing diborane production during the hydrogen release of metal borohydrides: The example of alloyed Al(BH4)3. *International Journal of Hydrogen Energy*, 41(28), p.12440. Available at: http://dx.doi.org/10.1016/j.ijhydene.2015.12.159.

Hartman, M.R. et al., 2007. Structure and vibrational dynamics of isotopically labeled

lithium borohydride using neutron diffraction and spectroscopy. , 180, pp.1298–1305.

Harvey, K.B. & McQuaker, N.R., 1971. Infrared and Raman Spectra of Potassium and Sodium Borohydride. *Canadian Journal of Chemistry*, 49(20), pp.3272–3281. Available at: http://www.nrcresearchpress.com/doi/abs/10.1139/v71-545.

Harvey, K.B. & McQuaker, N.R., 1971. Low Temperature Infrared and Raman Spectra of Lithium Borohydride. *Canadian Journal of Chemistry*, 49(20), pp.3282–3286. Available at: http://www.nrcresearchpress.com/doi/10.1139/v71-546.

He, L. et al., 2015. Synthesis of a Bimetallic Dodecaborate LiNaB12H12 with Outstanding Superionic Conductivity. *Chemistry of Materials*, 27(16), pp.5483–5486. Available at: http://pubs.acs.org/doi/10.1021/acs.chemmater.5b01568.

Hensens, O.D. & Goldberg, I.H., 1988. Mechansim of Activation of the Antitumor Antibiotic Neocarzinostatin by Mercaptan and Sodium Borohydirdes. , XLII(5).

Her, J.-H. et al., 2008. Crystal Structure of Li2B12H12 : a Possible Intermediate Species in the Decomposition of LiBH4. *Inorganic Chemistry*, 47(21), pp.9757–9759. Available at: http://dx.doi.org/10.1021/cm100536a.

Her, J.H. et al., 2009. Role of cation size on the structural behavior of the alkali-metal dodecahydro-closo-dodecaborates. *Journal of Physical Chemistry C*, 113(26), pp.11187–11189.

Hirscher, M. ed., 2010. *Handbook of Hydrogen Storage: New Materials for Future Energy Storage*, Wiley-VCH Verlag GmbH & Co. KGaA.

Hoffmann, E. de & Stroobant, V., 2007. *Mass Spectrometry: Principles and Applications* 3rd ed., Wiley.

Hofmann, K. & Albert, B., 2005. Crystal structures of M2[B10H10] (M = Na, K, Rb) via real-space simulated annealing powder techniques. *Zeitschrift für Kristallographie - Crystalline Materials*, 220(2/3). Available at: http://www.degruyter.com/view/j/zkri.2005.220.issue-2-3/zkri.220.2.142.59144/zkri.220.2.142.59144.xml.

Hofmann, R. & Hoppe, R., 1987. Ein neues Oxogermanat: Li8GeO6 = Li8O2 (GeO4) (Mit einer Bemerkung ueber Li8SiO6 und Li4GeO4). *Zeitschrift fuer Anorganische und Allgemeine Chemie*, 555, pp.118–128.

Holladay, J.D. et al., 2009. An overview of hydrogen production technologies. *Catalysis Today*, 139(4), pp.244–260.

Housecroft, C. & Sharpe, A.G., 2012. *Inorganic Chemistry* 4th ed., Pearson.

Hu, J. et al., 2014. Beneficial effects of stoichiometry and nanostructure for a LiBH4-MgH2 hydrogen storage system. *Journal of Materials Chemistry A*, 2(207890), p.66. Available at: http://pubs.rsc.org/en/content/articlelanding/2014/ta/c3ta13775a%5Cnhttp://pubs.rsc.org/en/Content/ArticleLanding/2014/TA/C3TA13775A#!divAbstract%5Cnhttp://pubs.rsc.org/en/content/articlepdf/2014/ta/c3ta13775a%5Cnhttp://xlink.rsc.org/?DOI=c3ta13775a.

Huang, Z.-Q. et al., 2016. First-principles calculated decomposition pathways for LiBH4 nanoclusters. *Scientific Reports*, 6(April), p.26056. Available at: http://www.nature.com/articles/srep26056.

Huen, P. et al., 2017. Hydrogen Storage Stability of Nanoconfined MgH2 upon Cycling. *Inorganics*, 5(3), p.57. Available at: http://www.mdpi.com/2304-6740/5/3/57.

Hull, A.W., 1917. Crystal structure of nickel. *Physical Review*, 10, pp.661–696.

Humphries, T.D. et al., 2013. Reversible Hydrogenation Studies of NaBH4 Milled with Ni-Containing Additives. *The Journal of Physical Chemistry C*, 117(12), pp.6060–6065. Available at: http://pubs.acs.org/doi/10.1021/jp312105w.

Hussain, A., Arif, S.M. & Aslam, M., 2017. Emerging renewable and sustainable energy technologies: State of the art. *Renewable and Sustainable Energy Reviews*, 71(January), pp.12–28. Available at: http://dx.doi.org/10.1016/j.rser.2016.12.033.

Hwang, S.J. et al., 2008. NMR confirmation for formation of [B12H12]2- complexes during hydrogen desorption from metal borohydrides. *Journal of Physical Chemistry C*, 112(9), pp.3164–3169.

Ibikunle, A., Goudy, A.J. & Yang, H., 2009. Hydrogen storage in a CaH2/LiBH4 destabilized metal hydride system. *Journal of Alloys and Compounds*, 475(1–2), pp.110–115.

Imre, B., 2009. Eutectic system phase diagram. *Wikipedia*. Available at: https://en.wikipedia.org/wiki/Eutectic_system#/media/File:Eutectic_system_phase_diagram.svg [Accessed March 25, 2018].

Jain, I.P., Jain, P. & Jain, A., 2010. Novel hydrogen storage materials: A review of lightweight complex hydridespuye. *Journal of Alloys and Compounds*, 503(2), pp.303–339. Available at: http://dx.doi.org/10.1016/j.jallcom.2010.04.250.

Jain, I.P., Lal, C. & Jain, A., 2010. Hydrogen storage in Mg: A most promising material. *International Journal of Hydrogen Energy*, 35(10), pp.5133–5144. Available at: http://dx.doi.org/10.1016/j.ijhydene.2009.08.088.

James, B.D. & Wallbridge, M.G.H., 1970. Metal Tetrahydroborates. In *Progress in Inorganic Chemistry, Volume 11*. Hoboken, NJ, USA.: John Wiley & Sons, pp. 99–231. Available at: http://doi.wiley.com/10.1002/9780470166123.ch3.

Jansen, M., 1982. Zur Kristallstruktur von Kaliumdisilicat. *Zeitschrift fuer Kristallographie*, 160, pp.127–133.

Javadian, P., Zlotea, C., et al., 2015. Hydrogen storage properties of nanoconfined LiBH4-Mg2NiH4 reactive hydride composites. *Journal of Physical Chemistry C*, 119(11), pp.5819–5826.

Javadian, P., Sheppard, D.A., et al., 2015. Hydrogen storage properties of nanoconfined LiBH4-NaBH4. *International Journal of Hydrogen Energy*, 40(43), pp.14916–14924.

Javadian, P. et al., 2017. Reversibility of LiBH4 Facilitated by the LiBH4–Ca(BH4)2 Eutectic. *The Journal of Physical Chemistry C*, 121(34), pp.18439–18449. Available at: http://pubs.acs.org/doi/abs/10.1021/acs.jpcc.7b06228.

Javadian, P. & Jensen, T.R., 2014. Enhanced hydrogen reversibility of nanoconfined LiBH4–Mg(BH4)2. *International Journal of Hydrogen Energy*, 39(18), pp.9871–

9876. Available at: http://linkinghub.elsevier.com/retrieve/pii/S036031991400620X.

Jensen, S.R.H. et al., 2015. Phase Diagram for the NaBH4–KBH4 System and the Stability of a Na1− xKxBH4 Solid Solution. *The Journal of Physical Chemistry C*, 119(50), pp.27919–27929. Available at: http://pubs.acs.org/doi/10.1021/acs.jpcc.5b09851.

Jensen, W.B., 1996. Electronegativity from Avogadro to Pauling: Part 1: Origins of the Electronegativity Concept. *Journal of Chemical Education*, 73(1), p.11. Available at: http://pubs.acs.org/doi/abs/10.1021/ed073p11.

Jiang, H.L. et al., 2010. Liquid-Phase chemical hydrogen storage: Catalytic hydrogen generation under ambient conditions. *ChemSusChem*, 3(5), pp.541–549.

Jiang, Y., Wang, Y. & Zeng, L., 1996. Analysis of Raman Spectra of LiB3O5 Single Crystals. *Journal of Raman Spectroscopy*, 27(8), pp.601–607. Available at: http://doi.wiley.com/10.1002/%28SICI%291097-4555%28199608%2927%3A8%3C601%3A%3AAID-JRS993%3E3.0.CO%3B2-P.

de Jongh, P.E. & Eggenhuisen, T.M., 2013. Melt Infiltration: an Emerging Technique for the Preparation of Novel Functional Nanostructured Materials. *Advanced Materials*, 25(46), pp.6672–6690. Available at: http://doi.wiley.com/10.1002/adma.201301912.

Jung, W., 1977. Darstellung und Kristallstruktur von MgNi2.5B2 und Li1.2Ni2.5B2. *Zeitschrift fuer Naturforschung, Teil B. Anorganische Chemie, Organische Chemie*, pp.1371–1374.

Jung, W., 1980. Die Kristallstruktur von Li3Ni20B6 und Li3Ni16B8. *Zeitschrift fuer Kristallographie*, pp.113–120.

Kahlenberg, V. et al., 1999. The Crystal Structure of δ-Na2Si2O5. *Journal of Solid State Chemistry*, 146(2), pp.380–386. Available at: http://linkinghub.elsevier.com/retrieve/pii/S0022459699983652.

Kalantzopoulos, G.N. et al., 2014. Destabilization effect of transition metal fluorides on sodium borohydride. *Phys. Chem. Chem. Phys.*, 16(38), pp.20483–20491. Available at: http://dx.doi.org/10.1039/C4CP02899F%0Ahttp://xlink.rsc.org/?DOI=C4CP02899F.

Kane, M., 2014. Toyota Mirai Fuel Cell Sedan Priced At $57,500 – Specs, Videos. *InsideEVs.com*. Available at: http://insideevs.com/toyota-mirai-fuel-cell-sedan-priced-at-57500-specs-videos/ [Accessed October 3, 2017].

Kato, S. et al., 2010. Effect of the surface oxidation of LiBH4 on the hydrogen desorption mechanism. *Physical Chemistry Chemical Physics*, 12(36), p.10950. Available at: http://xlink.rsc.org/?DOI=c000299b.

El Kharbachi, A. et al., 2012. A thermodynamic assessment of LiBH4. *Calphad: Computer Coupling of Phase Diagrams and Thermochemistry*, 39, pp.80–90.

El Kharbachi, A. et al., 2011. Above room temperature heat capacity and phase transition of lithium tetrahydroborate. *Thermochimica Acta*, 520(1–2), pp.75–79. Available at: http://dx.doi.org/10.1016/j.tca.2011.02.043.

Kim, K.C. & Sholl, D.S., 2010. Crystal Structures and Thermodynamic Investigations of LiK(BH4)2, KBH4, and NaBH4 from First-Principles Calculations. *The Journal of Physical Chemistry C*, 114(1), pp.678–686. Available at: http://pubs.acs.org/doi/abs/10.1021/jp909120p.

Kirubakaran, A., Jain, S. & Nema, R.K., 2009. A review on fuel cell technologies and power electronic interface. *Renewable and Sustainable Energy Reviews*, 13(9), pp.2430–2440.

Kissinger, H.E., 1957. Reaction Kinetics in Differential Thermal Analysis. , 303(5), pp.1702–1706.

Klebanoff, L., 2016. *Hydrogen Storage Technology: Materials and Applications* 1st ed., CRC Press.

Klechikov, A.G. et al., 2015. Hydrogen storage in bulk graphene-related materials.

Microporous and Mesoporous Materials, 210, pp.46–51.

Klein, D. et al. eds., 2017. *The Paris Agreement on Climate Change: Analysis and Commentary*, OUP Oxford.

Knighten, G. V et al., 2007. Designed synthesis of 3D covalent organic frameworks. , (April), pp.268–273.

Kojima, Y. & Haga, T., 2003. Recycling process of sodium metaborate to sodium borohydride. *International Journal of Hydrogen Energy*, 28(9), pp.989–993.

Kowada, Y., Tatsumisago, M. & Minami, T., 1989. Raman spectra of rapidly quenched glasses in the systems lithium borate-lithium silicate-lithium phosphate (Li3BO3-Li4SiO4-Li3PO4 and Li4B2O5-Li6Si2O7-Li4P2O7). *The Journal of Physical Chemistry*, 93(5), pp.2147–2151. Available at: http://pubs.acs.org/doi/abs/10.1021/j100342a085.

Krüger, H., Kahlenberg, V. & Kaindl, R., 2007. Li2Si3O7: Crystal structure and Raman spectroscopy. *Journal of Solid State Chemistry*, 180(3), pp.922–928. Available at: http://linkinghub.elsevier.com/retrieve/pii/S0022459606006554.

Kudlmann, U. & Roberg, W., 1994. OPTICAL PROPERTIES OF AMORPHOUS BORON. , 55(7), pp.579–587.

Kumar, R.S. & Cornelius, A.L., 2005. Structural transitions in NaBH4 under pressure. *Applied Physics Letters*, 87(26), pp.1–3.

Kumar, R.S., Eun-Ja, K. & Cornelius, A.L., 2008. Structural phase transitions in the potential hydrogen storage compound K B H4 under compression. *Journal of Physical Chemistry C*, 112, pp.8452–8457.

Kumar, S., Kojima, Y. & Dey, G.K., 2017. Synergic effect of ZrCl4 on thermal dehydrogenation kinetics of KBH4. *Journal of Alloys and Compounds*, 718, pp.134–138. Available at: http://linkinghub.elsevier.com/retrieve/pii/S0925838817317127.

Kurko, S. et al., 2013. Hydrogen sorption properties of MgH2/NaBH4 composites.

International Journal of Hydrogen Energy, 38(27), pp.12140–12145.

Kutz, M. ed., 2015. *Mechanical Engineers' Handbook, Volume 4: Energy and Power* 4th ed.,

De la Mora, P., Castro, M. & Tavizon, G., 2002. Comparative study of the electronic structure of alkaline-earth borides (MeB2; Me = Mg, Al, Zr, Nb, and Ta) and their normal-state conductivity. *Journal of Solid State Chemistry*, 169(2), pp.168–175.

Lang, J. et al., 2012. Differential Scanning Calorimetry (DSC) and Synchrotron X-ray Diffraction Study of Unmilled and Milled LiBH4: A Partial Release of Hydrogen at Moderate Temperatures. *Crystals*, 2, pp.1–21.

Langmi, H.W. et al., 2014. Hydrogen Storage in Metal-Organic Frameworks: A Review. *Electrochimica Acta*, 128(2014), pp.368–392. Available at: http://linkinghub.elsevier.com/retrieve/pii/S0013468613021622.

Larkin, P., 2011. *Infrared and Raman Spectroscopy: Principles and Spectral Interpretation* 1st ed. Elsevier, ed., Elsevier.

Lee, H.S. et al., 2011. Enhanced desorption and absorption properties of eutectic LiBH4-Ca(BH4)2 infiltrated into mesoporous carbon. *Journal of Physical Chemistry C*, 115(40), pp.20027–20035.

Lee, J.Y. et al., 2009. Decomposition Reactions and Reversibility of the LiBH4−Ca(BH4)2 Composite. *The Journal of Physical Chemistry C*, 113(4), pp.15080–15086. Available at: http://dx.doi.org/10.1021/jp904400b.

Leites, L.A., 1992. Vibrational Spectroscopy of Carboranes and Parent Boranes and Its Capabilities in Carborane Chemistry. *Chemical Reviews*, 92(2), pp.279–323.

Lemke, B.P. & Haneman, D., 1978. Dangling bonds on silicon. *Physical Review B*, 17(4), pp.1893–1907. Available at: https://link.aps.org/doi/10.1103/PhysRevB.17.1893.

Lemmon, E.W., Huber, M.L. & Leachman, J.W., 2008. Revised Standardized Equation for Hydrogen Gas Densities for Fuel Consumption Applications. *Journal of*

Research of the National Institute of Standards and Technology, 113(6), p.341. Available at: https://nvlpubs.nist.gov/nistpubs/jres/113/6/V113.N06.A05.pdf.

Leng, Y., 2008. *Materials Characterization*, Chichester, UK: John Wiley & Sons, Ltd. Available at: http://doi.wiley.com/10.1002/9780470823002.

Ley, M. et al., 2015. Melting Behavior and Thermolysis of NaBH4−Mg(BH4)2 and NaBH4−Ca(BH4)2 Composites. *Energies*, 8(4), pp.2701–2713. Available at: http://www.mdpi.com/1996-1073/8/4/2701/.

Ley, M.B., Roedern, E. & Jensen, T.R., 2014. Eutectic melting of LiBH4-KBH4. *Physical chemistry chemical physics : PCCP*, 16(44), pp.24194–9. Available at: http://www.ncbi.nlm.nih.gov/pubmed/25293724.

Li, D.M.B.H.M. et al., 2015. Thermal Decomposition of Anhydrous Alkali Metal. , 12(October), pp.12429–12438.

Li, H. et al., 2014. Improved Dehydrogenation and Rehydrogenation Properties of LiBH4 by Nanosized Ni Addition. *MATERIALS TRANSACTIONS*, 55(8), pp.1134–1137. Available at: https://www.jstage.jst.go.jp/article/matertrans/55/8/55_MG201407/_article.

Li, H.W. et al., 2011. Recent progress in metal borohydrides for hydrogen storage. *Energies*, 4(1), pp.185–214.

Li, Z.P. et al., 2003. Preparation of potassium borohydride by a mechano-chemical reaction of saline hydrides with dehydrated borate through ball milling. *Journal of Alloys and Compounds*, 354(1–2), pp.243–247. Available at: http://linkinghub.elsevier.com/retrieve/pii/S0925838802013464.

Liu, C. et al., 2010. Preparation and Characterization of Nanomaterials for Sustainable Energy Production. , 4(10), pp.5517–5526.

Liu, X. et al., 2010. Controlling the decomposition pathway of LiBH4 via confinement in highly ordered nanoporous carbon. *Journal of Physical Chemistry C*, 114(33), pp.14036–14041.

Liu, X. et al., 2011. Systematic pore-size effects of nanoconfinement of LiBH4: Elimination of diborane release and tunable behavior for hydrogen storage applications. *Chemistry of Materials*, 23(5), pp.1331–1336.

Liu, Y. et al., 2017. Study of the decomposition of a 0.62LiBH 4 –0.38NaBH 4 mixture. *International Journal of Hydrogen Energy*, 42(35), pp.22480–22488. Available at: http://linkinghub.elsevier.com/retrieve/pii/S0360319917311059.

Lototskyy, M. V. et al., 2014. Metal hydride hydrogen compressors: A review. *International Journal of Hydrogen Energy*, 39(11), pp.5818–5851. Available at: http://dx.doi.org/10.1016/j.ijhydene.2014.01.158.

Lototskyy, M. V. et al., 2017. The use of metal hydrides in fuel cell applications. *Progress in Natural Science: Materials International*, 27(1), pp.3–20. Available at: http://dx.doi.org/10.1016/j.pnsc.2017.01.008.

Lototskyy, M. & Yartys, V.A., 2015. Comparative analysis of the efficiencies of hydrogen storage systems utilising solid state H storage materials. *Journal of Alloys and Compounds*, 645, pp.S365–S373. Available at: http://linkinghub.elsevier.com/retrieve/pii/S0925838814029788.

Louër, D., 2017. Powder X-Ray Diffraction, Applications. In *Encyclopedia of Spectroscopy and Spectrometry*. Elsevier, pp. 723–731. Available at: http://linkinghub.elsevier.com/retrieve/pii/B9780128032244002570.

Luck, R.L. & Schelter, E.J., 1999. Potassium borohydride. *Acta Crystallographica Section C Crystal Structure Communications*, 55(12), p.IUC9900151. Available at: http://scripts.iucr.org/cgi-bin/paper?S010827019909842X.

Luo, W. et al., 2011. A single-component liquid-phase hydrogen storage material. *Journal of the American Chemical Society*, 133(48), pp.19326–19329.

Ma, Y. et al., 2016. Enhanced hydrogen storage properties of LiBH4 generated using a porous Li3BO3 catalyst. *Journal of Alloys and Compounds*, 689, pp.187–191. Available at: http://dx.doi.org/10.1016/j.jallcom.2016.07.313.

Mahato, N. et al., 2015. Progress in material selection for solid oxide fuel cell

technology: A review. *Progress in Materials Science*, 72, pp.141–337. Available at: http://dx.doi.org/10.1016/j.pmatsci.2015.01.001.

Manickam, K., Grant, D.M. & Walker, G.S., 2015. Optimization of AB2 type alloy composition with superior hydrogen storage properties for stationary applications. *International Journal of Hydrogen Energy*, 40(46), pp.16288–16296. Available at: http://linkinghub.elsevier.com/retrieve/pii/S0360319915024878.

Mao, J. et al., 2012. Hydrogen De-/absorption improvement of NaBH4 catalyzed by titanium-based additives. *Journal of Physical Chemistry C*, 116(1), pp.1596–1604.

Mao, J. et al., 2011. Improved hydrogen storage properties of NaBH4 destabilized by CaH2 and Ca(BH4)2. *Journal of Physical Chemistry C*, 115(18), pp.9283–9290.

Mao, J. & Gregory, D., 2015. Recent Advances in the Use of Sodium Borohydride as a Solid State Hydrogen Store. *Energies*, 8(1), pp.430–453. Available at: http://www.mdpi.com/1996-1073/8/1/430/.

Mao, J.F., Yu, X.B., et al., 2009. Enhanced hydrogen storage performances of NaBH4-MgH2 system. *Journal of Alloys and Compounds*, 479(1–2), pp.619–623.

Mao, J.F. et al., 2009. Improvement of the LiAlH4−NaBH4 System for Reversible Hydrogen Storage. *The Journal of Physical Chemistry C*, 113(24), pp.10813–10818. Available at: http://pubs.acs.org/doi/abs/10.1021/jp808269v.

Mao, J.F., Guo, Z.P., et al., 2009. Reversible hydrogen storage in titanium-catalyzed LiAlH4-LiBH4 system. *Journal of Alloys and Compounds*, 487(1–2), pp.434–438.

Marks, T.J. & Kolb, J.R., 1977. Covalent transition metal, lanthanide, and actinide tetrahydroborate complexes. *Chemical Reviews*, 77(2), pp.263–293. Available at: http://pubs.acs.org/doi/abs/10.1021/cr60306a004.

Martelli, P. et al., 2010. Stability and decomposition of NaBH4. *Journal of Physical Chemistry C*, 114(15), pp.7173–7177.

Matsuo, M. et al., 2007. Lithium superionic conduction in lithium borohydride accompanied by structural transition. *Applied Physics Letters*, 91(22), pp.1–4.

Mattuci, 2015. Vector diagram of PEM and PA FC operation. *Wikipedia*. Available at: https://en.wikipedia.org/wiki/Proton-exchange_membrane_fuel_cell#/media/File:Proton_Exchange_Fuel_Cell_Diagram.svg [Accessed March 24, 2018].

Mauron, P. et al., 2008. Stability and reversibility of LiBH4. *Journal of Physical Chemistry B*, 112(3), pp.906–910.

McDonald, W.S. & Cruickshank, D.W.J., 1967. A reinvestigation of the structure of sodium metasilicate, Na2SiO3. *Acta Crystallographica*, 22(1), pp.37–43. Available at: http://scripts.iucr.org/cgi-bin/paper?S0365110X67000076.

Meggouh, M. et al., 2015. Investigation of the dehydrogenation behavior of the 2LiBH4:CaNi5 multicomponent hydride system. *International Journal of Hydrogen Energy*, 40(7), pp.2989–2996. Available at: http://linkinghub.elsevier.com/retrieve/pii/S0360319914034351.

Miwa, K. et al., 2004. First-principles study on lithium borohydride LiBH4. *Physical Review B*, 69(24), p.245120. Available at: https://link.aps.org/doi/10.1103/PhysRevB.69.245120.

Mohr, S.H. et al., 2015. Projection of world fossil fuels by country. *Fuel*, 141, pp.120–135. Available at: http://dx.doi.org/10.1016/j.fuel.2014.10.030.

Mohring, R.M. & Luzader, R.E., 2001. A Sodium Borohydride On-board Hydrogen Generator for Powering Fuel Cell and Internal Combustion Engine Vehicles. *Papers Papers 19902002*, (724).

Moiseenko, V.N., Vdovin, A. V. & Dergachov, M.P., 2000. Raman scattering in lithium borate crystals. In V. S. Gorelik & A. D. Kudryavtseva, eds. p. 36. Available at: http://proceedings.spiedigitallibrary.org/proceeding.aspx?doi=10.1117/12.378133.

Mori, D. & Hirose, K., 2009. Recent challenges of hydrogen storage technologies for fuel cell vehicles. *International Journal of Hydrogen Energy*, 34(10), pp.4569–4574. Available at: http://dx.doi.org/10.1016/j.ijhydene.2008.07.115.

Mosegaard, L. et al., 2008. Reactivity of LiBH4: In Situ Synchrotron Radiation Powder

X-ray Diffraction Study. *Journal of Physical Chemistry C*, 112(4), pp.1299–1303. Available at: http://dx.doi.org/10.1021/jp076999v.

Muetterties, E.L. et al., 1962. Chemistry of Boranes. III. The Infrared and Raman Spectra of B12H12- and Related Anions. *Journal of the American Chemical Society*, 84(13), pp.2506–2508. Available at: http://pubs.acs.org/doi/abs/10.1021/ja00872a011.

Muetterties, E.L. et al., 1964. Chemistry of Boranes. VIII. Salts and Acids of B 10 H 10 -2 and B 12 12 -2. *Inorganic Chemistry*, 3(3), pp.444–451. Available at: http://pubs.acs.org/doi/abs/10.1021/ic50013a034%5Cnhttp://pubs.acs.org/doi/abs/10.1021/ic50013a030%5Cnhttp://pubs.acs.org/doi/abs/10.1021/ic50013a030.

Muir, S.S. & Yao, X., 2011. Progress in sodium borohydride as a hydrogen storage material: Development of hydrolysis catalysts and reaction systems. *International Journal of Hydrogen Energy*, 36(10), pp.5983–5997. Available at: http://dx.doi.org/10.1016/j.ijhydene.2011.02.032.

Nakamori, Y. et al., 2006. Correlation between thermodynamical stabilities of metal borohydrides and cation electronegativites: First-principles calculations and experiments. *Physical Review B - Condensed Matter and Materials Physics*, 74(4), p.45126.

Nakamori, Y. et al., 2007. Thermodynamical stabilities of metal-borohydrides. *Journal of Alloys and Compounds*, 446–447, pp.296–300.

Nakamori, Y. & Orimo, S.-I., 2004. Destabilization of Li-based complex hydrides. *Journal of Alloys and Compounds*, 370(1–2), pp.271–275.

Nale, A. et al., 2011. On the decomposition of the 0.6LiBH4-0.4Mg(BH4)2 eutectic mixture for hydrogen storage. *International Journal of Hydrogen Energy*, 36(21), pp.13676–13682.

National Renewable Energy Laboratory, 2007. *Go / No-Go Recommendation for Sodium Borohydride for On-Board Vehicular Hydrogen Storage*,

Netzsch, DSC 204 HP Phoenix® – High-pressure DSC. Available at:

https://www.netzsch-thermal-analysis.com/us/products-solutions/differential-scanning-calorimetry/dsc-204-hp-phoenix/ [Accessed November 1, 2017a].

Netzsch, STA 449 F3 Jupiter®. Available at: https://www.netzsch-thermal-analysis.com/en/products-solutions/simultaneous-thermogravimetry-differential-scanning-calorimetry/sta-449-f3-jupiter/ [Accessed November 1, 2017b].

Ngene, P., Adelhelm, P., et al., 2010. LiBH4 / SBA-15 Nanocomposites Prepared by Melt Infiltration under Hydrogen Pressure : Synthesis and Hydrogen Sorption Properties. *The Journal of Physical Chemistry C*, 114(13), pp.6163–6168.

Ngene, P., van den Berg, R., et al., 2011. Reversibility of the hydrogen desorption from NaBH4 by confinement in nanoporous carbon. *Energy & Environmental Science*, 4(10), p.4108.

Ngene, P., Verkuijlen, M.H.W., et al., 2011. The role of Ni in increasing the reversibility of the hydrogen release from nanoconfined LiBH4. *Faraday Discussions*, 151, p.47. Available at: http://xlink.rsc.org/?DOI=c0fd00028k.

Ngene, P., van Zwienen, M.R. & de Jongh, P.E., 2010. Reversibility of the hydrogen desorption from LiBH4: a synergetic effect of nanoconfinement and Ni addition. *Chemical communications (Cambridge, England)*, 46, pp.8201–8203.

Ni, M. et al., 2007. A review and recent developments in photocatalytic water-splitting using TiO2 for hydrogen production. *Renewable and Sustainable Energy Reviews*, 11(3), pp.401–425.

Niaz, S., Manzoor, T. & Pandith, A.H., 2015. Hydrogen storage: Materials, methods and perspectives. *Renewable and Sustainable Energy Reviews*, 50, pp.457–469.

Nickels, E.A., 2010. *Structural and Thermogravimetric Studies of Group I and II Borohydrides*. University of Oxford.

Nickels, E.A. et al., 2008. Tuning the Decomposition Temperature in Complex Hydrides: Synthesis of a Mixed Alkali Metal Borohydride. *Angewandte Chemie International Edition*, 47(15), pp.2817–2819. Available at: http://doi.wiley.com/10.1002/anie.200704949.

Nielsen, T.K., Besenbacher, F. & Jensen, T.R., 2011. Nanoconfined hydrides for energy storage. *Nanoscale*, 3(5), p.2086. Available at: http://xlink.rsc.org/?DOI=c0nr00725k.

Noritake, T. et al., 2002. Chemical bonding of hydrogen in MgH2. *Applied Physics Letters*, 81(11), pp.2008–2010. Available at: http://aip.scitation.org/doi/10.1063/1.1506007.

Nöth, H. & Wrackmeyer, B., 1978. *Nuclear Magnetic Resonance Spectroscopy of Boron Compounds* H. Nöth & B. Wrackmeyer, eds., Berlin, Heidelberg: Springer Berlin Heidelberg. Available at: http://link.springer.com/10.1007/978-3-642-66757-2.

Nunes, H.X. et al., 2016. Hydrogen generation and storage by aqueous sodium borohydride (NaBH4) hydrolysis for small portable fuel cells (H2–PEMFC). *International Journal of Hydrogen Energy*, 41(34), pp.15426–15432. Available at: http://dx.doi.org/10.1016/j.ijhydene.2016.06.173.

Nygård, M.M., 2016. *Calibration of the Sieverts apparatus at IFE*, Kjeller, Norway.

Nystrom, R.F., Chaikin, S.W. & Brown, W.G., 1949. Lithium Borohydride as a Reducing Agent. *Journal of the American Chemical Society*, 71(9), pp.3245–3246. Available at: http://pubs.acs.org/doi/abs/10.1021/ja01177a514.

O'Hayre, R. et al., 2017. *Fuel Cell Fundamentals* 3rd ed., Wiley.

Ohba, N. et al., 2006. First-principles study on the stability of intermediate compounds of LiBH4. *Physical Review B*, 74(7), p.75110. Available at: https://link.aps.org/doi/10.1103/PhysRevB.74.075110.

Olympus, 2007. Olympus Launches LEXT OLS3100 Confocal Laser Scanning Microscope Greater simplicity with higher precision. Available at: https://www.olympus-global.com/en/news/2007a/nr070125lext31e.html [Accessed November 1, 2017].

Opalka, S.M. et al., 2009. Experimental and theoretical screening of nanoscale oxide reactivity with LiBH4. *Nanotechnology*, 20, p.204024.

Orimo, S. et al., 2005. Dehydriding and rehydriding reactions of. *Journal of Alloys and Compounds*, 404–406, pp.427–430. Available at: http://linkinghub.elsevier.com/retrieve/pii/S0925838805009230.

Orimo, S.-I. et al., 2007. Complex hydrides for hydrogen storage. *Chemical reviews*, 107(10), pp.4111–4132.

Orimo, S., Nakamori, Y. & Züttel, A., 2004. Material properties of MBH4. *Materials Science and Engineering: B*, 108(1–2), pp.51–53. Available at: http://linkinghub.elsevier.com/retrieve/pii/S0921510703005403.

Orimo, S.I. et al., 2006. Experimental studies on intermediate compound of LiBH4. *Applied Physics Letters*, 89(2), p.21920.

Ott, K.C., 2010. *Final Report for the DOE Chemical Hydrogen Storage Center of Excellence*, Los Alamos. Available at: https://www.energy.gov/sites/prod/files/2014/03/f11/chemical_hydrogen_storage_coe_final_report.pdf.

Ozturk, Z. et al., 2015. Hydrogen storage in heat welded random CNT network structures. *International Journal of Hydrogen Energy*, 40(1), pp.403–411. Available at: http://dx.doi.org/10.1016/j.ijhydene.2014.10.148.

Parker, S.F., 2010. Spectroscopy and bonding in ternary metal hydride complexes-Potential hydrogen storage media. *Coordination Chemistry Reviews*, 254(3–4), pp.215–234.

Paskevicius, M. et al., 2013. Eutectic melting in metal borohydrides. *Physical Chemistry Chemical Physics*, 15(45), pp.19774–19789.

Paskevicius, M. et al., 2013. First-order phase transition in the Li2B12H12 system. *Physical Chemistry Chemical Physics*, 15(38), p.15825. Available at: http://xlink.rsc.org/?DOI=c3cp53090f.

Paskevicius, M. et al., 2017. Metal borohydrides and derivatives – synthesis, structure and properties. *Chem. Soc. Rev.*, 46(5), pp.1565–1634. Available at: http://xlink.rsc.org/?DOI=C6CS00705H.

Pauling, L., 1932. THE NATURE OF THE CHEMICAL BOND. IV. THE ENERGY OF SINGLE BONDS AND THE RELATIVE ELECTRONEGATIVITY OF ATOMS. *Journal of the American Chemical Society*, 54(9), pp.3570–3582. Available at: http://pubs.acs.org/doi/abs/10.1021/ja01348a011.

Pawley, J.B. ed., 2006. *Handbook Of Biological Confocal Microscopy*, Boston, MA: Springer US. Available at: http://link.springer.com/10.1007/978-0-387-45524-2.

Pei, Z. wei et al., 2017. NaNH2–NaBH4 hydrogen storage composite materials synthesized via liquid phase ball-milling: Influence of Co–Ni–B catalyst on the dehydrogenation performances. *International Journal of Hydrogen Energy*, 42(21), pp.14725–14733. Available at: http://dx.doi.org/10.1016/j.ijhydene.2017.04.124.

Peighambardoust, S.J., Rowshanzamir, S. & Amjadi, M., 2010. *Review of the proton exchange membranes for fuel cell applications*, Elsevier Ltd. Available at: http://dx.doi.org/10.1016/j.ijhydene.2010.05.017.

Pendolino, F. et al., 2009. Effect of Boron on the Activation Energy of the Decomposition of LiBH4. *Journal of Physical Chemistry C*, 113, pp.17231–17234.

Pendolino, F., 2013. Thermal study on decomposition of LiBH4 at non-isothermal and non-equilibrium conditions: Simultaneous evaluation of kinetic and thermodynamic parameters. *Journal of Thermal Analysis and Calorimetry*, 112(3), pp.1207–1211.

Peru, F. et al., 2013. Ammonia-free infiltration of NaBH4 into highly-ordered mesoporous silica and carbon matrices for hydrogen storage. *Journal of Alloys and Compounds*, 580(SUPPL1), pp.S309–S312. Available at: http://dx.doi.org/10.1016/j.jallcom.2013.02.141.

Pinkerton, F.E. et al., 2007. Phase boundaries and reversibility of LiBH4/MgH2 hydrogen storage material. *Journal of Physical Chemistry C*, 111(35), pp.12881–12885.

Pinkerton, F.E. & Meyer, M.S., 2008. Reversible hydrogen storage in the lithium borohydride-calcium hydride coupled system. *Journal of Alloys and Compounds*,

464(1–2), pp.4–7.

Pistidda, C. et al., 2014. Effect of NaH/MgB2 ratio on the hydrogen absorption kinetics of the system NaH + MgB2. *International Journal of Hydrogen Energy*, 39(10), pp.5030–5036.

Pitt, M.P. et al., 2013. Thermal stability of Li2B12H12 and its role in the decomposition of LiBH4. *Journal of the American Chemical Society*, 135(18), pp.6930–6941.

Price, T.E.C. et al., 2010. Enhanced kinetics for the LiBH4:MgH2 multi-component hydrogen storage system – The effects of stoichiometry and decomposition environment on cycling behaviour. *International Journal of Hydrogen Energy*, 35(9), pp.4154–4161. Available at: http://linkinghub.elsevier.com/retrieve/pii/S0360319910003642.

Price, T.E.C. et al., 2011. The Effect of H2 Partial Pressure on the Reaction Progression and Reversibility of Lithium-Containing Multicomponent Destabilized Hydrogen Storage Systems. *Journal of the American Chemical Society*, 133(34), pp.13534–13538. Available at: http://pubs.acs.org/doi/abs/10.1021/ja204381n.

Puszkiel, J.A. et al., 2017. Changing the dehydrogenation pathway of LiBH4–MgH4 via nanosized lithiated TiO 2. *Physical Chemistry Chemical Physics*, 19(11), pp.7455–7460. Available at: http://xlink.rsc.org/?DOI=C6CP08278E.

Racu, A.-M. et al., 2008. High-resolution Raman spectroscopy study of phonon modes in LiBH4 and LiBD4. *The journal of physical chemistry. A*, 112(40), pp.9716–9722.

Raman, C. V. & Krishnan, K.S., 1928. A New Type of Secondary Radiation. *Nature*, 121(3048), pp.501–502. Available at: http://www.nature.com/doifinder/10.1038/121501c0.

Ravnsbœk, D. et al., 2009. A series of mixed-metal borohydrides. *Angewandte Chemie - International Edition*, 48(36), pp.6659–6663.

Reed, D., 2010. *An investigation into the synthesis and characterisation of metal borohydrides for hydrogen storage*. Available at: http://etheses.bham.ac.uk/1008/.

Reed, D. & Book, D., 2009. In-situ Raman study of the thermal decomposition of LiBH4. *MRS Proceedings*, 1216.

Remhof, A. et al., 2012. Towards room temperature, direct, solvent free synthesis of tetraborohydrides. *Journal of Physics: Conference Series*, 340, p.12111. Available at: http://stacks.iop.org/1742-6596/340/i=1/a=012111?key=crossref.992e00ac7aebd1305cd8d1fbe46b994e.

Ren, J. et al., 2017. Current research trends and perspectives on materials-based hydrogen storage solutions: A critical review. *International Journal of Hydrogen Energy*, 42(1), pp.289–311. Available at: http://dx.doi.org/10.1016/j.ijhydene.2016.11.195.

Renaudin, G. et al., 2004. Structural and spectroscopic studies on the alkali borohydrides MBH4 (M = Na, K, Rb, Cs). *Journal of Alloys and Compounds*, 375(1–2), pp.98–106.

Renewable, O. of E.E.&, HYDROGEN STORAGE. Available at: http://energy.gov/eere/fuelcells/hydrogen-storage [Accessed October 10, 2016].

Renishaw, WiRE 4 Software for Raman Spectroscopy from Renishaw. Available at: http://www.renishaw.com/en/raman-software--9450 [Accessed November 1, 2017].

Retsch, 2017a. *Materials and Material Analyses*, Available at: https://www.retsch.com/dltmp/www/53e4b558-acc0-4661-9d7f-636500000000-b6c762a3fae3/material_analyses_of_grinding_tools_en_de.pdf.

Retsch, 2017b. Planetary Ball Mill PM 400. Available at: https://www.retsch.com/products/milling/ball-mills/planetary-ball-mill-pm-400/function-features/ [Accessed October 31, 2017].

Richet, P., Mysen, B. & Andrault, D., 1996. Melting and premelting of silicates: Raman spectroscopy and X-ray diffraction of Li2SiO3 and Na2SiO3. *Physics and chemistry of minerals*, 23(3), pp.157–172. Available at: http://www.springerlink.com/index/V22577W444003867.pdf.

Rietveld, H.M., 1969. A profile refinement method for nuclear and magnetic structures. *Journal of Applied Crystallography*, 2(2), pp.65–71. Available at: http://scripts.iucr.org/cgi-bin/paper?S0021889869006558.

Rietveld, H.M., 1967. Line profiles of neutron powder-diffraction peaks for structure refinement. *Acta Crystallographica*, 22(1), pp.151–152. Available at: http://scripts.iucr.org/cgi-bin/paper?S0365110X67000234.

Roedern, E. et al., 2015. Effect of Eutectic Melting, Reactive Hydride Composites, and Nanoconfinement on Decomposition and Reversibility of LiBH4-KBH4. *Journal of Physical Chemistry C*, 119(46), pp.25818–25825.

Roedern, E. et al., 2016. Solid state synthesis, structural characterization and ionic conductivity of bimetallic alkali-metal yttrium borohydrides MY(BH4)4 (M = Li and Na). *Journal of Materials Chemistry A: Materials for energy and sustainability*, 4, pp.8793–8802. Available at: http://dx.doi.org/10.1039/C6TA02761J.

Rosli, R.E. et al., 2017. A review of high-temperature proton exchange membrane fuel cell (HT-PEMFC) system. *International Journal of Hydrogen Energy*, 42(14), pp.9293–9314. Available at: http://linkinghub.elsevier.com/retrieve/pii/S0360319915313069.

Roszak, R. et al., 2016. Hydrogen storage by adsorption in porous materials: Is it possible? *Colloids and Surfaces A: Physicochemical and Engineering Aspects*, 496, pp.69–76. Available at: http://dx.doi.org/10.1016/j.colsurfa.2015.10.046.

Rude, L.H. et al., 2013. Hydrogen–fluorine exchange in NaBH4–NaBF4. *Physical Chemistry Chemical Physics*, 15(41), p.18185. Available at: http://xlink.rsc.org/?DOI=c3cp52815d.

Rude, L.H. et al., 2011. Tailoring properties of borohydrides for hydrogen storage: A review. *Physica Status Solidi (A) Applications and Materials Science*, 208(8), pp.1754–1773.

Rzepka, M., Lamp, P. & de la Casa-Lillo, M.A., 1998. Physisorption of Hydrogen on

Microporous Carbon and Carbon Nanotubes. *The Journal of Physical Chemistry B*, 102(52), pp.10894–10898. Available at: http://pubs.acs.org/doi/abs/10.1021/jp9829602.

Sadhasivam, T. et al., 2017. Dimensional effects of nanostructured Mg/MgH2 for hydrogen storage applications: A review. *Renewable and Sustainable Energy Reviews*, 72(November 2015), pp.523–534.

Sandrock, G., 1999. Panoramic overview of hydrogen storage alloys from a gas reaction point of view. *Journal of Alloys and Compounds*, 293, pp.877–888.

Sandrock, G. & Bowman, R.C., 2003. Gas-based hydride applications: Recent progress and future needs. *Journal of Alloys and Compounds*, 356–357, pp.794–799.

Sasaki, S., Fujino, K. & Takeuchi, Y., 1971. X-ray determination of electron-density distributions in oxides, Mg O, Mn O, Co O, and Ni O, and atomic scattering factors of their constituent atoms. *Proceedings of the Japan Academy*, 55, pp.43–48.

Scherrer, P., 1918. Bestimmung der Grösse und der inneren Struktur von Kolloidteilchen mittels Röntgenstrahlen. *Göttinger Nachrichten Gesell*, pp.98–100.

Schlapbach, L. & Züttel, a, 2001. Hydrogen-storage materials for mobile applications. *Nature*, 414(6861), pp.353–358.

Schlesinger, H.I., Brown, H.C., Abraham, B., et al., 1953. New Developments in the Chemistry of Diborane and the Borohydrides. I. General Summary 1. *Journal of the American Chemical Society*, 75(1), pp.186–190. Available at: http://pubs.acs.org/doi/abs/10.1021/ja01097a049.

Schlesinger, H.I., Brown, H.C., Hoekstra, H.R., et al., 1953. Reactions of Diborane with Alkali Metal Hydrides and Their Addition Compounds. New Syntheses of Borohydrides. Sodium and Potassium Borohydrides 1. *Journal of the American Chemical Society*, 75(1), pp.199–204. Available at: http://pubs.acs.org/doi/abs/10.1021/ja01097a053.

Schlesinger, H.I. & Brown, H.C., 1940. Metallo Borohydrides. III. Lithium

Borohydride. *Journal of the American Chemical Society*, 62(12), pp.3429–3435. Available at: http://pubs.acs.org/doi/abs/10.1021/ja01869a039.

Schlesinger, H.I., Brown, H.C. & Finholt, A.E., 1953. The Preparation of Sodium Borohydride by the High Temperature Reaction of Sodium Hydride with Borate Esters 1. *Journal of the American Chemical Society*, 75(1), pp.205–209. Available at: http://pubs.acs.org/doi/abs/10.1021/ja01097a054.

Schlesinger, H.I., Sanderson, R.T. & Burg, A.B., 1940. Metallo Borohydrides. I. Aluminum Borohydride. *Journal of the American Chemical Society*, 62(12), pp.3421–3425. Available at: http://pubs.acs.org/doi/abs/10.1021/ja01869a037.

Semenenko, K.N., Chavgun, A.P. & Surov, V.N., 1971. Interaction of sodium tetrahydroborate with potassium and lithium tetrahydroborate. *Russian Journal of Inorganic Chemistry*, 16, pp.271–273.

Sethio, D., Lawson Daku, L.M. & Hagemann, H., 2017. Computational study of the vibrational spectroscopy properties of boron-hydrogen compounds: Mg(B3H8)2 , CB9H10− and CB11H12−. *International Journal of Hydrogen Energy*, 42(35), pp.22496–22501. Available at: http://linkinghub.elsevier.com/retrieve/pii/S0360319917309254.

Shafiee, S. & Topal, E., 2009. When will fossil fuel reserves be diminished? *Energy Policy*, 37(1), pp.181–189.

Shao, J. et al., 2014. Low-Temperature reversible hydrogen storage properties of LiBH4: A synergetic effect of nanoconfinement and nanocatalysis. *Journal of Physical Chemistry C*, 118(21), pp.11252–11260.

Sheppard, D.A., Humphries, T.D. & Buckley, C.E., 2016. Sodium-based hydrides for thermal energy applications. *Applied Physics A: Materials Science and Processing*, 122(4), pp.1–13.

Shim, J.H. et al., 2010. Effect of hydrogen back pressure on dehydrogenation behavior of LiBH4-based reactive hydride composites. *Journal of Physical Chemistry Letters*, 1(1), pp.59–63.

Siegel, D.J., Wolverton, C. & Ozoliņš, V., 2007. Thermodynamic guidelines for the prediction of hydrogen storage reactions and their application to destabilized hydride mixtures. *Physical Review B - Condensed Matter and Materials Physics*, 76(13), pp.1–6.

Sigma Aldrich, 2018. Sigma Aldrich. Available at: https://www.sigmaaldrich.com/ [Accessed March 24, 2018].

Sivaev, I.B., 2017. Chemistry of closo- Dodecaborate Anion [B12H12]2- : A Review. , (July).

Smith, D.O., 1956. Development of a Vibrating‐Coil Magnetometer. *Review of Scientific Instruments*, 27(5), pp.261–268. Available at: http://aip.scitation.org/doi/10.1063/1.1715538.

Smith, E. & Dent, G., 2005. *Modern Raman Spectroscopy: A Practical Approach*, Chichester : J. Wiley.

Smith, M.B. & Bass, G.E., 1963. Heats and Free Energies of Formation of the Alkali Aluminum Hydrides and of Cesium Hydride. *Journal of Chemical & Engineering Data*, 8(3), pp.342–346. Available at: http://pubs.acs.org/doi/abs/10.1021/je60018a020.

Smith, R.I. et al., 1990. The structure of metastable lithium disilicate, Li2Si2O5. *Acta Crystallographica Section C Crystal Structure Communications*, 46(3), pp.363–365. Available at: http://scripts.iucr.org/cgi-bin/paper?S010827018900750X.

Soldate, A.M., 1947. Crystal Structure of Sodium Borohydride. *Journal of the American Chemical Society*, 69(5), pp.987–988. Available at: http://pubs.acs.org/doi/abs/10.1021/ja01197a002.

Soloveichik, G.L., 2007. Metal Borohydrides as Hydrogen Storage Materials. *Material Matters*, p.11. Available at: http://www.sigmaaldrich.com/technical-documents/articles/material-matters/metal-borohydrides.html [Accessed October 18, 2017].

Somer, M. et al., 2010. α- and β-Na2[BH4][NH2]: Two modifications of a complex

hydride in the system NaNH2–NaBH4; syntheses, crystal structures, thermal analyses, mass and vibrational spectra. *Journal of Alloys and Compounds*, 491(1–2), pp.98–105. Available at: http://linkinghub.elsevier.com/retrieve/pii/S0925838809022701.

Soule, D.E., Nezbeda, C.W. & Czanderna, A.W., 1964. High Sensitivity Faraday Susceptibility Apparatus. *Review of Scientific Instruments*, 35(11), pp.1504–1510. Available at: http://aip.scitation.org/doi/10.1063/1.1719194.

Soulié, J.-P. et al., 2002. Lithium borohydride LiBH4. *Journal of Alloys and Compounds*, 346(1–2), pp.200–205. Available at: http://linkinghub.elsevier.com/retrieve/pii/S0925838802005212.

Spencer, P.J., 2008. A brief history of CALPHAD. , 32, pp.1–8.

Stasinevich, D.S. & Egorenko, G.A., 1968. Thermographic investigation of alkali metal and magnesium tetrahydroborates at pressures up to 10atm. *Russian Journal of Inorganic Chemistry*, 13, pp.341–343.

Stavila, V. et al., 2010. Probing the structure , stability and hydrogen storage properties of calcium dodecahydro- closo -dodecaborate. *Journal of Solid State Chemistry*, 183(5), pp.1133–1140. Available at: http://dx.doi.org/10.1016/j.jssc.2010.03.026.

Stockmayer, W.H. & Stephenson, C.C., 1953. The Nature of the Gradual Transition in Sodium Borohydride. *The Journal of Chemical Physics*, 21(7), pp.1311–1312. Available at: http://aip.scitation.org/doi/10.1063/1.1699207.

Sundermeyer, W., 1965. Fused Salts and Their Use as Reaction Media. *Angewandte Chemie International Edition in English*, 4(3), pp.222–238. Available at: http://doi.wiley.com/10.1002/anie.196502221.

Suryanarayana, C., 2001. Mechanical alloying and milling. *Progress in Materials Science*, 46(1–2), pp.1–184. Available at: http://linkinghub.elsevier.com/retrieve/pii/S0079642599000109.

Suwarno et al., 2017. Confinement Effects for Lithium Borohydride: Comparing Silica and Carbon Scaffolds. *Journal of Physical Chemistry C*, 121(8), pp.4197–4205.

Swanson, D.K. & Prewitt, C.T., 1983. The crystal structure of K2 Si(VI) Si(IV)3 O9. *American Mineralogist*, 68, pp.581–585.

Takahashi, M. et al., 1989. Raman spectra of rapidly quenched Li4SiO4-Li2WO4 glasses. *Journal of Non-Crystalline Solids*, 107, pp.330–333.

Takeichi, N. et al., 2003. "Hybrid hydrogen storage vessel", a novel high-pressure hydrogen storage vessel combined with hydrogen storage material. *International Journal of Hydrogen Energy*, 28, pp.1121–1129. Available at: http://linkinghub.elsevier.com/retrieve/pii/S0360319902002161.

Tang, W.S., Unemoto, A., et al., 2015. Unparalleled lithium and sodium superionic conduction in solid electrolytes with large monovalent cage-like anions. *Energy & Environmental Science*, 8, pp.3637–3645. Available at: http://dx.doi.org/10.1039/C5EE02941D.

Tang, W.S., Udovic, T.J. & Stavila, V., 2015. Altering the structural properties of A2B12H12 compounds via cation and anion modifications. *Journal of Alloys and Compounds*, 12, pp.S200–S204. Available at: http://dx.doi.org/10.1016/j.jallcom.2015.01.061%5Cnhttp://linkinghub.elsevier.com/retrieve/pii/S0925838815001164.

Tegel, M. et al., 2017. An efficient hydrolysis of MgH2-based materials. *International Journal of Hydrogen Energy*, 42(4), pp.2167–2176.

Teprovich, J.A. et al., 2015. Bi-functional Li2B12H12 for energy storage and conversion applications: solid-state electrolyte and luminescent down-conversion dye. , pp.22853–22859.

Thermo-Calc Software, 1997. Thermo-Calc Software. Available at: http://www.thermocalc.com/.

Thermo Scientific, 2011. *Thermo Scientific ProLab Benchtop Gas Analysis Mass Spectrometer*, Available at: https://assets.thermofisher.com/TFS-Assets/LSG/Specification-Sheets/D01817~.pdf.

Thomas, K.M., 2007. Hydrogen adsorption and storage on porous materials. *Catalysis*

Today, 120(3–4 SPEC. ISS.), pp.389–398.

Tiritiris, I. & Schleid, T., 2003. Die Dodekahydro-closo-Dodekaborate M2[B12H12] der schweren Alkalimetalle (M+ = K+, Rb+, NH4+, Cs+) und ihre formalen Iodid-Addukte M3I[B12H12] (≡ MI · M2[B12H12]). *Zeitschrift für anorganische und allgemeine Chemie*, 629(78), pp.1390–1402. Available at: http://doi.wiley.com/10.1002/zaac.200300098.

Tuan, L., Nguyen, C.K. & Huan, T.D., 2014. First-principles prediction for the stability of LiK(BH 4) 2. , 1544(8), pp.1539–1544.

U.S. Department of Energy, 2017a. Hydrogen Delivery. *FUEL CELL TECHNOLOGIES OFFICE*.

U.S. Department of Energy, 2017b. Hydrogen Storage. Available at: https://energy.gov/eere/fuelcells/hydrogen-storage [Accessed October 2, 2017].

U.S. Department of Energy, 2017c. Technology Validation. *FUEL CELL TECHNOLOGIES OFFICE*. Available at: https://energy.gov/eere/fuelcells/technology-validation [Accessed October 29, 2017].

Umegaki, T. et al., 2009. Boron- and nitrogen-based chemical hydrogen storage materials. *International Journal of Hydrogen Energy*, 34(5), pp.2303–2311. Available at: http://dx.doi.org/10.1016/j.ijhydene.2009.01.002.

Unemoto, A., Matsuo, M. & Orimo, S.I., 2014. Complex hydrides for electrochemical energy storage. *Advanced Functional Materials*, 24(16), pp.2267–2279.

Uniteed Nations Framework Convention on Climate Change, 2015. The Paris Agreement. Available at: http://unfccc.int/paris_agreement/items/9485.php [Accessed October 29, 2017].

Urbanczyk, R. et al., 2016. Design and operation of an aluminium alloy tank using doped Na3AlH6 in kg scale for hydrogen storage. *Journal of Power Sources*, 324, pp.589–597. Available at: http://dx.doi.org/10.1016/j.jpowsour.2016.05.102.

Urgnani, J. et al., 2008. Hydrogen release from solid state NaBH4. *International Journal of Hydrogen Energy*, 33(12), pp.3111–3115.

Vajo, J.J., Skeith, S.L. & Mertens, F., 2005. Reversible storage of hydrogen in destabilized LiBH 4. *Journal of Physical Chemistry B*, 109(9), pp.3719–3722.

Varin, R.A. & Chiu, C., 2005. Structural stability of sodium borohydride (NaBH4) during controlled mechanical milling. *Journal of Alloys and Compounds*, 397(1–2), pp.276–281. Available at: http://linkinghub.elsevier.com/retrieve/pii/S0925838805000320.

Varley, J.B. et al., 2017. Understanding Ionic Conductivity Trends in Polyborane Solid Electrolytes from Ab Initio Molecular Dynamics.

Vetrano, J.B., 1971. Hydrides as neutron moderator and reflector materials. *Nuclear Engineering and Design*, 14(3), pp.390–412. Available at: http://linkinghub.elsevier.com/retrieve/pii/0029549370901597.

Vines, J.E., 2016. *The effect of carbon and silicon-based additives on the hydrogen storage properties of Lithium Borohydride*. University of Birmingham.

Vlasse, M. et al., 1986. The crystal structure of SiB6. *Journal of Solid State Chemistry*, 63(1), pp.31–45. Available at: http://linkinghub.elsevier.com/retrieve/pii/0022459686901490.

Voellenkle, H., Wittmann, A. & Nowotny, H.N., 1969. Die Kristallstruktur der Verbindung Li6(Si2O7). *Monatshefte fuer Chemie*, 100, pp.295–303.

Voronko, Y.K., Sobol, A.A. & Shukshin, V.E., 2013. Raman spectroscopy study of the phase transformations of LiB3O5 and Li2B4O7 during heating and melting. *Inorganic Materials*, 49(9), pp.923–929. Available at: http://link.springer.com/10.1134/S0020168513090203.

Walker, G. ed., 2008. *Solid-State Hydrogen Storage: Materials and Chemistry* 1st ed.,

Wallace, A.P., 2012. Sodium Silicide and the Development of the Portable Hydrogen Energy Market. In *Board of Investments (BOI)*. pp. 219–230. Available at:

http://ecst.ecsdl.org/cgi/doi/10.1149/1.4705498.

Wang, H. et al., 2016. Tuning kinetics and thermodynamics of hydrogen storage in light metal element based systems - A review of recent progress. *Journal of Alloys and Compounds*, 658, pp.280–300. Available at: http://dx.doi.org/10.1016/j.jallcom.2015.10.090.

Wang, J. et al., 2016. Effect of nano-sized Ce2S3 on reversible hydrogen storage properties of LiBH4. *International Journal of Hydrogen Energy*, 41(30), pp.13156–13162. Available at: http://dx.doi.org/10.1016/j.ijhydene.2016.06.061.

Wang, Y. & Wang, Y., 2017. Recent advances in additive-enhanced magnesium hydride for hydrogen storage. *Progress in Natural Science: Materials International*, 27(1), pp.41–49.

Wellen, R.M.R. & Canedo, E.L., 2014. On the Kissinger equation and the estimate of activation energies for non-isothermal cold crystallization of PET. , 40, pp.33–38.

Werthmann, R. & Hoppe, R., 1981. Ueber K2SiO3 - das erste Cyclotrisilicat eines Alkalimetalls - sowie Rb2SiO3, Cs2SiO3, Rb2GeO3 und Cs2GeO3. *Revue de Chimie Minerale*, 18, pp.593–607.

White, J.L. et al., 2016. Understanding and Mitigating the Effects of Stable Dodecahydro-closo-dodecaborate Intermediates on Hydrogen-Storage Reactions. *Journal of Physical Chemistry C*, 120(45), pp.25725–25731.

Wiles, D.B. & Young, R.A., 1981. A new computer program for Rietveld analysis of X-ray powder diffraction patterns. *Journal of Applied Crystallography*, 14(2), pp.149–151. Available at: http://scripts.iucr.org/cgi-bin/paper?S0021889881008996.

Wood, C.D. et al., 2007. Hydrogen storage in microporous hypercrosslinked organic polymer networks. *Chemistry of Materials*, 19(8), pp.2034–2048.

Wu, C. et al., 2012. Characterizations of composite NaNH2–NaBH4 hydrogen storage materials synthesized via ball milling. *International Journal of Hydrogen Energy*, 37(1), pp.889–893. Available at:

http://linkinghub.elsevier.com/retrieve/pii/S036031991100797X.

Wu, D.-H. et al., 2015. Structural evolution and electronic mechanism for KBH4 phase transition from first-principles calculations. *Chemical Physics Letters*, 620, pp.88–91. Available at: http://dx.doi.org/10.1016/j.cplett.2014.12.029.

Wu, H. et al., 2015. Structural behavior of Li2B10H10. *Journal of Physical Chemistry C*, 119(12), pp.6481–6487.

Wunderlich, J.A. & Lipscomb, W.N., 1960. Structure of B12H12−2 ion. *Journal of the American Chemical Society*, 82(16), pp.4427–4428.

Xia, G.L. et al., 2009. Enhanced hydrogen storage performance of LiBH4–Ni composite. *Journal of Alloys and Compounds*, 479(1–2), pp.545–548. Available at: http://linkinghub.elsevier.com/retrieve/pii/S0925838809000115.

Xiang, M. et al., 2017. Study on xLiBH4-NaBH4 (x = 1.6, 2.3, and 4) composites with enhanced lithium ionic conductivity. *Journal of Alloys and Compounds*, 729, pp.936–941. Available at: http://linkinghub.elsevier.com/retrieve/pii/S0925838817329924.

Xiong, G. et al., 1993. Infrared reflectance and Raman spectra of lithium triborate single crystal. *Journal of Raman Spectroscopy*, 24(11), pp.785–789. Available at: http://doi.wiley.com/10.1002/jrs.1250241111.

Xu, J. et al., 2013. Reversible hydrogen desorption from LiBH4 catalyzed by graphene supported Pt nanoparticles. *Dalton Transactions*, 42(36), p.12926. Available at: http://xlink.rsc.org/?DOI=c3dt50933h.

Xu, X. et al., 2017. Hydrogen storage behavior of LiBH4 improved by the confinement of hierarchical porous ZnO/ZnCo2O4 nanoparticles. *Journal of Power Sources*, 359, pp.134–141.

Yadav, M. & Xu, Q., 2012. Liquid-phase chemical hydrogen storage materials. *Energy & Environmental Science*, 5(12), p.9698. Available at: http://xlink.rsc.org/?DOI=c2ee22937d.

Yan, Y. et al., 2013. Controlling the Dehydrogenation Reaction toward Reversibility of the LiBH4–Ca(BH4)2 Eutectic System. *The Journal of Physical Chemistry C*, 117(17), pp.8878–8886. Available at: http://pubs.acs.org/doi/full/10.1021/jp401628g%5Cnhttp://pubs.acs.org/doi/abs/10.1021/jp401628g.

Yan, Y. et al., 2018. Direct Rehydrogenation of LiBH4 from H-Deficient Li2B12H12−x. *Crystals*, 8(3), p.131. Available at: http://www.mdpi.com/2073-4352/8/3/131.

Yan, Y. et al., 2012. Pressure and temperature dependence of the decomposition pathway of LiBH4. *Physical Chemistry Chemical Physics*, 14(18), pp.6514–6519.

Yan, Y., Rentsch, D., Battaglia, C., et al., 2017. Synthesis, stability and Li-ion mobility of nanoconfined Li2B12H12. *Dalton Trans.*, 46(37), pp.12434–12437. Available at: http://xlink.rsc.org/?DOI=C7DT02946B.

Yan, Y. et al., 2015. The role of MgB12H12 in the hydrogen desorption process of Mg(BH4)2. *Chem. Commun.*, 51(4), pp.700–702. Available at: http://www.ncbi.nlm.nih.gov/pubmed/25417944%5Cnhttp://xlink.rsc.org/?DOI=C4CC05266H.

Yan, Y., Rentsch, D. & Remhof, A., 2017. Controllable decomposition of Ca(BH4)2 for reversible hydrogen storage. *Physical Chemistry Chemical Physics*, 19(11), pp.7788–7792. Available at: http://xlink.rsc.org/?DOI=C7CP00448F.

Yang, C. & Ogden, J., 2007. Determining the lowest-cost hydrogen delivery mode. *International Journal of Hydrogen Energy*, 32(2), pp.268–286.

Yang, F.S. et al., 2010. Design of the metal hydride reactors - A review on the key technical issues. *International Journal of Hydrogen Energy*, 35(8), pp.3832–3840. Available at: http://dx.doi.org/10.1016/j.ijhydene.2010.01.053.

Yang, J. et al., 2010. High capacity hydrogenstorage materials: attributes for automotive applications and techniques for materials discovery. *Chem. Soc. Rev.*, 39(2), pp.656–675. Available at: http://xlink.rsc.org/?DOI=B802882F.

Yang, J., Sudik, A. & Wolverton, C., 2007. Destabilizing LiBH4 with a metal (M = Mg, Al, Ti, V, Cr, or Sc) or metal hydride (MH2 = MgH2, TiH2, or CaH 2). *Journal of Physical Chemistry C*, 111(51), pp.19134–19140.

Yang, Z., Xia, Y. & Mokaya, R., 2007. Enhanced hydrogen storage capacity of high surface area zeolite-like carbon materials. *Journal of the American Chemical Society*, 129(6), pp.1673–1679.

Yoshida, T. & Kojima, K., 2015. Toyota MIRAI Fuel Cell Vehicle and Progress Toward a Future Hydrogen Society. *Interface magazine*, 24(2), pp.45–49. Available at: http://inter.ecsdl.org/cgi/doi/10.1149/2.F03152if.

Young, K. hsiung & Nei, J., 2013. The current status of hydrogen storage alloy development for electrochemical applications. *Materials*, 6(10), pp.4574–4608.

Young, R.A. & Wiles, D.B., 1982. Profile shape functions in Rietveld refinements. *Journal of Applied Crystallography*, 15(4), pp.430–438. Available at: http://scripts.iucr.org/cgi-bin/paper?S002188988201231X.

Yu, X.B. et al., 2007. Improved hydrogen storage properties of LiBH4 destabilized by carbon. *Applied Physics Letters*, 90(3), pp.2005–2008.

Yu, X.B., Grant, D.M. & Walker, G.S., 2009. Dehydrogenation of LiBH 4 Destabilized with Various Oxides. , pp.17945–17949.

Yu, X.B., Granty, D.M. & Walker, G.S., 2008. Low-temperature dehydrogenation of LiBH4 through destabilization with TiO2. *Journal of Physical Chemistry C*, 112(29), pp.11059–11062.

Yuan, P.P., Liu, B.H. & Li, Z.P., 2011. A comparative study of LiBH4-based composites with metal hydrides and fluorides for hydrogen storage. *International Journal of Hydrogen Energy*, 36(23), pp.15266–15272. Available at: http://dx.doi.org/10.1016/j.ijhydene.2011.09.001.

Zachariasen, W.H., 1964. The crystal structure of lithium metaborate. *Acta Crystallographica*, 17(6), pp.749–751. Available at: http://scripts.iucr.org/cgi-bin/paper?S0365110X64001839.

Zavorotynska, O. et al., 2011. Vibrational properties of MBH4 and MBF4 crystals (M = Li, Na, K): A combined DFT, infrared, and Raman study. *Journal of Physical Chemistry C*, 115(38), pp.18890–18900.

Zeng, K. & Zhang, D., 2010. Recent progress in alkaline water electrolysis for hydrogen production and applications. *Progress in Energy and Combustion Science*, 36(3), pp.307–326. Available at: http://dx.doi.org/10.1016/j.pecs.2009.11.002.

Zhai, B. et al., 2016. Enhanced hydrogen desorption properties of LiBH4-Ca(BH4)2 by a synergetic effect of nanoconfinement and catalysis. *International Journal of Hydrogen Energy*, 41(39), pp.17462–17470. Available at: http://dx.doi.org/10.1016/j.ijhydene.2016.06.170.

Zhang, B.J. & Liu, B.H., 2010. Hydrogen desorption from LiBH4 destabilized by chlorides of transition metal Fe, Co, and Ni. *International Journal of Hydrogen Energy*, 35(14), pp.7288–7294. Available at: http://dx.doi.org/10.1016/j.ijhydene.2010.04.165.

Zhang, B.J., Liu, B.H. & Li, Z.P., 2011. Destabilization of LiBH4 by (Ce, La)(Cl, F)3 for hydrogen storage. *Journal of Alloys and Compounds*, 509(3), pp.751–757.

Zhang, J. et al., 2015. Superior destabilization effects of LiBH4 with the addition of nano-sized nickel ferrite NiFe2O4. *RSC Adv.*, 5(99), pp.81212–81219. Available at: http://xlink.rsc.org/?DOI=C5RA17893B.

Zhang, L. et al., 2014. Fast hydrogen release under moderate conditions from $NaBH_4$ destabilized by fluorographite. *RSC Adv.*, 4(5), pp.2550–2556. Available at: http://xlink.rsc.org/?DOI=C3RA45833D.

Zhang, Y. et al., 2008. Enhanced Hydrogen Storage Performance of LiBH4-SiO2-TiF3 Composite. *Society*, pp.4005–4010.

Zhang, Y. & Book, D., 2013. Hydrogen storage properties of ball-milled graphite with 0.5 wt% Fe. *International Journal of Energy Research*, 37(7), pp.720–725. Available at: http://doi.wiley.com/10.1002/er.1903.

Zhang, Z.G., Wang, H. & Zhu, M., 2011. Hydrogen release from sodium borohydrides

at low temperature by the addition of zinc fluoride. *International Journal of Hydrogen Energy*, 36(14), pp.8203–8208. Available at: http://dx.doi.org/10.1016/j.ijhydene.2011.04.070.

Zhao-Karger, Z. et al., 2013. Altered reaction pathways of eutectic LiBH4-Mg(BH4)2 by nanoconfinement. *Journal of Materials Chemistry A*, 1, p.3379. Available at: http://pubs.rsc.org/en/content/articlelanding/2013/ta/c2ta00542e%5Cnhttp://pubs.rsc.org/en/Content/ArticleLanding/2013/TA/c2ta00542e#!divAbstract%5Cnhttp://pubs.rsc.org/en/content/articlepdf/2013/ta/c2ta00542e%5Cnhttp://xlink.rsc.org/?DOI=c2ta00542e.

Zhao, Y. et al., 2014. A synergistic effect between nanoconfinement of carbon aerogels and catalysis of CoNiB nanoparticles on dehydrogenation of LiBH4. *International Journal of Hydrogen Energy*, 39(2), pp.917–926.

Zhu, M. et al., 2013. Thermodynamic tuning of mg-based hydrogen storage alloys: A review. *Materials*, 6(10), pp.4654–4674.

Zou, J. et al., 2012. Reversible hydrogen storage in a 3NaBH4/YF3 composite. *International Journal of Hydrogen Energy*, 37(22), pp.17118–17125. Available at: http://linkinghub.elsevier.com/retrieve/pii/S0360319912018502.

Züttel, A. et al., 2003. Hydrogen storage properties of LiBH4. *Journal of Alloys and Compounds*, 356–357, pp.515–520. Available at: http://linkinghub.elsevier.com/retrieve/pii/S0925838802012537.

Züttel, A. et al., 2003. LiBH4 a new hydrogen storage material. *Journal of Power Sources*, 118(1–2), pp.1–7. Available at: http://linkinghub.elsevier.com/retrieve/pii/S0378775303000545.

Züttel, A., 2003. Materials for hydrogen storage. *Materials Today*, 6(9), pp.24–33. Available at: http://www.sciencedirect.com/science/article/B6X1J-49BY31B-S/2/eb64f188c33a7538e402bb0fd7bce014.

Züttel, A., Borgschulte, A. & Orimo, S.I., 2007. Tetrahydroborates as new hydrogen storage materials. *Scripta Materialia*, 56(10), pp.823–828.

Züttel, A., Borgschulte, A. & Schlapbach, L. eds., 2008. *Hydrogen as a Future Energy Carrier* 1st ed., Wiley VCH.

LIST OF PUBLICATIONS

Publications

- **Yinzhe Liu**, Michael Heere, Luis Contreras Vasquez, Christos Paterakis, Magnus H. Sørby, Bjørn Hauback, David Book (2018) Dehydrogenation and rehydrogenation of a $0.62LiBH_4$-$0.38NaBH_4$ mixture with nano-sized Ni, *International Journal of Hydrogen Energy*, accepted
- **Yinzhe Liu**, Daniel Reed, Christos Paterakis, Luis Contreras Vasquez, Marcello Baricco, David Book (2017) Study of the decomposition of a $0.62LiBH_4$–$0.38NaBH_4$ mixture, *International Journal of Hydrogen Energy*, 42(35), 22480-22488
- Luis F. Contreras Vasquez, **Yinzhe Liu**, Christos Paterakis, Daniel Reed, David Book (2017) Hydrogen sorption properties of $Li_xNa_{1-x}MgH_3$ (x = 0, 0.2, 0.5 & 0.8), *International Journal of Hydrogen Energy*, 42(35), 22589-22597
- Christos Paterakis, Sheng Guo, Michael Heere, **Yinzhe Liu**, Luis F. Contreras, Magnus H. Sørby, Bjørn C. Hauback, Daniel Reed, David Book (2017) Study of the $NaBH_4$–NaBr system and the behaviour of its low temperature phase transition, *International Journal of Hydrogen Energy*, 42(35), 22538-22543

Oral Presentations (selected)

- **Yinzhe Liu**, Michael Heere, Daniel Reed, Magnus H. Sørby, Bjørn Hauback, David Book (2017) Study of the decomposition and rehydrogenation of a $0.62LiBH_4$-$0.38NaBH_4$ mixture with nano-sized Ni, *The European Materials Research Society (E-MRS) 2017 Fall Meeting*, Warsaw, Poland
- **Yinzhe Liu**, Daniel Reed, David Book (2017) Study of the Decomposition of a 0.62:0.38 Lithium and Sodium Borohydride Mixture with Nano-sized Ni, *11th Int. Symposium Hydrogen & Energy*, Hawaii, U.S.A
- **Yinzhe Liu**, Anna Wołczyk, Daniel Reed, Marcello Baricco, David Book (2016) Decomposition Mechanism of a Eutectic Lithium and Sodium Borohydride Mixture, *International Symposium on metal-Hydrogen Systems (MH2016)*, Interlaken, Switzerland

Poster Presentations

- **Yinzhe Liu,** Daniel Reed, David Book (2015) Raman studies on dehydrogenation processes in lithium borohydride, *Fuel Cell & Hydrogen Technical Conference (FCH2) 2015*, Birmingham, U.K.
- **Yinzhe Liu,** Daniel Reed, David Book (2015) Raman studies on dehydrogenation processes in lithium borohydride, *8th German-Japanese 8th International Symposium on Nanostructures (OZ-15)*, Kyoto, Japan